frontiers | Research Topics

Model-informed drug development and evidence-based translational pharmacology

Edited by
Yu-Wei Lin, S. Y. Amy Cheung, Songwen Tan, Weiguo Li, Chuanpin Chen, Amal Kaddoumi and Xiu-Li Guo

Published in
Frontiers in Pharmacology

ISSN 1664-8714
ISBN 978-2-83250-587-8
DOI 10.3389/978-2-83250-587-8

About Frontiers

Frontiers is more than just an open access publisher of scholarly articles: it is a pioneering approach to the world of academia, radically improving the way scholarly research is managed. The grand vision of Frontiers is a world where all people have an equal opportunity to seek, share and generate knowledge. Frontiers provides immediate and permanent online open access to all its publications, but this alone is not enough to realize our grand goals.

Frontiers journal series

The Frontiers journal series is a multi-tier and interdisciplinary set of open-access, online journals, promising a paradigm shift from the current review, selection and dissemination processes in academic publishing. All Frontiers journals are driven by researchers for researchers; therefore, they constitute a service to the scholarly community. At the same time, the *Frontiers journal series* operates on a revolutionary invention, the tiered publishing system, initially addressing specific communities of scholars, and gradually climbing up to broader public understanding, thus serving the interests of the lay society, too.

Dedication to quality

Each Frontiers article is a landmark of the highest quality, thanks to genuinely collaborative interactions between authors and review editors, who include some of the world's best academicians. Research must be certified by peers before entering a stream of knowledge that may eventually reach the public - and shape society; therefore, Frontiers only applies the most rigorous and unbiased reviews. Frontiers revolutionizes research publishing by freely delivering the most outstanding research, evaluated with no bias from both the academic and social point of view. By applying the most advanced information technologies, Frontiers is catapulting scholarly publishing into a new generation.

What are Frontiers Research Topics?

Frontiers Research Topics are very popular trademarks of the *Frontiers journals series*: they are collections of at least ten articles, all centered on a particular subject. With their unique mix of varied contributions from Original Research to Review Articles, Frontiers Research Topics unify the most influential researchers, the latest key findings and historical advances in a hot research area.

Find out more on how to host your own Frontiers Research Topic or contribute to one as an author by contacting the Frontiers editorial office: frontiersin.org/about/contact

Model-informed drug development and evidence-based translational pharmacology

Topic editors

Yu-Wei Lin — Monash University, Australia
S. Y. Amy Cheung — Certara, United States
Songwen Tan — Central South University, China
Weiguo Li — Harbin Institute of Technology, China
Chuanpin Chen — Central South University, China
Amal Kaddoumi — Auburn University, United States
Xiu-Li Guo — Shandong University, China

Topic coordinators

Yu Lin — Australian National University, Australia
Jinxin Zhao — Monash University, Australia
Fenglin Liu — Korea University of Technology and Education, Republic of Korea
Xiao Zhu — Fudan University, China

Citation

Lin, Y.-W., Cheung, S. Y. A., Tan, S., Li, W., Chen, C., Kaddoumi, A., Guo, X.-L., eds. (2023). *Model-informed drug development and evidence-based translational pharmacology*. Lausanne: Frontiers Media SA. doi: 10.3389/978-2-83250-587-8

Table of contents

frontiers | Frontiers in Pharmacology

TYPE Editorial
PUBLISHED 12 December 2022
DOI 10.3389/fphar.2022.1086551

OPEN ACCESS

EDITED AND REVIEWED BY
Alastair George Stewart,
The University of Melbourne, Australia

*CORRESPONDENCE
Songwen Tan,
stan0309@uni.sydney.edu.au
Chuanpin Chen,
ccpin2000@hotmail.com
Amal Kaddoumi,
kaddoumi@auburn.edu
Xiu-Li Guo,
guoxl@sdu.edu.cn
Yu-Wei Lin,
yu-wei.lin@monash.edu
S. Y. Amy Cheung,
amy.cheung@certara.com

†These authors have contributed equally to this work and share senior authorship

SPECIALTY SECTION
This article was submitted to Translational Pharmacology, a section of the journal Frontiers in Pharmacology

RECEIVED 01 November 2022
ACCEPTED 05 December 2022
PUBLISHED 12 December 2022

CITATION
Zhao J, Zhu X, Tan S, Chen C, Kaddoumi A, Guo X-L, Lin Y-W and Cheung SYA (2022), Editorial: Model-informed drug development and evidence-based translational pharmacology. *Front. Pharmacol.* 13:1086551. doi: 10.3389/fphar.2022.1086551

Editorial: Model-informed drug development and evidence-based translational pharmacology

Jinxin Zhao[1], Xiao Zhu[2], Songwen Tan[3*†], Chuanpin Chen[3*†], Amal Kaddoumi[4*†], Xiu-Li Guo[5*†], Yu-Wei Lin[1,6,7,8*†] and S. Y. Amy Cheung[8*†]

[1]Biomedicine Discovery Institute, Infection and Immunity Program and Department of Microbiology, Monash University, Melbourne, VIC, Australia, [2]Department of Clinical Pharmacy and Pharmacy Administration, School of Pharmacy, Fudan University, Shanghai, China, [3]Xiangya School of Pharmaceutical Sciences, Central South University, Changsha, China, [4]Department of Drug Discovery and Development, Harrison College of Pharmacy, Auburn University, Auburn, AL, United States, [5]Department of Pharmacology, School of Pharmaceutical Science, Shandong University, Jinan, China, [6]Malaya Translational and Clinical Pharmacometrics Group, Faculty of Pharmacy, University of Malaya, Kuala Lumpur, Malaysia, [7]Department of Clinical Pharmacy and Pharmacy Practice, Faculty of Pharmacy, University of Malaya, Kuala Lumpur, Malaysia, [8]Integrated Drug Development, Certara, NJ, United States

KEYWORDS

model informed drug development, pharmacometrics, artificial intelligence, machine learing, translational pharmacology

Editorial on the Research Topic
Model-informed drug development and evidence-based translational pharmacology

1 Introduction

Model-informed drug development (MIDD) is unarguably the cornerstone of pharmacological research in the 21st century (Marshall et al., 2016; Bi et al., 2019; Lesko, 2021; Rayner et al., 2021; Madabushi et al., 2022). It refers to the strategic creation and integration of mathematical models with throughout plan of execution (key questions, assumption, modelling approach and documentation) to facilitate the decision-making process in pharmaceutical research (Marshall et al., 2016; Madabushi et al., 2022). The applications of MIDD range from novel target identification, formulation design, non-clinical and clinical development and biopharmaceutical research to trial design and cost-effectiveness evaluations (Madabushi et al., 2022). MIDD is also increasingly used to evaluate causal links between drug physiochemical properties, disease/pathogen biology and patient physiology. This has facilitated an integrated approach for effective trial designs

and data-to-knowledge transformation while also helping narrow knowledge gaps and maximise the therapeutic potential of drug candidates (Wang et al., 2008; Lesko, 2021; Madabushi et al., 2022).

This multifaceted tool has revolutionised the scope of recent drug discovery and development efforts. Over the last decade, the application of MIDD methodologies has become a popular approach for drug development and applied pharmacotherapy projects in industry, academia and, more notably, in global regulatory agencies (e.g., FDA, EMA, ICH, PMDA and NMPA) (Sato et al., 2017; Li et al., 2019; Marshall et al., 2019; Madabushi et al., 2022). At least 90% of all US FDA-approved pharmacological agents have an MIDD-based research origin (Madabushi et al., 2022). Most recently, its applications have been crucial for rapid vaccine and treatment development against the COVID-19 pandemic (Xiong et al., 2022).

This research topic aims to bring together scientists from academia, industry, and regulatory authorities to discuss the most recent advancements in MIDD and their multidimensional role in drug discovery and development. This editorial seeks to discuss current research trends in the field of MIDD and translational pharmacology and share our perspective on the importance of MIDD in modern drug discovery and development.

2 Application of model-informed drug development (MIDD)

There is a long-standing history of applying MIDD to inform regulatory decisions at the FDA (Madabushi et al., 2022). In the early 90s, the utilities of MIDD were limited and focused only on product characterisation. The scope of MIDD applications rapidly expanded in the first decade of the 21st century. Since 2013, the FDA has published numerous regulatory guidelines on MIDD, which include characterising safety, guiding trial design, guiding dose selection and assisting effectiveness evaluation (Madabushi et al., 2022). The applications of MIDD are continuously evolving and, in the late 21st century, physiologically based pharmacokinetic (PBPK) modelling and simulations have become prevalent, in addition to classical pharmacometrics applications in modern drug development (Madabushi et al., 2022). In the modern era, the rise of novel mechanistic-based methodologies, such as quantitative systems pharmacology (QSP), is another significant development (Bradshaw et al., 2019).

3 Utilities of model-informed drug development (MIDD)

The rampant increase in MIDD-related publications over the last few years is a testament to the piqued interest in the scientific community. MIDD techniques enable the integration of data from clinical trials and non-clinical investigations in a drug development programme. Modelling techniques that are frequently employed include population pharmacokinetics (popPK) modelling, PBPK modelling and exposure-response modelling (Marshall et al., 2016; Keizer et al., 2018; Bi et al., 2019; Marshall et al., 2019; Darwich et al., 2021; Lesko, 2021; Madabushi et al., 2022). Currently, several stages in the development of new drugs have also made use of emerging modelling techniques, such as QSP modelling and artificial intelligence (AI)/machine learning (ML) (Madabushi et al., 2022). Drug development is complex, and a combination of different modelling approaches must often be utilised to adequately address questions that arise at various stages.

Pharmacometrics is the core of MIDD and is the science of developing mathematical models to quantitatively describe relationship exposure and response (Madabushi et al., 2022). In the absence of exposure, kinetic–pharmacodynamic (K-PD) models are used to predict the time course and magnitude of drug effects (Ooi et al., 2020). Kang et al. successfully demonstrated the utility of a K-PD model in describing the anticancer effect of BoNT/A1 in a syngeneic mouse model transplanted with melanoma cells (B16-F10). The developed K-PD model adequately captured the dynamics of tumour growth, and simulation studies were conducted to determine the optimal dose under various dosing scenarios.

Pharmacometrics is not only applicable to oncology but is also widely utilised in anti-infective programmes (Rayner et al., 2021). Mathematical modelling has been employed for the last decade to optimise dosing regimens for antibiotic therapy against multidrug-resistant ‘superbugs’ (Bulman et al., 2022; Yow et al.). These models include PopPK models, QSP, system-based models, and mechanism-based PK/PD models (Rayner et al., 2021). With antibiotics, inappropriate dosing may result in therapeutic failure or toxicities. Precision dosing, which customises doses to individual patients, is crucial for antibiotics, especially those with a narrow therapeutic index. Treatment response in individuals for antibiotics depends on three determinants: the patient, bacterium and antibiotic (Wicha et al., 2021). These factors determine the optimal dose of an antibiotic to maximise efficacy and minimise toxicity and the emergence of resistance. For some antibiotics, treatment responses vary greatly between individuals due to genotype, disease characteristics and patient population. Variability in individual responses to antibiotics demands precision dosing. The traditional ‘one dose fits all’ does not consider these variabilities; hence, therapy for patients may be suboptimal (Yow et al.). Particularly in the case of special populations, therapeutic drug monitoring (TDM) is often used to ensure that the exposure of the drug is optimal by comparing plasma concentration levels against a therapeutic range (Smith et al., 2021; Wicha et al., 2021). Based on this, recommendations are made that often involve dose adjustments to optimise outcomes. Several limitations are associated with the traditional TDM

approach—the most significant often relying on trough samples, which is a suboptimal surrogate of overall drug exposure (Wicha et al., 2021). Model-informed precision dosing (MIPD) utilises pharmacometrics principles to integrate various sources of information to streamline the TDM process and maximise therapeutic success (Keizer et al., 2018; Wicha et al., 2021; Bulman et al., 2022). In MIPD, the measured drug concentrations from TDM are used to derive the individual PK parameters that account for the interindividual differences using Bayesian estimation (Smith et al., 2021). These individual PK parameters are specific to the patient of interest and can be used to derive a personalised dosing regimen. Numerous techniques have been proposed for MIPD, including model-averaging (Uster et al., 2021) and hybrid ML/PK approach (Hughes and Keizer, 2021). In this reach topic, Yow et al. presented an excellent overview of various strategies for optimising antimicrobial therapy and the urgent need for implementation of MIPD for antibiotics in clinics.

Unlike the traditional pharmacometric models, which rely largely on available preclinical or clinical PK data and model structures that are selected based on statistical methods and biological plausibility grounds, QSP is a quantitative approach that incorporates mechanistic information of a biological system and drug mechanism to predict and define disease pathophysiology and therapeutic interventions (Sorger et al., 2011; Bradshaw et al., 2019; Helmlinger et al., 2019; Azer et al., 2021; Aghamiri et al., 2022). QSP models can be utilised throughout various stages of drug development (Bradshaw et al., 2019). In the early drug discovery stage, QSP models can be used to identify novel targets. QSP models can be applied in the translational stage to bridge non-clinical to clinical work and are subsequently used to study the source of variability in response in the clinical development stage. Rieger et al. implemented a novel QSP model of human hepatocyte lipid metabolism and demonstrated the suitability of the model in generating a virtual population that closely resembles patients with non-alcoholic fatty liver disease. The treatment intervention was also validated by simulating pioglitazone and diet intervention in the virtual population. As outlined by the authors, the benefits of the QSP model lie in its size and speed, which enables the simulations of large virtual patient populations for hypothesis testing to respond to critical drug development questions in a timely manner (Rieger et al.). Currently, QSP modelling to inform key decisions in drug development is still evolving, and only a handful of successful examples are available in the literature (Sorger et al., 2011; Bradshaw et al., 2019; Helmlinger et al., 2019; Aghamiri et al., 2022). As QSP continues to evolve, the acceptability of QSP for external and internal decision making will undoubtedly increase.

Lastly, the use of AI and ML has been increasing in the pharmaceutical industry to overcome the high failure rate in drug development (Zhang et al., 2017; Koromina et al., 2019; Saikin et al., 2019; Liu et al., 2020; Talevi et al., 2020; Gupta et al., 2021; Kashyap and Siddiqi, 2021). As such, the industry is beginning to explore and implement various AI and ML frameworks to supplement or be integrated into current drug discovery and development processes (Liu et al., 2020; Talevi et al., 2020). Yu et al. developed and demonstrated the utility of a supervised machine learning model to categorise and examine the magnetic resonance imaging features of brain tumours. Implementation of AI/MI in drug discovery and development will assist with the interpretation of clinical data and can standardise results across labs, thereby reducing biases and human errors (Zhang et al., 2017; Koromina et al., 2019; Saikin et al., 2019; Liu et al., 2020; Talevi et al., 2020; Gupta et al., 2021; Kashyap and Siddiqi, 2021). The future prospect of the utility of AI/MI in drug discovery and development remains unclear. There is an urgent need to bring together scientists from academia, industry, and regulatory authorities to outline critical research priorities and work towards best practices with respect to the use of AI/MI and to resolve any regulatory hurdles associated with the use of AI/MI in drug development. The development of standards for AI/MI and the implementation of best practices will undoubtedly boost confidence in the community in adopting AI/MI to facilitate and aid drug discovery and development (Liu et al., 2020).

4 Conclusion

MIDD has developed into an effective method to aid modern drug discovery and development. It plays a critical role in regulatory decision making and is gaining more acceptance in the community. Incorporating and leveraging newer techniques, such as MI/AI, are on the rise and will undoubtedly reshape drug development in the long term.

Author contributions

All authors listed have made a substantial, direct, and intellectual contribution to the work and approved it for publication.

Acknowledgments

We thank George Frimpong Boafo and Marlene Davis Ekpo for the assistance of manuscript outline preparation.

Conflict of interest

The authors declare that the research was conducted in the absence of any commercial or financial relationships that could be construed as a potential conflict of interest.

Publisher's note

References

Aghamiri, S. S., Amin, R., and Helikar, T. (2022). Recent applications of quantitative systems pharmacology and machine learning models across diseases. *J. Pharmacokinet. Pharmacodyn.* 49, 19–37. doi:10.1007/s10928-021-09790-9

Azer, K., Kaddi, C. D., Barrett, J. S., Bai, J. P. F., Mcquade, S. T., Merrill, N. J., et al. (2021). History and future perspectives on the discipline of quantitative systems pharmacology modeling and its applications. *Front. Physiol.* 12, 637999. doi:10.3389/fphys.2021.637999

Bi, Y., Liu, J., Li, L., Yu, J., Bhattaram, A., Bewernitz, M., et al. (2019). Role of model-informed drug development in pediatric drug development, regulatory evaluation, and labeling. *J. Clin. Pharmacol.* 59 (1), S104-S111–s111. Suppl. doi:10.1002/jcph.1478

Bradshaw, E. L., Spilker, M. E., Zang, R., Bansal, L., He, H., Jones, R. D. O., et al. (2019). Applications of quantitative systems pharmacology in model-informed drug discovery: Perspective on impact and opportunities. *CPT. Pharmacometrics Syst. Pharmacol.* 8, 777–791. doi:10.1002/psp4.12463

Bulman, Z. P., Wicha, S. G., Nielsen, E. I., Lenhard, J. R., Nation, R. L., Theuretzbacher, U., et al. (2022). Research priorities towards precision antibiotic therapy to improve patient care. *Lancet. Microbe* 3, e795–e802. doi:10.1016/S2666-5247(22)00121-5

Darwich, A. S., Polasek, T. M., Aronson, J. K., Ogungbenro, K., Wright, D. F. B., Achour, B., et al. (2021). Model-informed precision dosing: Background, requirements, validation, implementation, and forward trajectory of individualizing drug therapy. *Annu. Rev. Pharmacol. Toxicol.* 61, 225–245. doi:10.1146/annurev-pharmtox-033020-113257

Gupta, R., Srivastava, D., Sahu, M., Tiwari, S., Ambasta, R. K., and Kumar, P. (2021). Artificial intelligence to deep learning: Machine intelligence approach for drug discovery. *Mol. Divers.* 25, 1315–1360. doi:10.1007/s11030-021-10217-3

Helmlinger, G., Sokolov, V., Peskov, K., Hallow, K. M., Kosinsky, Y., Voronova, V., et al. (2019). Quantitative systems pharmacology: An exemplar model-building workflow with applications in cardiovascular, metabolic, and oncology drug development. *CPT. Pharmacometrics Syst. Pharmacol.* 8, 380–395. doi:10.1002/psp4.12426

Hughes, J. H., and Keizer, R. J. (2021). A hybrid machine learning/pharmacokinetic approach outperforms maximum a posteriori Bayesian estimation by selectively flattening model priors. *CPT. Pharmacometrics Syst. Pharmacol.* 10, 1150–1160. doi:10.1002/psp4.12684

Kashyap, K., and Siddiqi, M. I. (2021). Recent trends in artificial intelligence-driven identification and development of anti-neurodegenerative therapeutic agents. *Mol. Divers.* 25, 1517–1539. doi:10.1007/s11030-021-10274-8

Keizer, R. J., Ter Heine, R., Frymoyer, A., Lesko, L. J., Mangat, R., and Goswami, S. (2018). Model-informed precision dosing at the bedside: Scientific challenges and opportunities. *CPT. Pharmacometrics Syst. Pharmacol.* 7, 785–787. doi:10.1002/psp4.12353

Koromina, M., Pandi, M. T., and Patrinos, G. P. (2019). Rethinking drug repositioning and development with artificial intelligence, machine learning, and omics. *Omics* 23, 539–548. doi:10.1089/omi.2019.0151

Lesko, L. J. (2021). Perspective on model-informed drug development. *CPT. Pharmacometrics Syst. Pharmacol.* 10, 1127–1129. doi:10.1002/psp4.12699

Li, L., Han, H., Wang, J., Wei, C., Wang, Y., Li, M., et al. (2019). Model informed drug development and regulation in China: Challenges and opportunities. *CPT. Pharmacometrics Syst. Pharmacol.* 8, 59–61. doi:10.1002/psp4.12368

Liu, Q., Zhu, H., Liu, C., Jean, D., Huang, S. M., Elzarrad, M. K., et al. (2020). Application of machine learning in drug development and regulation: Current status and future potential. *Clin. Pharmacol. Ther.* 107, 726–729. doi:10.1002/cpt.1771

Madabushi, R., Seo, P., Zhao, L., Tegenge, M., and Zhu, H. (2022). Review: Role of model-informed drug development approaches in the lifecycle of drug development and regulatory decision-making. *Pharm. Res.* 39, 1669–1680. doi:10.1007/s11095-022-03288-w

Marshall, S. F., Burghaus, R., Cosson, V., Cheung, S. Y., Chenel, M., Dellapasqua, O., et al. (2016). Good practices in model-informed drug discovery and development: Practice, application, and documentation. *CPT. Pharmacometrics Syst. Pharmacol.* 5, 93–122. doi:10.1002/psp4.12049

Marshall, S., Madabushi, R., Manolis, E., Krudys, K., Staab, A., Dykstra, K., et al. (2019). Model-informed drug discovery and development: Current industry good practice and regulatory expectations and future perspectives. *CPT. Pharmacometrics Syst. Pharmacol.* 8, 87–96. doi:10.1002/psp4.12372

Ooi, Q. X., Hasegawa, C., Duffull, S. B., and Wright, D. F. B. (2020). Kinetic-pharmacodynamic model for drugs with non-linear elimination: Parameterisation matters. *Br. J. Clin. Pharmacol.* 86, 196–198. doi:10.1111/bcp.14154

Rayner, C. R., Smith, P. F., Andes, D., Andrews, K., Derendorf, H., Friberg, L. E., et al. (2021). Model-informed drug development for anti-infectives: State of the art and future. *Clin. Pharmacol. Ther.* 109, 867–891. doi:10.1002/cpt.2198

Saikin, S. K., Kreisbeck, C., Sheberla, D., Becker, J. S., and Aspuru-Guzik, A. (2019). Closed-loop discovery platform integration is needed for artificial intelligence to make an impact in drug discovery. *Expert Opin. Drug Discov.* 14, 1–4. doi:10.1080/17460441.2019.1546690

Sato, M., Ochiai, Y., Kijima, S., Nagai, N., Ando, Y., Shikano, M., et al. (2017). Quantitative modeling and simulation in PMDA: A Japanese regulatory perspective. *CPT. Pharmacometrics Syst. Pharmacol.* 6, 413–415. doi:10.1002/psp4.12203

Smith, N. M., Chan, A., Wilkinson, L. A., Chua, H. C., Nguyen, T. D., De Souza, H., et al. (2021). Open-source maximum a posteriori-bayesian dosing AdDS to current therapeutic drug monitoring: Adapting to the era of individualized therapy. *Pharmacotherapy* 41, 953–963. doi:10.1002/phar.2631

Sorger, P. K., Allerheiligen, S. R., Abernethy, D. R., Altman, R. B., Brouwer, K. L., Califano, A., et al. (2011). Quantitative and systems pharmacology in the post-genomic era: New approaches to discovering drugs and understanding therapeutic mechanisms, *An NIH white paper by the QSP workshop group*. Bethesda, MD, USA: NIH, 1–47.

Talevi, A., Morales, J. F., Hather, G., Podichetty, J. T., Kim, S., Bloomingdale, P. C., et al. (2020). Machine learning in drug discovery and development Part 1: A primer. *CPT. Pharmacometrics Syst. Pharmacol.* 9, 129–142. doi:10.1002/psp4.12491

Uster, D. W., Stocker, S. L., Carland, J. E., Brett, J., Marriott, D. J. E., Day, R. O., et al. (2021). A model averaging/selection approach improves the predictive performance of model-informed precision dosing: Vancomycin as a case study. *Clin. Pharmacol. Ther.* 109, 175–183. doi:10.1002/cpt.2065

Wang, Y., Bhattaram, A. V., Jadhav, P. R., Lesko, L. J., Madabushi, R., Powell, J. R., et al. (2008). Leveraging prior quantitative knowledge to guide drug development decisions and regulatory science recommendations: Impact of FDA pharmacometrics during 2004-2006. *J. Clin. Pharmacol.* 48, 146–156. doi:10.1177/0091270007311111

Wicha, S. G., Märtson, A.-G., Nielsen, E. I., Koch, B. C. P., Friberg, L. E., Alffenaar, J.-W., et al., and The International Society of Anti-Infective Pharmacology, and The PK/PD study group of the European Society of Clinical Microbiology, and Infectious Diseases (2021). From therapeutic drug monitoring to model-informed precision dosing for antibiotics. *Clin. Pharmacol. Ther.* 109, 928–941. doi:10.1002/cpt.2202

Xiong, Y., Fan, J., Kitabi, E., Zhang, X., Bi, Y., Grimstein, M., et al. (2022). Model-informed drug development approaches to assist new drug development in the COVID-19 pandemic. *Clin. Pharmacol. Ther.* 111, 572–578. doi:10.1002/cpt.2491

Zhang, L., Tan, J., Han, D., and Zhu, H. (2017). From machine learning to deep learning: Progress in machine intelligence for rational drug discovery. *Drug Discov. Today* 22, 1680–1685. doi:10.1016/j.drudis.2017.08.010

frontiers in Pharmacology

ORIGINAL RESEARCH
published: 15 December 2021
doi: 10.3389/fphar.2021.808144

Mechanism of Hedyotis Diffusa in the Treatment of Cervical Cancer

Kai Qian[1,2†], Dan Fu[2†], Baorui Jiang[2], Yue Wang[2], Fei Tian[2], Li Song[2] and Lei Li[1,2]*

[1]Department of Cardiology, Institute of Cardiovascular Development and Translational Medicine, The Second Affiliated Hospital of Wenzhou Medical University, Wenzhou, China, [2]Medical College of YiChun University, Yichun, China

Cervical cancer is one of the most common malignant tumors among women in the world. In clinical practice, Hedyotis diffusa has pharmacological effects in treating cervical cancer, but its components are relatively complex, and the mechanism of Hedyotis diffusa in treating cervical cancer is still unclear. In this work, the potential active components and mechanism of Hedyotis diffusa in the treatment of cervical cancer were explored by means of network pharmacology. By constructing its active ingredient-target network, and enriching and analyzing the targets, we found the key targets and their effective components (beta-Sitosterol and Quercetin) that play a therapeutic role. Finally, we evaluated the prognostic value of the core target genes through survival analysis. Our work initially explored the therapeutic mechanism of cervical cancer, which lays a theoretical foundation for further exploring its pharmacological action and its clinical application.

Keywords: hedyotis diffusa, component, cervical cancer, mechanism, network pharmacology

OPEN ACCESS

Edited by:
Songwen Tan,
Central South University, China

Reviewed by:
Yan Zhang,
Hunan Normal University, China
Guoxiang Tong,
Changsha Medical University, China

****Correspondence:***
Lei Li
lileiii@hotmail.com

†These authors have contributed equally to this work

Specialty section:
This article was submitted to Translational Pharmacology, a section of the journal Frontiers in Pharmacology

Received: *03 November 2021*
Accepted: *15 November 2021*
Published: *15 December 2021*

Citation:
Qian K, Fu D, Jiang B, Wang Y, Tian F, Song L and Li L (2021) Mechanism of Hedyotis Diffusa in the Treatment of Cervical Cancer. Front. Pharmacol. 12:808144. doi: 10.3389/fphar.2021.808144

INTRODUCTION

Cervical cancer is the fourth most common female malignant tumor and the most common cause of cancer death in the world (Bray et al., 2018). About half a million women develop cervical cancer every year and about 300,000 people die from the disease every year (Cohen et al., 2019). The incidence and mortality rates of cervical cancer in developed countries are much lower than those in developing countries, which is mainly due to the lack of screening and prevention programs for cervical cancer in many developing countries (Denny, 2012). Cervical cancer is considered as the only one which is known cause and can be preventable among human cancers. Although we know that the high-risk subtype of human papillomavirus (HPV) is the main cause of cervical cancer, the incidence and mortality of cervical cancer have not been significantly reduced (Walboomers et al., 1999). Cervical cancer patients are mainly treated by surgery, radiotherapy and chemotherapy. And novel immunotherapy, such as antibody targeted therapy and adoptive cell therapy, has unsatisfactory efficacy (Dyer et al., 2019). Surgical resection of tumors is mainly applied to early-stage patients, but most patients diagnosed with cervical cancer are generally advanced and lose the best treatment time, so chemotherapy and radiotherapy are the main treatment methods (Li et al., 2016). However, most chemotherapeutic drugs have severe toxic and side effects and long-term use will result in drug resistance, which seriously affect the efficacy. By contrast, Chinese medicinal active ingredients have the advantages of multiple pathways, multiple targets and small adverse reactions in the anti-tumor aspect, and may be more suitable for clinical treatment of cancer patients (Nie et al., 2016). Hedyotis diffusa is panicum miliaceum of Rubiaceae, widely distributed in subtropical regions (Li et al., 2013), and it is a famous traditional Chinese medicine for the treatment of inflammation-related diseases such as hepatitis and appendicitis in China (Chen et al., 2016).

Herba hedyotidis diffusae has various pharmacological activity, such as anticancer activity (Liu et al., 2010), antioxidant activity (Lu et al., 2000),immunomodulatory effect (Lin CC. et al., 2011) and anti-inflammatory activity (Ye et al., 2015),etc. At present, more and more clinical researches prove that the oldenlandia diffusa has remarkable anticancer activity (Gupta et al., 2004). Qiao Yan Cai et al. studied the molecular mechanism of Hedyotis diffusa in the treatment of colon cancer, and the results showed that Hedyotis diffusa exerts the curative effect mainly by regulating the expression of several important genes in the Signal Transducer and Activator of Transcription 3 signaling pathway. Hedyotis diffusa can inhibit the phosphorylation of Signal Transducer and Activator of Prescription 3, thereby promoting the apoptosis of tumor cells and inhibiting the proliferation of tumor cells to achieve the curative effect of treating colon cancer (Cai et al., 2012). Studies have shown that one of the mechanisms of Hedyotis diffusa's participation in tumor treatment is to inhibit tumor angiogenesis (Lin J. et al., 2011). As for the mechanism of treating cervical cancer,proto-oncogene c-Sre is a member of Sre-familykinases, which is a kind of non-receptor protein tyrosine kinase and plays an important role in regulating cell growth, development, differentiation and other biological functions. Studies have shown that proto-oncogene c-Sre can induce malignant transformation of cells. Studies have found that down-regulating the activity of c-Sre kinase can effectively inhibit the proliferation of cervical cancer cells (Kong et al., 2011). However, due to the complex components of Hedyotis diffusa, the mechanism for its treatment of most cancers including cervical cancer is not clear. Network pharmacology was first proposed by the British pharmacologist Hopkins in 2007. It is a new subject based on system biology theory and multi-directional pharmacology theory, which integrates information network science and computer science. And it has the overall and systematic research characteristics (Hopkins, 2008). Network pharmacology can be used to analyze biological system networks, predict and infer the correlation between targets and networks, and then construct a "drug-target-disease" interaction network, which can comprehensively and systematically clarify the intervention and influence of drugs on diseases (Zhang et al., 2014). In this study, with the help of network pharmacology, the effective active compounds of Hedyotis diffusa for treating cervical cancer were systematically screened out, and the pharmacological effects of Hedyotis diffusa for treating cervical cancer with multiple targets, multiple pathways and multiple mechanisms were preliminarily revealed.

METHODS

Collection of Effective Components and Targets

In TCMSP (http://tcmspw.com/tcmsp.php) database, the chemical components of Herba Hedyotis were collected by retrieving the key word "Herba Hedyotis" and taking oral bioavailability greater than or equal to 30% and drug-like property of 0.18 as screening conditions, the ineffective components were removed. Finally, target information corresponding to the active components is collected through HERB (http://herb.ac.cn/) database and the network of component targets is visualized by Cytoscape.

Acquisition of Cervical Cancer-Related Targets

By searching the keyword "cervical cancer" in GeneCards database (https://www.genecards.org/), we collected 7,110 related targets. Finally, we used Venn diagram to display the disease targets and drug component action targets, and got 175 common targets.

Functional Enrichment Analysis

Functional enrichment analysis included the GO functional enrichment analysis and KEGG pathway analysis. The GO functional enrichment analysis mainly included three parts: biological process (BP), molecular function (MF), cellular component (CC). Pathway enrichment analysis and GO enrichment analysis were performed using DAVID database to obtain the results of the top 20 FDR rankings, respectively, and the enrichment results were visualized using BioFormatics (www.bioinformatics.com.cn).

Construction of Protein Interaction Network and Extraction of Core Targets

Import the intersection targets into STRING database and build PPI network. Then, using cytoHubba in Cytoscape to extract the top ten targets in PPI network by MCC algorithm, and then performing pathway enrichment analysis on the extracted core targets.

Prognostic Information of Core Targets

KaplanMeie-plotter is a popular website tool based on EGA, TCGA and GEO databases, which is used to evaluate the survival of gene pairs. The prognosis of 10 core targets in cervical cancer was obtained by GEPIA2 (gepia2. cancer-pku.cn), and the targets with p value less than or equal to 0.05 were selected.

RESULTS

Related Targets of Hedyotis Diffusa in the Treatment of Cervical Cancer

We screened 7,110 cervical cancer-related targets from Gene Cards database. Six components of Hedyotis diffusa and its 203 action targets were collected through TCMSP database and HERB database, among which there were 175 cervical cancer-related targets (**Figure 1**). Here, we show the interaction between components and targets in the form of network, as shown in **Figure 1**. Red squares represent drug components, and circles represent component action targets, among which orange targets represent cervical cancer-related targets and green circles represent non-cervical cancer-related targets. It can be seen that most of the targets in the whole target network are related to cervical cancer, suggesting that Hedyotis diffusa has certain pertinence in the treatment of cervical cancer.

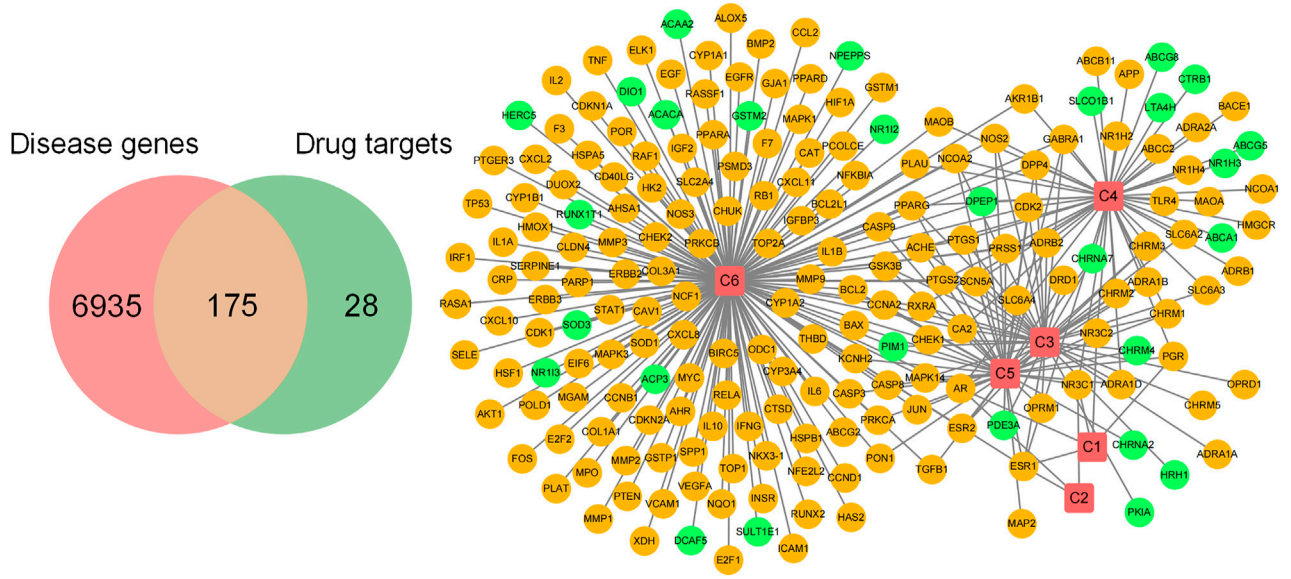

FIGURE 1 | Screening of therapeutic targets and construction of its component-target network.

Functional Enrichment Analysis of Therapeutic Targets for Cervical Cancer

GO function enrichment and KEGG pathway enrichment of the above 175 common targets were analyzed by DAVID database (https://david.ncifcrf.gov/home.jsp) (**Figure 2**). GO analysis includes biological processes (BP), cellular components (CC) and molecular functions (MF), which together describe the functions of gene products.

As shown in **Figure 2**, the pathway enrichment analysis of Hedyotis diffusa in treating cervical cancer mainly involves Pathways in cancer, Hepatitis B, Bladder cancer, Prostate cancer, Pancreatic cancer, TNF signaling pathway, HIF-1 signaling pathway, Non-small cell lung cancer, Chagas disease (American trypanosomiasis), Leishmaniasis and so on. GO analysis mainly involves response to drug, positive regulation of transcription from RNA polymerase II promoter, positive regulation of transcription, DNA-templated, positive regulation of gene expression, extracellular space, membrane raft, cell surface, nucleoplasm, enzyme binding, protein binding, transcription factor binding, etc.

Enrichment analysis showed that Hedyotis diffusa may act on multiple targets through various signal pathways and play a role in the treatment of cervical cancer. At the same time, it also provides reference value for further searching for key core targets and compounds.

Construction of Protein-Protein Interaction Network and Analysis of its Core Targets

We introduced the screened 175 common target genes into STRING, and set the minimum confidence level to 0.4. PPI network was constructed by the algorithm of STRING database, and the relationship between protein was visualized in the form of network. As shown in **Figure 3**, the network graph has 175 nodes and 3,424 edges, and the average node degree is 39.1, and the *p* value is less than 1.0e-16. Nodes represent target proteins, and each line represents the interaction between target proteins. The thickness of the connecting line represents.

In addition, cytoHubba was used for topology analysis of PPI networks, and the top ten core targets were extracted, which were successively AKT1, VEGFA, TNF, IL6, PTGS2, JUN, IL1B, CASP3, MAPK3, and MMP9(**Figure 4**). Later, we further enriched the pathways for the core targets, with the following results: TNF signaling pathway, Hepatitis B, Pertussis, Pathways in cancer, Chagas disease (American trypanosomiasis), etc. We found that the first-ranked pathways not only had the most significant statistical significance, but also involved more core targets. In addition, this pathway also appeared in our previous enrichment results of the entire PPI network, and it was ranked high, suggesting that Hedyotis diffusa may play an important role by mediating multiple pathways in the treatment of cervical cancer, and TNF signaling pathway may play a key role in the entire treatment network.

Prognostic Analysis of Core Targets and Construction of Component Target Network

In order to further determine the role of the core target in the network, we analyzed the overall survival of the core target by using GEPIA2. As shown in **Figure 5**, the results show that four of the 10 core targets have prognostic value in cervical cancer, namely VEGFA, IL1B, IL6, and JUN. The prognosis of all these targets is poor (HR = 1.7), and the low expression in cervical cancer has a good overall survival time. It also suggests that the components interacting with these targets may play the role of small molecule inhibitors, thus mediating the development of cervical cancer.

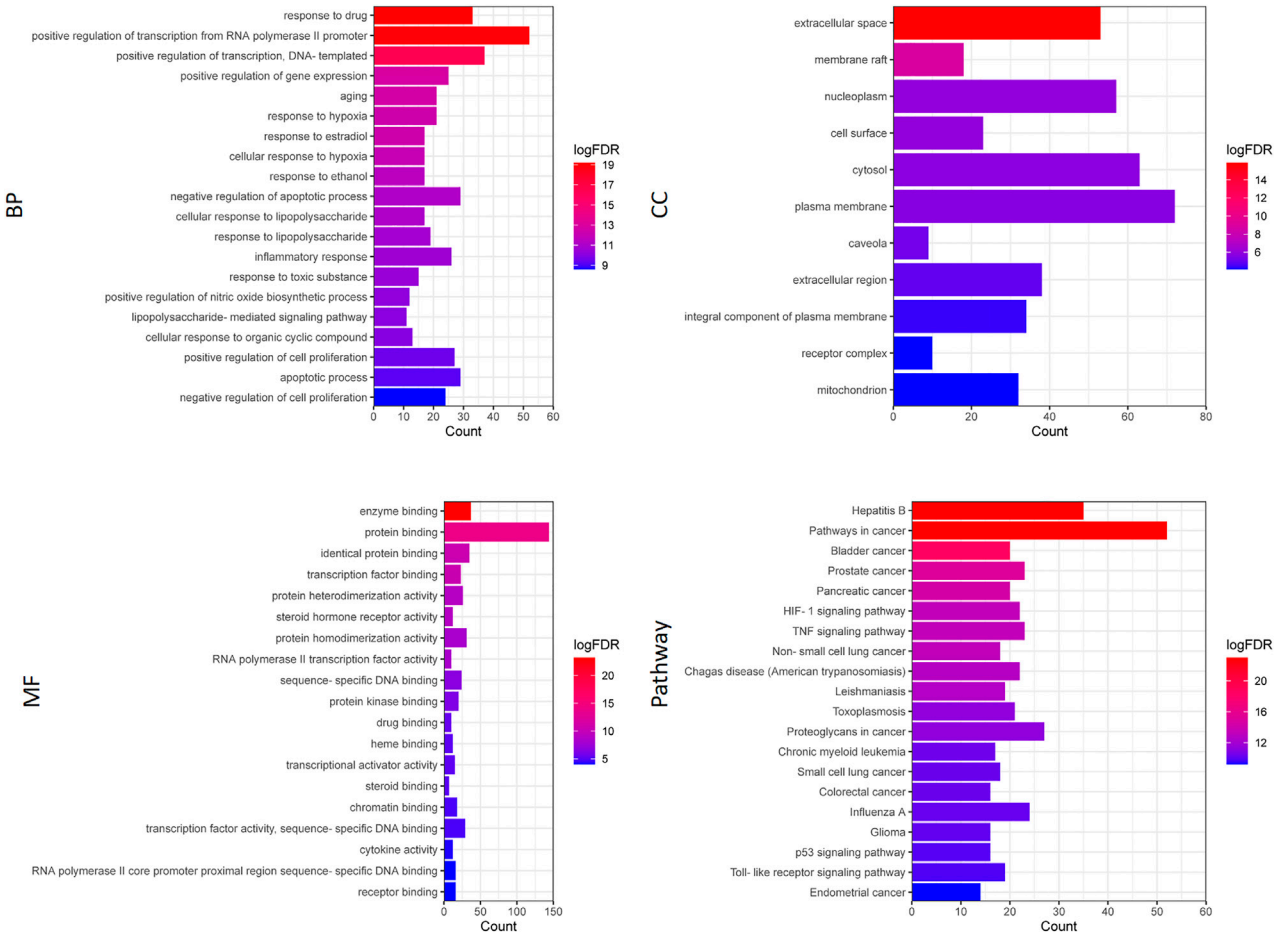

FIGURE 2 | KEGG pathway analysis and GO enrichment analysis.

In addition, we also constructed the core target-related component network (**Figure 6**). Only four components (C3, C4, C5, C6) were found to act on the core targets, among which C5(beta-Sitosterol) and C6(Quercetin) acted on the targets with poor prognosis. In addition, whether in the previous component-target network (**Figure 1**), or in the core target component network (**Figure 6**). Compared with other components, both C5 and C6 have larger degree value and more targets, suggesting that these two components play a leading role in the whole network. The above analysis results show that various active ingredients contained in Hedyotis diffusa interfere with the progress of cervical cancer by acting on its target network to mediate various pathways, thus exerting curative effects. Among them, beta-Sitosterol and Quercetin may play a key role, and the analysis results need further verification by subsequent experiments.

DISCUSSION

Cervical cancer is a common gynecological malignant tumor, with the mortality rate second only to that of ovarian cancer, and it is one of the malignant tumors threatening the health of women. Western medicine currently mainly adopts radiotherapy, chemotherapy and surgery, while radiotherapy and chemotherapy tolerance has become one of the main causes for the treatment failure, cancer metastasis and recurrence of cervical cancer (Vänskä et al., 2021). In recent years, Chinese medicine has been widely used in clinical due to its advantages of multi-channel, multi-target and small adverse reactions. Modern studies have shown that Hedyotis diffusa has the effects of anti-tumor, anti-oxidation, anti-inflammation and enhance the body's non-specific immune function. Hedyotis diffusa is often used to treat various tumors in clinic, especially gynecological tumors like cervical cancer, and has obtained good clinical efficacy. However its mechanism of action in the treatment of cervical cancer has not yet been elucidated. Based on the multi-component, multi-target, multi-channel research ideas, this work elucidated the potential mechanism of Hedyotis diffusa in the treatment of cervical cancer from the microscopic point of view by means of network pharmacology. In this study, six important active components related to cervical cancer were screened from Hedyotis diffusa Willd, which correspond to 175 targets of cervical cancer. The six important active ingredients in

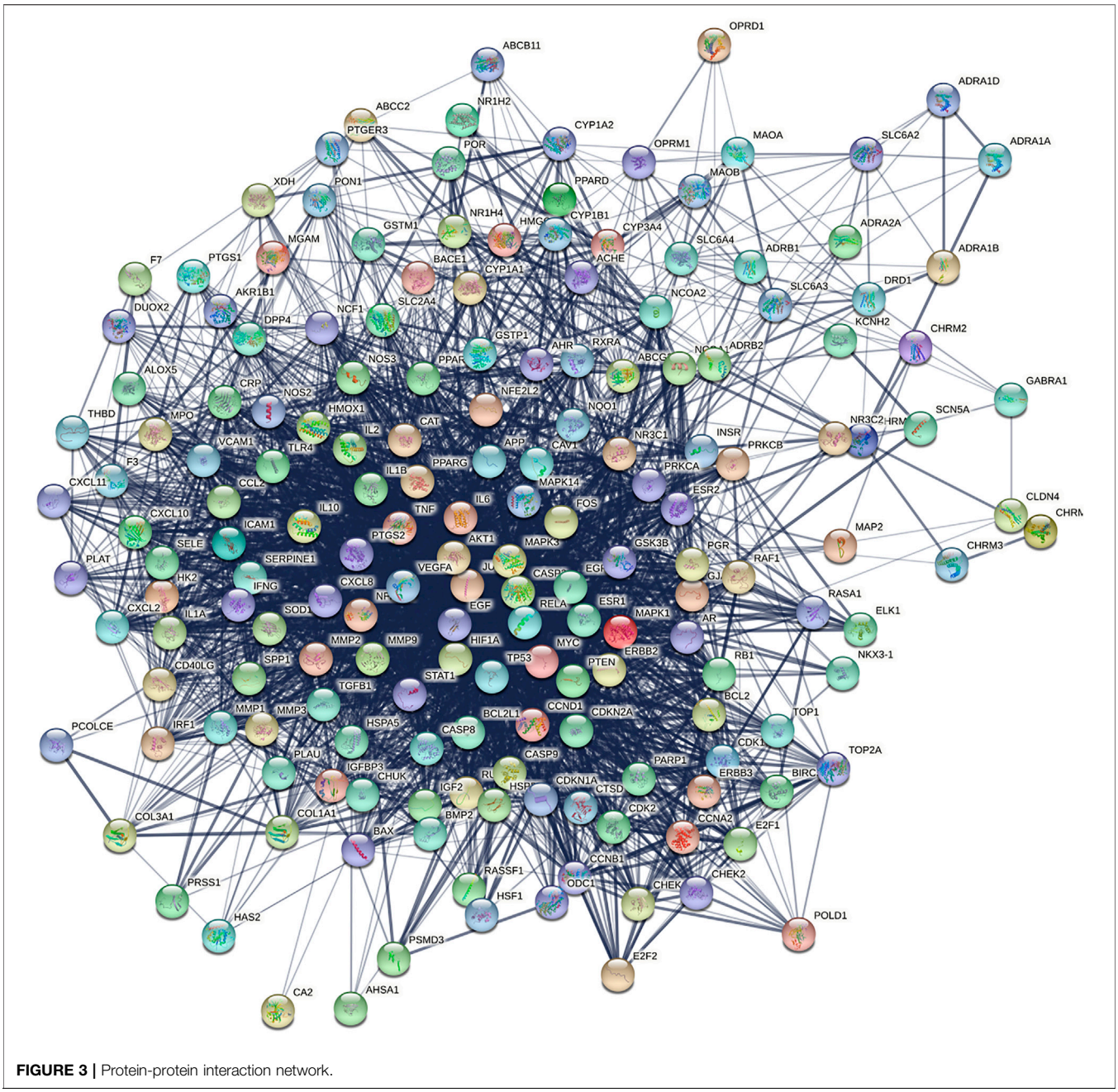

FIGURE 3 | Protein-protein interaction network.

Hedyotis diffusa for treating cervical cancer were beta-Sitosterol,Quercetin, Poriferasterol,Stigmasterol, 2-methoxy-3-methyl-9,10-anthraquinone and (4aS,6aR,6aS,6bR,8aR,10R,12aR,14bS)-10-hydroxy-2,2,6a,6b,9,9,12a-heptamethyl-1,3,4,5,6,6a,7,8,8a,10,11,12,13,14b-tetradecahydropicene-4a-carboxylic acid, of which the first two components played a more important role in the treatment of cervical cancer than other components. Quercetin is a kind of flavonoid, which widely exists in many fruits and vegetables in nature, and has many pharmacological activities such as anti-tumor, anti-virus, anti-inflammation, anti-oxidation and so on (Gibellini et al., 2011). Madhumitha Kedhari Sundaram et al. studied the mechanism of quercetin in the treatment of cervical cancer through relevant experiments. The results showed that quercetin could induce DNA damage, reduce the activity of cancer cells, and promote the apoptosis of cancer cells by promoting G2-M cell cycle arrest. In addition, quercetin can also block PI3K and other signaling pathways and inhibit the activity of anti-apoptotic proteins to promote cancer cell apoptosis (Darband et al., 2020). Related studies have shown that beta-Sitosterol has curative effect on a variety of cancers, such as cervical cancer, breast cancer, colon cancer, prostate cancer, and so on (Choudhary and Tran, 2011). Studies by Dali Cheng et al. have shown that beta-Sitosterol can inhibit the proliferation of cervical cancer cells and promote the apoptosis of cervical cancer

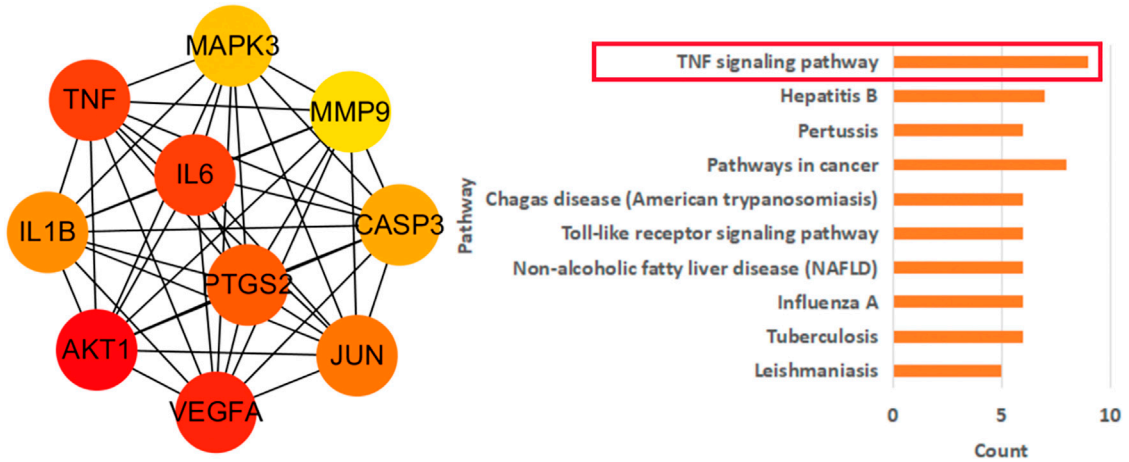

FIGURE 4 | Core target network and its pathway analysis.

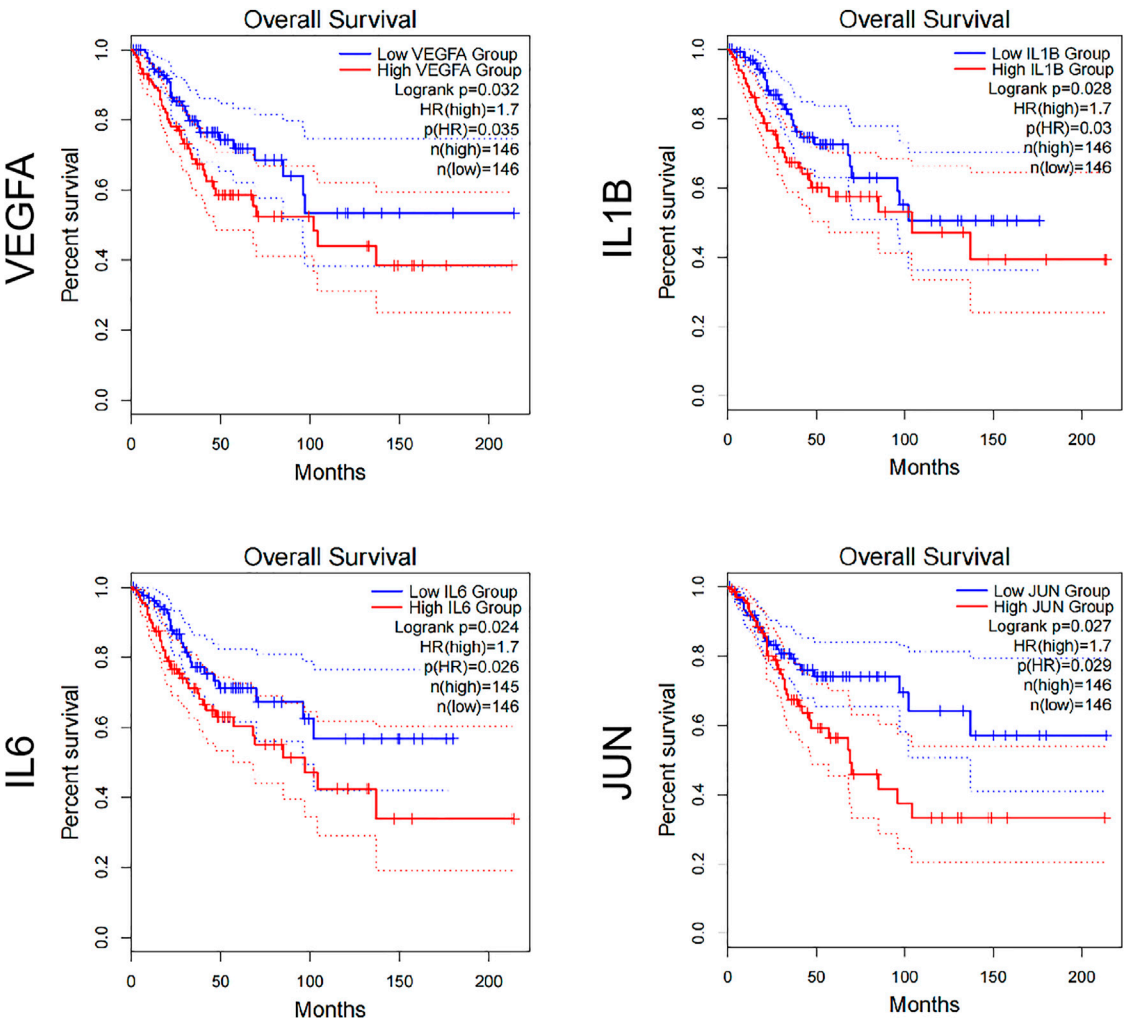

FIGURE 5 | Overall survival of core target.

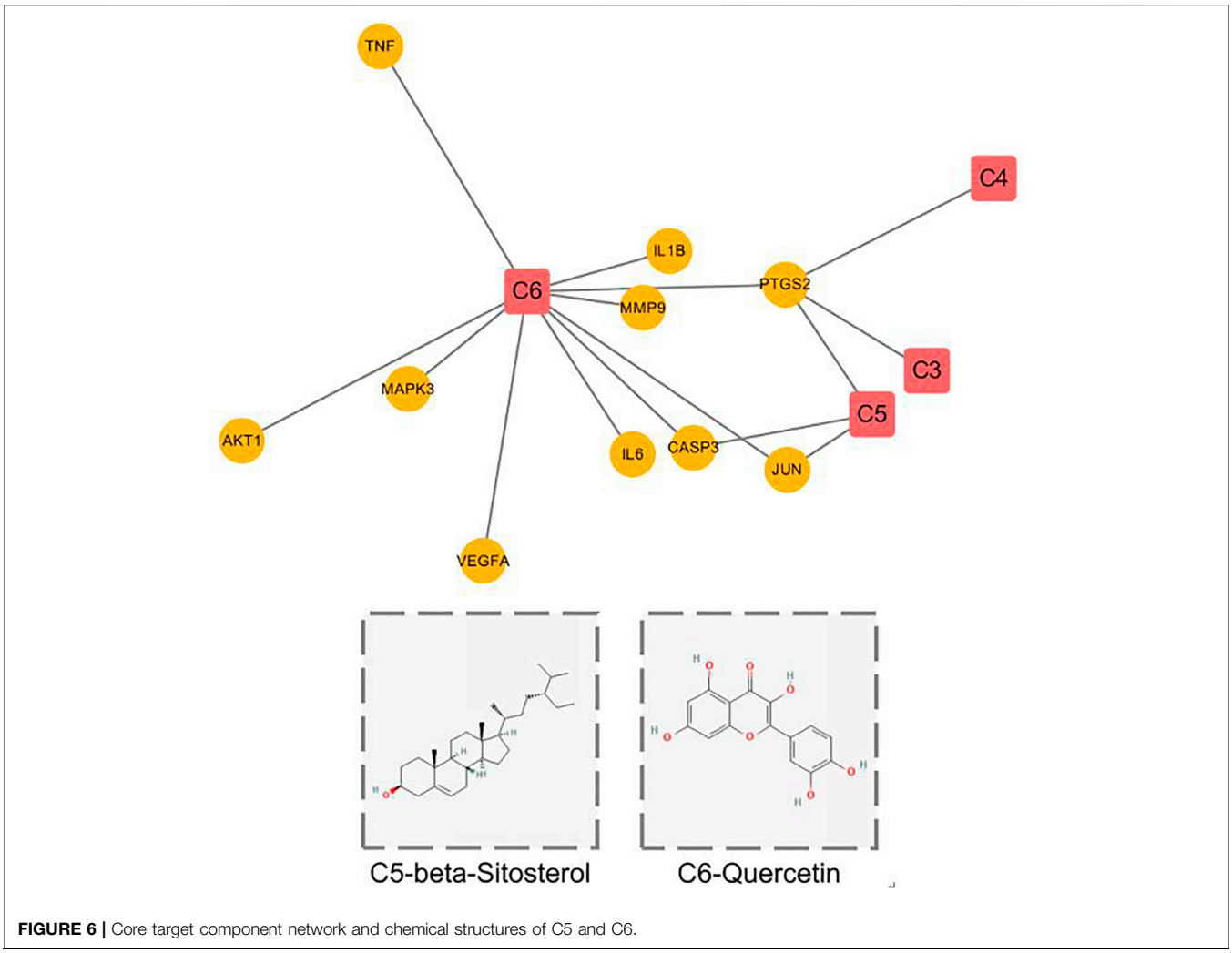

FIGURE 6 | Core target component network and chemical structures of C5 and C6.

cells. which is mainly related to the expression of P53 and HPVE six proteins (Cheng et al., 2015). The core targets of Hedyotis diffusa in treating cervical cancer mainly included AKT1, VEGFA, TNF, IL6, PTGS2, JUN, IL1B, CASP3, MAPK3, and MMP9. In addition, by analyzing the survival prognosis of the core targets, we found that the four genes with poor prognosis were namely VEGFA, IL1B, IL6 and JUN. VEGFA, as a member of VEGF family, is the most potential signaling protein to promote angiogenesis (Bagri et al., 2010). Baohuan Chen et al. found that VEGFA may inhibit the proliferation and metastasis of cervical cancer cells through Akt/mTor/PI3k signaling pathway (Chen et al., 2014). IL6, a multifunctional cytokine, plays an important role in regulating the growth of tumor cells (Kishimoto, 1989). Lin-Hung Wei et al. showed that IL-6 can regulate the expression of apoptosis protein Mcl-1 in cervical cancer cells and promote the occurrence of cervical cancer (Wei et al., 2001). Recent studies have shown that mi R-125 can inhibit the progression of cervical cancer by inhibiting the VEGF and PI3K-Akt signaling pathways (Fu et al., 2020). IL1B, a pro-inflammatory cytokine, is related to tumorigenesis. Studies have shown that the level of IL1B in plasma of patients with cervical cancer was significantly higher than that of the control group, and the expression level of IL1B played an important role in the carcinogenesis of cervical cancer (Qian et al., 2010). In order to further verify our screening results, we selected C6- quercetin, an important active compound in the treatment of cervical cancer by Hedyotis diffusa, for molecular docking with the core targets IL1B and IL6 which have prognostic value for cervical cancer respectively. Generally, when the binding energy is less than 0, the compound and protein can spontaneously combine, and the lower the binding energy, the greater the possibility of interaction between the compound and protein. Docking score ≤ -5.0 kJmol−1 indicates that it has good binding activity. The molecular docking results are shown in **Figure 7**, IL1B-quercetin (−8.2) and IL6-quercetin (−7.1). The results show that the core component C6- quercetin predicted in this study has strong binding ability with key targets (IL1B and IL6) and the binding ability of C6- quercetin with target IL1B is stronger, which further confirms the reliability of the prediction results of network pharmacology. The main signal pathways involved

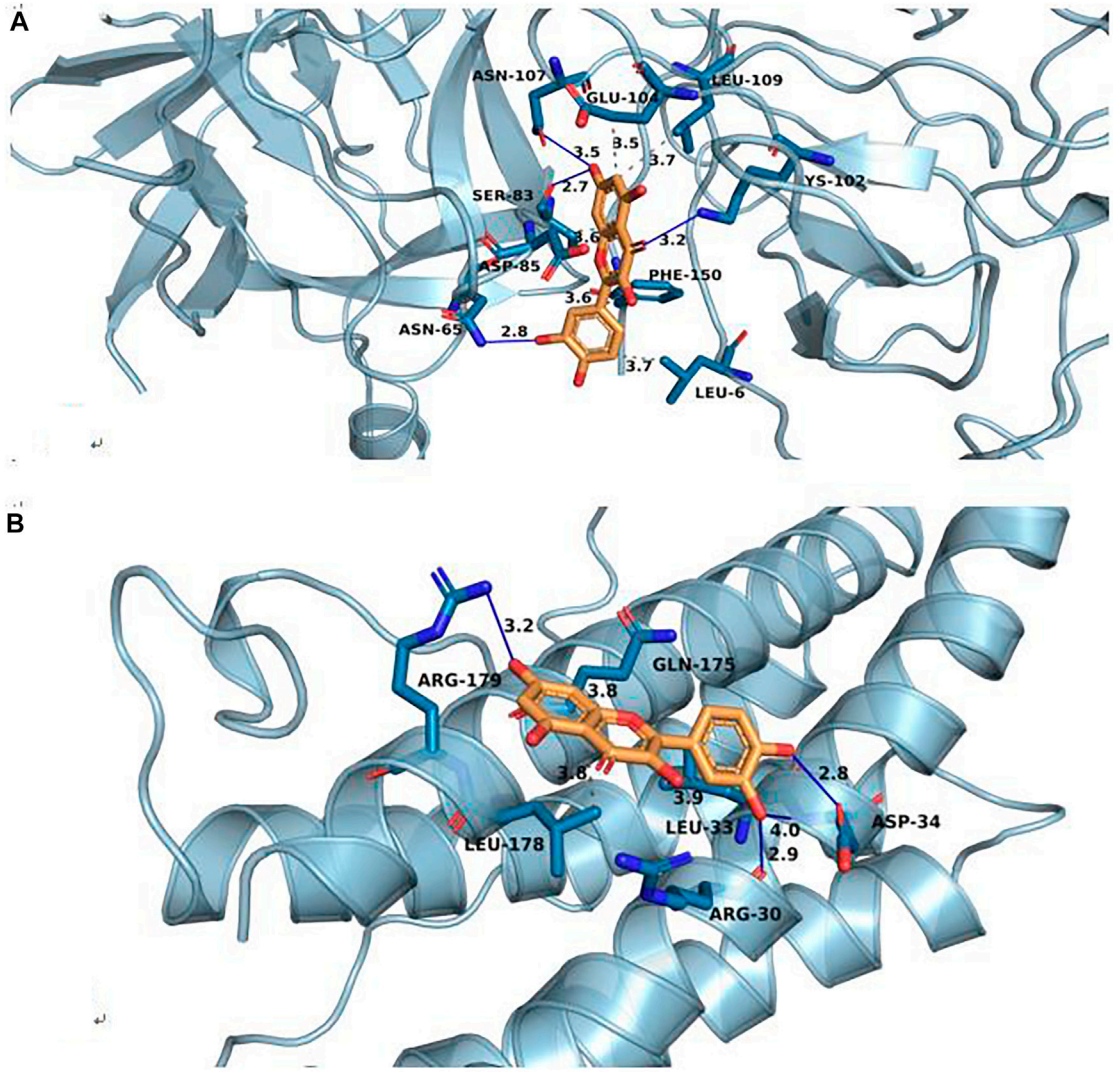

FIGURE 7 | Molecular docking of IL1B-Quercetin **(A)** and IL6_Quercetin **(B)**.

in the treatment of cervical cancer by Hedyotis diffusa were pathways in cancer, hepatitis B and blader C. Pathways in cancer, Hepatitis B, Bladder cancer, Prostate cancer, Pancreatic cancer, TNF signaling pathway, HIF-1 signaling pathway, Non-small cell lung cancer, Chagas disease (American trypanosomiasis), Leishmaniasis and so on.

Through the above analysis, we finally screened the active product capable of interfering with the progression of cervical cancer from Herba Hedyotis, and initially explored the multi-pathway action mechanism of Herba Hedyotis in the treatment of cervical cancer by the analysis method of network pharmacology, which provided reference value and theoretical basis for future clinical research. The experimental research method is reasonable, but the potential mechanism of *Melastoma dodecandrum* against cervical cancer is not yet clear, and further experiments are needed.

DATA AVAILABILITY STATEMENT

The original contributions presented in the study are included in the article/Supplementary Material, further inquiries can be directed to the corresponding authors.

AUTHOR CONTRIBUTIONS

All authors listed have made a substantial, direct, and intellectual contribution to the work and approved it for publication.

FUNDING

This study was supported by Key projects of workstation of He Lin (Grant No. 18331101) Natural Foundation of Zhejiang Provincial China (LGF18H300005) and Natural Foundation of Jiangxi Provincial China (20202BABL216078\20195656).

REFERENCES

Bagri, A., Kouros-Mehr, H., Leong, K. G., and Plowman, G. D. (2010). Use of Anti-VEGF Adjuvant Therapy in Cancer: Challenges and Rationale. *Trends. Mol. Med.* 16, 122–132. doi:10.1016/j.molmed.2010.01.004

Bray, F., Ferlay, J., Soerjomataram, I., Siegel, R. L., Torre, L. A., and Jemal, A. (2018). Global Cancer Statistics 2018: GLOBOCAN Estimates of Incidence and Mortality Worldwide for 36 Cancers in 185 Countries. *CA. Cancer J. Clin.* 68, 394–424. doi:10.3322/caac.21492

Cai, Q., Lin, J., Wei, L., Zhang, L., Wang, L., Zhan, Y., et al. (2012). Hedyotis Diffusa Willd Inhibits Colorectal Cancer Growth *In Vivo* via Inhibition of STAT3 Signaling Pathway. *Int. J. Mol. Sci.* 13, 6117–6128. doi:10.3390/ijms13056117

Chen, B., Zhang, C., Dong, P., Guo, Y., and Mu, N. (2014). Molecular Regulation of Cervical Cancer Growth and Invasion by VEGFa. *Tumour. Biol.* 35, 11587–11593. doi:10.1007/s13277-014-2463-2

Chen, R., He, J., Tong, X., Tang, L., and Liu, M. (2016). The Hedyotis Diffusa Willd. (Rubiaceae): A Review on Phytochemistry, Pharmacology, Quality Control and Pharmacokinetics. *Molecules* 21, 710. doi:10.3390/molecules21060710

Cheng, D., Guo, Z., and Zhang, S. (2015). Effect of β-sitosterol on the Expression of HPV E6 and P53 in Cervical Carcinoma Cells. *Contemp. Oncol. (Pozn)* 19, 36–42. doi:10.5114/wo.2015.50011

Choudhary, S. P., and Tran, L. S. (2011). Phytosterols: Perspectives in Human Nutrition and Clinical Therapy. *Curr. Med. Chem.* 18, 4557–4567. doi:10.2174/092986711797287593

Cohen, P. A., Jhingran, A., Oaknin, A., and Denny, L. (2019). Cervical Cancer. *Lancet* 393, 169–182. doi:10.1016/S0140-6736(18)32470-X

Darband, S. G., Sadighparvar, S., Yousefi, B., Kaviani, M., Ghaderi-Pakdel, F., Mihanfar, A., et al. (2020). Quercetin Attenuated Oxidative DNA Damage through NRF2 Signaling Pathway in Rats with DMH Induced colon Carcinogenesis. *Life Sci.* 253, 117584. doi:10.1016/j.lfs.2020.117584

Denny, L. (2012). Cervical Cancer: Prevention and Treatment. *Discov. Med.* 14, 125–131. PMID: 22935209.

Dyer, B. A., Zamarin, D., Eskandar, R. N., and Mayadev, J. M. (2019). Role of Immunotherapy in the Management of Locally Advanced and Recurrent/Metastatic Cervical Cancer. *J. Natl. Compr. Canc. Netw.* 17, 91–97. doi:10.6004/jnccn.2018.7108

Fu, K., Zhang, L., Liu, R., Shi, Q., Li, X., and Wang, M. (2020). MiR-125 Inhibited Cervical Cancer Progression by Regulating VEGF and PI3K/AKT Signaling Pathway. *World J. Surg. Oncol.* 18, 115. doi:10.1186/s12957-020-01881-0

Gibellini, L., Pinti, M., Nasi, M., Montagna, J. P., De Biasi, S., Roat, E., et al. (2011). Quercetin and Cancer Chemoprevention. *Evid. Based. Complement. Alternat. Med.* 2011, 591356. doi:10.1093/ecam/neq053

Gupta, S., Zhang, D., Yi, J., and Shao, J. (2004). Anticancer Activities of Oldenlandia Diffusa. *J. Herb. Pharmacother.* 4, 21–33. PMID: 15273074. doi:10.1080/j157v04n01_03

Hopkins, A. L. (2008). Network Pharmacology: the Next Paradigm in Drug Discovery. *Nat. Chem. Biol.* 4, 682–690. doi:10.1038/nchembio.118

Kishimoto, T. (1989). The Biology of Interleukin-6. *Blood* 74, 1–10. PMID: 2473791. doi:10.1182/blood.v74.1.1.1

Kong, L., Deng, Z., Zhao, Y., Wang, Y., Sarkar, F. H., and Zhang, Y. (2011). Down-regulation of Phospho-Non-Receptor Src Tyrosine Kinases Contributes to Growth Inhibition of Cervical Cancer Cells. *Med. Oncol.* 28, 1495–1506. doi:10.1007/s12032-010-9583-3

Li, H., Wu, X., and Cheng, X. (2016). Advances in Diagnosis and Treatment of Metastatic Cervical Cancer. *J. Gynecol. Oncol.* 27, e43. doi:10.3802/jgo.2016.27.e43

Li, M., Wong, Y. L., Jiang, L. L., Wong, K. L., Wong, Y. T., Lau, C. B., et al. (2013). Application of Novel Loop-Mediated Isothermal Amplification (LAMP) for Rapid Authentication of the Herbal tea Ingredient Hedyotis Diffusa Willd. *Food Chem.* 141, 2522–2525. doi:10.1016/j.foodchem.2013.05.085

Lin, C. C., Kuo, C. L., Lee, M. H., Hsu, S. C., Huang, A. C., Tang, N. Y., et al. (2011a). Extract of Hedyotis Diffusa Willd Influences Murine Leukemia WEHI-3 Cells *In Vivo* as Well as Promoting T- and B-Cell Proliferation in Leukemic Mice. *In Vivo* 25, 633–640. PMID: 21709007.

Lin, J., Wei, L., Xu, W., Hong, Z., Liu, X., and Peng, J. (2011b). Effect of Hedyotis Diffusa Willd Extract on Tumor Angiogenesis. *Mol. Med. Rep.* 4, 1283–1288. doi:10.3892/mmr.2011.577

Liu, Z., Liu, M., Liu, M., and Li, J. (2010). Methylanthraquinone from Hedyotis Diffusa WILLD Induces Ca(2+)-Mediated Apoptosis in Human Breast Cancer Cells. *Toxicol. Vitro* 24, 142–147. doi:10.1016/j.tiv.2009.08.002

Lu, C. M., Yang, J. J., Wang, P. Y., and Lin, C. C. (2000). A New Acylated Flavonol Glycoside and Antioxidant Effects of Hedyotis Diffusa. *Planta. Med.* 66, 374–377. doi:10.1055/s-2000-8544

Nie, J., Zhao, C., Deng, L. I., Chen, J., Yu, B., Wu, X., et al. (2016). Efficacy of Traditional Chinese Medicine in Treating Cancer. *Biomed. Rep.* 4, 3–14. doi:10.3892/br.2015.537

Qian, N., Chen, X., Han, S., Qiang, F., Jin, G., Zhou, X., et al. (2010). Circulating IL-1beta Levels, Polymorphisms of IL-1B, and Risk of Cervical Cancer in Chinese Women. *J. Cancer Res. Clin. Oncol.* 136, 709–716. doi:10.1007/s00432-009-0710-5

Vänskä, S., Luostarinen, T., Lagheden, C., Eklund, C., Kleppe, S. N., Andrae, B., et al. (2021). Differing Age-specific Cervical Cancer Incidence between Different Types of Human Papillomavirus: Implications for Predicting the Impact of Elimination Programs. *Am. J. Epidemiol.* 190, 506–514. doi:10.1093/aje/kwaa121

Walboomers, J. M., Jacobs, M. V., Manos, M. M., Bosch, F. X., Kummer, J. A., Shah, K. V., et al. (1999). Human Papillomavirus Is a Necessary Cause of Invasive Cervical Cancer Worldwide. *J. Pathol.* 189, 12–19. doi:10.1002/(SICI)1096-9896(199909)189:1<12:AID-PATH431>3.0.CO;2-F

Wei, L. H., Kuo, M. L., Chen, C. A., Chou, C. H., Cheng, W. F., Chang, M. C., et al. (2001). The Anti-apoptotic Role of Interleukin-6 in Human Cervical Cancer Is Mediated by Up-Regulation of Mcl-1 through a PI 3-K/Akt Pathway. *Oncogene* 20, 5799–5809. doi:10.1038/sj.onc.1204733

Ye, J. H., Liu, M. H., Zhang, X. L., and He, J. Y. (2015). Chemical Profiles and Protective Effect of Hedyotis Diffusa Willd in Lipopolysaccharide-Induced Renal Inflammation Mice. *Int. J. Mol. Sci.* 16, 27252–27269. doi:10.3390/ijms161126021

Zhang, S., Shan, L., Li, Q., Wang, X., Li, S., Zhang, Y., et al. (2014). Systematic Analysis of the Multiple Bioactivities of Green Tea through a Network Pharmacology Approach. *Evid. Based. Complement. Alternat. Med.* 2014, 512081. doi:10.1155/2014/512081

Conflict of Interest: The authors declare that the research was conducted in the absence of any commercial or financial relationships that could be construed as a potential conflict of interest.

frontiers in Pharmacology

ORIGINAL RESEARCH
published: 04 January 2022
doi: 10.3389/fphar.2021.793349

Model-Based Anticancer Effect of Botulinum Neurotoxin Type A1 on Syngeneic Melanoma Mice

Won-Ho Kang[1,2†], *Hyo-Jeong Ryu*[1,2†], *Seongsung Kwak*[1] *and Hwi-Yeol Yun*[2*]

[1]Department of Pharmacology and Toxicology, Gwangyo R&D Center, Medytox Inc., Suwon, South Korea, [2]Department of Pharmacy, College of Pharmacy, Chungnam National University, Deajon, South Korea

In recent, Botulinum Neurotoxin A1 (BoNT/A1) has been suggested as a potential anticancer agent due to neuronal innervation in tumor cells. Although potential BoNT/A1's mechanism of action for the tumor suppression has been gradually revealed so far, there were no reports to figure out the exposure-response relationships because of the difficulty of its quantitation in the biological matrix. The main objectives of this study were to measure the anticancer effect of BoNT/A1 using a syngeneic mouse model transplanted with melanoma cells (B16-F10) and developed a kinetic-pharmacodynamic (K-PD) model for quantitative exposure-response evaluation. To overcome the lack of exposure information, the K-PD model was implemented by the virtual pharmacokinetic compartment link to the pharmacodynamic compartment of Simeoni's tumor growth inhibition model and evaluated using curve-fitting for the tumor growth-time profile after intratumoral injection of BoNT/A1. The final K-PD model was adequately explained for a pattern of tumor growth depending on represented exposure parameters and simulation studies were conducted to determine the optimal dose under various scenarios considering dose strength and frequency. The optimal dose range and regimen of ≥13.8 units kg^{-1} once a week or once every 3 days was predicted using the final model in B16-F10 syngeneic model and it was demonstrated with an extra *in-vivo* experiment. In conclusion, the K-PD model of BoNT/A1 was well developed to optimize the dosing regimen for evaluation of anticancer effect and this approach could be expandable to figure out quantitative interpretation of BoNT/A1's efficacy in various xenograft and/or syngeneic models.

Keywords: botulinum neurotoxin, melanoma, pharmacokinetics, pharmacodynamics, K-PD modeling, tumor growth inhibition, NONMEM

OPEN ACCESS

Edited by:
Mark Rogge,
University of Florida, United States

Reviewed by:
Shuowei Cai,
University of Massachusetts Dartmouth, United States
Aleksander Czogalla,
University of Wrocław, Poland

****Correspondence:***
Hwi-Yeol Yun
hyyun@cnu.ac.kr

†These authors have contributed equally to this work and share first authorship

Specialty section:
This article was submitted to Translational Pharmacology, a section of the journal Frontiers in Pharmacology

Received: *12 October 2021*
Accepted: *22 November 2021*
Published: *04 January 2022*

Citation:
Kang W-H, Ryu H-J, Kwak S and Yun H-Y (2022) Model-Based Anticancer Effect of Botulinum Neurotoxin Type A1 on Syngeneic Melanoma Mice. Front. Pharmacol. 12:793349. doi: 10.3389/fphar.2021.793349

INTRODUCTION

Botulinum neurotoxins (BoNTs) are generated by the anaerobic bacterium *Clostridium botulinum*. There are seven antigenically distinct botulinum toxin serotypes (A to G), of which BoNT type A1 (BoNT/A1) has traditionally been indicated for use in cosmetics and various diseases such as axillary hyperhidrosis, chronic migraine, and neurogenic detrusor overactivity (Nigam and Nigam, 2010; Chen, 2012; Walker and Dayan, 2014; Pirazzini et al., 2017; Kwak et al., 2020).

Owing to the increased understanding of the pharmacological importance of neovascularization and neuronal signaling in maintaining the tumor microenvironment there are several studies on the anticancer effect of BoNT/A1. It has been studied in various tumor types, including glioblastoma,

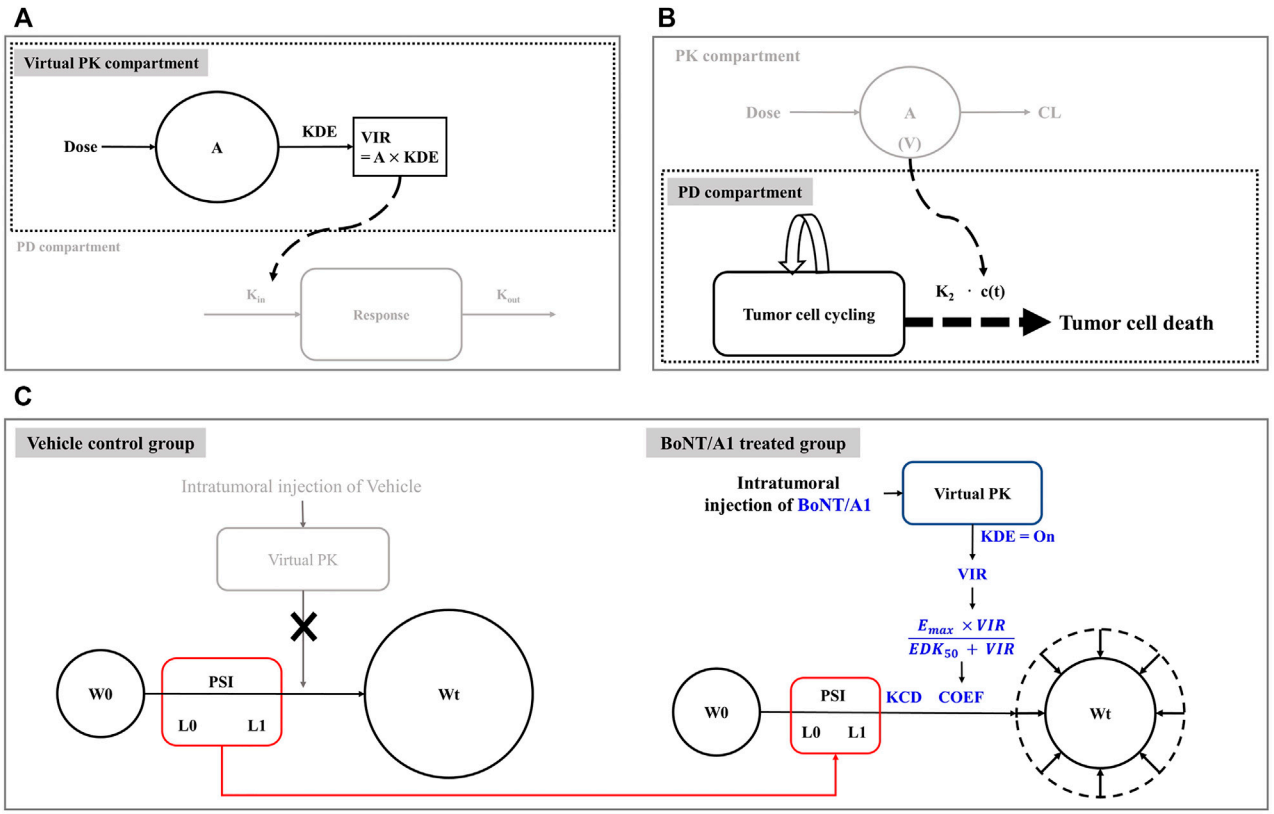

FIGURE 1 | Model structures related to this study. **(A)** Typical K-PD model structure. **(B)** Simeoni's tumor growth inhibition model structure. **(C)** Final K-PD model structure.

neuroblastoma, prostate, breast, and colorectal cancer (Nam et al., 2012; Proietti et al., 2012; Ulloa et al., 2015; Rust et al., 2016; Mittal and Jabbari, 2020). Additionally, several studies have shown that, similar to normal organs and tissues, solid tumors require innervation from the sympathetic and parasympathetic nervous systems to sustain the tumor microenvironment and facilitate cancer development, metastasis, and disease progression (Magnon et al., 2013; Coarfa et al., 2018; Faulkner et al., 2019; Reavis et al., 2020; Wang et al., 2020). Since BoNT/A1 causes denervation via cholinergic signaling pathway interference (Simpson, 2013; Kwak et al., 2020), exploring its anticancer properties is possible. In particular, various acetylcholine receptor subtypes occur in melanomas (Lucianò and Tata, 2020). More recently, it has been suggested that the presence of dorsal root ganglion neurons allows melanoma to grow significantly faster *in vivo*, and innervation plays a direct role in tumorigenesis by suppressing the immune response in melanoma (Keskinov et al., 2016; Reavis et al., 2020). Furthermore, a phase I clinical trial, including metastatic melanoma cancer patients, reported promising tumor inhibition activity administering a combination of pembrolizumab (PD-1 antibody) and propranolol, a non-selective beta-adrenergic blocking agent (Gandhi et al., 2021). Thus, we could conceptualize a relationship between tumor growth and innervation in melanoma. Additionally, melanoma can directly and precisely inject BoNT/A1 into the tumor site; therefore, we focused on it.

Although many studies have explored its anticancer effect and mechanism of action, quantitative exposure-response studies on BoNT/A1 have not been reported, as it is difficult to quantify the blood concentration of BoNT/A1 because of the extremely small volumes injected into the local tissue. Therefore, the regulatory agencies have approved BoNT/A1 products based on less in-depth PK data (Ravichandran et al., 2006; U.S. Food and Drug Administration, 2009; U.S. Food and Drug Administration, 2010; U.S. Food and Drug Administration, 2011). The lack of PK data is compounded by the difficulty of pharmacometrics research, including the prediction of exposure-response relationships.

To overcome these issues, the kinetic-pharmacodynamic model (K-PD), also referred to as the kinetic drug action model, can provide an alternative. The K-PD model was established based on the link between virtual pharmacokinetic (PK) and pharmacodynamic (PD) compartments. The virtual PK compartment was reversely defined, depending on the curve fit for the PD compartment observation values (Jacqmin et al., 2007; Population Approach Group Europe, 2021; Pillai et al., 2004; González-Sales et al., 2017; Lixoft, 2021a, https://mlxtran.lixoft.com/examples/k-pd-models/). The typical K-PD model structure is shown in **Figure 1A**. The main advantage of the K-PD model is that quantitative analysis is possible even with a lack of PK

information; however, pharmacometricians can only establish the exposure-response model to determine the optimal dosing regimen.

This study used a modified Simeoni tumor growth inhibition model as a PD model for our final model build-up and we set it up based on information from the Simeoni perturbed (treated group) and unperturbed (control group) model. In the unperturbed model, tumor growth was exponential in its early phase and linear in its late phase (Simeoni et al., 2004; Mo et al., 2014; Lixoft, 2021b, https://mlxtran.lixoft.com/model-libraries/tgi-library; Li et al., 2016). **Eq. 1** provides a mathematical understanding of the overall tumor growth phenomenon, including exponential and linear growth. The perturbed model combined the drug effect on tumor growth with the unperturbed model. Here, the drug effect was revealed by the drug moving from the PK compartment, i.e., the intrinsic tumor growth aspect explained by the unperturbed model could be controlled by the inhibition ability of the drug flowing into the PD compartment. **Eq. 2** provides a mathematical understanding of intrinsic tumor growth and drug inhibition.

$$\frac{dW(t)}{dt} = \frac{\lambda_0 \cdot W(t)}{\left[1 + \left(\frac{\lambda_0}{\lambda_1} \cdot W(t)\right)^{\psi}\right]^{1/\psi}} \quad (1)$$

$$\frac{dW(t)}{dt} = \frac{\lambda_0 \cdot W(t)}{\left[1 + \left(\frac{\lambda_0}{\lambda_1} \cdot W(t)\right)^{\psi}\right]^{1/\psi}} - k_2 \cdot c(t) \cdot x(t) \quad (2)$$

where W(t) represents the tumor volume at time t, and λ0 and λ1 are exponential and linear growth rate constants, respectively. x(t) represents the proliferating portion of W(t). k_2 is the tumor degradation rate constant. c(t) represents the drug concentration input from the PK compartment. The power coefficient Ψ (PSI) was assumed to be 20 as a switch between the exponential and linear tumor growth phases. In Simeoni's experience, when the value was fixed 20, it was considered to be a sharp function as a switch (Simeoni et al., 2004). The original typical structure of Simeoni's model was shown in **Figure 1B**.

The first objective of this study was to develop a novel tumor growth inhibition model to explain the anticancer effect of BoNT/A1 in a melanoma syngeneic mouse model. Second, to predict the relationship of exposure-response based on our developed K-PD model, and finally, to obtain a quantitatively appropriate therapeutic dose range and regimen for single- and multiple-dose studies. Furthermore, we considered that the K-PD modeling approaches will inform pharmacometricians on the feasibility of a K-PD model build-up for BoNT/A1.

MATERIALS AND METHODS

Tumor Growth Inhibition in Syngeneic Melanoma Mice

Male C57BL/6 mice (six-week-old) were purchased from Orient Bio, Inc. (Seongnam-si, Republic of Korea) and kept in an environment with a 12-h light/dark cycle, controlled temperature (23 ± 3°C), relative humidity (55 ± 15%), and given free access to food and water. The B16-F10 (KCLB#80008) mouse melanoma cell line was obtained from the Korean Cell Line Bank (KCLB) and cultured in Dulbecco's Modified Eagle Medium (11965-092, Gibco) supplemented with 10% fetal bovine serum (FBS, 10082-147, Gibco) and 1% penicillin and streptomycin (15140-122, Gibco) in a humidified atmosphere containing 5% CO_2 at 37°C.

Thirty-five mice with tumor volumes above 25 mm^3 were selected and assigned to one of five treatment groups, with seven mice per group. The mice were anesthetized with ketamine hydrochloride (100 mg kg^{-1}) and xylazine (10 mg kg^{-1}) by intraperitoneal injection prior to B16-F10 tumor cell implantation. Approximately 5×10^5 B16-F10 cells in 1 ml phosphate-buffered saline were subcutaneously implanted into their right flank. The group assignment, performed 8 days post B16-F10 tumor implantations, was based on the tumor volume in the right flank of the tumor-bearing mice.

BoNT/A1 (CORETOX® 100 U, Medytox Inc. Rep, Korea) was injected intratumorally on the day following the group assignment. The tumor volume at the inoculation site was determined by measuring the surface length and width of the tumor mass using a digital Vernier caliper (CD-15APX, Mitutoyo, Japan) and calculating according to **Eq. 3** (Jensen et al., 2008; Faustino-Rocha et al., 2013; Pierrillas et al., 2016). The tumor volumes were measured and recorded twice a week (**Table 1**). All experimental procedures were approved by the Institutional Animal Care and Use Committee of Medytox Inc. (IACUC, Approval No. A-2020-004, January 29, 2020) before the initiation of the study.

$$Tumor\ volume\ (mm^3) = \frac{length\ (mm) \cdot width^2\ (mm^2)}{2} \quad (3)$$

Establishment of Tumor Growth Inhibition Model Using Virtual PK Concept

We established tumor inhibition models using a virtual PK compartment for mouse syngeneic melanoma models (**Figure 1C**). The modeling was performed using non-linear mixed-effects modeling (NONMEM) version 7.4 (ICON Development Solutions, Ellicott City, MD, United States), Pirania ver 2.9.8 (Princeton, NJ, United States), and Pearl-Speaks-non-linear mixed-effects modeling (PsN) ver 4.9.0 (Husargatan, Uppsala, Sweden). The statistical and graphical analyses were performed using R software ver. 3.6.1 (Welthandelsplatz, Vienna, Austria), R Studio ver. 1.2.1335, and GraphPad Prism ver. 7.05.

We combined the Simeoni tumor growth inhibition model with the virtual PK model to explain the tumor growth aspect after intratumoral injection of BoNT/A1 (**Figure 1C**). In the vehicle control group, we assumed that the growth of tumor cells followed the exponential (L0) and linear (L1) phases (**Figure 1C**). The growth rate constants L0 and L1 were assumed to be the same in the vehicle control and treated groups because the tumor growth rate is an intrinsic value for its growth. In the BoNT/A1-treated group, we assumed that BoNT/A1 from the virtual PK

TABLE 1 | Study design for tumor growth inhibition using a syngeneic melanoma mouse model.

Group	Test articles	Dose (U kg^{-1})	Number of animals	Inoculation time (h) for tumor cell	Dosing route	Dosing time (h)	Measurement time (h)
G1	Vehicle	0	7	0	I.T.[a]	192	192, 264, 336, 432
G2	BoNT/A1	1.5	7				
G3	BoNT/A1	5	7				
G4	BoNT/A1	15	7				
G5	BoNT/A1	50	7				

[a]*I.T.: intratumoral injection.*

compartment inhibited intrinsic tumor growth, i.e., we hypothesized that the efficiencies and rates of tumor growth inhibition were generated by BoNT/A1 delivered through the virtual PK compartment. As mentioned in the introduction, in the K-PD model, all PK functions can be implicated by the virtual infusion rate instead of the typical PK parameters such as clearance, volume of distribution, absorption rate constant, and bioavailability, when the drug concentration data is unavailable.

Differential equations were used to describe the tumor growth pattern after intratumoral BoNT/A1 injection.

$$\frac{dA(1)}{dt} = -KDE \cdot A(1) \tag{4}$$

$$VIR = A(1) \cdot KDE \tag{5}$$

$$COEF = \frac{E_{max} \cdot VIR}{EDK_{50} + VIR} \tag{6}$$

$$\frac{dA(2)}{dt} = W0 + \frac{L_0 \cdot A(2)}{\left[1 + \left(\frac{L_0}{L_1} \cdot A(2)\right)^{\psi}\right]^{1/\psi}} - KCD \cdot COEF \cdot A(2) \tag{7}$$

where A (1) and KDE represent the quantity of BoNT/A1 and degradation rate constant in the virtual PK compartment, respectively, and the virtual infusion rate (VIR) represents the virtual infusion rate from the virtual PK compartment to the PD compartment. W0 represents the tumor volume at the coefficient for the drug effect by describing the general Emax equation. KCD represents the cancer degradation rate constant. To summarize the function in the final K-PD model, when cancer cells grow by L0 and L1, BoNT/A1 flows into the PD compartment by VIR. Subsequently, BoNT/A1 within the PD compartment generated an inhibitory effect on cancer growth, defined by COEF and KCD (**Figure 1C**).

Model Diagnostics and Evaluation

We checked the goodness-of-fit (GOF) plot of the final K-PD model vehicle and treated the model for two types of tumors. A visual predictive check (VPC) was also performed to evaluate the final K-PD model. Using the final K-PD model, 1,000 simulated replicates of the original dataset were generated, and the fifth percentile, median, and 95th percentile calculated from the simulated tumor volume were compared to the observed tumor volume. In addition, a bootstrap analysis was conducted to evaluate the internal model. The final K-PD model was compared with the 95% confidence intervals in the bootstrap analysis.

Simulation Studies for Optimal Dosing Regimen

We conducted exploratory simulation studies based on the final K-PD model to establish an effective dose range and adequate dose regimen. First, the tumor growth-time profile was simulated for a single BoNT/A1 dose in the range of 0.0025–3,200 units kg^{-1} (U kg^{-1}) to calculate the 50% effective dose (ED_{50}), maximum effective dose (ED_{max}), and the hill slope sigmoidity for the profiles. We then calculated the PD parameters using the sigmoid E_{max} model (**Eq. 8**) with tumor growth inhibition (TGI) for each dose. Consequently, we defined an adequate dose range using the ED_{50} value and maximum injectable dose ($D_{max\text{-}inj.}$) converted from the human dose (ClinicalTrials.gov., 2020) based on body surface area between species. That is, the $D_{max\text{-}inj}$ was calculated using equation (**Eq. 9**) modified from the FDA guidelines relating to estimating the maximum safe starting dose in initial clinical trials (U.S. Food and Drug Administration. Center for Drug Evaluation and Research. U.S., 2005)

$$Effect = \frac{ED_{max} \times Dose^{\gamma}}{ED_{50} + Dose^{\gamma}} \tag{8}$$

$$Mouse\ D_{max-inj.} = Human\ D_{max-inj.} \times \frac{Human\ K_m\ (37)}{Mouse\ K_m(3)} \tag{9}$$

Second, we conducted a simulation study of the tumor growth pattern after multiple BoNT/A1 doses in various scenarios. We simulated three different dose regimens, once a day (Q.D.), once every 3 days (Q.3.D.), and once per week (Q.W.) in our study design. The dose range in the multiple-dose simulation study was 6–74 U kg^{-1} with ED_{50} and $D_{max\text{-}inj.}$ obtained from the single-dose simulation. The study designs are presented in detail in **Table 2**.

RESULTS

Tumor Growth Profiles in Syngeneic Mice

The change in tumor volume over time was determined from *in vivo* TGI experiments using syngeneic melanoma mouse models. The tumor growth patterns after BoNT/A1 injection are shown in **Figure 2**. Overall, the tumors grew slowly in the early stage and

TABLE 2 | Final melanoma syngeneic mouse K-PD model simulation scenarios and results.

Dosing frequency	Dose strength	Dose regimen	Dosing time (h)	Tumor growth inhibition[a] (%)
Single	0	Q.D.[b]	192	0
	0.0025			14.92
	0.005			14.93
	0.02			15.01
	0.1			15.5
	1			20.63
	10			38.32
	50			53.47
	200			65.19
	400			69.6
	800			73.66
	1,600			76.94
	3,200			79.52
Multiple	6	Q.D.	192, 216, 240, 264, 288, 312, 336, 360, 384, 408, 432, 456	77.27
	13.8			81.17
	31.7			82.03
	74			82.91
	6	Q.3.D.[c]	192, 264, 336, 408	64.92
	13.8			74.78
	31.7			78.67
	74			81.53
	6	Q.W.[d]	192, 360	42.14
	13.8			59.61
	31.7			67.09
	74			74.13

B16-F10 tumor cell inoculation time was 0 h in every scenario. Administration route was intratumoral injection in every scenario.

[a]*TGI values were calculated based on tumor volume at 468 h, when tumor volume of the vehicle control group >2000 mm^3, standard for euthanasia.*

[b]*Q. D. once a day.*

[c]*Q. 3. D. once every 3 days.*

[d]*Q. W. once a week; TGI, tumor growth inhibition.*

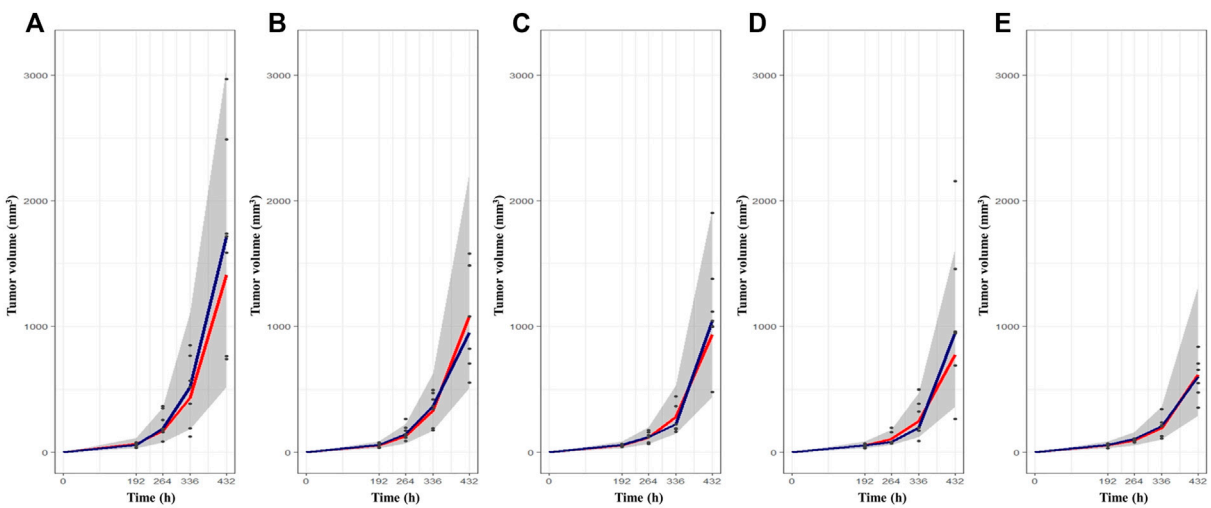

FIGURE 2 | The tumor growth-time profiles after BoNT/A1 injection and visual check prediction (VPC) results for final K-PD model. **(A)** Vehicle control group. **(B)** BoNT/A1 1.5 U kg^{-1} treated group. **(C)** BoNT/A1 5 U BoNT/A1 1.5 U kg^{-1} treated group. **(D)** BoNT/A1 15 U kg^{-1} treated group **(E)** BoNT/A1 50 U kg^{-1} treated group. Black dot, observed tumor volume; Gray shade, 90% simulation intervals; Blue line, observed median value; Red line, simulated median value.

TABLE 3 | Parameters estimated via final K-PD model and bootstrap validation.

Group	Parameter	Unit	Estimates (%RSE)	IIV (%RSE)	Bootstrap median (2.5–97.5% Percentile)
Vehicle group	L0	h^{-1}	0.013 (8.9%)	13.5% (21.9%)	0.013 (0.011–0.021)
	L1	h^{-1}	16.7 (15.6%)	—	16.4 (9.9–23.5)
	W0	mm^3	0.0736 (14.9%)	—	0.0727 (0.0203–0.0965)
	Proportional error	N/A	0.285 (8.9%)		—
BoNT/A1 treated group	KDE	h^{-1}	0.0292 (37.3%)	—	0.0278 (0.0098–0.0597)
	L0	h^{-1}	0.013 FIX	8.8% (17.2%)	—
	L1	h^{-1}	16.7 FIX	62.2% (43.9%)	—
	KCD	h^{-1}	0.0427 (45.7%)	—	0.0442 (0.0360–2.2053)
	WO	mm^3	0.0631 (4.3%)		0.0632 (0.0583–0.0683)
	EMAX	mol	0.164 (35.1%)		0.170 (0.138–8.470)
	EDK50	Unit/h	0.00116 (93.1%)		0.00127 (0.00016–24.8405)
	Proportional error	N/A	0.246 (6.9%)		—

IIV, inter-individual variability; RSE, relative standard error.

then rapidly when they exceeded a specific tumor volume. **Figure 2A** shows that the tumor growth pattern in each vehicle control group changed from an exponential to a linear function at a tumor volume of approximately 500 mm^3. Additionally, a large magnitude of inter-individual variability within the data in the syngeneic melanoma mouse model was found; and at the last measurement, the coefficient of variation between the observations was approximately 47% in the vehicle control group. We used population PK-PD analyses in the model build-up to explain these magnitudes of inter-individual variability; furthermore, as the BoNT/A1 dose increased from 1.5 to 50 U kg^{-1}, the tumor's size decreased (**Figures 2B–E**). Note that, for all test groups, we designated the endpoint of tumor growth observation to be the time point (432 h) at which the tumor volume of the vehicle control group approached 2000 mm^3 since this is the IACUC-recommended time point for euthanasia, considering animal ethics and welfare.

Tumor Growth Inhibition Modeling

The dataset for the tumor growth pattern in the syngeneic melanoma mouse was applied to our novel TGI modeling system. Our final K-PD model best described the tumor volume from tumor volume-time profiles, which indicated a combination of the modified Simeoni TGI model with a virtual PK compartment. The estimated parameters are summarized in **Table 3**.

L0 and L1 were 0.013 and 16.7 h^{-1}, respectively, in the B16-F10 syngeneic mouse model. The B16-F10 tumor cells grew rapidly during the linear growth phase following the exponential growth phase in the early stage of cancer cell transplantation. In the BoNT/A1-treated groups, the KDE was estimated at 0.0292 h^{-1} (low value) since BoNT/A1 was injected directly into the tumor tissue, the site of the TGI response. The E_{max} and EDK_{50} in the E_{max} formula reflecting the VIR [VIR = −KDE*A (1)] were 0.164 mol and 0.00116 U h^{-1}, respectively. An EDK_{50} of 0.00116 U h^{-1} indicated that a small quantity of BoNT/A1 would be sufficient for B16-F10 growth inhibition because the EDK_{50} showed *in vivo* potency, defined as the infusion rate resulting in a 50% inhibition coefficient.

Model Diagnostics and Evaluation

The VPCs with 95% prediction intervals using the final K-PD models are shown in **Figure 2**. The VPC plot indicated that most of the values were within the 95% prediction interval of the simulation data. The results indicated that the predictive performance was appropriate for the final K-PD models to explain TGI in the syngeneic melanoma model data. The values were similar to those generated from 1,000 bootstrap replications, indicating good precision in the final K-PD models (**Table 3**). The basic GOF plots for the final K-PD models are shown in **Supplementary Figure S1**. Individual and population predictions were evenly distributed across the line of identity, indicating good model fitting.

Simulation Studies for Optimal Dosing Regimen

Simulation Study for Single BoNT/A1 Dose

The tumor growth-time profiles were simulated at single BoNT/A1 doses ranging from 0.0025 to 3200 U kg^{-1} using our novel K-PD model. In all groups, exponential growth was observed after tumor transplantation and linear growth toward the late stage. In addition, an increase in tumor suppression was observed with an increasing BoNT/A1 dosage (**Figure 3A**). The TGI rate of each BoNT/A1 treatment group was calculated based on 468 h, when the tumor volume of the vehicle group exceeded 2000 mm^3 (**Table 2**). The dose-response relationship estimated with a typical sigmoidal E_{max} equation had an ED_{50} of 31.7 U kg^{-1}. The mouse $D_{max\text{-}inj.}$ was 74 U kg^{-1} calculated from human $D_{max\text{-}inj.}$ (ClinicalTrials.gov. 2020) at 6 U kg^{-1} (360 U) using an inter-species conversion factor on the basis of body surface area (U.S. Food and Drug Administration. Center for Drug Evaluation and Research. U.S., 2005). Consequently, we identified the dose range of 31.7–74 U kg^{-1} as a therapeutically meaningful range for the BoNT/A1 single-injection study (**Figure 3B**).

Simulation Study for Multiple BoNT/A1 Doses

The simulations at four different dose regimens, including ED_{50} and $D_{max\text{-}inj.}$ in three-dose regimen conditions, revealed the results shown in **Figure 4** and **Table 2**. First, when the BoNT/

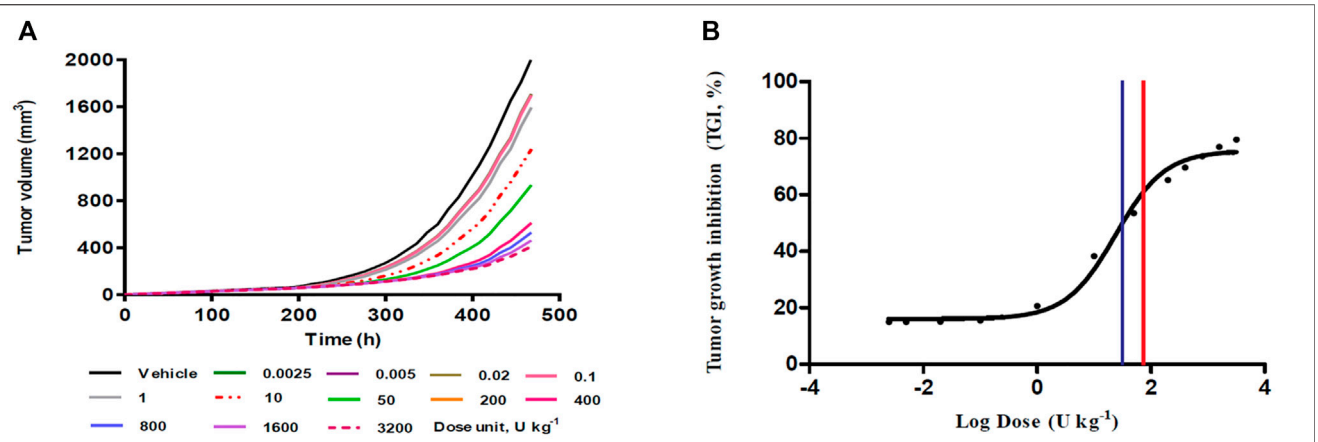

FIGURE 3 | Single-dose simulation study. **(A)** Tumor growth-time profiles **(B)** Dose-response relationship from single-dose (%) simulation. Blue vertical line in the panel **(B)**, 31.7 U kg^{-1} as a predicted ED_{50}; red vertical line in the panel **(B)**, 74 U kg^{-1} as a predicted maximum injectable dose ($D_{max\text{-}inj.}$).

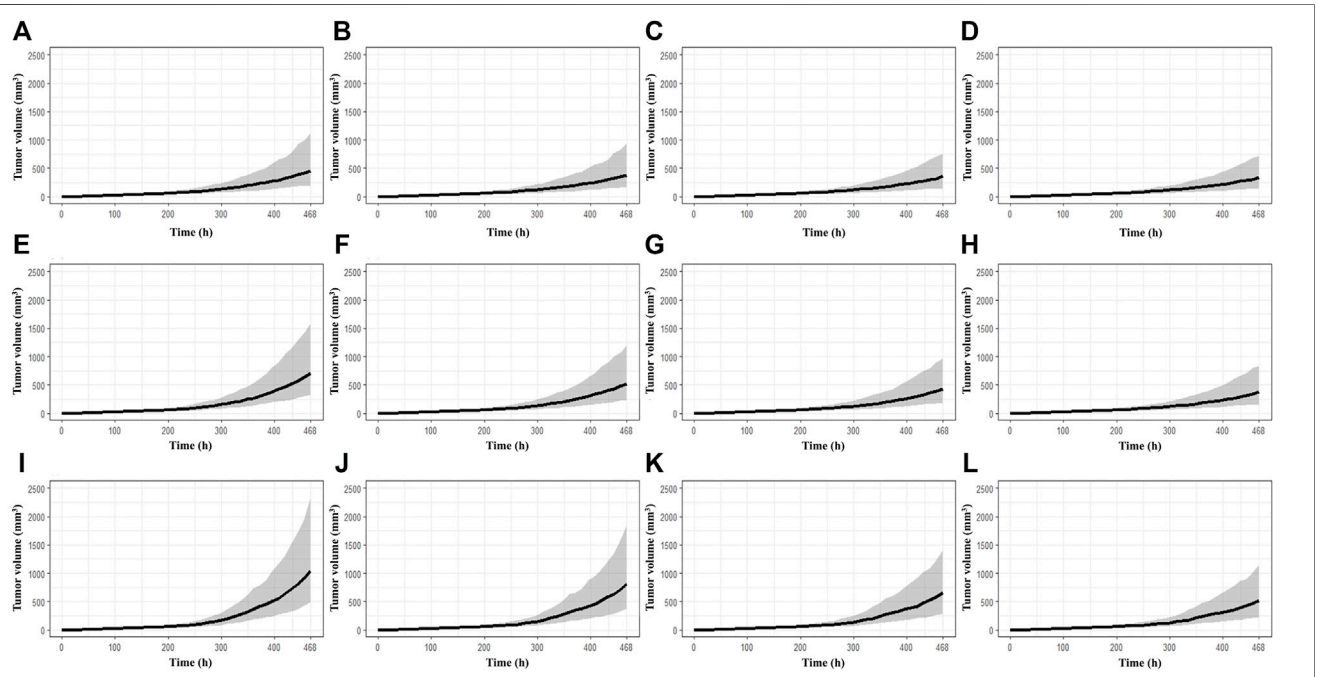

FIGURE 4 | Multiple-dose simulation study. **(A)** BoNT/A1 6 U kg^{-1} for Q.D. **(B)** BoNT/A1 13.8 U kg^{-1} for Q.D. **(C)** BoNT/A1 31.7 U kg^{-1} for Q.D. **(D)** BoNT/A1 74 U kg^{-1} for Q.D. **(E)** BoNT/A1 6 U kg^{-1} for Q.3.D. **(F)** BoNT/A1 13.8 U kg^{-1} for Q.3.D. **(G)** BoNT/A1 31.7 U kg^{-1} for Q.3.D. **(H)** BoNT/A1 74 U kg^{-1} for Q.3.D. **(I)** BoNT/A1 6 U kg^{-1} for Q.W. **(J)** BoNT/A1 13.8 U kg^{-1} for Q.W. **(K)** BoNT/A1 31.7 U kg^{-1} for Q.W. **(L)** BoNT/A1 74 U kg^{-1} for Q.W.

A1 dose was increased from 6 to 74 U kg^{-1} in the Q.D. dose regimen scenarios, the TGI was 77.27–82.92%, and a significant anticancer effect was observed at all doses (**Figures 4A–D**). Second, when the dose was increased from 6 to 74 U kg^{-1} in the Q.3.D. scenarios, the TGI (%) value was 64.92–81.53%, and there was a meaningful anticancer effect depending on the dose escalation in those scenarios (**Figures 4E–H**). Finally, the TGI of Q.W. was 42.14–74.14% at the same dose range in previous studies. These results indicated a good dose-dependent escalation in anticancer effect (**Figures 4I–L**). The dose-response relationships for the three different dose regimens are shown in **Figure 5**. In the Q.D. dose regimen scenario, a high TGI of ≥77% was maintained at all dose ranges. For the Q.3.D. dose regimen, a high TGI of ≥74% was observed in all dose

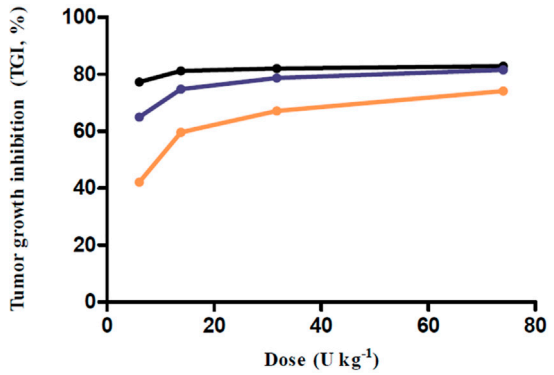

FIGURE 5 | Dose-response relationship for multiple-dose simulations. Black line, Q.D. as a dose regimen; Blue line, Q.3.D. as a dose regimen; Orange line, Q.W. as a dose regimen; Every closed circle, observed TGI values.

ranges except at 6 U kg^{-1}, which was 64%. Q.W. the last dose regimen scenario among our repeated simulation studies, showed a significant logarithmic TGI increase of between 6 and 74 U kg^{-1}.

DISCUSSION

As with BoNT/A1, because the plasma drug-time-concentration profile might not always be available to correlate exposure with the biomarker or clinical endpoints during the drug discovery and development process, pharmacometricians needed to examine alternatives for cases in which PK data are unavailable. Using the syngeneic melanoma mouse model, we attempted to establish a mathematical model to explain the anticancer effect in a diseased mouse model when BoNT/A1 was intratumorally injected in a situation where PK data were not available. We attempted to combine the virtual PK part of the K-PD model with the PD part of the Simeoni TGI model. Our final K-PD model predicted the anticancer effects well. First, our final K-PD model estimated that the tumor growth rates L0 and L1 were fast for the dataset of the syngeneic melanoma mice. In addition, the virtual PK parameters were also well and stably estimated while performing curve-fitting using only the tumor volume as a dependent variable. While performing NONMEM iterations, the virtual PK parameters were also stably estimated. Meanwhile, we considered L0 and L1 omega in the final K-PD model to account for the large inter-individual variability (IIV) in tumor growth profiles (**Figure 2**). In developing the model, the IIV for the other parameters was considered, but it had little effect on decreasing the objective function value. Therefore, we only reflected IIV on L0 and L1 in our final K-PD model.

Based on the established K-PD model, we simulated various scenarios. First, a simulation study of a single BoNT/A1 administration was conducted. Due to the BoNT neurotoxicity in this simulation study, the dose was gradually increased to a high dose (0.0025–3200 U kg^{-1}) that could not be injected in an actual experiment, thereby securing a dose-response profile for the anti-melanoma effect—using the calculated ED_{50} and the mouse $D_{max\text{-}inj.}$ converted from the human, $D_{max\text{-}inj.}$ we confirmed that the therapeutic dose range of BoNT/A1 in syngeneic melanoma mice was approximately 31.7–74 U kg^{-1} (**Figure 3**; **Table 2**). Second, we conducted another simulation study on multiple BoNT/A1 doses from 6 to 74 U kg^{-1} in three-dose regimens (Q.D. Q.3.D., and Q.W.). The results confirmed the dose-proportional and superior anticancer effect in the all-dose regimen scenarios (**Figure 5**; **Table 2**). Overall, we considered that the minimum meaningful dose in syngeneic melanoma mice is ≥13.8 U kg^{-1} (0.27 U). We considered that the adequate administration interval could be Q.3.D. or Q.W. In the case of Q.D. there could be a neurotoxicological concern due to the injection of dense BoNT/A1. Meanwhile, in some BoNT/A1 products such as Dysport® (Ipsen, United States), there was a precedent in which repeated toxicity tests were conducted by once-daily intramuscular administration for 14 days in rats, but the No Observed Adverse Effect Level (NOAEL) in this study was low such as 1 U Rat^{-1} (~5 U kg^{-1}) (U.S. Food and Drug Administration, 2009). Therefore, there were still concerns concerning neurotoxicity in Q.D. even though there were differences in animal species and administration sites in the tests. Furthermore, our results indicated that BoNT/A1 alone had a highly significant anticancer effect; therefore, it could be difficult to confirm the synergistic effect with other anticancer drugs such as PD-1 or PD-L1 antibody.

Fortunately, the predicted optimal dosing regimen was verified through additional *in-vivo* results in the B16-F10 syngeneic mouse model by performing an *in vivo* anticancer efficacy study with single or multiple intratumoral BoNT/A1 injections. The anticancer efficacy study conducted using BoNT/A1 injections at three doses (**Supplementary Table S1**) showed that most tumor volumes were within the 90% simulation interval estimated using our model (**Supplementary Figure S2**). Furthermore, when we compared the average observed values at 432 h, the final measurement time, with the simulation median value and interval, we found that all average observation values were within the 90% prediction interval (**Supplementary Table S2**). Based on the above results, we again found that our final K-PD model had appropriate predictive power. Furthermore, we applied our K-PD model to the TGI data obtained from another syngeneic model with inoculated 4T-1 breast cancer cells and validated the model, as it explained the tumor growth aspect accurately. Even when BoNT/A1's inhibitory effect in the 4T-1 syngeneic model was slightly lower than that of B16-F10, our K-PD model exhibited a good curve-fitting for the 4T-1 tumor volume-time curve (in-house results). In addition, in a syngeneic model inoculated with MBT2 cells, which are ovarian cancer cells, the tumor growth rates, such as L1 and L0, were high and similar to that of B16-F10. Hence, for such tumor cell line types, we presume that growth rate constants similar to that of B16-F10 can be used (in-house results).

A previous study had identified the BoNT/A1 antitumoral effect in prostate cancer via the mouse xenograft experiment and clinical trials (Coarfa et al., 2018). As the result of the study, there was a reduction of tumor incidence and size where BoNT/A1's dose was 0.45 U *via* intratumoral injection route to the xenograft mouse and there were meaningful findings which were not only nerve density decrease but apoptosis increases in prostate cancer when 100 U of BoNT/A1 was treated to the patients in clinical trials. Although our

targeted cancer is different from this previous study, we considered that the results could be indirectly applied to our case because we have obtained a similar efficacious dose of BoNT/A1. In detail, we could expect a similar or lower effective dose (≤100 U) in the clinical study for melanoma patients considering the effective dose (100 U) of BoNT/A1 for prostate cancer patients since the minimum efficacious dose (0.27 U) in the syngeneic melanoma mouse was similar or a little lower than 0.45 U in the xenograft prostate mouse.

We are currently trying to expand the indications of BoNT/A1 by targeting melanoma that can be locally injectable. Although BoNT/A1 rarely elicits adverse events such as facial and palpebral edema, injection site pain, eye pain, erythema, psoriasis, skin infections, vertigo, nausea, fever, blepharitis, xerostomia, itching, and asthenia, we speculate that the minimum efficacious dose (0.27 U = 13.8 U Kg^{-1} ≈ 1.1 U Kg^{-1} for human) that we arrived at could be used for melanoma treatment in clinical trials considering the risk-to-benefit aspect.

There were some potential limitations in this study. First, our concept for the model development was applied only to B16-F10 melanoma tumors. Hence, it was unclear whether our concept for the combination model build-up could be applied to other tumors. Second, in this study, we used only tumor volume as a PD marker. However, if we had obtained the survival rate or the level of other biomarkers related to cancer growth, we would have succeeded in developing better models, such as disease progression models. Since a study to obtain these factors is planned, in this study, we focused on the development of models that could satisfactorily explain the change in tumor volume. Third, regarding the pharmacological mechanism of the anticancer effect of BoNT/A1, there have been various reports of BoNT/A1's effects on apoptosis, phosphorylation process, and neuron denervation (Proietti et al., 2012; Bandala et al., 2013; Coarfa et al., 2018). Therefore, we have planned on performing *in-vitro* studies clarifying the pharmacological mechanism behind the anticancer effect. We believe that this investigation on the mechanism of tumor treatment could facilitate the development of more elaborate pharmacometrics models.

CONCLUSION

We developed a mathematical model to explain the tumor-suppressing effect of BoNT/A1 in B16-F10 melanoma cancer cells. The virtual PK compartment of the K-PD model was used as the model setup for the PK part in a situation where PK data were not available, and the PD part of the Simeoni TGI model was used to explain the tumor growth aspect in our dataset. Hence, novel tumor growth inhibition models for BoNT/A1 were established by combining the PK and PD parts of each model. Furthermore, our final K-PD models were well curve-fitted for each animal experiment data set and showed adequate predictive power for both single and repeated BoNT/A1 injection data. Moreover, we hypothesize that this approach could be scalable for pharmacometricians to use in PK-PD modeling for BoNT/A1.

DATA AVAILABILITY STATEMENT

The original contributions presented in the study are included in the article/**Supplementary Material**, further inquiries can be directed to the corresponding author.

ETHICS STATEMENT

The animal study was reviewed and approved by the Institutional Animal Care and Use Committee of Medytox. Inc.

AUTHOR CONTRIBUTIONS

W-HK and H-JR contributed equally to this study as the first authors. W-HK, H-JR, and SK conducted the animal experiments. W-HK and H-YY conceptualized and developed the final K-pD model. W-HK and H-JR conducted the modeling and simulation studies. W-HK, H-JR, and SK conducted statistical and graphical analyses. W-HK, H-JR, and H-YY wrote the original draft of the manuscript. All authors contributed to, reviewed, and approved the manuscript.

FUNDING

This research was funded by the Chungnam National University (CNU) and the Institute of Information and Communications Technology Planning and Evaluation (IITP) grant funded by the Korean government (MSIT) (No. 2020-0-01441, Artificial Intelligence Convergence Research Center (Chungnam National University)). This study was funded from the Chungnam National university and the Institute of Information and Communucations Technology Planning and Evaluation (ITTP) granted funded by the Korean government (MSIT). Every author declares that industry and institute, where authors has been employed and funded, was not involved for the study design, collection, analysis, interpretation of data, the writing of this article or the decision to submit it for publication.

SUPPLEMENTARY MATERIAL

The Supplementary Material for this article can be found online at: https://www.frontiersin.org/articles/10.3389/fphar.2021.793349/full#supplementary-material

REFERENCES

Bandala, C., Perez-Santos, J. L., Lara-Padilla, E., Delgado Lopez, G., and Anaya-Ruiz, M. (2013). Effect of Botulinum Toxin A on Proliferation and Apoptosis in the T47D Breast Cancer Cell Line. *Asian Pac. J. Cancer Prev.* 14, 891–894. doi:10.7314/apjcp.2013.14.2.891

Chen, S. (2012). Clinical Uses of Botulinum Neurotoxins: Current Indications, Limitations and Future Developments. *Toxins (Basel)* 4, 913–939. doi:10.3390/toxins4100913

ClinicalTrials.gov (2020). ClinicalTrials. Available: https://clinicaltrials.gov/ct2/show/NCT03289702 (Accessed October 12, 2021).

Coarfa, C., Florentin, D., Putluri, N., Ding, Y., Au, J., He, D., et al. (2018). Influence of the Neural Microenvironment on Prostate Cancer. *Prostate* 78, 128–139. doi:10.1002/pros.23454

Faulkner, S., Jobling, P., March, B., Jiang, C. C., and Hondermarck, H. (2019). Tumor Neurobiology and the War of Nerves in Cancer. *Cancer Discov.* 9, 702–710. doi:10.1158/2159-8290.CD-18-1398

Faustino-Rocha, A., Oliveira, P. A., Pinho-Oliveira, J., Teixeira-Guedes, C., Soares-Maia, R., da Costa, R. G., et al. (2013). Estimation of Rat Mammary Tumor Volume Using Caliper and Ultrasonography Measurements. *Lab. Anim. (Ny)* 42, 217–224. doi:10.1038/laban.254

Gandhi, S., Pandey, M. R., Attwood, K., Ji, W., Witkiewicz, A. K., Knudsen, E. S., et al. (2021). Phase I Clinical Trial of Combination Propranolol and Pembrolizumab in Locally Advanced and Metastatic Melanoma: Safety, Tolerability, and Preliminary Evidence of Antitumor Activity. *Clin. Cancer Res.* 27, 87–95. doi:10.1158/1078-0432.CCR-20-2381

González-Sales, M., Nekka, F., Tanguay, M., Tremblay, P. O., and Li, J. (2017). Modelling the Dose-Response Relationship: the Fair Share of Pharmacokinetic and Pharmacodynamic Information. *Br. J. Clin. Pharmacol.* 83, 1240–1251. doi:10.1111/bcp.13225

Jacqmin, P., Snoeck, E., van Schaick, E. A., Gieschke, R., Pillai, P., Steimer, J. L., et al. (2007). Modelling Response Time Profiles in the Absence of Drug Concentrations: Definition and Performance Evaluation of the K-PD Model. *J. Pharmacokinet. Pharmacodyn.* 34, 57–85. doi:10.1007/s10928-006-9035-z

Jensen, M. M., Jørgensen, J. T., Binderup, T., and Kjaer, A. (2008). Tumor Volume in Subcutaneous Mouse Xenografts Measured by microCT Is More Accurate and Reproducible Than Determined by 18F-FDG-microPET or External Caliper. *BMC Med. Imaging* 8, 16. doi:10.1186/1471-2342-8-16

Keskinov, A. A., Tapias, V., Watkins, S. C., Ma, Y., Shurin, M. R., and Shurin, G. V. (2016). Impact of the Sensory Neurons on Melanoma Growth *In Vivo*. *PLoS One* 11, e0156095. doi:10.1371/journal.pone.0156095

Kwak, S., Kang, W. H., Rhee, C. H., Yang, G. H., and Cruz, D. J. M. (2020). Comparative Pharmacodynamics Study of 3 Different Botulinum Toxin Type A Preparations in Mice. *Dermatol. Surg.* 46, e132–e138. doi:10.1097/DSS.0000000000002402

Li, J. Y., Ren, Y. P., Yuan, Y., Ji, S. M., Zhou, S. P., Wang, L. J., et al. (2016). Preclinical PK/PD Model for Combined Administration of Erlotinib and Sunitinib in the Treatment of A549 Human NSCLC Xenograft Mice. *Acta Pharmacol. Sin.* 37, 930–940. doi:10.1038/aps.2016.55

Lixoft (2021a). Lixoft. Available: https://mlxtran.lixoft.com/examples/k-pd-models/(Accessed October 12, 2021).

Lixoft (2021b).Lixoft. Available: https://mlxtran.lixoft.com/model-libraries/tgi-library/(Accessed October 12, 2021).

Lucianò, A. M., and Tata, A. M. (2020). Functional Characterization of Cholinergic Receptors in Melanoma Cells. *Cancers* 12, 3141. doi:10.3390/cancers12113141

Magnon, C., Hall, S. J., Lin, J., Xue, X., Gerber, L., Freedland, S. J., et al. (2013). Autonomic Nerve Development Contributes to Prostate Cancer Progression. *Science* 341, 1236361. doi:10.1126/science.1236361

Mittal, S. O., and Jabbari, B. (2020). Botulinum Neurotoxins and Cancer-A Review of the Literature. *Toxins (Basel)* 12, 32. doi:10.3390/toxins12010032

Mo, G., Gibbons, F., Schroeder, P., and Krzyzanski, W. (2014). Lifespan Based Pharmacokinetic-Pharmacodynamic Model of Tumor Growth Inhibition by Anticancer Therapeutics. *PLoS One* 9, e109747. doi:10.1371/journal.pone.0109747

Nam, H. J., Kang, J. K., Chang, J. S., Lee, M. S., Nam, S. T., Jung, H. W., et al. (2012). Cells Transformed by PLC-Gamma 1 Overexpression Are Highly Sensitive to clostridium Difficile Toxin A-Induced Apoptosis and Mitotic Inhibition. *J. Microbiol. Biotechnol.* 22, 50–57. doi:10.4014/jmb.1107.07018

Nigam, P. K., and Nigam, A. (2010). Botulinum Toxin. *Indian J. Dermatol.* 55, 8–14. doi:10.4103/0019-5154.60343

Pierrillas, P. B., Tod, M., Amiel, M., Chenel, M., and Henin, E. (2016). Improvement of Parameter Estimations in Tumor Growth Inhibition Models on Xenografted Animals: a Novel Method to Handle the Interval Censoring Caused by Measurement of Smaller Tumors. *AAPS J.* 18, 404–415. doi:10.1208/s12248-015-9862-1

Pillai, G., Gieschke, R., Goggin, T., Jacqmin, P., Schimmer, R. C., and Steimer, J. L. (2004). A Semimechanistic and Mechanistic Population PK-PD Model for Biomarker Response to Ibandronate, a New Bisphosphonate for the Treatment of Osteoporosis. *Br. J. Clin. Pharmacol.* 58, 618–631. doi:10.1111/j.1365-2125.2004.02224.x

Pirazzini, M., Rossetto, O., Eleopra, R., and Montecucco, C. (2017). Botulinum Neurotoxins: Biology, Pharmacology, and Toxicology. *Pharmacol. Rev.* 69, 200–235. doi:10.1124/pr.116.012658

Population Approach Group Europe (2021). Population Approach Group Europe. Available: https://www.page-meeting.org/pdf_assets/7711-Navin%20Goyal_Page%202012.pdf (Accessed October 12, 2021).

Proietti, S., Nardicchi, V., Porena, M., and Giannantoni, A. (2012). Botulinum Toxin Type-A Toxin Activity on Prostate Cancer Cell Lines. *Urologia* 79, 135–141. doi:10.5301/RU.2012.9254

Ravichandran, E., Gong, Y., Al Saleem, F. H., Ancharski, D. M., Joshi, S. G., and Simpson, L. L. (2006). An Initial Assessment of the Systemic Pharmacokinetics of Botulinum Toxin. *J. Pharmacol. Exp. Ther.* 318, 1343–1351. doi:10.1124/jpet.106.104661

Reavis, H. D., Chen, H. I., and Drapkin, R. (2020). Tumor Innervation: Cancer Has Some Nerve. *Trends. Cancer* 6, 1059–1067. doi:10.1016/j.trecan.2020.07.005

Rust, A., Leese, C., Binz, T., and Davletov, B. (2016). Botulinum Neurotoxin Type C Protease Induces Apoptosis in Differentiated Human Neuroblastoma Cells. *Oncotarget* 7, 33220–33228. doi:10.18632/oncotarget.8903

Simeoni, M., Magni, P., Cammia, C., De Nicolao, G., Croci, V., Pesenti, E., et al. (2004). Predictive Pharmacokinetic-Pharmacodynamic Modeling of Tumor Growth Kinetics in Xenograft Models after Administration of Anticancer Agents. *Cancer Res.* 64, 1094–1101. doi:10.1158/0008-5472.can-03-2524

Simpson, L. (2013). The Life History of a Botulinum Toxin Molecule. *Toxicon* 68, 40–59. doi:10.1016/j.toxicon.2013.02.014

Ulloa, F., Gonzàlez-Juncà, A., Meffre, D., Barrecheguren, P. J., Martínez-Mármol, R., Pazos, I., et al. (2015). Blockade of the SNARE Protein Syntaxin 1 Inhibits Glioblastoma Tumor Growth. *PLoS One* 10, e0119707. doi:10.1371/journal.pone.0119707

U.S. Food and Drug Administration (2009). U.S. Food and Drug Administration. Availableat: https://www.accessdata.fda.gov/drugsatfda_docs/nda/2009/125274s000_PharmR.pdf (Accessed October 12, 2021).

U.S. Food and Drug Administration (2010). U.S. Food and Drug Administration. Availableat: https://www.accessdata.fda.gov/drugsatfda_docs/nda/2010/125360s000PharmR.pdf (Accessed October 12, 2021).

U.S. Food and Drug Administration (2011). U.S. Food and Drug Administration. Availableat: https://www.accessdata.fda.gov/drugsatfda_docs/bla/2011/103000Orig1s5232.pdf (Accessed October 12, 2021).

U.S. Food and Drug Administration. Center for Drug Evaluation and Research. U.S (2005). Guidance for Industry: Estimating the Maximum Safe Starting Dose in Initial Clinical Trials for Therapeutics in Adult Healthy Volunteers. Availableat: https://www.fda.gov/media/72309/download (Accessed October 12, 2021).

Walker, T. J., and Dayan, S. H. (2014). Comparison and Overview of Currently Available Neurotoxins. *J. Clin. Aesthet. Dermatol.* 7, 31–39.

Wang, W., Li, L., Chen, N., Niu, C., Li, Z., Hu, J., et al. (2020). Nerves in the Tumor Microenvironment: Origin and Effects. *Front. Cel Dev. Biol.* 8, 601738. doi:10.3389/fcell.2020.601738

Conflict of Interest: Author W-HK, H-JR and SK are employed by Medytox Inc.

The remaining author declares that the research was conducted in the absence of any commercial or financial relationships that could be construed as a potential conflict of interest.

Publisher's Note: All claims expressed in this article are solely those of the authors and do not necessarily represent those of their affiliated organizations, or those of the publisher, the editors and the reviewers. Any product that may be evaluated in this article, or claim that may be made by its manufacturer, is not guaranteed or endorsed by the publisher.

frontiers in Pharmacology

MINI REVIEW
published: 25 January 2022
doi: 10.3389/fphar.2022.842775

Feasibility of Growth Factor Agent Therapy in Repairing Motor Injury

*Qiaoyin Tan[1], Jiayu Li[2], Yuwen Liu[3], Xiaojuan Zhu[1] and Weide Shao[2]**

[1]College of Teacher Education, Zhejiang Normal University, Jinhua, China, [2]College of Physical Education and Health Sciences, Zhejiang Normal University, Jinhua, China, [3]Department of General Surgery, The First Affiliated Hospital of Jiangxi Medical College, Shangrao, China

Growth factors (GF), with the activity of stimulating cell growth, play a significant role in biology, medicine, and exercise physiology. In the process of exercise, human tissues are impacted, making cells suffer damage. Growth factor can accelerate the repair of damaged cells and regulate the synthesis of protein, so biological preparations of growth factors can be added to traditional therapies. A combination of growth factor biologics and conventional therapies may improve the efficiency of injury repair, but growth factor biologics may not produce any results. The feasibility of growth factor biologics in the treatment of motor injury was discussed. The research have shown that: 1) GF biological agent therapy is a very promising treatment for motor injury, which is based on the power of autologous growth factor (GFs) to accelerate tissue healing, promote muscle regeneration, increase angiogenesis, reduce fibrosis, and make the muscle injury rapid recovery. 2) There are various methods for delivering the higher dose of GF to the injured tissue, but most of them depend on the platelet release of GF. At the site of injury, there are several ways to deliver higher doses of GF to the injured tissue. 3) At present, the inhibition of GF is mainly through signal transduction inhibitors and inhibition of transcription factor production. 4) Pattern of GF during wound repair: GF directly regulates many key steps of normal wound repair, including inflammatory cell chemotaxis, division and proliferation of fibroblasts, keratinocytes and vascular endothelial cells, formation of new blood vessels, and synthesis and degradation of intercellular substances. 5) When GF promotes chronic wound healing, in most cases, certain GF can be used targeted only when *in vivo* regulation still cannot meet the need for repair.

Keywords: growth factor, growth factor agent therapy, motor injury, restorative therapy, repair therapy

OPEN ACCESS

Edited by:
Weiguo Li,
Harbin Institute of Technology, China

Reviewed by:
Yan Zhang,
Hunan Normal University, China
Yunrun Liu,
Hong Kong Baptist University, Hong Kong SAR, China

****Correspondence:***
Weide Shao
txsh@zjnu.cn

Specialty section:
This article was submitted to Translational Pharmacology, a section of the journal Frontiers in Pharmacology

Received: *24 December 2021*
Accepted: *05 January 2022*
Published: *25 January 2022*

Citation:
Tan Q, Li J, Liu Y, Zhu X and Shao W (2022) Feasibility of Growth Factor Agent Therapy in Repairing Motor Injury. Front. Pharmacol. 13:842775. doi: 10.3389/fphar.2022.842775

INTRODUCTION OF GROWTH FACTOR

Growth factors, which are cytokines with activity of stimulating cell growth, are composed of polypeptides and protein and are used to regulate cell growth and other cell functions. They are found in platelets, various adult and embryonic tissues, and most cultured cells (Burnouf et al., 2013). It can directly reach the nucleus to repair genes and promote cell division, reproduction and regeneration (Escobar et al., 2015). The general characteristic of GF biological preparations is that it can bind to cell membrane specific receptors and modulate the growth and development of cells. At present, Fibroblast growth factor (FGF), bone morphogenetic protein (BMP), nerve growth factor (NGF), granulocyte colony stimulating factor (G-CSF), platelet-derived growth factor (PDGF), transforming growth factor -α and transforming growth factor -β are all GF related to sports injury. Sports injuries are generally caused by professional sports and recreational sports injuries. Muscle

injury usually occurs after eccentric contraction, resulting in injury of tendon joint. When the degree of injury is different, the doctor's treatment method will also change. But mainly limited to ice compress, oppression, elevation, anti-inflammatory drugs, rest, and activities (Kasemkijwattana et al., 2000). Motor injury generally exists in muscle tissue, bone and other parts of the human body. The spontaneous regeneration ability of muscle tissues and bones is poor, and usually they cannot be fully recovered after injury (Lyu et al., 2020). Once the muscle and bone are damaged, due to the formation of adhesion and scar, the normal biological and biomechanical properties of tendon and bone cannot be completely regained (Giannotti et al., 2015). These abnormal arrangements and structures are often the risk factors for re-injury. Sports-related injuries include acute and chronic injuries. For soft tissues including muscles and ligaments, no matter what kind of injury is, it includes four processes: hemostasis, inflammation, proliferation of cells and matrix, wound maturation and remodeling. The difference lies in the time limit. In the above-mentioned processes, the cell and matrix proliferation stage can be said to be the most important stage of wound healing, determining whether the function of soft tissues is likely to return to the previous level. In addition, the stages of wound maturation and remodeling may involve the formation of scar tissue. Moreover, physiopathologic and metabolic factors in the body can affect any process of injury repair, resulting in prolonged time. In the process of potentially unfavorable repair, it leads to the instability of the soft tissue structure and the weakening of its function, resulting in re-injury. (Middleton et al., 2012)Movement-related GF can affect the cycle conversion of target cells to accelerate the division and proliferation of cells (Creaney and Hamilton, 2008), and promote the synthesis of DNA, RNA and protein in tissue repair cells, which can effectively eliminate low density lipoprotein in blood (Evanson et al., 2014). It plays a significant regulatory part in wound inflammation and infection, wound healing, differentiation of various cells (Gigante et al., 2013), and apoptosis of aging cells in the human body (Bachl et al., 2009).

GF formulations have described a number of fascinating results in sports medicine (Bisciotti et al., 2013), however, the biological characteristics of many different GF preparations are not well understood. A variety of GF preparations can be used in combination, which makes the effect better in the repair of sports injury. However, the effect of using GF preparation in the treatment of motor injury may also be poor, so we must pay attention to the implementation of the course of treatment and the role of the site. In this paper, the source, properties, action mechanism and possible effects of GF preparations in the field of sports injury were introduced in detail. The course results of future GF preparations for the treatment of sport injury were also summarized in order to promote the development of GF preparation therapy.

PERFORMANCE OF GROWTH FACTOR

Bone morphogenetic protein-2 and PDGF are the barrier membranes of osteogenic growth factors, and they have studied the loading and release kinetics of growth factors more through soaking in GF solution and culturing the membrane followed by freeze-drying, or mixing with polymer before evaporation to incorporate GF into the membrane (Zumstein et al., 2011). Membrane materials and other reagents are important factors that affect the adsorption capacity of the membrane, as well as the concentration of heparin, crosslinking agent and GF. Notably, there were two stages of release of GF from the membrane: the first stage consisted of a sudden release (approximately 1 day) and the second stage consisted of a slow release. In addition, the ability to exert biological activity at GFs concentrations controlled by release in the membrane has also been demonstrated by many studies. For example, white blood cell and platelet-rich fibrin (L-PRF) contains growth factors. L-PRF clots were slowly released with increasing GF1, PDGF-AB over the first 8 h, and within the first 7 days increased complete release of growth factors GF1, VEGF, and MPO and then decreased to near zero at Day 28.

Studies have shown that there are several methods for delivering higher doses of GF to injured tissues, but most rely on platelet release of GF. The alpha particles of platelets contain GF [insulin-like GF-1, vascular endothelial GF, and transformed GF-β (1)],etc. Platelet-rich plasma is usually analyzed for peripheral blood using different types of centrifugation, and different separation methods result in different distributions of platelet and leukocyte counts (Pochini et al., 2016). A standard L-PRF centrifugation protocol at 400 ×g has been shown to have the highest concentrations of platelets and leukocytes (Zumstein et al., 2012).

Plasma (PRGF) therapy, direct injection and hydrogel incorporation can be realized at the injury site as can be seen in **Figure 1**. 1) Plasma treatment refers to the reinfusion of plasma in the body. After removing red and white blood cell, platelets, and liquid components from that blood, the remaining material contain large amounts of growth factors, coagulation factors, albumin, globulin, and various antibodies. 2) Direct injection, which can be used as a liquid injection preparation for damaging tendons or joints (Singh et al., 2020). Pure platelet-rich fibrin (P-PRF) and leukocyte and platelet-rich fibrin (L-PRF) are leukocyte-free and leukocyte-containing solid fibrin-based products, respectively, that can be used as bioactive healing biomaterials (Creaney et al., 2011). 3) Hydrogel therapy. Treatment of motor injury requires consistent skeletal muscle regeneration, complete healing as far as possible, and reduction of tissue fibrosis (Hwang et al., 2013). It has been studied that stem cells and basic fibroblast growth factor (BFGF) are incorporated into hydrogels to observe muscle cell regeneration in animal models of muscle tearing (Caballé-Serrano et al., 2019). The results showed that the rapid twitch muscle contraction at the injury site was markedly improved, and fibrosis was markedly reduced. Combined treatment with GF hydrogel results in restoration of function, revascularization and innervation with minimal fibrosis of the torn muscle. Thus, some of the GF hydrogel preparations could be used as a hopeful treatment for muscle cells' regeneration, and this part of the study needs to be further developed.

In terms of the effect of activator on promoting the use of GF, some studies have found that the activator used in combination

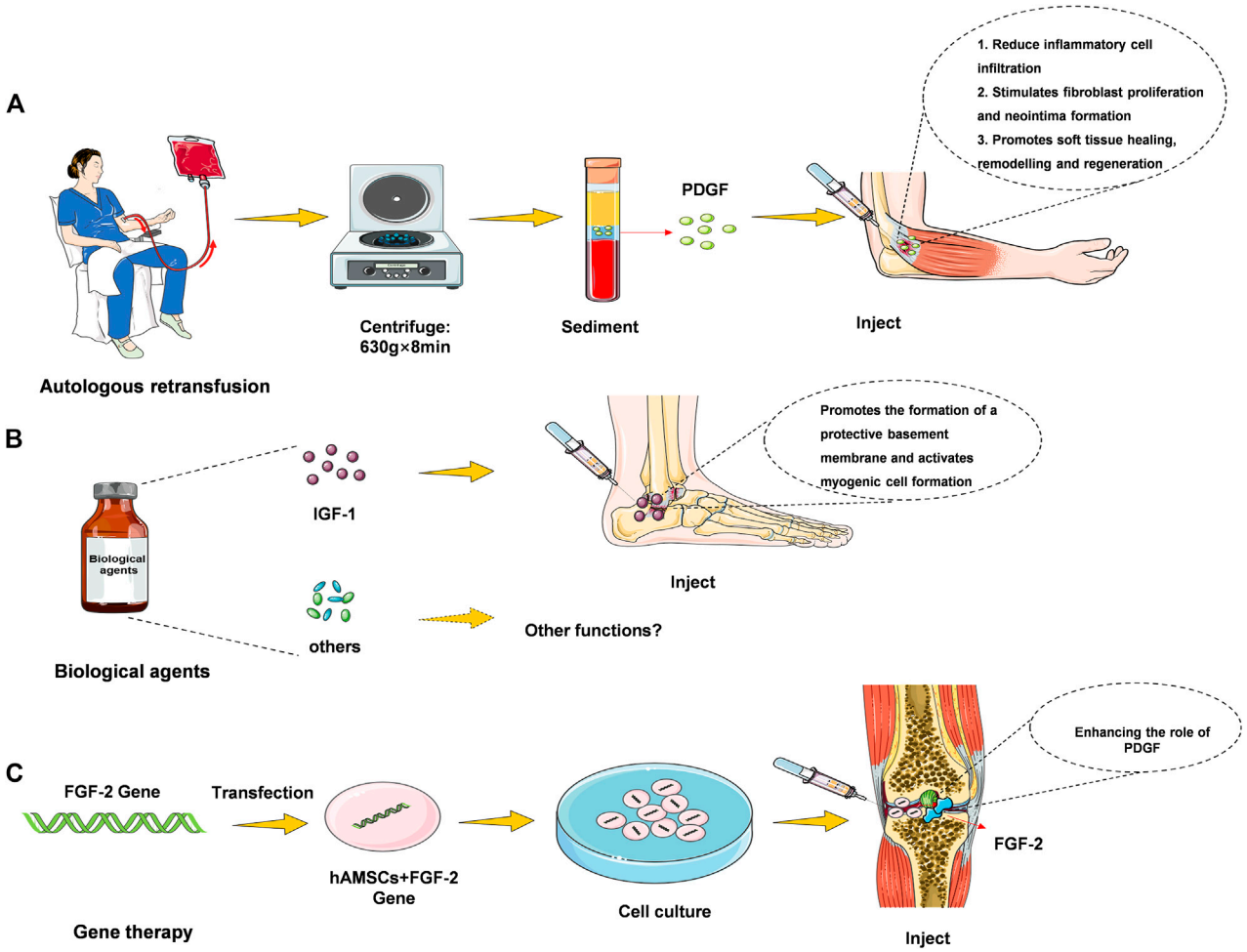

FIGURE 1 | Feasibility of growth factor preparation in the repair of sports injury.

with PRP is effective for promoting the concentration of GF. Such as the effect of activator calcium chloride on the concentration of GF, activated and inactive calcium chloride prepared by PRP under each condition, activated with calcium chloride resulted in significant increases in PDGF antibody and IGF-1 concentrations, and calcium chloride activated PRP resulted in the release of platelet-differentiated GF (Hamilton et al., 2015). The use of these activators affects the outcome after treatment of motor injury and is recommended for consideration in future treatment.

INHIBITION OF GROWTH FACTOR

GF is the key to regulate cell signaling pathway. Currently, the inhibition of GF is exerted through signal transduction inhibitors. It can interfere with the process of protein-protein interaction between GF and its receptor by targeting the extracellular protein-binding domain of GF receptor. Such as the signal transduction inhibitor compound CJJ300, inhibits tgf-beta signals by disrupting the process of formation of signal complexes that transform gf-beta (tgf-beta) (Wu et al., 2020). The compounds can be used for treating the elimination of downstream signals during the transmission of cell signaling pathways, the phosphorylation of GF in key factors of the pathways and the induction of molecular markers. Through these effects, signaling inhibitors can significantly inhibit cell migration.

In addition, there is a method for producing an inhibitory effect on GF by inhibition of a transcription factor. Mechanical GF (MGF) can significantly promote the migration of chondrocytes from growth plates, accompanied by YAP activation. YAP is a transcription regulator that modulate cell proliferation, survival, and differentiation, in order to control organ development and tissue regeneration (Jing et al., 2018). Knocking out YAP with the YAP inhibitor YAP siRNA inhibits MGF-induced migration. MGF promotes YAP activation through RhoA GTPase-mediated cytoskeletal recombination, and C3 toxin can also be used to inhibit RhoA and eliminate MGF-induced YAP activation.

TABLE 1 | Therapeutic use of growth factor preparation.

Growth factor	Extraction method	Save method	Disposal method	Treatment site	Treatment	Biological effect	Mechanism of action	References
Plasma rich in growth factors (PRGF)	630 g centrifuge 8 min to get the middle layer	stored at −80°C	10% calcium chloride activation	Achilles tendon of sheep injury	Infiltration injection	Regulating the inflammatory reaction of the achilles tendon injury, accelerating the tendon healing process and shortening the recovery time	Reduce tendon inflammatory cell infiltration	Daniel Aguilar-García et al.(2018) (Aguilar-Garcia et al. (2018)
Fibroblast growth factor (FGF-2)	NM	NM	HAMSCs were transfected with a lentivirus carrying the FGF-2 gene and combined with autologous platelet-rich plasma (PRP)	Rabbit bone-tendon interface	Local injection	HAMSCs transfected with FGF-2 gene in combination with autologous PRP can enhance tendon-to-bone healing	FGF-2 and PRP have synergistic effect	Jun Zhang et al.(2020) (Zhang et al. (2020)
(PRGF-Endoret)	460 g centrifuge 8 min to get the middle layer	stored at −80°C	10% calcium chloride activation	Medial collateral ligament of rabbit	Local injection	Local application of PRGF-Endoret advances early pace of ligament healing and recovery of structural features in rabbit models	PRGF-Endoret stimulates fibroblast proliferation and neovascularization	Tomokazu Yoshioka et al.(2013) (Yoshioka et al. (2013)
Insulin-like growth factor 1 (IGF-1)	NM	NM	NM	NM	Local injection	Exogenous insulin-like growth factor -1 accelerates the process of skeletal muscle post-traumatic repair induced by treadmill exercise	It can promote the formation of protective film of basement membrane, activate myoblasts to form myofilaments and myotubes, and promote fusion into muscle fibers	Wang, Qing et al.(2021) (Wang and Wang (2021)
Bevacizumab, an anti-vascular endothelial growth factor (VEGF) preparation	NM	NM	NM	Knee joint of rat with chronic athletic arthritis injury	Intra-articular injection	Bevacizumab Treatment Improves Cartilage Degradation in Rats Suffering from Chronic Exercise-induced Arthritis Injury	Bevacizumab treatment resulted in marked decreases in cytokine interleukin (IL)-1β, tumor necrosis factor (TNF)-α, matrix metalloproteinase (MMP)-1 and MMP-3 levels, and marked increases in transforming growth factor (TGF)-β1 levels	Lei Shang et al.(2018) (Shang et al. (2018)
(PRGF-Endoret)	460 g centrifuge 8 min to get the middle layer	stored at −80°C	10% calcium chloride activation	Knee joint with anterior cruciate ligament (ACL) tear	Intra-articular injection	PRGF-Endoret Promotes Exercise Recovery in Athletes with Cases of Instability Caused by ACL Tears	NM	Roberto Seijas et al.(2014) (Seijas et al. (2014)
(PRGF)	460 g centrifuge 8min to get the middle layer	stored at −80°C	10% calcium chloride activation	Knee joint cartilage of young football player	Intra-articular injection	Promote that complete healing of the articular cartilage to be obviously accelerate	NM	Mikel Sánchez et al.(2003) (Mikel Sanchez et al., 2003)
(PRGF)	460 g centrifuge 8 min to get	stored at −80°C	10% calcium chloride activation	Ankle joint of player with anterior tibiofibular	Intra-articular injection	Combined joint re-stabilization with less long-term residual pain	NM	Lior Laver et al.(2015) (Laver et al. (2015)

(Continued on following page)

TABLE 1 | (*Continued*) Therapeutic use of growth factor preparation.

Growth factor	Extraction method	Save method	Disposal method	Treatment site	Treatment	Biological effect	Mechanism of action	References
	the middle layer			ligament (AITFL) injury				
(PRGF)	460 g centrifuge 8 min to get the middle layer	stored at −80°C	10% calcium chloride activation	Type III injured ankle ligament	Intra-articular injection	Lower the ankle to show signs of instability and return to previous athletic activity	The entry of growth factors into the injured tissue promotes the healing and remodeling of the soft tissues for regeneration. At lower interleukin levels, the inflammatory healing phase is inhibited, pain is alleviated, and the process of repair and regeneration is accelerated	R Frei et al.(2008) (Frei et al. (2008)

With the development of GF biological agents, many studies began to study GF inhibitors to achieve the purpose of inhibiting GF and controlling its action mechanism.

THE EFFECTS OF GROWTH FACTOR PREPARATION

Positive Impact

Pattern of GF in the process of wound repair: GF directly regulates many key steps of normal wound repair, including inflammatory cell tropism, division and proliferation of fibroblasts, keratinocytes and vascular endothelial cells, formation of new blood vessels, and synthesis and degradation of intercellular substance (Mishra et al., 2012). The presence of GF contributes to the healing and remodeling of the soft tissues, and regeneration can begin before leukocytes infiltrate the affected sites. At low interleukin levels, the inflammatory phase of healing is inhibited, pain is alleviated, and the process of repair and regeneration is accelerated (Sanchez et al., 2009). GF mimics the clotting physiological events of thrombin-induced fibrin formation and platelet activation and has the key advantage of not having tissue necrosis effects and being biodegradable by body enzymes. Clinically, most of the platelet-rich GF biomaterials are used to achieve wound healing (Seijas et al., 2014), repair soft and hard tissues (Scala et al., 2014), and stimulate bone tissue regeneration (Zhang et al., 2020). They have recently been evaluated in the repair of knee osteoarthritis and muscle damage (Huang et al., 2020), and platelet GF opens up new prospects for regenerative medicine.

When being applied to the repair of articular cartilage injury and meniscus injury, the patients can move more smoothly when being injected with the GF, and the discomfort is obviously relieved (Shang et al., 2018); and the method is quite effective for treating pain of patients with osteoarthritis. In the area between the pits and the fixed fragments injected with a number of growth factors in autologous plasma, in the case with a poor prognosis, the complete healing of the articular cartilage was significantly accelerated, the functional results were good, and the asymptomatic motor activity could be quickly restored (Sanchez et al., 2003). When being applied to the injury of anterior cruciate ligament and achilles tendon, the GF biological preparation promotes the process of "ligament ingrowth, creeping substitution and bone tendon healing" of the injured ligament (Rizzello et al., 2012) and the surgically reconstructed ligament (Anitua et al., 2014). Studies have found that bone marrow mesenchymal stem cells transfected with FGF-2 gene compound with autologous PRP transplantation can promote extraarticular tendon-bone healing, particularly for acute exercise-related tendon-ligament injury (Laver et al., 2015). The use of PRGF for fear of partial anterior cruciate ligament tears, with the preservation of an intact bundle, can guarantee a high success rate in the recovery from the motor injury (Volpi et al., 2010; Yoshioka et al., 2013).

It has more obvious effect when being used for the treatment of "heel pain" of plantar fasciitis compared with the "local sealing treatment". Local injection of exogenous insulin-like growth factor-1 (IGF-1) can stimulate the proliferation of myoblasts and accelerate the process of repair (Wang and Wang, 2021). It can be used for the treatment of shoulder arthritis (subacromial and bilateral tendonitis), traumatic or degenerative joint swelling and synovitis, and helps to relieve swelling and pain. The level of evidence is determined by the number of high-quality studies with consistent findings. Patients with ankylosing spondylitis used in the knee joint and sacroiliac joint, have achieved good curative effect, in addition to pain relief, laboratory indicators of erythrocyte sedimentation rate and C-reactive protein also fell to the normal range after 1 month of treatment (Aguilar-Garcia et al., 2018). Regarding the treatment of tendonitis and tenosynovitis, for patients who are resistant to first-line physical therapy such as eccentric load, ABI or PRP injection is an effective second-line treatment to improve clinical results (Sandrey, 2014). The GF biological preparation can also be applied to the treatment of shoulder, elbow, wrist, hip, knee, ankle, sacroiliac joint, vertebral joint and the like (Frei et al., 2008).

Negative Effect

1) The surrounding environment of wound healing contains protein GF. Its content changes during the whole release process. When the effect of GF is inhibited, wound repair will encounter obstacles (Shen et al., 2021). 2) The surrounding environment of chronic trauma contains low GF activity. 3) When GF promotes the healing of chronic wounds, in most cases, exogenous GF does not necessarily need to be supplied for wound repair, and only when *in vivo* regulation still cannot meet the need for repair, such as some hard-to-heal injuries, can certain GF be used pointedly. For example, local application of IGF-1 in human body has been proved to rapidly stimulate tendon collagen synthesis. Then can IGF-1 injection enhance tendon synthesis and tissue structure in patients with patellar tendon disease? Although clinical responses were small and rapid with IGF-1 injection in combination with training, no additional long-term effects of intratendon IGF-1 on structure and clinical outcome were observed in patients with patellar tendon disease (Olesen et al., 2021). As another example of meniscus injury, the local application of vascular growth factor, vascular endothelial growth factor could theoretically promote healing of the meniscus tear in the avascular zone, however, no meniscus healed completely in this treatment group. It was found that topical application of vascular endothelial growth factor through PDLLA-coated sutures did not promote meniscus healing (Petersen et al., 2007).

Therefore, GF may not always be a hopeful tool for repairing damage, which is related to the site of sports injury, the design of treatment, the number and type of growth factor injections, and further research is needed to clarify the ineffective mechanism.

CONCLUSION AND PROSPECT

Muscle damage is a common cause of long-term severe pain and limb disability. Recovery from muscle damage caused directly or indirectly by exercise is a complex but well-defined process that includes degeneration, inflammation, regeneration, and fibrosis. Biological agents, such as IGF-1, MGF, PDGF, and TGF-β have been discussed in clinical treatment. They have the potential not only to treat athletic injuries but also to be a centre of interest for stimulant abusers as biotechnologies that achieve good athletic performance but are not yet fully understood.

The research have shown that: 1) GF biological agent therapy is a very promising treatment for motor injury, which is based on the power of autologous growth factor (GFs) to accelerate tissue healing, promote muscle regeneration, increase angiogenesis, reduce fibrosis, and make the muscle injury rapid recovery. 2) There are various methods for delivering the higher dose of GF to the injured tissue, but most of them depend on the platelet release of GF. At the site of injury, there are several ways to deliver higher doses of GF to the injured tissue. 3) At present, the inhibition of GF is mainly through signal transduction inhibitors and inhibition of transcription factor production. 4) Pattern of GF during wound repair: GF directly regulates many key steps of normal wound repair, including inflammatory cell chemotaxis, division and proliferation of fibroblasts, keratinocytes and vascular endothelial cells, formation of new blood vessels, and synthesis and degradation of intercellular substances. 5) When GF promotes chronic wound healing, in most cases, certain GF can be used targeted only when *in vivo* regulation still cannot meet the need for repair.

To date, most treatments for muscle injury with GF biologics have been due to limited experimental and clinical data or only empirical trials. Therefore, we need more experimental studies, including the specific GFs to quantify the release of PRP, angiogenesis, myogenesis and functional recovery data, as well as other mechanisms of GF repair, to finally verify the repair hypothesis of GF biological agents in the treatment of muscle injury and open a new journey for its wide clinical application. Currently, there is a large amount of data on the pathophysiology of muscle injury in the relevant studies.

AUTHOR CONTRIBUTIONS

All authors listed have made a substantial, direct, and intellectual contribution to the work and approved it for publication.

REFERENCES

Aguilar-García, D., Fernández-Sarmiento, J. A., Granados, M. d. M., Morgaz, J., Navarrete, R., Carrillo, J. M., et al. (2018). Effect of Plasma Rich in Growth Factors on the Early Phase of Healing of Surgically Severed Achilles Tendon in Sheep: Histological Study. *J. Appl. Anim. Res.* 46 (1), 471–478. doi:10.1080/09712119.2017.1337017

Anitua, E., Sánchez, M., Aguirre, J. J., Prado, R., Padilla, S., and Orive, G. (2014). Efficacy and Safety of Plasma Rich in Growth Factors Intra-articular Infiltrations in the Treatment of Knee Osteoarthritis. *Arthrosc. J. Arthroscopic Relat. Surg.* 30 (8), 1006–1017. doi:10.1016/j.arthro.2014.05.021

Bachl, N., Derman, W., Engebretsen, L., Goldspink, G., Kinzlbauer, M., Tschan, H., et al. (2009). Therapeutic Use of Growth Factors in the Musculoskeletal System in Sports-Related Injuries. *J. Sports Med. Phys. Fitness* 49 (4), 346–357.

Bisciotti, G. N., Eirale, C., and Sannicandro, I. (2013). Role of Growth Factors in Tendon Repair. *Medicina Dello Sport* 66 (3), 407–429.

Burnouf, T., Goubran, H. A., Chen, T. M., Ou, K. L., El-Ekiaby, M., and Radosevic, M. (2013). Blood-derived Biomaterials and Platelet Growth Factors in Regenerative Medicine. *Blood Rev.* 27 (2), 77–89. doi:10.1016/j.blre.2013.02.001

Caballé-Serrano, J., Abdeslam-Mohamed, Y., Munar-Frau, A., Fujioka-Kobayashi, M., Hernández-Alfaro, F., and Miron, R. (2019). Adsorption and Release Kinetics of Growth Factors on Barrier Membranes for Guided Tissue/bone Regeneration: A Systematic Review. *Arch. Oral Biol.* 100, 57–68. doi:10.1016/j.archoralbio.2019.02.006

Creaney, L., and Hamilton, B. (2008). Growth Factor Delivery Methods in the Management of Sports Injuries: the State of Play. *Br. J. Sports Med.* 42 (5), 314–320. doi:10.1136/bjsm.2007.040071

Creaney, L., Wallace, A., Curtis, M., and Connell, D. (2011). Growth Factor-Based Therapies Provide Additional Benefit beyond Physical Therapy in Resistant Elbow Tendinopathy: a Prospective, Single-Blind, Randomised Trial of Autologous Blood Injections versus Platelet-Rich Plasma Injections. *Br. J. Sports Med.* 45 (12), 966–971. doi:10.1136/bjsm.2010.082503

Escobar, G. L., Garuz, A. T., Anzalas, G. F., Villagra, V., Gudelis, M., and Pérez, L. T. (2015). Growth Factor's Treatment in Musculoskeletal Injuries. *Med. Sci. Sports Exerc.* 47 (5), 652. doi:10.1249/01.mss.0000478495.22477.a8

Evanson, J. R., Guyton, M. K., Oliver, D. L., Hire, J. M., Topolski, R. L., Zumbrun, S. D., et al. (2014). Gender and Age Differences in Growth Factor Concentrations from Platelet-Rich Plasma in Adults. *Mil. Med.* 179 (7), 799–805. doi:10.7205/milmed-d-13-00336

Frei, R., Biosca, F. E., Handl, M., and Trc, T. (2008). Conservative Treatment Using Plasma Rich in Growth Factors (PRGF) for Injury to the Ligamentous Complex of the Ankle. *Acta Chir Orthop. Traumatol. Cech* 75 (1), 28–33.

Giannotti, S., Dell'Osso, G., Bottai, V., Ghilardi, M., Bugelli, G., Lazzerini, I., et al. (2015). Treatment of Tendon Injuries of the Lower Limb with Growth Factors Associated with Autologous Fibrin Scaffold or Collagenous Scaffold. *Surg. Technol. Int.* 26, 324–328.

Gigante, A., Cianforlini, M., Manzotti, S., and Ulisse, S. (2013). The Effects of Growth Factors on Skeletal Muscle Lesions. *Joints* 1 (4), 180–186. doi:10.11138/jts/2013.1.4.180

Hamilton, B., Tol, J. L., Knez, W., and Chalabi, H. (2015). Exercise and the Platelet Activator Calcium Chloride Both Influence the Growth Factor Content of Platelet-Rich Plasma (PRP): Overlooked Biochemical Factors that Could Influence PRP Treatment. *Br. J. Sports Med.* 49 (14), 957–960. doi:10.1136/bjsports-2012-091916

Huang, J., Zhao, L., and Chen, D. (2020). "Growth Factors and Osteoarthritis," in *Encyclopedia of Bone Biology*. Editor M. Zaidi (Oxford: Academic Press), 632–640. doi:10.1016/b978-0-12-801238-3.11191-2

Hwang, J. H., Kim, I. G., Piao, S., Jung, A. R., Lee, J. Y., Park, K. D., et al. (2013). Combination Therapy of Human Adipose-Derived Stem Cells and Basic Fibroblast Growth Factor Hydrogel in Muscle Regeneration. *Biomaterials* 34 (25), 6037–6045. doi:10.1016/j.biomaterials.2013.04.049

Jing, X., Ye, Y., Bao, Y., Zhang, J., Huang, J., Wang, R., et al. (2018). Mechano-growth Factor Protects against Mechanical Overload Induced Damage and Promotes Migration of Growth Plate Chondrocytes through RhoA/YAP Pathway. *Exp. Cell Res* 366 (2), 81–91. doi:10.1016/j.yexcr.2018.02.021

Kasemkijwattana, C., Menetrey, J., Bosch, P., Somogyi, G., Moreland, M. S., Fu, F. H., et al. (2000). Use of Growth Factors to Improve Muscle Healing after Strain Injury. *Clin. Orthop. Relat. Res.* 370, 272–285. doi:10.1097/00003086-200001000-00028

Laver, L., Carmont, M. R., McConkey, M. O., Palmanovich, E., Yaacobi, E., Mann, G., et al. (2015). Plasma Rich in Growth Factors (PRGF) as a Treatment for High Ankle Sprain in Elite Athletes: a Randomized Control Trial. *Knee Surg. Sports Traumatol. Arthrosc.* 23 (11), 3383–3392. doi:10.1007/s00167-014-3119-x

Lyu, J., Chen, L., Zhang, J., Kang, X., Wang, Y., Wu, W., et al. (2020). A Microfluidics-Derived Growth Factor Gradient in a Scaffold Regulates Stem Cell Activities for Tendon-To-Bone Interface Healing. *Biomater. Sci.* 8 (13), 3649–3663. doi:10.1039/d0bm00229a

Middleton, K. K., Barro, V., Muller, B., Terada, S., and Fu, F. H. (2012). Evaluation of the Effects of Platelet-Rich Plasma (PRP) Therapy Involved in the Healing of Sports-Related Soft Tissue Injuries. *Iowa Orthop. J.* 32, 150–163.

Mishra, A., Harmon, K., Woodall, J., and Vieira, A. (2012). Sports Medicine Applications of Platelet Rich Plasma. *Curr. Pharm. Biotechnol.* 13 (7), 1185–1195. doi:10.2174/138920112800624283

Olesen, J. L., Hansen, M., Turtumoygard, I. F., Hoffner, R., Schjerling, P., Christensen, J., et al. (2021). No Treatment Benefits of Local Administration of Insulin-like Growth Factor-1 in Addition to Heavy Slow Resistance Training in Tendinopathic Human Patellar Tendons: A Randomized, Double-Blind, Placebo-Controlled Trial with 1-Year Follow-Up. *Am. J. Sports Med.* 49 (9), 2361–2370. doi:10.1177/03635465211021056

Petersen, W., Pufe, T., Stärke, C., Fuchs, T., Kopf, S., Neumann, W., et al. (2007). The Effect of Locally Applied Vascular Endothelial Growth Factor on Meniscus Healing: Gross and Histological Findings. *Arch. Orthop. Trauma Surg.* 127 (4), 235–240. doi:10.1007/s00402-005-0024-2

Pochini, A. C., Antonioli, E., Bucci, D. Z., Sardinha, L. R., Andreoli, C. V., Ferretti, M., et al. (2016). Analysis of Cytokine Profile and Growth Factors in Platelet-Rich Plasma Obtained by Open Systems and Commercial Columns. *Einstein (Sao Paulo)* 14 (3), 391–397. doi:10.1590/s1679-45082016ao3548

Rizzello, G., Longo, U. G., Petrillo, S., Lamberti, A., Khan, W. S., Maffulli, N., et al. (2012). Growth Factors and Stem Cells for the Management of Anterior Cruciate Ligament Tears. *Open Orthop. J.* 6, 525–530. doi:10.2174/1874325001206010525

Sánchez, M., Anitua, E., Orive, G., Mujika, I., and Andia, I. (2009). Platelet-Rich Therapies in the Treatment of Orthopaedic Sport Injuries. *Sports Med.* 39 (5), 345–354. doi:10.2165/00007256-200939050-00002

Sánchez, M., Azofra, J., Anitua, E., Andía, I., Padilla, S., Santisteban, J., et al. (2003). Plasma Rich in Growth Factors to Treat an Articular Cartilage Avulsion: a Case Report. *Med. Sci. Sports Exerc.* 35 (10), 1648–1652. doi:10.1249/01.MSS.0000089344.44434.50

Sandrey, M. A. (2014). Autologous Growth Factor Injections in Chronic Tendinopathy. *J. Athl Train* 49 (3), 428–430. doi:10.4085/1062-6050-49.3.06

Scala, M., Lenarduzzi, S., Spagnolo, F., Trapasso, M., Ottonello, C., Muraglia, A., et al. (2014). Regenerative Medicine for the Treatment of Teno-Desmic Injuries of the Equine. A Series of 150 Horses Treated with Platelet-Derived Growth Factors. *In Vivo* 28 (6), 1119–1123.

Seijas, R., Ares, O., Cuscó, X., Alvarez, P., Steinbacher, G., and Cugat, R. (2014). Partial Anterior Cruciate Ligament Tears Treated with Intraligamentary Plasma Rich in Growth Factors. *World J. Orthop.* 5 (3), 373–378. doi:10.5312/wjo.v5.i3.373

Shang, L., Xu, Y., Shao, C., Ma, C., and Feng, Y. (2018). Anti-Vascular Endothelial Growth Factor (VEGF) Antibody Ameliorates Cartilage Degradation in a Rat Model of Chronic Sports Arthritic Injury. *Med. Sci. Monit.* 24, 4073–4079. doi:10.12659/msm.906954

Shen, Z., Tsao, H., LaRue, S., Liu, R., Kirkpatrick, T. C., Souza, L. C., et al. (2021). Vascular Endothelial Growth Factor And/or Nerve Growth Factor Treatment Induces Expression of Dentinogenic, Neuronal, and Healing Markers in Stem Cells of the Apical Papilla. *J. Endod.* 47 (6), 924–931. doi:10.1016/j.joen.2021.02.011

Singh, N., Pandey, C. R., Tamang, B., and Singh, R. (2020). Scranton Type V Osteochondral Defects of Talus: Does One-Stage Arthroscopic Debridement, Microfracture and Plasma Rich in Growth Factor Cause the Healing of Cyst and Cessation of Progression to Osteoarthritis? *Malays Orthop. J.* 14 (2), 64–71. doi:10.5704/moj.2007.014

Volpi, P., Quaglia, A., Schoenhuber, H., Melegati, G., Corsi, M. M., Banfi, G., et al. (2010). Growth Factors in the Management of Sport-Induced Tendinopathies: Results after 24 Months from Treatment. A Pilot Study. *J. Sports Med. Phys. Fitness* 50 (4), 494–500.

Wang, Q., and Wang, F. (2021). Rehabilitation Therapy with Insulin-Like Growth Factor after Acute Skeletal Muscle Injury. *Rev. Bras Med. Esporte* 27 (3), 295–298. doi:10.1590/1517-8692202127032021_0135

Wu, H., Sun, Y., Wong, W. L., Cui, J., Li, J., You, X., et al. (2020). The Development of a Novel Transforming Growth Factor-β (TGF-β) Inhibitor that Disrupts Ligand-Receptor Interactions. *Eur. J. Med. Chem.* 189, 112042. doi:10.1016/j.ejmech.2020.112042

Yoshioka, T., Kanamori, A., Washio, T., Aoto, K., Uemura, K., Sakane, M., et al. (2013). The Effects of Plasma Rich in Growth Factors (PRGF-Endoret) on Healing of Medial Collateral Ligament of the Knee. *Knee Surg. Sports Traumatol. Arthrosc.* 21 (8), 1763–1769. doi:10.1007/s00167-012-2002-x

Zhang, J., Liu, Z., Tang, J., Li, Y., You, Q., Yang, J., et al. (2020). Fibroblast Growth Factor 2-induced Human Amniotic Mesenchymal Stem Cells Combined with Autologous Platelet Rich Plasma Augmented Tendon-To-Bone Healing. *J. Orthop. Translat* 24, 155–165. doi:10.1016/j.jot.2020.01.003

Zumstein, M. A., Berger, S., Schober, M., Boileau, P., Nyffeler, R. W., Horn, M., et al. (2012). Leukocyte- and Platelet-Rich Fibrin (L-PRF) for Long-Term Delivery of Growth Factor in Rotator Cuff Repair: Review, Preliminary Results and Future Directions. *Curr. Pharm. Biotechnol.* 13 (7), 1196–1206. doi:10.2174/138920112800624337

Zumstein, M. A., Bielecki, T., and Dohan Ehrenfest, D. M. (2011). The Future of Platelet Concentrates in Sports Medicine: Platelet-Rich Plasma, Platelet-Rich Fibrin, and the Impact of Scaffolds and Cells on the

Long-Term Delivery of Growth Factors. *Oper. Tech. Sports Med.* 19 (3), 190–197. doi:10.1053/j.otsm.2011.01.001

Conflict of Interest: The authors declare that the research was conducted in the absence of any commercial or financial relationships that could be construed as a potential conflict of interest.

Publisher's Note: All claims expressed in this article are solely those of the authors and do not necessarily represent those of their affiliated organizations, or those of the publisher, the editors and the reviewers. Any product that may be evaluated in this article, or claim that may be made by its manufacturer, is not guaranteed or endorsed by the publisher.

frontiers in Pharmacology

ORIGINAL RESEARCH
published: 08 February 2022
doi: 10.3389/fphar.2022.819728

Anti-Inflammatory and Anti-asthmatic Effects of TMDCT Decoction in Eosinophilic Asthma Through Treg/Th17 Balance

Yumei Zhou[1], *Haihong Zhao*[1], *Tieshan Wang*[2], *Xiaoshan Zhao*[1], *Ji Wang*[1]* *and Qi Wang*[1]*

[1]National Institute of TCM Constitution and Preventive Medicine, School of Chinese Medicine, Beijing University of Chinese Medicine, Beijing, China, [2]Beijing Research Institute of Chinese Medicine, Beijing University of Chinese Medicine, Beijing, China

Tuo-Min-Ding-Chuan decoction (TMDCT) is a Traditional Chinese Medicine (TCM) formula consisting of twelve herbs that can relieve the symptoms and treat allergic asthma. Yet, the underlying mechanism of action is still unclear. In this study, we investigated the effect of TMDCT in regulating Treg/Th17 cells immune balance and explored potential metabolic and gut biomarkers associated with Treg and Th17 cells in eosinophilic asthma mice treated by TMDCT. We found that TMDCT increases Treg cells percentage and decreases Th17 cells percentage in the ovalbumin (OVA) -induced eosinophilic asthma mice model. Furthermore, Imidazoleacetic acid, DL-glutamine, L-pyroglutamic acid, 2-deoxy-D-glucose were preliminary identified as biomarkers in plasma metabolites treated by TMDCT, meanwhile genus *Desulfovibrio*, genus *Butyricimonas* and genus *Prevotella 9* were preliminary identified as gut microbiota biomarkers after TMDCT treatment. These results provide an experimental foundation for the treatment of allergic asthma with Chinese herbal compounds.

Keywords: Tuo-Min-Ding-Chuan decoction, Treg/Th17, eosinophilic asthma, anti-inflammatory, anti-asthmatic

OPEN ACCESS

Edited by:
Songwen Tan,
Central South University, China

Reviewed by:
Wenhu Zhou,
Central South University, China
Muhammad Shahzad,
University of Health Sciences, Pakistan

***Correspondence:**
Ji Wang
doctorwang2009@126.com
Qi Wang
wangqi710@126.com

Specialty section:
This article was submitted to Translational Pharmacology, a section of the journal Frontiers in Pharmacology

Received: *22 November 2021*
Accepted: *24 January 2022*
Published: *08 February 2022*

Citation:
Zhou Y, Zhao H, Wang T, Zhao X, Wang J and Wang Q (2022) Anti-Inflammatory and Anti-asthmatic Effects of TMDCT Decoction in Eosinophilic Asthma Through Treg/Th17 Balance. Front. Pharmacol. 13:819728. doi: 10.3389/fphar.2022.819728

INTRODUCTION

Asthma is a chronic inflammatory disease which is difficult to control affects more than 300 million people worldwide. With current rising trends, it is expected that this number will reach 400 million people by 2025. According to some reports, there are nearly 250,000 asthma-related deaths each year, many of which are avoidable (Christiansen and Zuraw, 2019).

Inflammatory disorder in allergic asthma is characterized by broncho-construction, bronchial hyper-responsiveness, and even tissue damage and the most common type of asthma (National Asthma Education and Prevention Program, 2007). If not properly treated, allergic asthma can progress to chronic obstructive lung disease or other disease associated with airways and lung tissue. The burden of allergic diseases has increased over recent years, as evidenced by a high incidence of patients suffering from these diseases and incurring high financial costs (Bousquet et al., 2016). Over the years, anti-inflammatory drugs have been developed, such as inhaled steroids and bronchodilators that can relieve symptoms. Yet, existing drugs cannot completely cure the patient, and have an elevated recurrence rate. Moreover, conventional drugs have been associated with certain side effects. E.g., an inhaled corticosteroid (ICS), the dominant treatment in type 2-high asthmatic inflammation, can suppress the endocrine system, which assists body's immune system fight against infection, while long-term steroid treatments can lead to anxiety and depression.

Allergic asthma is induced by an abnormal type 2 immune response to inhaled allergens, such as house dust mites (HDM), grass pollen, animal dander, and mold (Caminati et al., 2018). In the airway, the inflammatory response is mainly caused by Th2 type inflammation, inducing cytokines IL-4, IL-5, and IL-13 overexpression, which consequently activate the expression of IgE and the infiltration of eosinophils and mast cells in the airway.

Previous studies have shown that the imbalance of Th1/Th2 cells may be involved in the pathogenesis of airway inflammation in asthma (Berker et al., 2017). Besides that, some recent studies suggested that insufficient Th1 cell differentiation is not the only cause leading to over-differentiation and activation of Th2 cells. It has been discovered that Treg cells have an essential role in regulating the body's immune balance. Dysfunctional Treg cells, unable to effectively suppress excessive Th2 response, may lead to asthma and other allergic diseases.

Th2-type inflammation is involved in all types of asthma (mild, moderate, and severe). Also, inflammation caused by Th17 cells has been associated with a progression of asthma (Israel and Reddel, 2017). The imbalance between Treg cells and Th cells such as Th1, Th2 and Th17 cell responses in allergic asthma is associated with the development of allergic asthma (Noval Rivas and Chatila, 2016). Genetic and immunological evidence suggested that Treg cells can promote tolerance to allergens and prevent allergic disorders (Palomares et al., 2014). Thus, it is believed that the inflammation of allergic asthma inflammation and increasing Treg cells number or stimulating the proliferation of immunosuppressive cells such as Treg cells is a new strategy for the treatment of allergic asthma.

Recently, some new drugs with the ability to exert Treg cells in the body's immune system or stimulate differentiation of Treg cells have been tested. Although great development has been achieved using allergen immunotherapy (AIT) and other immunotherapy, treatment of allergic asthma and its recurrence remains challenging. New treatment options that can regulate the immune balance of Treg/Th17 are currently emerging.

TMDCT is a TCM formula consisting of twelve herbs that can relieve the symptoms and treat allergic asthma. Nevertheless, the underlying mechanism of action is still unclear. TMDCT contain 12 kinds of traditional Chinese medicine, it can suppresses inflammation of allergic asthma and inhibit the degranulation of mast cell (Qin et al., 2021). In our study, we investigated the effect of TMDCT in regulating Treg/Th17 cells balance and explored potential metabolic and gut biomarkers associated with Treg and Th17 cells in eosinophilic asthma mice treated with TMDCT using non-targeted metabolome and 16S rDNA technology.

MATERIALS AND METHODS

Mice

BALB/c mice (female, 6–8 weeks old, 17–20 g) were obtained from Beijing Vital River Laboratory Animal Technology Co., Ltd in China. Keeping mice in specific pathogen-free conditions in Beijing University of Chinese Medicine. All mice were kept at a controlled room (25 ± 1°C, 45–60% humidity). All animal studies were conducted in accordance with the institutional animal care regulations of Beijing University of Chinese Medicine and were conducted in accordance with AAALAC and IACUC guidelines.

OVA-Induced Allergic Asthma Mice Model and Grouping

The OVA-induced eosinophilic asthma BALB/c mice model was constructed following a previously described approach (Dumas et al., 2018). Briefly, mice were intraperitoneally injected with 2 mg of OVA (Sigma-Aldrich, Cat#A5503) mixed with 2 mg Imject™ Alum Adjuvant (Invitrogen, Cat#77161) and PBS on day 0 and day 14. From the 21st to 25th days post-injection, in the challenge phase, mice are continuously nebulized with 1% OVA for 30 min as shown in **Figure 1A**.

OVA-induced allergic asthma mice were then divided in the following groups: High-dose TMDCT group (40.56 g/kg/d TMDCT (H group)), Middle-dose TMDCT treatment group (20.28 g/kg/d TMDCT (M group)), Low-dose TMDCT treatment group (10.14 g/kg/d TMDCT (L group)), and positive group (dexamethasone 1 mg/kg/d). TMDCT, containing 12 kinds of Chinese medicine, was prepared as previously described (Qin et al., 2021). TMDCT and dexamethasone (1 mg/kg/d, a positive drug for suppressing eosinophilic asthma) were given daily at the same time from the 21st to 25th days 1 hour before challenge.

Detection of Measured Airway Responsiveness

We used 0, 6.25, 12.5, 25, and 50 mg/ml methacholine (mch) (Sigma, Cat#A2251) to detect enhanced pause (Penh), which reflected lung function according to noninvasive measurement of airway hyperresponsiveness by whole-body phelthysmography (WBP-4MR, TOW, China) (Sun et al., 2021).

Histological Sections and Pathology Scoring

Lungs were fixed with 4% paraformaldehyde (PFA) at 4°C, after paraffin-embedded sections and stained them with hematoxylin and eosin (HE) (to examine cell infiltration detection) or periodic acid-schiff stain (PAS) (to examine mucus production) in lung tissues. Scoring of inflammatory cells and goblet cells was performed in at least three different fields for each lung section as described (Duan et al., 2004). The mean scores were calculated using five animals.

Bronchoalveolar Lavage Fluid, Serum Cytokines, and the Culture Supernatant of Treg and Th17 Cells Cytokines Analysis

Twenty-four hours after the last aerosol challenge, bronchoalveolar lavage (BAL) fluid was collected by syringe three times with 1 ml PBS containing 1% BSA. Eosinophils in BAL fluid were counted by cell sorting and counting instrument. Cytokine levels of IL-4, IL-5, IL-13, IL-10, IL-17A, IL-6 in BALF

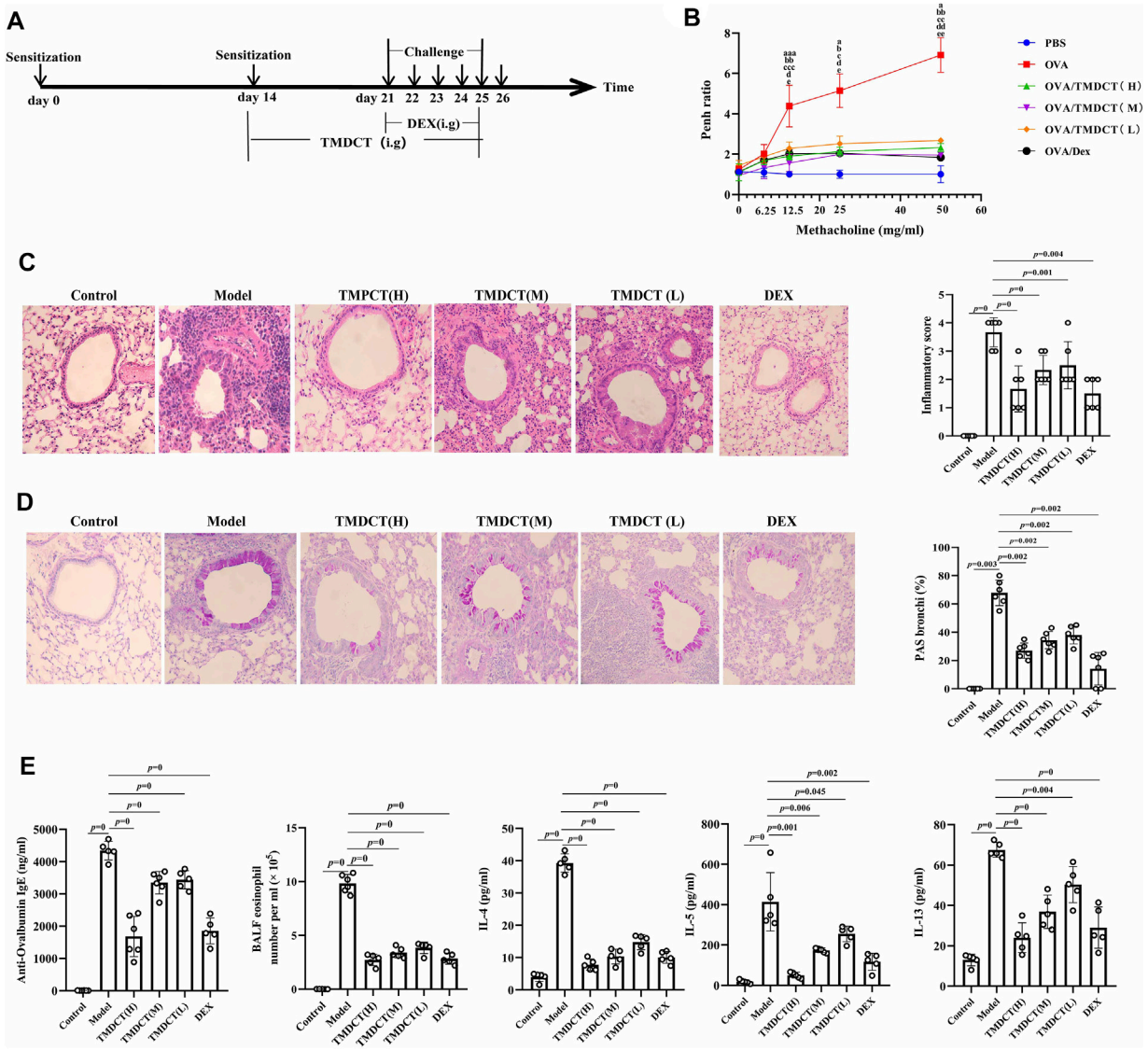

FIGURE 1 | TMDCT can alleviate allergic inflammation in eosinophilic asthma BALB/c mice. **(A)** Experimental protocol for eosinophilic asthma induced by OVA and treatment administration. **(B)** Lung function experiments. Detection the Penh value when the methacholine concentration is 0, 6.25, 12.5, 25, 50 mg/ml respectively. Penh ratio (average Penh in the 5-minute interval with methacholine divided by the average Penh in the 5-minute interval with PBS). a, $p < 0.05$ vs. Control; aa, $p < 0.01$ vs. Control; aaa, $p \leq 0.001$ vs. Control. b, $p < 0.05$ vs. TMDCT(H); bb, $p < 0.01$ vs. TMDCT(H); bbb, $p \leq 0.001$ vs. TMDCT(H). c, $p < 0.05$ vs. TMDCT(M); cc, $p < 0.01$ vs. TMDCT(M); ccc, $p \leq 0.001$ vs. TMDCT(M). d, $p < 0.05$ vs. TMDCT(L); dd, $p < 0.01$ vs. TMDCT(L); ddd, $p \leq 0.001$ vs. TMDCT(L). **(C)** Left: HE staining of lung tissues; Right: Inflammatory score results. **(D)** Left: PAS staining of lung tissues; Right: Total lung inflammation was defined as the average of the peribronchial and perivascular inflammation scores. **(E)** Detection if specific OVA-IgE in serum; eosinophils count in BALF; detection of cytokines IL-4, IL-5, IL-13. All the values are expressed as mean +/- SEM. n = 4-5 animals per group.

were analyzed using a premixed AimPlex™ multiplex-assay kit (Cat#T2C0710709), TGF-β was analyzed using a premixed AimPlex™ multiplex-assay kit (Cat#B111206); OVA-specific IgE in serum was detected by ELISA kit (Cayman, Cat#500840).

Flow Cytometry Detection of Treg and Th17 Cells in Spleen Tissues

The spleen tissue was aseptically removed and prepared into a single-cell suspension. For Th17 ($CD3^+CD4+IL17A+$) cells and Treg cells ($CD3^+CD4^+$ CD25 + FOXP3+) detection, the cells were stimulated by cocktail A for 4 h (BD, Cat# 550583). Samples were then washed and re-suspended in 1 × PBS stained with FVS 780 (BD, Cat#565388) to discriminate viable cells and then incubated with various surface markers. Consequently, samples were fixed by eBioscience Fix/Perm (Cat#00-5523-00) or BD Fix/Perm buffer kit (Cat#554714) to destroy the cell membrane and then were stained with FOXP3 (eBioscience, Cat#17-5773-82), IL-17A (BD, Cat# 564169). In the study, CD3 (BD, Cat# 557,666), CD4 (BD, Cat# 552,775) and CD25 (BD, Cat# 558642) were used.

Finally, samples were analyzed with the LSR Fortessa cell analyzer (BD) and BD FACSDiva 8.0.3 software.

Real-Time PCR Detection of Foxp3 and RORγt mRNA

Foxp3 and RORγt mRNA in the lung tissues were detected. RNA extraction kit (Tiangen Biotech (Beijing) co, LTD, Cat#DP419) was used. RNA reverse transcription into cDNA using a cDNA Synthesis Kit (ThermoFisher, Cat#K1622). The primers sequence was the following: β-actin (FP: GACCCAGATCATGTTTG AGACCT; RP: TCCAGGGAGGAAGAGGATGC); RORγ (FP: CGCACCAACCT CTTTTCACG; RP: TGGCAAACTCCACCA CATACTG); Foxp3 (FP: CTTCAAGT ACCACAATATGCGACC; RP: GCGAACATGCGAGT AAACCAA).

Untargeted Metabolomics Detection of Plasma

Plasma was collected with 1.5 ml Eppendorf Tubes containing EDTA (ethylene diamine tetraacetic acid), which were centrifuged at 4°C by 1,500 g, 15 min. Rremove the protein by Methanol/acetonitrile (1:1, v/v) and centrifuged at 14000g, 4°C for 15 min. All LC-MS analyses were performed at Shanghai Applied Protein Technology Co., Ltd.

R package (ropls) was used to analyzed the processed data. Unsupervised principal component analysis (PCA) and supervised orthogonal partial least squares discriminant analysis (OPLS-DA) were used to evaluate sample stability. The VIP (variables in the projection) value of the OPLS-DA model was calculated, metabolites with VIP $>$ 1, p-value $<$ 0.05 is considered to be the significant changed metabolites.

After multivariate and univariable analysis, searched the significant metabolites in the Human Metabolome database (http://www.hmdb.ca), METLIN (https://metlin. scripps.edu), KEGG (http://www.kegg.com) and Chemspider (http://www. chemspider.com/). Cytoscape software was used to perform enrichment analysis and visualization. Pearson correlation analysis was used to perform and determine the correlation between two variables. KEGG enrichment analysis was performed using MetaboAnalyst (www.metaboanalyst.ca). The volcano plot and clustering analysis were performed using R.

Gut Microbiota Analysis

Using CTAB/SDS method to extracte the total genome DNA. Then, the V3-V4 regions in 16S rDNA were amplified using a specific primer included in the barcode. Next, an Illumina Miseq/ HiSeq2500 platform was used to build a library. We used PCoA (Principal Co-ordinates Analysis) to study the similarity or difference of sample community composition, and LEfSe (LDA Effect Size) to quantify the biomarkers in different groups.

Statistical Analysis

In this study, t-test, one-way ANOVA test (Turkey or Dunnett), Wilcoxon rank-sum test, Kruskal–Wallis test or Wilcoxon rank-sum test was used. p value $<$ 0.05 was considered as statistically significant. Pearson analysis with R3.4.2 Heatmap was used to analyze the correlation between metabolites and other index, the correlation between gut microbiota and other index.

RESULTS

TMDCT Alleviates Airway Inflammation in BALB/C Mice With Eosinophilic Asthma

To evaluate the treatment effect of TMDCT in treating eosinophilic asthma, an OVA-induced eosinophilic asthma model was constructed as described in **Figure 1A**. The most significant effect of TMDCT(H) group in reducing cell infiltration (**Figure 1C**) and decreasing goblet cell hyperplasia was observed in the TMDCT(H) group (**Figure 1D**), further indicating that TMDCT can alleviate airway inflammation. Moreover, TMDCT reduced airway resistance (Penh ratio), which indicated that lung function in TMDCT with a high concentration group had the best effect (**Figure 1B**).

To investigate the role of TMDCT in allergic airway inflammation, we detected OVA-specific IgE levels in serum. TMDCT significantly decreased OVA-specific IgE concentration in serum (**Figure 1E**). Additionally, the eosinophils number in BALF was reduced, and IL-5 levels were decreased in BALF of the TMDCT group, especially in the H group (**Figure 1E**). Also, TMDCT significantly reduced IL-4 and IL-13 cytokines in BALF. These data suggested that TMDCT could alleviate allergic airway inflammation.

TMDCT can Increase Treg Cells Percentage and Decrease Th17 Cells Percentage in the Spleen

Th17 and Treg cells have important role in driving and restraining airway inflammation in patients with asthma (Seumois et al., 2020). To further investigate whether TMDCT can regulate immune response, we detected Treg and Th17 cells percentage in spleen tissues. Surprisingly, TMDCT increased Treg cells percentage and decreased Th17 cells percentage; the most significant effect was seen in the TMDCT(H) group (**Figures 2B,C**).

Next, we analyzed TGFβ, IL-10, IL-6, and IL17A cytokines in BALF. As shown in **Figure 2A**, TMDCT stimulated TGFβ and IL-10 and suppressed IL-6 and IL17A (p value were all $<$0.05), which is consistent with the Treg and Th17 percentage detection.

At the mRNA level, TMDCT increased the Foxp3 (transcription factor of Treg cells) and decreased RORγt (transcription factor of Th17 cells) relative expression (**Figure 2D**). These data suggested that TMDCT could decrease Th17 cells percentage, and increase Treg cells percentage in spleen tissues, among them TMDCT(H) has the best effect.

Identification Plasma Metabolites of TMDCT

To further explore the mechanism of TMDCT in regulating the immune balance in eosinophilic asthma, we examined potential plasma metabolite biomarkers of TMDCT. The TMDCT with a

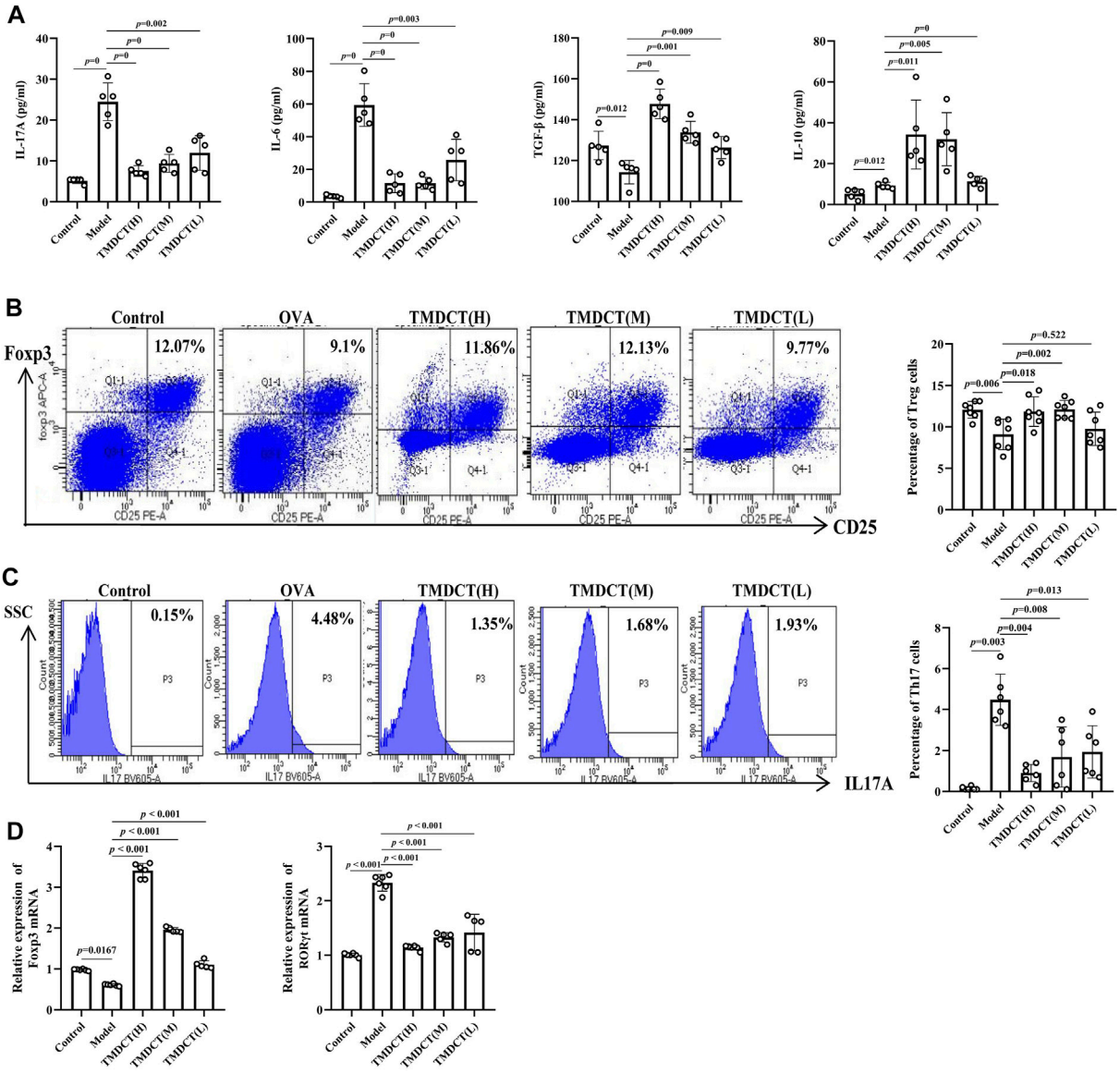

FIGURE 2 | TMDCTregulate Treg/Th17 balance in eosinophilic asthma BALB/c mice. **(A)** Detection of cytokines (IL-17A, IL-6, TGF-β, IL-10). **(B,C)** Left: intracellular staining FOXP3+ and IL-17 in CD4+ T cells in spleen tissue. Right: statistic data of FOXP3+, IL-17+ percentages. **(D)** Real-time PCR data of FOXP3 and RORγt mRNA expression in lung tisue. All the values are expressed as mean +/- SEM. n = 5-7 animals per group.

high concentration was used, and the untargeted metabolomics technology was used in this experiment. As seen in **Figure 3A**, OPLA-DA analysis found the following: 0.3 < Q2<0.384 (in POS mode) < 0.5, 0.3 < Q2=0.329 (in NEG mode) < 0.5, suggesting that the detected model was stable. The upregulated and downregulated metabolites in positive and negative mode can be shown in **Figure 3B**, Hierarchical cluster of significant difference metabolites (VIP >1, *p*-value < 0.05) analysis (**Figure 3C**) further suggested that metabolites in TMDCT or model group had a similar function; they participated in similar metabolite pathway or cell pathway. Finally, six differential metabolites in positive mode and 16 differential metabolites in the negative mode were detected (**Table 1**).

Next, we performed a KEGG enrichment analysis. As shown in **Figure 3D**, several pathways were identified. The significant metabolism pathway were our interest.

Metabolic Biomarkers in Plasma Associated With Treg and Th17 Cells in Eosinophilic Asthma Mice Treated With TMDCT

To understand the mechanism of TMDCT in regulating Treg/Th17 cells balance, the different metabolites between TMDCT and model group were used for correlation analysis, including Penh value (Mch:12.5, 25, 50 mg/ml), OVA-IgE, Eosinophils,

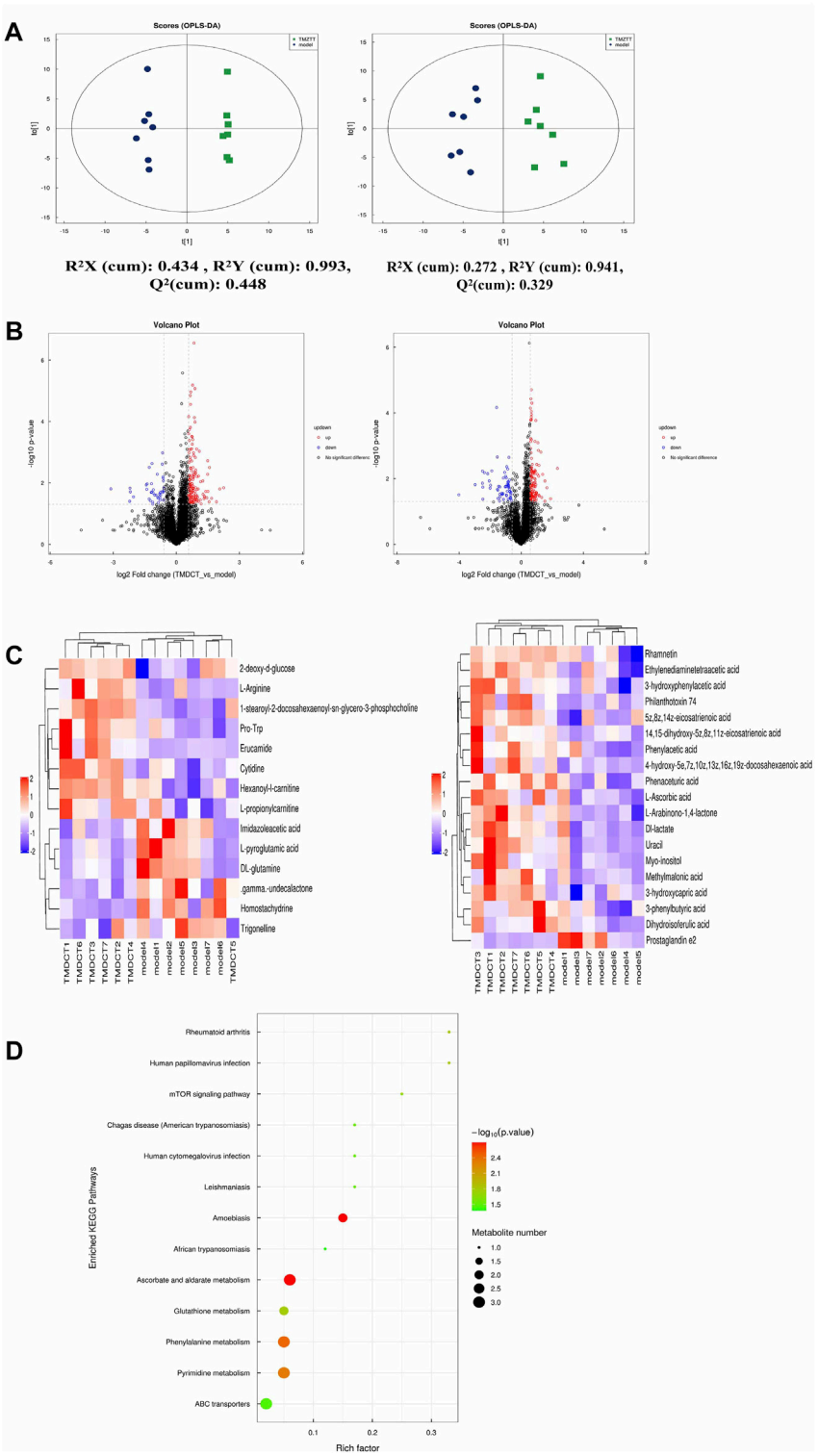

FIGURE 3 | Untarget plasma metabolism detection. **(A)** OPLS-DA analysis of LC/MS data in positive mode (left) and negative mode (right) from TMDCT(H) vs. Model. **(B)** Volcano map of differential metabolites in positive and negative mode. The metabolites with FC > 1.5, *p* value <0.05 are indicated by rose red, satisfying FC < 0.67, *p* value < 0.05 are shown in blue. **(C)** Hierarchical clustering heat map in positive mode (left) and negative mode (right). **(D)** Enriched KEGG pathways based on significant different metabolites between TMDCT(H) group and Model group. n =7 animals per group.

TABLE 1 | Differentiated plasma metabolites between model and TMDCT groups.

Name	ESI	VIP	Fold change	*p* Value
1-Stearoyl-2-docosahexaenoyl-sn-glycero-3-phosphocholine	+	8.885118	1.227872	2.63E-06
Cytidine	+	1.081076	1.403976	0.008353
Homostachydrine	+	1.038925	0.655271	0.008604
Pro-Trp	+	1.147062	1.587755	0.012893
Imidazoleacetic acid	+	1.009063	0.890448	0.019436
L-Arginine	+	1.963909	1.903922	0.023805
.gamma.-undecalactone	+	1.286511	0.830919	0.024305
Trigonelline	+	1.412927	0.751799	0.029667
DL-glutamine	+	2.401136	0.898755	0.030164
Hexanoyl-L-carnitine	+	1.586371	1.42347	0.031471
Erucamide	+	7.243441	3.201381	0.031635
L-pyroglutamic acid	+	3.855271	0.90852	0.032281
L-propionylcarnitine	+	2.100705	1.363916	0.03821
2-deoxy-D-glucose	+	1.228756	1.07907	0.039665
Phenaceturic acid	−	1.163085	1.433406	0.004378
L-Arabinono-1,4-lactone	−	1.619284	1.612233	0.005725
4-hydroxy-5e,7z,10z,13z,16z,19z-docosahexaenoic acid	−	1.555208	1.803301	0.006093
Uracil	−	4.134414	1.766824	0.006679
Ethylenediaminetetraacetic acid	−	20.93969	1.229205	0.006782
Philanthotoxin 74	−	1.093587	1.866347	0.010424
3-hydroxycapric acid	−	2.141189	1.513555	0.011763
5z,8z,14z-eicosatrienoic acid	−	1.640482	1.35079	0.013645
3-hydroxyphenylacetic acid	−	4.039256	1.598082	0.014398
Phenylacetic acid	−	2.600282	1.531541	0.016176
DL-lactate	−	7.134456	1.584984	0.018574
Prostaglandin e2	−	3.913766	0.249951	0.019496
L-Ascorbic acid	−	1.732841	1.944992	0.031862
Rhamnetin	−	2.374967	1.098614	0.034419
Myo-inositol	−	1.164396	1.312587	0.037616
14,15-dihydroxy-5z,8z,11z-eicosatrienoic acid	−	1.339304	1.790195	0.041816
Methylmalonic acid	−	1.270319	1.796966	0.04481
Dihydroisoferulic acid	−	1.221032	1.52335	0.047058
3-phenylbutyric acid	−	1.854654	1.270711	0.049813

Treg and Th17 cells percentage. In our study, L-Arabinono-1,4-lactone, Myo-inositol, DL-lactate, Uracil and 1-stearoyl-2-docosahexaenoyl-sn-glycero-3-phosphocholine were associated with Penh value (Mch: 12.5, 25, 50 mg/ml), OVA-IgE, Eosinophils, Treg and Th17 cells percentage (**Figure 4A**). There were obviously different ($p < 0.05$) in 1-stearoyl-2-docosahexaenoyl-sn-glycero-3-phosphocholine and Ethylenediaminetetraacetic acid either between the model and control group, or the model group and the TMDCT group (**Figure 4B**), they were all associated with OVA-IgE, Penh value (Mch: 12.5 mg/ml, 25 mg/ml, 50 mg/ml) and Eosinophil numbers while they has no correaltion with Treg or Th17 cells percentage (**Figure 4A**). Moreover, Imidazoleacetic acid, DL-glutamine, L-pyroglutamic acid were all increased in model group compared with control group, while they were all decreased in TMDCT treatment group (p value were all <0.05). Besides that, Imidazoleacetic acid, DL-glutamine, L-pyroglutamic acid were all associated with OVA-IgE, Penh value (Mch: 12.5 mg/ml, 25 mg/ml, 50 mg/ml), Eosinophil numbers and Th17 cells percentage (p value all <0.05). As shown in **Figure 4B**, 2-deoxy-D-glucose was decreased in model group when compared with control group ($p < 0.05$), while it increased in TMDCT treatment group ($p < 0.05$), it is also associated with OVA-IgE, Penh value (Mch: 12.5 mg/ml, 25 mg/ml, 50 mg/ml), Eosinophil number and Th17 cells percentage (p value all <0.05). The above four metabolites were not correlated with Treg cells, which indicated that they could also affect the Treg/Th17 balance in eosinophilic asthma. The changed metabolites were enriched to phenylalanine metabolism, pyrimidine metabolism, ascorbate and aldarate metabolism pathway, histidine metabolism, glutathione metabolism and metabolic pathways (**Figure 3D**).

Variation of Gut Microbiota and Key Phylotypes of Gut Microbiota in Response to OVA-Induced Eosinophilic Asthma Mice Treated by TMDCT

Gut bacteria have an essential role in the action of drugs. Thus, we detected gut microbiota in the Control group and TMDCT (H) group. As shown in **Figures 5A,B**, the differences in gut microbiota were found between the control and the model group. LEfSe (LDA Effect Size) software was used to discover high-dimensional biomarkers and reveal genome characteristics. LDA ˃ two was used as selection criteria in the study. Through STAMP analysis, we found that genus Rikenellaceae_*RC9_gut_group* ($p = 0.0497$), genus *Bifidobacterium* ($p = 0.0462$), genus *Rikenella* ($p = 0.0496$), genus *mouse gut metagenome* ($p = 0.0196$), genus *Butyricimonas* ($p = 0.0323$), genus *Prevotella* ($p = 0.0339$), genus *Enterococcus* ($p = 0.0029$),

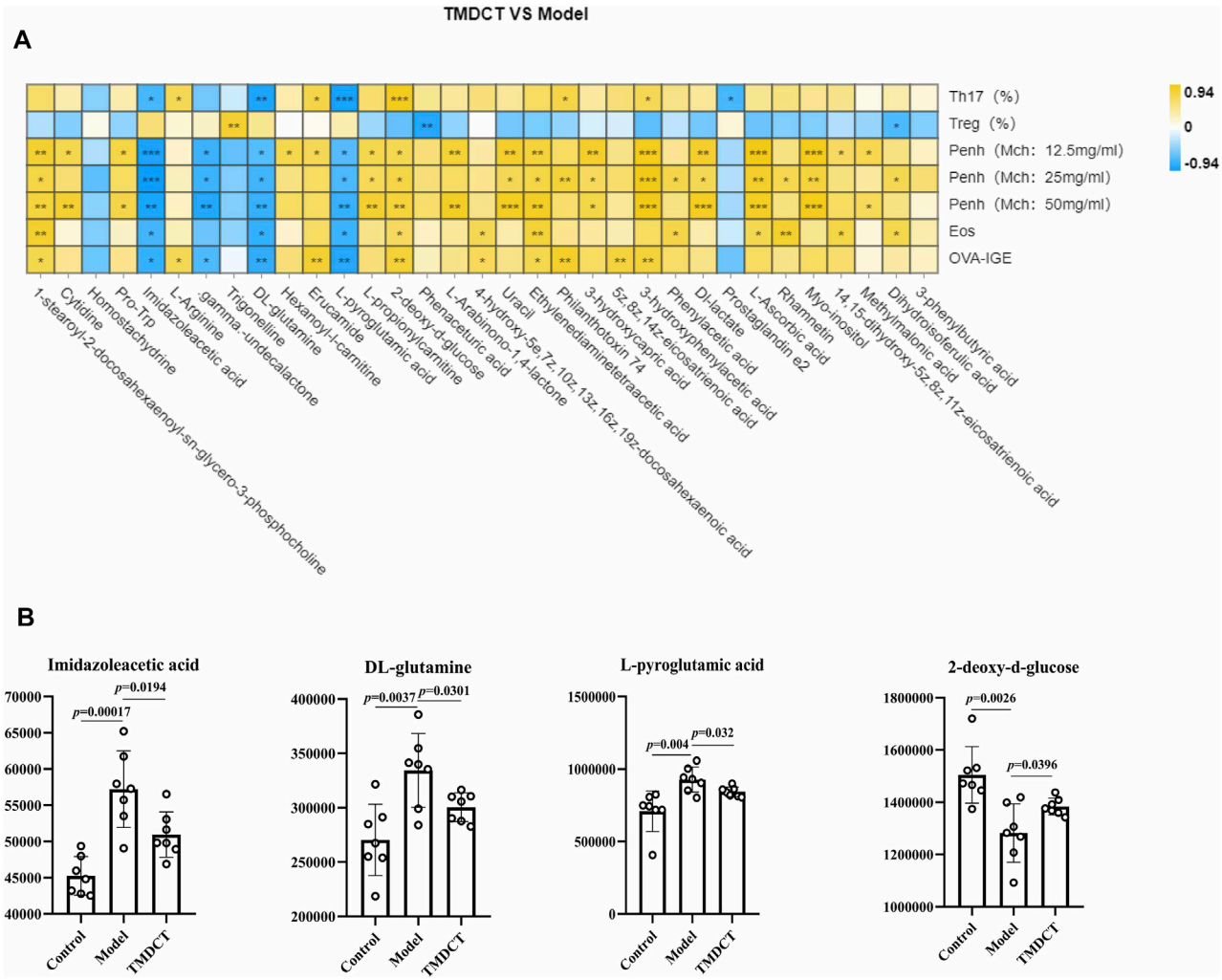

FIGURE 4 | Biomarker selection of plasma metabolites associated with Treg/Th17 balance. **(A)** Correlation analysis of differential plasma metabolites with specific OVA-IgE, Penh value (Mch: 12.5, 25, 50 mg/ml), Eosinophil number in BALF, Treg and Th17 cells percentage.*$p < 0.05$, **$p < 0.01$, ***$p < 0.001$. **(B)** Biomarker in plasma metabolites associated with Treg/Th17 balance. n = 7 animals per group.

genus *Peptoniphilus* (p = 0.0092), genus *Dialister* (p = 0.0175), genus *Corynebacterium* (p = 0.0082), genus *Dermabacter* (p = 0.0341), genus *Varibaculum* (p = 0.0255) were different in the TMDCT group compared to the model group in **Figures 5C,D**.

We used Pearson correlation analysis with R 3.4.2 Heatmap software to analyze the correlation. As shown in **Figure 6**, genus *Desulfovibrio*, genus *Muribaculum* and genus *Prevotella 9* were all associated with Penh value (Mch:12.5, 25, 50 mg/ml), OVA-IgE, Eosinophils number in BALF and Th17 cells percentage. These results indicated a correlation with Treg/Th17 balance in eosinophilic asthma treated by TMDCT.

DISCUSSION

TMDCT is a prescription of professor Qi Wang used to treat allergic asthma which has significant clinical effect. Yet, its mechanism of action still remains unclear. We further investigated the role of TMDCT in regulating Treg/Th17 cells balance in eosinophilic asthma.

The generation and maintenance of Treg cells and their suppressive cytokines (TGF-β, IL-10) are essential for the induction of allergen tolerance in allergic disease (Palomares et al., 2017). In addition, FOXP3+ Treg cells play a key role in maintaining peripheral tolerance by inhibiting the responsiveness to allergens (Noval Rivas and Chatila, 2016). It is also suggested that allergen-specific immunotherapy regimens increase the numbers of Treg cells (Radulovic et al., 2008). Moreover, some studies found that Treg cells have an irreplaceable role in preventing airway inflammation of allergic asthma (Tortola et al., 2019; Sun et al., 2020). While increasing immunosuppressive function of immunosuppressive cells such as Treg or Breg cells may be essential in a complete cure for allergic asthma.

IL-17A is upregulated in allergic asthma patients, and the upregulation of IL-17A is correlated with the severity of allergic

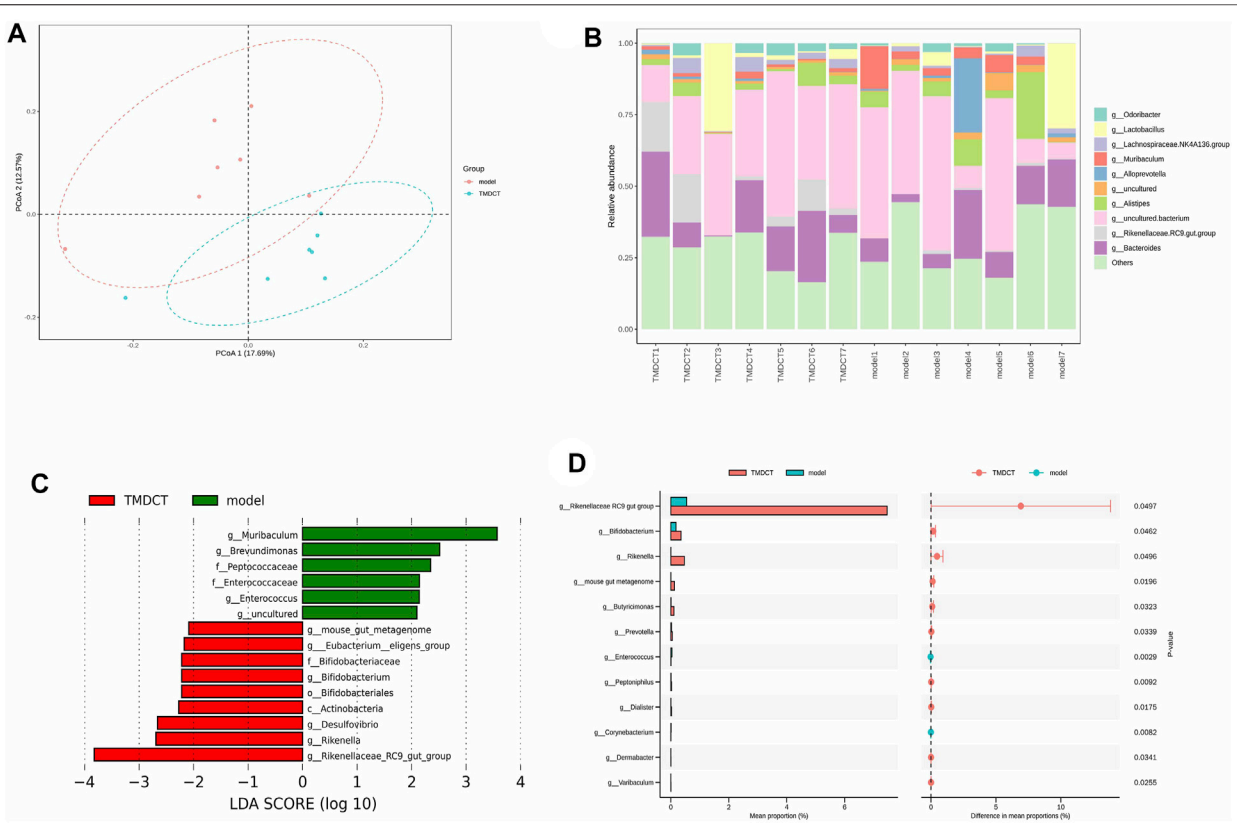

FIGURE 5 | TMDCT significantly changed gut microbiota composition. **(A)** Principal Co-ordinates Analysis (PCoA) analysis in each group. **(B)** Relative abundance of gut microbiota in each group. **(C)** Key phylotypes of gut microbiota in response to TMDCT interventions (LDA method was used). **(D)** Significantly difference gut microbiota analysis, STAMP difference analysis method was used. n = 7 animals per group.

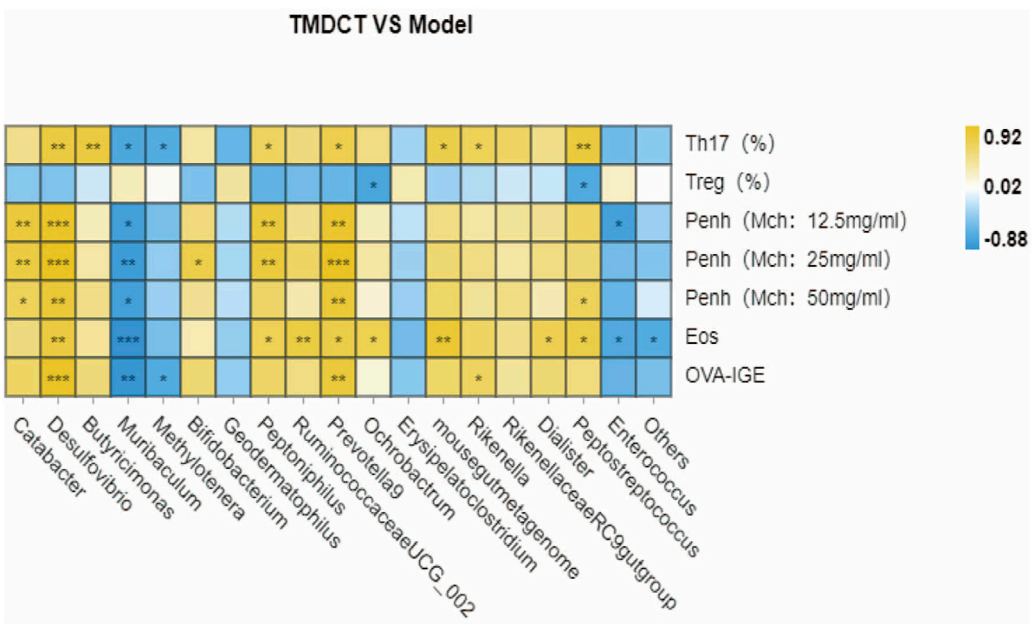

FIGURE 6 | Biomarker selection of gut microbiota associated with Treg/Th17 balance. Correlation of differentiated microbial phylotypes and specific OVA-IgE, Penh value (Mch:12.5, 25, 50 mg/ml), Eosinophil number in BALF, Treg and Th17 cells percentage. *$p < 0.05$, **$p < 0.01$, *** $p < 0.001$.

asthma. TGF-β induces the synthesis of the transcription factor of RORγt, which is specific for the Th17 cells (Ivanov et al., 2006). In this study, IL17A and TGF-β, transcription factor RORγt of Th17 cells, and transcription factor FOXP3 of Treg cells were used to analyze the balance of Treg/Th17 cells after TMDCT treatment. Our data suggested that TMDCT can suppress the symptoms of eosinophilic asthma and regulate the balance of Treg/Th17 cells. Interestingly, dexamethasone has similar anti-inflammatory and anti-asthma effects when compared with TMDCT in our study. TMDCT can also treat eosinophilic asthma by regulating Treg/Th17 immune balance the same as dexamethasone does (Kianmehr et al., 2017). While there are too many drawbacks of dexamethasone, a new drug should be explored.

Next, we used non-targeted metabolome to explore potential metabolic biomarkers in the plasma that were associated with Treg and Th17 cells in eosinophilic asthma mice treated with TMDCT. Imidazoleacetic acid, DL-glutamine, 2-deoxy-D-glucose, L-pyroglutamic acid were identified as plasma biomarkers of TMDCT and were all associated with Treg/Th17 cells balance. They were enriched in phenylalanine metabolism, pyrimidine metabolism, ascorbate and aldarate metabolism pathway, histidine metabolism, glutathione metabolism and metabolic pathways, etc. All of the plasma metabolites preliminary proved that TMDCT could regulate Treg/Th17 balance in eosinophilic asthma, which is also the advantage of multi-target effects of traditional Chinese medicine TMDCT. Previous studies found that glutamine can distinct regulate Th17 differentiation (Johnson et al., 2018), which can better explain the reasons for the change in Th17 cells percentage which is consistent with our results. While, until now there are no study found imidazoleacetic acid, 2-deoxy-D-glucose, L-pyroglutamic acid neithor can regulate Treg, Th17 cells nor regulate the differentiation of Treg or Th17 cells, which are not found associated with Treg/Th17 balance in allergic asthma.

Gut, lung, and skin microbiome exposures can also influence the occurrence and the development of allergy disease (Kemter and Nagler, 2019). The gut microbiota is essential in systemic immune regulatory network of allergic disease (Sommer and Bäckhed, 2013) and can regulate drug pharmacokinetics, such as absorption and distribution (Sousa et al., 2008; Tremaroli and Bäckhed, 2012; El Aidy et al., 2015; Zhang et al., 2018). Besides that, the gut-lung axis transfers metabolites and immunomodulatory signals between the gut and lungs. Many studies have shown an increase in the number of respiratory diseases due to deviations in gut ecology (Reddy et al., 2012; Budden et al., 2017). Omics technologies, including metabolomics, can be used to begin to understand relevant molecular changes. In this study, we used omics technology to detect the effect on of TMDCT in regulating Treg/Th17 cells, and then used Non-targeted metabolome and 16S rRNA technology to analyze the biomarkers after TMDCT treatment and relative factors correlated with Treg/Th17 balance. We found that gut microbiota genus Rikenellaceae_ *RC9_gut_group*, genus *Bifidobacterium*, genus *Rikenella*, genus *mouse gut metagenome*, genus *Butyricimonas*, genus *Prevotella*, genus *Enterococcus*, genus *Peptoniphilus*, genus *Dialister*, genus *Corynebacterium*, genus *Dermabacter*, genus *Varibaculum* were significantly different after TMDCT treatment.

Bifidobacterium is anti-inflammatory bacteria that can relieve allergic asthma in mice by regulating Th1/Th2 balance (Wang et al., 2020). Allergic patients with chronic asthma usually have low levels of *Bifidobacterium* (Hevia et al., 2016).

Oral administration of *Enterococcus faecalis* can suppress allergic asthmatic response associated with attenuation of Th17 cell development (Zhang et al., 2012). Fecal transplantation containing gut Rikenellaceae *bacteria* can alleviate acute liver injury in mice through regulating Treg/Th17 balance(Liu et al., 2021), while it cannot alleviate eosinophilic asthma. *Corynebacterium* may regulate Th17/Treg cells in the intestinal mucosal immunity (Zhang et al., 2019); However, there are still no studies in allergic asthma. So far, we have not find relevant research about genus *Desulfovibrio*, genus *Muribaculum* or genus *Prevotella 9* are related with Th17 cells percentage in eosinophilic asthma disease, they were the gut microbiota biomarker after TMDCT treatment.

This study has some limitations. First, only the BALB/c eosinophilic asthma model was used in this study. The effect of TMDCT should be further examined in other asthma models. Also, clinical research and other allergic asthma models are required to prove the mechanism of TMDCT in treating allergic asthma. Much more study of the biomarkers of TMDCT treatment should be developed to further explain the mechanism of TMDCT in treating allergic asthma, which will be a new strategy to treat allergic asthma.

DATA AVAILABILITY STATEMENT

The datasets presented in this study can be found in online repositories. The names of the repository/repositories and accession number(s) can be found below: https://www.ncbi.nlm.nih.gov/, PRJNA799688.

ETHICS STATEMENT

The animal study was reviewed and approved by Beijing University of Chinese Medicine.

AUTHOR CONTRIBUTIONS

YZ, JW, XZ and QW conceived and designed the experiments; YZ, HZ and TW performed the experiments; YZ analyzed the data and wrote the paper. All authors have read and agreed to the published version of the manuscript.

FUNDING

This work was supported by the General program of National Natural Science Foundation of China (No.81973715, 82174243), the General project of Beijing Natural Science Foundation (No.7202110), China Postdoctoral Science Foundation (No. 2021M690476) and the Innovation Team and Talents Cultivation Program of National Administration of Traditional Chinese Medicine (No: ZYYCXTD-C-202001).

REFERENCES

Berker, M., Frank, L. J., Geßner, A. L., Grassl, N., Holtermann, A. V., Höppner, S., et al. (2017). Allergies - A T Cells Perspective in the Era beyond the TH1/TH2 Paradigm. *Clin. Immunol.* 174, 73–83. doi:10.1016/j.clim.2016.11.001

Bousquet, J., Hellings, P. W., Agache, I., Bedbrook, A., Bachert, C., Bergmann, K. C., et al. (2016). ARIA 2016: Care Pathways Implementing Emerging Technologies for Predictive Medicine in Rhinitis and Asthma across the Life Cycle. *Clin. Transl Allergy* 6, 47. doi:10.1186/s13601-016-0137-4

Budden, K. F., Gellatly, S. L., Wood, D. L., Cooper, M. A., Morrison, M., Hugenholtz, P., et al. (2017). Emerging Pathogenic Links between Microbiota and the Gut-Lung axis. *Nat. Rev. Microbiol.* 15, 55–63. doi:10.1038/nrmicro.2016.142

Caminati, M., Pham, D. L., Bagnasco, D., and Canonica, G. W. (2018). Type 2 Immunity in Asthma. *World Allergy Organ. J.* 11, 13. doi:10.1186/s40413-018-0192-5

Christiansen, S. C., and Zuraw, B. L. (2019). Treatment of Hypertension in Patients with Asthma. Reply. *N. Engl. J. Med.* 381, 2279–1057. doi:10.1056/NEJMra180034510.1056/NEJMc1913646

Duan, W., Chan, J. H., Wong, C. H., Leung, B. P., and Wong, W. S. (20041950). Anti-inflammatory Effects of Mitogen-Activated Protein Kinase Kinase Inhibitor U0126 in an Asthma Mouse Model. *J. Immunol.* 172, 7053–7059. doi:10.4049/jimmunol.172.11.7053

Dumas, A., Bernard, L., Poquet, Y., Lugo-Villarino, G., and Neyrolles, O. (2018). The Role of the Lung Microbiota and the Gut-Lung axis in Respiratory Infectious Diseases. *Cell Microbiol* 20, e12966. doi:10.1111/cmi.12966

El Aidy, S., van den Bogert, B., and Kleerebezem, M. (2015). The Small Intestine Microbiota, Nutritional Modulation and Relevance for Health. *Curr. Opin. Biotechnol.* 32, 14–20. doi:10.1016/j.copbio.2014.09.005

Hevia, A., Milani, C., López, P., Donado, C. D., Cuervo, A., González, S., et al. (2016). Allergic Patients with Long-Term Asthma Display Low Levels of Bifidobacterium Adolescentis. *PloS one* 11, e0147809. doi:10.1371/journal.pone.0147809

Israel, E., and Reddel, H. K. (2017). Severe and Difficult-To-Treat Asthma in Adults. *N. Engl. J. Med.* 377, 965–976. doi:10.1056/NEJMra1608969

IvanovII, McKenzie, B. S., Zhou, L., Tadokoro, C. E., Lepelley, A., Lafaille, J. J., et al. (2006). The Orphan Nuclear Receptor RORgammat Directs the Differentiation Program of Proinflammatory IL-17+ T Helper Cells. *Cell* 126, 1121–1133. doi:10.1016/j.cell.2006.07.035

Johnson, M. O., Wolf, M. M., Madden, M. Z., Andrejeva, G., Sugiura, A., Contreras, D. C., et al. (2018). Distinct Regulation of Th17 and Th1 Cell Differentiation by Glutaminase-dependent Metabolism. *Cell* 175, 1780–e19. doi:10.1016/j.cell.2018.10.001

Kemter, A. M., and Nagler, C. R. (2019). Influences on Allergic Mechanisms through Gut, Lung, and Skin Microbiome Exposures. *J. Clin. Invest.* 129, 1483–1492. doi:10.1172/jci.12461010.1172/JCI124610

Kianmehr, M., Haghmorad, D., Nosratabadi, R., Rezaei, A., Alavinezhad, A., and Boskabady, M. H. (2017). The Effect of Zataria Multiflora on Th1/Th2 and Th17/T Regulatory in a Mouse Model of Allergic Asthma. *Front. Pharmacol.* 8, 458. doi:10.3389/fphar.2017.00458

Liu, Y., Fan, L., Cheng, Z., Yu, L., Cong, S., Hu, Y., et al. (2021). Fecal Transplantation Alleviates Acute Liver Injury in Mice through Regulating Treg/Th17 Cytokines Balance. *Sci. Rep.* 11, 1611. doi:10.1038/s41598-021-81263-y

NationalAsthmaEducationandPreventionProgram (2007). Expert Panel Report 3 (EPR-3): Guidelines for the Diagnosis and Management of Asthma-Summary Report 2007. *J. Allergy Clin. Immunol.* 120, S94–S138. doi:10.1016/j.jaci.2007.09.043

Noval Rivas, M., and Chatila, T. A. (2016). Regulatory T Cells in Allergic Diseases. *J. Allergy Clin. Immunol.* 138, 639–652. doi:10.1016/j.jaci.2016.06.003

Palomares, O., Akdis, M., Martín-Fontecha, M., and Akdis, C. A. (2017). Mechanisms of Immune Regulation in Allergic Diseases: the Role of Regulatory T and B Cells. *Immunol. Rev.* 278, 219–236. doi:10.1111/imr.12555

Palomares, O., Martín-Fontecha, M., Lauener, R., Traidl-Hoffmann, C., Cavkaytar, O., Akdis, M., et al. (2014). Regulatory T Cells and Immune Regulation of Allergic Diseases: Roles of IL-10 and TGF-β. *Genes Immun.* 15, 511–520. doi:10.1038/gene.2014.45

Qin, J., Lv, M., Jiang, Z., Meng, X., Wang, Y., Cui, J., et al. (2021). Tuo-Min-Ding-Chuan Decoction Alleviate Ovalbumin-Induced Allergic Asthma by Inhibiting Mast Cell Degranulation and Down-Regulating the Differential Expression Proteins. *Front. Pharmacol.* 12, 725953. doi:10.3389/fphar.2021.725953

Radulovic, S., Jacobson, M. R., Durham, S. R., and Nouri-Aria, K. T. (2008). Grass Pollen Immunotherapy Induces Foxp3-Expressing CD4+ CD25+ Cells in the Nasal Mucosa. *J. Allergy Clin. Immunol.* 121, 1467–e1. doi:10.1016/j.jaci.2008.03.013

Reddy, A. T., Lakshmi, S. P., and Reddy, R. C. (2012). Murine Model of Allergen Induced Asthma. *JoVE*, 14 (63). e3771. doi:10.3791/3771

Seumois, G., Ramírez-Suástegui, C., Schmiedel, B. J., Liang, S., Peters, B., Sette, A., et al. (2020). Single-cell Transcriptomic Analysis of Allergen-specific T Cells in Allergy and Asthma. *Sci. Immunol.* 5. eaba6087. doi:10.1126/sciimmunol.aba6087

Sommer, F., and Bäckhed, F. (2013). The Gut Microbiota-Mmasters of Host Development and Physiology. *Nat. Rev. Microbiol.* 11, 227–238. doi:10.1038/nrmicro2974

Sousa, T., Paterson, R., Moore, V., Carlsson, A., Abrahamsson, B., and Basit, A. W. (2008). The Gastrointestinal Microbiota as a Site for the Biotransformation of Drugs. *Int. J. Pharm.* 363, 1–25. doi:10.1016/j.ijpharm.2008.07.009

Sun, L., Fan, M., Huang, D., Li, B., Xu, R., Gao, F., et al. (2021). Clodronate-loaded Liposomal and Fibroblast-Derived Exosomal Hybrid System for Enhanced Drug Delivery to Pulmonary Fibrosis. *Biomaterials* 271, 120761. doi:10.1016/j.biomaterials.2021.120761

Sun, L., Fu, J., Lin, S. H., Sun, J. L., Xia, L., Lin, C. H., et al. (2020). Particulate Matter of 2.5 μm or Less in Diameter Disturbs the Balance of TH17/regulatory T Cells by Targeting Glutamate Oxaloacetate Transaminase 1 and Hypoxia-Inducible Factor 1α in an Asthma Model. *J. Allergy Clin. Immunol.* 145, 402–414. doi:10.1016/j.jaci.2019.10.008

Tortola, L., Pawelski, H., Sonar, S. S., Ampenberger, F., Kurrer, M., and Kopf, M. (2019). IL-21 Promotes Allergic Airway Inflammation by Driving Apoptosis of FoxP3+ Regulatory T Cells. *J. Allergy Clin. Immunol.* 143, 2178–e5. doi:10.1016/j.jaci.2018.11.047

Tremaroli, V., and Bäckhed, F. (2012). Functional Interactions between the Gut Microbiota and Host Metabolism. *Nature* 489, 242–249. doi:10.1038/nature11552

Wang, W., Luo, X., Zhang, Q., He, X., Zhang, Z., and Wang, X. (2020). Bifidobacterium Infantis Relieves Allergic Asthma in Mice by Regulating Th1/Th2. *Med. Sci. Monit.* 26, e920583. doi:10.12659/msm.920583

Zhang, B., An, J., Shimada, T., Liu, S., and Maeyama, K. (2012). Oral Administration of *Enterococcus faecalis* FK-23 Suppresses Th17 Cell Development and Attenuates Allergic Airway Responses in Mice. *Int. J. Mol. Med.* 30, 248–254. doi:10.3892/ijmm.2012.1010

Zhang, J., Zhang, J., and Wang, R. (2018). Gut Microbiota Modulates Drug Pharmacokinetics. *Drug Metab. Rev.* 50, 357–368. doi:10.1080/03602532.2018.1497647

Zhang, L., Song, P., Zhang, X., Metea, C., Schleisman, M., Karstens, L., et al. (2019). Alpha-Glucosidase Inhibitors Alter Gut Microbiota and Ameliorate Collagen-Induced Arthritis. *Front. Pharmacol.* 10, 1684. doi:10.3389/fphar.2019.01684

Conflict of Interest: The authors declare that the research was conducted in the absence of any commercial or financial relationships that could be construed as a potential conflict of interest.

Publisher's Note: All claims expressed in this article are solely those of the authors and do not necessarily represent those of their affiliated organizations, or those of the publisher, the editors and the reviewers. Any product that may be evaluated in this article, or claim that may be made by its manufacturer, is not guaranteed or endorsed by the publisher.

frontiers in Pharmacology

ORIGINAL RESEARCH
published: 08 February 2022
doi: 10.3389/fphar.2022.803602

Tissue Pharmacokinetic Properties and Bystander Potential of Hypoxia-Activated Prodrug CP-506 by Agent-Based Modelling

Victoria Jackson-Patel[1,2*†], *Emily Liu*[1†], *Matthew R. Bull*[1,2], *Amir Ashoorzadeh*[1,2], *Gib Bogle*[2,3], *Anna Wolfram*[1], *Kevin O. Hicks*[1,2], *Jeff B. Smaill*[1,2] *and Adam V. Patterson*[1,2]

[1]*Auckland Cancer Society Research Centre, Faculty of Medical and Health Sciences, University of Auckland, Auckland, New Zealand,* [2]*Maurice Wilkins Centre for Molecular Biodiscovery, University of Auckland, Auckland, New Zealand,* [3]*Auckland Bioengineering Institute, University of Auckland, Auckland, New Zealand*

OPEN ACCESS

Edited by:
S. Y. Amy Cheung, Certara, United States

Reviewed by:
Shawn D. Spencer, Philadelphia College of Osteopathic Medicine (PCOM), United States
Noor Ayad Hussein, Stanford University, United States

***Correspondence:**
Victoria Jackson-Patel
v.jackson@auckland.ac.nz

†These authors have contributed equally to this work

Specialty section:
This article was submitted to Translational Pharmacology, a section of the journal Frontiers in Pharmacology

Received: *28 October 2021*
Accepted: *04 January 2022*
Published: *08 February 2022*

Citation:
Jackson-Patel V, Liu E, Bull MR, Ashoorzadeh A, Bogle G, Wolfram A, Hicks KO, Smaill JB and Patterson AV (2022) Tissue Pharmacokinetic Properties and Bystander Potential of Hypoxia-Activated Prodrug CP-506 by Agent-Based Modelling. Front. Pharmacol. 13:803602. doi: 10.3389/fphar.2022.803602

Hypoxia-activated prodrugs are bioactivated in oxygen-deficient tumour regions and represent a novel strategy to exploit this pharmacological sanctuary for therapeutic gain. The approach relies on the selective metabolism of the prodrug under pathological hypoxia to generate active metabolites with the potential to diffuse throughout the tumour microenvironment and potentiate cell killing by means of a "bystander effect". In the present study, we investigate the pharmacological properties of the nitrogen mustard prodrug CP-506 in tumour tissues using *in silico* spatially-resolved pharmacokinetic/pharmacodynamic (SR-PK/PD) modelling. The approach employs a number of experimental model systems to define parameters for the cellular uptake, metabolism and diffusion of both the prodrug and its metabolites. The model predicts rapid uptake of CP-506 to high intracellular concentrations with its long plasma half-life driving tissue diffusion to a penetration depth of 190 µm, deep within hypoxic activating regions. While bioreductive metabolism is restricted to regions of severe pathological hypoxia (<1 µM O_2), its active metabolites show substantial bystander potential with release from the cell of origin into the extracellular space. Model predictions of bystander efficiency were validated using spheroid co-cultures, where the clonogenic killing of metabolically defective "target" cells increased with the proportion of metabolically competent "activator" cells. Our simulations predict a striking bystander efficiency at tissue-like densities with the *bis*-chloro-mustard amine metabolite (CP-506M-Cl_2) identified as a major diffusible metabolite. Overall, this study shows that CP-506 has favourable pharmacological properties in tumour tissue and supports its ongoing development for use in the treatment of patients with advanced solid malignancies.

Keywords: CP-506, SN36506, PR-104 (PubChem CID: 11455973), PR-104A (PubChem CID: 9848786), bystander effect, hypoxia-activated prodrug, agent-based modelling (ABM), multicellular spheroids

INTRODUCTION

Heterogeneous tumour oxygenation has long been recognized as a major impediment to the development of effective cancer therapies (Hockel et al., 1996; Nordsmark et al., 2005; Wilson and Hay, 2011; Marusyk et al., 2012). Given the prevalence of tumour hypoxia (Fukumura and Jain, 2007; Pries et al., 2009) and its association with treatment failure (Vaupel and Mayer, 2007), the use of hypoxia-activated prodrugs is a noteworthy approach to improve clinical outcomes. Hypoxia-activated prodrugs are designed to preferentially target regions of severe hypoxia, allowing tumour dose intensification by circumventing the normal tissue toxicities (Denny, 2005; Denny, 2010) that traditionally limit the potential for dose-escalation with conventional chemotherapeutic regimens (Rowinsky, 2000; Crawford, 2013).

Essentially, most hypoxia-activated prodrugs are comprised of a bioreductive switch or trigger unit that deactivates or masks the cytotoxic effector under aerobic conditions. Computational studies have elegantly shown that the efficacy of a hypoxia-activated prodrug is a delicate balance between its cellular affinity (reversible binding or sequestration), metabolic stability (prodrug activation rate and O_2-dependence), potency and diffusion capabilities of the released effector (Hicks et al., 1998; Hicks et al., 2003; Foehrenbacher et al., 2013a; Foehrenbacher et al., 2013b; Hong et al., 2018a; Hong et al., 2019). In which, the prodrug must penetrate relatively long distances through the extravascular compartment in order to reach the cells that are sufficiently hypoxic for its metabolic activation and subsequent cytotoxicity. The localization of the hypoxic target cells and the relative degree of effector redistribution (known as the bystander effect) determine the resultant cell killing. The limited success of earlier clinical candidates reflects, in part, the complexity of this design criteria (Marcu and Olver, 2006; Spiegelberg et al., 2019; Li et al., 2021).

A noteworthy example is the nitroaromatic compound PR-104A. Experimental studies showed that PR-104A is readily metabolised by endogenous one-electron reductases (e.g. cytochrome P450 oxidoreductase (POR) and other diflavin oxidoreductases) into a radical species that spontaneously converts under hypoxic conditions into DNA cross-linking metabolites (notably hydroxylamine PR-104H and amine PR-104M) (Guise et al., 2007; Patterson et al., 2007; Singleton et al., 2009; Guise et al., 2012). Computational studies indicated favourable pharmacokinetic properties for both single agent and combinatorial activity owing to its strict oxygen dependence (the half-maximal activation occurs at KO_2 = 0.126 μM O_2) and bystander efficiency in experimental models (Hicks et al., 2007; Foehrenbacher et al., 2013a; Foehrenbacher et al., 2013b). A sizeable bystander effect was shown using various multicellular layer (MCL) (Foehrenbacher et al., 2013a), spheroid co-culture (Hong et al., 2018b) and tumour xenograft models (Patterson et al., 2007; Foehrenbacher et al., 2013a). Combinatorial activity was noted with radiation (Hicks et al., 2007) as well as various systemic agents (Patterson et al., 2007; Abbattista et al., 2015).

Despite its promising preclinical activity, PR-104A, when administered to patients as its phosphate pre-prodrug form PR-104, failed to demonstrate significant clinical efficacy due to its myelotoxicity profile. The principal toxicities of neutropenia and thrombocytopenia aligned with those of conventional therapies resulting in additive toxicity rather than efficacy upon co-administration (Jameson et al., 2010; Abou-Alfa et al., 2011; Mckeage et al., 2011; Mckeage et al., 2012). A retrospective study identified an alternative route of PR-104A activation involving two-electron metabolism by aldo-keto reductase 1C3 (AKR1C3) that bypasses the oxygen-dependent step in the activation schematic (Guise et al., 2010). The off-target activation of PR-104A was specific to the human AKR1C3 orthologue explaining the clear oversight during its preclinical development (Guise et al., 2010; Van Der Wiel et al., 2021).

CP-506 is a second-generation PR-104A analogue that is rationally designed to be resistant to AKR1C3 activation in human tissues (Van Der Wiel et al., 2021). The mechanism of activation involves an initial one-electron reduction by endogenous oxidoreductases to a nitro radical anion intermediate that acts as a direct oxygen sensor, as previously described for PR-104A (Patterson et al., 2007). Experimental studies have shown that this reaction is catalysed efficiently by cytochrome P450 oxidoreductase (POR), although a number of other flavoenzymes can also contribute (Van Der Wiel et al., 2021). Further reduction leads to the formation of various DNA cross-linking metabolites selectively under hypoxic conditions. While CP-506 shows similar potency to PR-104A in anti-proliferative assays, the oxygen-dependence of prodrug activation and cytotoxicity is more favourable with complete inhibition above 1 μM O_2 and through the physiological O_2 concentration range (Van Der Wiel et al., 2021).

In the present study, we investigate the extravascular transport properties and bystander efficiency of CP-506 in tumour tissues by coupling various experimental and computational modelling approaches. The experimental framework involves a series of novel *in vitro* systems to measure reaction-diffusion in cells and 3D tumour models. Then, a well-validated in silico spatially-resolved pharmacokinetic/pharmacodynamic (SR-PK/PD) modelling approach (Hicks et al., 1997; Hicks et al., 2006; Hicks et al., 2010; Foehrenbacher et al., 2013b) was applied to estimate parameters for the cellular uptake, metabolism and diffusion of CP-506 and its active metabolites in the tumour tissue (Foehrenbacher et al., 2013a; Hong et al., 2018b). A cellular PK model was first developed by quantifying the extracellular (C_e) to intracellular (C_i) partitioning ratio for CP-506 and its formed metabolites in monolayer cultures treated under normoxic (21% O_2) and anoxic conditions (<1 ppm O_2). The derived reaction and diffusion terms were then scaled to tissue-like densities based on the transport of the prodrug and its effectors across multicellular layer (MCL) cultures maintained under supraoxic (95% O_2) and hypoxic conditions (<1 ppm O_2). Next, the parameter estimates were validated by comparing theoretical predictions to experimental determinations of clonogenic cell killing in spheroid co-cultures by agent-based modelling (ABM) (Hong et al., 2018b). Differences in fluorescent protein expression (mRuby vs. EGFP), antibiotic resistance genes

(puromycin vs. geneticin) and POR expression (high vs. null) were used to delineate between the subpopulations of metabolically competent "activator" and metabolically defective "target" cells to interpret experimental findings. We conclude by simulating the spatial gradients of CP-506 and its active metabolites in a transverse section of a representative spheroid. Our findings illustrate the superior tissue pharmacokinetic properties of CP-506 relative to PR-104A and support its future clinical evaluation in patients with advanced solid malignancies.

MATERIALS AND METHODS

Compounds

CP-506 (2-[(2-bromoethyl)-5-[(4-ethyl-1-piperazinyl)carbonyl]-2-(methylsulfonyl)-4-nitro anilino]ethyl methanesulfonate), CP-506H (2-((2-bromoethyl)(5-(4-ethylpiperazine-1-carbonyl)-4-(hydroxyamino)-2-(methylsulfonyl)phenyl)amino)ethyl methanesulfonate) and CP-506M (2-((4-amino-5-(4-ethylpiperazine-1-carbonyl)-2-(methylsulfonyl)phenyl)(2-bromoethyl)amino)ethyl methanesulfonate) and their respective deuterated (D8) standards (prepared from D8-1-ethylpiperazine) were manufactured by Mercachem (Nijmegen, the Netherlands) employing a synthetic route developed at the University of Auckland as previously described (Van Der Wiel et al., 2021). The downstream metabolites CP-506H-$(OH)_2$ (5-(bis(2-hydroxyethyl)amino)-2-(hydroxyamino)-4-(methylsulfonyl)phenyl)(4-ethylpiperazin-1-yl)methanone), CP-506M-$(OH)_2$ (2-amino-5-(bis(2-hydroxyethyl)amino)-4-(methylsulfonyl)phenyl)(4-ethylpiperazin-1-yl)methanone), CP-506H-Cl_2 (5-(bis(2-chloroethyl)amino)-2-(hydroxyamino)-4-(methylsulfonyl)phenyl)(4-ethylpiperazin-1-yl)methanone), CP-506M-Cl_2 (2-amino-5-(bis(2-chloroethyl)amino)-4-(methylsulfonyl)phenyl)(4-ethylpiperazin-1-yl)methanone) and their respective deuterated (D8) standards (prepared from D8-diethanolamine) were synthesized at the University of Auckland as described in the supplementary methods. Stock solutions were prepared in DMSO (CP-506, CP-506H and CP-506M) or acetonitrile (CP-506H-Cl_2, CP-506H-$(OH)_2$, CP-506M-Cl_2, CP-506M-$(OH)_2$) to concentrations of up to 100 mM and stored at −80°C until use. Working solutions were made by dilution into culture medium immediately before drug addition on the day of the experiment.

Cell Culture

The HCT-116 cell line was purchased from the American Type Culture Collection (Manassas, VA). A POR-overexpressing clone (POR-R) was generated by transfecting the parental cell line with a pBRP expression vector encoding an N-terminal truncated soluble version of the human POR gene (Foehrenbacher et al., 2013a; Guise et al., 2020). Ectopic expression is driven by the human cytomegalovirus (CMV) major immediate-early promoter. Downstream of POR is a human elongation factor-1 alpha (EF-1 alpha) promoter, which drives expression of mRuby and the puromycin resistance gene *pac* (puromycin N-acetyltransferase). A POR-null clone (PORG-ko) was generated as previously described (Su et al., 2013). POR-null clones were then transfected with a pEGFP-N1 plasmid encoding enhanced green fluorescent protein (EGFP) and geneticin resistance to permit identification upon co-culture (Hong et al., 2018b). Cell lines were maintained by weekly subculture in T-flasks containing alpha minimal essential medium (αMEM) with 5% foetal bovine serum (FBS) for a maximum of 24 passages or 90 days (whichever came first). The culture medium was further supplemented with 1 mg/ml geneticin or 2 μM puromycin for the routine maintenance of the POR-null and POR-overexpressing clones respectively. All cultures were re-established from STR-authenticated, mycoplasma negative frozen stocks.

Anti-Proliferative IC_{50} Assays

Cells (700–1,000 per well) were seeded with 100 μl culture medium into 96-well plates and left to attach for 2 h in a humidified 37°C incubator. Compounds were prepared in culture medium and serially diluted (1:3) in the well volume. Plates were returned to a humidified 37°C incubator for the duration of the drug exposure (4 h). Aerobic experiments were performed under standard tissue culture conditions (21% O_2), and the anoxic experiments were performed in parallel in a 5% H_2/Pd catalyst anaerobic chamber (Shellab Bactron, Sheldon manufacturing Inc., Cornelius, OR) using pre-equilibrated media and plasticware. All anoxia experiments were conducted using a catalyst-scrubbed anaerobic chamber, unless otherwise specified, with gas oxygen measurements of <1 ppm O_2. Cells were then washed three times and left to grow for 96 h before cell density determination using a sulforhodamine B (SRB) assay (Vichai and Kirtikara, 2006). To this end, the cells were fixed by layering 50 μl of trichloroacetic acid (40% w/v in MilliQ water) on top of the culture media (150 μl) in each well for 1 h at 4°C. Plates were rinsed under running tap water and stained with 50 μl of SRB (0.4% w/v in MilliQ water containing 1% v/v acetic acid) for 30 min at room temperature. Plates were rapidly destained by rinsing three times in tap water containing 1% (v/v) acetic acid. The stain was solubilized by adding 100 μl of 10 mM unbuffered Tris base to each well with gentle rocking for 1 h. Plates were read on a Biotek ELx808 Absorbance Microplate Reader at 490 nm using KC4 software. The IC_{50} value (concentration required to reduce staining to 50% of the untreated control on the same plate) for each compound was determined by interpolation using a 4-parameter logistic regression model.

Monolayer Clonogenic Assays

Cells (4.8×10^5 cells) were seeded with 2 ml culture medium into 6-well plates and left to attach for 2 h in a humidified 37°C incubator. Compounds were then prepared in culture medium and added in a 500 μl volume to each well. Plates were returned to a humidified 37°C incubator for the duration of the drug exposure (4 h). Aerobic and anoxic experiments were performed as described above. Plates were then removed from the anaerobic chamber and processed alongside the aerobic cultures. Cells were detached from monolayer by trypsinisation and plated at serial dilutions in 6-well plates. Cells were left to grow in a standard 37°C incubator for 10 days until the controls formed discrete

colonies comprised of at least 50 cells. Colonies were visualized by staining with methylene blue (2 g/L in 50% aqueous ethanol) for 30 min. The number of colonies with at least 50 cells was manually counted to determine the plating efficiency. The surviving fraction was determined as the ratio of plating efficiency of treated cells to that of the controls.

Cellular Metabolism Assay

Aerobic and anoxic conditions were achieved as described above. Cells (5×10^5 per well) were seeded with 350 µl medium in duplicate into 24-well plates and left to attach for 2 h in a humidified 37°C incubator. A working solution of CP-506 was prepared in culture medium to achieve a 100 µM concentration in each well after the addition of a 500 µl volume. Plates were exposed to drug for 1 h in a humidified 37°C incubator. Metabolism was then halted by the addition of two-volumes of ice-cold acetonitrile containing 2 µM of internal standard for each analyte. Samples were stored at −80°C until LC-MS/MS analysis.

Media Stability Studies

The stability of each compound was determined in stirred medium (without serum) maintained under aerobic conditions by the constant supply of a humidified gas mixture comprised of 21% O_2, 5% CO_2 with balance N_2. Vials were spiked with 100 µM of the relevant compound, and samples were collected using a positive displacement pipettor for up to 3 h thereafter. The collected samples were then treated with two-volumes of ice-cold acetonitrile containing 2 µM of the relevant deuterated (D8) internal standard and stored at −80°C until LC-MS/MS analysis.

Cellular Uptake Studies

The intracellular/extracellular partitioning ratio for CP-506 and its major metabolites was determined in monolayer cultures of POR-overexpressing HCT-116 cells, as described previously (Hong et al., 2018b). Briefly, cells (5×10^5 per well) were seeded with 350 µl medium into 24-well plates and left to attach for 2 h in a humidified 37°C incubator. Stock solutions of CP-506 were diluted and added with 50 µl medium to the well volume to achieve a final concentration of 100 µM. Samples were harvested at various time points for up to 3 h thereafter. Aerobic experiments were performed under standard tissue culture conditions (21% O_2), and the anoxic experiments in parallel in a H_2/Pd-catalyst-scrubbed anaerobic chamber as described. The well volume was spiked with [^{3}H]-mannitol immediately before sample harvest and treated with two-volumes of ice-cold acetonitrile containing 2 µM of the deuterated (D8) internal standards for each CP-506, CP-506H and CP-506M. The cell monolayer was then treated with 100 µl of this crashing solution. Samples were stored at −80°C until LC-MS/MS analysis. The cellular exclusion of [^{3}H]-mannitol was used to account for the contribution of the extracellular medium toward determinations of the intracellular concentration, as described previously (Foehrenbacher et al., 2013a).

Multicellular Layer Flux Studies

The extravascular transport properties of CP-506 and its formed metabolites were investigated using a custom-designed diffusion apparatus, as described previously (Hicks et al., 2006). Briefly, MCL cultures were established by seeding 1×10^6 POR-R cells onto collagen-coated Millicell-CM inserts for 3 days. Established MCLs were placed at the interface of the two media-filled compartments of diffusion chambers. Diffusion chambers were placed in a 37°C water bath and gassed with a supraoxic (95% O_2, 5% CO_2) or anoxic (5% CO_2, bal N_2) mixture for at least 1 h prior to drug addition. Flux was initiated by the addition of internal standard ([^{14}C]-urea) and 20 µM CP-506 to the donor compartment. Samples (100 µl) were collected from both the donor and receiver compartments for up to 5 h thereafter. At each time point, a 25 µl aliquot was mixed with emulsifier-safe water-accepting scintillant and assayed for radioactivity using a Perkin Elmer Tricard 2910 TR liquid scintillation analyser. The remaining sample was treated with two volumes of ice-cold acetonitrile (containing 2 µM of the relevant deuterated internal standards) and stored at −80°C until LC-MS/MS analysis. Similar experiments were performed using collagen-coated inserts without MCLs to deduce the chemical stability and diffusion coefficient of CP-506 across the bare support membrane.

Spheroid Growth and Survival Assays

Spheroid cultures were established by seeding 3×10^3 cells with 100 µl medium into ultra-low attachment, round bottom 96-well plates (Corning Inc, Corning, NY). Plates were briefly centrifuged (200 g, 5 min) to facilitate cell aggregation and grown in a standard incubator (37°C, 21% O_2, 5% CO_2) for 4 days before experiments. The culture medium was then aspirated, and the established spheroids taken into a H_2/Pd-catalyst anaerobic chamber. Spheroids were washed three times with anoxia pre-equilibrated medium and left to settle for 1 h in a humidified 37°C incubator. Spheroids were removed from the anaerobic chamber after a 4 h drug exposure and washed three times with fresh culture medium. The growth of representative spheroids was monitored for 10 days using a published method of image analysis for volume determination (Mao et al., 2018). The remainder were enzymatically dissociated and plated at serial dilutions in 6-well plates containing 2 µM puromycin or 1 mg/ml geneticin for positive selection of POR-R and PORko-G cells, respectively. Colonies were visualized after 10 days of drug-free proliferation by staining with methylene blue (2 g/L in 50% aqueous ethanol) for 30 min. The number of colonies with at least 50 cells was manually counted to determine the plating efficiency. The surviving fraction was determined as the ratio of the plating efficiency of treated cells to that of the controls.

Flow Cytometric Detection of EF5 Binding in Multicellular Spheroids

Spheroid cultures were established by seeding 3×10^3 cells into ultra-low attachment, round bottom 96-well plates, as described above. The culture medium was then aspirated, and the established spheroids taken into the H_2/Pd-catalyst anaerobic chamber. Spheroids were washed three times with anoxia pre-equilibrated medium and left to settle for 1 h in a humidified 37°C incubator. Spheroids were then treated with 100 µM EF5 for 4 h at

37°C. Plates were removed from the anaerobic chamber and washed three times with fresh culture medium. Spheroids were then dissociated by trypsinisation, washed three times with 0.1 M PBS and fixed in 4% formaldehyde. Samples were blocked with PBS containing 0.3% Tween-20 (PBS-T) and 10% FBS for 1 h at 4°C. EF5 adducts were then stained with 10 μg/ml Alexa Fluor 488-conjugated Elk3-51 antibody (supplied by Prof. Cameron Koch, University of Pennsylvania) diluted in incubation buffer (5% FBS, PBS-T *v/v*) overnight at 4°C. After a further three washes in PBS-T, cells were stored in 500 μl of PBS at 4°C until analysis on a BD Accuri flow cytometer (BD Biosciences, Franklin Lakes, NJ). A primary gate was set based on forward and side scatter to exclude cellular debris, dead cells and doublets. A secondary gate was set based on the selective metabolism and binding of EF5 in monolayer cultures treated under anaerobic conditions (<1 ppm O_2) compared to standard tissue culture conditions (37°C, 21% O_2, 5% CO_2) to define EF5-positive events.

Flow Cytometric Analysis of Fluorescent Protein Expression

The relative proportion of POR-R ("activator") and PORko-G ("target") cells in spheroid co-cultures was quantified by the flow cytometric detection of EGFP expression in paired samples. Established spheroids were enzymatically dissociated and re-suspended in 500 μl of 0.1 M PBS for analysis on a BD Accuri flow cytometer (BD Biosciences, Franklin Lakes, NJ). A primary gate was set based on forward and side scatter to exclude cellular debris, dead cells and doublets. A secondary gate was set based on the basal fluorescence of the parental HCT-116 cell line to define GFP-positive events.

Western Immunoblotting

Cellular lysates were prepared from log-phase cultures using modified radioimmuno-precipitation assay (RIPA) buffer (50 mM Tris-HCl, 1% NP-40, 0.25% sodium deoxycholate, 150 mM NaCl, 1mM EDTA, 1 mM Na_3VO_4, 1 mM NaF, 1:100 protease inhibitor cocktail (Roche, Basel, Switzerland)). Cellular lysates were then diluted in sample buffer (4 x LDS sample buffer containing 5% β-mercaptoethanol) and loaded with equal amounts of protein (30 μg) into BOLT precast gels (Thermofisher Scientific, Carlsbad, CA). Proteins were separated at 100 V for 1 h using BOLT MES SDS running buffer (Thermofisher Scientific, Carlsbad, CA) and transferred at 100 V for 1 h onto polyvinylidene difluoride (PVDF) membranes (pre-soaked in 100% methanol for 5 min) using ice-cold transfer buffer (14.4 g glycine, 3 g Trisma base, 200 ml methanol, 800 ml MilliQ water). Membranes were incubated with blocking solution for 1 h followed by the relevant primary antibody overnight at 4°C. Membranes were then washed three times with 0.1 M TBS-T (48 g Tris-HCl, 11.2 g Trisma base, 176 g NaCl, 20 ml Tween-20, 1800 ml MilliQ water (*w/v*)) and incubated with the appropriate HRP-conjugated secondary antibody for 1 h at room temperature. After a further three washes with 0.1 M TBS-T, bands were visualized with Supersignal West Pico Chemiluminescent substrate (Thermofisher Scientific, Carlsbad, CA) using a ChemiDoc MP Imaging System (Biorad Laboratories, Hercules, CA). Band densitometry was performed using Image J software (Schneider et al., 2012). Additional details regarding the antibodies and blocking solutions used in this study can be found in **Supplementary Table S1**.

LC-MS/MS Analysis of CP-506 and Metabolites

The LC system for tandem MS consisted of an Agilent 1200 autosampler (4°C) and binary pump, a 3.0 × 50 mm, 1.8-micron Zorbax SB-C18 column (Agilent; PN: 827975-302) and 2.1 × 7 mm guard column (Alltech, IL) maintained at 35°C, at a pressure of <400 bar and flow rate of 0.3 ml/min. The mobile phase comprised a gradient of 0.01% formic acid in 80% acetonitrile - 20% water, v/v (solvent A), and 0.01% formic acid in water (solvent B). Initial mobile phase composition was 20% solvent A and 80% solvent B, increasing to 60% A (0–3 min) then 80% A (3–5.45 min), returning to initial conditions (5.5–6 min). Post-run time was 1 min, and the total run time was 9 min. Mass spectrometric detection was carried out using an Agilent 6410 triple quadrupole mass spectrometer equipped with a multimode ionization (MMI) source. The mass spectrometer was operated in electrospray positive ionization mode using multiple reaction monitoring (MRM), with Q1 & Q3 set to unit resolution (0.7 μm). The electrospray ionization parameters, optimized for the parent molecular ion ([M+H]+) abundance were: drying gas temperature 325°C, vaporiser temperature 150°C, drying gas flow 5 L/min, nebuliser pressure 50 psi, capillary voltage 1.8 kV, Delta EMV 300 V. Ultra-pure nitrogen was used as collision gas. The divert valve feature of the Agilent 6410 triple quadrupole mass spectrometer was utilised to prevent the eluate from entering the ionisation source chamber during the first 0.5 min of each run. For CP-506 samples, positively charged ions representing the [M+H]+ for CP-506 and CP-506-D8 were collisionally dissociated to form specific product ions which were monitored in MS2 (unit resolution). The MRM transition, ionization mode, collision energy, dwell time, fragmentor voltage and retention time for all compounds is provided in **Supplementary Table S2**. Agilent MassHunter software (v.4.04.00) was used for data acquisition and chromatographic peak integration.

Cellular Pharmacokinetic Model

An agent-based model (ABM) employing a one-dimensional approximation for monolayers was used to develop a cellular PK model, as described in further detail elsewhere (Hong et al., 2018b; Mao et al., 2018). The mathematical framework assumes that solute concentrations in the medium are dependent only on the depth (on the *z* coordinate) and not the lateral position (*x,y*) so that all cells are exposed to the same concentration of nutrients and drugs within the monolayer culture. Moreover, all cells have the same rate of metabolism and volume growth at any instance with variability allowed in cell volume, rate of cell division and cell death. Monolayer ABM simulations were performed on a desktop Windows PC (Intel core I7 processor) from a Qt (Qt

Company, https://www.qt.io/) graphical user interface passing parameters to a DLL built with Fortran95. The monolayer ABM uses a finite difference method to solve reaction-diffusion equations for each compound (N) in the medium and cells. Parameters for the cellular uptake and metabolism were fitted to the concentration-time profiles of CP-506 and its metabolites in monolayer cultures of POR-R cells using a linear (first order) cell transport and metabolism model. Terms for the extracellular instability of CP-506 and its metabolites were set at their respective values in media stability studies, and media diffusion coefficients were estimated from the support membrane diffusion coefficients described below. Experimental data describing the kinetics of CP-506 uptake under aerobic conditions was fitted by adjusting the permeability coefficients k_{in} and k_{out} for each compound. These values were fixed for anoxic experiments to allow for parameter estimation of the rate of intracellular CP-506 metabolism (k_{met0}) as well as the intracellular/extracellular partitioning ratio (k_{in} and k_{out}) and metabolic instability (k_{met0}) for its cytotoxic metabolites.

Pro(drug) Transport Model

Drug transport in MCLs was modelled as a one-dimensional diffusion with reaction across four consecutive compartments (stirred donor, POR-R MCL, collagen-coated teflon support membrane and stirred receiver) using a custom designed MatLab routine (Foehrenbacher et al., 2013a). Model parameters were derived by fitting **Eq. 1** and **Eq. 2** to the measured concentration-time profile of internal standard [^{14}C]-urea, CP-506, CP-506H and CP-506M in MCL flux studies. The flux of CP-506 and its metabolites across POR-R MCLs was described using Fick's second law with a reaction term:

$$\frac{\partial C_{eN}}{\partial t} = D_N \frac{\partial^2 C_{eN}}{\partial x^2} - k_{lossN} C_{eN} - \varphi\left(k_{inN} C_{eN} - k_{outN} C_{iN}\right) \quad (1)$$

$$\frac{\partial C_{iN}}{\partial t} = k_{met0(N-1)} C_{i(N-1)} + \varphi\left(k_{inN} C_{eN} - k_{outN} C_{iN}\right) - k_{met0N} C_{iN} \quad (2)$$

where C is the concentration of the diffusing substance at position x and time t in the extracellular (e) or intracellular (i) compartment, D is the diffusion coefficient through either a bare support membrane (without cells) (D_{suo}) or extracellular space of a POR-R MCL (D_{MCL}), k_{loss} is the rate constant for first-order loss (instability) in culture medium, k_{in} and k_{out} are the rate constants for transmembrane transport and k_{met0} is the rate constant for intracellular metabolism and instability for each compound (N). For metabolites, N-1 represents the previous compound from which the current compound is produced by metabolism. Experimental data was fitted iteratively to derive a tissue diffusion coefficient (D_{MCL}) and metabolic scaling factor (φ_i) to restrain parameter estimates from the cellular PK model (K_{in}, K_{out}, K_{met0}). The diffusion coefficient for CP-506 across the bare support membrane (D_{sup}) was determined by solving **Eq. 1** with a reaction term only for chemical instability. MCL thicknesses were estimated by fitting the measured [^{14}C]-urea concentrations to those predicted by **Eq. 1** and **Eq. 2** without instability or metabolism by using the known diffusion coefficient (D_{MCL}) for [^{14}C]-urea in HCT-116 MCLs (Wilson et al., 2004). The diffusion coefficient (D_{MCL}) for CP-506 in POR-R MCLs was then fitted from the measured concentrations in the donor and receiver compartments of supraoxic experiments by assuming one-directional diffusion in the extracellular space. The metabolic scaling factor (φ_i) was then fitted from the measured concentrations in the donor and receiver compartment of anoxic experiments by fixing parameter estimates to the diffusion coefficient (D_{MCL}) from supraoxic experiments.

Simulations of CP-506 Diffusion and Efficacy in Spheroid Cultures

The spheroid ABM is described in further detail elsewhere (Hong et al., 2018b; Mao et al., 2018). The model employs two 3D grids and two solvers, a coarse grid represents the culture medium and is embedded with a much finer grid that represents the spheroid in a small cubic region at the bottom of the well. The spheroid grows in a specified volume and depth of unstirred medium containing dissolved oxygen. The geometry of the model is lattice-based, in which cells occupy cubic sites on a regular 3D lattice and grow in volume at a rate dependent on the local oxygen concentration. Autonomous cell mobility and cell-cell forces are not simulated. Cell motion occurs only as a result of cell division. Cells divide when the volume reaches a pre-set value (V_{div}) and the resultant daughter cell occupies an adjacent empty lattice site. If a vacancy does not exist, cells are moved radially outward to create one. The oxygen concentration at the air-medium boundary is defined by the gas phase of the culture environment. As the spheroid grows and total oxygen consumption increases, concentration gradients within the culture medium and spheroid interior steepen with significantly lower concentrations within the spheroid core. When oxygen concentrations fall below a critical level (<0.15 μM), cells are tagged to die and cytolysis occurs after a further 24 h leading to the central necrosis observed in *in vitro* spheroids. Spheroid ABM simulations were performed on a desktop Windows PC (Intel core I7 processor) from a Qt (Qt Company, https://www.qt.io/) graphical user interface passing parameters to a DLL built with Fortran95. The solution of the coarser grid provides the boundary conditions for the solution of the intracellular and extracellular concentrations within the spheroid lattice. Oxygen and drug are transported by diffusion from the boundary into the spheroid interior through the intercellular space in parallel with their uptake into cells. The model allows specification of two mass transfer constants to characterise the uptake (K_{in}) and efflux (K_{out}) rates for each compound. Prodrug metabolism is restricted to the intracellular compartment and dependent on the local oxygen concentration. Parameter estimates for the cellular uptake and metabolism of CP-506 in monolayer cultures were used to fit clonogenic survival data to estimate the kill probability rate constant (k_d), as described previously for PR-104A (Hong et al., 2018b). The kill probability (model 4 in the ABM program (Mao et al., 2018)) was assumed proportional to the intracellular concentration of the bioreductive metabolites ($k_d C_N$) and was set to zero for the prodrug. The same k_d was assumed for each of the major metabolites (CP-506H, CP-506M and CP-506M-Cl_2), and that the intrinsic sensitivity of the cell lines was identical with differences only in the oxygen- and POR-dependent first order rate constant for the metabolic consumption (k_{met0}) of CP-506. Parameter estimates were used alongside the *in vitro* determined drug pharmacokinetic

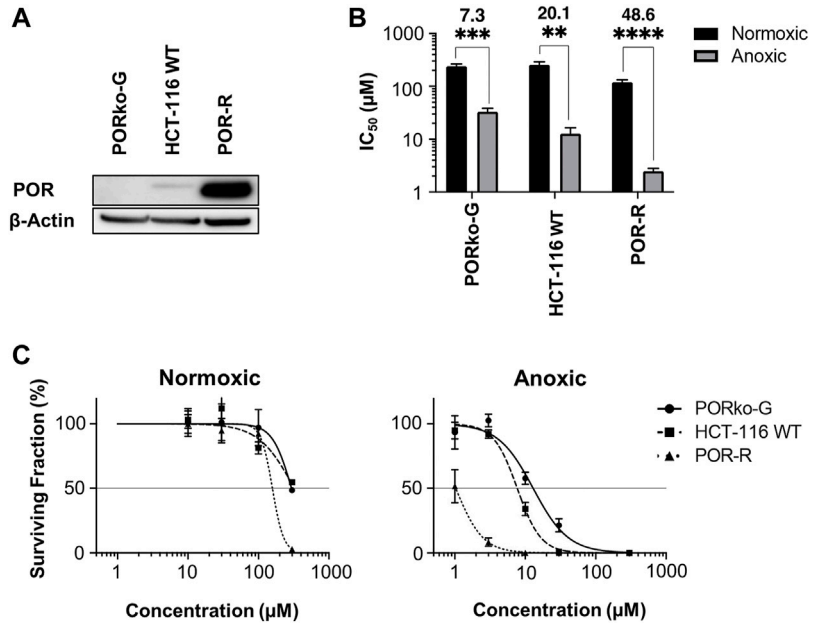

FIGURE 1 | Hypoxia-dependent cellular cytotoxicity of CP-506 is influenced by POR expression. **(A)** Western blot analysis of POR expression in HCT-116 cells upon gene knockout (PORko-G) and ectopic overexpression (POR-R) as compared to the parental cell line (HCT-116 WT). **(B)** Anti-proliferative potency after exposure of monolayer cultures (700 – 1000 cells per well) to CP-506 for 4 h under normoxic (21% O_2) and anoxic conditions (<1 ppm O_2). IC_{50} values were determined after 96 h of drug-free proliferation as the drug concentration required to inhibit cellular proliferation by 50% of the untreated controls. Values are the mean ± SEM of triplicate wells for three independent experiments. ANOVA tests were performed using GraphPad Prism 8 (p-value ≤ 0.01; ***, p-value ≤ 0.001; ****, p-value ≤ 0.0001). **(C)** Clonogenic survival after exposure of monolayer cultures (4.8×10^5 cells per well) to CP-506 for 4 h under normoxic (21% O_2) and anoxic conditions (<1 ppm O_2). IC_{50} values were interpolated from the fitted dose response curve as the concentration required to reduce the clonogenic surviving fraction to 50% of the untreated controls (shown by the reference line). Values are the mean ± SEM of duplicate wells for three independent experiments.

terms to predict the killing of "activator" (POR-R) and "target" (PORko-G) cells in spheroid co-cultures.

Statistical Analysis

All statistical tests were performed using GraphPad Prism 8. Individual tests used are specified in the relevant figures.

RESULTS

The Hypoxia-Dependent Metabolism and Cellular Cytotoxicity of CP-506 is Influenced by Cytochrome P450 Oxidoreductase Expression

Given the primary role of POR in CP-506 metabolism (Van Der Wiel et al., 2021), a panel of isogenic cell lines with variable levels of POR expression was used to investigate the extravascular transport properties of CP-506 and its metabolites in an *in vitro* setting. Consistent with the genetic modifications, protein expression was elevated by 11-fold in the POR-overexpressing cell line (POR-R) relative to wild-type cells (HCT-116 WT) and was undetectable in the POR-knockout line (PORko-G) (**Figure 1A**). The impact of POR expression on the sensitivity of HCT-116 cells to CP-506 was examined using both an anti-proliferative (**Figure 1B**) and clonogenic endpoint (**Figure 1C**). Both assays demonstrate hypoxia-selective cellular cytotoxicity, with a marked increase in the sensitivity of HCT-116 cells to CP-506 under anoxic conditions. A 13-fold differential in anoxic sensitivity was noted between the PORko-G and POR-R cell lines by anti-proliferative assay. Aerobic IC_{50} values were 240 ± 26, 257 ± 37 and 120 ± 13 μM for the PORko-G, HCT-116 WT and POR-R cell lines, respectively (p-value ≤ 0.01). Values under anoxic conditions were 7.3-fold, 20.1-fold and 48.6-fold lower at 33.1 ± 5.6, 12.8 ± 3.7 and 2.5 ± 0.3 μM, respectively (p-value ≤ 0.01). Clonogenic assays showed a similar trend with a 22-fold differential in anoxic sensitivity between the PORko-G and POR-R cell lines. Clonogenic IC_{50} values under anoxia were 17.1 ± 3.4, 7.4 ± 0.5 and 0.8 ± 0.3 μM for the PORko-G, HCT-116 WT and POR-R cell lines respectively.

The mass spectrometric detection of reduced metabolites accompanied the selective cytotoxicity of CP-506 in hypoxic cultures. Although a number of species were detected (**Figure 2**), the hydroxylamine CP-506H, amine CP-506M and dichloro-amine CP-506M-Cl_2 were the major metabolites present at concentrations sufficient for comparison between cell lines. Rates of metabolite formation reflected differences in POR expression, with metabolite concentrations 5.5- (CP-506H) to 8.6-fold (CP-506M-Cl_2) higher in POR-R cells and 4.1- (CP-506M) to 17.7-fold (CP-506M-Cl_2) lower in PORko-G cells than HCT-116 WT cells after a 1 h treatment period (**Figure 3A**). Authentic standards of the six identified metabolites (**Figure 2**)

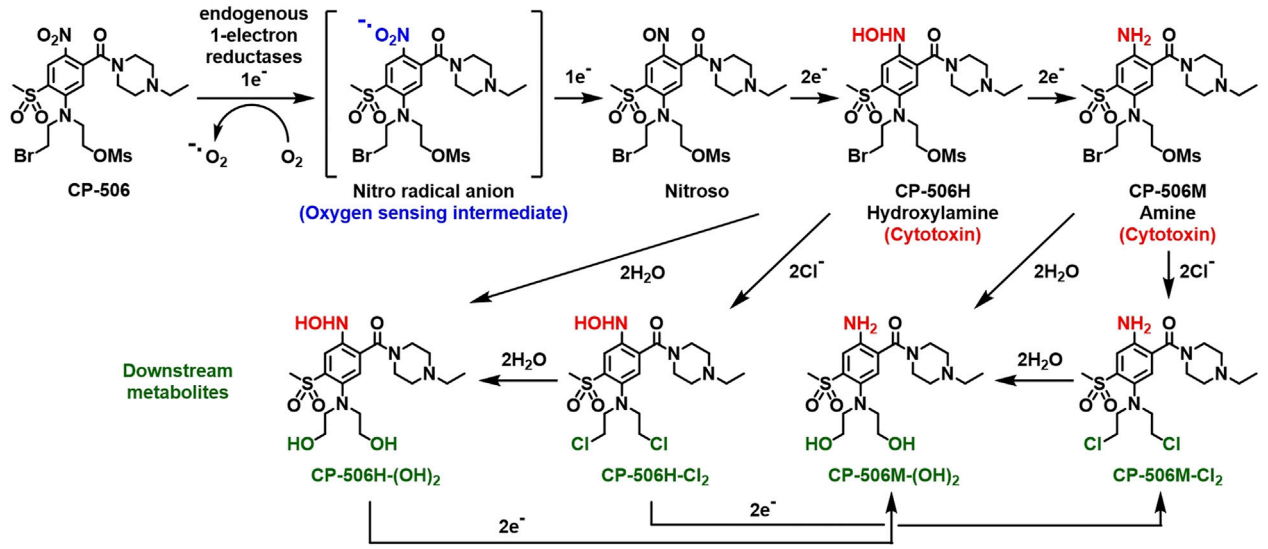

FIGURE 2 | Schematic representation of the activation sequence for CP-506. CP-506 is metabolised by endogenous one-electron reductases into a nitro radical anion that is readily back-oxidised in the presence of molecular oxygen. Under hypoxia, the nitro radical anion is further metabolised to its corresponding hydroxylamine (CP-506H) and amine (CP-506M) metabolites. The major metabolites are highly reactive. Each arm of the bromomesylate mustard can react with chloride ions and/or undergo aqueous hydrolysis providing the major observed downstream metabolites, CP-506H-Cl_2, CP-506H-$(OH)_2$, CP-506M-Cl_2, and CP-506M-$(OH)_2$.

were synthesized (see **Supplementary Material**) and shown to have marked differences in intrinsic stability in stirred medium at 37°C (**Figure 3B**). While the prodrug CP-506 showed no loss of mass balance for over 360 min in stirred medium, half-lives ($T_{1/2}$) for the reduced metabolites were significantly shorter at 2.5, 10.5, 7.6, 141.3, 271.1 and 393.9 min for the diol-hydroxylamine CP-506H-$(OH)_2$, hydroxylamine CP-506H, amine CP-506M, dichloro-hydroxylamine CP-506H-Cl_2, dichloro-amine CP-506M-Cl_2 and diol-amine CP-506M-$(OH)_2$ respectively. Anti-proliferative IC_{50} assays were performed to estimate the relative contribution of each metabolite toward the cellular cytotoxicity of CP-506 under hypoxic conditions (**Figure 3C**). Both diol-containing metabolites were essentially inactive (IC_{50} > 30 μM), consistent with the absence of appropriate mustard leaving groups required for formation of the cytotoxic intermediates. The dichloro-hydroxylamine CP-506H-Cl_2 metabolite also exhibited limited potency. The major cytotoxic metabolites (IC_{50} < 10 μM) were the hydroxylamine CP-506H, amine CP-506M, and dichloro-amine CP-506M-Cl_2. The former two metabolites were short-lived ($T_{1/2}$ of 7–11 min) while the latter had relatively high stability ($T_{1/2}$ of 271 min).

Cellular Pharmacokinetic Model for CP-506 in Tumour Tissues

A cellular PK model was developed based on the extracellular and intracellular concentration-time profile for CP-506 and its reduced metabolites in monolayer cultures. Experiments were performed using POR-R cells to allow for greater sensitivity in metabolite detection. Under aerobic conditions, the cellular uptake of CP-506 was described by a simple two compartment model with the loss of mass balance in the extracellular medium (C_e) coupled with a respective increase in the intracellular concentration (C_i) (**Figure 4A**). The rate of cellular uptake was fastest during the first 30 min after drug addition and plateaued thereafter. The cellular uptake of CP-506 was not concentration-dependent, with steady-state C_i/C_e ratios of 50-fold across the C_o range of 0.3–30 μM initial concentrations. No net metabolism nor intrinsic instability were observed under aerobic conditions. In anoxic experiments, the cellular uptake of CP-506 was accompanied by the appearance of metabolites CP-506H and CP-506M in the intracellular compartment (**Figure 4B**). The loss of mass balance was reiterated in the lower steady-state C_i/C_e ratio of 40-fold. The formed metabolites were released from the cell of origin into the extracellular medium indicating bystander potential. However, the mass balance was dominated by the intracellular fraction indicating that the cellular efflux of these metabolites is a passive process. A first order kinetic model describing the cellular uptake and metabolism of CP-506 (**Figure 4C**) was fitted to the *in vitro* data with excellent correlation between the experimental data and model-predicted fits (R^2 = 0.9596) (lines in **Figure 4B**). The model assumed that the high intracellular concentrations of CP-506 are driven by its large cell uptake factor, and that metabolic loss of CP-506 is O_2-dependent and restricted to the intracellular compartment. Once formed, the downstream metabolites can diffuse freely between the two compartments. The stability varies between compounds with the half-life ($T_{1/2}$) of CP-506 significantly longer than that of its metabolites. The rate of CP-506 metabolism and metabolite uptake is higher than the rate of cellular efflux resulting in the high intracellular concentrations observed under anoxic conditions. Model estimates of the uptake and metabolism parameters for CP-506 and its metabolites are provided in

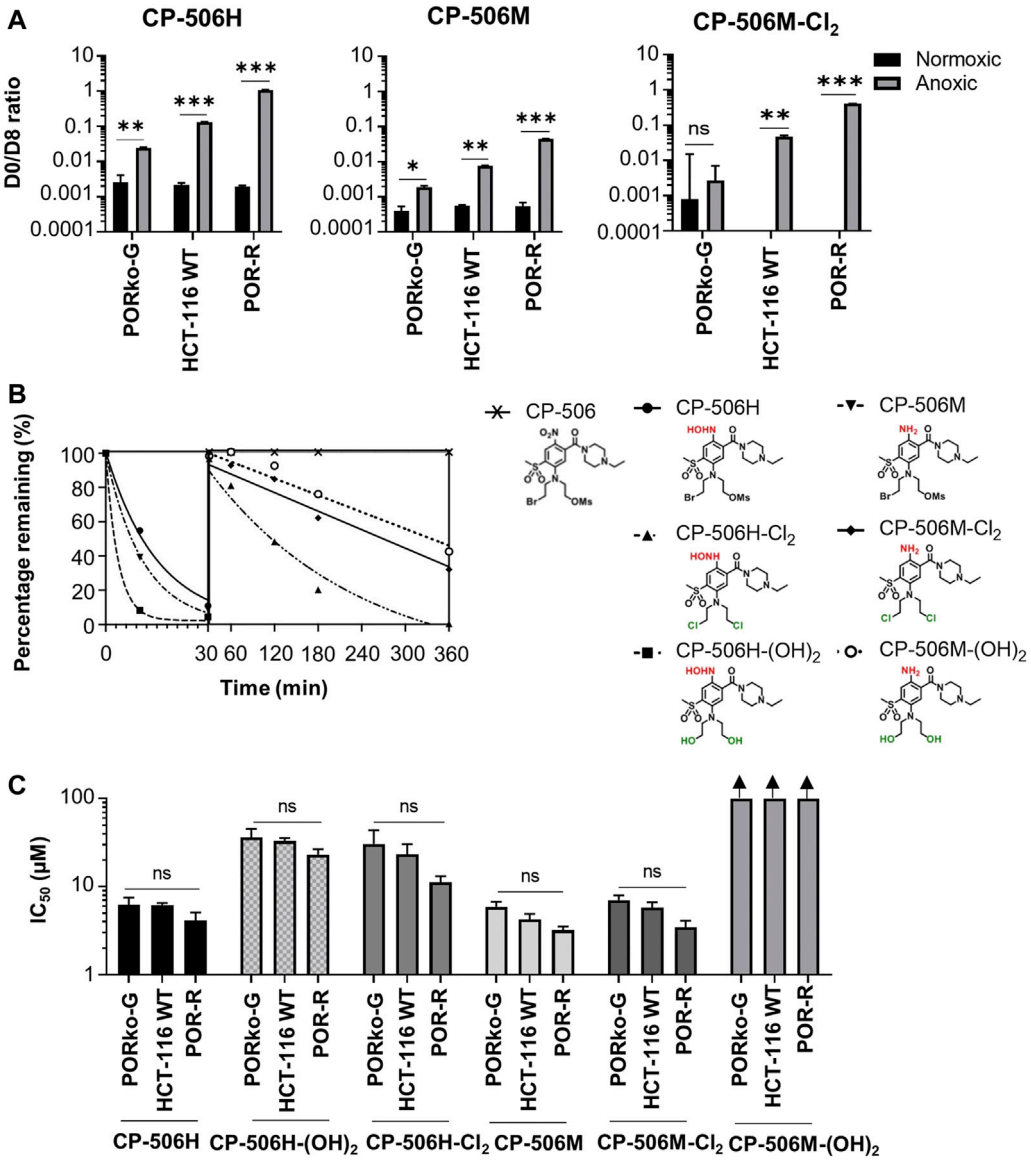

FIGURE 3 | Hypoxia-dependent metabolism of CP-506 leads to the formation of a multitude of short-lived species with variable cytotoxicity. **(A)** Bioreductive metabolism of CP-506 under normoxic (21% O_2) and anoxic conditions (<1 ppm O_2). Concentrations of CP-506 and its metabolites (CP-506H, CP-506M and CP-506M-Cl_2) were quantified by mass spectrometry with reference to the appropriate deuterated (D8) internal standard. Values are the mean ± SEM for three independent experiments. **(B)** Stability of CP-506 metabolites in culture medium (without cells) at 37°C. Concentrations were determined by mass spectrometry using standard curves generated from authenticated stocks. **(C)** Anti-proliferative potency after exposure of monolayer cultures to CP-506 metabolites for 5 days under normoxic conditions (21% O_2). IC_{50} values are the mean ± SEM of duplicate wells for three independent experiments. T-tests were performed using GraphPad Prism 8 (ns, p-value > 0.05; *, p-value ≤ 0.05; **, p-value ≤ 0.01; ***, p-value ≤ 0.001).

Supplementary Table S3. Cell uptake studies considered only the major metabolites (CP-506H and CP-506M) due to the retrospective identification and synthesis of the downstream metabolites and deuterated internal standards thereof. For inclusion in the cellular PK model, the rate constants for the cellular uptake, cellular efflux and extracellular instability of CP-506M-Cl_2 were fixed to the fitted values for the stable downstream metabolites of PR-104A (termed "metabolite 2") (Foehrenbacher et al., 2013a; Hong et al., 2018b). Parameter estimates were later refined based on the accrued stability and MCL transport data for spheroid simulations as described below.

Extravascular Transport Model for CP-506 in Tumour Tissues

The cellular uptake and metabolism parameters from monolayer assays were scaled to tissue-like densities based on the concentration-time profile of CP-506 and its formed metabolites in the donor and receiver compartment of

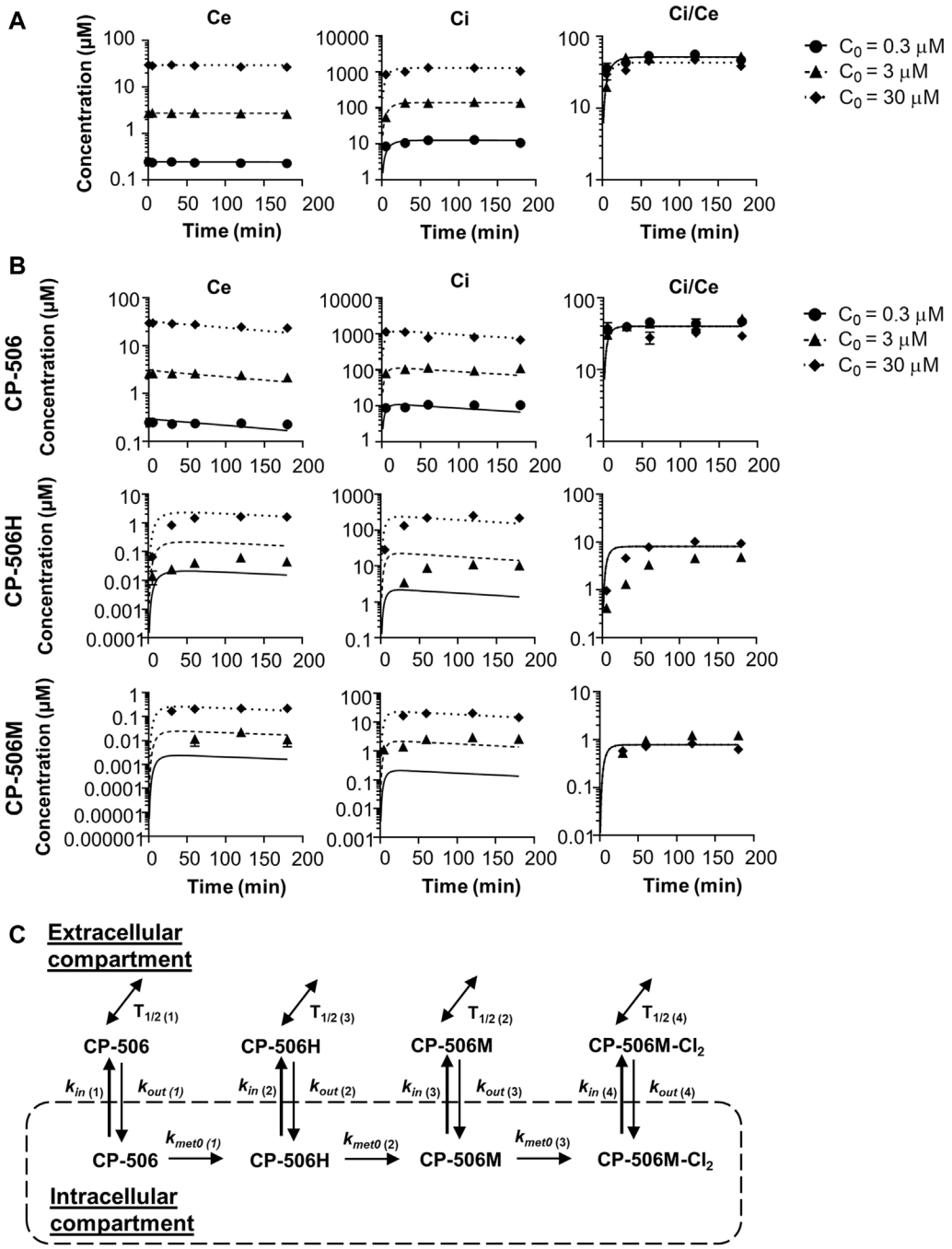

FIGURE 4 | Cellular PK model of CP-506 in the tumor tissues. **(A)** Cellular uptake of CP-506 in monolayer cultures of POR-R cells after exposure to a range of initial concentrations (C_o) under normoxic conditions (21% O_2). Concentrations were determined in the extracellular medium and cellular extracts by mass spectrometry. Graphs show the concentration-time profile of CP-506 in the extracellular volume (C_e), intracellular volume (C_i) and resultant C_i/C_e ratio over the experiment duration (3 h). Values represent the mean ± SEM of three independent experiments. Lines show the corresponding estimates from the cellular PK model as fitted to the experimental data. **(B)** Hypoxia-selective metabolism of CP-506 and release of CP-506 metabolites into the extracellular medium of POR-R cells under anoxic conditions (<1 ppm O_2). Graphs show the concentration-time profile of CP-506 and its metabolites CP-506H and CP-506M in the extracellular volume (C_e), intracellular volume (C_i) and resultant C_i/C_e ratio over the experiment duration (3 h). Data points have been censored if below the lower limits of quantification (LLOQ, 0.01 μM). Lines show the corresponding estimates from the cellular PK model. **(C)** Cellular PK model for CP-506. The concentration of CP-506 and its metabolites in the extracellular and intracellular compartments is defined by the permeability rate constants (k_{in} and k_{out}). The bioreductive metabolism of CP-506 (k_{met0}) is O_2-dependent and restricted to the intracellular compartment. The stability of each compound is defined by their respective half-life ($T_{1/2}$). Model estimates for the given parameters are provided in **Supplementary Table S3**.

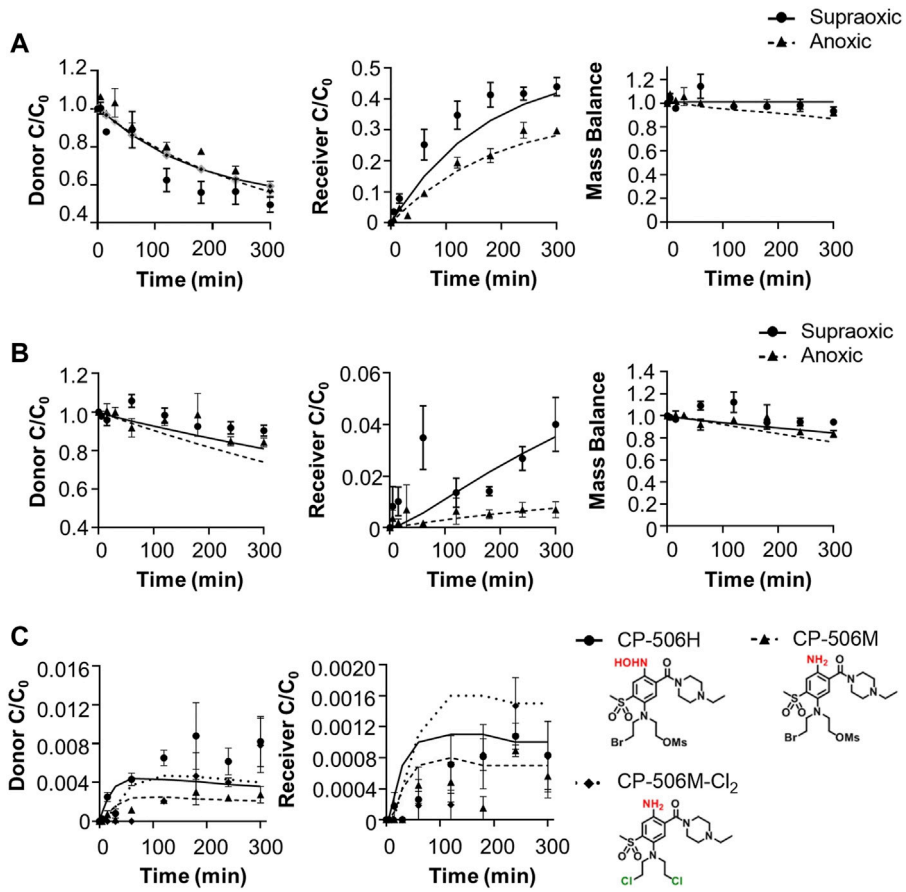

FIGURE 5 | Extravascular transport of CP-506 and its formed metabolites (CP-506H, CP-506M and CP-506M-Cl_2) across support membranes with or without a MCL culture. Flux was initiated by the addition of CP-506 (C_o = 17.4 ± 1.3 μM) and internal standard [^{14}C]-urea into the donor compartment of diffusion chambers maintained under supraoxic (95% O_2, 5% CO_2) and anoxic (5% CO_2, bal N_2) conditions. The concentration-time profile of CP-506 in the donor and receiver compartments of diffusion chambers was determined by mass spectrometry. Mass balance was calculated as the sum of the donor and receiver compartments. Lines are the concentrations predicted from the developed (pro)drug transport model. Values are mean ± SEM of three independent diffusion chambers. **(A)** Concentration-time profile of CP-506 across bare support membranes (without cells) maintained under supraoxic and anoxic conditions. **(B)** Concentration-time profile of CP-506 across POR-R MCLs maintained under supraoxic and anoxic conditions. **(C)** Concentration-time profile for the formed metabolites of CP-506 (CP-506H, CP-506M and CP-506M-Cl_2) in POR-R MCLs under anoxic conditions.

diffusion chambers containing multicellular layers maintained under supraoxic (95% O_2, 5% CO_2) and anoxic conditions (5% CO_2, bal N_2). Initial experiments were performed using collagen-coated inserts without cells to determine the chemical stability and diffusion coefficient of CP-506 across the bare support membrane (D_{sup}) (**Figure 5A**). Irrespective of oxygen tension, the extravascular transport of CP-506 across the bare support membrane was described using a simple Fickian diffusion model without loss of mass balance between the media compartments of the diffusion chambers (donor, receiver). Differences in stirring rate resulted in a lower D_{sup} for anoxic experiments ((0.717 ± 0.01) x 10^{-6} cm^2 s^{-1}) compared to supraoxic experiments ((1.32 ± 0.19) x 10^{-6} cm^2 s^{-1}), however this discrepancy was accounted for in D_{MCL} calculations. MCL cultures were established from POR-R cells to allow for greater sensitivity in metabolite detection. The predicted thickness of the MCL cultures (L_{MCL}) was 101.7 ± 6.9 μm, as estimated from the acquired flux data and established D_{MCL} (3.67 x 10^{-7} cm^2 s^{-1}, (Wilson et al., 2004)) for internal standard [^{14}C]-urea. Drug transport in the MCL was modelled as a one-dimensional diffusion with reaction in the extracellular and intracellular compartments, with the integrated reaction term used to describe the loss of mass balance due to cellular uptake and metabolism. The cellular uptake of CP-506 slowed extravascular transport across the MCL, as indicated by the estimated D_{MCL} of (1.93 ± 0.011) x 10^{-7} cm^2s^{-1} for supraoxic experiments (**Figure 5B**). The rate of diffusion was further reduced by reductive metabolism with its major metabolites detected in both the donor and receiver compartments of anoxic experiments (**Figure 5C**). A metabolic scaling factor (φ_i) of 0.3 was derived to scale the metabolic parameters from the previous monolayer-based assays. A summary of the determined extravascular transport parameters for CP-506 across POR-R MCLs is provided in **Supplementary Table S4**.

Bystander Potential of CP-506 in Spheroid Co-cultures

Predictions based on the tissue pharmacokinetics of CP-506 in experimental model systems were compared to determinations of

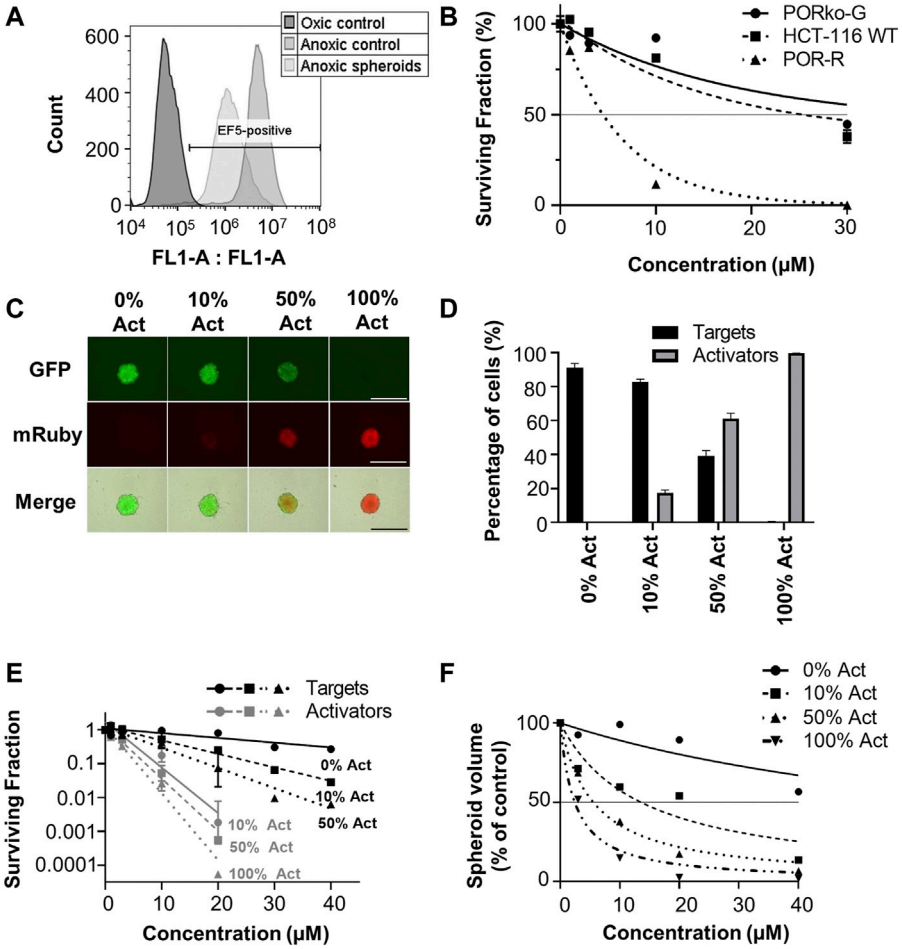

FIGURE 6 | Bystander efficiency of CP-506 in spheroid co-cultures. Multicellular spheroids were established by seeding differing proportions of target (PORko-G) and activator cells (POR-R) and growing for 4 days in ultra-low attachment, round bottom 96-well plates. **(A)** Flow cytometric analysis of EF5 binding upon the enzymatic dissociation of anoxia pre-equilibrated POR-R spheroids. The hypoxic population was defined by the hypoxia-selective metabolism and binding of EF5 in monolayer controls. **(B)** Clonogenic survival after exposure of spheroid cultures to CP-506 for 4 h under anoxic conditions (<1 ppm O_2). IC_{50} values were interpolated from the fitted dose response curve as the concentration required to reduce the plating efficiency to 50% of the untreated controls (shown by the reference line). Values are the mean ± SEM for three independent experiments. **(C)** Fluorescent microscope images of representative spheroids showing target (GFP-positive) and activator cells (mRuby-positive) at the anticipated proportions based on their initial seeding densities. Images were acquired at 4 X objective using a JuliStage Real-Time Cell History Recorder (NanoEnTek, Seoul, Korea). Scale bar indicates 1 mm. **(D)** Flow cytometric detection of target and activator cells in spheroid co-cultures based on GFP expression. The parental cell line (HCT-116 WT) was used as a negative control. Values are the mean ± SEM for three independent experiments. **(E)** Clonogenic survival of target and activator cells (Act) in spheroid co-cultures treated with CP-506 for 4 h under anoxic conditions (<1 ppm O_2). Spheroids were then enzymatically dissociated and plated in parallel in media supplemented with 2 μM puromycin or 1 mg/ml geneticin to select for activator and target cells respectively. Values are the mean ± SEM for three independent experiments. **(F)** Growth delay after exposure of spheroid co-cultures to CP-506 for 4 h under anoxic conditions (<1 ppm O_2). Spheroid volumes were quantified at endpoint (day 14 post-treatment) using a previously described method of image analysis (Mao et al., 2018). Values are the mean ± SEM for three independent experiments.

clonogenic cell survival and growth delays in spheroid co-cultures. Experiments were performed under strict anoxia to eliminate oxygen gradients to ensure that the established concentration gradients of CP-506 and its reduced metabolites reflect their respective pharmacokinetic properties rather than metabolic potential due to oxygen availability. This notion was confirmed by the flow cytometric detection of EF5 adducts (<1 μM O_2) upon the enzymatic dissociation of anoxic spheroids (**Figure 6A**). Preliminary dose ranging experiments identified a 22-fold differential in anoxic sensitivity between PORko-G and POR-R spheroids by clonogenic endpoint reflecting the intrinsic differences in metabolic potential between the cell lines (**Figure 6B**).

Spheroid co-cultures were established by seeding "activator" POR-R cells and "target" PORko-G cells at differing proportions growing for 4 days in ultra-low attachment, round bottom 96-well plates. At this point, fluorescent imaging showed intimate mixtures of red and green fluorescent cells in proportions broadly consistent with the respective seeding densities of activator and target cells (**Figure 6C**). A flow cytometric analysis of representative spheroids showed that activator cells were overrepresented by 5–10% due to

TABLE 1 | CP-506 PK/PD parameters used for ABM simulations.

Parameter (unit)	Description	Estimate			
		CP-506	**CP-506H**	**CP-506M**	**CP-506M-Cl_2**
D_s (cm^2s^{-1})[a]	Diffusion coefficient in spheroid	$1.93 \times 10^{-7} \pm 1.8 \times 10^{-8}$	$1.93 \times 10^{-7} \pm 1.8 \times 10^{-8}$	$1.93 \times 10^{-7} \pm 1.8 \times 10^{-8}$	$1.93 \times 10^{-7} \pm 1.8 \times 10^{-8}$
D_M (cm^2s^{-1})[b]	Diffusion coefficient in medium	$1.32 \times 10^{-6} \pm 0.19 \times 10^{-6}$	$1.32 \times 10^{-6} \pm 0.19 \times 10^{-6}$	$1.32 \times 10^{-6} \pm 0.19 \times 10^{-6}$	$1.32 \times 10^{-6} \pm 0.19 \times 10^{-6}$
k_{in} (min^{-1})[c]	Rate constant for transfer from the extracellular to intracellular volume	3.7	0.9	0.9	0.9[d]
k_{out} (min^{-1})[c]	Rate constant for transfer from the intracellular to extracellular volume	0.06	0.25	0.4	0.3[d]
Half-life (h)[e]	Time required to reduce the concentration of drug to half of its initial value	30	0.18	0.13	4.52
Activator k_{met0} (min^{-1})[c]	Rate constant for the maximum rate of metabolism in POR-R cells under anoxia	0.12	0.09	0.1	0.1[d]
Target k_{met0} (min^{-1})[f]	Rate constant for the maximum rate of metabolism in PORko-G cells under anoxia	0.0019	0.09	0.1	0.1[d]
$k_{d\ M}$[f]	Kill probability rate constant in monolayer cultures	0	0.01	0.01	0.01
$k_{d\ S}$[f]	Kill probability rate constant in spheroid cultures	0	0.0256	0.0256	0.0256

[a]*D_{MCL} fitted to the concentration-time profile of CP-506 in the donor and receiver compartment of diffusion chambers bearing POR-R MCLs maintained under supraoxic conditions. Parameter estimates were assumed equivalent for the active metabolites due to their similar physiochemical properties – Refer to* ***Figure 5****.*

[b]*D_{sup} fitted to the concentration-time profile of CP-506 in the donor and receiver compartment of diffusion chambers bearing bare support membranes maintained under supraoxic conditions. Parameter estimates were assumed equivalent for the active metabolites due to their similar physiochemical properties – Refer to* ***Figure 5****.*

[c]*Parameters estimated from the extracellular/intracellular partitioning of CP-506 and its active metabolites in monolayer cultures maintained under supraoxic or anoxic conditions – Refer to* ***Figure 4****.*

[d]*Extracellular/intracellular partitioning parameters of CP-506M-Cl_2 were assumed equivalent to the measured metabolites or derived from published estimates for PR-104A metabolites (Foehrenbacher et al., 2013a; Hong et al., 2018b).*

[e]*Stability of CP-506 and its active metabolites in stirred culture medium at 37°C – Refer to* ***Figure 3****.*

[f]*Parameters estimated from the clonogenic survival of monolayer or spheroid cultures following exposure to CP-506 under anoxic conditions – Refer to* ***Figure 7****.*

the longer doubling time of the target cells (21.7 ± 0.04 vs. 22.95 ± 0.38 h, respectively) (**Figure 6D**).

Established spheroids were exposed to CP-506 for 4 h under anoxic conditions. Treated spheroids were then enzymatically dissociated for a clonogenic endpoint or tracked using an image analysis method of volume determination. Clonogenic survival assays showed increased killing of both target and activator cells with the proportion of activator cells in the co-culture (**Figure 6E**). Growth delay assays illustrated a similar trend with an increase in the proportion of activator cells leading to greater spheroid growth inhibition at each concentration relative to the DMSO-only control (**Figure 6F**). IC_{50} values for inhibition of spheroid growth were >40 μM, 13.6 μM, 5.6 μM and 2.4 μM for spheroid co-cultures comprised of 0%, 10%, 50% and 100% activator cells respectively.

A summary of the parameters used for ABM simulations is provided in **Table 1**. Here, the *in vitro* determined terms for the cellular uptake, metabolism and transport of CP-506 were used to simulate the killing of activator and target cells in anoxic spheroids. The clonogenic cell survival data from monolayer-based assays was used to estimate the kill probability parameter (k_d) and was well-fitted with the monolayer ABM (R^2 = 0.9685; **Figure 7A**). This assumed uniform solute concentrations and equipotent metabolites (same k_d) with a lower anoxic first-rate constant for metabolic consumption (k_{met0}) fitted for target compared to activator cells (0.0019 min^{-1} vs. 0.12 min^{-1} respectively) (**Figure 7B**). However, a higher k_d was required to model the experimental data from spheroid co-cultures (0.01 vs. 0.0256 respectively). The spheroid ABM assumed that diffusion occurs through the unstirred medium and extracellular spaces with the metabolic activation of CP-506 restricted to the intracellular space (**Figure 7C**). CP-506 and its metabolites can exchange across the plasma membrane with the reduced metabolites sufficiently stable to diffuse from the cell of origin. Simulated spheroids were exposed to CP-506 for 4 h under anoxic conditions with oxygen gradients restored upon treatment withdrawal. Best efforts recapitulated trends in target cell killing (R^2 = 0.9733) but slightly underestimated activator cell killing (R^2 = 0.7703; **Figure 7D**).

To understand how its pharmacological properties may impact tissue distribution in in vivo tumours, spatial gradients of CP-506 and its reduced metabolites were modelled in a transverse section of a representative spheroid comprised of 50% activators (**Figure 8**). Simulations show intracellular concentrations as a function of penetration depth after a 4 h exposure under anoxic conditions. The model predicts a rapid decline in the intracellular concentration of CP-506 from the spheroid periphery toward the spheroid core (613-fold range). Concentrations are negligible beyond a penetration depth of 190 μm. Concentrations of the formed metabolites CP-506H and CP-506M largely reflect the spatial gradient of CP-506 within the spheroid, with concentrations naturally higher in the peripheral cells. The decline in the intracellular concentration is however less pronounced compared

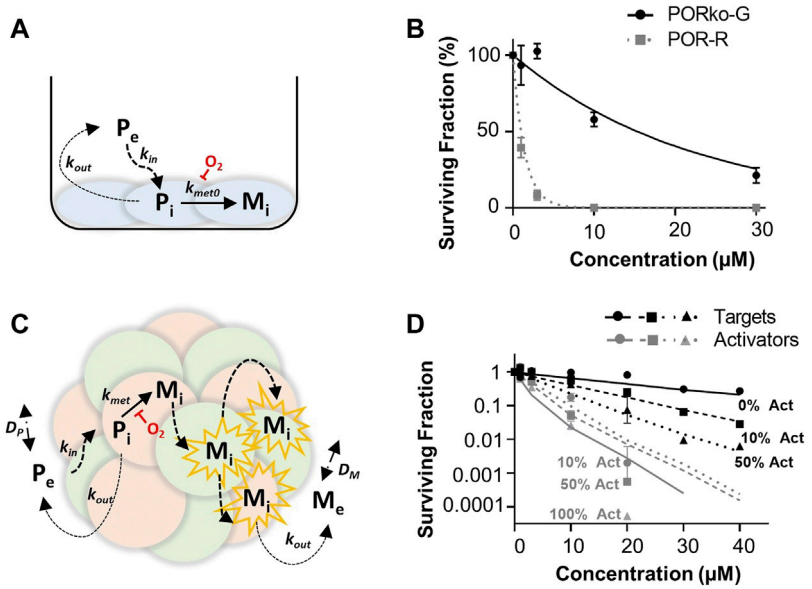

FIGURE 7 | ABM simulations of clonogenic cell survival in monolayer and spheroid cultures following CP-506 treatment. **(A)** Schematic representation of the cellular uptake, metabolism and diffusion of CP-506 in monolayer cultures. Exchange of the extracellular prodrug (P_e) and intracellular prodrug (P_i) between cell membranes is defined by permeability rate constants k_{in} and k_{out} with metabolism of P_i to intracellular metabolites (M_i) defined by the first order rate constant k_{met0} and is strictly oxygen-dependent. **(B)** Model predictions (lines) compared to experimental determinations (symbols) of clonogenic survival in monolayer cultures of target (PORko-G) and activator (POR-R) cells exposed to CP-506 for 4 h under anoxic conditions (<1 ppm O_2) determined from the monolayer ABM by fitting k_d for POR-R cells and the k_{met0} parameter for PORko-G cells (data redrawn from **Figure 2C**). **(C)** Schematic representation of the cellular uptake, metabolism and diffusion of CP-506 in spheroid co-cultures. Diffusion of extracellular prodrug (P_e) and intracellular prodrug (P_i) across cell membranes is defined by permeability rate constants k_{in} and k_{out}. P_i is metabolized to intracellular metabolites (M_i) in activator cells (red) defined by a first order rate constant k_{met0} which is oxygen-dependent. M_i can diffuse to nearby target cells (green) by the extracellular route to elicit bystander killing and can diffuse out into the extracellular compartment, M_e. In the extracellular compartment P_e and M_e can diffuse as defined by their diffusion coefficients D_P and D_M respectively. **(D)** Model predictions (lines) compared to experimental determinations (symbols) of clonogenic survival in spheroid co-cultures comprised of differing proportions of activator (act) and target cells (data re-drawn from **Figure 6E**).

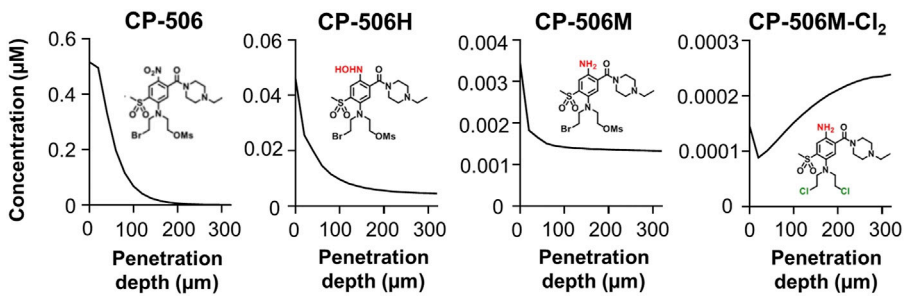

FIGURE 8 | ABM simulations of the intracellular concentration gradients of CP-506 and its reduced metabolites in a transverse section of a multicellular spheroid. Model predictions of the intracellular concentration gradients of CP-506 and its reduced metabolites CP-506H, CP-506M and CP-506M-Cl_2 as a function of penetration depth in a spheroid co-culture comprised of 50% activators after exposure to 20 μM CP-506 for 4 h under anoxic conditions (<1 ppm O_2).

to CP-506, with concentrations in the innermost cells only 3- (CP-506M) to 10-fold (CP-506H) lower than that of the peripheral cells. Intracellular concentrations of the downstream metabolite CP-506M-Cl_2 mirror the spatial gradients of CP-506H and CP-506M, with concentrations markedly higher in the spheroid core. Collectively, these findings indicate that the reduced metabolites of CP-506 are sufficiently stable to diffuse from their hypoxic activating cells to neighbouring populations to potentiate cell killing by means of a bystander effect.

DISCUSSION

This study demonstrates that CP-506 exhibits favourable tissue pharmacokinetic properties, with a high cell uptake factor, maximal activation under extreme hypoxia, long half-life and good aqueous stability; all properties consistent with the observed anti-tumour efficacy of CP-506 (Van Der Wiel et al., 2021). These optimal properties are comparable or superior to the first generation analogue PR-104A (Patterson et al., 2007; Patel et al., 2011) but

without the potential for off-target aerobic activation by AKR1C3 in normal tissues. The clinical development of PR-104 was halted due to dose-limiting myelotoxicity at suboptimal plasma exposures (Jameson et al., 2010; Abou-Alfa et al., 2011; Mckeage et al., 2012) with AKR1C3 expression in human bone marrow progenitor cells implicated as the probable cause (Birtwistle et al., 2009; Guise et al., 2010; Van Der Wiel et al., 2021). CP-506 thus represents an optimised PR-104 analogue designed to undergo metabolic activation exclusively under hypoxic conditions (Van Der Wiel et al., 2021).

Here, we employ a series of novel experimental systems to solve reaction-diffusion equations to define parameters for the cellular uptake, metabolism and diffusion of CP-506 and its active metabolites (**Figure 2**) in tumour tissue. Model predictions were validated by comparing theoretical predictions to experimental determinations of clonogenic cell survival in spheroid co-cultures comprised of varying proportions of metabolically competent "activator" and metabolically defective "target" cells.

The cellular uptake of CP-506 in monolayer cultures was described by a first order kinetic model with a constant cell uptake (C_i/C_e) ratio of 50-fold (**Figure 4A**). The physiochemical properties of CP-506 imply that the high affinity cellular uptake is due to lysosomal sequestration reflecting ionization of the piperazine nitrogen (pKb = 7.79). The developed prodrug transport model suggests that the high cell uptake factor is offset by the intrinsic stability of CP-506 in the absence of reductive metabolism (**Figure 5B**), where the extended half-life affords the long equilibrium time required for delivery of effective concentrations to distal, metabolically active hypoxic cells (<1 μM O_2) (Van Der Wiel et al., 2021).

The reliance on severe hypoxia (<1 μM O_2) for CP-506 metabolism and cytotoxicity (Van Der Wiel et al., 2021) ensures selective activation in tumour tissues. A number of flavoenzymes have been implicated in the nitroreduction of CP-506 in an *in vitro* setting (Van Der Wiel et al., 2021), including POR which is a major enzyme responsible for the hypoxia-selective metabolism of PR-104A in cancer cell lines (Guise et al., 2007; Guise et al., 2012). Here, we reaffirm the role of POR in CP-506 metabolism using paired cell lines with variable levels of protein expression. Forced overexpression of soluble POR heightened protein expression levels by 11-fold with corresponding increase in the rate of CP-506 metabolite formation (**Figure 3A**) and cellular cytotoxicity (**Figure 1B**) under hypoxic conditions. POR gene knockdown had the converse effect, with metabolite production suppressed up to 151-fold (CP-506M-Cl_2, **Figure 3A**) relative to the POR-overexpressing cell line resulting in a 20-fold differential in anoxic sensitivity by clonogenic endpoint in both monolayer (**Figure 1C**) and spheroid-based assays (**Figure 6B**).

The hypoxia-selective metabolism of CP-506 leads to the formation of a series of reactive cytotoxic species (**Figure 2**). By direct exogenous exposure of cell monolayers to each authentic metabolite, we identify the amine CP-506M, hydroxylamine CP-506H and dichloro-amine CP-506M-Cl_2 as the major cytotoxic metabolites (**Figure 3**). Our spheroid-based assays provide the first direct evidence of a bystander effect, with reduced growth kinetics (**Figure 6F**) and increased target and activator cell killing (**Figure 6E**) correlating with the proportion of activator cells in the co-culture. These findings are consistent with metabolite redistribution via efflux of the formed metabolites from metabolically enhanced "activator" cells followed by rapid uptake into neighbouring POR-null "target" cell populations leading to widespread cell killing. Moreover, heightened "activator" cell killing with escalating proportions of activators indicates that metabolic consumption of CP-506 does not impede its extravascular transport to the most distal regions of the tumour tissue resulting in minimal spatial heterogeneity in metabolite distribution. This interpretation is supported by the appearance of the active metabolites in the media compartments of our experimental model systems (**Figure 4**, **Figure 5**), although the attained parameters slightly underestimate activator cell killing (**Figure 7D**). This implies that the extravascular transport properties of CP-506 are likely superior to that anticipated by our experimental model systems. It may also indicate missing variables in our bystander model, analogous to the implied requirement for metabolites with low potency but high stability for PR-104A (Foehrenbacher et al., 2013a). Despite these caveats, our simulations predict a striking bystander efficiency at tissue-like densities (**Figure 8**). Although reaction (cellular uptake and metabolism) within the tumour tissue completely depletes intracellular concentrations of CP-506 beyond a penetration depth of 190 μm, concentrations of the formed metabolites were fairly homogenous throughout the simulated spheroid. In fact, intracellular concentrations of the major metabolites were only 3- (CP-506M) to 10-fold (CP-506H) lower at a penetration depth of 300 μm, essentially compensating for the CP-506 concentration gradient.

CP-506 is metabolically converted under hypoxic conditions into a series of short-lived reduced metabolites (**Figure 2**), but the relative contribution of each toward the bystander efficiency of CP-506 is not yet known. In principle, the bystander potential of each metabolite is dependent on multiple factors including its rate of intracellular production, stability, potency and membrane permeability. Of the metabolites examined, CP-506H-Cl_2 and CP-506M-Cl_2 demonstrated at least a 10-fold longer half-life than CP-506H or CP-506M (**Figure 3B**), reflecting the slower leaving group efficiency of the *bis*-chloro-mustard metabolites. Analogous to the dichloro metabolites of PR-104A (Hong et al., 2018b), the dichloro-hydroxylamine CP-506H-Cl_2 and dichloro-amine CP-506M-Cl_2 are predicted to be approximately 10-fold more lipophilic than their corresponding Br/OMs mustard metabolites CP-506H and CP-506M, indicating that they will more readily permeate membranes and exit the cell of origin. Notably, the stability of CP-506H-Cl_2 was relatively poor in comparison to CP-506M-Cl_2, reflecting the tendency of the hydroxylamine moiety to undergo further reduction to its amine derivative, CP-506M-Cl_2. In an analogous manner, the diol-hydroxylamine CP-506H-$(OH)_2$ was undetectable in anoxic cultures indicating rapid conversion to its six-electron reduction product CP-506M-$(OH)_2$ (**Figure 3B**). Despite the long half-life of CP-506M-$(OH)_2$, the cell line panel was not sensitive to concentrations up to 100 μM (**Figure 3C**), consistent with the hydroxyl moieties failing to act as leaving groups (and the hydrophilic nature of the metabolite). This identifies CP-506M-$(OH)_2$ as an inert terminal metabolite. Collectively these data also indicate the reduction from CP-506H-Cl_2 to CP-506M-Cl_2 proceeds faster than its hydrolysis to CP-506H-$(OH)_2$. Taken together, the superior physicochemical properties of CP-506M-Cl_2 are consistent with the simulated accumulation of CP-506M-Cl_2 in the spheroid

core and identify it as the major bystander mediator of CP-506, perhaps with CP-506H and CP-506M playing minor secondary roles.

While the concentration-dependence of "activator" and "target" cell killing with CP-506 is comparable to previous determinations for PR-104A (Hong et al., 2018b), it is important to note any difference in plasma pharmacokinetics are not accounted for in the current modelling paradigm. Although PR-104A showed favourable activity in murine xenograft models (Patterson et al., 2007), safe human exposure levels were only 10–29% of those observed in mice (Guise et al., 2010), most likely due to off-target aerobic activation of PR-104A by human AKR1C3 in myeloid progenitor cells. The resistance of CP-506 to AKR1C3 bioactivation predicts for significantly higher plasma exposures in human trial without dose-limiting myelotoxicity. When coupled with the favourable extravascular transport properties of CP-506 and its bystander metabolite(s), as described in this study, marked single agent activity would be anticipated. Substantial anti-tumour activity of CP-506 has indeed been reported using clinically-relevant doses and schedules in murine xenograft models of diverse cancer types with variable hypoxic fractions reflecting the superior physicochemical properties and murine pharmacokinetics of CP-506 (Van Der Wiel et al., 2021). Current research efforts are exploring this further using a well-validated *in silico* spatially-resolved pharmacokinetic/pharmacodynamic modelling approach (Foehrenbacher et al., 2013a), where experimental inputs are used to model the spatial gradients of a prodrug and its cytotoxic effectors with respect to molecular oxygen in a representative mapped tumour microvascular network.

Overall, this study uses a series of novel experimental systems along with computational modelling to investigate the extravascular transport properties and bystander efficiency of nitrogen mustard prodrug CP-506 and its active metabolites in the tumour tissues. We show that CP-506 possesses favourable tissue pharmacokinetic properties for anti-tumour activity including a long half-life, high cell uptake factor, tissue diffusion, selective activation under severe hypoxia and a substantial bystander potential. Our findings endorse the ongoing clinical development of CP-506 (NCT04954599) for use in the treatment of patients with advanced solid malignancies.

DATA AVAILABILITY STATEMENT

The raw data supporting the conclusion of this article will be made available by the authors, without undue reservation.

AUTHOR CONTRIBUTIONS

Compound synthesis: AA; Compound analysis: AA, MB, VJ-P, and EL; Conceptualization and experimental design: VJ-P, KH, EL, AP, JS, and AA; Data curation: VJ-P, EL, AW and AA; Modelling and analysis: VJ-P, EL, AW and KH. Funding acquisition: AP and JS; Experimental investigation: EL, AW, VJ-P, and MB; Methodology: KH, VJ-P, EL, and MB; Project administration: AP and JS; Resources: AP and JS; Software development and maintenance: GB. Supervision: AP, KH, and VJ-P. Visualization: EL, AW, and VJ-P; Writing—original draft: EL, VJ-P, KH, JS, and AA; Writing—review and editing: AP, JS, AA, VJ-P, EL, and KH.

SUPPLEMENTARY MATERIAL

The Supplementary Material for this article can be found online at: https://www.frontiersin.org/articles/10.3389/fphar.2022.803602/full#supplementary-material

REFERENCES

Abbattista, M. R., Jamieson, S. M., Gu, Y., Nickel, J. E., Pullen, S. M., Patterson, A. V., et al. (2015). Pre-clinical Activity of PR-104 as Monotherapy and in Combination with Sorafenib in Hepatocellular Carcinoma. *Cancer Biol. Ther.* 16 (4), 610–622. doi:10.1080/15384047.2015.1017171

Abou-Alfa, G. K., Chan, S. L., Lin, C. C., Chiorean, E. G., Holcombe, R. F., Mulcahy, M. F., et al. (2011). PR-104 Plus Sorafenib in Patients with Advanced Hepatocellular Carcinoma. *Cancer Chemother. Pharmacol.* 68 (2), 539–545. doi:10.1007/s00280-011-1671-3

Birtwistle, J., Hayden, R. E., Khanim, F. L., Green, R. M., Pearce, C., Davies, N. J., et al. (2009). The Aldo-Keto Reductase AKR1C3 Contributes to 7,12-Dimethylbenz(a)anthracene-3,4-Dihydrodiol Mediated Oxidative DNA Damage in Myeloid Cells: Implications for Leukemogenesis. *Mutat. Res.* 662, 67–74. doi:10.1016/j.mrfmmm.2008.12.010

Crawford, S. (2013). Is it Time for a New Paradigm for Systemic Cancer Treatment? Lessons from a century of Cancer Chemotherapy. *Front. Pharmacol.* 4, 68–18. doi:10.3389/fphar.2013.00068

Denny, W. A. (2005). Hypoxia-activated Anticancer Drugs. *Expert Opin. Ther. Patents* 15 (6), 635–646. doi:10.1517/13543776.15.6.635

Denny, W. A. (2010). Hypoxia-activated Prodrugs in Cancer Therapy: Progress to the Clinic. *Future Oncol.* 6 (3), 419–428. doi:10.2217/fon.10.1

Foehrenbacher, A., Patel, K., Abbattista, M. R., Guise, C. P., Secomb, T. W., Wilson, W. R., et al. (2013). The Role of Bystander Effects in the Antitumor Activity of the Hypoxia-Activated Prodrug PR-104. *Front. Oncol.* 3, 263. doi:10.1016/s0959-8049(12)71601-510.3389/fonc.2013.00263

Foehrenbacher, A., Secomb, T. W., Wilson, W. R., and Hicks, K. O. (2013). Design of Optimized Hypoxia-Activated Prodrugs Using Pharmacokinetic/pharmacodynamic Modeling. *Front. Oncol.* 3, 314. doi:10.3389/fonc.2013.00314

Fukumura, D., and Jain, R. K. (2007). Tumor Microenvironment Abnormalities: Causes, Consequences, and Strategies to Normalize. *J. Cel. Biochem.* 101 (4), 937–949. doi:10.1002/jcb.21187

Guise, C. P., Wang, A. T., Theil, A., Bridewell, D. J., Wilson, W. R., and Patterson, A. V. (2007). Identification of Human Reductases that Activate the Dinitrobenzamide Mustard Prodrug PR-104A: a Role for NADPH: cytochrome P450 Oxidoreductase under Hypoxia. *Biochem. Pharmacol.* 74 (6), 810–820. doi:10.1016/j.bcp.2007.06.014

Guise, C. P., Abbattista, M. R., Singleton, R. S., Holford, S. D., Connolly, J., Dachs, G. U., et al. (2010). The Bioreductive Prodrug PR-104A Is Activated under Aerobic Conditions by Human Aldo-Keto Reductase 1C3. *Cancer Res.* 70 (4), 1573–1584. doi:10.1158/0008-5472.CAN-09-3237

Guise, C. P., Abbattista, M. R., Tipparaju, S. R., Lambie, N. K., Su, J., Li, D., et al. (2012). Diflavin Oxidoreductases Activate the Bioreductive Prodrug PR-104A under Hypoxia. *Mol. Pharmacol.* 81 (1), 31–40. doi:10.1124/mol.111.073759

Guise, C. P., Abbattista, M. R., Anderson, R. F., Li, D., Taghipouran, R., Tsai, A., et al. (2020). Subcellular Location of Tirapazamine Reduction Dramatically Affects Aerobic but Not Anoxic Cytotoxicity. *Molecules* 25 (21), 4888. doi:10.3390/molecules25214888

Hicks, K. O., Ohms, S. J., van Zijl, P. L., Denny, W. A., Hunter, P. J., and Wilson, W. R. (1997). An Experimental and Mathematical Model for the Extravascular Transport of a DNA Intercalator in Tumours. *Br. J. Cancer* 76 (7), 894–903. doi:10.1038/bjc.1997.481

Hicks, K. O., Fleming, Y., Siim, B. G., Koch, C. J., and Wilson, W. R. (1998). Extravascular Diffusion of Tirapazamine: Effect of Metabolic Consumption Assessed Using the Multicellular Layer Model. *Int. J. Radiat. Oncol. Biol. Phys.* 42 (3), 641–649. doi:10.1016/s0360-3016(98)00268-5

Hicks, K. O., Pruijn, F. B., Sturman, J. R., Denny, W. A., and Wilson, W. R. (2003). Multicellular Resistance to Tirapazamine Is Due to Restricted Extravascular Transport: A Pharmacokinetic/pharmacodynamic Study in HT29 Multicellular Layer Cultures. *Cancer Res.* 63 (18), 5970–5977.

Hicks, K. O., Pruijn, F. B., Secomb, T. W., Hay, M. P., Hsu, R., Brown, J. M., et al. (2006). Use of Three-Dimensional Tissue Cultures to Model Extravascular Transport and Predict *In Vivo* Activity of Hypoxia-Targeted Anticancer Drugs. *J. Natl. Cancer Inst.* 98 (16), 1118–1128. doi:10.1093/jnci/djj306

Hicks, K. O., Myint, H., Patterson, A. V., Pruijn, F. B., Siim, B. G., Patel, K., et al. (2007). Oxygen Dependence and Extravascular Transport of Hypoxia-Activated Prodrugs: Comparison of the Dinitrobenzamide Mustard PR-104A and Tirapazamine. *Int. J. Radiat. Oncol. Biol. Phys.* 69 (2), 560–571. doi:10.1016/j.ijrobp.2007.05.049

Hicks, K. O., Siim, B. G., Jaiswal, J. K., Pruijn, F. B., Fraser, A. M., Patel, R., et al. (2010). Pharmacokinetic/pharmacodynamic Modeling Identifies SN30000 and SN29751 as Tirapazamine Analogues with Improved Tissue Penetration and Hypoxic Cell Killing in Tumors. *Clin. Cancer Res.* 16 (20), 4946–4957. doi:10.1158/1078-0432.CCR-10-1439

Hockel, M., Schlenger, K., Aral, B., Mitze, M., Schaffer, U., and Vaupel, P. (1996). Association between Tumor Hypoxia and Malignant Progression in Advanced Cancer of the Uterine Cervix. *Cancer Res.* 56 (19), 4509–4515.

Hong, C. R., Dickson, B. D., Jaiswal, J. K., Pruijn, F. B., Hunter, F. W., Hay, M. P., et al. (2018). Cellular Pharmacology of Evofosfamide (TH-302): A Critical Re-evaluation of its Bystander Effects. *Biochem. Pharmacol.* 156, 265–280. doi:10.1016/j.bcp.2018.08.027

Hong, C. R., Bogle, G., Wang, J., Patel, K., Pruijn, F. B., Wilson, W. R., et al. (2018). Bystander Effects of Hypoxia-Activated Prodrugs: Agent-Based Modeling Using Three Dimensional Cell Cultures. *Front. Pharmacol.* 9, 1013–1016. doi:10.3389/fphar.2018.01013

Hong, C. R., Wilson, W. R., and Hicks, K. O. (2019). An Intratumor Pharmacokinetic/Pharmacodynamic Model for the Hypoxia-Activated Prodrug Evofosfamide (TH-302): Monotherapy Activity Is Not Dependent on a Bystander Effect. *Neoplasia* 21 (2), 159–171. doi:10.1016/j.neo.2018.11.009

Jameson, M. B., Rischin, D., Pegram, M., Gutheil, J., Patterson, A. V., Denny, W. A., et al. (2010). A Phase I Trial of PR-104, a Nitrogen Mustard Prodrug Activated by Both Hypoxia and Aldo-Keto Reductase 1C3, in Patients with Solid Tumors. *Cancer Chemother. Pharmacol.* 65 (4), 791–801. doi:10.1007/s00280-009-1188-1

Li, Y., Zhao, L., and Li, X. F. (2021). The Hypoxia-Activated Prodrug TH-302: Exploiting Hypoxia in Cancer Therapy. *Front. Pharmacol.* 12, 636892. doi:10.3389/fphar.2021.636892

Mao, X., McManaway, S., Jaiswal, J. K., Patel, P. B., Wilson, W. R., Hicks, K. O., et al. (2018). An Agent-Based Model for Drug-Radiation Interactions in the Tumour Microenvironment: Hypoxia-Activated Prodrug SN30000 in Multicellular Tumour Spheroids. *Plos Comput. Biol.* 14 (10), e1006469–30. doi:10.1371/journal.pcbi.1006469

Marcu, L., and Olver, I. (2006). Tirapazamine: From Bench to Clinical Trials. *Curr. Clin. Pharmacol.* 1 (1), 71–79. doi:10.2174/157488406775268192

Marusyk, A., Almendro, V., and Polyak, K. (2012). Intra-tumour Heterogeneity: a Looking Glass for Cancer? *Nat. Rev. Cancer* 12 (5), 323–334. doi:10.1038/nrc3261

Mckeage, M. J., Gu, Y., Wilson, W. R., Hill, A., Amies, K., Melink, T. J., et al. (2011). A Phase I Trial of PR-104, a Pre-prodrug of the Bioreductive Prodrug PR-104A, Given Weekly to Solid Tumour Patients. *BMC Cancer* 11 (1), 432. doi:10.1186/1471-2407-11-432

Mckeage, M. J., Jameson, M. B., Ramanathan, R. K., Rajendran, J., Gu, Y., Wilson, W. R., et al. (2012). PR-104 a Bioreductive Pre-prodrug Combined with Gemcitabine or Docetaxel in a Phase Ib Study of Patients with Advanced Solid Tumours. *BMC Cancer* 12, 496. doi:10.1186/1471-2407-12-496

Nordsmark, M., Bentzen, S. M., Rudat, V., Brizel, D., Lartigau, E., Stadler, P., et al. (2005). Prognostic Value of Tumor Oxygenation in 397 Head and Neck Tumors after Primary Radiation Therapy. An International Multi-center Study. *Radiother. Oncol.* 77 (1), 18–24. doi:10.1016/j.radonc.2005.06.038

Patel, K., Choy, S. S., Hicks, K. O., Melink, T. J., Holford, N. H., and Wilson, W. R. (2011). A Combined Pharmacokinetic Model for the Hypoxia-Targeted Prodrug PR-104A in Humans, Dogs, Rats and Mice Predicts Species Differences in Clearance and Toxicity. *Cancer Chemother. Pharmacol.* 67 (5), 1145–1155. doi:10.1007/s00280-010-1412-z

Patterson, A. V., Ferry, D. M., Edmunds, S. J., Gu, Y., Singleton, R. S., Patel, K., et al. (2007). Mechanism of Action and Preclinical Antitumor Activity of the Novel Hypoxia-Activated DNA Cross-Linking Agent PR-104. *Clin. Cancer Res.* 13 (13), 3922–3932. doi:10.1158/1078-0432.CCR-07-0478

Pries, A. R., Cornelissen, A. J., Sloot, A. A., Hinkeldey, M., Dreher, M. R., Höpfner, M., et al. (2009). Structural Adaptation and Heterogeneity of normal and Tumor Microvascular Networks. *Plos Comput. Biol.* 5 (5), e1000394–11. doi:10.1371/journal.pcbi.1000394

Rowinsky, E. K. (2000). The Pursuit of Optimal Outcomes in Cancer Therapy in a New Age of Rationally Designed Target-Based Anticancer Agents. *Drugs* 60 Suppl 1, 1–2. doi:10.2165/00003495-200060001-00001

Schneider, C. A., Rasband, W. S., and Eliceiri, K. W. (2012). NIH Image to ImageJ: 25 Years of Image Analysis. *Nat. Methods* 9 (7), 671–675. doi:10.1038/nmeth.2089

Singleton, R. S., Guise, C. P., Ferry, D. M., Pullen, S. M., Dorie, M. J., Brown, J. M., et al. (2009). DNA Cross-Links in Human Tumor Cells Exposed to the Prodrug PR-104A: Relationships to Hypoxia, Bioreductive Metabolism, and Cytotoxicity. *Cancer Res.* 69 (9), 3884–3891. doi:10.1158/0008-5472.CAN-08-4023

Spiegelberg, L., Houben, R., Niemans, R., de Ruysscher, D., Yaromina, A., Theys, J., et al. (2019). Hypoxia-activated Prodrugs and (Lack of) Clinical Progress: The Need for Hypoxia-Based Biomarker Patient Selection in Phase III Clinical Trials. *Clin. Transl. Radiat. Oncol.* 15, 62–69. doi:10.1016/j.ctro.2019.01.005

Su, J., Gu, Y., Pruijn, F. B., Smaill, J. B., Patterson, A. V., Guise, C. P., et al. (2013). Zinc finger Nuclease Knock-Out of NADPH:cytochrome P450 Oxidoreductase (POR) in Human Tumor Cell Lines Demonstrates that Hypoxia-Activated Prodrugs Differ in POR Dependence. *J. Biol. Chem.* 288 (52), 37138–37153. doi:10.1074/jbc.M113.505222

Van Der Wiel, A. M. A., Jackson-Patel, V., Niemans, R., Yaromina, A., Liu, E., Marcus, D., et al. (2021). Selectively Targeting Tumor Hypoxia with the Hypoxia-Activated Prodrug CP-506. *Mol. Cancer Ther.* 20, 2372–2383. doi:10.1158/1535-7163.MCT-21-0406

Vaupel, P., and Mayer, A. (2007). Hypoxia in Cancer: Significance and Impact on Clinical Outcome. *Cancer Metastasis Rev.* 26 (2), 225–239. doi:10.1007/s10555-007-9055-1

Vichai, V., and Kirtikara, K. (2006). Sulforhodamine B Colorimetric Assay for Cytotoxicity Screening. *Nat. Protoc.* 1 (3), 1112–1116. doi:10.1038/nprot.2006.179

Wilson, W. R., and Hay, M. P. (2011). Targeting Hypoxia in Cancer Therapy. *Nat. Rev. Cancer* 11 (6), 393–410. doi:10.1038/nrc3064

Wilson, W. R., Pullen, S. M., Hogg, A., Hobbs, S. M., Pruijn, F. B., and Hicks, K. O. (2004). *In Vitro* and *In Vivo* Models for Evaluation of GDEPT: Quantifying Bystander Killing in Cell Cultures and Tumors. *Methods Mol. Med.* 90, 403–431. doi:10.1385/1-59259-429-8:403

Conflict of Interest: JS and AP have previously served as scientific consultants to Convert Pharmaceuticals. JS, AP, and AA are co-inventors on patents assigned to Health Innovation Ventures (PCT: WO2014031012A1; Granted patents: EP2888227B1, US10202408B2, CA2886574C, US9873710B2, AU 2013/306514B2, US9505791B2).

The remaining authors declare that the research was conducted in the absence of any commercial or financial relationships that could be construed as a potential conflict of interest.

Publisher's Note: All claims expressed in this article are solely those of the authors and do not necessarily represent those of their affiliated organizations, or those of the publisher, the editors and the reviewers. Any product that may be evaluated in this article, or claim that may be made by its manufacturer, is not guaranteed or endorsed by the publisher.

frontiers | Frontiers in Pharmacology

ORIGINAL RESEARCH
published: 08 April 2022
doi: 10.3389/fphar.2022.884495

A Supervised ML Applied Classification Model for Brain Tumors MRI

Zhengyu Yu[1,2], *Qinghu He*[3], *Jichang Yang*[3] *and Min Luo*[1,3]*

[1]Department of Nephrology, The Second Xiangya Hospital, Central South University, Changsha, China, [2]Faculty of Engneering and IT, University of Technology Sydney, Sydney, NSW, Australia, [3]Department of Rehabilitation Medicine and Health Care, Hunan University of Medicine, Huaihua, China

Brain Tumor originates from abnormal cells, which is developed uncontrollably. Magnetic resonance imaging (MRI) is developed to generate high-quality images and provide extensive medical research information. The machine learning algorithms can improve the diagnostic value of MRI to obtain automation and accurate classification of MRI. In this research, we propose a supervised machine learning applied training and testing model to classify and analyze the features of brain tumors MRI in the performance of accuracy, precision, sensitivity and F1 score. The result presents that more than 95% accuracy is obtained in this model. It can be used to classify features more accurate than other existing methods.

OPEN ACCESS

Edited by:
Weiguo Li,
Harbin Institute of Technology, China

Reviewed by:
Yan Zhang,
Hunan Normal University, China
Yunrun Liu,
Hong Kong Baptist University, Hong Kong SAR, China

***Correspondence:**
Min Luo
xyluomin@csu.edu.cn

Specialty section:
This article was submitted to Translational Pharmacology, a section of the journal Frontiers in Pharmacology

Received: 26 February 2022
Accepted: 28 March 2022
Published: 08 April 2022

Citation:
Yu Z, He Q, Yang J and Luo M (2022) A Supervised ML Applied Classification Model for Brain Tumors MRI. Front. Pharmacol. 13:884495. doi: 10.3389/fphar.2022.884495

Keywords: brain tumor, magnetic resonance imaging, machine learning algorithms, classification, automation

INTRODUCTION

In the human body, the brain is a complex organ. When brain tumors originate, uncontrolled cell division occurs in an abnormal series of cells forms in the brain (Logeswari and Karnan, 2010). That abnormal series of cells will destroy healthy cells and influent the general activity of the brain. Benign tumors and malignant tumors Brain are two classifications of brain tumors. Benign tumors grow slowly and originate in the brain; They are considered non-progressive or non-cancerous. Benign tumors cannot extend to any other organs inside the body. In contrast, malignant tumors are progressive and cancerous. They grow unexpectedly in an indeterminate manner. Primary malignant tumors can grow themselves. In addition, malignant tumors also can grow in other organs inside the body and spread to the brain.

MRI is an imaging technology that can generate high-quality images of human anatomy. MRI provides extensive information for medical diagnosis and research (Zhang et al., 2011). The automation and accurate classification of MRI images has dramatically improved the diagnostic value of MRI (Scapaticci et al., 2012). However, one type of MRI cannot provide full details for brain tumours that contain many different tissues (Sudharani et al., 2016). Different weighted images are combined to develop the image segmentation of brain tumors. Three weighted MRI images (T1, T2, and FLAIR, in **Figure 1**) are used for image segmentation of the skull on different axial slices (Vannier et al., 1988; Clark et al., 1994; Dou et al., 2007).

As one of the best imaging methods, researchers use MRI to analyze the progression of a brain tumor during the stages of detection and treatment. As MRI generates high resolution, brain structure information, such as brain tissue abnormalities, is detailed. Therefore, MRI significantly influences automatic analysis for medical images (Zacharaki et al., 2009; Litjens et al., 2017). Since medical images can be scanned and loaded into a computer, researchers have proposed different

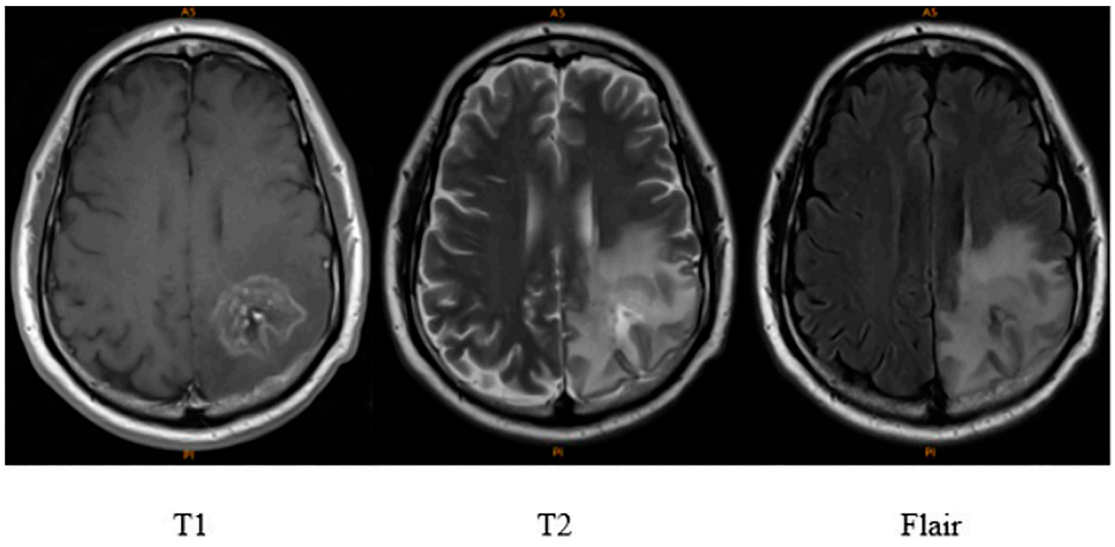

FIGURE 1 | Comparison of T1, T2 and flair of brain tumors MRI (Clark et al., 2013; Scarpace et al., 2022).

automated methods of observation and classification for brain tumor by exploiting brain MRI images (Litjens et al., 2017).

Recently, two categories of research have been proposed. First is unsupervised classification, such as fuzzy c-means and self-organization feature maps (Ibrahim et al., 2013). Second is supervised classification, such as K Nearest Neighbours (KNN) and Support Vector Machine (SVM) (Cocosco et al., 2003; Chaplot et al., 2006). According to the results in classification accuracy, the performance of supervised classification is better than unsupervised classification (Zhang and Wu, 2008; Ibrahim et al., 2013). Nevertheless, most of the classification accuracy is less than 95% (Yeh and Fu, 2008). In the past decades, SVM and Neural Network (NN) become popular due to the outstanding performance for detecting and classifying brain tumors (Ibrahim et al., 2013). Recently, deep learning methods have established novel modeling in machine learning. Complex relationships can be displayed effectively without the need for many nodes by deep architectures, such as SVM and KNN. In this case, they have rapidly developed into the most advanced technologies in various health research fields (such as medical image analysis, medical informatics, and bioinformatics) (Pan et al., 2015; Ravì et al., 2016; Litjens et al., 2017).

MATERIALS AND METHODS

Supervised machine learning algorithms applied classification method is proposed to classify whether the cysts are detected from the MRI of brain tumors. **Figure 2** illustrates the workflow diagram for the training and testing models of the classification method. The process is summarised below:

1) Extract datasets of Brain tumors MRI images. The datasets are from the Repository of Molecular Brain Neoplasia Data (REMBRANDT) in this research (Clark et al., 2013; Scarpace et al., 2022).
2) Extract features. **Table 1** presents that there are 30 features extracted from brain tumors MRI, including 21 categorical features and 9 numerical features. Feature 8 is selected as a target feature; The rest are selected as attributes.
3) Machine learning algorithm classification comparison. Supervised machine learning algorithms applied classification methods, such as Decision Tree (DT), SVM, KNN and NN have been compared to estimate the performance for each training model. Cross-validations are computed on different folds to avoid overfitting. 80% of the datasets are used for training model. The result indicates that the model using DT is the most accurate.
4) The testing model is evaluated by using 20% of the datasets; in this stage, feature 8 is also selected as a target feature; the rest of the features are selected as attributes. The results present that the performance of the DT model with 30 cross-validation folds is the best.
5) After the final model has been evaluated, the result is predicted that the accuracy of the final model is 95.9%.

Datasets

The dataset we used for the research is REMBRANDT (Scarpace et al., 2022). It is accessed from The Cancer Imaging Archive (TCIA) database (Clark et al., 2013). REMBRANDT is purposed to explore the link between the data from genomic characterization and clinical information. and clinical information. REMBRANDT consists of pre-surgical MRI for 130 patients, including 174 studies, 1,483 series, and 110,020 images. **Table 1** presents 30 extracted features from brain tumors MRI, including 21 categorical features and 9 numerical features.

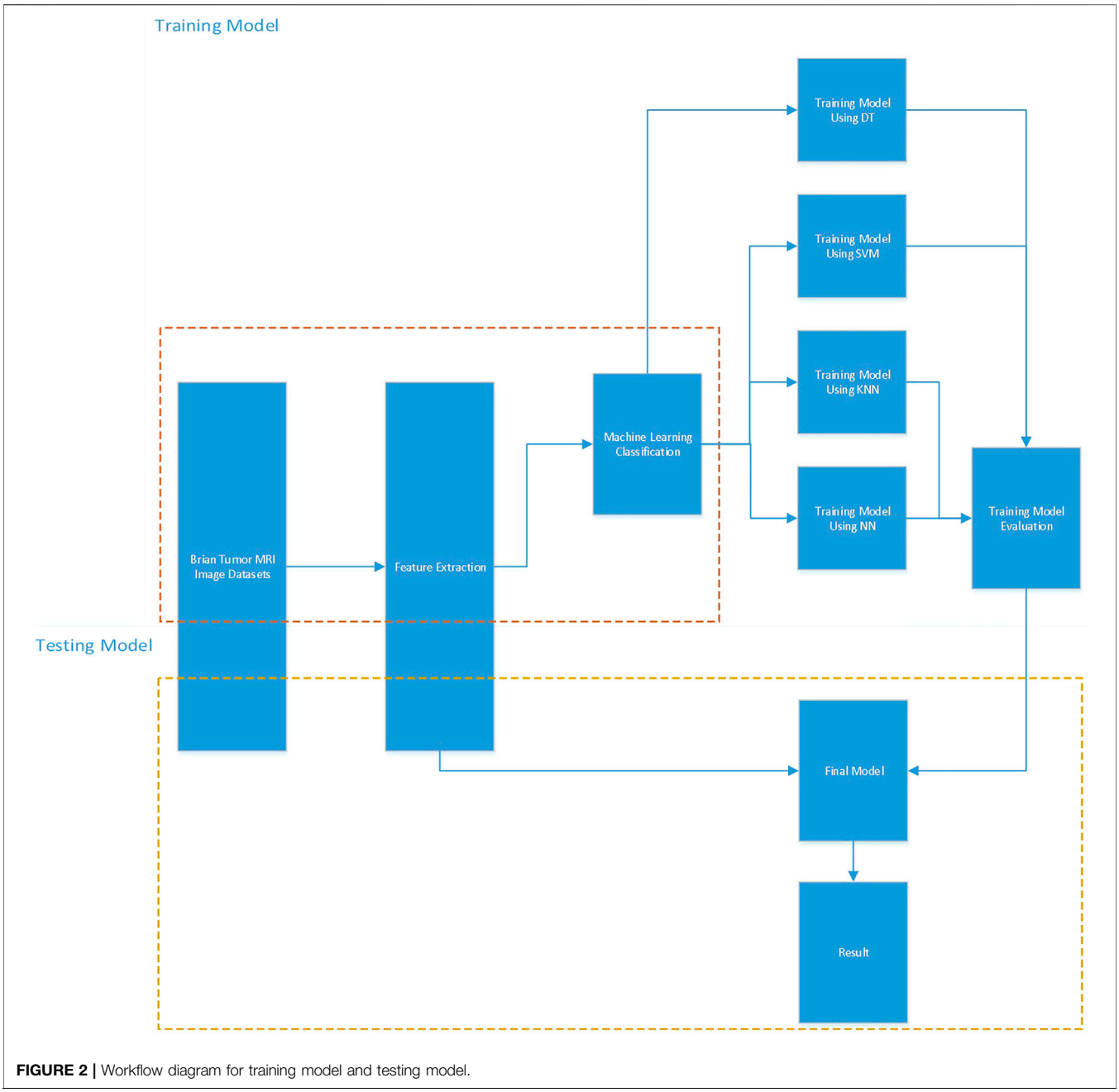

FIGURE 2 | Workflow diagram for training model and testing model.

Training Algorithms Methods

The DT classifier is a supervised machine learning technique to make decisions in a multistage way. The decision tree's fundamental concept includes spreading a complicated decision into a group of more straightforward decisions. The result from this technique could be similar to the intended desired result (Hastie et al., 2009).

The DT technique is a widely used data mining methodology to classify multiple covariates or predict a target variable by algorithms. Branda-like segments are classified *via* decision tree to consist of an inverted tree containing leaf node, interal node and the root node. The decision tree algorithm can efficiently determine complex and large data sets as its non-parametric structure. The data for the study is separated for training and validation when the data set size is too large. The training data sets are built for the decision tree model, whereas the validation data sets are built to approach the optimal final solution by appropriate tree size (Boser et al., 1992; Song and Lu, 2015).

SVM is a commonly used machine learning methodology that classifies data mining problems by its relative flexibility and simplicity (Hearst et al., 1998). SVMs have been processed in

TABLE 1 | Data features extracted from brain tumors MRI.

Number	Features	Type	Number	Features	Type
1	Tumor Location	Categorical	2	Side of Tumor Epicenter	Categorical
3	Eloquent Brain	Categorical	4	Enhancement Quality	Categorical
5	Proportion Enhancing	Numerical	6	Proportion nCET	Numerical
7	Proportion Necrosis	Numerical	8	Cyst(s)	Categorical
9	Multifocal or Multicentric	Categorical	10	T1/FLAIR RATIO	Categorical
11	Thickness of enhancing margin	Categorical	12	Definition of the enhancing margin	Categorical
13	Definition of the non-enhancing margin	Categorical	14	Proportion of Edema	Numerical
15	Edema Crosses Midline	Categorical	16	Hemorrhage	Categorical
17	Diffusion	Categorical	18	Pial invasion	Categorical
19	Ependymal invasion	Categorical	20	Cortical involvement	Categorical
21	Deep WM invasion	Categorical	22	nCET tumor Crosses Midline	Categorical
23	Enhancing tumor Crosses Midline	Categorical	24	Satellites	Categorical
25	Calvarial remodeling	Categorical	26	Extent of resection of enhancing tumor	Numerical
27	Extent resection of nCET	Numerical	28	Extent resection of vasogenic edema	Numerical
29 and 30	Lesion Size	Numerical			

TABLE 2 | Confusion matrix for the classifier method.

		Actual class	
		Positive class	**Negative class**
Predicted Class	Positive Class	True Positive (TP)	False Positive (FP)
	Negative Class	False Negative (FN)	True Negative (TN)

TABLE 3 | Performance of DT classifier.

	Accuracy (%)	Precision (%)	Sensitivity (%)	F1-Score (%)
5 folds	91.1	95.9	94.6	95.3
10 folds	94.2	96.3	97.6	96.9
15 folds	93.7	94.8	98.6	96.7
20 folds	91.1	93.5	97.3	95.4
25 folds	94.9	96.1	98.6	97.3
30 folds	96.2	97.3	98.6	97.9

a wide variety of biomedical applications. For instance, SVM can help automatically classify microarray gene data sets, where the gene expression profile can be examined if they are derived from peripheral fluid or a tumour sample for the result of diagnosis or prognosis. In brain diseases search, SVMs are usually applied by multivoxel pattern analysis due to the low possibility of overfitting when processing images with high dimensions. Recently, SVMs have been developed to predict prognosis and diagnosis in brain disorders research (Orrù et al., 2012).

KNN is an effective and high-performance learning technique to classify and cluster data from a large scale in big data applications (Zhang et al., 2017). The original KNN technique typically set a value of K and select the nearest samples with the influential group. In selecting K nearest samples, KNN is calculated the similarity of all samples for training (Guo et al., 2003). This algorithm costs high memory of the computer and time to process extensive data. Nevertheless, KNN is one of the top techniques in data mining due to its significant performance (Deng et al., 2016).

NN has been introduced as a vital tool for classification in recent research. NN is non-linear and self-adaptive. It is flexible in a complex data environment and can alter itself based on data without explaining of classification functions (Cybenko, 1989; Hornik, 1991). Moreover, NN has the advantage of performing statistical analysis and establishing classification functions with their capability of estimating the probabilities of posterior (Richard and Lippmann, 1991; Zhang, 2000).

RESULTS AND DISCUSSION

The confusion matrix is applied to determine the accuracy, precision, sensitivity and F1 score for the performance of the classifier method. **Table 2** shows the confusion matrix for the classifier method.

The accuracy, precision, sensitivity and F1 score are calculated by equations below:

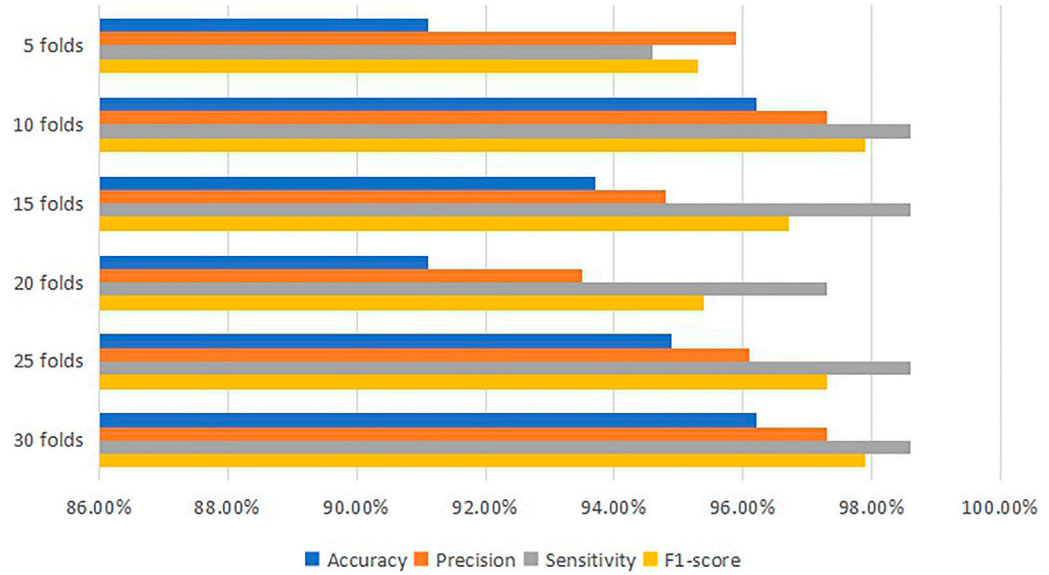

FIGURE 3 | Comparison diagram for the performance of DT classifier.

TABLE 4 | Performance of SVM classifier.

	Accuracy (%)	Precision (%)	Sensitivity (%)	F1-Score (%)
5 folds	94.9	94.9	100	97.4
10 folds	93.7	93.7	100	96.7
15 folds	94.9	94.9	100	97.4
20 folds	94.9	94.9	100	97.4
25 folds	93.7	93.7	100	96.7
30 folds	94.9	94.9	100	97.4

$$\text{Accuracy} = \frac{TP + TN}{TP + TN + FP + FN} \quad (1)$$

$$\text{Precision} = \frac{TP}{TP + FP} \quad (2)$$

$$\text{Sensitivity} = \frac{TP}{TP + FN} \quad (3)$$

$$\text{F1} - \text{score} = \frac{2TP}{2TP + FP + FN} \quad (4)$$

DT Classifier

After processing the training model, the machine learning classifier using DT algorithms indicates that the most accurate model is 96.2% at 30 folds cross-validation. **Table 3** and **Figure 3** present the value of accuracy, precision, sensitivity and F1-score for each fold cross-validation. At 30 folds cross-validation, 96.2% accuracy, 97.3% precision, 98.6% sensitivity and 97.9% F1-score are obtained.

SVM Classifier

After the training model has been computed by SVM algorithms, **Table 4** and **Figure 4** indicate that the most accurate model is 94.9% at 5, 15, 20 and 30 folds cross-validation. They all obtain 94.9% accuracy, 94.9% precision, 100% sensitivity and 97.4% F1-score.

KNN Classifier

In this case, the training model has been processed by KNN Classifier, **Table 5** and **Figure 5** present that the most accurate model is 93.7% which are at 10 and 20 folds, 25 and 30 folds cross-validation. 93.7% accuracy, 94.8% precision, 98.6% sensitivity and 96.6% F1-score are obtained for all of them.

NN Classifier

Table 6 and **Figure 6** are generated from the training model by NN classifier, they present that the most accurate model is 92.4% which is at 10 cross-validation with 94.7% precision, 97.3% sensitivity and 95.9%.

Testing Model

All the classifiers are trained in the previous section. DT training model at 30 folds cross-validation with 96.2% accuracy is selected, which is the highest accurate model among the results. In this research, the testing model is used for evaluation with the rest of the datasets to verify the model's performance.

As **Table 7** presented, the accuracy of DT classifier at 30 folds cross-validation in the testing model is 95.9%. Although this is lower than the score in the training model due to the overfitting classification, it is still the best model with the highest performance.

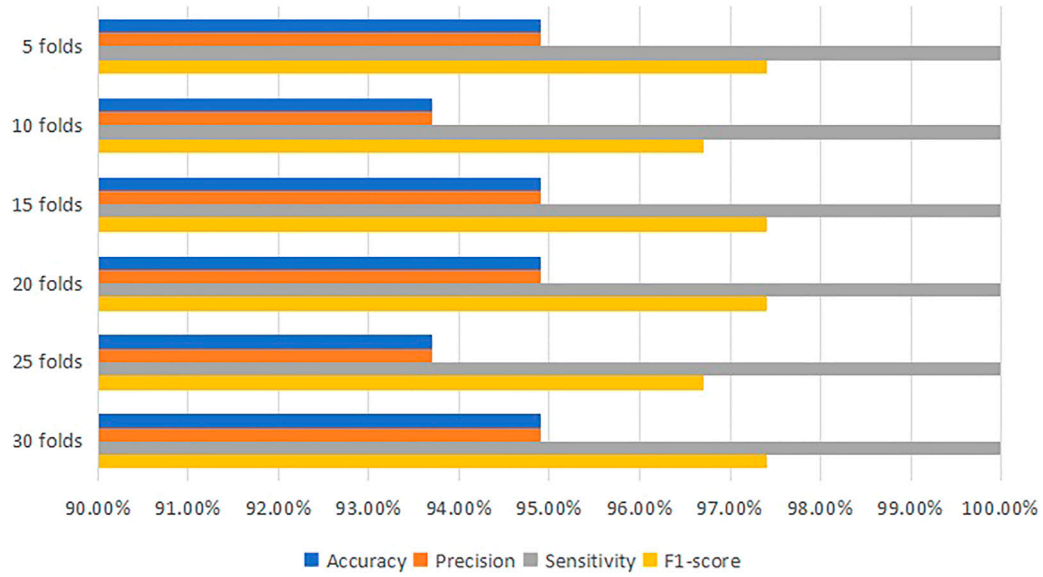

FIGURE 4 | Comparison diagram for the performance of SVM classifier.

TABLE 5 | Performance of KNN classifier.

	Accuracy (%)	Precision (%)	Sensitivity (%)	F1-Score (%)
5 folds	92.4	94.7	97.3	95.9
10 folds	93.7	94.8	98.6	96.6
15 folds	92.4	94.7	97.3	95.9
20 folds	93.7	94.8	98.6	96.6
25 folds	93.7	94.8	98.6	96.6
30 folds	93.7	94.8	98.6	96.6

TABLE 6 | Performance of NN classifier.

	Accuracy (%)	Precision (%)	Sensitivity (%)	F1-Score (%)
5 folds	86.1	95.7	89.2	92.3
10 folds	92.4	94.7	97.3	95.9
15 folds	88.6	95.8	91.9	93.8
20 folds	89.9	95.8	93.2	94.5
25 folds	88.6	94.5	93.2	93.8
30 folds	83.5	94.2	87.8	90.9

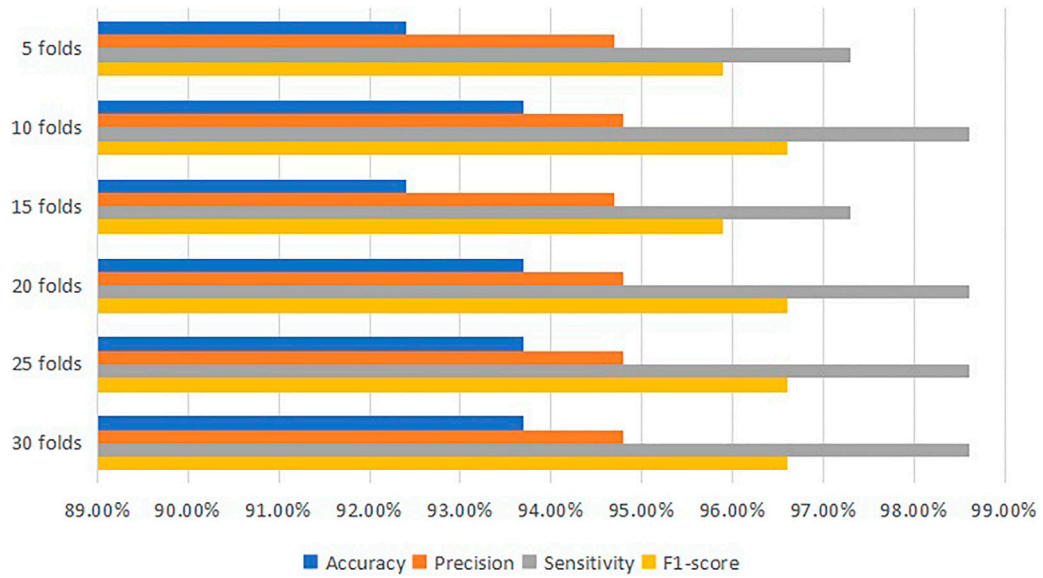

FIGURE 5 | Comparison diagram for the performance of KNN classifier.

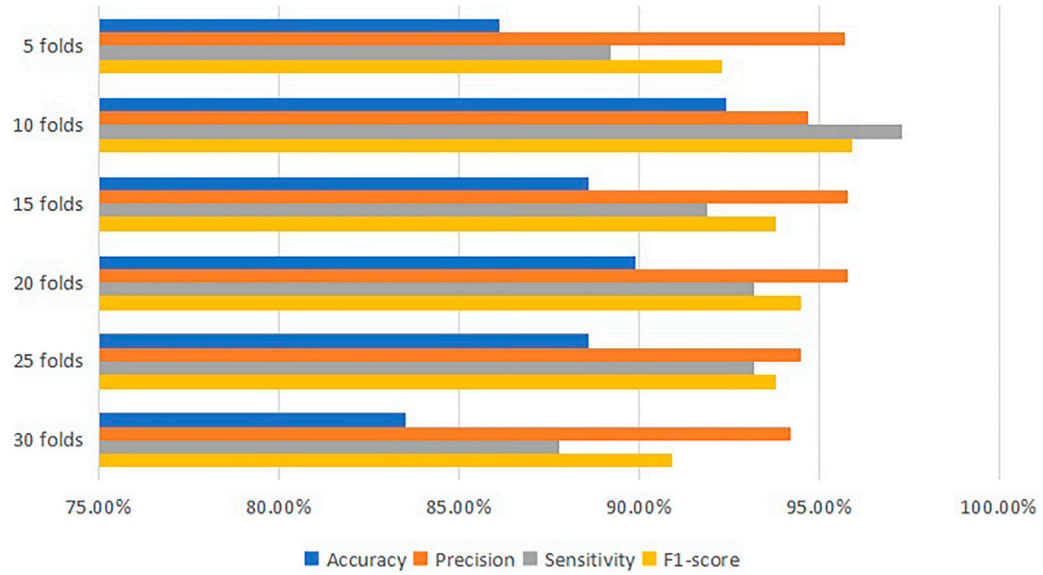

FIGURE 6 | Comparison diagram for the performance of NN classifier.

TABLE 7 | Performance of Testing model.

DT	Training (%)	Testing (%)
30 folds	96.2	95.9

CONCLUSION

This article proposes a supervised machine learning applied classification model for brain tumors MRI. This model is developed to obtain higher classification performance of accuracy, precision, sensitivity and F1 score for the classification of features of brain tumors MRI. The optimized classification model with the most accurate result is developed by comparing with different supervised machine learning algorithms at different folds of cross-validation. After testing, the best performance of the model is obtained. This classification model can be used in other features of brain tumors MRI to obtain the most accurate result.

DATA AVAILABILITY STATEMENT

The original contributions presented in the study are included in the article/Supplementary Material, further inquiries can be directed to the corresponding author.

AUTHOR CONTRIBUTIONS

ZY contributed to conception and design of the study, and wrote the first draft of the manuscript. QH, JY, and ML contributed to manuscript revision, read, and project management. All authors approved the submitted version.

FUNDING

This work was supported by the Foundation of The Second Xiangya Hospital (XYEYY20200812), Central South University.

REFERENCES

Boser, B. E., Guyon, I. M., and Vapnik, V. N. (1992). "A Training Algorithm for Optimal Margin Classifiers," in Proceedings of the fifth annual workshop on Computational learning theory, Pittsburgh, PA, July 27–29, 1992, 144–152. doi:10.1145/130385.130401

Chaplot, S., Patnaik, L. M., and Jagannathan, N. R. (2006). Classification of Magnetic Resonance Brain Images Using Wavelets as Input to Support Vector Machine and Neural Network. *Biomed. signal Process. Control* 1 (1), 86–92. doi:10.1016/j.bspc.2006.05.002

Clark, K., Vendt, B., Smith, K., Freymann, J., Kirby, J., Koppel, P., et al. (2013). The Cancer Imaging Archive (TCIA): Maintaining and Operating a Public Information Repository. *J. Digit Imaging* 26 (6), 1045–1057. doi:10.1007/s10278-013-9622-7

Clark, M. C., Hall, L. O., Goldgof, D. B., Clarke, L. P., Velthuizen, R. P., and Silbiger, M. S. (1994). MRI Segmentation Using Fuzzy Clustering Techniques. *IEEE Eng. Med. Biol. Mag.* 13 (5), 730–742. doi:10.1109/51.334636

Cocosco, C. A., Zijdenbos, A. P., and Evans, A. C. (2003). A Fully Automatic and Robust Brain MRI Tissue Classification Method. *Med. Image Anal.* 7 (4), 513–527. doi:10.1016/s1361-8415(03)00037-9

Cybenko, G. (1989). Approximation by Superpositions of a Sigmoidal Function. *Math. Control. Signal. Syst.* 2 (4), 303–314. doi:10.1007/bf02551274

Deng, Z., Zhu, X., Cheng, D., Zong, M., and Zhang, S. (2016). Efficient K NN Classification Algorithm for Big Data. *Neurocomputing* 195, 143–148. doi:10.1016/j.neucom.2015.08.112

Dou, W., Ruan, S., Chen, Y., Bloyet, D., and Constans, J.-M. (2007). A Framework of Fuzzy Information Fusion for the Segmentation of Brain Tumor Tissues on MR Images. *Image Vis. Comput.* 25 (2), 164–171. doi:10.1016/j.imavis.2006.01.025

Guo, G., Wang, H., Bell, D., Bi, Y., and Greer, K. (2003). "KNN Model-Based Approach in Classification," in OTM Confederated International Conferences" On the Move to Meaningful Internet Systems, Sicily, November 3–7, 2003 (Springer), 986–996. doi:10.1007/978-3-540-39964-3_62

Hastie, T., Tibshirani, R., Friedman, J. H., and Friedman, J. H. (2009). *The Elements of Statistical Learning: Data Mining, Inference, and Prediction*. Heidelberg: Springer.

Hearst, M. A., Dumais, S. T., Osuna, E., Platt, J., and Scholkopf, B. (1998). Support Vector Machines. *IEEE Intell. Syst. Their Appl.* 13 (4), 18–28. doi:10.1109/5254.708428

Hornik, K. (1991). Approximation Capabilities of Multilayer Feedforward Networks. *Neural networks* 4 (2), 251–257. doi:10.1016/0893-6080(91)90009-t

Ibrahim, W. H., Osman, A. A. A., and Mohamed, Y. I. (2013). "MRI Brain Image Classification Using Neural Networks," in 2013 international conference on computing, electrical and electronic engineering (ICCEEE), Khartoum, August 26–28, 2013 (IEEE), 253–258. doi:10.1109/icceee.2013.6633943

Litjens, G., Kooi, T., Bejnordi, B. E., Setio, A. A. A., Ciompi, F., Ghafoorian, M., et al. (2017). A Survey on Deep Learning in Medical Image Analysis. *Med. Image Anal.* 42, 60–88. doi:10.1016/j.media.2017.07.005

Logeswari, T., and Karnan, M. (2010). An Improved Implementation of Brain Tumor Detection Using Segmentation Based on Hierarchical Self Organizing Map. *Ijcte* 2 (4), 591–595. doi:10.7763/ijcte.2010.v2.207

Orrù, G., Pettersson-Yeo, W., Marquand, A. F., Sartori, G., and Mechelli, A. (2012). Using Support Vector Machine to Identify Imaging Biomarkers of Neurological and Psychiatric Disease: a Critical Review. *Neurosci. Biobehav Rev.* 36 (4), 1140–1152. doi:10.1016/j.neubiorev.2012.01.004

Pan, Y., Huang, W., Lin, Z., Zhu, W., Zhou, J., Wong, J., et al. (2015). "Brain Tumor Grading Based on Neural Networks and Convolutional Neural Networks," in 2015 37th Annual International Conference of the IEEE Engineering in Medicine and Biology Society (EMBC), Milano, August 25–29 (IEEE), 699–702. doi:10.1109/embc.2015.7318458

Ravì, D., Wong, C., Deligianni, F., Berthelot, M., Andreu-Perez, J., Lo, B., et al. (2016). Deep Learning for Health Informatics. *IEEE J. Biomed. Health Inform.* 21 (1), 4–21. doi:10.1109/JBHI.2016.2636665

Richard, M. D., and Lippmann, R. P. (1991). Neural Network Classifiers Estimate Bayesian A Posteriori Probabilities. *Neural Comput.* 3 (4), 461–483. doi:10.1162/neco.1991.3.4.461

Scapaticci, R., Di Donato, L., Catapano, I., and Crocco, L. (2012). A Feasibility Study on Microwave Imaging for Brain Stroke Monitoring. *Pier B* 40, 305–324. doi:10.2528/pierb12022006

Scarpace, L., Flanders, A. E., Jain, R., Mikkelsen, T., and Andrews, D. W. (2022). Data from: Rembrandt. The Cancer Imaging Archive.

Song, Y. Y., and Lu, Y. (2015). Decision Tree Methods: Applications for Classification and Prediction. *Shanghai Arch. Psychiatry* 27 (2), 130–135. doi:10.11919/j.issn.1002-0829.215044

Sudharani, K., Sarma, T. C., and Prasad, K. S. (2016). Advanced Morphological Technique for Automatic Brain Tumor Detection and Evaluation of Statistical Parameters. *Proced. Tech.* 24, 1374–1387. doi:10.1016/j.protcy.2016.05.153

Vannier, M., Speidel, C., and Rickman, D. (1988). Magnetic Resonance Imaging Multispectral Tissue Classification. *Physiology* 3 (4), 148–154. doi:10.1152/physiologyonline.1988.3.4.148

Yeh, J., and Fu, J. (2008). A Hierarchical Genetic Algorithm for Segmentation of Multi-Spectral Human-Brain MRI. *Expert Syst. Appl.* 34 (2), 1285–1295. doi:10.1016/j.eswa.2006.12.012

Zacharaki, E. I., Wang, S., Chawla, S., Soo Yoo, D., Wolf, R., Melhem, E. R., et al. (2009). Classification of Brain Tumor Type and Grade Using MRI Texture and Shape in a Machine Learning Scheme. *Magn. Reson. Med.* 62 (6), 1609–1618. doi:10.1002/mrm.22147

Zhang, G. P. (2000). Neural Networks for Classification: a Survey. *IEEE Trans. Syst. Man. Cybern. C* 30 (4), 451–462. doi:10.1109/5326.897072

Zhang, S., Li, X., Zong, M., Zhu, X., and Wang, R. (2017). Efficient kNN Classification with Different Numbers of Nearest Neighbors. *IEEE Trans. Neural Netw. Learn. Syst.* 29 (5), 1774–1785. doi:10.1109/TNNLS.2017.2673241

Zhang, Y.-D., and Wu, L. (2008). Weights Optimization of Neural Network via Improved BCO Approach. *Pier* 83, 185–198. doi:10.2528/pier08051403

Zhang, Y., Wu, L., and Wang, S. (2011). Magnetic Resonance Brain Image Classification by an Improved Artificial Bee colony Algorithm. *Pier* 116, 65–79. doi:10.2528/pier11031709

Conflict of Interest: The authors declare that the research was conducted in the absence of any commercial or financial relationships that could be construed as a potential conflict of interest.

Publisher's Note: All claims expressed in this article are solely those of the authors and do not necessarily represent those of their affiliated organizations, or those of the publisher, the editors and the reviewers. Any product that may be evaluated in this article, or claim that may be made by its manufacturer, is not guaranteed or endorsed by the publisher.

frontiers | Frontiers in Pharmacology

OPINION
published: 26 April 2022
doi: 10.3389/fphar.2022.897635

Stem Cells as a Novel Biomedicine for the Repair of Articular Meniscus: Pharmacology and Applications

*Qiaoyin Tan[1], Cuicui Wu[2], Lei Li[2], Yijie Liang[3], Xiaoyong Bai[3] and Weide Shao[2]**

[1]College of Teacher Education, Zhejiang Normal University, Jinhua, China, [2]College of Physical Education and Health Sciences, Zhejiang Normal University, Jinhua, China, [3]Nova Doctors Group, Hunan Carnation Biotechnology Co., Ltd., Carnation Hospital, Changsha, China

Keywords: stem cells, repair and maintenance, articular meniscus, novel biomedicine, biological agent, stem cell therapy

OPEN ACCESS

Edited by:
Weiguo Li,
Harbin Institute of Technology, China

Reviewed by:
Yunrun Liu,
Hong Kong Baptist University, Hong Kong SAR, China
Huali Chen,
Hunan Provincial People's Hospital, China

****Correspondence:***
Weide Shao
txsh@zjnu.cn

Specialty section:
This article was submitted to Translational Pharmacology, a section of the journal Frontiers in Pharmacology

Received: *16 March 2022*
Accepted: *23 March 2022*
Published: *26 April 2022*

Citation:
Tan Q, Wu C, Li L, Liang Y, Bai X and Shao W (2022) Stem Cells as a Novel Biomedicine for the Repair of Articular Meniscus: Pharmacology and Applications. Front. Pharmacol. 13:897635. doi: 10.3389/fphar.2022.897635

INTRODUCTION

Meniscus is a kind of fibrocartilage composite tissue which plays an important role in the stability, load distribution and shock absorption of the knee joint. In addition, meniscus can absorb the impact and provide nutrition. Meniscus is mainly composed of water, collagen, glycosaminoglycan, etc. Meniscal injury is one of the most common sports injuries. After meniscal injury, traditional repair, suture or meniscectomy are currently used for clinical treatment. However, due to the limited number of blood vessels, it is difficult to heal, and may even lead to knee arthritis and osteoarthritis. Therefore, the field of meniscal in which alternative regenerative medicine is being studied has attracted attention, especially stem cells as the best source of cells to help stimulate the regeneration of natural tissues of meniscal. although only limited relevant research has been conducted at present, mesenchymal stem cells are a very good idea for repairing human joint meniscus injury (Prabhath et al., 2021).

Stem cells have been studied by more and more experts and scholars due to their unique characteristics, such as self-renewal, proliferation and differentiation, immune regulation and plasticity. However, these cells are limited in their clinical application due to their tumorigenesis. However, among the various stem cell types, mesenchymal stem cells (MSCs) have a lower risk of formation due to the teratoma they carry (Huldani et al., 2022)Without any ethical issues, and its readily available sources, have been the subject of most therapeutic application studies. Studies have isolated, cultured and amplified bone marrow mesenchymal stem cells from animals such as sheep and used them in various transformation models for human medical applications (Gugjoo and Amarpal, 2018). There are also many studies that have evaluated MSCs including cartilage, tendon and construct (Gugjoo et al., 2020).

The research summarizes the repair methods of meniscal injury, especially the application of mesenchymal stem cells in the meniscal injury of joint. Many researchers have used a variety of methods to treat meniscal injury with stem cells in animal experiments, to promote the healing of meniscal. Although some results have been achieved, it cannot be widely used in human body, and it is hoped that it can be applied to clinical practice in the near future.

REPAIR METHOD

Scaffold and Stem Cell Combination

Meniscal repair techniques have had limited success in previous years due to technical reasons and local vascularization of the meniscus. Then with that development of meniscus repair technique, there is a new technique by suturing the meniscus-capsule complex to the edge of the tibial plateau. This can reduce the meniscal extrusion of the centralizing technique in the treatment of meniscal injury (Ozeki et al., 2021).

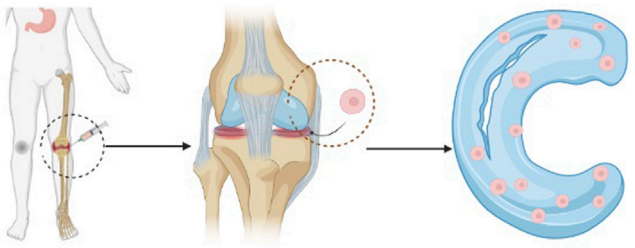

FIGURE 1 | Proces schematic of stem cell injection method.

However, in this way, the scaffold was completely resorbed and no new tissue was formed. Therefore, the combined repair method of scaffolds and stem cells can make up for the defects. Stem cells have strong self-renewal ability and multi-directional differentiation potential, and it is expected to treat meniscus defects by combining with scaffold materials (Arredondo et al., 2021).

Recent advances in stem cell technology have expanded the ability of meniscal stenting. Extracellular matrix of acellular meniscus (MECM) can significantly promote the survival and proliferation of meniscal fibrochondrocytes and increase the *in vitro* expression of type II collagen and proteoglycans. At the same time, the PCL scaffold printed in 3D was used to construct the bionic acellular scaffold with both micro-structure and micro-environment. This cell-free PCL-MECM scaffold demonstrated excellent biocompatibility and yielded good biomechanical properties similar to those of the natural meniscus. Regeneration of the new meniscus in the PCL-MECM scaffold transplanted to the knee and subjected to medial meniscectomy may be a promising approach in rabbit and sheep models. (Guo et al., 2021). In conclusion, the 3D cell printing technique, PCL-MECM scaffold combined with stem cells, helped to generalize the meniscus tissue specificity with respect to the shape and microenvironment of meniscus regeneration (Chae et al., 2021). Composite nanofiber scaffold based on mesenchymal stem cells (MSCs) and tissue engineering constructs (TEC) is helpful to prevent meniscus extrusion and protect cartilage. This meniscus defect is always repaired with fibrocartilage tissue. (Shimomura et al., 2019). Some studies have evaluated the role of polyvinyl alcohol/chitosan (PVA/Ch) scaffolds implanted by adipose-derived mesenchymal stem cells (ASC) and articular chondrocytes (AC) in meniscal regeneration. The results showed that AC/stent group had the best results, followed by AC-ASC/stent group and ASC/stent group (Moradi et al., 2017). Although further research is needed in preclinical application, the results of these studies in clinical meniscal biomaterial repair strategy are promising.

In conclusion, there is a growing recognition of the previous view that menisci cannot be repaired, and that treatment can be performed using repair techniques and bio-enhancing that combine stents with stem cell injection.

Stem Cell Injection

Many studies have tried to repair meniscus with mesenchymal stem cells. As shown in **Figure 1** many people are interested in treating meniscus injury with biological agents such as mesenchymal stem cells and platelet-rich plasma. (Baria et al., 2017). Therapeutic procedures and adjuvant drugs include mechanical stimulation of healing reactions, bone marrow aspirate concentrates, fibrin reinforcement, mesenchymal stem cells, platelet-rich plasma, and other drugs under development used alone or in combination. In particular mesenchymal stem cells, have great research potential for improving and repairing joint meniscus (Mlynarek et al., 2018).

As for the mechanism of stem cells promoting the repair of articular meniscus, there is a tissue engineering strategy based on mesenchymal stem cells (MSC) to test its feasibility for cartilage regeneration. Some studies have derived new stem cell sources from arthroscopic irrigation (AFF-MSCs), which may contain significant amounts of MSCs from synovial and synovial fluid. The experiment prove that wrapping that stem cell with the one-step rapid crosslinking polypeptide DA/HA hydrogel has very encouraging cartilage regeneration potential (Li et al., 2018) Other acellular matrix (DCM) derived from meniscal can induce synovial fluid-derived mesenchymal stem cells (SF-MSCs) to differentiate into meniscal fibrochondrocytes (MFC). (Liang et al., 2018). ECM components from the inner and outer areas of meniscus can promote cartilage formation of mesenchymal stem cells in three-dimensional photo-crosslinked hydrogel. These findings suggest that acellular meniscus ECM has region-specific biological activity. (Rothrauff et al., 2017). In addition to mesenchymal stem cells, allogeneic three-dimensional shaped adipose-derived stem cells (ADSCs) were implanted into the rabbit model with a partially meniscectomy. The results showed that he survived in rabbits and adhered to the defect area, which promoted the histological healing of meniscus (Toratani et al., 2017).

Many studies on repairing meniscal with stem cells show the effectiveness. However, the relationship between MSC life span, persistence at the injured site and therapeutic effect is still unclear (Colbath et al., 2017). The effect of mECM on the response of microencapsulated MSCs and the integrated meniscal repair indicated that mECM hydrogel could be a very promising carrier. MSCs can be transported for long-term repair of meniscal tissue. (Zhong et al., 2020). In addition, ECM hydrogel derived from specific tissues can be injected to provide a bionic environment for cell delivery and realize seamless regeneration of tissue defects. Human bone marrow mesenchymal stem cells (hMSCs) in the meniscus ECM hydrogel facilitate tissue regeneration after injection. It can prevent that development of joint space stenosis and osteoarthritis. Therefore, the study recommends the use of tissue-specific meniscal ECM-derived hydrogels to deliver therapeutic hMSCs for the treatment of meniscal injury. (Yuan et al., 2017). These studies are of great value for exploring its clinical application.

CONCLUSION

Mesenchymal stem cells (MSCs) have brought hope for cartilage regeneration and achieved good results in animal models. However, based on the internal and external effectiveness of

current animal research, there is no evidence that stem cells can form meniscal similar to primitive human meniscus in human body. Therefore, more in-depth research is needed. In addition, whether the manufacturing process of stem cells is standard, whether the clinical methods of bone tissue engineering can be developed on a large scale, and whether the preclinical research can be effectively transformed into clinical trials need further research.

DISCUSSIONS

The research on tissue regeneration technology of stem cells to repair meniscal injury is just started, and has not been widely applied to clinical practice. The therapeutic effect of stem cell repair of meniscus cannot be accurately evaluated. In addition, the high cost of stem cell purification and storage, as well as the need for multiple injections of treatment, are also factors that cannot be fully implemented at present. However, human studies are promising, and MSCs have great potential in the musculoskeletal system. In the next few years, mesenchymal stem cells may play an important role in meniscus repair.

AUTHOR CONTRIBUTIONS

All authors listed have made a substantial, direct, and intellectual contribution to the work and approved it for publication.

REFERENCES

Arredondo, R., Poggioli, F., Martínez-Díaz, S., Piera-Trilla, M., Torres-Claramunt, R., Tío, L., et al. (2021). Fibronectin-coating Enhances Attachment and Proliferation of Mesenchymal Stem Cells on a Polyurethane Meniscal Scaffold. *Regen. Ther.* 18, 480–486. doi:10.1016/j.reth.2021.11.001

Baria, M. R., Sellon, J. L., Lueders, D., and Smith, J. (2017). Sonographically Guided Knee Meniscus Injections: Feasibility, Techniques, and Validation. *PM R.* 9 (10), 998–1005. doi:10.1016/j.pmrj.2016.12.012

Chae, S., Lee, S. S., Choi, Y. J., Hong, D. H., Gao, G., Wang, J. H., et al. (2021). 3D Cell-Printing of Biocompatible and Functional Meniscus Constructs Using Meniscus-Derived Bioink. *Biomaterials* 267, 120466. doi:10.1016/j.biomaterials.2020.120466

Colbath, A. C., Frisbie, D. D., Dow, S. W., Kisiday, J. D., McIlwraith, C. W., and Goodrich, L. R. (2017). Equine Models for the Investigation of Mesenchymal Stem Cell Therapies in Orthopaedic Disease. *Oper. Tech. Sports Med.* 25 (1), 41–49. doi:10.1053/j.otsm.2016.12.007

Gugjoo, M. B., Amarpal, fnm., Fazili, M. u. R., Shah, R. A., Saleem Mir, M., and Sharma, G. T. (2020). Goat Mesenchymal Stem Cell Basic Research and Potential Applications. *Small Ruminant Res.* 183, 106045. doi:10.1016/j.smallrumres.2019.106045

Gugjoo, M. B., and Amarpal, A. (2018). Mesenchymal Stem Cell Research in Sheep: Current Status and Future Prospects. *Small Ruminant Res.* 169, 46–56. doi:10.1016/j.smallrumres.2018.08.002

Guo, W., Chen, M., Wang, Z., Tian, Y., Zheng, J., Gao, S., et al. (2021). 3D-printed Cell-free PCL-MECM Scaffold with Biomimetic Micro-structure and Micro-environment to Enhance *In Situ* Meniscus Regeneration. *Bioactive Mater.* 6 (10), 3620–3633. doi:10.1016/j.bioactmat.2021.02.019

Huldani, H., Abdalkareem Jasim, S., Olegovich Bokov, D., Kamal Abdelbasset, W., Nader Shalaby, M., Thangavelu, L., et al. (2022). Application of Extracellular Vesicles Derived from Mesenchymal Stem Cells as Potential Therapeutic Tools in Autoimmune and Rheumatic Diseases. *Int. Immunopharmacol* 106, 108634. doi:10.1016/j.intimp.2022.108634

Li, J., Huang, Y., Song, J., Li, X., Zhang, X., Zhou, Z., et al. (2018). Cartilage Regeneration Using Arthroscopic flushing Fluid-Derived Mesenchymal Stem Cells Encapsulated in a One-step Rapid Cross-Linked Hydrogel. *Acta Biomater.* 79, 202–215. doi:10.1016/j.actbio.2018.08.029

Liang, Y., Idrees, E., Szojka, A. R. A., Andrews, S. H. J., Kunze, M., Mulet-Sierra, A., et al. (2018). Chondrogenic Differentiation of Synovial Fluid Mesenchymal Stem Cells on Human Meniscus-Derived Decellularized Matrix Requires Exogenous Growth Factors. *Acta Biomater.* 80, 131–143. doi:10.1016/j.actbio.2018.09.038

Mlynarek, R. A., Gomoll, A. H., and Farr, J. (2018). Meniscus Repair Enhancement Options. *Oper. Tech. Sports Med.* 26 (4), 279–287. doi:10.1053/j.otsm.2018.10.010

Moradi, L., Vasei, M., Dehghan, M. M., Majidi, M., Farzad Mohajeri, S., and Bonakdar, S. (2017). Regeneration of Meniscus Tissue Using Adipose Mesenchymal Stem Cells-Chondrocytes Co-culture on a Hybrid Scaffold: *In Vivo* Study. *Biomaterials* 126, 18–30. doi:10.1016/j.biomaterials.2017.02.022

Ozeki, N., Seil, R., Krych, A. J., and Koga, H. (2021). Surgical Treatment of Complex Meniscus Tear and Disease: State of the Art. *J. ISAKOS* 6 (1), 35–45. doi:10.1136/jisakos-2019-000380

Prabhath, S., Alappatt, K., Shetty, A., and Sumalatha, S. (2021). An Exploratory Study of the Histomorphogenesis and Zonal Vascular Changes in the Human Fetal Medial Meniscus. *Translational Res. Anat.* 25, 100148. doi:10.1016/j.tria.2021.100148

Rothrauff, B. B., Shimomura, K., Gottardi, R., Alexander, P. G., and Tuan, R. S. (2017). Anatomical Region-dependent Enhancement of 3-dimensional Chondrogenic Differentiation of Human Mesenchymal Stem Cells by Soluble Meniscus Extracellular Matrix. *Acta Biomater.* 49, 140–151. doi:10.1016/j.actbio.2016.11.046

Shimomura, K., Rothrauff, B. B., Hart, D. A., Hamamoto, S., Kobayashi, M., Yoshikawa, H., et al. (2019). Enhanced Repair of Meniscal Hoop Structure Injuries Using an Aligned Electrospun Nanofibrous Scaffold Combined with a Mesenchymal Stem Cell-Derived Tissue Engineered Construct. *Biomaterials* 192, 346–354. doi:10.1016/j.biomaterials.2018.11.009

Toratani, T., Nakase, J., Numata, H., Oshima, T., Takata, Y., Nakayama, K., et al. (2017). Scaffold-Free Tissue-Engineered Allogenic Adipose-Derived Stem Cells Promote Meniscus Healing. *Arthroscopy* 33 (2), 346–354. doi:10.1016/j.arthro.2016.07.015

Yuan, X., Wei, Y., Villasante, A., Ng, J. J. D., Arkonac, D. E., Chao, P. G., et al. (2017). Stem Cell Delivery in Tissue-specific Hydrogel Enabled Meniscal Repair in an Orthotopic Rat Model. *Biomaterials* 132, 59–71. doi:10.1016/j.biomaterials.2017.04.004

Zhong, G., Yao, J., Huang, X., Luo, Y., Wang, M., Han, J., et al. (2020). Injectable ECM Hydrogel for Delivery of BMSCs Enabled Full-Thickness Meniscus Repair in an Orthotopic Rat Model. *Bioact Mater.* 5 (4), 871–879. doi:10.1016/j.bioactmat.2020.06.008

Conflict of Interest: YL and XB were employed by the Company Hunan Carnation Biotechnology Co., Ltd.

The remaining authors declare that the research was conducted in the absence of any commercial or financial relationships that could be construed as a potential conflict of interest.

frontiers | Frontiers in Pharmacology

ORIGINAL RESEARCH
published: 02 May 2022
doi: 10.3389/fphar.2022.887822

LINC00586 Represses ASXL1 Expression Thus Inducing Epithelial-To-Mesenchymal Transition of Colorectal Cancer Cells Through LSD1-Mediated H3K4me2 Demethylation

Fengting Liu[1], *Xiaofang Ma*[2,3], *Xiyun Bian*[2,3], *Chunyan Zhang*[2,3], *Xiaozhi Liu*[2,3]* and *Qiang Liu*[1]*

[1]Tianjin Key Laboratory of Radiation Medicine and Molecular Nuclear Medicine, Institute of Radiation Medicine, Chinese Academy of Medical Sciences and Peking Union Medical College, Tianjin, China, [2]Medical Research Center, The Fifth Central Hospital of Tianjin, Tianjin, China, [3]Tianjin Key Laboratory of Epigenetics for Organ Development in Preterm Infants, The Fifth Central Hospital of Tianjin, Tianjin, China

OPEN ACCESS

Edited by:
Songwen Tan,
Central South University, China

Reviewed by:
Lijuan Wen,
Hainan Medical University, China
Fangping Wu,
Hunan University of Medicine, China

***Correspondence:**
Xiaozhi Liu
lxz7997@126.com
Qiang Liu
liuqiang@irm-cams.ac.cn

Specialty section:
This article was submitted to Translational Pharmacology, a section of the journal Frontiers in Pharmacology

Received: 02 March 2022
Accepted: 12 April 2022
Published: 02 May 2022

Citation:
Liu F, Ma X, Bian X, Zhang C, Liu X and Liu Q (2022) LINC00586 Represses ASXL1 Expression Thus Inducing Epithelial-To-Mesenchymal Transition of Colorectal Cancer Cells Through LSD1-Mediated H3K4me2 Demethylation. Front. Pharmacol. 13:887822. doi: 10.3389/fphar.2022.887822

Colorectal cancer (CRC) is a major public health problem on a global scale by virtue of its relatively high incidence. The transition of tumor cells from an epithelial to a mesenchymal-like phenotype, so-called epithelial-to-mesenchymal transition (EMT), is a key hallmark of human cancer metastasis, including CRC. Understanding the signaling events that initiate this phenotypic switch may provide opportunities to limit the metastasis of CRC. In this study, we aim to identify long non-coding RNA (lncRNA) mediated epigenetic regulation under the context of CRC. 54 paired samples of tumor tissues and surrounding non-tumor tissues were collected from CRC patients. Cultured human CRC cells HCT116 and LoVo were assayed for their viability and migration using CCK-8 tests and transwell migration assays. The expression of EMT-specific markers (E-cadherin, N-cadherin and vimentin) was analyzed biochemically by RT-qPCR and immunoblot analyses. Interaction among LINC00586, LSD1, and ASXL1 was determined by RNA immunoprecipitation and chromatin immunoprecipitation. *In vivo* analysis of LINC00586 was performed in nude mice xenografted with HCT116 cells. LINC00586 was overexpressed in CRC tissues and associated with patient survival. LINC00586 knockdown repressed HCT116 and LoVo cell viability, migration, their phenotypic switch from epithelial to a mesenchymal, and tumorigenesis *in vivo*. We demonstrated LINC00586 recruited the LSD1 into the ASXL1 promoter region and epigenetically silenced the ASXL1 expression. An ASXL1 gene resisting to LINC00586 attack was demonstrated in cultured HCT116 and LoVo cells and mouse xenograft models of human CRC. Overall, discovery of the LINC00586/LSD1/ASXL1 axis partially explains epigenetic mechanism regulating EMT in CRC, providing a therapeutic target to limit CRC metastasis.

Keywords: colorectal cancer, epithelial-to-mesenchymal transition, LINC00586, LSD1, ASXL1

INTRODUCTION

Colorectal cancer (CRC) is known as the common type of gastrointestinal tract cancers worldwide (Rabeneck et al., 2020). The American Cancer Society updates CRC occurrence that approximately 147,950 individuals will be diagnosed with CRC and 53,200 will die from the disease in 2020 (Siegel et al., 2020). About 90% of CRC-related deaths are attributed to distant metastasis (Ding et al., 2018). Routine clinical management of patients with metastatic colorectal cancer includes oxaliplatin-containing therapy followed by irinotecan-containing therapy at progression (Pfeiffer et al., 2020; Saleh et al., 2020). Although the advancement has been achieved for treating metastatic CRC patients, their overall survival remains unsatisfactory (Basile et al., 2020). A process of tumor cells switch from an epithelial to a mesenchymal-like phenotype is termed epithelial mesenchymal transition (EMT), which is a distinctive feature of human cancers including CRC (Mittal, 2018; Kim et al., 2020). Yet, it still needs to make great efforts to discover and improve therapeutic targets for some obstacles to effective therapy (Fan and Liu, 2017). It is an urgent need to develop the potential effective targets for CRC diagnosis and therapy, such as long non-coding RNAs (lncRNAs) that exert great effects on the progression of CRC.

LncRNAs play a crucial role in the regulation of tumorigenesis, and their aberrant expression underpins the progression of CRC (Galamb et al., 2020). LINC00586, also known as BRAF-activated lncRNA (BANCR), is a 693 bp lncRNA located on chromosome 9, being implicated in the development of CRC and demonstrated to promote the tumorigenesis in CRC (Ma et al., 2018). A previous study clarified that LINC00586 induces the migration of CRC cells and promotes the process of EMT (Guo et al., 2014). Of note, researchers performed quantitative proteomics strategy to globally identify LINC00586-regulated proteins in HeLa cells and found 569 differentially expressed proteins (DEPs) in HeLa cells upon knockout of BANCR (Wang et al., 2022). Nevertheless, the detailed molecular mechanism underlying LINC00586 waits to be further elucidated. LncRNAs as critical contributors in the epigenetic mechanisms are involved in the initiation, progression and metastasis of CRC (Ghafouri-Fard et al., 2021). Furthermore, lncRNAs function in many cases as transcriptional regulators by binding to histone-modifying complexes, to DNA binding proteins (including transcription factors), and even to RNA polymerase II (Long et al., 2017). Transcriptional Regulator 1 (ASXL1), based on the RNA-protein interaction prediction tool (http://pridb.gdcb.iastate.edu/RPISeq/). It has been previously addressed that depleted ASXL1 might be related to lymphatic invasion of CRC, which suggests that ASXL1 is likely to function as a tumor suppressor in CRC (Lee et al., 2020). A direct interaction of ASXL1 with histone H3 demethylase lysine-specific demethylase 1 (LSD1) through the N-terminal region nearby the HP1-binding site was previously reported (Lee et al., 2010). LSD1 could participate in the regulation of CRC by interacting with tetraspanin 8 (Zhang et al., 2020). LSD1 was found to downregulate CDH-1 expression by epigenetic modification and consequently facilitate the metastasis of colon cancer cells (Ding et al., 2013). Taken above into consideration, we aim at investigating the role of LINC00586 in progression of CRC by recruitment of LSD1 into the ASXL1 promoter region and epigenetically silencing the ASXL1 expression. For this purpose, we determine expression pattern of LINC00586 in CRC tissue sample and its association with CRC progression and prognosis. We also tested the effect of LINC00586 on CRC cells *in vitro* setting. To further validate results *in vivo*, we xenografted human CRC cells into nude mice to examine the effect of LINC00586 on the *in vivo* tumorigenesis of CRC cells.

MATERIALS AND METHODS

Ethics Statement

Human tissue specimens were collected from CRC patients who signed informed consent for a protocol approved by the Ethics committee of the hospital. The experiments involved animals were performed with the approval from the institutional animal care and use committee of the hospital.

Human Tissue Specimen Collection

Tumor tissues and matched surrounding non-tumor tissues were collected from 54 CRC patients who were admitted into our hospital between June 2017 and June 2018. The diagnosis of these CRC patients was confirmed by histopathological examinations and their clinical stages were the 7th edition of American Joint Committee on Cancer (AJCC) Cancer Staging Manual, TNM staging criteria for CRC (Edge and Compton, 2010). None received radiotherapy and chemotherapy before tissue specimen collection. Medical records were available from each patient. All patients were followed up 36 months by telephone or hospital visit until June 2021. The follow-up ranged from 2 to 36 months.

Cell Harvest and Transient Transfection

Normal human colon epithelial cells (FHC) and human CRC cell lines (HCT116, LoVo, HT-29, SW480, and SW620) were purchased from the Cell bank in Shanghai Institutes of Chinese Academy of Sciences and harvested in the RPMI-1640 supplemented with 10% fetal bovine serum (FBS) and 1% antibiotics (penicillin/streptomycin). Cell harvest was performed in the incubator (37°C, 5 %CO_2). siRNA against LINC00586 and pcDNA expression vector containing the full-length of human LINC00586 transcripts were purchased from GenePharma (Shanghai, China) and delivered into HCT116 and LoVo cells to specifically blunt and overexpress LINC00586 in CRC cells, respectively, using lipofectamine 3000 reagent (Invitrogen, United States) according to the manufacturer's recommendation. Likewise, ASXL1 overexpression was achieved in HCT116 and LoVo cells using pcDNA expression vector containing the full-length of human ASXL1 gene (Shanghai GenePharma Co., Ltd., China).

Real-Time Quantitative PCR (RT-qPCR) Analysis

Total RNA was extracted from tissues and cells using TRIzol reagents (Invitrogen). cDNA was generated using PrimeScript RT

TABLE 1 | Primer sequences used for RT-qPCR.

Target	Primer sequences (5′-3′)
LINC00586	F: ACAGGACTCCATGGCAAACG
	R: ATGAAGAAAGCCTGGTGCAGT
ASXL1	F: GGTCCTGTCTCAGTCCCTCA
	R: ATAACCACGGGGTCAGAGGT
E-cadherin (human)	F: AAGGCACGCCTGTCGAAGCA
	R: ACGTTGTCCCGGGTGTCATCCT
N-cadherin (human)	F: TGCGCGTGAAGGTTTGCCAGT
	R: TGGCGTTCTTTATCCCGGCGT
Vimentin (human)	F: ACCGCACACAGCAAGGCGAT
	R: CGATTGAGGGCTCCTAGCGGTT
E-cadherin (mouse)	F: TACCATGCTGGTAGGGTGGA
	R: GTGGGAGTCAAATCCCGGTT
N-cadherin (mouse)	F: ACCACTGGCAAGTTCACAGC
	R: TGTACCCCAACTAGTCGCCA
Vimentin (mouse)	F: TCCACCCCTAGCCTGATACC
	R: TGCTGACTTAAAGGGGACCA
GAPDH	F: AACGGATTTGGTCGTATTGGG
	R: TCGCTCCTGGAAGATGGTGAT

F, forward; R, reverse.

kit (RR036A, Takara) as per the manufacturer's protocol. qRT-PCR was performed with the SYBR®Premix ExTaqTM II (RR820A, Takara) on the ABI PRISM®7300 System (Applied Biosystems). Data were normalized to fold change of GAPDH, a house-keeping gene, and relative expressions of mRNAs of interest were determined using the delta-delta comparative threshold cycle (ΔΔCt) methods. Primers are listed in **Table 1**.

Subcellular Fractionation

HCT116 and LoVo cells were harvested for subcellular RNA isolation. Cell cytoplasm and nuclear fractionation was performed with SurePrep™ Nuclear or Cytoplasmic RNA Purification Kit (Fisher Scientific, MA) in accordance with provider's manual. RNA quality and quantity were determined with Nanodrop 2000 (Invitrogen, MA). The U6 and GAPDH transcripts were employed as nuclear and cytosolic controls, respectively.

Immunoblotting

The whole-cell protein was extracted from cell lysates in protease inhibitors-contained radioimmunoprecipitation buffer. After SDS-PAGE separation and membrane transfer, the protein was probed with the following primary antibodies (Abcam, United Kingdom): Anti-ASXL1 antibody (ab228009), anti-SEMA6B antibody (ab180215), anti-E-cadherin antibody (ab15148), anti-N-cadherin antibody (ab18203), anti-vimentin antibody (ab137321), and anti-GAPDH antibody (ab9485). Immunoblots were exposed to horseradish peroxidase-coupled goat anti-rabbit immunoglobulin and enhanced chemiluminescence detection reagents (EMD Millipore, United States). Gray value of target protein bands was quantified using ImageJ software, with GAPDH used for normalization.

Cell Viability Assays

A commercially available CCK-8 kit was used to examine the viability of HCT116 and LoVo cells. In brief, HCT116 and LoVo cells were independently cultured for 0, 24, 48, and 72 h, with 10 μL CCK-8 solution added at the end of each culture for an additional incubation 2 h. Absorbance (at 450 nm) was determined using the Microplate reader, with growth curves depicted.

Cell Migration Assays

Transwell chamber systems of 24-well plate with an 8-μm pore were performed for cell migration assays. In brief, HCT116 and LoVo cells were adjusted using the serum-free DMEM (100 μL) and 200 μL of cell suspension were added into the upper chambers. Following 24-hour incubation at 37°C, the cells that transferred to Matrigel-coated lower chamber containing 10% FBS-supplemented DMEM (Invitrogen) were subject to 4% paraformaldehyde fixation and 0.05% crystal violet staining. Stained cells were counted in six random fields per well using the inverted microscope.

RNA Immunoprecipitation

LINC00586 binding with LSD1 was evaluated using the Magna RIP™RNA-Binding Protein Immunoprecipitation Kit (Millipore, United States) following the manufacturer's recommendation. In brief, two parts of cell extracts were incubated with either anti-LSD1 antibody (ab17721, Abcam) or nonspecific rabbit IgG (ab2410, Abcam) and immunoprecipitated with magnetic Protein A/G beads. Following proteinase k incubation, the immunoprecipitated RNA and total RNA from the whole cell lysates (input controls) were extracted for RT-qPCR analysis.

Chromatin Immunoprecipitation-qPCR

Enrichment of LSD1 and H3K27me3 in the ASXL1 promoter region was evaluated by the EZ ChIP™Chromatin Immunoprecipitation Kit (Millipore) following the manufacturer's recommendation. In brief, HCT116 and LoVo cells were fixed with 10% formaldehyde for 10 min to generate DNA-protein cross-links. Cell lysates were then sonicated to generate chromatin fragments. The chromatin fragments were incubated with Protiein G Agarose (1 h) and then centrifuged (5,000 g, 1 min). Cell extracts were split into four parts of which one was used as "Input" and others were probed with anti-LSD1 antibody (ab17721, Abcam), anti-H3K27me3 antibody (ab6002) or nonspecific rabbit IgG (ab2410, Abcam) at 4°C overnight. The DNA-protein complexes were precipitated by using protein G Agarose. The immunoprecipitation was de-crosslinked, and the DNA samples were extracted for real-time qPCR analysis.

Constructs, Lentivirus Production, and Transduction

The recombinant lentivirus harboring shRNA targeting LINC00586 (5′-GGAGTGGCGACTATAGCAAAC-3′), scramble shRNA (5′-TTCTCCGAACGTGTCACGT-3′), the full length of human ASXL1 gene (NCBI reference sequence ID, NM_015338.6), or the full length of human LINC00586 transcripts (NCBI reference sequence ID, NR_047671.2) were constructed and purchased from Shanghai GeneChem Co., Ltd. (shanghai, China). The recombinant lentivirus (LV-sh-LINC00586, LV-ASXL1, and LV-LINC00586) were produced in 293T cells. Supernatants containing lentiviruses were

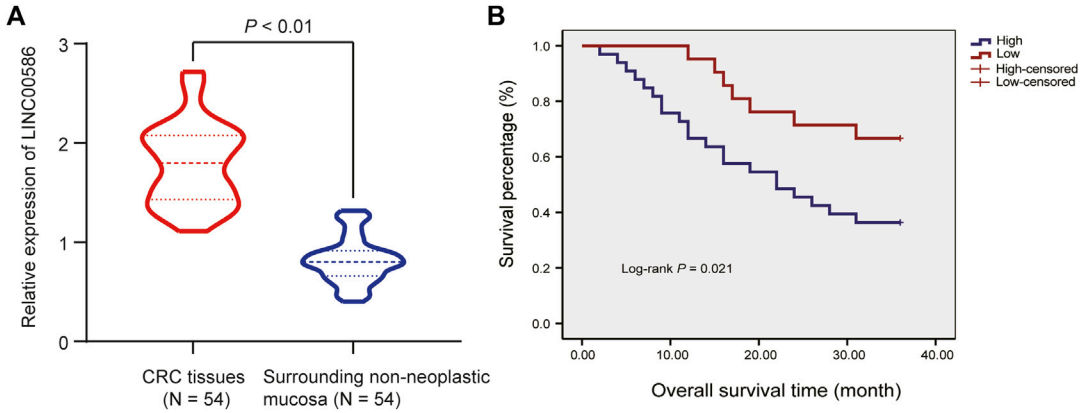

FIGURE 1 | High expression of LINC00586 is associated with CRC progression and unfavorable prognosis. **(A)** The expression of LINC00586 was analyzed by real-time qPCR in CRC tissues (n = 54) and surrounding non-neoplastic mucosa (n = 54). **(B)** Overall survival and disease-free survival probabilities of 54 CRC patients were estimated according to LINC00586 expression using the Kaplan-Meier method and analyzed by Log-rank test. *p < 0.05 by paired t test.

harvested 48 h later. We performed subsequent purification using ultracentrifugation. HCT116 cells were transduced with the recombinant lentivirus plus 5 μg/ml of Polybrene (Huang et al., 2018). The infected HCT116 cells were selected by puromycin (1 μg/ml), and the puromycin-resistant colonies were subsequently selected, expanded, and analyzed.

Mouse Xenograft Models of CRC

A total of 25 BALB/c mice aged 6–8 weeks and weighing 18–25 g (Hunan SJA Laboratory Animal Co., Ltd., China) were kept under specific pathogen-free conditions. HCT116 cells transduced with the recombinant lentivirus (2×10^6 cells for each cell line) were resuspended in 200 ml phosphate buffered saline and subcutaneously injected into BALB/c mice. 2 weeks after implantation, the mice were euthanized, with CRC xenografts collected. The mice were euthanized by exposure to prolonged inhalatory anesthesia. Tremendous efforts were done to minimize pain the included animals suffered.

Statistical Analysis

Measurement data were presented as mean ± standard deviation of three independent experiments (each in triplicate) and analyzed by paired or unpaired t-test, a one-way analysis of variance (ANOVA) with Tukey's test, and repeated measurements ANOVA with Bonferroni corrections as required. Percentage or frequency was used to report enumeration data and chi-square test was used for statistical comparisons. Survival curves were plotted using Kaplan-Meier's method, and statistical differences were identified by a log-rank test. Cox's proportional hazards model was employed to identify the independent factors. Statistical comparisons were processed by SPSS 21.0

TABLE 2 | Correlation of LINC00586 expression with the clinical characteristics of CRC patients.

Clinical characteristics	Case	LINC00586 expression		Statistics	p value
		High (n = 33)	Low (n = 21)		
Age	54	50.78 ± 12.19	50.12 ± 13.29	t = 0.186	0.853
Gender	—	—	—	χ^2 = 0.691	0.406
Male	39	22	17	—	—
Female	15	11	4	—	—
Tumor size	—	—	—	χ^2 = 0.362	0.547
<4 cm	14	10	4	—	—
≥4 cm	40	23	17	—	—
Lymph node metastasis	—	—	—	χ^2 = 5.479	0.019*
No	24	10	14	—	—
Yes	30	23	7	—	—
Tumor differentiation	—	—	—	χ^2 = 0.084	0.772
High and medium	41	25	16	—	—
Low and none	13	8	5	—	—
TNM stage	—	—	—	χ^2 = 7.154	0.007*
I-II	25	10	15	—	—
III-IV	29	23	6	—	—

Data were analyzed using t *test or chi-square test (*p < 0.05).*

TABLE 3 | Cox regression analysis of independent prognostic factors for CRC.

	B	SE	Wald	df	Sig.	Exp(B)	95.0% CI	
							Upper	Lower
LINC00586	−1.610	0.813	3.919	1	0.048	0.200	0.041	0.984
LNM	−2.381	1.159	4.221	1	0.040	0.092	0.010	0.896
TNM	−1.634	0.817	3.998	1	0.046	0.195	0.039	0.968

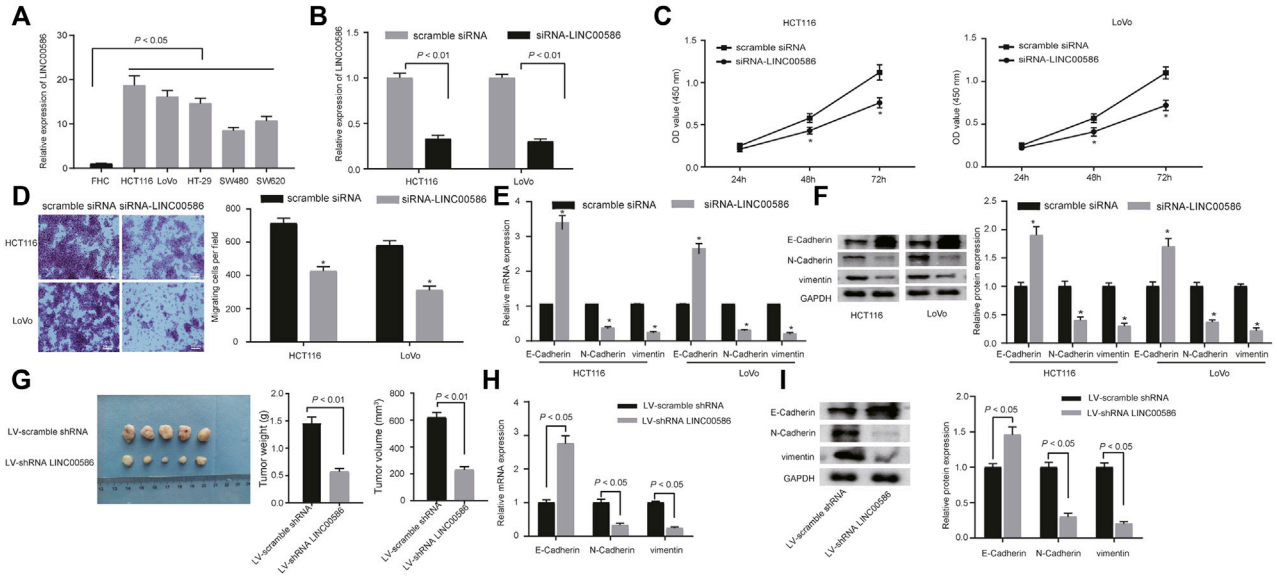

FIGURE 2 | LINC00586 knockdown suppresses CRC cell viability, invasion, EMT, and tumorigenicity. **(A)** The expression of LINC00586 was analyzed by real-time qPCR in a panel of CRC cell lines (HCTl16, LoVo, HT-29, SW480, and SW620) and FHC. **(B)** Verification of LINC00586 knockdown in HCTl16 and LoVo cells by real-time qPCR. **(C)** The viability of HCTl16 and LoVo cells was examined by CCK-8 test upon LINC00586 knockdown. **(D)** Representative view (× 200) of HCTl16 and LoVo cells migrating from upper transwell chambers into lower ones and statistics of migrating cells upon LINC00586 knockdown. **(E)** The mRNA expression of E-Cadherin, N-Cadherin, and vimentin by real-time qPCR in HCTl16 and LoVo cells upon LINC00586 knockdown. **(F)** Immunoblots of E-Cadherin, N-Cadherin, vimentin, and their quantitative analysis in HCTl16 and LoVo cells upon LINC00586 knockdown. **(G)** Effects of LINC00586 knockdown on tumor growth in a xenograft mouse model. HCTl16 cells were infected with the recombinant lentivirus harboring shRNA targeting LINC00586 or scramble shRNA and then injected into the nude mice ($n = 5$), and the tumors were obtained 2 weeks after xenograft implantation and weighed. **(H)** The mRNA expression of E-Cadherin, N-Cadherin, and vimentin by real-time qPCR in CRC xenograft tissue sections upon LINC00586 knockdown. **(I)** Immunoblots of E-Cadherin, N-Cadherin, vimentin, and their quantitative analysis in CRC xenograft tissue sections upon LINC00586 knockdown. *$p < 0.05$ by unpaired t test or by repeated measurements ANOVA with Bonferroni corrections [only for **(C)**].

software (IBM, Armonk, NY, United States), with two-tailed $p < 0.05$ as a level of statistical significance.

RESULTS

High Expression of LINC00586 was Associated With CRC Progression and Unfavorable Prognosis

We first set out to quantify the expression of LINC00586 in the clinical patient tissue samples. The real-time qPCR revealed an elevated LINC00586 in CRC tissues compared with surrounding non-neoplastic mucosa (**Figure 1A**). The expression of LINC00586 was associated with tumor node metastasis (TNM) and lymph node metastasis (LNM) of CRC patients ($p < 0.05$, **Table 2**). The median expression level of LINC00586 in tumor tissues was used to classify 54 CRC patients with high or low expression of LINC00586. The Kaplan-Meier curve was depicted to show CRC patient prognosis according to LINC00586 patients. Patients with high LINC00586 expression had shorter overall survival than those with low LINC00586 expression ($p < 0.05$, **Figure 1B**). Cox regression analysis revealed high LINC00586 expression, TNM, and LNM were independent prognostic factors for CRC ($p < 0.05$, **Table 3**). These data suggested that high expression of LINC00586 was associated with CRC progression and unfavorable prognosis.

LINC00586 Knockdown Suppressed CRC Cell Viability, Invasion, EMT, and Tumorigenicity

We next analyzed the expression of LINC00586 in a panel of CRC cell lines (HCT116, LoVo, HT-29, SW480, and SW620) and FHC

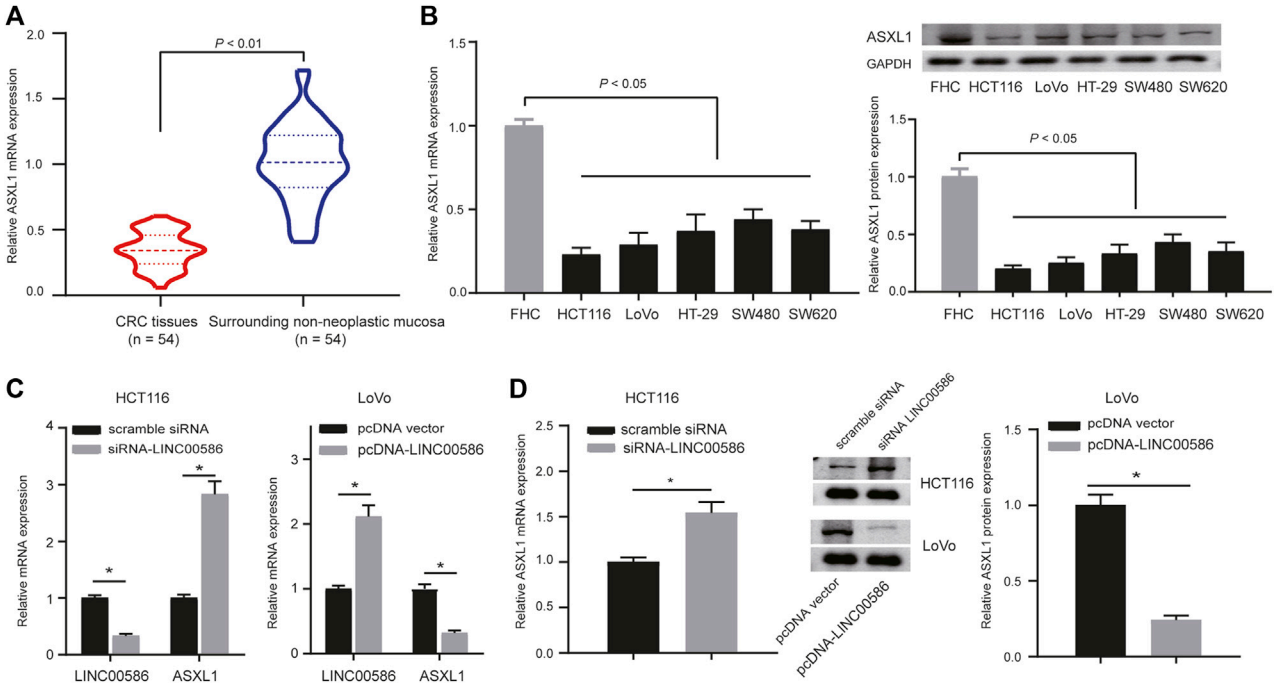

FIGURE 3 | High expression of LINC00586 inhibits the expression of ASXL1 in CRC cells. **(A)** The mRNA and protein expression of ASXL1 was analyzed by real-time qPCR and immunoblotting analysis in CRC tissues ($n = 54$) and surrounding non-neoplastic mucosa ($n = 54$). **(B)** The mRNA and protein expression of ASXL1 was analyzed by real-time qPCR and immunoblotting analysis in a panel of CRC cell lines (HCTl16, LoVo, HT-29, SW480, and SW620) and FHC. **(C,D)**, The mRNA and protein expression of ASXL1 was analyzed by real-time qPCR **(C)** and immunoblotting analysis **(D)** in HCTl16 and LoVo cells upon LINC00586 knockdown or overexpression. *$p < 0.05$ by unpaired t test or by one-way ANOVA with Tukey's test [only for **(B)**].

by real-time qPCR. We observed a significant elevation of LINC00586 in all CRC cell lines when comparable to FHC (**Figure 2A**). HCT116 cells followed by LoVo possessed greatest fold change in LINC00586 expression. To experimentally examine the contribution of LINC00586 to CRC development, we constructed LINC00586-deficient stable CRC cells by delivering siRNA targeting LINC00586 into HCT116 and LoVo cells (**Figure 2B**). The cell viability evaluated by CCK-8 test was decreased by LINC00586 knockdown in HCT116 and LoVo cells (**Figure 2C**). Consistently, our transwell migration assays demonstrated HCT116 and LoVo cell migration was reduced upon LINC00586 knockdown (**Figure 2D**). We next characterized the functional role of LINC00586 in the process of EMT by determining the EMT markers E-Cadherin, N-Cadherin, and vimentin. The results of real-time PCR and immunoblotting analysis showed that LINC00586 knockdown resulted in an elevated E-Cadherin concomitant with declined N-Cadherin and vimentin in HCT116 and LoVo cells (**Figures 2E,F**). To further consolidate our preliminary observations *in vivo*, we xenografted LINC00586-deficient HCT116 cells into nude mice to examine the effect of LINC00586 on the *in vivo* tumorigenesis of HCT116 cells. As expected, lentivirus-mediated LINC00586 knockdown led to smaller tumors and displayed less weight and volume than corresponding control in mouse xenograft models (**Figure 2G**). Real-time PCR and immunoblotting analysis likewise revealed an elevated E-Cadherin concomitant with declined N-Cadherin and vimentin in CRC xenograft tissue sections upon LINC00586 knockdown (**Figures 2H,I**). Overall, these results support the notion that LINC00586 knockdown suppressed CRC cell viability, invasion, EMT, and tumorigenicity.

High Expression of LINC00586 Underpins ASXL1 Inhibition in CRC Cells

Subsequently, we are interested in the mechanism behind the regulation of LINC00586 in CRC. A computer-based RNA-protein interaction prediction (http://pridb.gdcb.iastate.edu/RPISeq/) revealed the binding relationship between LINC00586 and ASXL1. We next analyzed the expression of ASXL1 in the clinical patient samples and CRC cell lines. The real-time qPCR and immunoblotting analysis revealed lower expression levels of ASXL1 in CRC tissues (**Figure 3A**) and all CRC cell lines (**Figure 3B**) than surrounding non-neoplastic mucosa and FHC. To investigate whether ASXL1 could be regulated by LINC00586 in CRC cells, we determined mRNA and protein expression of ASXL1 in HCT116 and LoVo cells upon LINC00586 overexpression and knockdown by real-time qPCR and immunoblotting analysis. The results showed that LINC00586 knockdown upregulated ASXL1 expression, whereas ectopic expression of LINC00586 downregulated ASXL1 expression in HCT116 and LoVo cells (**Figures 3C,D**). Taken together, high expression of LINC00586 may underpins ASXL1 inhibition in the setting of CRC.

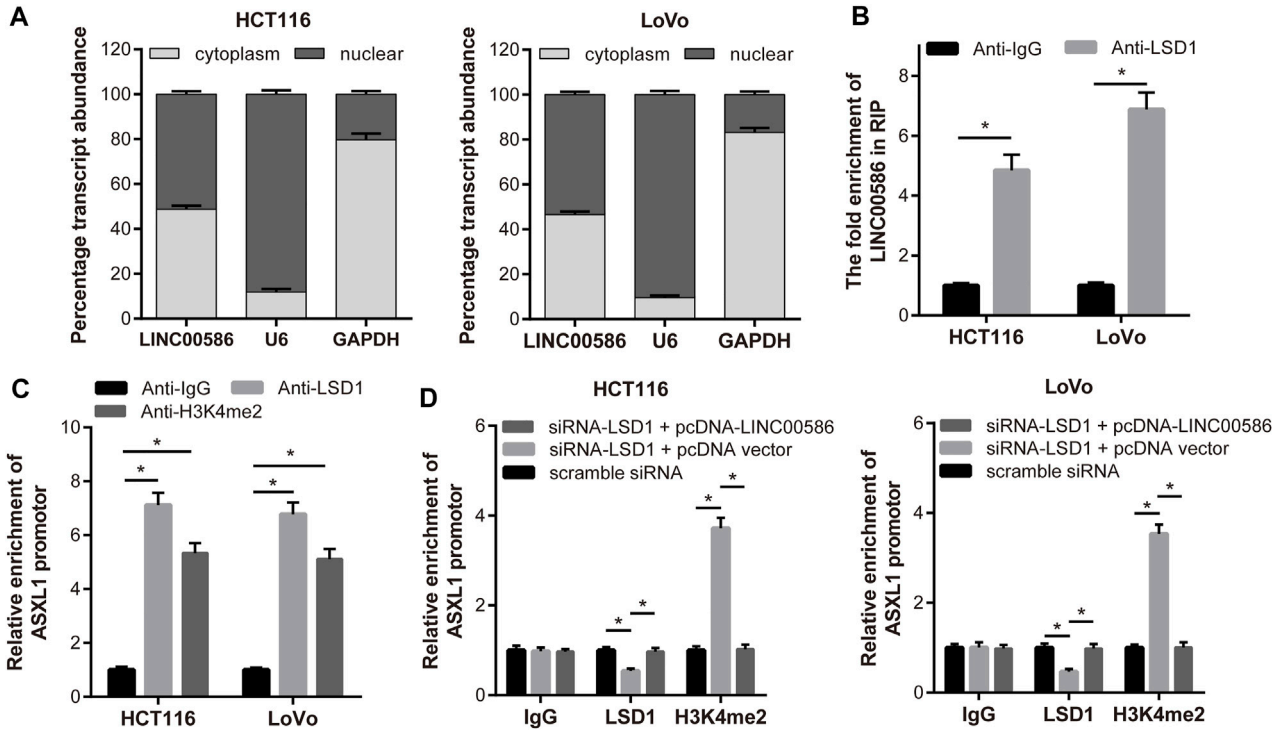

FIGURE 4 | LINC00586 epigenetically silenced ASXL1 transcription through LSD1-mediated H3K4me2 demethylation. **(A)** Relative LINC00586 expression levels in nuclear and cytosolic fractions of HCTl16 and LoVo cells were determined by real-time qPCR. Nuclear controls: U6; Cytosolic controls: GAPDH. **(B)** RIP assay was performed to determine LINC00586 binding with LSD1. A significant enrichment of endogenous LINC00586 was detected in the anti-LSD1 RIP fraction (relative to nonspecific IgG control) in HCTl16 and LoVo cells. **(C)** HCTl16 and LoVo cells were subject to ChIP-PCR assays using anti-LSD1, anti-H3K4me2 or nonspecific IgG control for ASXL1 enrichment. **(D)** ChIP-PCR assays of ASXL1 enrichment in HCTl16 and LoVo cells following LSD1 knockdown and/or LINC00586 overexpression. *$p < 0.05$ by unpaired t test or by one-way ANOVA with Tukey's test.

LINC00586 Epigenetically Silenced ASXL1 Transcription Through LSD1-Mediated H3K4me2 Demethylation

In this part, we set out to recapitulate the molecular mechanism by which LINC00586 regulated ASXL1 transcription. Considering that mechanisms of lncRNAs are largely dependent of specific cell locations, we first analyzed the subcellular localization of LINC00586 in both HCT116 and LoVo cells. As depicted in **Figure 4A**, we detected abundant LINC00586 transcripts in both cytoplasm and nuclear fractions, suggesting that LINC00586 may exert transcriptional regulation function on ASXL1. Given the critical role of LSD1 in epigenetic regulation of multiple target genes by lncRNAs, we performed RIP-qPCR assays and detected significant enrichment of endogenous LINC00586 in the anti-LSD1 RIP fraction (**Figure 4B**). Accordingly, LSD1 binding with the promoter region of ASXL1 was tested by ChIP assays using anti-LSD1, anti-H3K4me2, or nonspecific IgG control. We found a significant enrichment of ASXL1 in immunoprecipitated complex of anti-LSD1 antibody and anti-H3K4me2 antibody (**Figure 4C**), whereas we detected a reduced ASXL1 enrichment in anti-LSD1 immunoprecipitations but an increased enrichment in anti-H3K4me2 immunoprecipitations in HCT116 and LoVo cells transfected with siRNA targeting LSD1 compared with scramble siRNA (**Figure 4D**). Additionally, the ASXL1 enrichment in anti-LSD1 immunoprecipitations and anti-H3K4me2 immunoprecipitations upon LSD1 knockdown was greatly compromised by subsequent LINC00586 overexpression. All these data showed that LINC00586 epigenetically silenced ASXL1 transcription through LSD1-mediated H3K4me2 demethylation.

LINC00586 Modulated CRC Cell Viability, Invasion, EMT, and Tumorigenicity by Inhibiting ASXL1

Since the observations of LINC00586 epigenetically silencing ASXL1 transcription, we aim at dissecting out whether LINC00586 is implicated in the development of CRC by inhibiting ASXL1. For this purpose, we first delivered pcDNA-ASXL1 into CRC cells to achieve ASXL1 overexpression in HCT116 and LoVo cells (**Figure 5A**). HCT116 and LoVo cells with ASXL1 overexpression were assayed to evaluate their viability and migration *in vitro*. The CCK-8 test and transwell migration assays revealed that ASXL1 overexpression suppressed CRC cell viability and migration (**Figures 5B,C**). Real-time qPCR and immunoblotting analysis results revealed an elevated E-Cadherin along with declined N-Cadherin and vimentin in HCT116 and LoVo cells upon ASXL1 overexpression (**Figures**

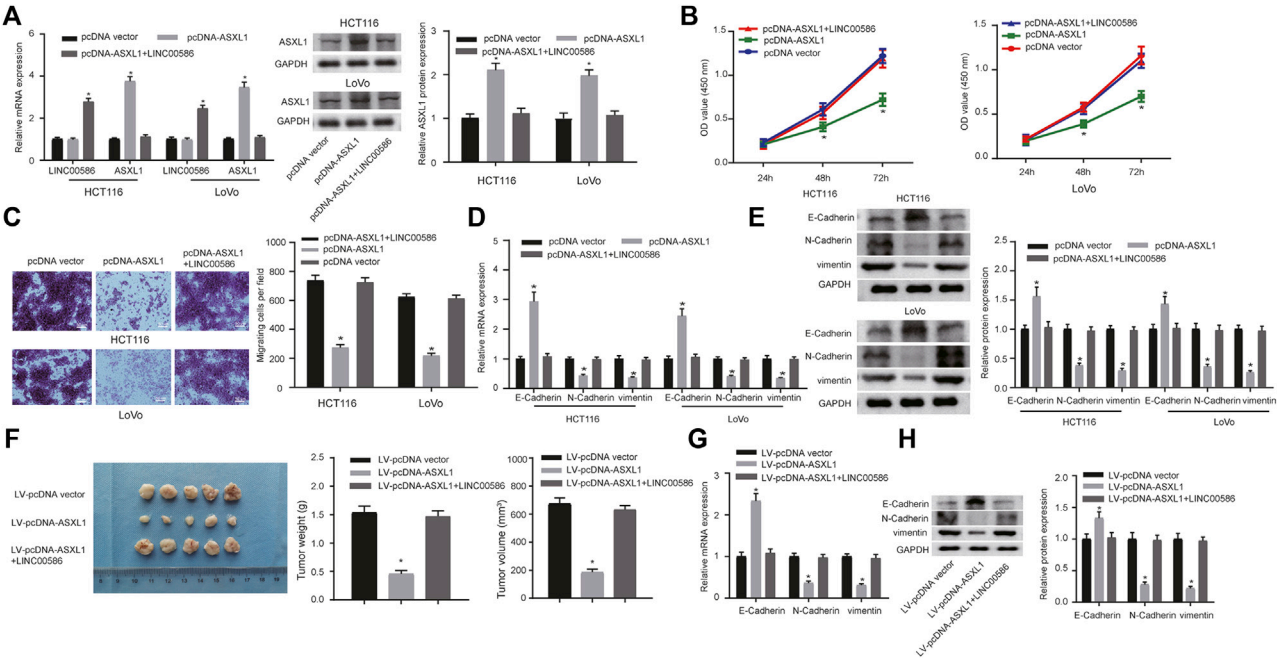

FIGURE 5 | LINC00586 modulates CRC cell viability, invasion, EMT, and tumorigenicity by inhibiting ASXL1. **(A)** The mRNA and protein expression of ASXL1 was determined in HCTl16 and LoVo cells upon ASXL1 overexpression and/or LINC00586 overexpression by real-time qPCR and immunoblotting analysis. **(B)** The viability of HCTl16 and LoVo cells was examined by CCK-8 test upon ASXL1 overexpression and/or LINC00586 overexpression. **(C)** Representative view (× 200) of HCTl16 and LoVo cells migrating from upper transwell chambers into lower ones and statistics of migrating cells upon ASXL1 overexpression and/or LINC00586 overexpression. **(D)** The mRNA expression of E-Cadherin, N-Cadherin, and vimentin by real-time qPCR in HCTl16 and LoVo cells upon ASXL1 overexpression and/or LINC00586 overexpression. **(E)** Immunoblots of E-Cadherin, N-Cadherin, vimentin, and their quantitative analysis in HCTl16 and LoVo cells upon ASXL1 overexpression and/or LINC00586 overexpression. **(F)** HCTl16 cells were infected with the recombinant lentivirus harboring the full length of human ASXL1 gene alone or in combination with the recombinant lentivirus harboring human LINC00586 transcripts and injected into the nude mice (n = 5), and the tumors were obtained 2 weeks after xenograft implantation and weighed. **(G)** The mRNA expression of E-Cadherin, N-Cadherin, and vimentin by real-time qPCR in CRC xenograft tissue sections upon ASXL1 overexpression and/or LINC00586 overexpression. **(H)** Immunoblots of E-Cadherin, N-Cadherin, vimentin, and their quantitative analysis in CRC xenograft tissue sections upon ASXL1 overexpression and/or LINC00586 overexpression.

5D,E). More importantly, we observed ASXL1 overexpression coincident with LINC00586 overexpression not only significantly decreased the expression of ASXL1 but also compromised the inhibitory effects of ASXL1 on HCT116 and LoVo cell viability, migration, and the process of EMT. The *in vivo* analysis demonstrated ASXL1 overexpression attenuated the growth of subcutaneous xenotransplanted tumors of HCT116 cells (**Figure 5F**). Real-time qPCR (**Figure 5G**) and immunoblotting analysis (**Figure 5H**) likewise revealed an elevated E-Cadherin concomitant with declined N-Cadherin and vimentin in CRC xenograft tissue sections upon ASXL1 overexpression. We next established mouse xenograft models of HCT116 cells transfected with pcDNA-ASXL1+LINC00586 expression vector. Results revealed ensuing LINC00586 overexpression abrogated the tumor suppressive effects of ASXL1 on mouse xenograft models. Furthermore, we found the effects of ASXL1 on the expression of EMT markers were partially lost by subsequent LINC00586 overexpression mouse xenograft models. The aforementioned results unveiled that LINC00586 promoted CRC cell viability, invasion, EMT, and tumorigenicity by inhibiting ASXL1.

DISCUSSION

Increasing importance of lncRNAs, over 200 nucleotides in length, has been attached to the pathology of CRC, functioning as diagnostic and therapeutic biomarkers (Kim and Croce, 2018; Sun et al., 2018). LncRNAs are controllers of gene expression as well as a regulator of cell development, which includes cell migration, proliferation and apoptosis in carcinoma (Liz and Esteller, 2016). The aim of the current study was to explore the functional role of LINC00586 and the underlying mechanism in modulation of CRC cells to affect the development and progression of CRC. Collectively, the experimental data demonstrated that the LINC00586 promoted CRC cell viability, invasion, EMT, and tumorigenicity in association with ASXL1.

A fundamental finding of our study was to determine the expression profile of LINC00586. Previous evidence has manifested that lncRNAs are essential regulators of oncogenesis in CRC, which suggests that lncRNAs can function as biomarkers for CRC diagnosis (Silva-Fisher et al., 2020; Wu et al., 2020). It has been previously revealed that LINC00586 (BANCR) was aberrantly in

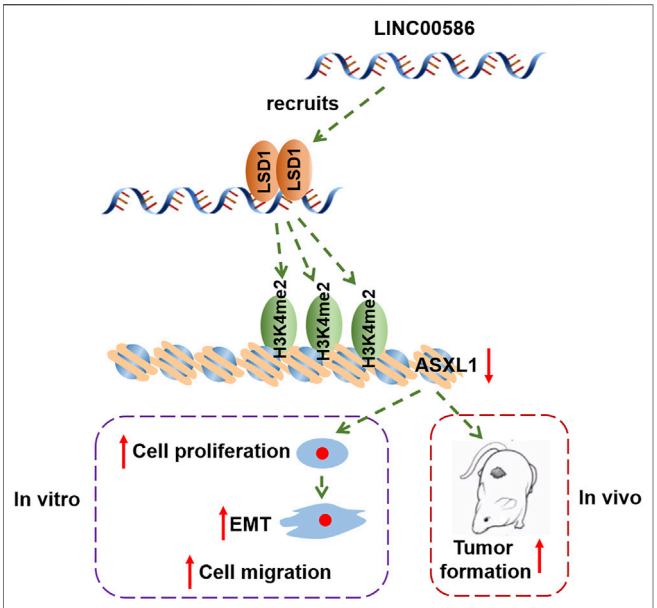

FIGURE 6 | The graphical summary of the mechanism of LINC00586 in regulating CRC progression. LINC00586 epigenetically silenced ASXL1 transcription through LSD1-mediated H3K4me2 demethylation, thereby leading to the development and progression of CRC.

various cancers (Zou et al., 2017). For instance, prior work reports that LINC00586 is highly expressed in melanoma cell lines and tissues, while knockdown of LINC00586 inhibits proliferation of melanoma cells (Li et al., 2014). Consistent with our study, it has been pointed out that LINC00586 is also highly expressed in CRC tissues and cell lines, the overexpression of which could promote cell migration by boosting EMT in ERK-dependent manner (Guo et al., 2014). Furthermore, LINC00586 has been identified to be associated with lymph node metastasis and poor survival of CRC patients (Shen et al., 2017). Likewise, we further found that knockdown of LINC00586 was able to suppress viability, invasion and EMT of CRC cells. All of these findings made our statement that LINC00586 played a pathogenic role in CRC reasonable.

Subsequently, mechanistic investigation showed that LINC00586 knockdown upregulated ASXL1 expression, whereas ectopic expression of LINC00586 downregulated ASXL1 expression in CRC cells. Aberrantly expressed ASXL1 has also been identified in CRC previously (Lee et al., 2019). However, we were the first reporting the regulatory relationship between LINC00586 and ASXL1. Moreover, ASXL1 can regulate H3K4me2 and H3K27me3 (Abdel-Wahab and Dey, 2013), which partially supports our proposal that LINC00586 epigenetically silenced ASXL1 transcription through LSD1-mediated H3K4me2 demethylation. LSD1 knockdown is reported to decline the proliferative rate of CRC cells (Ding et al., 2021). However, previous work also shows that low LSD1 expression and high H3K9me3 and H3K27me3 expression are both associated with more advanced stage of CRC (Carvalho et al., 2018). Therefore, how LSD1 exerted its function in the regulation of LINC00586/ASXL1 remains to be further investigated in the future study. Additionally, the data derived from our study showed that overexpression of ASXL1 was linked to the therapeutic role in CRC, which was manifested by elevated E-Cadherin and declined N-Cadherin and Vimentin levels. ASXL1 has already been identified as a tumor suppressor in CRC, which plays a crucial role in regulating the biological functions of CRC cells (Lee et al., 2020). Meanwhile, E-cadherin is a well-known epithelial marker, while N-cadherin and Vimentin are regarded as mesenchymal markers. Suppressed EMT is associated with reduced N-Cadherin and Vimentin levels as well as increased E-Cadherin expression (Lin et al., 2020). Furthermore, EMT is a critical mechanism affecting invasion, migration, and metastasis of tumors, also being involved in the occurrence CRC (Spaderna et al., 2006). Therefore, it was reasonable to infer that overexpressed ASXL1 could inhibit EMT in CRC, thus attenuating the progression of CRC. We further confirmed our molecular mechanism underlying LINC00586 in CRC xenograft tissue sections.

In conclusion, the study provided evidence that LINC00586 knockdown suppressed CRC cell viability, invasion, EMT, and tumorigenicity by mediating ASXL1 expression through LSD1-mediated H3K4me2 demethylation (**Figure 6**). This study offers a novel insight into the molecular mechanism underlying CRC for theoretical evidence for development of targeted therapies. However, further investigation is still warranted if we want to provide more safe and efficient lncRNA-targeted ways for cancer diagnosis and therapy.

DATA AVAILABILITY STATEMENT

The original contributions presented in the study are included in the article/Supplementary Material, further inquiries can be directed to the corresponding authors.

ETHICS STATEMENT

The studies involving human participants were reviewed and approved by the Chinese Academy of Medical Sciences and Peking Union Medical College. The patients/participants provided their written informed consent to participate in this study. The animal study was reviewed and approved by the Chinese Academy of Medical Sciences and Peking Union Medical College.

AUTHOR CONTRIBUTIONS

FTL: Conception and design, manuscript writing; XZL and QL: Administrative support, collection and assembly of data; XFM: Provision of study materials or patients; XYB and CYZ: Data analysis and interpretation, checking of entered data for accuracy.

FUNDING

The study was supported by grant from National Natural Science Foundation of China (Grant Nos 81901526 and 32171239), Tianjin Natural Science Foundation of China (Grant Nos 18JCQNJC12800, 19JCZDJC35200, and

19JCQNJC11900), Tianjin Special Project of New Generation Artificial Intelligence Technology (Grant No. 18ZXZNSY00260), and funded by Tianjin Key Medical Discipline Construction Project.

REFERENCES

Abdel-Wahab, O., and Dey, A. (2013). The ASXL-BAP1 Axis: New Factors in Myelopoiesis, Cancer and Epigenetics. *Leukemia* 27, 10–15. doi:10.1038/leu.2012.288

Basile, D., Bartoletti, M., Polano, M., Bortot, L., Gerratana, L., Di Nardo, P., et al. (2020). Prognostic Role of Visceral Fat for Overall Survival in Metastatic Colorectal Cancer: A Pilot Study. *Clin. Nutr.* 40 (1), 286–294. doi:10.1016/j.clnu.2020.05.019

Carvalho, S., Freitas, M., Antunes, L., Monteiro-Reis, S., Vieira-Coimbra, M., Tavares, A., et al. (2018). Prognostic Value of Histone marks H3K27me3 and H3K9me3 and Modifying Enzymes EZH2, SETDB1 and LSD-1 in Colorectal Cancer. *J. Cancer Res. Clin. Oncol.* 144, 2127–2137. doi:10.1007/s00432-018-2733-2

Ding, D., Li, C., Zhao, T., Li, D., Yang, L., and Zhang, B. (2018). LncRNA H19/miR-29b-3p/PGRN Axis Promoted Epithelial-Mesenchymal Transition of Colorectal Cancer Cells by Acting on Wnt Signaling. *Mol. Cells* 41, 423–435. doi:10.14348/molcells.2018.2258

Ding, J., Zhang, Z. M., Xia, Y., Liao, G. Q., Pan, Y., Liu, S., et al. (2013). LSD1-Mediated Epigenetic Modification Contributes to Proliferation and Metastasis of Colon Cancer. *Br. J. Cancer* 109, 994–1003. doi:10.1038/bjc.2013.364

Edge, S. B., and Compton, C. C. (2010). The American Joint Committee on Cancer: The 7th Edition of the AJCC Cancer Staging Manual and the Future of TNM. *Ann. Surg. Oncol.* 17, 1471–1474. doi:10.1245/s10434-010-0985-4

Fan, Q., and Liu, B. (2017). Identification of the Anticancer Effects of a Novel Proteasome Inhibitor, Ixazomib, on Colorectal Cancer Using a Combined Method of Microarray and Bioinformatics Analysis. *Onco Targets Ther.* 10, 3591–3606. doi:10.2147/OTT.S139686

Ghafouri-Fard, S., Hussen, B. M., Gharebaghi, A., Eghtedarian, R., and Taheri, M. (2021). LncRNA Signature in Colorectal Cancer. *Pathol. Res. Pract.* 222, 153432. doi:10.1016/j.prp.2021.153432

Ding, X., Zhang, J., Feng, Z., Tang, Q., and Zhou, X. (2021). MiR-137-3p Inhibits Colorectal Cancer Cell Migration by Regulating a KDM1A-Dependent Epithelial-Mesenchymal Transition. *Dig. Dis. Sci.* 66 (7), 2272–2282. doi:10.1007/s10620-020-06518-6

Galamb, O., Kalmar, A., Sebestyen, A., Danko, T., Kriston, C., Furi, P., et al. (2020). Promoter Hypomethylation and Increased Expression of the Long Non-coding RNA LINC00152 Support Colorectal Carcinogenesis. *Pathol. Oncol. Res.* 26 (4), 2209–2223. doi:10.1007/s12253-020-00800-8

Guo, Q., Zhao, Y., Chen, J., Hu, J., Wang, S., Zhang, D., et al. (2014). BRAF-Activated Long Non-Coding RNA Contributes to Colorectal Cancer Migration by Inducing Epithelial-Mesenchymal Transition. *Oncol. Lett.* 8, 869–875. doi:10.3892/ol.2014.2154

Huang, Y., Yu, S., Cao, S., Yin, Y., Hong, S., Guan, H., et al. (2018). MicroRNA-222 Promotes Invasion and Metastasis of Papillary Thyroid Cancer through Targeting Protein Phosphatase 2 Regulatory Subunit B Alpha Expression. *Thyroid* 28, 1162–1173. doi:10.1089/thy.2017.0665

Kim, T., and Croce, C. M. (2018). Long Noncoding RNAs: Undeciphered Cellular Codes Encrypting Keys of Colorectal Cancer Pathogenesis. *Cancer Lett.* 417, 89–95. doi:10.1016/j.canlet.2017.12.033

Kim, T. W., Lee, Y. S., Yun, N. H., Shin, C. H., Hong, H. K., Kim, H. H., et al. (2020). MicroRNA-17-5p Regulates EMT by Targeting Vimentin in Colorectal Cancer. *Br. J. Cancer* 123 (7), 1123–1130. doi:10.1038/s41416-020-0940-5

Lee, J. H., Ahn, B. K., Baik, S. S., and Lee, K. H. (2019). Comprehensive Analysis of Somatic Mutations in Colorectal Cancer with Peritoneal Metastasis. *In Vivo* 33, 447–452. doi:10.21873/invivo.11493

Lee, J. H., Lee, J. H., Ahn, B. K., Paik, S. S., Kim, H., and Lee, K. H. (2020). Loss of ASXL1 Expression Is Associated with Lymph Node Metastasis in Colorectal Cancer. *Indian J. Pathol. Microbiol.* 63, 221–225. doi:10.4103/IJPM.IJPM_822_19

Lee, S. W., Cho, Y. S., Na, J. M., Park, U. H., Kang, M., Kim, E. J., et al. (2010). ASXL1 Represses Retinoic Acid Receptor-Mediated Transcription through Associating with HP1 and LSD1. *J. Biol. Chem.* 285, 18–29. doi:10.1074/jbc.M109.065862

Li, R., Zhang, L., Jia, L., Duan, Y., Li, Y., Bao, L., et al. (2014). Long Non-Coding RNA BANCR Promotes Proliferation in Malignant Melanoma by Regulating MAPK Pathway Activation. *PLoS One* 9, e100893. doi:10.1371/journal.pone.0100893

Lin, L., Wang, D., Qu, S., Zhao, H., and Lin, Y. (2020). miR-370-3p Alleviates Ulcerative Colitis-Related Colorectal Cancer in Mice through Inhibiting the Inflammatory Response and Epithelial-Mesenchymal Transition. *Drug Des. Devel Ther.* 14, 1127–1141. doi:10.2147/DDDT.S238124

Liz, J., and Esteller, M. (2016). lncRNAs and microRNAs with a Role in Cancer Development. *Biochim. Biophys. Acta* 1859, 169–176. doi:10.1016/j.bbagrm.2015.06.015

Long, Y., Wang, X., Youmans, D. T., and Cech, T. R. (2017). How Do lncRNAs Regulate Transcription? *Sci. Adv.* 3, eaao2110. doi:10.1126/sciadv.aao2110

Ma, S., Yang, D., Liu, Y., Wang, Y., Lin, T., Li, Y., et al. (2018). LncRNA BANCR Promotes Tumorigenesis and Enhances Adriamycin Resistance in Colorectal Cancer. *Aging (Albany NY)* 10, 2062–2078. doi:10.18632/aging.101530

Mittal, V. (2018). Epithelial Mesenchymal Transition in Tumor Metastasis. *Annu. Rev. Pathol.* 13, 395–412. doi:10.1146/annurev-pathol-020117-043854

Pfeiffer, P., Yilmaz, M., Möller, S., Zitnjak, D., Krogh, M., Petersen, L. N., et al. (2020). TAS-102 with or without Bevacizumab in Patients with Chemorefractory Metastatic Colorectal Cancer: An Investigator-Initiated, Open-Label, Randomised, Phase 2 Trial. *Lancet Oncol.* 21, 412–420. doi:10.1016/S1470-2045(19)30827-7

Rabeneck, L., Chiu, H. M., and Senore, C. (2020). International Perspective on the Burden of Colorectal Cancer and Public Health Effects. *Gastroenterology* 158, 447–452. doi:10.1053/j.gastro.2019.10.007

Saleh, M., Cassier, P. A., Eberst, L., Naik, G., Morris, V. K., Pant, S., et al. (2020). Phase I Study of Ramucirumab Plus Merestinib in Previously Treated Metastatic Colorectal Cancer: Safety, Preliminary Efficacy, and Pharmacokinetic Findings. *Oncologist* 25 (11), e1628–e1639. doi:10.1634/theoncologist.2020-0520

Shen, X., Bai, Y., Luo, B., and Zhou, X. (2017). Upregulation of lncRNA BANCR Associated with the Lymph Node Metastasis and Poor Prognosis in Colorectal Cancer. *Biol. Res.* 50, 32. doi:10.1186/s40659-017-0136-5

Siegel, R. L., Miller, K. D., Goding Sauer, A., Fedewa, S. A., Butterly, L. F., Anderson, J. C., et al. (2020). Colorectal Cancer Statistics, 2020. *CA Cancer J. Clin.* 70, 145–164. doi:10.3322/caac.21601

Silva-Fisher, J. M., Dang, H. X., White, N. M., Strand, M. S., Krasnick, B. A., Rozycki, E. B., et al. (2020). Long Non-Coding RNA RAMS11 Promotes Metastatic Colorectal Cancer Progression. *Nat. Commun.* 11, 2156. doi:10.1038/s41467-020-15547-8

Spaderna, S., Schmalhofer, O., Hlubek, F., Berx, G., Eger, A., Merkel, S., et al. (2006). A Transient, EMT-Linked Loss of Basement Membranes Indicates Metastasis and Poor Survival in Colorectal Cancer. *Gastroenterology* 131, 830–840. doi:10.1053/j.gastro.2006.06.016

Sun, Z., Liu, J., Chen, C., Zhou, Q., Yang, S., Wang, G., et al. (2018). The Biological Effect and Clinical Application of Long Noncoding RNAs in Colorectal Cancer. *Cell Physiol Biochem* 46, 431–441. doi:10.1159/000488610

Wang, B., Wang, M., Jia, S., Li, T., Yang, M., and Ge, F. (2022). Systematic Survey of the Regulatory Networks of the Long Noncoding RNA BANCR in Cervical Cancer Cells. *J. Proteome Res.* 21 (4), 1137–1152. doi:10.1021/acs.jproteome.2c00009

Wu, H., Qin, W., Lu, S., Wang, X., Zhang, J., Sun, T., et al. (2020). Long Noncoding RNA ZFAS1 Promoting Small Nucleolar RNA-Mediated 2'-O-Methylation via

NOP58 Recruitment in Colorectal Cancer. *Mol. Cancer* 19, 95. doi:10.1186/s12943-020-01201-w

Zhang, H. S., Liu, H. Y., Zhou, Z., Sun, H. L., and Liu, M. Y. (2020). TSPAN8 Promotes Colorectal Cancer Cell Growth and Migration in LSD1-Dependent Manner. *Life Sci.* 241, 117114. doi:10.1016/j.lfs.2019.117114

Zou, Y., Li, J., Chen, Y., Xiao, H., Zhang, F., Yu, D., et al. (2017). BANCR: A Novel Oncogenic Long Non-Coding RNA in Human Cancers. *Oncotarget* 8, 94997–95004. doi:10.18632/oncotarget.22031

Conflict of Interest: The authors declare that the research was conducted in the absence of any commercial or financial relationships that could be construed as a potential conflict of interest.

Publisher's Note: All claims expressed in this article are solely those of the authors and do not necessarily represent those of their affiliated organizations, or those of the publisher, the editors and the reviewers. Any product that may be evaluated in this article, or claim that may be made by its manufacturer, is not guaranteed or endorsed by the publisher.

frontiers | Frontiers in Pharmacology

ORIGINAL RESEARCH
published: 05 May 2022
doi: 10.3389/fphar.2022.908212

Analgesic Effects and Safety of Dexmedetomidine Added to Nalbuphine or Sufentanil Patient-Controlled Intravenous Analgesia for Children After Tonsillectomy Adenoidectomy

*Yingping Jia, Rui Zhou, Zhengchen Li, Yuanyuan Wang, Sandong Chen, Liyuan Zhao, Yi Shao and Jinlian Qi**

Department of Anesthesiology, Children's Hospital of Henan, Zhengzhou, China

OPEN ACCESS

Edited by:
Songwen Tan,
Central South University, China

Reviewed by:
Yongxia Liu,
Yanan University Affiliated Hospital, China
Kai Chen,
Yinzhou No.2 Hospital, China

****Correspondence:***
Jinlian Qi
jinlian_qi11@163.com

Specialty section:
This article was submitted to Translational Pharmacology, a section of the journal Frontiers in Pharmacology

Received: *30 March 2022*
Accepted: *18 April 2022*
Published: *05 May 2022*

Citation:
Jia Y, Zhou R, Li Z, Wang Y, Chen S, Zhao L, Shao Y and Qi J (2022) Analgesic Effects and Safety of Dexmedetomidine Added to Nalbuphine or Sufentanil Patient-Controlled Intravenous Analgesia for Children After Tonsillectomy Adenoidectomy. Front. Pharmacol. 13:908212. doi: 10.3389/fphar.2022.908212

Tonsillectomy is a frequently performed surgical procedure in children, requiring postoperative analgesia. This study evaluated the efficacy and safety of nalbuphine or sufentanil combined with dexmedetomidine for patient-controlled intravenous analgesia (PCIA) after pediatric tonsillectomy adenoidectomy. A total of 400 patients undergoing tonsillectomy with and without adenoidectomy were included in the study. Patients received a PCIA pump (0.5 mg/kg nalbuphine, 2 μg/kg dexmedetomidine and 0.9% sodium chloride to a total volume of 100 ml) for postoperative pain management were classified into Group ND (n = 200). Patients received a PCIA pump (2 μg/kg sufentanil, 2 μg/kg dexmedetomidine and 0.9% sodium chloride to a total volume of 100 ml) for postoperative pain management were classified into Group SD (n = 200). More stable hemodynamic changes were noted in Group ND than Group SD from 1 h to 48 h after operation. At 6, 12, 24, and 48 h after operation, the children in Group ND had higher Ramsay sedation scores than those in Group SD. The times to push the PCIA button in Group ND and Group SD were 2.44 ± 0.74 and 2.62 ± 1.00, showing significant differences (p = 0.041). The VASR scores of children in Group ND were significantly lower within 6, 12, and 24 h than those in Group SD ($p < 0.05$). The VASC scores of children in Group ND were significantly lower within four time points (2, 6, 12, and 24 h) than those in Group SD ($p < 0.05$). At 1st day after surgery, the children in Group ND had lower levels of serum ACTH, IL-6, and COR levels than those in Group SD ($p < 0.001$). The incidence rates of nausea and vomiting, and pruritus were significantly higher in Group SD than Group ND (5.00% vs. 11.00%, p = 0.028; 1.00% vs. 4.50%, p = 0.032). The total incidence rate of adverse reactions was significantly higher in Group SD than Group ND (15.00% vs. 31.00%, p = 0.0001). The study demonstrated that dexmedetomidine added to nalbuphine PCIA enhanced the analgesic effects, attenuated the postoperative pain, and reduced the stress response after pediatric tonsillectomy adenoidectomy.

Keywords: tonsillectomy, adenoidectomy, patient-controlled intravenous analgesia, dexmedetomidine, nalbuphine, sufentanil

INTRODUCTION

Tonsillectomy with or without adenoidectomy is one of the commonest surgical procedures in children, and recovery from tonsillectomy involves significant and prolonged pain and appears to be more troublesome than other types of childhood surgical procedures (Mitchell et al., 2019). Postoperative pain continues to increase the risk of developing short- and long-term complications, such as delayed behavioral and clinical recovery, including an increased risk of incision bleeding (Batoz et al., 2016). The post-tonsillectomy children may refuse to speak and eat due to intense pain in the throat, which affects nutrition intake and psychological condition, ultimately resulting in poor quality of life (Blackshaw et al., 2020). Moreover, due to the lack of nutrition caused by less eating, the patient's resistance decreases, increases the chance of postoperative infection, and also affects the healing of postoperative wounds. Well-established principles for successful management of postoperative pain for children include multimodal analgesia, adequate dosage, administration at regular intervals, and use of appropriate route of administration (Krauss et al., 2016; Makhlouf et al., 2019). A variety of analgesic classes, each present their own risk profiles and unique side effects when used for postoperative analgesia in children undergoing tonsillectomy (Cohen and Sommer, 2016). For example, codeine is no longer approved for children aged less than 12 years undergoing tonsillectomy due to obstructive sleep apnea syndrome resulting from clinically relevant polymorphisms in CYP2D6 activity in Europe and United States (Tobias et al., 2016). Paracetamol in combination with a non-steroidal anti-inflammatory drug attenuated the pain after tonsillectomy in children more efficiently (Jotić et al., 2019), while further studies of morphine addition showed mixed results (Kelly et al., 2015; Oremule et al., 2015). Additionally, administration of opioids has been associated with adverse reactions, such as the risk of respiratory depression in case of overdosing and postoperative nausea and vomiting (Kiyatkin, 2019). Postoperative administration of traditional non-steroidal anti-inflammatory drugs such as ketoroic acid and ibuprofen increases the risk of re-operation and bleeding after tonsillectomy (Kokki, 2003). All these represent a major barrier to use in pediatric outpatient surgery. In addition to adverse reactions, parents worries about safety issues around pain medication and refusal of children to take medication make the relief of post-tonsillectomy pain challenging (Lee et al., 2020; Yu and Kim, 2021).

Sufentanil is a newly synthesized μ-opioid receptor agonist, which is widely used in many operation and postoperative analgesia due to its strong analgesic effect, long duration, and fewer side effects than morphine (Giaccari et al., 2020). Nalbuphine is a classical opioid receptor agonist-antagonist acting as an agonist of κ-receptors and an antagonist of μ-receptors. Nalbuphine has increasingly become a commonly used clinical analgesic drug, especially for the management of visceral pain because of its agonist-antagonist effects and good analgesic effects (Chen et al., 2021). Dexmedetomidine is a selective adrenergic agonist that has less effect on respiratory function, has anti-anxiety, anti-sympathetic nerve and analgesic and sedative properties (Weerink et al., 2017). Previous studies reported the application of dexmedetomidine combined with sufentanil or dexmedetomidine combined with nalbuphine for postoperative analgesia, and both of two postoperative analgesia protocols showing good analgesic effects, reduced doses of sufentanil and nalbuphine, and low incidences of adverse effects (Zhao and Li, 2020; Wang et al., 2022). Patient-controlled analgesia (PCA) is a system that effectively delivers pain relief at a patient's preferred dose and schedule by allowing them to administer a predetermined bolus dose of medication on-demand at the press of a button (Weibel et al., 2017). PCA has been used since the early 1970s and its application in hospitals has been increasing due to its proven advantages over conventional intramuscular injections (Momeni et al., 2006). PCA has been reported to not only relieve multiple categories of pain, including acute, such as postoperative or labor pain, or chronic, such as palliative care or cancer pain, but also improve pain relief, greater patient satisfaction, less sedation and fewer postoperative complications (Motamed, 2022). Recent evidence has showed the efficacy of patient-controlled intravenous analgesia (PCIA) after pediatric surgery, including pediatric moyamoya surgery (Lim et al., 2020), pediatric thoracotomy for malignancy (Gonzalez et al., 2016), and Nuss surgery (Min et al., 2012). However, limited clinical evidence demonstrated the application of dexmedetomidine combined with sufentanil or dexmedetomidine combined with nalbuphine after pediatric tonsillectomy adenoidectomy. In this study, we analyzed 400 patients undergoing tonsillectomy with and without adenoidectomy who received a PCIA pump (0.5 mg/kg nalbuphine, 2 μg/kg dexmedetomidine and 0.9% sodium chloride to a total volume of 100 ml) for postoperative pain management and a PCIA pump (2 μg/kg sufentanil, 2 μg/kg dexmedetomidine and 0.9% sodium chloride to a total volume of 100 ml) for postoperative pain management, respectively.

MATERIALS AND METHODS

Participants

Pediatric patients undergoing tonsillectomy with and without adenoidectomy at the Children's Hospital of Henan between January 2018 and June 2021, American Society of anaesthesiologists physical status (ASA-PS) grade I or II, aged 3–6 years were recruited into the study. Children were excluded from enrollment if their parents or guardians were unwilling to receiving postoperative analgesia with PCIA. Children were also excluded for the following reasons: intellectual disability, neurological diseases with agitation-like symptoms, respiratory inhibition diseases or bronchial asthma, cardiac, renal or hepatic disease, severe circulatory system or blood system dysfunction, allergic to study drug administration, body weight >40 kg, or major life changes 1 month before surgery, such as divorce of parents and death of parents. This single center study was approved by the Institutional Review Board of Children's Hospital of Henan.

Anaesthesia Protocols

All children fasted for at least 6 h and received no pre-medication before procedure. After the child was transferred to the operating room, non-invasive blood pressure (BP), electrocardiogram, heart rate (HR), pulse oxygen saturation (SpO_2), end-tidal

carbon dioxide partial pressure, and bispectral index (VISTA™ monitoring system, Aspect Medical Systems Inc., Norwood, MA, United States) were continuously monitored. Before anesthesia induction, the child was given intramuscular injection of 0.01 mg/kg atropine and intravenous injection of 1 mg/kg ketamine1 min later. Once consciousness was lost, anesthesia was induced by 2.5 mg/kg propofol, 2 μg/kg fentanyl, and 0.15 mg/kg cisatracurium. Three minutes later, the child was given endotracheal intubation and then mechanically ventilated with volume-controlled ventilation mode aiming at maintain the tidal volume 8–10 ml/kg, the respiratory rate 20 to 25 times/min, oxygen flow 2L/min, the end-tidal carbon dioxide partial pressure at 30–35 mmHg, and the SpO_2 > 97%. Anesthesia was maintained with 9–15 μg/kg/h propofol and 0.05–0.2 μg/kg/h remifentanil by continuous infusion with a BIS target range of 40–60. Hemodynamic changes were monitored at 5-min intervals throughout the procedure. If systolic blood pressure values decreased 20% below the preoperative baseline value or decreased to 90 mmHg, the child was administered with 10 ml/kg Ringer's solution and 0.1 mg/kg ephedrine. If the heart rate decreased to 60 beats/min, which was considered bradycardia, and accordingly the child was administered with 0.01 mg/kg atropine.

Postoperative Analgesia Protocols

All children received PCIA for postoperative pain management with nalbuphine plus dexmedetomidine hydrochloride (Group ND) or sufentanil plus dexmedetomidine hydrochloride (Group SD). At the end of the operation, the child was connected with the wireless analgesic pump system (Rehn Medtech, Jiangsu, China) composed of a patient-controlled analgesia pump transmitting signals, base stations receiving the wireless data, and the monitoring center. The monitoring data from each user are transmitted to the monitoring center in the doctor's office online. The physicians can then analyze and deal with the data. The PCIA formula for the child allocated into Group ND consisted of nalbuphine 0.5 mg/kg, dexmedetomidine 2 μg/kg and 0.9% sodium chloride to a total volume of 100 ml. The PCIA formula for the child allocated into Group SD consisted of sufentanil 2 μg/kg, dexmedetomidine 2 μg/kg and 0.9% sodium chloride to a total volume of 100 ml. Upon arrival at the general ward, all children and their parents or guardians were instructed on the use of the PCIA pump (Apon, ZZB-I, Medical technology Corporation, Jiangsu, China), and all children were encouraged to push the PCIA button to self-administer their own PCA medications and thus to achieve a rescue analgesic when they were not tolerant to pain throughout 48 h after operation. The PCIA was programmed to deliver a 2 ml bolus on demand, with a lock-out interval of 15 min and a background infusion rate of 2 ml/h. All children were given 2 ml i.v. of PCIA solution immediately after they were attached a PCIA pump. The PCIA was used for the first 48 h postoperatively and thus allowed either a continuous background infusion of nalbuphine 0.01 mg/kg/h with a bolus of nalbuphine 0.005 mg/kg or a continuous background infusion of sufentanil 0.04 μg/kg/h with a bolus of sufentanil 0.02 μg/kg with a continuous background infusion of dexmedetomidine 0.04 μg/kg/h with a bolus of dexmedetomidine 0.02 μg/kg for the child allocated into Group ND and Group SD. The parents received full guidance from anesthesiologists about how to assess pain and push the PCIA button.

Pain Assessment

Ramsay sedation scores: The Ramsay sedation scale was used to estimate the restlessness scores from 1 to 6 (1, anxious and not reassurable; 2, cooperative, tranquil, and oriented; 3, responds to command; 4, asleep with brisk response to a light glabellar tap or loud auditory stimulus; 5, asleep with sluggish response to a light glabellar tap or loud auditory stimulus; 6, non-responsive). A score of 2–4 indicates good analgesic effect. A score of 5–6 indicates excessive sedation.

Visual analogue score (VAS) at rest (VASR) and at coughing (VASC): VASR was assessed with the child lying supine for static pain intensity and VASC was assessed during change from coughing for dynamic pain intensity. VAS is a 10 cm horizontal "vernier" ranging from 0 to 10 where 0 is defined as no pain, < 3 as sustainable mild pain, 4 to 6 as sustainable but sleep-disturbing pain, and 7 to 10 as unbearable pain to a maximum level of pain. When responding to a VAS item, respondents specify their level of agreement to a statement by indicating a position along a continuous line between two end-points.

Enzyme Linked Immunosorbent Assay

Fasting venous blood was obtained from each child in the morning on the day before operation, first and second day after operation, respectively. The serum levels of adrenocorticotropic hormone (ACTH), interleukin-6 (IL-6), and cortisol (COR) were detected using ELISA kits (R&D Systems, United States).

Outcome Variables

Hemodynamic measurements including SBP, DBP, HR and SpO_2, Ramsay sedation scores, VASR and VASC were recorded at 1, 2, 6, 12, 24, 36, and 48 h after arrival to the ward. The times to push the PCIA button and the incidence of adverse reactions including nausea and vomiting, respiratory depression, cardiovascular events, pruritus and dizziness, were recorded during the studied period. Nausea and vomiting scores were recorded as previously described (Apfel et al., 1999), ranging from 1 to 4 (1, the absence of nausea and vomiting; 2, feel nausea without vomiting; 3, vomiting less than two times; 4, severe vomiting more than two times). Respiratory depression was defined as respiratory depression (ventilatory frequency <10 breath/min lasting for more than 10 min or SpO_2 < 90%). Cardiovascular events refer to drugrelated bradycardia (HR < 60 beats/min for more than 10 min), and hypotension (>20% decrease in systolic BP or >15% decrease in diastolic BP from preoperative baseline). If severe adverse reactions appeared, the use of PCIA was stopped temporarily and the child was observed continuously for 30 min. If the adverse reactions were presented more than 30 min or a further severe, the child was treated with appropriate medications. Nausea and vomiting were treated with metoclopramide. Respiratory depression was treated with naloxone and oxygen. Hypotension or bradycardia was treated

TABLE 1 | Patient characteristics between Group ND and Group SD.

Characteristics	ND (n = 200)	SD (n = 200)	t/Z	*P*
Age (year)	5.04 ± 0.88	5.08 ± 0.83	0.468	0.640
Gender (male/%)	131 (65.50%)	125 (62.50%)	0.625	0.532
Weight (kg)	20.29 ± 4.04	20.31 ± 3.50	0.053	0.958
ASA-PS grade (n)	-	-	0.817	0.414
Grade I	52	45	-	-
Grade II	148	155	-	-
Type of surgery (n)	-	-	0.717	0.474
Tonsillectomy	82	75	-	-
Tonsillectomyandadenoidectomy	118	125	-	-
Duration of operation (min)	35.72 ± 16.83	34.42 ± 15.11	0.813	0.417
Length of anesthesia (min)	44.21 ± 20.18	42.89 ± 18.37	0.684	0.494

ASA-PS, American Society of anaesthesiologists physical status; Data of mean ± standard deviation were analyzed by unpaired t *test and data of number with percentage were analyzed by chi-square test or Fisher's exact test.*

with volume expansion, ephedrine, or atropine. Pruritus was evaluated and treated with diphenhydramine, as appropriate.

Statistical Analysis

A sample size calculation was performed using PASS 15.0 (NCSS, LLC, Kaysville, Utah, United States) before participant recruitment. Under the supervision of the ethical committee a preliminary trial with 30 pediatric patients under general anesthesia was performed, in which the standard deviation of VASC after tonsillectomy adenoidectomy was found to be 2. With a one-tailed α of 0.05 and power of 90%, to gain a difference of no less than 1 in VAS after tonsillectomy adenoidectomy between two equal groups, a total of 86 patients in each group were required. Assuming a dropout rate of 20%, at least 120 children for each group should be recruited in this study.

All statistical analysis was performed Graphpad Prism 8 (GraphPad Software, CA, United States) for Windows. Measurement data are examined by Shapiro Wilk test for normal distribution and shown as mean ± standard deviation and analyzed by paired or unpaired *t* test when normally distributed. Categorical data were shown by number with percentage and analyzed by chi-square test or Fisher's exact test. The level of $p < 0.05$ reflects the presence of significant difference.

RESULTS

A total of 400 patients undergoing tonsillectomy with and without adenoidectomy fulfilled the inclusion and excluded criteria were included in the study. The patient characteristics between Group ND (n = 200) and Group SD (n = 200) are summarized in **Table 1**. There was no difference identified in demographic data including age, gender, weight, ASA-PS grade, duration of operation, length of anesthesia, and transfusion volume between two groups.

Hemodynamic measurements including SBP, DBP, HR and SpO_2 at 1, 2, 6, 12, 24, and 48 h after arrival to the ward were shown in **Table 2**. With regard to SBP, the children in Group SD exhibited significant changes at indicated time points, while those in Group ND exhibited significant changes only at 2, 12, and 24 h after surgery ($p < 0.05$). As for DBP, no evidence of hypotension was found in each group, while the children in Group SD exhibited significant changes in DBP among each time points ($p < 0.05$). The children in Group ND exhibited no significant change at each time point ($p > 0.05$). It was found that the children in Group ND exhibited significant changes in HR only at 6 h after surgery ($p < 0.05$), but those in

TABLE 2 | Hemodynamic measurements of children at 1, 2, 6, 12, 24, and 48 h after arrival to the ward between Group ND and Group SD.

Hemodynamic Measurements	ND (n = 200)	SD (n = 200)
SBP (mmHg)		
1 h after surgery	100.83 ± 8.27	101.04 ± 8.32
2 h after surgery	97.48 ± 3.25*	99.02 ± 7.41*
6 h after surgery	96.83 ± 3.68	89.17 ± 4.92*
12 h after surgery	98.79 ± 4.36*	100.20 ± 6.20*
24 h after surgery	95.30 ± 5.82*	94.88 ± 6.12*
48 h after surgery	94.68 ± 7.04	89.83 ± 4.33*
DBP (mmHg)		
1 h after surgery	51.34 ± 5.19	52.74 ± 6.80*
2 h after surgery	50.83 ± 5.27	49.76 ± 6.11*
6 h after surgery	49.20 ± 6.05	47.64 ± 6.14*
12 h after surgery	48.68 ± 7.70	45.41 ± 4.56*
24 h after surgery	46.88 ± 5.76	43.75 ± 3.22*
48 h after surgery	47.83 ± 5.13	45.53 ± 6.01*
HR (beat/min)		
1 h after surgery	80.53 ± 10.76	78.86 ± 5.27
2 h after surgery	81.22 ± 9.33	81.29 ± 7.40*
6 h after surgery	83.80 ± 8.79*	83.61 ± 8.12*
12 h after surgery	84.02 ± 9.35	86.14 ± 7.90*
24 h after surgery	83.17 ± 6.80	84.65 ± 8.03
48 h after surgery	84.54 ± 7.22	82.64 ± 5.05*
SpO_2 (%)		
1 h after surgery	97.83 ± 1.33	98.17 ± 1.26
2 h after surgery	98.33 ± 1.25	99.00 ± 1.46
6 h after surgery	98.01 ± 1.20	98.53 ± 1.25
12 h after surgery	98.47 ± 1.29	98.11 ± 1.18
24 h after surgery	97.76 ± 1.06	97.94 ± 1.21
48 h after surgery	98.11 ± 1.41	98.57 ± 1.32

**indicates* p *< 0.05 by paired* t *test in comparison with the previous time point.*

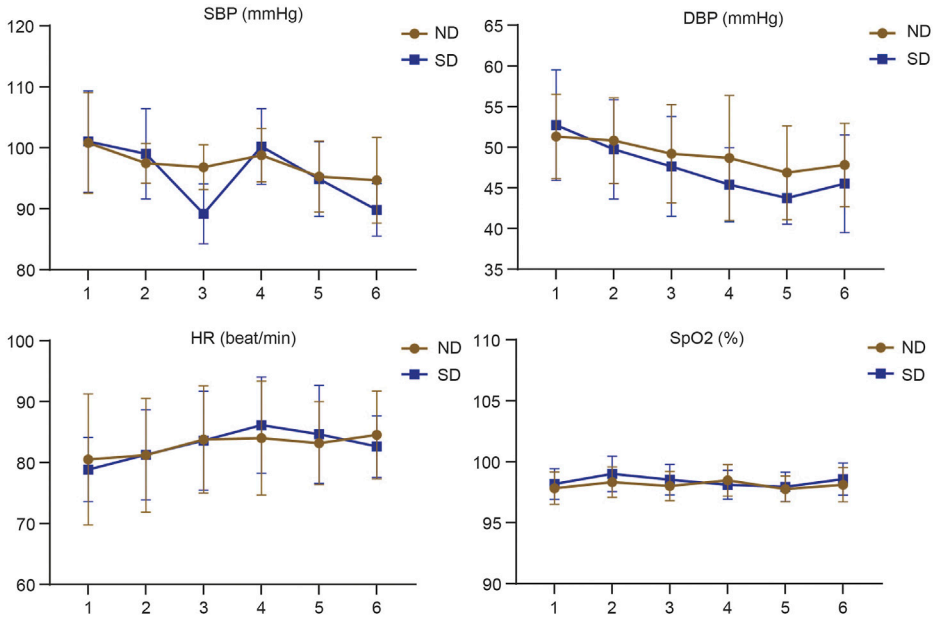

FIGURE 1 | Hemodynamic changes assessed by SBP, DBP, HR and SpO_2 of children at 1, 2, 6, 12, 24, and 48 h after operation between Group ND and Group SD.

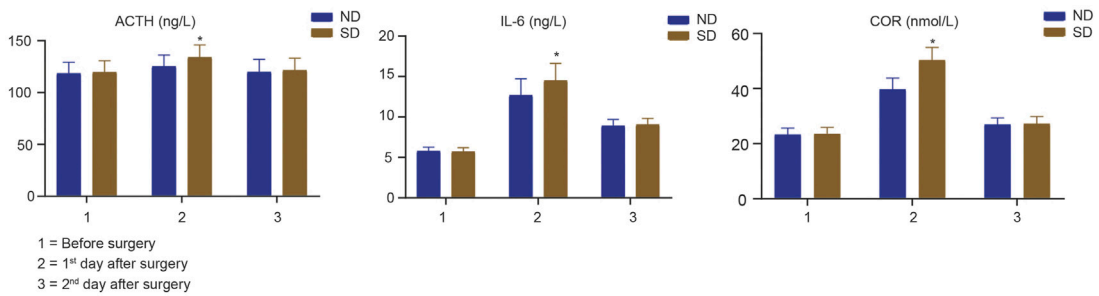

FIGURE 2 | The serum ACTH, IL-6, COR levels in children first day before surgery, first and second day after operation between Group ND and Group SD were determined by ELISA methods. * indicates $p < 0.05$.

Group SD exhibited significant changes at indicated time points ($p < 0.05$). No remarkable changes were found in both groups at indicated time points ($p > 0.05$) after surgery. These data suggested that more stable hemodynamic changes were noted in pediatric patients receiving nalbuphine combined with dexmedetomidine than sufentanil combined with dexmedetomidine for PCIA (**Figure 1**).

Ramsay sedation scores of children at 1, 2, 6, 12, 24, and 48 h after arrival to the ward between Group ND and Group SD were listed in **Table 3**. No evidence of distinct difference was found regarding Ramsay sedation scores of children between Group ND and Group SD at 1 and 2 h after surgery ($p > 0.05$). At 6, 12, 24, and 48 h after surgery, the children allocated into Group ND had higher Ramsay sedation scores than those allocated into Group SD ($p < 0.05$). No case with excessive sedation (Ramsay sedation scores ≥5) was observed. These data revealed a more analgesic effect conferred by nalbuphine combined with dexmedetomidine than sufentanil combined with dexmedetomidine for PCIA.

TABLE 3 | Ramsay sedation scores of children at 1, 2, 6, 12, 24, and 48 h after arrival to the ward between Group ND and Group SD.

	ND (n = 200)	SD (n = 200)	t	*P*
1 h after surgery	3.31 ± 0.50	3.26 ± 0.45	1.051	0.294
2 h after surgery	3.26 ± 0.48	3.18 ± 0.52	1.599	0.111
6 h after surgery	3.17 ± 0.47	3.02 ± 0.40	3.437	0.006
12 h after surgery	3.08 ± 0.41	2.99 ± 0.29	2.534	0.012
24 h after surgery	2.32 ± 0.57	2.19 ± 0.23	2.991	0.003
48 h after surgery	2.05 ± 0.50	1.93 ± 0.15	3.251	0.001

Statistical analysis was performed by unpaired t *test.*

TABLE 4 | VAS scores of children at 1, 2, 6, 12, 24, and 48 h after arrival to the ward between Group ND and Group SD.

VAS Scores	ND (n = 200)	SD (n = 200)	t	*P*
VASR				
1 h after surgery	2.36 ± 0.52	2.44 ± 0.58	1.452	0.147
2 h after surgery	2.50 ± 0.57	2.60 ± 0.60	1.709	0.088
6 h after surgery	2.81 ± 0.59	3.01 ± 0.63	3.277	0.001
12 h after surgery	3.06 ± 0.50	3.20 ± 0.55	2.644	0.008
24 h after surgery	2.86 ± 0.49	2.98 ± 0.53	2.351	0.019
48 h after surgery	2.29 ± 0.43	2.35 ± 0.45	1.363	0.174
VASC				
1 h after surgery	2.55 ± 0.60	2.62 ± 0.62	1.147	0.252
2 h after surgery	2.88 ± 0.57	3.03 ± 0.60	2.563	0.011
6 h after surgery	3.27 ± 0.66	3.53 ± 0.68	3.880	0.001
12 h after surgery	3.60 ± 0.66	3.78 ± 0.68	2.686	0.008
24 h after surgery	3.39 ± 0.60	3.52 ± 0.63	2.113	0.035
48 h after surgery	2.62 ± 0.57	2.72 ± 0.60	1.709	0.088

Statistical analysis was performed by unpaired t *test.*

The times to push the PCIA button in Group ND and Group SD were 2.44 ± 0.74 and 2.62 ± 1.00, showing significant difference between two groups (t = 2.046, $p = 0.041$).

VAS scores of children at 1, 2, 6, 12, 24, and 48 h after operation between Group ND and Group SD were shown in **Table 4**. There was no significant difference of VASR scores within 1 and 2 h post operation and of VASC scores within 1 h post operation between the two groups ($p > 0.05$). The VASR scores of children in Group ND were significantly lower within 6, 12, and 24 h than those in Group SD ($p < 0.05$). The VASC scores of children in Group ND were significantly lower within four time points (2, 6, 12, and 24 h) than those in Group SD ($p < 0.05$). No significant difference regarding both scores within 48 h post operation between the two groups ($p > 0.05$). These results indicated that nalbuphine combined with dexmedetomidine in PCIA could relieve the postoperative pain compared with sufentanil combined with dexmedetomidine in PCIA for pediatric tonsillectomy adenoidectomy.

The ACTH, IL-6, COR levels in the serum extracted from each child first day before surgery, first and second day after surgery between Group ND and Group SD were determined by ELISA methods. As shown in **Figure 2**, two groups exhibited no significant difference with regard to serum levels of ACTH, IL-6, COR in children first day before surgery ($p > 0.05$). At 1st day after surgery, the children in Group ND had lower levels of serum ACTH (t = 6.516, $p < 0.001$), IL-6 (t = 8.685, $p < 0.001$), and COR (t = 23.880, $p < 0.001$) levels than those in Group SD. At 2nd day after surgery, no significant difference was noted in serum levels of ACTH, IL-6, and COR in children between two groups ($p > 0.05$). These data suggested that nalbuphine combined with dexmedetomidine in PCIA could reduce stress response of pediatric patients undergoing tonsillectomy adenoidectomy.

The children may suffer several adverse reactions, including nausea and vomiting, dizziness and headache, respiratory depression, dry mouth, restlessness, and pruritus. As shown in **Table 5**, no child suffered respiratory depression. There were 10 cases of nausea and vomiting, 8 cases of dizziness and headache, 7 cases of dry mouth, 3 cases of restlessness, and 2 cases of pruritus in Group ND. There were 22 cases of nausea and vomiting, 12 cases of dizziness and headache, 12 cases of dry mouth, 7 cases of restlessness, and 9 cases of pruritus in Group SD. The incidence rates of nausea and vomiting, and pruritus were significantly higher in Group SD than Group ND (5.00% vs. 11.00%, $p = 0.028$; 1.00% vs. 4.50%, $p = 0.032$), while the incidence rates of dizziness and headache, dry mouth, and restlessness were not ($p > 0.05$). The total incidence rate of adverse reactions was significantly higher in Group SD than Group ND (15.00% vs. 31.00%, $p = 0.0001$). These data revealed the safety of nalbuphine combined with dexmedetomidine in PCIA for postoperative pain management in pediatric tonsillectomy adenoidectomy.

DISCUSSION

Alleviating the pain after tonsillectomy in children has always been a challenge and the choice of postsurgical analgesic agents remains controversial. Opioid analgesics are widely used in PCIA in clinic, including fentanyl, morphine, and sufentanil. Although these analgesics present good analgesic effect, they may be associated with various adverse reactions such as respiratory depression especially for children with obstructive sleep apnea (Chidambaran et al., 2017), excessive sedation, blood pressure drop, gastrointestinal peristalsis, nausea and vomiting, skin pruritus, urinary retention (Sadhasivam et al., 2015). The use of alternative nonsteroidal anti-inflammatory drugs such as ketorolac and ibuprofen contributes to the increased risk of hemorrhage after tonsillectomy (Møiniche et al., 2003; Tan and Tunkel, 2017). Naborphine, as a new type of synthetic opioid, has emerged its clinical value in recent years. Nalbuphine is a powerful analgesic showing low side effects and low dependence in animals and humans, and it has been shown to be effective against the respiratory inhibitory without attenuation of analgesia (Klepper et al., 1986; Narver, 2015; Haw et al., 2016). Previous studies have confirmed that combination of dexmedetomidine and sufentanil on spinal anesthesia (Karimi et al., 2021) or nalbuphine combined with dexmedetomidine in the postoperative treatment of laparoscopic oophorocystectomy (Liu et al., 2021) achieved good clinical effects such as longer postoperative analgesia, reduced use of analgesic, and slight hemodynamic changes. This study attempted to investigate the impacts of sufentanil or nalbuphine combined with dexmedetomidine on the children after tonsillectomy.

Under the condition of PCIA, drugs can be infused according to the specified time and concentration, leading to lower dosage, improvements on the efficacy and safety of drugs, and decrease in side effects. PCIA has been proved to be an excellent method of postoperative pain relief in adults and children undergoing surgical intervention (Morlion et al., 2018). In this study, we adopted PCIA method with different analgesics for the patients who underwent tonsillectomy for postoperative pain management. Perioperative haemodynamic monitoring is the cornerstone of optimizing tissue perfusion and preventing metabolic deterioration. Hemodynamic instability is related to cardiac dysfunction (Pang et al., 2019). Dexmedetomidine inhibits the release of norepinephrine through stimulating presynaptic and postsynaptic α 2 receptors, which in turn slows the patient's heart rate and reduces blood pressure, and then maintain the stability of hemodynamics of

TABLE 5 | The incidence of adverse reactions in children receiving PCA between Group ND and Group SD.

Group	Nausea and vomiting	Dizziness and headache	Respiratory depression	Dry mouth	Restlessness	Pruritus	Total
ND (n = 200)	10 (5.00%)	8 (4.00%)	0	7 (3.50%)	3 (1.50%)	2 (1.00%)	30 (15.00%)
SD (n = 200)	22 (11.00%)	12 (6.00%)	0	12 (6.00%)	7 (3.50%)	9 (4.50%)	62 (31.00%)
P	0.028	0.358	0	0.240	0.200	0.032	0.0001

Statistical analysis was performed by chi-square test or Fisher's exact test.

patients (Weerink et al., 2017). The present study found that the children received sufentanil and dexmedetomidine showed significant changes regarding SBP at time points including 1, 2, 6, 12, 24, and 48 h after arrival to the ward, and the children treated with nalbuphine and dexmedetomidine had significant changes of SBP only at 2, 12, and 24 h after arrival. The two groups presented the absence of hypotension. However, significant changes in DBP at each time points were found in the Group SD but not in the Group ND. As for the HR, the Group SD exhibited significant changes at all points while the Group ND revealed significant changes only at 6 h after arrival. The two groups showed slight changes in SpO_2 at indicated time points after arrival. These findings suggested that the children had more stable hemodynamics after administration of nalbuphine and dexmedetomidine. Naborphine is a new synthetic opioid drug, which belongs to agonist-antagonist drugs. It exerts analgesic effect mainly through stimulation of k receptor and it has significant antagonism to μ receptor, which relatively reduces adverse reactions induced by μ receptor-related opioids such as respiratory depression, nausea and vomiting, skin pruritus, and hemodynamic instability (Wu et al., 2021). Etches (1994) indicated that the incidence of respiratory depression is 0.1%–1% regardless of the route of administration of opioids, and the degree of respiratory depression is associated with dose. This study confirmed that no patient had respiratory depression in the two groups, which might be benefited from the use of dexmedetomidine resulting in decrease use of opioids. The two groups showed no significant difference in the incidence rates of dizziness and headache, dry mouth, and restlessness. However, Group ND revealed significantly lower incidence rates of nausea and vomiting, and pruritus than the Group SD. These outcomes were indirectly supported by other studies indicating the addition of nalbuphine in parturients undergoing cesarean delivery contributed to lower incidence of postoperative adverse reactions including nausea, vomiting and pruritus (Ibrahim et al., 2019). Tubog et al. (2019) also proved that reduced incidence of pruritus induced by neuraxial opioids was relevant with the use of nalbuphine.

Postoperative pain experience will have a long-term impact on children, such as long-term behavioral changes and reduced pain tolerance, which will directly affect the development and growth of children's emotional and activity ability in the future (Howard, 2003). Therefore, it is very important to do a good job in perioperative analgesia. In this study, it was observed that the two groups showed slight difference in Ramsay sedation scores at 1 and 2 h after arrival to the ward. However, the Group ND had higher Ramsay sedation scores at 6, 12, 24, and 48 h after arrival than the Group SD, and there was no one with Ramsay sedation scores ≥5 in the two groups. The results demonstrated the analgesic effect of naborphine combined with dexmedetomidine is better than that of sufentanil combined with dexmedetomidine. VAS is a scale developed to obtain more variable measurements. It uses linear continuum to measure potential features and is widely used to measure postoperative pain intensity (Sung and Wu, 2018). We compared VAS scores of each groups at different time points including 1, 2, 6, 12, 24, and 48 h after operation. The Group ND presented significantly lower VASR scores (6, 12, 24 h) and VASC scores (2, 6, 12, and 24 h) than the Group SD. Previous study of orthognathic surgery revealed that the patients who received naborphine had significant lower VAS scores, and higher Ramsay scores than the patients who treated with sufentanil (Xi et al., 2020). The results indirectly confirmed our above findings.

Surgical trauma can also cause various body reactions, including activation of leukocytes and synthesis of cell factors. Cytokines are involved in a variety of reaction processes *in vivo*, and IL-6 is an important pro-inflammatory cytokine in body reactions (Jawa et al., 2011; Yuan, 2018). Pro-inflammatory cytokine release promotes phagocytosis of macrophages to remove invading pathogens and necrotic tissue cells. However, its overexpression will cause the expansion of inflammation, which is not conducive to the recovery of the body. Dexmedetomidine, as a α2 adrenoceptor agonist, has been shown to reduce systemic inflammation induced by sepsis *in vivo* (Sun et al., 2019) and *in vitro* (Mei et al., 2021). In our study, at first day after surgery, lower levels of serum IL-6 was found in the Group ND than that in the Group SD, and slight difference was observed at second day after surgery between two groups. Liu et al. manifested naborphine with high dose (1.5 mg/kg) plus dexmedetomidine (4 μg/kg) was beneficial to reduce IL-6 levels at first day after laparoscopic oophorocystectomy (Liu et al., 2021). The present study also confirmed that nalbuphine combined with dexmedetomidine significantly reduced levels of ACTH and COR at the first day after surgery, which suggested this administration could reduce stress response after tonsillectomy.

Several study limitations should be noted when interpreting our data. First, included surgical and anesthetic protocols were done by several surgeons and anesthesiologists. Although they all had the same experience with pediatric tonsillectomy adenoidectomy and anaesthesia, bias on surgical outcomes may be considered. Second, due to retrospective nature, our data were obtained through past records, which may introduce potential bias by patient selection. Third, we investigated only one dose of study drugs, and a dose-response study was not performed. Thus, there might be a better dose for a more effective combination, and further prospective studies will be required to evaluate dose-dependent effects. Fourth, we failed to analyze pediatric patients receiving PCIA of single dose of

nalbuphine, sufentanil or dexmedetomidine and compared them with combination groups. Fifth, this was a single-center study, and thus more high-quality, multi-center, large-simple randomized trials are still warranted to optimize PCIA protocols for being more practical in clinical practice.

The results of this study revealed that in PCIA mode, naborphine combined with dexmedetomidine presented better clinical efficacy than the combination of dexmedetomidine and sufentanil after tonsillectomy. Dexmedetomidine and naborphine can further enhanced analgesic effect, maintain hemodynamics, reduce the incidence of nausea and vomiting, and decrease stress response.

DATA AVAILABILITY STATEMENT

The original contributions presented in the study are included in the article/Supplementary Material, further inquiries can be directed to the corresponding author.

ETHICS STATEMENT

The studies involving human participants were reviewed and approved by Children's Hospital of Henan. Written informed consent to participate in this study was provided by the participants' legal guardian/next of kin.

AUTHOR CONTRIBUTIONS

YPJ: conception and design, manuscript writing; RZ and ZCL: collection and assembly of data; YYW and SDC: provision of study materials or patients; LYZ and YS: data analysis and interpretation, checking of entered data for accuracy; JLQ: manuscript reviewing and revising.

FUNDING

The study was supported by the project (LHGJ20190956).

REFERENCES

Apfel, C. C., Läärä, E., Koivuranta, M., Greim, C. A., and Roewer, N. (1999). A Simplified Risk Score for Predicting Postoperative Nausea and Vomiting: Conclusions from Cross-Validations between Two Centers. *Anesthesiology* 91 (3), 693–700. doi:10.1097/00000542-199909000-00022

Batoz, H., Semjen, F., Bordes-Demolis, M., Bénard, A. K., and Nouette-Gaulain, K. (2016). Chronic Postsurgical Pain in Children: Prevalence and Risk Factors. A Prospective Observational Study. *Br. J. Anaesth.* 117 (4), 489–496. doi:10.1093/bja/aew260

Blackshaw, H., Springford, L. R., Zhang, L. Y., Wang, B., Venekamp, R. P., and Schilder, A. G. (2020). Tonsillectomy versus Tonsillotomy for Obstructive Sleep-Disordered Breathing in Children. *Cochrane Database Syst. Rev.* 4, CD011365. doi:10.1002/14651858.CD011365.pub2

Chen, C., Tang, W., Ye, W., Zhong, W., and Li, Y. (2021). ED50 of Propofol Combined with Nalbuphine on the Sedative Effect in Painless Hysteroscopy. *Pain Ther.* 10 (2), 1235–1243. doi:10.1007/s40122-021-00280-x

Chidambaran, V., Sadhasivam, S., and Mahmoud, M. (2017). Codeine and Opioid Metabolism: Implications and Alternatives for Pediatric Pain Management. *Curr. Opin. Anaesthesiol.* 30 (3), 349–356. doi:10.1097/ACO.0000000000000455

Cohen, N., and Sommer, D. D. (2016). Post-tonsillectomy Pain Control: Consensus or Controversy? *Pain Manag.* 6 (1), 31–37. doi:10.2217/pmt.15.58

Etches, R. C. (1994). Respiratory Depression Associated with Patient-Controlled Analgesia: A Review of Eight Cases. *Can. J. Anaesth.* 41 (2), 125–132. doi:10.1007/BF03009805

Giaccari, L. G., Coppolino, F., Aurilio, C., Esposito, V., Pace, M. C., Paladini, A., et al. (2020). Sufentanil Sublingual for Acute Post-Operative Pain: A Systematic Literature Review Focused on Pain Intensity, Adverse Events, and Patient Satisfaction. *Pain Ther.* 9 (1), 217–230. doi:10.1007/s40122-020-00166-4

Gonzalez, K. W., Dalton, B. G., Millspaugh, D. L., Thomas, P. G., and St Peter, S. D. (2016). Epidural versus Patient-Controlled Analgesia after Pediatric Thoracotomy for Malignancy: A Preliminary Review. *Eur. J. Pediatr. Surg.* 26 (4), 340–343. doi:10.1055/s-0035-1554805

Haw, A. J., Meyer, L. C., and Fuller, A. (2016). Nalbuphine and Butorphanol Reverse Opioid-Induced Respiratory Depression but Increase Arousal in Etorphine-Immobilized Goats (*Capra hircus*). *Vet. Anaesth. Analg.* 43 (5), 539–548. doi:10.1111/vaa.12343

Howard, R. F. (2003). Current Status of Pain Management in Children. *JAMA* 290 (18), 2464–2469. doi:10.1001/jama.290.18.2464

Ibrahim, A. S., Aly, M. G., Thabet, M. E., and Abdelaziz, M. R. (2019). Effect of Adding Nalbuphine to Intrathecal Bupivacaine with Morphine on Postoperative Nausea and Vomiting and Pruritus after Elective Cesarean Delivery: A Randomized Double Blinded Study. *Minerva Anestesiol.* 85 (3), 255–262. doi:10.23736/S0375-9393.18.12751-9

Jawa, R. S., Anillo, S., Huntoon, K., Baumann, H., and Kulaylat, M. (2011). Interleukin-6 in Surgery, Trauma, and Critical Care Part II: Clinical Implications. *J. Intensive Care Med.* 26 (2), 73–87. doi:10.1177/0885066610384188

Jotić, A., Savić Vujović, K., Milovanović, J., Vujović, A., Radin, Z., Milić, N., et al. (2019). Pain Management after Surgical Tonsillectomy: Is There a Favorable Analgesic? *Ear, Nose Throat J.* 98 (6), 356–361. doi:10.1177/0145561319846065

Karimi, M., Alipour, M., Jalaeian Taghaddomi, R., and Tavakolian, A. (2021). Effects of the Sufentanil and Dexmedetomidine Combination on Spinal Anesthesia in Patients Undergoing Lower Abdominal or Lower Extremity Surgery: A Double-Blind Randomized Controlled Trial. *Iran J. Med. Sci.* 46 (4), 263–271. doi:10.30476/ijms.2020.83681.1299

Kelly, L. E., Sommer, D. D., Ramakrishna, J., Hoffbauer, S., Arbab-Tafti, S., Reid, D., et al. (2015). Morphine or Ibuprofen for post-tonsillectomy Analgesia: A Randomized Trial. *Pediatrics* 135 (2), 307–313. doi:10.1542/peds.2014-1906

Kiyatkin, E. A. (2019). Respiratory Depression and Brain Hypoxia Induced by Opioid Drugs: Morphine, Oxycodone, Heroin, and Fentanyl. *Neuropharmacology* 151, 219–226. doi:10.1016/j.neuropharm.2019.02.008

Klepper, I. D., Rosen, M., Vickers, M. D., and Mapleson, W. W. (1986). Respiratory Function Following Nalbuphine and Morphine in Anaesthetized Man. *Br. J. Anaesth.* 58 (6), 625–629. doi:10.1093/bja/58.6.625

Kokki, H. (2003). Nonsteroidal Anti-inflammatory Drugs for Postoperative Pain: A Focus on Children. *Paediatr. Drugs* 5 (2), 103–123. doi:10.2165/00128072-200305020-00004

Krauss, B. S., Calligaris, L., Green, S. M., and Barbi, E. (2016). Current Concepts in Management of Pain in Children in the Emergency Department. *Lancet* 387 (10013), 83–92. doi:10.1016/S0140-6736(14)61686-X

Lee, J., Delaney, K., Napier, M., Card, E., Lipscomb, B., Werkhaven, J., et al. (2020). Child Pain Intensity and Parental Attitudes toward Complementary and Alternative Medicine Predict Post-Tonsillectomy Analgesic Use. *Children (Basel)* 7 (11), 236. doi:10.3390/children7110236

Lim, L., Jang, Y. E., Kim, E. H., Lee, J. H., Kim, J. T., and Kim, H. S. (2020). Comparison of the Effects of Sufentanil and Fentanyl in Intravenous Patient-Controlled Analgesia after Pediatric Moyamoya Surgery: A Retrospective Study. *Pediatr. Neurosurg.* 55 (1), 36–41. doi:10.1159/000504582

Liu, X., Song, J., Zhang, Y., Zhang, Y., and Hu, X. (2021). Different Doses of Nalbuphine Combined with Dexmedetomidine in Laparoscopic Oophorocystectomy. *Med. Sci. Monit.* 27, e930197. doi:10.12659/MSM.930197

Makhlouf, M. M., Garibay, E. R., Jenkins, B. N., Kain, Z. N., and Fortier, M. A. (2019). Postoperative Pain: Factors and Tools to Improve Pain Management in Children. *Pain Manag.* 9 (4), 389–397. doi:10.2217/pmt-2018-0079

Mei, B., Li, J., and Zuo, Z. (2021). Dexmedetomidine Attenuates Sepsis-Associated Inflammation and Encephalopathy via central α2A Adrenoceptor. *Brain Behav. Immun.* 91, 296–314. doi:10.1016/j.bbi.2020.10.008

Min, T. J., Kim, W. Y., Jeong, W. J., Choi, J. H., Lee, Y. S., Kim, J. H., et al. (2012). Effect of Ketamine on Intravenous Patient-Controlled Analgesia Using Hydromorphone and Ketorolac after the Nuss Surgery in Pediatric Patients. *Korean J. Anesthesiol.* 62 (2), 142–147. doi:10.4097/kjae.2012.62.2.142

Mitchell, R. B., Archer, S. M., Ishman, S. L., Rosenfeld, R. M., Coles, S., Finestone, S. A., et al. (2019). Clinical Practice Guideline: Tonsillectomy in Children (Update)-Executive Summary. *Otolaryngol. Head Neck Surg.* 160 (1_Suppl. l), 187–205. doi:10.1177/0194599818807917

Møiniche, S., Rømsing, J., Dahl, J. B., and Tramèr, M. R. (2003). Nonsteroidal Antiinflammatory Drugs and the Risk of Operative Site Bleeding after Tonsillectomy: A Quantitative Systematic Review. *Anesth. Analg.* 96 (1), 68. doi:10.1097/00000539-200301000-00015

Momeni, M., Crucitti, M., and De Kock, M. (2006). Patient-controlled Analgesia in the Management of Postoperative Pain. *Drugs* 66 (18), 2321–2337. doi:10.2165/00003495-200666180-00005

Morlion, B., Schafer, M., Betteridge, N., and Kalso, E. (2018). Non-Invasive Patient-Controlled Analgesia in the Management of Acute Postoperative Pain in the Hospital Setting. *Curr. Med. Res. Opin.* 34 (7), 1179–1186. doi:10.1080/03007995.2018.1462785

Motamed, C. (2022). Clinical Update on Patient-Controlled Analgesia for Acute Postoperative Pain. *Pharmacy* 10 (1), 22. doi:10.3390/pharmacy10010022

Narver, H. L. (2015). Nalbuphine, a Non-controlled Opioid Analgesic, and its Potential Use in Research Mice. *Lab. Anim. (NY)* 44 (3), 106–110. doi:10.1038/laban.701

Oremule, B., Johnson, M., Sanderson, L., Lutz, J., Dodd, J., and Hans, P. (2015). Oral Morphine for Pain Management in Paediatric Patients after Tonsillectomy and Adenotonsillectomy. *Int. J. Pediatr. Otorhinolaryngol.* 79 (12), 2166–2169. doi:10.1016/j.ijporl.2015.09.040

Pang, Q., Hendrickx, J., Liu, H. L., and Poelaert, J. (2019). Contemporary Perioperative Haemodynamic Monitoring. *Anaesthesiol. Intensive Ther.* 51 (2), 147–158. doi:10.5114/ait.2019.86279

Sadhasivam, S., Zhang, X., Chidambaran, V., Mavi, J., Pilipenko, V., Mersha, T. B., et al. (2015). Novel Associations between FAAH Genetic Variants and Postoperative central Opioid-Related Adverse Effects. *Pharmacogenomics J.* 15 (5), 436–442. doi:10.1038/tpj.2014.79

Sun, Y. B., Zhao, H., Mu, D. L., Zhang, W., Cui, J., Wu, L., et al. (2019). Dexmedetomidine Inhibits Astrocyte Pyroptosis and Subsequently Protects the Brain in *In Vitro* and *In Vivo* Models of Sepsis. *Cell Death Dis.* 10 (3), 167. doi:10.1038/s41419-019-1416-5

Sung, Y. T., and Wu, J. S. (2018). The Visual Analogue Scale for Rating, Ranking and Paired-Comparison (VAS-RRP): A New Technique for Psychological Measurement. *Behav. Res. Methods* 50 (4), 1694–1715. doi:10.3758/s13428-018-1041-8

Tan, G. X., and Tunkel, D. E. (2017). Control of Pain after Tonsillectomy in Children: A Review. *JAMA Otolaryngol. Head Neck Surg.* 143 (9), 937–942. doi:10.1001/jamaoto.2017.0845

Tobias, J. D., Green, T. P., and Coté, C. J.Section On Anesthesiology and Pain Medicine (2016). Codeine: Time to Say "No". *Pediatrics* 138 (4), e20162396. doi:10.1542/peds.2016-2396

Tubog, T. D., Harenberg, J. L., Buszta, K., and Hestand, J. D. (2019). Prophylactic Nalbuphine to Prevent Neuraxial Opioid-Induced Pruritus: A Systematic Review and Meta-Analysis of Randomized Controlled Trials. *J. Perianesth. Nurs.* 34 (3), 491–501 e8. doi:10.1016/j.jopan.2018.06.098

Wang, Y., Xu, W., Xia, W., Wei, L., Yang, D., Deng, X., et al. (2022). Comparison of the Sedative and Analgesic Effects of Dexmedetomidine-Remifentanil and Dexmedetomidine-Sufentanil for Liposuction: A Prospective Single-Blind Randomized Controlled Study. *Aesthet. Plast. Surg.* 46 (1), 524–534. doi:10.1007/s00266-021-02566-z

Weerink, M. A. S., Struys, M. M. R. F., Hannivoort, L. N., Barends, C. R. M., Absalom, A. R., and Colin, P. (2017). Clinical Pharmacokinetics and Pharmacodynamics of Dexmedetomidine. *Clin. Pharmacokinet.* 56 (8), 893–913. doi:10.1007/s40262-017-0507-7

Weibel, S., Jelting, Y., Afshari, A., Pace, N. L., Eberhart, L. H., Jokinen, J., et al. (2017). Patient-controlled Analgesia with Remifentanil versus Alternative Parenteral Methods for Pain Management in Labour. *Cochrane Database Syst. Rev.* 4, CD011989. doi:10.1002/14651858.CD011989.pub2

Wu, L., Yu, J., Wang, Q., and Lu, Y. (2021). Effects of Nalbuphine on the Cardioprotective Effect of Morphine in Rats. *Int. J. Cardiol.* 322, 207–210. doi:10.1016/j.ijcard.2020.08.064

Xi, M. Y., Li, S. S., Zhang, C., Zhang, L., Wang, T., and Yu, C. (2020). Nalbuphine for Analgesia after Orthognathic Surgery and its Effect on Postoperative Inflammatory and Oxidative Stress: A Randomized Double-Blind Controlled Trial. *J. Oral. Maxillofac. Surg.* 78 (4), 528–537. doi:10.1016/j.joms.2019.10.017

Yu, K. E., and Kim, J. S. (2021). Pediatric Postoperative Pain Management in Korea: Parental Attitudes toward Pain and Analgesics, Self-Efficacy, and Pain Management. *J. Pediatr. Nurs.* 58, e28–e36. doi:10.1016/j.pedn.2020.12.002

Yuan, S. M. (2018). Interleukin-6 and Cardiac Operations. *Eur. Cytokine Netw.* 29 (1), 1–15. doi:10.1684/ecn.2018.0406

Zhao, L., and Li, Y. (2020). Application of Dexmedetomidine Combined with Sufentanil in colon Cancer Resection and its Effect on Immune and Coagulation Function of Patients. *Oncol. Lett.* 20 (2), 1288–1294. doi:10.3892/ol.2020.11643

Conflict of Interest: The authors declare that the research was conducted in the absence of any commercial or financial relationships that could be construed as a potential conflict of interest.

Publisher's Note: All claims expressed in this article are solely those of the authors and do not necessarily represent those of their affiliated organizations, or those of the publisher, the editors and the reviewers. Any product that may be evaluated in this article, or claim that may be made by its manufacturer, is not guaranteed or endorsed by the publisher.

frontiers | Frontiers in Pharmacology

ORIGINAL RESEARCH
published: 18 May 2022
doi: 10.3389/fphar.2022.819747

Plasma Metabolites and Gut Microbiota Are Associated With T cell Imbalance in BALB/c Model of Eosinophilic Asthma

Yumei Zhou[1], *Tieshan Wang*[2], *Xiaoshan Zhao*[1], *Ji Wang*[1]* *and Qi Wang*[1]*

[1]National Institute of TCM Constitution and Preventive Medicine, School of Chinese Medicine, Beijing University of Chinese Medicine, Beijing, China, [2]Beijing Research Institute of Chinese Medicine, Beijing University of Chinese Medicine, Beijing, China

OPEN ACCESS

Edited by:
Songwen Tan,
Central South University, China

Reviewed by:
Wenhu Zhou,
Central South University, China
Wen Gu,
Shanghai Jiaotong University, China

***Correspondence:**
Ji Wang
doctorwang2009@126.com
Qi Wang
wangqi710@126.com

Specialty section:
This article was submitted to Translational Pharmacology, a section of the journal Frontiers in Pharmacology

Received: *22 November 2021*
Accepted: *19 April 2022*
Published: *18 May 2022*

Citation:
Zhou Y, Wang T, Zhao X, Wang J and Wang Q (2022) Plasma Metabolites and Gut Microbiota Are Associated With T cell Imbalance in BALB/c Model of Eosinophilic Asthma. Front. Pharmacol. 13:819747. doi: 10.3389/fphar.2022.819747

The pathogenesis of allergic asthma is complex, it is usually caused by immune system imbalance. Th1, Th2, regulatory T cells (Treg) and T helper 17 (Th17) cells have an important role in the pathogenesis of eosinophilic asthma. Yet, the exact role of Th1, Th2, Treg and Th17 cells in eosinophilic asthmatic disease is not fully understood. This study used an untargeted plasma metabolomics combine 16S rDNA technology to identify new biomarkers of plasma metabolites and gut microbiota in ovalbumin-induced eosinophilic allergic asthma in BALB/c mice to further explore the biomarkers in regulating the immune balance or the immune response. We discovered that malate, L-dihydroorotate were associated with Th1/Th2 and Treg/Th17 cells balance, imidazoleacetic acid was associated with Th1/Th2 cell balance, 1,5-anhydro-d-sorbitol was associated with Treg/Th17 cell balance. The results also found that genus *Candidatus Arthromitus of* gut microbiota were associated with Th1/2, Treg/Th17 balance, genus *Ruminiclostridium 6*, they were all associated with Th1/2 and Treg/Th17 cell balance, while the gut microbiota were not associated with penh value which reflect airway hyperresponsiveness (AHR) in the eosinophilic asthma mice model. Interestingly, the plasma metabolite biomarkers of malate, L-dihydroorotate are associated with genus Ruminiclostridium 6, they were all associated with Th1/2 and Treg/Th17 cell balance, while imidazoleacetic acid is associated with genus Ruminiclostridium 6 which is associated with Th1/2 balance. Among the differential plasma metabolites, 1,5-anhydro-d-sorbitol is associated with genus *Ruminiclostridium 6* and genus *Candidatus Arthromitus*. Among them, malate participate in the T cell activation, T cell differentiation and activation may be a new research direction in eosinophilic allergic asthma. We firstly study the gut microbiota and plasma metabolites markers of immune balance in eosinophilic asthma in mice model, laying a foundation for drug treatment in eosinophilic allergic asthma.

Keywords: eosinophilic asthma, Tcell imbalance, drug treatment, plasma metabolites, gut microbiota

INTRODUCTION

More than 300 million people worldwide are suffered from allergic asthma which is a long-term disease. Allergic asthma is also a chronic inflammatory condition characterized by high responsiveness to inhaled allergens in the respiratory tract (Matsumura et al., 2006). The in-depth immunologic characterization of patients and the emergency of biologics agents targeting type2-high cytokines have classified asthma patients into those with a high type 2 inflammatory response (type2-high group) and those with low or no type 2 inflammation (type2-low group). Type 2-high asthma is related to the over-expression cytokines of IL-4, IL-5, IL-9, and IL-13 which are usually produced by the innate immune system which can recognize allergens (including bacteria, viruses and allergens), and are essential in the effect phase of allergic reactions. Type2-high asthma is associated with excessive production of fractional exhaled nitric oxide (FeNO), mucus overproduction, increased eosinophil and mast cell infiltration, bronchial hyperresponsiveness, and excessive synthesis of IgE. In type 2-high allergic asthma, IL-4 and IL-13 are involved in mucus production and goblet cell hyperplasia in lung tissue, airway hyperresponsiveness, eosinophil invasion into the lungs, and IgE over-production (Woodruff et al., 2009; Pavord et al., 2019). The eosinophil in peripheral blood is often used as a marker to the treatment of type 2 asthma in allergic asthma patients. For example, most corticosteroid-treated asthma patients has been found eosinophilia in the sputum (Lambrecht et al., 2019).

There are two main types of allergic asthma, Th2 high asthma is predominantly eosinophilic, while Th2 low is predominantly neutrophilic and paucigranulocytic (Zhang et al., 2022). In allergic asthma patients, the appearance of Th2 cell response, the production of allergen-specific IgE, and the regulation of the recruitment of effector cells to the lung tissue are all related to the continuous immune tolerance of the allergen (Verbsky and Chatila, 2013; Lambrecht and Hammad, 2015). It is also currently believed that Th1/Th2 imbalance is one of the key immunological mechanisms. Increasing genetic and immunological evidence suggests that Treg cells have an essential role in inducing immune tolerance to allergens and preventing the occurrence and development of allergic asthma (Chatila et al., 2000; Torgerson et al., 2007; Jones et al., 2014; Palomares et al., 2014). Treg cells can inhibit allergic inflammation and play an important role in tissue remodeling (Gri et al., 2008; Nonaka et al., 2008). Treg cells can prevent effector T cells from flowing into inflammatory tissues through a cytokine-dependent manner (Ring et al., 2006). Treg can also reduce the induction of Th0/Th1 cells (Trautmann et al., 2002), thus eliminating bronchial epithelial cells and preventing tissue injury. Besides, Treg directly affects B cells through suppress the production of allergen-specific IgE (Meiler et al., 2008a), and inhibit the secretion of TGF-β, IL-10, CTLA-4 or histamine to perform these functions (Meiler et al., 2008b; Sakaguchi et al., 2009). In allergic asthma, it is well accepted that the generation and maintenance of Treg cells, the low expression of suppression cytokines such as IL-10, TGF-β and surface molecules are essential for the pathogenesis and the development of the disease. The induction of allergen tolerance is indispensable for allergic asthma (Palomares et al., 2017).

Th17 cells, as a subpopulation of $CD4^+$ T cells which can induce eosinophilic airway inflammation in asthma patients. Many studies have reported that the immune regulation Th17/Treg cells is correlated with asthma severity. Moreover, it has been suggested that Th17 cells could inhibit Treg cell-mediated tolerance and promote airway remodeling. Yet, the exact role of Treg and Th17 cells in eosinophilic asthmatic disease and airway remodeling are not fully understood (Zhao et al., 2013).

Metabolomics can perform high-dimensional molecular atlas analysis of diseases, and it is possible to define the endophenotype of diseases (Swietlik et al., 2021). In this study, we used an untargeted plasma metabolome to identify new biomarkers of plasma metabolites associated with the immune balance of Th1/2 and Treg/Th17 cells in a classical eosinophilic allergic asthma mice model. Besides, we also used 16S rDNA technology to analyze gut microbiota so as to further explore the role of gut microbiota in regulating the immune balance of Th1/2 and Treg/Th17 cells.

The pathogenesis of allergic asthma is complex, we can find OVA, OVA combine aluminum adjuvant, OVA combine Lipopolysaccharide (LPS), HDM (house dust mites) were used to construct allergic asthma mice model, while the immune response in the body are different. Until now, the allergic asthma induced by OVA is mainly predominantly infiltrated by eosinophils which can be demonstrated by my previous study (Zhou et al., 2022), while induced by HDM is maily infiltrated by neutrophils (Ma et al., 2021). When conducting research, different animal models are selected according to the different therapeutic effects of the drug. Although there are too much study focus on the gut microbiota or plasma metabolites in asthma disease, until now we have not found the biomarker of the gut microbiota or plasma metabolites associated with Th1/2 or Treg/Th17 immune balance in the animal study in eosinophilic asthma, which is critical for mechanism research and it is the foundation of drug therapy in eosinophilic asthma disease.

METHODS

Animals

BALB/c female mice (6–8 weeks old, 18–20 g) were obtained from Beijing Vital River Laboratory Animal Technology Co., Ltd. in China. All the animals were kept and all the animal studies were done according to institutional animal care regulations of Beijing University of Chinese Medicine and conducted according to the AAALAC and the IACUC guidelines.

Eosinophilic Asthma Mice Model Construction

The Eosinophilic asthma mice model was constructed according to our previously study (Zhou et al., 2022). Briefly, mice were sensitized intraperitoneally with 2 μg ovalbumin (OVA) and 2 mg Imject™ Alum Adjuvant (Invitrogen, Cat#77161) dissolved in 0.2 ml sterile PBS. The control group received

2 mg Alum Adjuvant in 0.2 ml of sterile PBS on 0 and 14 days, respectively. In the challenge phase, mice received 1% OVA dissolved in sterile PBS for 30 min from the 21st to 25th day by aerosol inhalation.

The Detection of Lung Function, Collection of Bronchoalveolar Lavage Fluid (BALF) and the Serum

The lung function detection was used to evaluate airway hyperresponsiveness (AHR). Briefly, on day 26 post-modeling, AHR was assessed by determining enhanced pause (Penh value). Briefly, mice were placed in the plethysmography chambers of a whole-body plethysmograph (WBP-4MR, TOW, China), after 2, 3 min acclimation, mice were exposed to aerosolized methacholine (Mch) with a series concentrations: 0, 6.25, 12.5, 25, and 50 mg/ml. Non-invasive measurement of airway hyperresponsiveness reflect lung function by whole-body phelthysmography was done according to a previously described approach (Sun et al., 2021).

Twenty-four hours after the last challenge with either OVA or PBS on the 26th day, bronchioalveolar lavage (BAL) of the lung was performed. Samples were centrifugated at 4°C, 1,200 rpm for 5 min resuspended in PBS. The supernatants of BAL fluids were analyzed by multiplex-assay ELISA kits containing IL-4, IL-5, IL-13, IL-17A, IL-6, IL-10, TGF-β and IFN-γ (Luminex, Univ, Cat#T2C0710709). OVA-specific IgE was detected according to the ELISA kit provided by Cayman (Cat#500840). Blood analyzer was used to count the number of Eosinophil cells.

Histopathology of Lungs

After 4% paraformaldehyde fixation and paraffin embedding of the lung tissue. HE (Hematoxylin and eosin), PAS (periodic acid–Schiff) staining were used to evaluate the inflammation and goblet cells hyperplasia. Inflammation grade was scored according to the following criteria: grade 0 (no inflammatory cells), grade 1 (some inflammatory cells), grade 2 (1-3 layer inflammatory cells surrounded bronchi), grade 3 (4, 5 layer of inflammatory cells surrounded bronchi) and grade 4 (more than five layers of inflammatory cells surrounded most bronchi). The pathological changes were quantified by the percentage of goblet cells in the epithelium using a five-point scoring system: grade 0 (no goblet cells), grade 1 (< 25% of airway), grade 2 (25–50% of airway), grade 3 (51–75% of airway) and grade 4 (>75% of airway). More than five bronchioles were counted in one pathological section, the inflammation scores or goblet cell hyperplasia scores was used in the study (Padrid et al., 1995).

Detection the Percentage of Th1, Th2, Treg and Th17 Cells

The percentage of Treg and Th17 cells in spleen tissue were detected by flow cytometry. Spleen tissues were prepared into a single cell suspension. CD3 (BD, Cat#557666), CD4 (BD, Cat#552775), CD25 (BD, Cat#558642), IFN-γ (BD, Cat#557735), IL-4 (BD, Cat#562915) were surface staining, while Foxp3 (eBioscience, Cat#17-5773-82) and IL-17A (BD, Cat#564169) were stained after the cell membrane was destroyed by eBioscience Fix/Perm (Cat#00-5523-00) or BD Fix/Perm buffer kit (Cat#554714) respectively. FVS 780 (BD, Cat#565388) was used to identify the live or dead cells. LSR Fortessa cell analyzer (BD) and BD FACSDiva 8.0.3 software were used to detect the percentage of Th1, Th2, Treg or Th17 cells.

Detection of IFN-γ, IL-4, RORγt and Foxp3 mRNA Relative Expression

TRIzol (Invitrogen) was used to extract total RNA in lung tissues according to manufacturer's instruction. The cDNA was synthesized with cDNA synthesis kit (K1622) (ThermoFisher) by reverse transcription according to the manufacturer's instructions. A realtime PCR assay was then performed in 1× superreal preMix plus (SYBR Green) (FP205-02) mixed with 0.2 mM forward and reverse primers. The mRNA amounts of test genes were normalized to the amount of β-actin. The primers in the study were shown below: β-actin (FP: GACCCAGATCATGTTTGAGACCT; RP: TCC AGGGAGGAAGAGGATGC); RORγt (FP: CGCACCAACCTCTTTTCA CG; RP: TGGCAAACTCCACCA CATACTG); Foxp3 (FP: CTTCAAGTACCACAA TATGCGACC; RP: GCGAACATGCGAGTAAACCAA); IFN-γ (FP: CTCAAGT GGCATAGATGTGGAAG; RP: TGACCTCAAACTTGGCAA TACTC); IL-4 (FP: GATAAGCTGCACCATGAATGAGT; RP: CCATTTGCATGATGCTCTTTAGG).

Sample Collection and Metabolomics Profiling

Blood was collected with anticoagulant tubes containing anticoagulant EDTA, and then centrifuged at 4°C, 1,500 g for 15 min. All the plasma was stored at −80°C. The plasma sample was collected and detected as described in our previous study (Zhou et al., 2022).

To evaluate the sample qualification, multivariate statistical analysis such as orthogonal partial least squares discriminant analysis (OPLS-DA) were used in the study. The R^2 and Q^2 values in the OPLS-DA model were used to assess the goodness of fit. Heatmap, cluster analysis, pathway analysis were conducted with the MetaboAnalyst web tool (https://www.metaboanalyst.ca/). Enrichment analysis was performed with the cytoscape software. Finally, we screen significantly different metabolites in plasma.

Gut Microbiota Analysis

Total genome DNA was extracted by CTAB/SDS method, and V3-V4 regions in the 16S rDNA of samples were amplified. The following primers were used: 16S V3-V4: 341F- 806R, 18S V9: 1380F-1510R, ITS1: ITS1F- ITS2R. 16S rDNA genes were amplified using the specific primer with the barcode. PCoA (Principal Co-ordinates Analysis) was used to study the similarity or difference of sample community

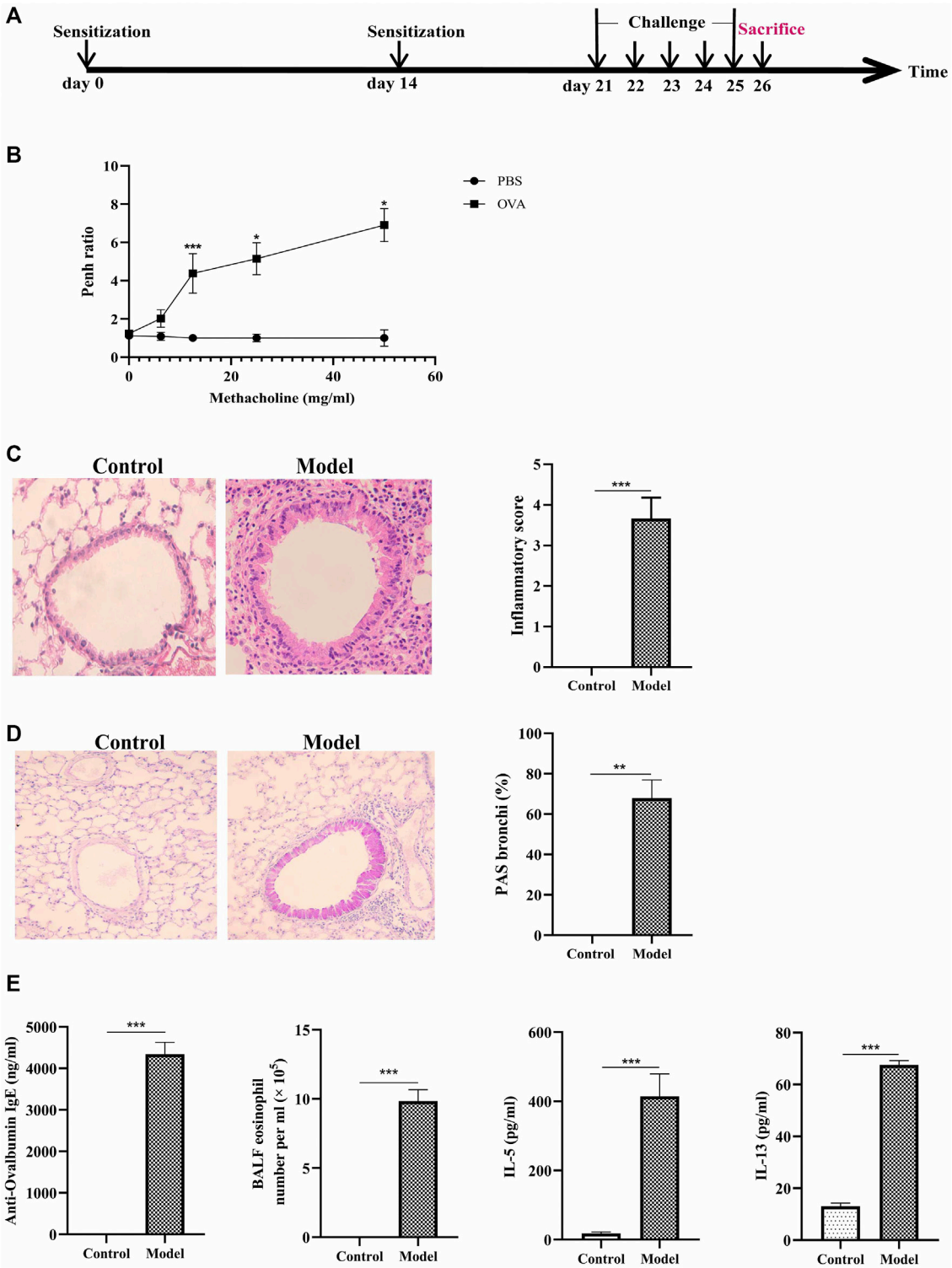

FIGURE 1 | Construction of eosinophilic asthma mice model and evalution of the model. **(A)** Experimental schema for eosinophilic asthma mice mode; **(B)** AHR in response to increasing doses of MCh by monitoring penh values. (average Penh over the 5-min time interval with methacholine divided by the average Penh over the 5-min interval with PBS); **(C)** HE (Hematoxylin/eosin) staining and inflammatory score of lung tissue; **(D)** PAS staining and goblet cell hyperplasia percentage of lung tissue; **(E)** Eosinophil counts in BALF, the detection of specific OVA-IgE, IL-5, IL-13 in control and model group, BALF was collected 24 h after last challenge, $^{*}p < 0.05$, $^{**}p < 0.01$, $^{***}p \leq 0.001$. All the values are expressed as mean±SEM. $n = 4$, 5 animals per group.

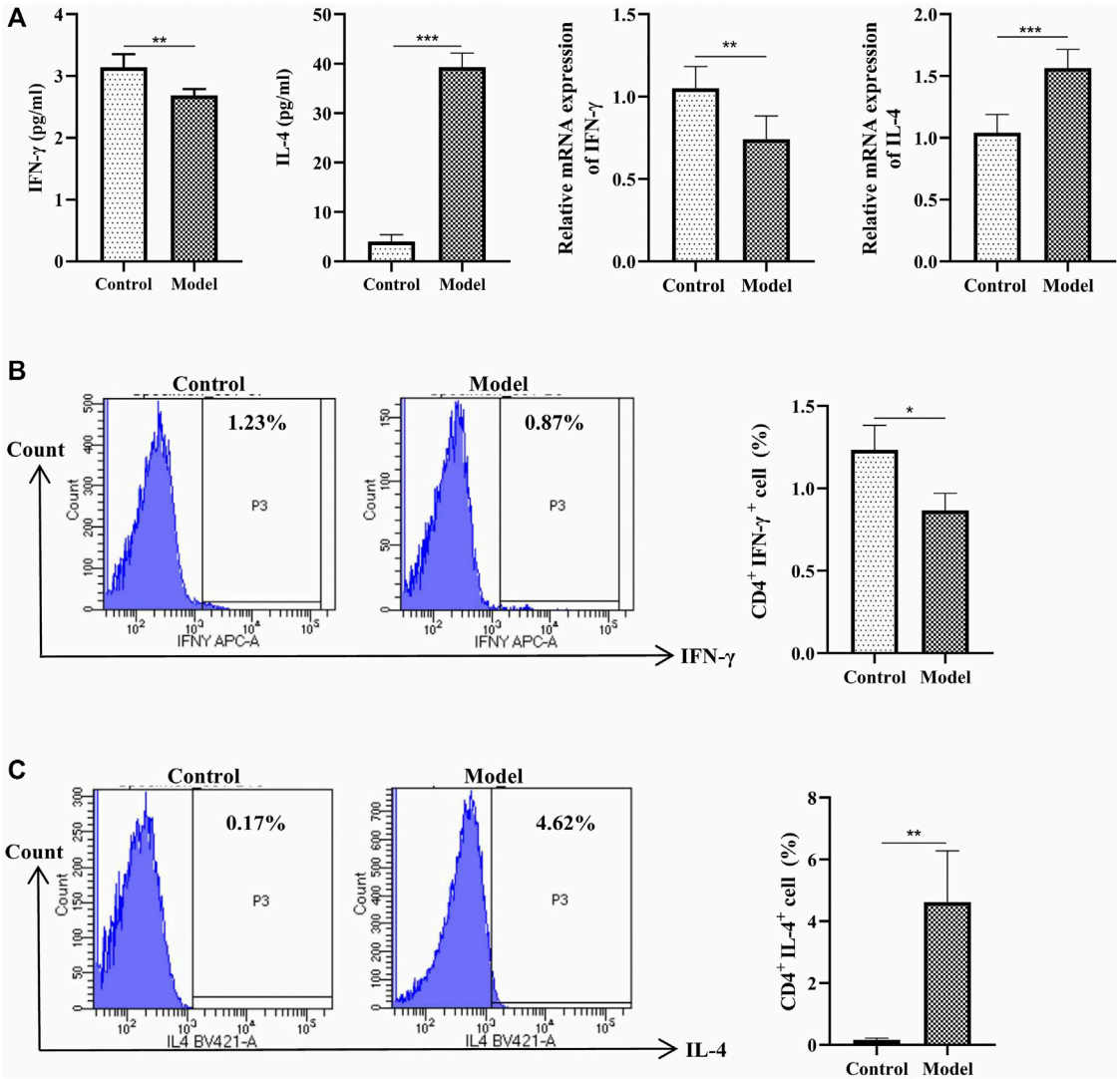

FIGURE 2 | Detection of Th1 and Th2 cells. **(A)** Left:Detection of IFN-γ, IL-4 in BALF, BALF was collected 24 h after last challenge, they were detected as described in the protocol; Right: Relative expression of IFN-γ mRNA and IL-4 mRNA detected by RT-qPCR **(B)**Left: Intracellular staining of CD4 and IFN-γ in the door $CD3^+$ T cells 24 h after last challenge; Right:Statistic data of Th1 cells 24 h after challenge; **(C)** Left: Intracellular staining of IL-4 and CD4 in the door $CD3^+$ T cells 24 h after last challenge; Right: Statistic data of Th2 cells 24 h after challenge. $^*p < 0.05$, $^{**}p < 0.01$, $^{***}p \leq 0.001$. All the values are expressed as mean±SEM. $n = 5$ animals per group.

composition. LEfSe ((LDA Effect Size) analysis method was used for the quantitative analysis of biomarkers in the two groups.

Statistical Analysis

All statistical analysis were performed by Prism 7.0 in this study. To analyze the difference between two groups, the *t*-test, one-way ANOVA test (Turkey or Dunnett), Wilcoxon rank-sum test were used. Data were shown as mean ± SD, and $p < 0.05$ was considered statistically significant. R software (version 3.5.1) by a hierarchical clustering algorithm and Pearson correlation analysis were used to describe the relevance between the gut microbiota, the metabolites, and the immunological index.

RESULT

OVA Sensitization Induced Eosinophilic Asthma in BALB/C Mice

To induce type-2 high allergic asthma (eosinophilic asthma), we immunized BALB/c mice with OVA and aluminum adjuvant (**Figure 1A**). The increasing of inflammatory cells and goblet cell hyperplasia were seen in the eosinophilic asthma model group (**Figures 1C,D**). The airway resistance was obvious in eosinophilic asthma compared to control mice which can be shown in **Figure 1B**.

Next, eosinophils and the related cytokines in BALF were detected in the two groups. The cytokines of IL-4, IL-5, and IL-

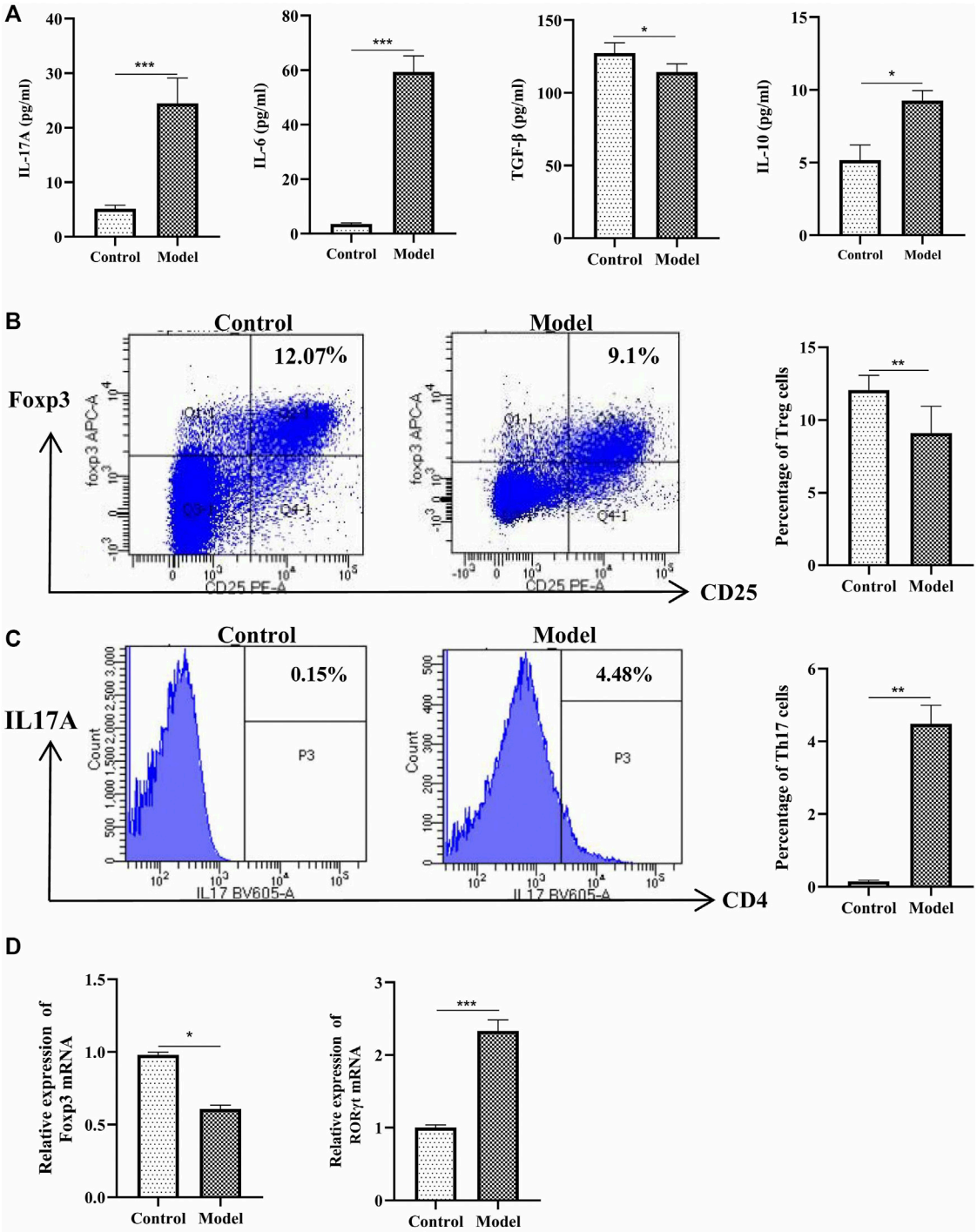

FIGURE 3 | Detection of Treg and Th17 cells. **(A)** Detection of IL-17A, IL-6, TGF-β and IL-10 in BALF, BALF was collected 24 h after last challenge, they were detected as described in the protocol; **(B)**Left:Intracellular staining of CD25 and Foxp3 in the door $CD4^+$ T cells 24 h after challenge; Right:Statistic data of Treg cells 24 h after challenge; **(C)** Left: Intracellular staining of IL17A and CD4 in the door $CD3^+$ T cells 24 h after challenge; Right: Statistic data of Th17 cells 24 h after challenge; **(D)** Relative expression of Foxp3 mRNA and RORγt mRNA detected by RT-qPCR. $^*p < 0.05$, $^{**}p < 0.01$, $^{***}p \leq 0.001$. All the values are expressed as mean±SEM. n = 4,5 animals per group.

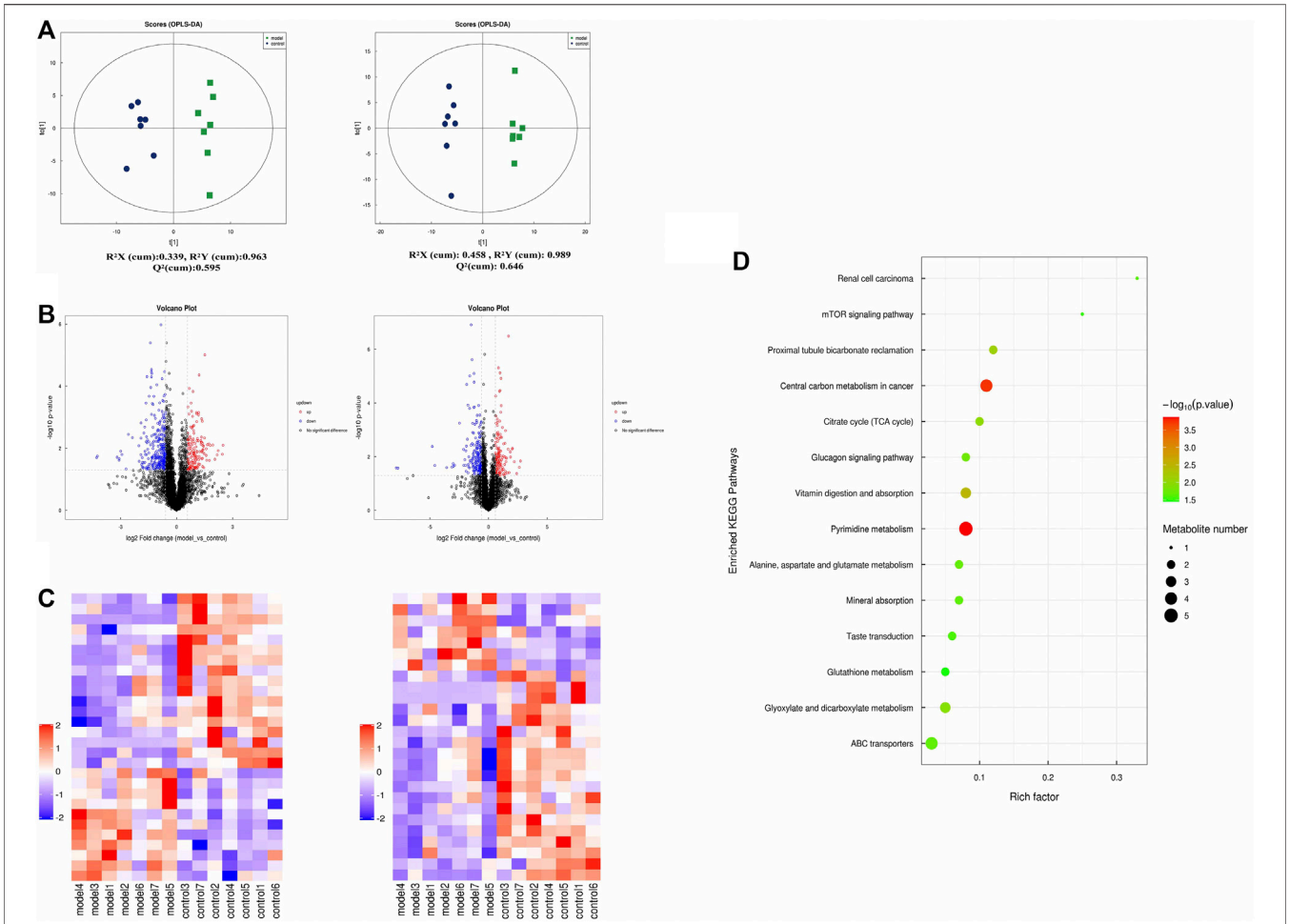

FIGURE 4 | Untargeted plasma metabolome detection. **(A)** The OPLS-DA scatter plot under positive and negative ion modes; **(B)** Volcano map of different metabolites in positive and negative ion mode. (The up-regulated differential metabolites were red, FC > 1.5, *p* value <0.05; The down-regulated differential metabolites were blue, FC < 0.67, *p* value <0.05.) **(C)** The clustering results of hierarchical cluster analysis based on the significantly different metabolites between groups under positive and negative modes. **(D)** Enriched KEGG pathways based on significant different metabolites between control group (*n* = 7) and model group (*n* = 7).

13 in BALF significantly increased in eosinophilic asthma mice compared to the mice in the control group (**Figure 1E**). Meanwhile, OVA-specific IgE in the serum of model group also increased (**Figure 1E**). These data suggested that the eosinophilic asthma mice model was successfully established.

The Imbalance of Th1/2, Treg/Th17 Cells Exist in the Eosinophilic Asthma Mice Model

The IFN-γ cytokine, the IFN-γ mRNA are downregulated, the cytokine of IL-4 and the IL-4 mRNA are upregulated (**Figure 2A**). Meawhile, the percentage of Th1 cells ($CD3^+CD4$+IFN-γ+) are decreased, while the percentage of Th2 cells ($CD3^+CD4^+$ IL-4+) are increased (**Figure 2B**). These data suggested an imbalance of Th1/Th2 is exist in this eosinophilic asthma mice model.

Next, we analyzed the percentage of Treg and Th17 cells in the OVA-induced eosinophilic asthma mice model. In our study, Treg cells were decreased significantly, while Th17 cells were increased significantly (**Figures 3B,C**). Moreover, associated cytokines of Treg cells (TGF-β, IL-10) were significantly decreased (**Figure 3A**), and the Th17 cells associated with cytokines IL17 and IL-6 in BALF were increased (**Figure 3A**). Consistently, at the mRNA level, the Treg-related transcription factor Foxp3 was downregulated, and Th17-related transcription factor RORγt was upregulated (**Figure 3D**). These data suggested an imbalance of Treg/Th17 in this eosinophilic asthma mice model.

Different Metabolites Plasma in Eosinophilic Asthma Mice Model

To further understand the related factor of eosinophilic asthma, an untargeted metabolomics assay was performed. OPLS-DA analysis, a supervised method for pattern recognition, was performed on the data comparing the control and the model groups. As shown in **Figure 4**, groups in positive and negative nodes were separated in the OPLS-DA score plots (**Figure 4A**)

TABLE 1 | Differentiated plasma metabolites between model and control groups.

Metabolites	ESI	VIP	Fold Change	*p* Value
Beta-octylglucoside	+	1.131464	0.378592156	4.03E-06
Pro-hyp	+	1.559487	0.481080359	9.01E-05
1-behenoyl-2-hydroxy-sn-glycero-3-phosphocholine	+	1.20523	0.706403289	0.000112
Imidazoleacetic acid	+	1.199073	1.264756258	0.000172
1-Palmitoyllysophosphatidylcholine	+	1.64467	0.790425533	0.001203
1-lignoceroyl-2-hydroxy-sn-glycero-3-phosphocholine	+	1.478166	0.700320405	0.002041
2-deoxy-d-glucose	+	3.343785	0.852229227	0.002636
Taurohyocholic acid	+	1.420785	1.881183802	0.002657
Fraxetin	+	1.046128	0.602647196	0.003539
DL-glutamine	+	2.706991	1.236530723	0.003757
L-pyroglutamic acid	+	4.784439	1.30721999	0.00428
Captopril	+	1.09852	1.60715764	0.010905
1-heptadecanoyl-sn-glycero-3-phosphocholine	+	1.245238	0.867062765	0.011883
2-methylbutyryl-l-carnitine	+	1.097752	0.695498651	0.015584
N.omega.-hydroxy-nor-l-arginine	+	3.761146	0.58632938	0.019692
Arachidonoylthiophosphorylcholine	+	3.194667	0.73748276	0.021846
Didodecyl 3,3′-thiodipropionate oxide	+	7.401258	0.118898778	0.024455
(+)-.alpha.-tocopherol	+	2.632343	1.31377735	0.027809
1,2-dipalmitoleoyl-sn-glycero-3-phosphocholine	+	1.021394	0.71138672	0.028041
1-hexadecyl-2-(9z-octadecenoyl)-sn-glycero-3-phosphocholine	+	2.118359	1.419830373	0.029925
Didodecyl 3,3′-thiodipropionate	+	9.705313	1.177332401	0.036962
DL-Indole-3-lactic acid	+	2.483305	0.510177656	0.037305
L-Norleucine	+	1.200297	2.192440841	0.04081
N-alpha-acetyl-l-lysine	+	1.143018	2.02499295	0.042362
Erucamide	+	4.504219	0.468475768	0.042909
Androstan-3-ol-17-one 3-glucuronide	+	1.229974	0.428586777	0.043986
3-hydroxyanthranilic acid	+	1.176436	1.56196739	0.04645
Flumethasone pivalate	+	1.466925	0.446652483	0.048715
Pyridoxal	–	1.041898	0.653730059	0.000499
Myo-inositol	–	1.132384	0.718497076	0.000858
1,5-anhydro-d-sorbitol	–	1.551254	0.667099073	0.00154
Taurocholate	–	5.049303	3.614488366	0.006614
Ethylenediaminetetraacetic acid	–	30.02436	0.671296218	0.006731
Leucine	–	3.909682	1.655640658	0.009614
Malate	–	3.36886	0.466826514	0.010515
L-Ascorbic acid	–	1.220481	0.548166624	0.010813
Pseudouridine	–	2.2885	1.283592485	0.013045
Citrate	–	5.707591	0.796622739	0.013066
Propanoic acid, 3-[[[2-[(aminoiminomethyl)amino]-4-thiazolyl]methyl]thio]-	–	1.979877	0.840032629	0.013144
Dihydroxyacetone	–	2.309582	0.796052851	0.013892
Indole-3-carboxaldehyde	–	1.869297	0.55207048	0.015098
Dihydroisoferulic acid	–	1.017208	0.745015711	0.018041
L-dihydroorotate	–	2.074576	0.78453178	0.021762
2,6-di-tert-butylphenol	–	7.03295	0.126136357	0.022794
Acetylglycine	–	1.816961	0.838562471	0.023526
Valerenic acid	–	4.909679	0.114797002	0.024352
Dodecanoic acid	–	2.350182	0.630639683	0.025552
Uridine	–	1.279404	1.392006018	0.028122
(r)-2-hydroxystearic acid	–	1.521972	1.599680456	0.030486
Glutamine	–	2.540492	1.199525586	0.034038
5a,6-anhydrotetracycline	–	1.489606	0.837611418	0.037084
Oleic acid	–	20.06777	1.317683351	0.037228
His-ser	–	2.790828	0.745949054	0.041775
N-acetyl-d-glucosamine 6-phosphate	–	1.008122	0.567914407	0.047293

with satisfactory goodness of fit. Overall, 55 different metabolites were detected; 18 metabolites were upregulated, and 37 metabolites were downregulated (**Figure 4B**; **Table 1**). The results of hierarchical cluster analysis are shown in **Figure 4C**; metabolites clustered in the same cluster have similar expression patterns, may have similar functions, or participate in the same metabolic process or cellular pathway.

In addition, metabolites were grouped through pathway analysis based on the KEGG database. Interestingly, 14 different KEGG pathways showed statistical significance (**Figure 4D**). Interestingly pyrimidine metabolism, vitamin digestion, and absorption, glyoxylate, and dicarboxylate metabolism pathway etc., were obviously upregulated in eosinophilic asthma mice.

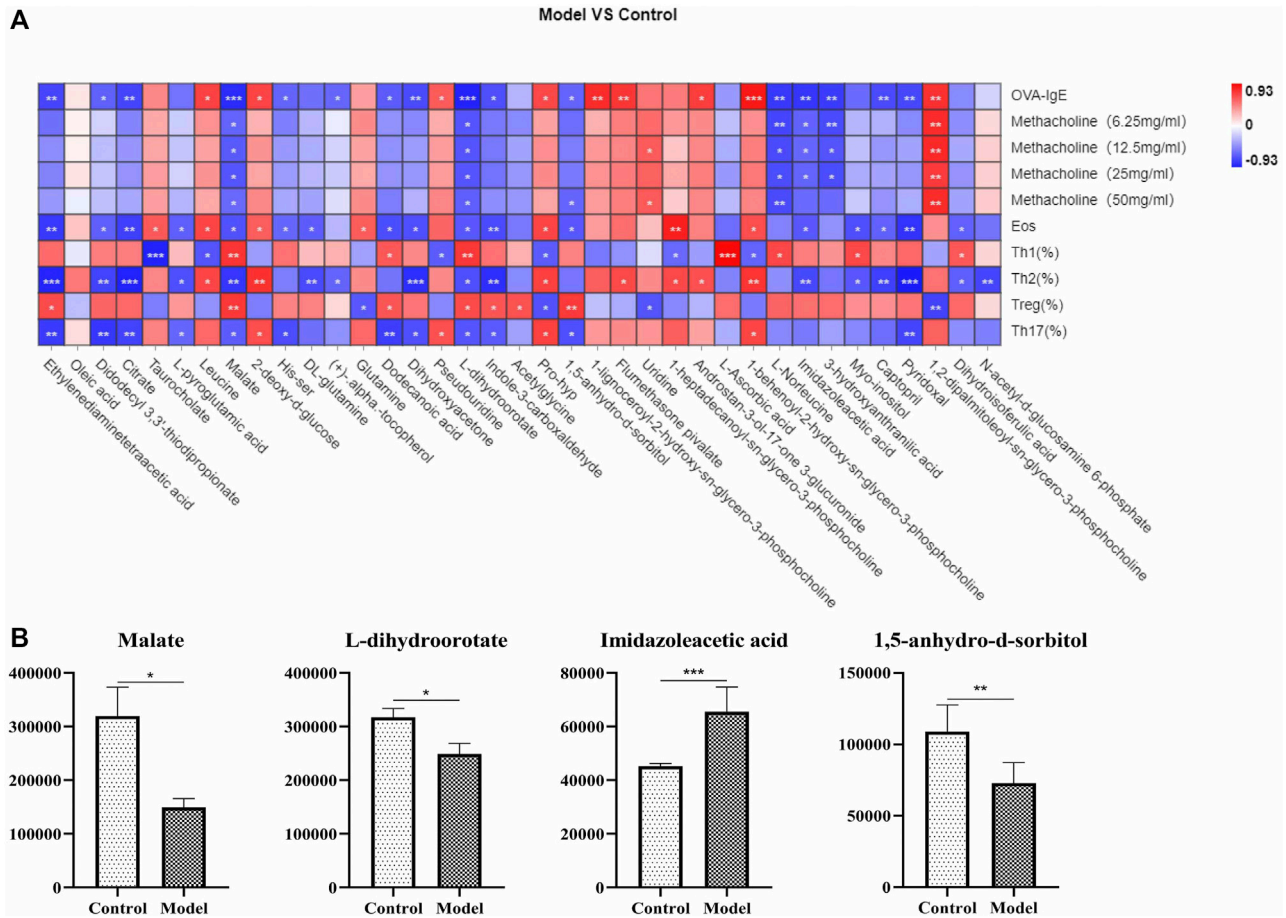

FIGURE 5 | Correlation analysis of metabolic biomarkers and Th1, Th2, Treg, Th17 cells in OVA induced eosinophilic asthma model. **(A)** Correlation plot showing the relationship between the differential metabolites in plasma and the key immune indicators of eosinophillic asthma including OVA-IgE, Penh value and eosinophil number in BALF. **(B)** Biomarkers of metabolic biomarkers in eosinophilic asthma associated with Th1, Th2, Treg and Th17 cells, followed by Malate, L-dihydroorotate, Imidazoleacetic acid and 1,5-anhydro-d-sorbitol. $^{*}p < 0.05$, $^{**}p < 0.01$, $^{***}p \leq 0.001$. All the values are expressed as mean±SEM. $n = 7$ animals per group.

Metabolites Biomarkers in Plasma Associated With Th1, Th2, Treg and Th17 Cells in Eosinophilic Asthma Mice Model

To further understand the metabolites associated with eosinophilic asthma, spearman analysis was performed using R software. To explore plasma biomarkers associated with Th1/2, Treg/Th17 balance, differential metabolites associated with Treg cells, Th17 cells, OVA-IgE, Penh value, and eosinophil number were analyzed (**Figure 5A**). In this study, malate, L-dihydroorotate were associated with Th1, Th2, Treg cells, Th17 cells, OVA-IgE, Penh value (Mch: 6.25, 12.5, 25, 50 mg/ml) and eosinophil number (Eos). Interestingly, imidazoleacetic acid in plasma of eosinophilic asthma mice model was upregulated and associated with Th2 cells in with OVA-IgE, Penh value (Mch:6.25, 12.5, 25 mg/ml) and eosinophil number (Eos) on a relevant basis. While 1,5-anhydro-d-sorbitol were downregulated and associated with Treg and Th17 cells based on related with OVA-IgE, Penh value (Mch: 50 mg/ml) and eosinophil number (Eos) (**Figure 5B**).

Variation of Gut Microbiota and the Biomarkers of Gut Microbiota in Response to OVA-Induced Eosinophilic Asthma Modeling

The pathogenesis of asthma is complex. To analyze this process, we profiled the overall variation of gut microbiota to determine whether OVA-induced eosinophilic asthma mice modeling may impact the microbial populations. As shown in **Figure 6** A and **Figure 6** B, the structure of the gut microbiota was changed. To explore potential biomarkers of eosinophilic asthma, microbial phylotypes in response to OVA-induced eosinophilic asthma mice modeling were identified with LEfSe. Specifically differentiated phylotypes between model and control group were identified: *g_Ruminiclostridium 6*, *c_Melainabacteria*, *o_Gastranaerophilales*, *g_Eubacterium_coprostannoligenes_group* in the control group; genus *Helicobacter*, family Helicobacteraceae, class order *Campylobacterales*, phylum *Epsilonbacteraeota*, genus *Parasutterella* were important microbiota in the eosinophilic asthma model group (**Figure 6C**).

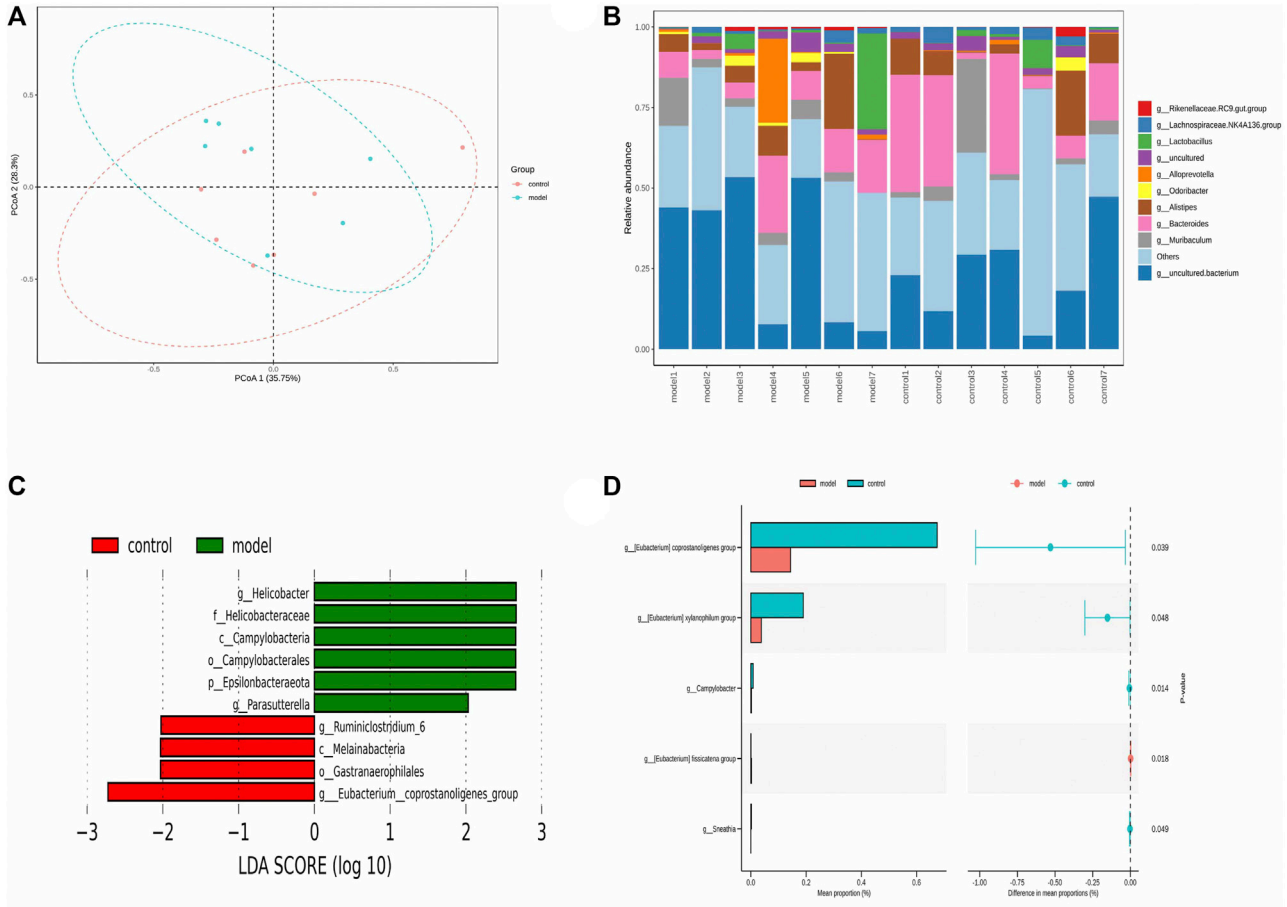

FIGURE 6 | Gut microbiota biomarker in OVA induced eosinophilic asthma BALB/c mice model. **(A)** Principal Co-ordinates Analysis (PCoA) of control group ($n = 7$) and model group ($n = 7$). **(B)** Community structure composition map of gut microbiota. **(C)** LEfSe (LDA Effect Size) analysis of different species in control group and model group (LDA > 2). **(D)** STAMP analysis of different gut microbiota ($p < 0.05$). $n = 7$ animals per group.

To further investigate the gut microbiota biomarkers, the STAMP difference analysis method was used to analyze the abundance of species in two groups. Different abundance was found in the Genus *Coprostanoligenes*, genus *Xylanophilum*, genus *Geodermatophilus*, genus *Campulobacter*, genus *fissicatena* group, and genus *Sneathia* ($p < 0.05$) (**Figure 6D**).

Variation of Gut Microbiota and Key Phylotypes of Gut Microbiota, Differential Plasma Metabolites Associated With Th1/2 and Treg/Th17

The pathogenesis of asthma is complex. To analyze this process, we profiled the overall variation of gut microbiota and plasma metabolites to determine whether OVA-induced eosinophilic asthma mice modeling may impact the immune balance of Th1/Th2 and Treg/Th17. Pearson associated analysis was used to further investigate the relationship between gut microbiota and eosinophilic asthma, gut microbiota and differential plasma metabolites. As shown in **Figure 7** A, genus *Ruminiclostridium 6* and genus *Candidatus Arthromitus* were associated with OVA-IgE, Eos, Th2 cells, Treg cells and Th17 cells. Interestingly, genus *Candidatus Arthromitus* is associated with OVA-IgE, Th2 cells and Th17 cells (**Figure 7A**). However, the differential gut microbiota biomarker are all irrelevant with penh value which was applied to calculate the AHR.

Interestingly, the plasma metabolite biomarkers of malate, L-dihydroorotate are associated with genus *Ruminiclostridium 6*, they were all associated with Th1/2 and Treg/Th17 cell balance, while imidazoleacetic acid is associated with genus *Ruminiclostridium 6* which is associated with Th1/2 balance. Among the differential plasma metabolites, 1,5-anhydro-d-sorbitol is associated with genus *Ruminiclostridium 6* and genus *Candidatus Arthromitus.*

DISCUSSION

Treg cells play an essential role in allergic asthma by suppressing T helper effector cells such as Th1, Th2, and Th17 cells; which can inhibit inflammatory cell infiltration in lung tissues and induce IgE switching to IgG4 (Palomares et al., 2010; Rauber et al., 2019).

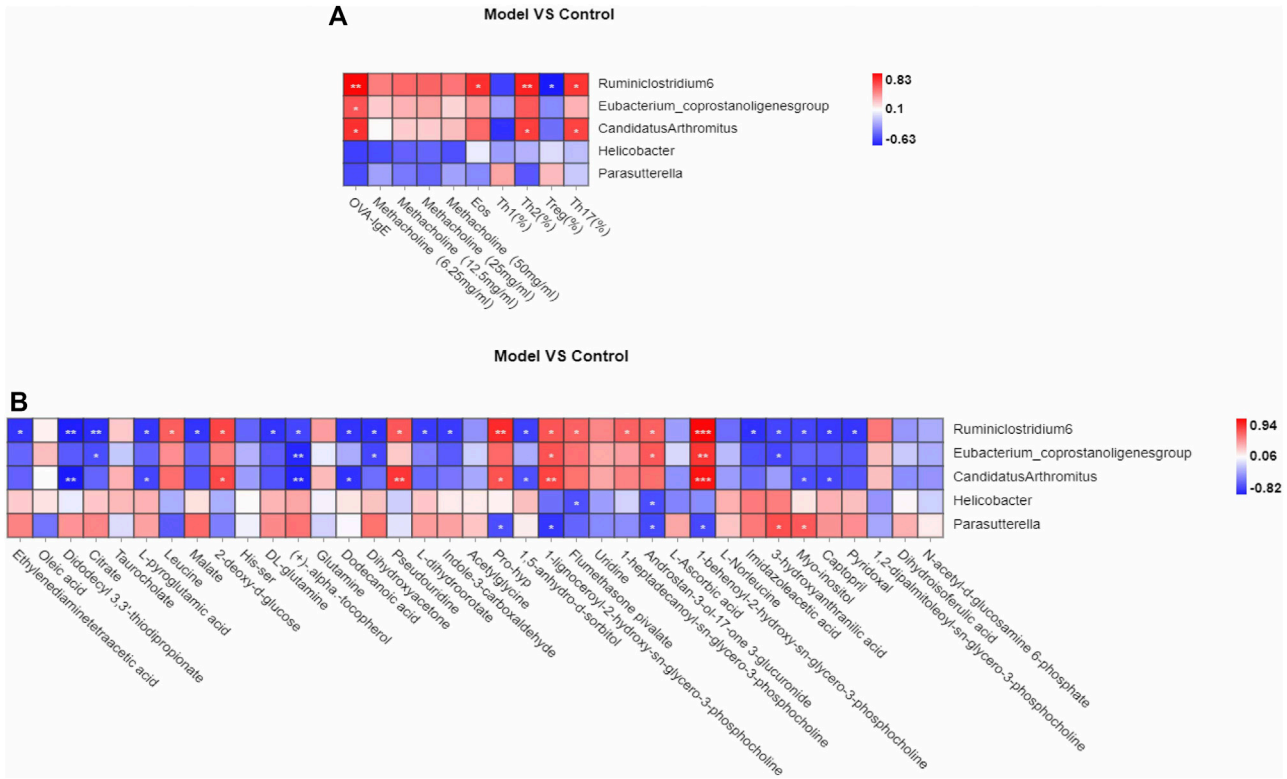

FIGURE 7 | Correlation analysis of Th1, Th2, Treg, Th17 cells, differential metabolites biomarker respectively with gut microbiota biomarkers in OVA induced eosinophilic asthma model. **(A)** Correlation analysis between gut microbiota biomarker and the key immune indicators of eosinophilic asthma including OVA-IgE, Penh value and eosinophil number in BALF, Th1, Th2, Treg and Th17 cells **(B)** Biomarkers of metabolic biomarkers associated with gut microbiota biomarkers in eosinophilic asthma mice model. *$p < 0.05$, **$p < 0.01$, ***$p \leq 0.001$. $n = 7$ animals per group.

Our study highlights the immune balance of Th1/2 and Treg/Th17 cells in eosinophilic asthma mice model.

In our study, we successfully constructed a eosinophilic asthma mice model predominantly infiltrated by eosinophils. The ovalbumin (OVA) sensitization model can mimic the prominent eosinophilic response of severe asthma in humans (Holgate and Polosa, 2006). The spleen is the largest secondary lymphoid organ in the body and T cells in the spleen organ are the key effectors of the adaptive immune system (Lewis et al., 2019). Therefore, we detected the Treg and Th17 cells in the spleen tissue to evaluate the immune balance of Treg/Th17 cells in the eosinophilic asthma mice model. Treg cells were decreased while Th17 cells were increased all obviously in the eosinophilic mice model group. To further confirm the imbalance of Treg/Th17, we also detected TGF-β, IL10, IL17A and IL-6 cytokines in BALF. TGF-β plays an important role in the maintenance and induction of Treg cells, while IL-10 is produced mainly by many immune cells such as monocytes, Treg, Breg cells, natural killer (NK) cells, macrophages, dendritic cells (DCs), and innate lymphoid cells (ILCs). We found that TGF-β and IL-10 were significantly decreased in the model group, which is consistent with other studies (Tagkareli et al., 2021). In clinical, IL-17A mRNA and IL-17A protein are all increased in asthmatic patients compared with healthy subjects. In this study, IL17A and IL-6 were upregulated in the eosinophilic asthma model group, which is consistent with the clinical results (Laan et al., 2002). Moreover, Foxp3 and RORγt as the transcription factor of Treg cells and Th17 cells were all detected. The Foxp3 mRNA expression was downregulated, while the RORγt mRNA expression was upregulated. The imbalance of Treg/Th17 cells existed in the eosinophilic asthma mice model, the imbalance of Th1/2 is also exist in the mice model of our study.

To explore new biomarkers of the eosinophilic asthma mice model, we used untargeted plasma metabolomics and 16S rDNA sequencing technology to examine the differential metabolites and microbiota between the eosinophilic asthma mice model and control group. A previous study found that 12/15-Lipoxygenase can regulate IL-33-induced eosinophilic asthma in mice (Miyata et al., 2021). In our study, 15 significant metabolism pathways associated with eosinophilic asthma were identified. Among them, 4 metabolites such as malate, L-dihydroorotate, imidazoleacetic acid and 1,5-anhydro-d-sorbitol were all associated with Treg/Th17 cell balance in eosinophilic asthma, while malate, L-dihydroorotate, imidazoleacetic acid were associated with Th1/2 cell balance in eosinophilic asthma. Malate is participate in the tricarboxylic acid (TCA), which is important in the synthesis of aspartate to maintain proliferation of the Th cells. It can combine with aspartate to regulate the

expression of genes associated with T cell activation (Bailis et al., 2019). While, there are no reports about the specific role of malate in allergic asthma disease, it may participate in the T cells differentiation of Th cells which is the essential immune mechanism of allergic asthma disease. Our data reported for the first time that malate, L-dihydroorotate, imidazoleacetic acid and 1,5-anhydro-d-sorbitol can act as biomarkers in eosinophilic asthma disease.

The "hygiene hypothesis" is the first that proposed a link between microbes and allergy disease (Stiemsma and Turvey, 2017). So far, more and more evidence has shown that there is an association between bacterial components and asthma. Studies have shown that the imbalance of "gut-lung axis" exist in asthma. Gut microbiota is linked to allergic asthma through regulating the immune response (Penders et al., 2007). In this study, genus *Ruminiclostridium 6*, genus *Candidatus Arthromitus* were associated with the immune balance of Th1/2 and Treg/Th17 in eosinophilic asthma, while genus *Candidatus Arthromitus* (also designated as Candidatus Savagella) is a type of segmented filamentous bacteria (SFB) can influence the immune response of the intestinal tract to resistance against some infectious diseases and it also can induce antigen-specific Th17 cells (Hedblom et al., 2018). To our surprise, genus *Ruminiclostridium 6*, genus *Candidatus Arthromitus* were all irrelevant with penh value which is the indicator of reactive airway hyperresponsiveness.

Interestingly, malate, L-dihydroorotate, imidazoleacetic acid and 1,5-anhydro-d-sorbitol are all associated with genus *Ruminiclostridium 6*. While 1,5-anhydro-d-sorbitol is associated with genus *Ruminiclostridium 6* and genus *Candidatus Arthromitus*. Until now, there are no related reports about them yet, while it will be a new research new research directions and new discoveries, we should combine experiments such as clinical trials and microbiota transplantation to verify our results because the gut microbiota of animals and humans is different. Besides that, more experiments are needed to confirm that these can act as biomarkers in eosinophilic asthma, they can be used as a new strategy for studying the mechanism and treatment foundation of eosinophilic asthma.

DATA AVAILABILITY STATEMENT

The original contributions presented in the study are publicly available. This data can be found here: NCBI, PRJNA825171.

ETHICS STATEMENT

The animal study was reviewed and approved by Beijing University of Chinese Medicine.

AUTHOR CONTRIBUTIONS

YZ, JW, XZ and QW conceived and designed the experiments; YZ, TW performed the experiments; JW and QW contributed reagents/materials/analysis tools; YZ analyzed the data and wrote the paper. All authors have read and agreed to the published version of the manuscript.

FUNDING

This work was supported by the General program of National Natural Science Foundation of China (No.81973715, 82174243), the General project of Beijing Natural Science Foundation (No.7202110) and the Innovation Team and Talents Cultivation Program of National Administration of Traditional Chinese Medicine (No: ZYYCXTD-C-202001).

REFERENCES

Bailis, W., Shyer, J. A., Zhao, J., Canaveras, J. C. G., Al Khazal, F. J., Qu, R., et al. (2019). Distinct Modes of Mitochondrial Metabolism Uncouple T Cell Differentiation and Function. *Nature* 571 (7765), 403–407. doi:10.1038/s41586-019-1311-3

Chatila, T. A., Blaeser, F., Ho, N., Lederman, H. M., Voulgaropoulos, C., Helms, C., et al. (2000). JM2, Encoding a fork Head-Related Protein, Is Mutated in X-Linked Autoimmunity-Allergic Disregulation Syndrome. *J. Clin. Invest.* 106, R75–R81. doi:10.1172/jci11679

Gri, G., Piconese, S., Frossi, B., Manfroi, V., Merluzzi, S., Tripodo, C., et al. (2008). CD4+CD25+ Regulatory T Cells Suppress Mast Cell Degranulation and Allergic Responses through OX40-Ox40l Interaction. *Immunity* 29, 771–781. doi:10.1016/j.immuni.2008.08.018

Hedblom, G. A., Reiland, H. A., Sylte, M. J., Johnson, T. J., and Baumler, D. J. (2018). Segmented Filamentous Bacteria - Metabolism Meets Immunity. *Front. Microbiol.* 9, 1991. doi:10.3389/fmicb.2018.01991

Holgate, S. T., and Polosa, R. (2006). The Mechanisms, Diagnosis, and Management of Severe Asthma in Adults. *Lancet* 368, 780–793. doi:10.1016/S0140-6736(06)69288-X

Jones, S. M., Burks, A. W., and Dupont, C. (2014). State of the Art on Food Allergen Immunotherapy: Oral, Sublingual, and Epicutaneous. *J. Allergy Clin. Immunol.* 133, 318–323. doi:10.1016/j.jaci.2013.12.1040

Laan, M., Palmberg, L., Larsson, K., and Lindén, A. (2002). Free, Soluble Interleukin-17 Protein during Severe Inflammation in Human Airways. *Eur. Respir. J.* 19, 534–537. doi:10.1183/09031936.02.00280902

Lambrecht, B. N., Hammad, H., and Fahy, J. V. (2019). The Cytokines of Asthma. *Immunity* 50, 975–991. doi:10.1016/j.immuni.2019.03.018

Lambrecht, B. N., and Hammad, H. (2015). The Immunology of Asthma. *Nat. Immunol.* 16, 45–56. doi:10.1038/ni.3049

Lewis, S. M., Williams, A., and Eisenbarth, S. C. (2019). Structure and Function of the Immune System in the Spleen. *Sci. Immunol.* 4, eaau6085. doi:10.1126/sciimmunol.aau6085

Ma, M., Li, G., Qi, M., Jiang, W., and Zhou, R. (2021). Inhibition of the Inflammasome Activity of NLRP3 Attenuates HDM-Induced Allergic Asthma. *Front. Immunol.* 12, 718779. doi:10.3389/fimmu.2021.718779

Matsumura, Y., Byrne, S. N., Nghiem, D. X., Miyahara, Y., and Ullrich, S. E. (2006). A Role for Inflammatory Mediators in the Induction of Immunoregulatory B Cells. *J. Immunol.* 177, 4810–4817. doi:10.4049/jimmunol.177.7.4810

Meiler, F., Klunker, S., Zimmermann, M., Akdis, C. A., and Akdis, M. (2008a). Distinct Regulation of IgE, IgG4 and IgA by T Regulatory Cells and Toll-like Receptors. *Allergy* 63, 1455–1463. doi:10.1111/j.1398-9995.2008.01774.x

Meiler, F., Zumkehr, J., Klunker, S., Rückert, B., Akdis, C. A., and Akdis, M. (2008b). *In Vivo* switch to IL-10-secreting T Regulatory Cells in High Dose Allergen Exposure. *J. Exp. Med.* 205, 2887–2898. doi:10.1084/jem.20080193

Miyata, J., Yokokura, Y., Moro, K., Arai, H., Fukunaga, K., and Arita, M. (2021). 12/15-Lipoxygenase Regulates IL-33-Induced Eosinophilic Airway Inflammation in Mice. *Front. Immunol.* 12, 687192. doi:10.3389/fimmu.2021.687192

Nonaka, M., Pawankar, R., Fukumoto, A., and Yagi, T. (2008). Heterogeneous Response of Nasal and Lung Fibroblasts to Transforming Growth Factor-Beta 1. *Clin. Exp. Allergy* 38, 812–821. doi:10.1111/j.1365-2222.2008.02959.x

Padrid, P., Snook, S., Finucane, T., Shiue, P., Cozzi, P., Solway, J., et al. (1995). Persistent Airway Hyperresponsiveness and Histologic Alterations after Chronic Antigen challenge in Cats. *Am. J. Respir. Crit. Care Med.* 151, 184–193. doi:10.1164/ajrccm.151.1.7812551

Palomares, O., Akdis, M., Martín-Fontecha, M., and Akdis, C. A. (2017). Mechanisms of Immune Regulation in Allergic Diseases: the Role of Regulatory T and B Cells. *Immunol. Rev.* 278, 219–236. doi:10.1111/imr.12555

Palomares, O., Martín-Fontecha, M., Lauener, R., Traidl-Hoffmann, C., Cavkaytar, O., Akdis, M., et al. (2014). Regulatory T Cells and Immune Regulation of Allergic Diseases: Roles of IL-10 and TGF-β. *Genes Immun.* 15, 511–520. doi:10.1038/gene.2014.45

Palomares, O., Yaman, G., Azkur, A. K., Akkoc, T., Akdis, M., and Akdis, C. A. (2010). Role of Treg in Immune Regulation of Allergic Diseases. *Eur. J. Immunol.* 40, 1232–1240. doi:10.1002/eji.200940045

Pavord, I., Bahmer, T., Braido, F., Cosío, B. G., Humbert, M., Idzko, M., et al. (2019). Severe T2-High Asthma in the Biologics Era: European Experts' Opinion. *Eur. Respir. Rev.* 28, 190054. doi:10.1183/16000617.0054-2019

Penders, J., Stobberingh, E. E., van den Brandt, P. A., and Thijs, C. (2007). The Role of the Intestinal Microbiota in the Development of Atopic Disorders. *Allergy* 62, 1223–1236. doi:10.1111/j.1398-9995.2007.01462.x

Rauber, M. M., Wu, H. K., Adams, B., Pickert, J., Bohle, B., Shamji, M. H., et al. (2019). Birch Pollen Allergen-specific Immunotherapy with Glutaraldehyde-Modified Allergoid Induces IL-10 Secretion and Protective Antibody Responses. *Allergy* 74, 1575–1579. doi:10.1111/all.13774

Ring, S., Schäfer, S. C., Mahnke, K., Lehr, H. A., and Enk, A. H. (2006). CD4+ CD25+ Regulatory T Cells Suppress Contact Hypersensitivity Reactions by Blocking Influx of Effector T Cells into Inflamed Tissue. *Eur. J. Immunol.* 36, 2981–2992. doi:10.1002/eji.200636207

Sakaguchi, S., Wing, K., and Yamaguchi, T. (2009). Dynamics of Peripheral Tolerance and Immune Regulation Mediated by Treg. *Eur. J. Immunol.* 39, 2331–2336. doi:10.1002/eji.200939688

Stiemsma, L. T., and Turvey, S. E. (2017). Asthma and the Microbiome: Defining the Critical Window in Early Life. *Allergy Asthma Clin. Immunol.* 13, 3. doi:10.1186/s13223-016-0173-6

Sun, L., Fan, M., Huang, D., Li, B., Xu, R., Gao, F., et al. (2021). Clodronate-loaded Liposomal and Fibroblast-Derived Exosomal Hybrid System for Enhanced Drug Delivery to Pulmonary Fibrosis. *Biomaterials* 271, 120761. doi:10.1016/j.biomaterials.2021.120761

Swietlik, E. M., Ghataorhe, P., Zalewska, K. I., Wharton, J., Howard, L. S., Taboada, D., et al. (2021). Plasma Metabolomics Exhibit Response to Therapy in Chronic Thromboembolic Pulmonary Hypertension. *Eur. Respir. J.* 57, 2003201. doi:10.1183/13993003.03201-2020

Tagkareli, S., Salagianni, M., Galani, I. E., Manioudaki, M., Pavlos, E., Thanopoulou, K., et al. (2021). CD103 Integrin Identifies a High IL-10-producing FoxP3(+) Regulatory T-Cell Population Suppressing Allergic Airway Inflammation. *Allergy* 77, 1150–1164. doi:10.1111/all.15144

Torgerson, T. R., Linane, A., Moes, N., Anover, S., Mateo, V., Rieux-Laucat, F., et al. (2007). Severe Food Allergy as a Variant of IPEX Syndrome Caused by a Deletion in a Noncoding Region of the FOXP3 Gene. *Gastroenterology* 132, 1705–1717. doi:10.1053/j.gastro.2007.02.044

Trautmann, A., Schmid-Grendelmeier, P., Krüger, K., Crameri, R., Akdis, M., Akkaya, A., et al. (2002). T Cells and Eosinophils Cooperate in the Induction of Bronchial Epithelial Cell Apoptosis in Asthma. *J. Allergy Clin. Immunol.* 109, 329–337. doi:10.1067/mai.2002.121460

Verbsky, J. W., and Chatila, T. A. (2013). Immune Dysregulation, Polyendocrinopathy, Enteropathy, X-Linked (IPEX) and IPEX-Related Disorders: an Evolving Web of Heritable Autoimmune Diseases. *Curr. Opin. Pediatr.* 25, 708–714. doi:10.1097/MOP.0000000000000029

Woodruff, P. G., Modrek, B., Choy, D. F., Jia, G., Abbas, A. R., Ellwanger, A., et al. (2009). T-helper Type 2-driven Inflammation Defines Major Subphenotypes of Asthma. *Am. J. Respir. Crit. Care Med.* 180, 388–395. doi:10.1164/rccm.200903-0392OC

Zhang, X., Xu, Z., Wen, X., Huang, G., Nian, S., Li, L., et al. (2022). The Onset, Development and Pathogenesis of Severe Neutrophilic Asthma. *Immunol. Cel Biol* 100 (3), 144–159. doi:10.1111/imcb.12522

Zhao, J., Lloyd, C. M., and Noble, A. (2013). Th17 Responses in Chronic Allergic Airway Inflammation Abrogate Regulatory T-Cell-Mediated Tolerance and Contribute to Airway Remodeling. *Mucosal Immunol.* 6, 335–346. doi:10.1038/mi.2012.76

Zhou, Y., Zhao, H., Wang, T., Zhao, X., Wang, J., and Wang, Q. (2022). Anti-Inflammatory and Anti-asthmatic Effects of TMDCT Decoction in Eosinophilic Asthma through Treg/Th17 Balance. *Front. Pharmacol.* 13, 819728. doi:10.3389/fphar.2022.819728

Conflict of Interest: The authors declare that the research was conducted in the absence of any commercial or financial relationships that could be construed as a potential conflict of interest.

Publisher's Note: All claims expressed in this article are solely those of the authors and do not necessarily represent those of their affiliated organizations, or those of the publisher, the editors and the reviewers. Any product that may be evaluated in this article, or claim that may be made by its manufacturer, is not guaranteed or endorsed by the publisher.

frontiers | Frontiers in Pharmacology

OPINION
published: 19 May 2022
doi: 10.3389/fphar.2022.898152

The Role of Growth Factors in the Repair of Motor Injury

*Qiaoyin Tan[1], Jiayu Li[2], Yanmin Yin[2] and Weide Shao[2]**

[1]College of Teacher Education, Zhejiang Normal University, Jinhua, China, [2]College of Physical Education and Health Sciences, Zhejiang Normal University, Jinhua, China

Keywords: growth factors, motor injury, repair of motor injury, post-injury rehabilitation, platelet-rich plasma

INTRODUCTION

Growth factors are a group of bioactive peptides secreted by the body. Growth factors stimulate cell growth and exert other biological effects by binding to specific, highly affinity cell membrane receptors. There are various growth factors, such as platelet-like growth factors (platelet-derived growth factor, PDGF, Osteosarcoma-derived growth factor ODGF), epidermal growth factors (epidermal growth factor, EGF, transforming growth factor, TGFα, and TGFβ), fibroblast growth factors (αFGF, βFGF), insulin-like growth factors (IGF-I, IGF-II), nerve growth factor (NGF), interleukin-like growth factor (IL-1, IL-3, etc.), erythropoietin (EPO), colony stimulating factor (CSF), etc. Growth factors play irreplaceable roles in individual growth, development and aging, including accelerating metabolism, inhibiting inflammatory response, and repairing damaged tissues and organs.

The human motor system is mainly composed of nerves, muscles, bones, joints, and other organs and tissues, which is the basis of maintaining normal motor function. With the development of the society and the accumulation of life and work pressure, chronic diseases such as diabetes, cardiovascular and cerebrovascular diseases, and cancer are like a layer of haze hanging over the top of the head of the public. Proper exercise, as a brilliant "prescription", plays an incomparable role in the treatment of chronic diseases in traditional Chinese medicine. The health of various sports tissues and organs is the prerequisite for the implementation of this prescription (Cacciata et al., 2019; Kirsch Micheletti et al., 2019). As an athlete, healthy sports function is an important guarantee for basic training and competition. Injuries in sports are common to both athletes and the public. For some severe athletic injuries, surgical treatment is considered the most effective way to restore motor function. However, the surgical trauma, long postoperative recovery time and functional limitation caused by scar tissue proliferation are all defects brought by surgery. In recent years, growth factors have been applied by scientists as a special treatment after exercise injury. The therapeutic effects and potentials demonstrated from *in vivo* animal tests to the current clinical applications are exciting. As a treatment with small trauma, mild side effects and easy operation, it has gradually replaced the traditional treatment in the treatment of part of the motor injury. Growth factors work admirably as a new treatment. At the same time, the difficulties and challenges in the future development of growth factors as a treatment for motor injury deserve attention.

FUNCTION

Muscle Injury

It is generally believed that the maintenance of skeletal muscle quality throughout life is the key to athletic health. Under normal physiological conditions, insulin-like growth factor -1 (IGF-1) can work together with androgens and mechanical muscle sensitivity to increase muscle mass (Gharahdaghi et al., 2020). During exercise, the relatively shallow positions of many muscles in

OPEN ACCESS

Edited by:
Songwen Tan,
Central South University, China

Reviewed by:
Hongwen Wu,
Liuzhou Workers Hospital, China
Huali Chen,
Hunan Provincial People's Hospital, China

****Correspondence:***
Weide Shao
txsh@zjnu.cn

Specialty section:
This article was submitted to Translational Pharmacology, a section of the journal Frontiers in Pharmacology

Received: *17 March 2022*
Accepted: *23 March 2022*
Published: *19 May 2022*

Citation:
Tan Q, Li J, Yin Y and Shao W (2022) The Role of Growth Factors in the Repair of Motor Injury. Front. Pharmacol. 13:898152. doi: 10.3389/fphar.2022.898152

TABLE 1 | The role of growth factors in the repair of motor injuries.

Organization	Growth factor and preparations	Function	Mechanism	Ref
Muscle	Insulin-like growth factor -1 (IGF-1) Insulin-like growth factor IGF-2 Fibroblast growth factor 6 (FGF6) Human epidermal growth factor (hEGF) Transforming growth factor -β (TGF-β) Hepatocyte growth factor (HGF) Autologous platelet rich plasma (PRP)	Repair muscle damage and increase muscle quality	Activation of mitogen-activated protein kinase (MAPK/ERK1/2) pathway and PI3K/Akt pathway; Regulating the number of MSCs; Directly promote that proliferation and differentiation of muscle cells; Regulation of inflammatory response	Kim and Lee, (2017), Choi et al., (2019), Ahmad et al., (2020), Wroblewski et al., (2021), Zofkie et al., (2021)
Bones, joints	Fibroblast growth factor (FGF) Bone morphogenetic protein (BMP) Insulin-like growth factor (IGF) Platelet derived growth factor (PDGF) Transforming growth factor -β(TGF-β) Vascular endothelial growth factor (VEGF) Autologous platelet rich plasma (PRP) Growth factor midkine (Mdk) Myelogenous growth factor (MYDGF)	Repair damaged bones and protect bone homeostasis; Promote that regeneration of the joint synovial membrane; Repair damaged ligaments	Assisting the recruitment and migration of mesenchymal cells, the coagulation of progenitor cells, and the differentiation and maturation of chondrocytes; Promote the migration of bone progenitor cells and induce proliferation, differentiation and matrix formation; Induce osteoblast proliferation and differentiation	Frei et al., (2008), Kon et al., (2010), Liedert et al., (2014), Seijas et al., (2014), Zubair et al., (2018), Xu et al., (2022)
Nerve	Nerve growth factor (NGF) TGF-β Platelet derived growth factor B (PDGF-B) Acidic fibroblast growth factor (aFGF) Fibroblast growth factor 21 (FGF21) Platelet derived growth factor (PDGF) Vascular endothelial growth factor -A (Vegf-A)	Repair damaged nerve and neuromuscular junction	Regulating the expression of nerve factors at the injury site; Promoting mitosis and pluripotency of nerve cells; Reducing the death of nerve cells; Regulate autophagy to promote endothelial cell repair	Golzadeh and Mohammadi, (2016), Ko et al., (2019), Lu et al., (2020), Zhu et al., (2020), Ye et al., (2021), Yokozeki et al., (2021)

the body make them more susceptible to acute injury from exposure to contusion, lacerations (Tidball, 2011). In addition, incorrect posture can also cause chronic muscle strain. The pathophysiological basis of muscle injury is mainly the direct mechanical damage to myofibrils caused by centrifugal contraction force and the destruction of muscle cell membrane (Tidball, 2011). There is evidence that a variety of growth factors play an important role in the repair of muscle injury (As shown in **Table 1**). Muscle satellite cells (MSCs), as the key participants in skeletal muscle regeneration, have the ability to secrete IGF-1 (Lee et al., 2018). IGF-1 secretion by MSCs is significantly increased after skeletal muscle injury. IGF-1 promotes the mitosis of myoblasts by mediating the mitogen-activated protein kinase (MAPK/ERK1/2) pathway and PI3K/Akt pathway, thereby repairing the damaged muscle cells in muscle fibers and then regenerating them (Ahmad et al., 2020). Like IGF-1, IGF-2 is necessary for muscle differentiation and development and functions in an autocrine manner with the same mechanism (Ahmad et al., 2020). Notably, the number of MSCs in each individual was different. William Zofkie et al. found that fibroblast growth factor 6 (FGF6) was necessary to regulate the number of MSCs in the postnatal period to establish a quiescent adult muscle stem cell bank (Zofkie et al., 2021). Another type of growth factor also plays an important role in

muscle cell mitosis. Recently, an *in vitro* cytological study found that the supplementation of human epidermal growth factor (hEGF) in primary human myogenic cell cultures can promote the structural and functional characteristics of tissue-engineered skeletal muscle and enhance the proliferation and differentiation of skeletal muscle cells *in vitro* (Wroblewski et al., 2021). This latest research is of interest. HEGF cannot be obtained by autocrine of muscle cells, and biotechnology-dominated synthesis of hEGF reagents is expected to bring new treatment options for the repair of muscle injury. However, the specific mechanism of human epidermal growth factor (hEGF) acting on muscle cells needs further investigation. After the injury of myofibrils and muscle cells caused by centrifugal contractions, the damaged muscle recovers through different processes, including degeneration, inflammation, regeneration, and fibrosis (Quintero et al., 2009; Wong et al., 2015). TGF-β is a cytokine that participates in muscle recovery and repair. TGF-β can inhibit muscle regeneration, regulate extracellular matrix remodeling and promote fibrosis by regulating skeletal muscle inflammation. While some studies have shown that inhibition of TGF-β after muscle injury promotes muscle regeneration and recovery, others have pointed out that inhibition of TGF-β actually decreases muscle strength as it leads to incomplete muscle regeneration (Kim and Lee, 2017). Exercise injury may lead to degenerative atrophy of skeletal muscle. A study has found that hepatocyte growth factor (HGF) may regulate the transition of macrophages to M2 phenotype and promote the regeneration of skeletal muscle in mice (Choi et al., 2019). Autologous platelet-rich plasma (PRP) injection has been studied for a variety of applications, including as an adjunct therapy for muscle injury. Platelets release growth factors, including FGF-2, TGF-β1, PDGF, and IGF-1, and when platelets are highly concentrated by centrifugation, the resulting PRP solution is considered to improve tissue healing.

Bone Damage

In the skeletal system, growth factors promote the production of large numbers of osteoblasts and inhibit osteoclasts, thereby ensuring the normal development of the skeletal system. Moreover, the role of growth factors in bone repair is widely recognized (see **Table 1**). Growth factors that act on bones, including mainly bone morphogenetic protein (BMP), fibroblast growth factor (FGF), insulin-like growth factor (IGF), platelet-derived growth factor (PDGF), transforming growth factor beta (TGF-β), and vascular endothelial growth factor (VEGF), are usually stored in the extracellular matrix (ECM), but are actively released by ECM, cells and platelets after injury (Devescovi et al., 2008). FGF is involved in the earliest stage-segment cartilage formation in bone development and is involved in assisting with the recruitment and migration of mesenchymal cells, the coagulation of progenitor cells, the differentiation and maturation of chondrocytes, and the formation of cartilage and bone during endochondral ossification (Goldring et al., 2006). BMP, PDGF, and IGF can promote the migration of bone progenitor cells and induce proliferation, differentiation and matrix formation (Devescovi et al., 2008). VEGF can promote cartilage to bone transformation, and can induce osteoblast proliferation and differentiation (Devescovi et al., 2008). TGF-β seems to have all the functions mentioned above during the process of bone repair. A Liedert et al. found that The growth factor midkine (Mdk) plays a key role in bone remodeling, and it is expressed in the processes of bone formation and fracture repair (Liedert et al., 2014). A recent *in vivo* animal study reported that myelogenous growth factor (MYDGF) protects bone mass by inhibiting osteoclastogenesis and promoting osteoblast differentiation, and is a positive modulator of bone homeostasis (Xu et al., 2022). Similarly, growth factors play an important role in the repair of joint injuries. A study reported by Ling Yu pointed out that BMP9 can stimulate the regeneration of joint synovial membrane and achieve the reconstruction of joint function. Autologous platelet-rich plasma (PRP) is the most widely used agent for the treatment of joint injuries and its effects are well recognized (Zubair et al., 2018). R Frei et al. demonstrated a favorable therapeutic effect of PRGF-rich plasma for the treatment of ankle ligament complex injury in a retrospective clinical trial. It can be used as a replacement for traditional surgery or as an adjunct to accelerate and improve the healing of traumatic lesions and postoperative conditions (Frei et al., 2008). Consistently, Roberto Seijas et al. by treating a patient with a partial anterior cruciate ligament tear with growth factor-rich intraligamentous plasma, they found that a professional soccer player's athletic ability could be restored to the level prior to the injury with the retention of an intact cingulate band (Seijas et al., 2014). In addition, PDGF also has a good effect in the treatment of degenerative diseases in the elderly. One study has confirmed that intra-articular injection of PRP is safe and has the potential to reduce the degree of joint degeneration, improving pain, and knee function and quality of life in young patients (Kon et al., 2010). Current sources for delivery of the GF mixture to bone repair sites are platelet gel and demineralized bone matrix. However, GF levels in these formulations were affected by donor-to-donor variability and formulation differences. Autologous GF generated by patients themselves during bone repair may interfere with the prosthetic device and even cause the implant to become loose due to tissue reaction around the prosthesis. In conclusion, GF is a key component of functional bone regeneration: Screening of basic research results and controlled clinical trials are accelerating the development of GF in orthopedic surgery.

Nerve Injury

In the nervous system, growth factors have the function of promoting the generation of brain nerve cells and dendrites, and enhancing the electrochemical signal transduction between the nerves and muscles. After motor injury, especially in the traumatic injury caused by violence, the nerve and neuromuscular junction at the injury site will be damaged, leading to the related complications. Some studies have found that some growth factors play an important role in the repair of nerve injury (see **Table 1**). Nerve growth factor (NGF) is best known for its remarkable effects on the repair of nerve cells (Jafari et al., 2019). Although TGF-β cannot directly participate in the repair after nerve injury, it can play a positive role by regulating

the expression of nerve factors at the injury site (Yokozeki et al., 2021). The results of an animal model study conducted by Atefeh Golzadeh et al. showed that local administration of platelet-derived growth factor B (PDGF-B) had a beneficial effect on the regeneration and functional recovery of peripheral nerves, but the specific biological mechanism was still unclear (Golzadeh and Mohammadi, 2016). Spinal cord injury is the most serious injury to motor-related nerves. The repair of damaged nerves by acidic fibroblast growth factor (aFGF) is due to its ability to promote mitosis and pluripotency of nerve cells, thus playing a role in the repair of nerves (Ko et al., 2019). Fibroblast growth factor 21 (FGF21) can also play a role in repairing nerves, mainly by reducing the death of nerve cells and promoting the healing of nerve injury (Zhu et al., 2020). A recent study has shown that exogenous platelet-derived growth factor (PDGF) can improve the recovery of neurovascular units after spinal cord injury by regulating autophagy to promote endothelial cell repair (Ye et al., 2021). There are also relevant literature reports on the role of growth factors in the repair of neuromuscular junction injury. Chuien-yilu et al. found through *in vivo* animal experiments that macrophage-derived vascular endothelial growth factor -A (Vegf-A) is a key component of recovery after neuromuscular junction injury, revealing a new therapeutic goal for repair after motor injury (Lu et al., 2020). Although some growth factors have not yet been studied in humans for the repair of neurological function, a positive effect on this aspect is expected.

DISCUSSION

Growth factors have shown unique clinical advantages in the treatment of motor injury. Currently, platelet-rich plasma (PRP) is the most widely used growth factor biologics and is a natural concentrate of growth factors derived from autologous blood. It has good curative effect in the treatment of various osteoarthritis, long-term chronic sports injury, pain caused by degenerative changes, and postoperative rehabilitation. Synergy between growth factors is feasible, and in addition to PRP, BMP-2 in combination with VEGF has been shown to play a positive role in the repair of muscle and bone injuries (Subbiah et al., 2020). Growth factors not only play an important role in the repair of muscle, bone and nerve injuries, but also play a potential role in the relief of post-injury pain. Previous studies have demonstrated the potential role of insulin-like growth factor (IGF) in the treatment of myofascial pain syndrome. Compared with traditional therapy, growth factor preparation therapy has the characteristics of less trauma, rapid recovery and good patient compliance. Although growth factors and their preparations are increasingly widely used in the treatment of motor injury, the specific mechanism is still not very clear. In particular, the specific role of each growth factor in motor injury should be elucidated. The accurate mechanism is to achieve the purpose of accurate treatment according to the injury situation in future treatment. Individual derived growth factors are limited and it is necessary to prepare growth factors and related formulations by other means. With the development of genetic engineering and biotechnology engineering, the demand for growth factors and their preparations will be met in the future. It is worth worrying that as a bioengineering preparation, its possible safety and usage standardization should be considered. In general, the effect of growth factors on exercise health is irreplaceable, and its prospect is bright. However, the understanding of the relationship between them is vague.

AUTHOR CONTRIBUTIONS

All authors listed have made a substantial, direct, and intellectual contribution to the work and approved it for publication.

REFERENCES

Ahmad, S. S., Ahmad, K., Lee, E. J., Lee, Y. H., and Choi, I. (2020). Implications of Insulin-like Growth Factor-1 in Skeletal Muscle and Various Diseases. *Cells* 9 (8). doi:10.3390/cells9081773

Cacciata, M., Stromberg, A., Lee, J. A., Sorkin, D., Lombardo, D., Clancy, S., et al. (2019). Effect of Exergaming on Health-Related Quality of Life in Older Adults: A Systematic Review. *Int. J. Nurs. Stud.* 93, 30–40. doi:10.1016/j.ijnurstu.2019.01.010

Choi, W., Lee, J., Lee, J., Lee, S. H., and Kim, S. (2019). Hepatocyte Growth Factor Regulates Macrophage Transition to the M2 Phenotype and Promotes Murine Skeletal Muscle Regeneration. *Front. Physiol.* 10, 914. doi:10.3389/fphys.2019.00914

Devescovi, V., Leonardi, E., Ciapetti, G., and Cenni, E. (2008). Growth Factors in Bone Repair. *Chir Organi Mov* 92 (3), 161–168. doi:10.1007/s12306-008-0064-1

Frei, R., Biosca, F. E., Handl, M., and Trc, T. (2008). Conservative Treatment Using Plasma Rich in Growth Factors (PRGF) for Injury to the Ligamentous Complex of the Ankle. *Acta Chir Orthop. Traumatol. Cech* 75 (1), 28–33.

Gharahdaghi, N., Phillips, B. E., Szewczyk, N. J., Smith, K., Wilkinson, D. J., and Atherton, P. J. (2020). Links between Testosterone, Oestrogen, and the Growth Hormone/Insulin-like Growth Factor Axis and Resistance Exercise Muscle Adaptations. *Front. Physiol.* 11, 621226. doi:10.3389/fphys.2020.621226

Goldring, M. B., Tsuchimochi, K., and Ijiri, K. (2006). The Control of Chondrogenesis. *J. Cel Biochem* 97 (1), 33–44. doi:10.1002/jcb.20652

Golzadeh, A., and Mohammadi, R. (2016). Effect of Local Administration of Platelet-Derived Growth Factor B on Functional Recovery of Peripheral Nerve Regeneration: A Sciatic Nerve Transection Model. *Dent Res. J. (Isfahan)* 13 (3), 225–232. doi:10.4103/1735-3327.182181

Jafari, M., Delaviz, H., Torabi, S., Mohammadi, J., and Gheitasi, I. (2019). The Effect of Muscle Graft with Nerve Growth Factor and Laminin on Sciatic Nerve Repair in Rats. *Basic Clin. Neurosci.* 10 (4), 333–344. doi:10.32598/bcn.9.10.145

Kim, J., and Lee, J. (2017). Role of Transforming Growth Factor-β in Muscle Damage and Regeneration: Focused on Eccentric Muscle Contraction. *J. Exerc. Rehabil.* 13 (6), 621–626. doi:10.12965/jer.1735072.536

Kirsch Micheletti, J., Bláfoss, R., Sundstrup, E., Bay, H., Pastre, C. M., and Andersen, L. L. (2019). Association between Lifestyle and Musculoskeletal Pain: Cross-Sectional Study Among 10,000 Adults from the General Working Population. *BMC Musculoskelet. Disord.* 20 (1), 609. doi:10.1186/s12891-019-3002-5

Ko, C. C., Tu, T. H., Wu, J. C., Huang, W. C., and Cheng, H. (2019). Acidic Fibroblast Growth Factor in Spinal Cord Injury. *Neurospine* 16 (4), 728–738. doi:10.14245/ns.1836216.108

Kon, E., Buda, R., Filardo, G., Di Martino, A., Timoncini, A., Cenacchi, A., et al. (2010). Platelet-rich Plasma: Intra-articular Knee Injections Produced Favorable Results on Degenerative Cartilage Lesions. *Knee Surg. Sports Traumatol. Arthrosc.* 18 (4), 472–479. doi:10.1007/s00167-009-0940-8

Lee, E. J., Jan, A. T., Baig, M. H., Ahmad, K., Malik, A., Rabbani, G., et al. (2018). Fibromodulin and Regulation of the Intricate Balance between Myoblast Differentiation to Myocytes or Adipocyte-like Cells. *FASEB J.* 32 (2), 768–781. doi:10.1096/fj.201700665R

Liedert, A., Schinke, T., Ignatius, A., and Amling, M. (2014). The Role of Midkine in Skeletal Remodelling. *Br. J. Pharmacol.* 171 (4), 870–878. doi:10.1111/bph.12412

Lu, C. Y., Santosa, K. B., Jablonka-Shariff, A., Vannucci, B., Fuchs, A., Turnbull, I., et al. (2020). Macrophage-Derived Vascular Endothelial Growth Factor-A Is Integral to Neuromuscular Junction Reinnervation after Nerve Injury. *J. Neurosci.* 40 (50), 9602–9616. doi:10.1523/JNEUROSCI.1736-20.2020

Quintero, A. J., Wright, V. J., Fu, F. H., and Huard, J. (2009). Stem Cells for the Treatment of Skeletal Muscle Injury. *Clin. Sports Med.* 28 (1), 1–11. doi:10.1016/j.csm.2008.08.009

Seijas, R., Ares, O., Cuscó, X., Alvarez, P., Steinbacher, G., and Cugat, R. (2014). Partial Anterior Cruciate Ligament Tears Treated with Intraligamentary Plasma Rich in Growth Factors. *World J. Orthop.* 5 (3), 373–378. doi:10.5312/wjo.v5.i3.373

Subbiah, R., Cheng, A., Ruehle, M. A., Hettiaratchi, M. H., Bertassoni, L. E., and Guldberg, R. E. (2020). Effects of Controlled Dual Growth Factor Delivery on Bone Regeneration Following Composite Bone-Muscle Injury. *Acta Biomater.* 114, 63–75. doi:10.1016/j.actbio.2020.07.026

Tidball, J. G. (2011). Mechanisms of Muscle Injury, Repair, and Regeneration. *Compr. Physiol.* 1 (4), 2029–2062. doi:10.1002/cphy.c100092

Wong, S., Ning, A., Lee, C., and Feeley, B. T. (2015). Return to Sport after Muscle Injury. *Curr. Rev. Musculoskelet. Med.* 8 (2), 168–175. doi:10.1007/s12178-015-9262-2

Wroblewski, O. M., Vega-Soto, E. E., Nguyen, M. H., Cederna, P. S., and Larkin, L. M. (2021). Impact of Human Epidermal Growth Factor on Tissue-Engineered Skeletal Muscle Structure and Function. *Tissue Eng. Part. A.* 27 (17-18), 1151–1159. doi:10.1089/ten.TEA.2020.0255

Xu, X., Li, Y., Shi, L., He, K., Sun, Y., Ding, Y., et al. (2022). Myeloid-derived Growth Factor (MYDGF) Protects Bone Mass through Inhibiting Osteoclastogenesis and Promoting Osteoblast Differentiation. *EMBO Rep.* 23 (3), e53509. doi:10.15252/embr.202153509

Ye, L. X., An, N. C., Huang, P., Li, D. H., Zheng, Z. L., Ji, H., et al. (2021). Exogenous Platelet-Derived Growth Factor Improves Neurovascular Unit Recovery after Spinal Cord Injury. *Neural Regen. Res.* 16 (4), 765–771. doi:10.4103/1673-5374.295347

Yokozeki, Y., Uchida, K., Kawakubo, A., Nakawaki, M., Okubo, T., Miyagi, M., et al. (2021). TGF-β Regulates Nerve Growth Factor Expression in a Mouse Intervertebral Disc Injury Model. *BMC Musculoskelet. Disord.* 22 (1), 634. doi:10.1186/s12891-021-04509-w

Zhu, S., Ying, Y., Ye, L., Ying, W., Ye, J., Wu, Q., et al. (2020). Systemic Administration of Fibroblast Growth Factor 21 Improves the Recovery of Spinal Cord Injury (SCI) in Rats and Attenuates SCI-Induced Autophagy. *Front. Pharmacol.* 11, 628369. doi:10.3389/fphar.2020.628369

Zofkie, W., Southard, S. M., Braun, T., and Lepper, C. (2021). Fibroblast Growth Factor 6 Regulates Sizing of the Muscle Stem Cell Pool. *Stem Cel. Rep.* 16 (12), 2913–2927. doi:10.1016/j.stemcr.2021.10.006

Zubair, U., Salam, O., and Zubair, Z. (2018). Role of Intra-articular Platelet Rich Plasma in the Management of Osteoarthritis: A Review. *Cureus* 10 (9), e3359. doi:10.7759/cureus.3359

Conflict of Interest: The authors declare that the research was conducted in the absence of any commercial or financial relationships that could be construed as a potential conflict of interest.

Publisher's Note: All claims expressed in this article are solely those of the authors and do not necessarily represent those of their affiliated organizations, or those of the publisher, the editors and the reviewers. Any product that may be evaluated in this article, or claim that may be made by its manufacturer, is not guaranteed or endorsed by the publisher.

frontiers | Frontiers in Pharmacology

ORIGINAL RESEARCH
published: 27 May 2022
doi: 10.3389/fphar.2022.911962

Chronic Cervicitis and Cervical Cancer Detection Based on Deep Learning of Colposcopy Images Toward Translational Pharmacology

Wei Huang[1], *Shasha Sun*[1], *Zhengyu Yu*[2], *Shanshan Lu*[1] *and Hao Feng*[3]*

[1]Department of Gynecology, Hunan Provincial People's Hospital (The First-Affiliated Hospital of Hunan Normal University), Changsha, China, [2]Faculty of Engineering and IT, University of Technology, Sydney, NSW, Australia, [3]Department of Dermatology, Hunan Provincial People's Hospital (The First-Affiliated Hospital of Hunan Normal University), Changsha, China

With the rapid development of deep learning, automatic image recognition is widely used in medical development. In this study, a deep learning convolutional neural network model was developed to recognize and classify chronic cervicitis and cervical cancer. A total of 10,012 colposcopy images of 1,081 patients from Hunan Provincial People's Hospital in China were recorded. Five different colposcopy image features of the cervix including chronic cervicitis, intraepithelial lesions, cancer, polypus, and free hyperplastic squamous epithelial tissue were extracted to be applied in our deep learning network convolutional neural network model. However, the result showed a low accuracy (42.16%) due to computer misrecognition of chronic cervicitis, intraepithelial lesions, and free hyperplastic squamous epithelial tissue with high similarity. To optimize this model, we selected two significant feature images: chronic cervicitis and cervical cancer to input into a deep learning network. The result indicates high accuracy and robustness with an accuracy of 95.19%, which can be applied to detect whether the patient has chronic cervicitis or cervical cancer based on the patient's colposcopy images.

Keywords: chronic cervicitis, cervical cancer, colposcopy images, deep learning, convolutional neural network model

OPEN ACCESS

Edited by:
Weiguo Li,
Harbin Institute of Technology, China

Reviewed by:
Yunrun Liu,
Hong Kong Baptist University, Hong Kong SAR, China
Hongwen Wu,
Liuzhou Workers Hospital, China

****Correspondence:***
Hao Feng
doctorfenghao@126.com

Specialty section:
This article was submitted to Translational Pharmacology, a section of the journal Frontiers in Pharmacology

Received: *03 April 2022*
Accepted: *21 April 2022*
Published: *27 May 2022*

Citation:
Huang W, Sun S, Yu Z, Lu S and Feng H (2022) Chronic Cervicitis and Cervical Cancer Detection Based on Deep Learning of Colposcopy Images Toward Translational Pharmacology. Front. Pharmacol. 13:911962. doi: 10.3389/fphar.2022.911962

INTRODUCTION

Cervical cancer is one of the most common gynecological malignancies with high mortality in women worldwide (Arbyn et al., 2020). According to 2020 Global Cancer statistics, cervical cancer ranks in the top four for both incidence (6.5%) and mortality (7.7%) among women (Sung et al., 2021). In recent years, the incidence of cervical cancer is declining in some developed countries. However, it is still high in developing countries. In China, the incidence of cervical cancer tends to be younger (Zhu et al., 2019). Chronic cervicitis is defined as the inflammation of the cervix. Patients with chronic cervicitis are very common (Woods et al., 2011; Hester and Middleman, 2019). Early screening for cervix precancerous lesions is essential to prevent or treat cervical cancer.

At present, colposcopy is the most commonly used cervical screening method for prescreening cervical cancer, especially in some underdeveloped areas (Holme et al., 2017; Mezei et al., 2017). However, as a visual diagnosis method, the diagnosis process of colposcopy is mainly dependent on the doctors' experience, which has strong subjectivity and poor repeatability (Wentzensen et al., 2017; Hu et al., 2019; Guo et al., 2020). In addition, cervical cancer is a large-scale screening disease

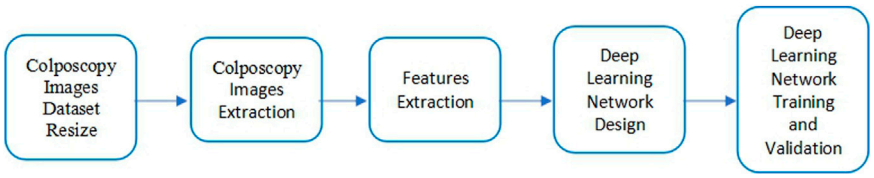

FIGURE 1 | Workflow diagram of the deep learning classification model.

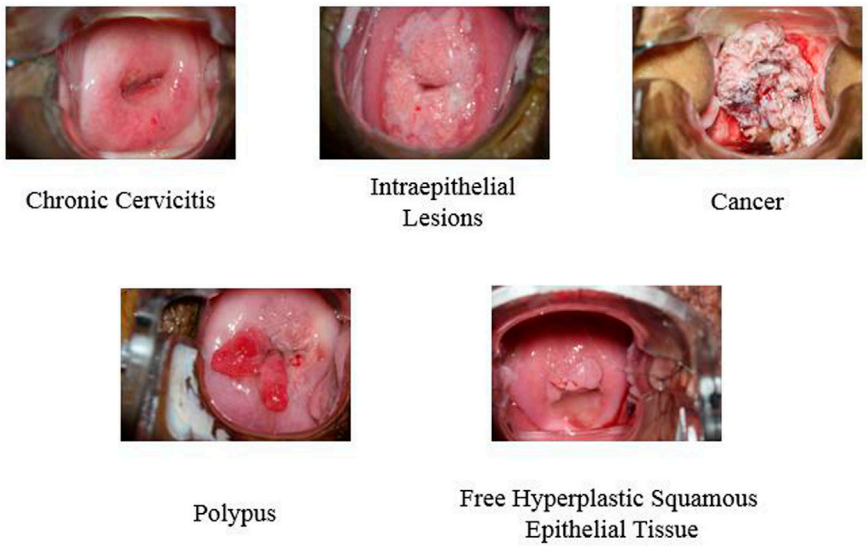

FIGURE 2 | Sample image of different features.

and has a huge workload, which leads to a certain possibility of missed diagnosis and misdiagnosis by medical workers (Zhang et al., 2020).

With the rapid development of deep learning, automatic diagnosis of lesions is being widely used in computer-aided diagnosis systems (Mehlhorn et al., 2012; Peng et al., 2021). The application of deep learning convolutional neural networks in colposcopy image analysis has been reported as an effective way to recognize the automatic diagnosis of cervical cancer and other pathology classification (Sato et al., 2018; Miyagi et al., 2020; Yan et al., 2021; Fu et al., 2022). Therefore, we attempted to develop and test a deep learning convolutional neural network model to recognize the classifications of different colposcopy images so as to detect whether the patient has chronic cervicitis or cervical cancer.

MATERIALS AND METHODS

A deep learning convolutional neural network model is proposed to recognize and classify whether the patient has chronic cervicitis or cervical cancer in this research, **Figure 1** illustrates the process of the workflow diagram of a deep learning classification model. The process stages are introduced as follows:

1. Resizing colposcopy images: Each original image from the hospital is around 10–20 MB with pixels (6,000 * 4,000), which contains more than 100 GB images in total. This is too large to process, so we resized each image to 500 KB with the same pixels and kept the quality as much as we could, eventually, the total size of all the images was reduced to 5GB, which was much faster to compute.
2. Extract colposcopy images: In the datasets, each patient has about 10 images recorded, some of them are duplicated and redundant and some of them are blurry and unclear. In order to improve the accuracy of the classification model, we selected the most significant image for each patient. In this stage, 1,081 images were selected from 10,012 colposcopy images.
3. Extract features. There are five features extracted from the clinical record for each patient, which include chronic cervicitis, intraepithelial lesions, cancer, polypus, and free hyperplastic squamous epithelial tissue for the cervix. All the images are allocated into different classes. The two most significant features are chronic cervicitis and cervical cancer.
4. Design a deep learning network: A deep learning convolutional neural network was designed to classify different classes of images. This network included eight layers including one image input layer, two convolution

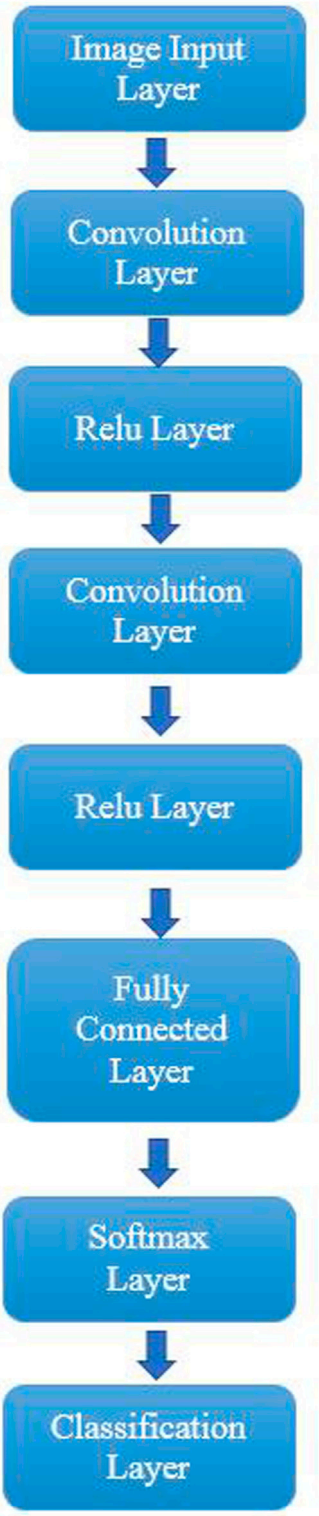

FIGURE 3 | Structure of the proposed deep learning network.

TABLE 1 | Descriptions of network layers.

Network layer	Description
Image input layer	To input and normalize images into a network
Convolution layers	To learn and recognize images patterns. It is the main block for convolutional neural networks
Relu layers	Relu (Rectified Linear Unit) is one of the activation functions, which outputs the positive part of the input
Fully connected layer	To connect previous layer with all the inputs to all the activation value in the next layer
Softmax layer	To turn the value between 0 and 1
Classification layer	To compute the class number from the input size

layers, two relu layers, one fully connected layer, one softmax layer, and one classification layer.

5. Train and validate the designed deep learning network: Five classes of images with different features were trained and validated, and the result indicated that the accuracy of the classification model was 42.16%, which was low, accurate, and unreliable. The reason was investigated, as a few images of chronic cervicitis, intraepithelial lesions and free hyperplastic squamous epithelial tissue were highly similar. Computer misrecognized them and hardly classified the features. To optimize this model, we selected the class of chronic cervicitis, as this class has the most numbers of patients, and selected the class of cancer, as this class has the most serious patients. We input these two classes of images into our designed deep learning network and process the training and validation. The result indicates that the accuracy of the classification model is 95.19%, which is highly accurate and robust.

Datasets

The dataset we used in the article is from Hunan Provincial People's Hospital in China, which contains 1,081 patients. About 10 colposcopy images have been recorded for each patient, and there are 10,012 images in total. Patients' clinical reports associated with images have been generated. Five different features have been extracted including chronic cervicitis, intraepithelial lesions, cancer, polypus, and free hyperplastic squamous epithelial tissue for the cervix. **Figure 2** illustrates a sample image of each feature.

Deep Learning Classification Model

A deep learning convolutional neural network is a network class which is usually used to process images. The convolutional neural network consists of multiple layers of neurons. Neurons are algorithms in mathematics, which processes multiple weighted inputs to generate an activation value of outputs.

We have designed a deep learning network to classify image features. This network contains eight layers with seven connections, including one image input layer, two convolution layers, two relu layers, one fully connected layer, one softmax

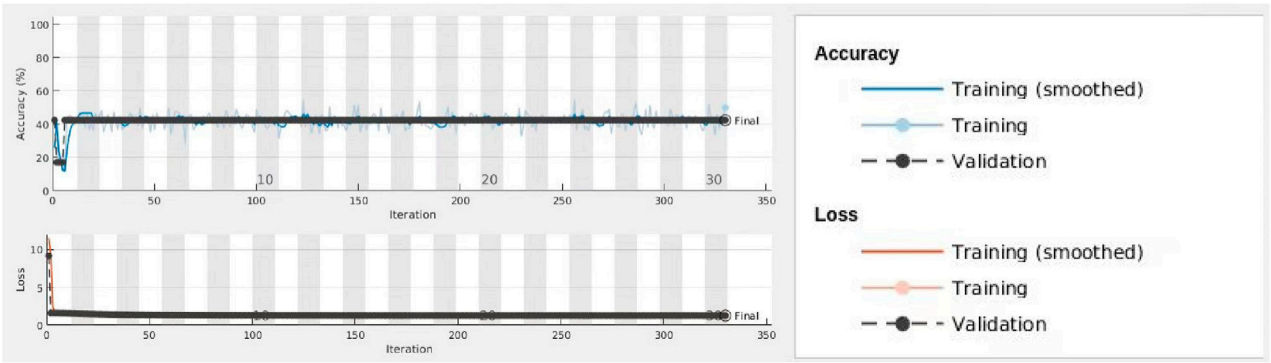

FIGURE 4 | Process of training and validation for all classes.

FIGURE 5 | Examples of similar images of different features.

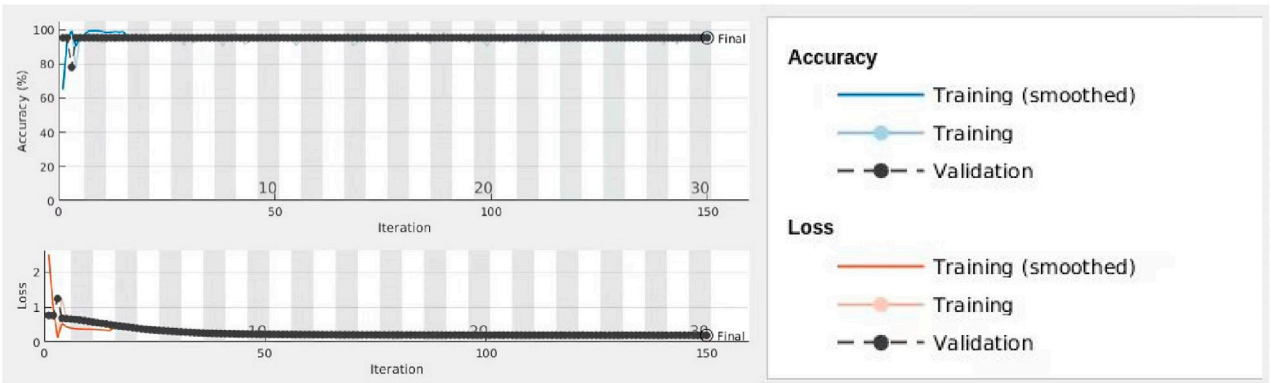

FIGURE 6 | Process of training and validation for chronic cervicitis and cancer classes.

layer, and one classification layer. The structure of the network is displayed in **Figure 3**, and the descriptions of each layer have been introduced in **Table 1**. The image input layer converted the image pixels into 227*227 and normalized image data. The convolution layer produced 32 filters with filter sizes [3 3]. The relu layer produced the same value as the input when the input value is not less than 0, otherwise it produced 0. The fully connected layer connected all the inputs from the previous layer, the number of outputs needs to be set up based on the number of classes. A softmax function was generated in the softmax layer. The classification layer was used to weight the elements and generated the cross-entropy loss to classify the features.

RESULTS AND DISCUSSION

In this research, we have five classes of images with different features. Initially, we inputted these five classes of images into the designed deep learning network to train and recognize the images. After the training process was validated, a

classification model was developed to classify images accurately. This model can be used to determine which feature the patient has according to the patient's colposcopy images. In the training process, we selected 70% images for training and 30% images for validation randomly. The result presented that classification accuracy was only 42.16% which is presented in **Figure 4**, due to some high similarity images occurring in the class of chronic cervicitis, intraepithelial lesions and free hyperplastic squamous epithelial tissue. **Figure 5** presents the example of similar images.

We inputted these two classes of images into the network and assigned 70% images for training and 30% images for validation randomly. **Figure 6** displays the process of training and validation. At the top diagram, the blue line indicated the smoothed training data for accuracy, the grey line indicated training data for accuracy, and the dotted black line is for the validation of accuracy. At the bottom diagram, the red line indicated the smoothed training data for loss. The pink line indicated training data for loss, and the dotted black line is for the validation of loss. The result indicate that the accuracy of this model is 95.19% which is much higher than the previous model. We believe this deep learning convolutional neural network based on classification model is high, accurate, and robust, which can be applied to detect whether the patient has chronic cervicitis or cervical cancer based on the patient's colposcopy images.

CONCLUSION

This present research proposed a deep learning convolutional neural network model for recognition and classification of chronic cervicitis and cervical cancer with colposcopy images. Initially, five classes of colposcopy images with different features which contained chronic cervicitis, intraepithelial lesions, cancer, polypus, and free hyperplastic squamous epithelial tissue were used in deep learning network. Due to high similarity of chronic cervicitis, intraepithelial lesions and free hyperplastic squamous epithelial tissue, the features of these images were misrecognized by the network, which resulted in low accuracy of the classification model. Then two significant features images were selected to train and recognize by our deep learning network model. The result showed high accuracy and robustness. Compared with previous network recognition, the proposed deep learning model is effective and has promising prospects, which provide an effective detection way of chronic cervicitis and cervical cancer based on the patient's colposcopy images.

DATA AVAILABILITY STATEMENT

The original contributions presented in the study are included in the article/supplementary material; further inquiries can be directed to the corresponding author.

ETHICS STATEMENT

The studies involving human participants were reviewed and approved by Hunan Provincial People's Hospital (The first-affiliated hospital of Hunan normal university). The patients/participants provided their written informed consent to participate in this study.

AUTHOR CONTRIBUTIONS

WH contributed to conception and design of the study and wrote the first draft of the manuscript. SS, ZY, and SL contributed to data collection and analysis. HF contributed to manuscript revision, read, and project management. All authors approved the submitted version.

FUNDING

This work was supported by the Plan of Hunan Provincial Science and Technology Innovation Guidance (No. 2018SK50724), and the Hunan Health Commission (No. B2019073).

REFERENCES

Arbyn, M., Weiderpass, E., Bruni, L., de Sanjosé, S., Saraiya, M., Ferlay, J., et al. (2020). Estimates of Incidence and Mortality of Cervical Cancer in 2018: a Worldwide Analysis. *Lancet Glob. Health* 8 (2), e191–e203. doi:10.1016/S2214-109X(19)30482-6

Fu, L., Xia, W., Shi, W., Cao, G. X., Ruan, Y. T., Zhao, X. Y., et al. (2022). Deep Learning Based Cervical Screening by the Cross-Modal Integration of Colposcopy, Cytology, and HPV Test. *Int. J. Med. Inf.* 159, 104675. doi:10.1016/j.ijmedinf.2021.104675

Guo, J., Fu, L., Zhao, J., Lei, L., Zhan, Q., Liu, M., et al. (2020). The Value of Microendoscopy in the Diagnosis of Cervical Precancerous Lesions and Cervical Microinvasive Carcinoma. *Arch. Gynecol. Obstet.* 302, 455–462. doi:10.1007/s00404-020-05565-8

Hester, E. E., and Middleman, A. B. (2019). A Clinical Conundrum: Chronic Cervicitis. *J. Pediatr. Adolesc. Gynecol.* 32 (3), 342–344. doi:10.1016/j.jpag.2018.12.004

Holme, F., Kapambwe, S., Nessa, A., Basu, P., Murillo, R., and Jeronimo, J. (2017). Scaling up Proven Innovative Cervical Cancer Screening Strategies: Challenges and Opportunities in Implementation at the Population Level in Low- and Lower-Middle-Income Countries. *Int. J. Gynaecol. Obstet.* 138, 63–68. doi:10.1002/ijgo.12185

Hu, L., Bell, D., Antani, S., Xue, Z., Yu, K., Horning, M. P., et al. (2019). An Observational Study of Deep Learning and Automated Evaluation of Cervical Images for Cancer Screening. *J. Natl. Cancer Inst.* 111 (9), 923–932. doi:10.1093/jnci/djy225

Mehlhorn, G., Kage, A., Münzenmayer, C., Benz, M., Koch, M. C., Beckmann, M. W., et al. (2012). Computer-assisted Diagnosis (CAD) in Colposcopy: Evaluation of a Pilot Study. *Anticancer Res.* 32 (12), 5221–5226.

Mezei, A. K., Armstrong, H. L., Pedersen, H. N., Campos, N. G., Mitchell, S. M., Sekikubo, M., et al. (2017). Cost-effectiveness of Cervical Cancer Screening Methods in Low- and Middle-Income Countries: A Systematic Review. *Int. J. Cancer* 141, 437–446. doi:10.1002/ijc.30695

Miyagi, Y., Takehara, K., Nagayasu, Y., and Miyake, T. (2020). Application of Deep Learning to the Classification of Uterine Cervical Squamous Epithelial Lesion from Colposcopy Images Combined with HPV Types. *Oncol. Lett.* 19 (2), 1602–1610. doi:10.3892/ol.2019.11214

Peng, G., Dong, H., Liang, T., Li, L., and Liu, J. (2021). Diagnosis of Cervical Precancerous Lesions Based on Multimodal Feature Changes. *Comput. Biol. Med.* 130, 104209. doi:10.1016/j.compbiomed.2021.104209

Sato, M., Horie, K., Hara, A., Miyamoto, Y., Kurihara, K., Tomio, K., et al. (2018). Application of Deep Learning to the Classification of Images from Colposcopy. *Oncol. Lett.* 15 (3), 3518–3523. doi:10.3892/ol.2018.7762

Sung, H., Ferlay, J., Siegel, R. L., Laversanne, M., Soerjomataram, I., Jemal, A., et al. (2021). Global Cancer Statistics 2020: GLOBOCAN Estimates of Incidence and Mortality Worldwide for 36 Cancers in 185 Countries. *CA A Cancer J. Clin.* 71 (3), 209–249. doi:10.3322/caac.21660

Wentzensen, N., Schiffman, M., Silver, M. I., Khan, M. J., Perkins, R. B., Smith, K. M., et al. (2017). ASCCP Colposcopy Standards: Risk-Based Colposcopy Practice. *J. Low. Genit. Tract. Dis.* 21 (4), 230–234. doi:10.1097/LGT.0000000000000334

Woods, J. L., Bailey, S. L., Hensel, D. J., and Scurlock, A. M. (2011). Cervicitis in Adolescents: Do Clinicians Understand Diagnosis and Treatment? *J. Pediatr. Adolesc. Gynecol.* 24 (6), 359–364. doi:10.1016/j.jpag.2011.06.006

Yan, L., Li, S., Guo, Y., Ren, P., Song, H., Yang, J., et al. (2021). Multi-state Colposcopy Image Fusion for Cervical Precancerous Lesion Diagnosis Using BF-CNN. *Biomed. Signal Process. Control[J]* 68, 102700. doi:10.1016/j.bspc.2021.102700

Zhang, T., Luo, Y., Li, P., Liu, P-Z., Du, Y-Z., Sun, P., et al. (2020). Cervical Precancerous Lesions Classification Using Pre-trained Densely Connected Convolutional Networks with Colposcopy Images. *Biomed. Signal Process. Control[J]* 55, 101566. doi:10.1016/j.bspc.2019.101566

Zhu, B., Liu, Y., Zuo, T., Cui, X., Li, M., Zhang, J., et al. (2019). The Prevalence, Trends, and Geographical Distribution of Human Papillomavirus Infection in China: the Pooled Analysis of 1.7 Million Women. *Cancer Med.* 8 (11), 5373–5385. doi:10.1002/cam4.2017

Conflict of Interest: The authors declare that the research was conducted in the absence of any commercial or financial relationships that could be construed as a potential conflict of interest.

Publisher's Note: All claims expressed in this article are solely those of the authors and do not necessarily represent those of their affiliated organizations, or those of the publisher, the editors, and the reviewers. Any product that may be evaluated in this article, or claim that may be made by its manufacturer, is not guaranteed or endorsed by the publisher.

frontiers | Frontiers in Pharmacology

MINI REVIEW
published: 08 June 2022
doi: 10.3389/fphar.2022.842525

Current Insights Into the Maintenance of Structure and Function of Intervertebral Disc: A Review of the Regulatory Role of Growth and Differentiation Factor-5

Bin Lv†, Weikang Gan†, Zhangrong Cheng†, Juntao Wu†, Yuhang Chen, Kangchen Zhao* and Yukun Zhang**

Department of Orthopaedics, Union Hospital, Tongji Medical College, Huazhong University of Science and Technology, Wuhan, China

OPEN ACCESS

Edited by:
Songwen Tan, Central South University, China

Reviewed by:
Peter Natesan Pushparaj, King Abdulaziz University, Saudi Arabia

***Correspondence:**
Yukun Zhang
zhangyukuncom@126.com
Kangchen Zhao
zhaokc_uh@hust.edu.cn
Bin Lv
dr_lvbin@sina.com

†*These authors have contributed equally to this work*

Specialty section:
This article was submitted to Translational Pharmacology, a section of the journal Frontiers in Pharmacology

Received: *23 December 2021*
Accepted: *08 April 2022*
Published: *08 June 2022*

Citation:
Lv B, Gan W, Cheng Z, Wu J, Chen Y, Zhao K and Zhang Y (2022) Current Insights Into the Maintenance of Structure and Function of Intervertebral Disc: A Review of the Regulatory Role of Growth and Differentiation Factor-5. Front. Pharmacol. 13:842525. doi: 10.3389/fphar.2022.842525

Intervertebral disc degeneration (IDD), characterized by conversion of genotypic and phenotypic, is a major etiology of low back pain and disability. In general, this process starts with alteration of metabolic homeostasis leading to ongoing inflammatory process, extracellular matrix degradation and fibrosis, diminished tissue hydration, and impaired structural and mechanical functionality. During the past decades, extensive studies have focused on elucidating the molecular mechanisms of degeneration and shed light on the protective roles of various factors that may have the ability to halt and even reverse the IDD. Mutations of GDF-5 are associated with several human and animal diseases that are characterized by skeletal deformity such as short digits and short limbs. Growth and differentiation factor-5 (GDF-5) has been shown to be a promise biological therapy for IDD. Substantial literature has revealed that GDF-5 can decelerate the progression of IDD on the molecular, cellular, and organ level by altering prolonged imbalance between anabolism and catabolism. GDF family members are the central signaling moleculars in homeostasis of IVD and upregulation of their gene promotes the expression of healthy nucleus pulposus (NP) cell marker genes. In addition, GDF signaling is able to induce mesenchymal stem cells (MSCs) to differentiate into NPCs and mobilize resident cell populations as chemotactic signals. This review will discuss the promising critical role of GDF-5 in maintenance of structure and function of IVDs, and its therapeutic role in IDD endogenous repair.

Keywords: intervertebral disc degeneration, growth and differentiation factor (GDF), nucleus pulposus, extracellular matrix, mesenchymal stem cell

INTRODUCTION

As a major public health concern, low back pain (LBP) is a leading reason for disability worldwide, affecting all-age population. LBP is associated with pathologies including intervertebral disc herniation, spine stenosis, and radiculopathy. Although the etiology of LBP is complex and multifactorial, intervertebral disc degeneration (IDD) has been cited as a leading pathological contributor to LBP. IDD is a common musculoskeletal degeneration that progresses with age, which

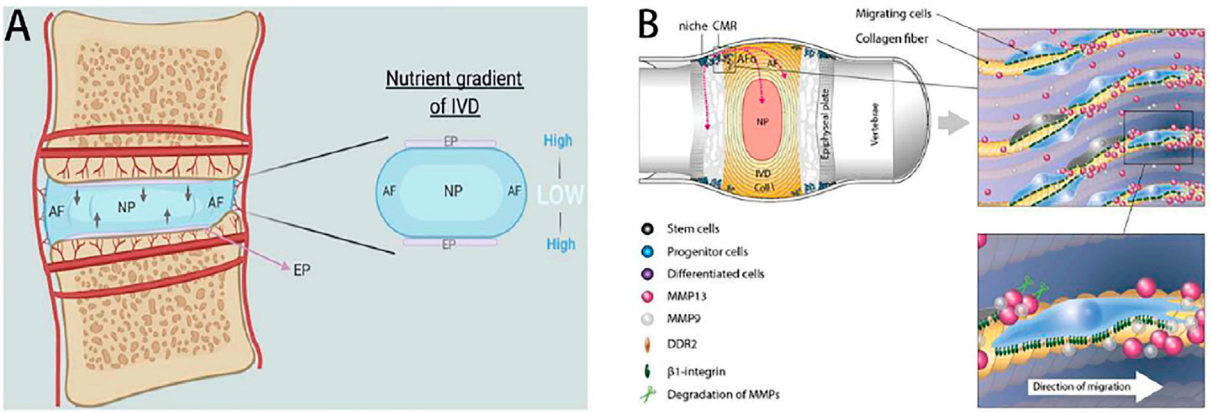

FIGURE 1 | Overview of IVDs structure and the cellular migration/directions during IVDs repair. **(A)** Avascular nature of the human IVDs. Reproduced from Rebecca et al.(Kritschil et al., 2021) with permission from Copyright 2021 Wiley. **(B)** Intervertebral disc stem cell niche and cells migrate to AF, the outer layer of collagen-rich fibers (COLL I). Cells migrate to the germinal region and interact with ECM along the alignment of collagen fibers. Moreover, the disorganization of collagen fibers and increasing of the interlamellar distances between collagen bundles in the annulus fibrosus were usually observed during the degeneration process that often results in disc bulging. Reproduced from Henriksson et al. (2015) with permission from Copyright 2015 Elsevier.

is the major cause of physical disability in aging populations. Serving as a shock absorber, intervertebral disc (IVD) is the fibrocartilaginous joint positioned between the vertebrae and composed of three structural components, sustaining mechanical strength and conferring spinal flexibility. It is estimated that 84% of the LBP cases experience symptom at least once throughout lives (Ahlholm et al., 2021). Consequently, there has been an increase in efforts to find innovative therapeutic strategies.

The injection of targeted proteins fully reverses tissue pathology in terms of its structural and functional complexity. The IVD is a complex fibrocartilaginous structure that links adjacent vertebrae and confers spinal mobility. Consisting of the annulus fibrosus (AF), nucleus pulposus (NP), and cartilage endplate (CEP), the IVD is the largest non-vascularized structure where cells retrieve nutrients and oxygen mainly by diffusion through CEP, readily advancing to nutritional deficiency in ageing population. A relatively low number of IVD cells are inactive metabolically, and therefore most of their properties depend on IVD extracellular matrix (ECM). The ECM is physiologically rich in proteoglycans, consisting of a protein core and a multitude of glycosaminoglycan (GAG) side chains, entrapped in the network of collagen fibres. Resident IVD cells are maintained under a high osmotic, hypoxic, and high-load microenvironment. Multifactorial including genetic, molecular, cellular and mechanical overloading contribute to an imbalance between production and degradation of the ECM, initially within the NP and eventually causing IDD (Mayer et al., 2013). Furthermore, increased catabolic processes of glycosaminoglycans (GAGs) decrease the swelling capacity of the NP. Thus, the altered mechanical loading of the IVD leads to vascularization and neoinnervation with infiltration of immune cells. Due to the limited self-repair capacity and harsh nutrient availability of IVD, the ECM degradation process is irreversible and requires restoration if IVD repair is pursued (**Figure 1**). For reasons that are not yet fully understood, very early after skeletal maturity, the IVD can undergo a degenerative process that manifests as cell death, extracellular matrix (ECM) changes and dehydration, culminating in failure of its biomechanical properties, thereby leading to pain and disability. Thus, they have a limited capacity for self-repair after damage or degeneration (Zhang et al., 2021a). The extracellular matrix (ECM) is mainly synthesized and secreted by NP cells (NPCs) and is composed of type II collagen (collagen II) and aggrecan, helping to resist compression and maintain disc height. Its pathogenesis is very complicated and it involves a variety of pathological processes, including apoptosis, cell proliferation, degradation of the extracellular matrix, inflammation, and degeneration of cartilage endplates, which will lead to complex biochemical and molecular changes in the intervertebral disc, including the reduction of proteoglycan content, the conversion of collagen type II to collagen type I, and the decrease of NP cell density. IDD is considered to arise from cell driven degeneration to the ECM of the central part of the IVD, which eventually result in structural damage, such as AF rupture, NP cells protruding. This process is concurrent with an in-growth of blood vessels and nociceptive nerve fibers into the IVDs, promoting immune cell infiltration and resulting in pain and contributing to the abnormity of IVDs mechanical function (Zhang et al., 2021a).

IDD is mainly characterized by apoptosis of function cells, an imbalance between ECM anabolism and catabolism, and the dysregulation of NPC survival (Wang et al., 2021). IDD leads to imbalance between anabolic and catabolic processes, altered extracellular matrix composition, loss of tissue hydration, aberrant activation of the inflammation, and impaired mechanical functionality. Unfortunately, current treatments are aimed at relieving symptoms instead of preserving disc structure and function. The hallmark of IDD is the gradual loss of ECM molecules-specifically the GAG-substituted

proteoglycans. While this loss is often associated with increased extracellular catabolism via metalloproteinases and pro-inflammatory cytokines, evidence suggests that IDD is related to dysregulation of the enzymes involved in GAG biosynthesis.

Any deviation from the homeostatic balance between the anabolic and catabolic factors in the normal, healthy disc will result in degenerative process of IVDs. Because IVD tissue homeostasis is maintained by a balance between anabolic and anti-catabolic process of IVD cells, current strategy to regenerate degenerative IVDs is to promote the anabolism and to suppress the catabolism induced by cytokines. Various growth factors have been demonstrated to shift the catabolic state to the anabolic state to regenerate IVDs. Recently, the injection of growth factors has been under serious consideration as a potential biological therapy to enhance IVD tissue regeneration. The feasibility, safety, and efficacy of injection of growth factors for IVD degeneration has been heavily investigated. We reviewed the role of chosen prototypical growth factors and growth factor combinations that have the capacity to improve IVD restoration. A number of growth factors have showed potential to modulate the anabolism and catabolism through multiple pathogenic mechanisms, including suppressing inflammatory process and down-regulating degrading enzymes, in both *in vitro* and animal studies of IVDs tissue engineering. Previous studies have been generated about the outcomes after the intradiscal administration of a series of growth factors: growth and differentiation factor-5 (GDF-5), bone morphogenetic protein-2 (BMP-2), and bone morphogenetic protein-7 (BMP-7), transforming growth factor beta-1 (TGF-β1), platelet-derived growth factor (PDGF), insulin-like growth factor-1 (IGF-1), basic fibroblast growth factor (bFGF), fibroblast growth factor-18 (FGF-18). Members of the transforming growth factor-β superfamily, IGF-1, GDF-5, BMP-2, BMP-7, and platelet-derived growth factor have all been investigated as possible therapeutic options for IVD regeneration. However, growth factors, including Transforming Growth Factor-β (TGF-β), Fibroblast Growth Factor (FGF), and Insulin-like Growth Factor-1 (IGF-1), may induce blood vessel in-growth and accelerate the process of IDD. Growth factors can be applied in IVD tissue regeneration via delivery of the "naked" or "embedded" proteins as well as prolonged supplement by vector- or cell-based gene therapy (Paesold et al., 2007).

The metabolic activity of IVDs is modulated and regulated by several growth factors, enzymes, and cytokines via either autocrine or paracrine manner (Wang et al., 2021). Studies have showed that injection of GDF-5 into the intervertebral disc of mice can effectively attenuate the IDD, which results in their response via BMPRII and will not stimulate blood vessel ingrowth (Fitzgerald et al., 2021). An increasing body of evidence indicates that GDF family members are central to IVD homeostatic processes and show up-regulation of healthy NP cell marker genes in degenerative cells, induce MSCs to differentiate into NP cells and even act as chemotactic signals mobilizing resident cell populations during disc injury repair. Furthermore, GDF-5 has been determined to induce the restoration of disc height and to increase the proteoglycan (PG) content in NP (Wang et al., 2021). This finding suggests that GDF-5 is more suitable for use in IDD treatment compared with the three other growth factors. In this review, we will focus the discussion on the basic structure, signaling pathways, function in cartilage and bone formation, and potential clinical application of GDF5 in bone tissue regeneration.

Overview of GDF-5

Growth and differentiation factor-5 (GDF-5), also known as CDMP1 or BMP14, is a divergent member of the transforming growth factor-beta (TGF-b) superfamily and is expressed under physiological conditions. GDF-5 is synthesized as a large precursor protein with seven cysteine residues, which contains two major domains: the N-terminal prodomain with a cleavage site and signal sequence and the active C-terminal domain. GDF-5 binds to two types of transmembrane serine/threonine kinase receptors to activate its signaling pathway (Genovesi et al., 2021). Specificly, upon GDF-5 binding to the extracellular part of the receptor complex, BMP ligands signal through a receptor complex consisting of two type I BMP receptors (BMPRs) and two type II BMPRs to activate the downstream Smad pathway (Xu et al., 2021). This spatialtemporal expression pattern of GDF-5 proves its essential role in the formation of bone and cartilage. Similar to other members of BMPs, the signaling cascade of GDF5 is originated through binding to type I and type II receptors and thus regulating the downstream intracellular biochemical processes. The intracellular Smad proteins become activated and then translocate into the nucleus to regulate the transcription of COL2A1 and ACAN, which encode for type II collagen and aggrecan, respectively (Massagué, 2000). Each BMP ligand has a varying affinity for each receptor subtype and GDF-5 is known to preferentially bind to the BMPR1b type I receptor and BMPR2 type II receptor. Like that of GDF5, these receptors are expressed in the developing rat ventral mesencephalon (VM) at embryonic day 11 and their expression continues throughout development until adulthood, at least up to postnatal day 90. Li et al. (2015) found that GDF-5 and BMPRII expressed both in normal and degenerated IVD, showing that gene therapy may produce be a physiological effects. They showed that GDF-5 might have an inhibition effect on degenerated human IVD.

GDF-5 plays a crucial role in developmental processes of organs including bone, cartilage, ligament, and soft tissue formation. Mutations of GDF-5 are associated with several human and animal diseases that are characterized by skeletal deformity such as short digits and short limbs. GDF-5 is emerging as a major mediator in the interzone of joint formation sites, and in the cartilage primordium in the early limb development. *In vitro* and *in vivo* studies showed that GDF-5 overexpression or treatment of recombinant protein stimulated chondrogenesis and osteogenesis.

Over the past decades, studies regarding the role of GDF-5 in progression of musculoskeletal diseases have been conducted. GDF-5 seems uniquely capable of stimulating beneficial effects on IVD and ECM without inducing ectopic ossification (Belykh et al., 2015).GDF-5-gene-deficient mice demonstrated abnormalities in IVD structure and ECM. Adenoviral

mediation of GDF-5 gene can stimulate NPCs growth. For instance, Liang et al. showed the therapeutic effects of gene delivery for intervention for IDD in a mice model by of adenovirus-mediated GDF-5 delivery. Their findings highlighted the physiological improvements that occurred to the IVD and showed the long-term expression of the target protein in the IDD (Liang et al., 2010). GDF-5 was observed in both normal and degenerated human IVD, particularly in the NPCs. In addition, degenerated human IVD cells show reduced number of cells expressing GDF-5. An investigation of polymorphisms in GDF-5 revealed that its variable expression and function are linked to osteoarthritis (Masuya et al., 2007). Williams et al. investigated SNP rs143383 (a T to C substitution at position 104) located within the promoter region of the GDF-5 gene. Their analysis showed that the T allele was associated with 1.72-fold increased risk of disc space narrowing and osteophyte production in women (Zhu et al., 2019). This result shows that GDF-5 is a convincing candidate gene for bone tissue engineering by promoting osteogenesis and angiogenesis.

Jodie et al. (Daniels et al., 2017) suggested that both GDF-5 and IL-1 could activate intracellular ERK signaling pathways in the degenerated IVD. Liu et al. (2016a) showed that microRNA-34a inhibition could increase GDF-5 expression to prevent IL-1β-induced ECM degradation in human NPCs. The commitment of hASCs is powerful and highly specific, as evidenced by the expression of NPCs-associated genes characteristic of normal human NPCs. Pauline et al. (Colombier et al., 2016) showed that the GDF-5 and TGF-β1 synergistically drive the human adipose stromal cells (hASCs) differentiate into NPCs-like cells. Enochson et al. (2014) showed that GDF-5 stimulation of human chondrocytes inhibited expression of the cartilage ECM degrading enzymes MMP-13 and ADAMTS-4 and stimulated the expression of cartilage anabolic genes ACAN and Sex determining region Y-Box9 (SOX9) via the canonical Wnt signaling pathway. Luo et al. (Enochson et al., 2014) showed that GDF-5 gene insertion displayed significant promise for applications in repairing the matrix of degenerated IVD cells (Luo et al., 2016).

GDF-5 Affects ECM Metabolism in IVD

Physiological NP matrix contains 70–90% water, while its dry weight consists of 20% collagen, mainly type II, and 30–50% proteoglycan. IVDs comprise three regions: a hydrophilic nucleus pulposus (NP), an outer fibrocartilaginous annulus fibrosus (AF), and bordered superiorly and inferiorly by hyaline cartilaginous endplates (CEP). Resident cells in both the NP and AF compartments produce and secrete the complex ECM molecules that accommodate the compressive and tensile mechanical loads, respectively.

Under pathological conditions, the inbalance between the synthesis and decomposition of the ECM decreased structural components (collagen II and aggrecan) and increased matrix-degrading enzymes (MMP-2, MMP-3, MMP-13, ADAMTS-4, and ADAMTS-5). IDD is closely related to the reduction of hydrophilic ECM molecules and the changes in the phenotype of IVD cells, leading to structural changes and instability of the spine (Bedore et al., 2014). ECM degradation is a key factor in the progression of IDD, contributing to loss of compression resistance and IVD height. ECM degradation produces various severe consequences. For instance, decreased levels of aggrecan and collagens cause various characteristic features of IDD, including NP dehydration and fibrosis, AF disorganization, and CEP calcification (Jing and Liu, 2021). In addition, loss of NP proteoglycan matrix coupled with increased breakdown products of proteoglycan attenuates the hygroscopic properties of ECM, leading to decreased water content, swelling pressure and ability to withstand load. Dehydration of the NP also suppresses the availability of nutrients and growth factors to the disc cells, leading to further impairment of IVD function (Bridgen et al., 2017).

Matrix metalloproteinases (MMPs), a family of zinc-dependent endopeptidases, are divided into six categories: collagenases, stromelysins, gelatinases, membrane-type MMPs, and unclassified types. Gelatinases (MMP-2 and MMP-9) degrades denatured collagen, laminin and gelatins. Stromelysins (MMP-3, MMP-10, and MMP-11) break down proteoglycans, collagens and gelatins. Collagen enzymes (MMP-1, MMP-8, MMP-13, and MMP-18) are predominantly cellulosic collagen. Membrane-type MMPs (MMP-14, MMP-17, MMP-24, and MMP-25) are localized to plasma membranes and have cytoplasmic domains. These MMPs play an important role in activation of signal transduction pathway and the other proteases.

MMPs are increasingly recognized as key elements in in disc tissue degradation and re-absorption. The researchers showed that MMPs played a dominant role in IDD and that elevated levels of MMP-2 and MMP-9 were associated with grading of degenerative disc disease. For instance, miR-155 is down-regulated in degenerative NP cells, and MMP-16 increased aggrecan and Col II degradation, resulting in the dehydration and IDD (Zhang et al., 2017). Mouse IVD cells were treated with GDF-5 protein and cDNA, and then IVD cell proliferation, proteoglycan production, and ECM–related gene expression were detected to assess therapeutic effect. GDF-5 can slow down the decomposition of ECM by suppressing the expression of MMP-3 (Tan et al., 2018). Stimulated with rhTGF-beta1, and to a lesser extent with GDF-5, BMSCs proliferated, and synthesized ECM rich in collagen (type I and III) when applied to a 3D hybrid construct (Jenner et al., 2007). Han et al. (2016) showed that aggrecan and collagen (type I and II) were higher expressed after GDF-5 treatment in terms of the mode of GDF-5 in promoting the chondrogenic differentiation of ADSCs. IL-1 treatment dose-dependently reduced GDF-5 gene expression in NP cells. The aggrecan and collagen II synthesis of NP cells were both upregulated after appropriate GDF-5 protein supplement, which is probably based on the mediation of ALK6 (Yang et al., 2020). The injection of GDF5-GMs *in situ* promoted ADSCs differentiation and induced the synthesis of an NP-like coat and ECM, restoring the IDD (Wu et al., 2018). Co-culture of dopamine modified and GDF-5 laden PCL-HA scaffolds and hBMSCs can promote hBMSCs' adhesion, proliferation, and chondrogenic differentiation (Xu et al., 2018). However, as reflected by increased expression of ECM mRNA levels, fibroblastic differentiation of MSCs is selectively increased in

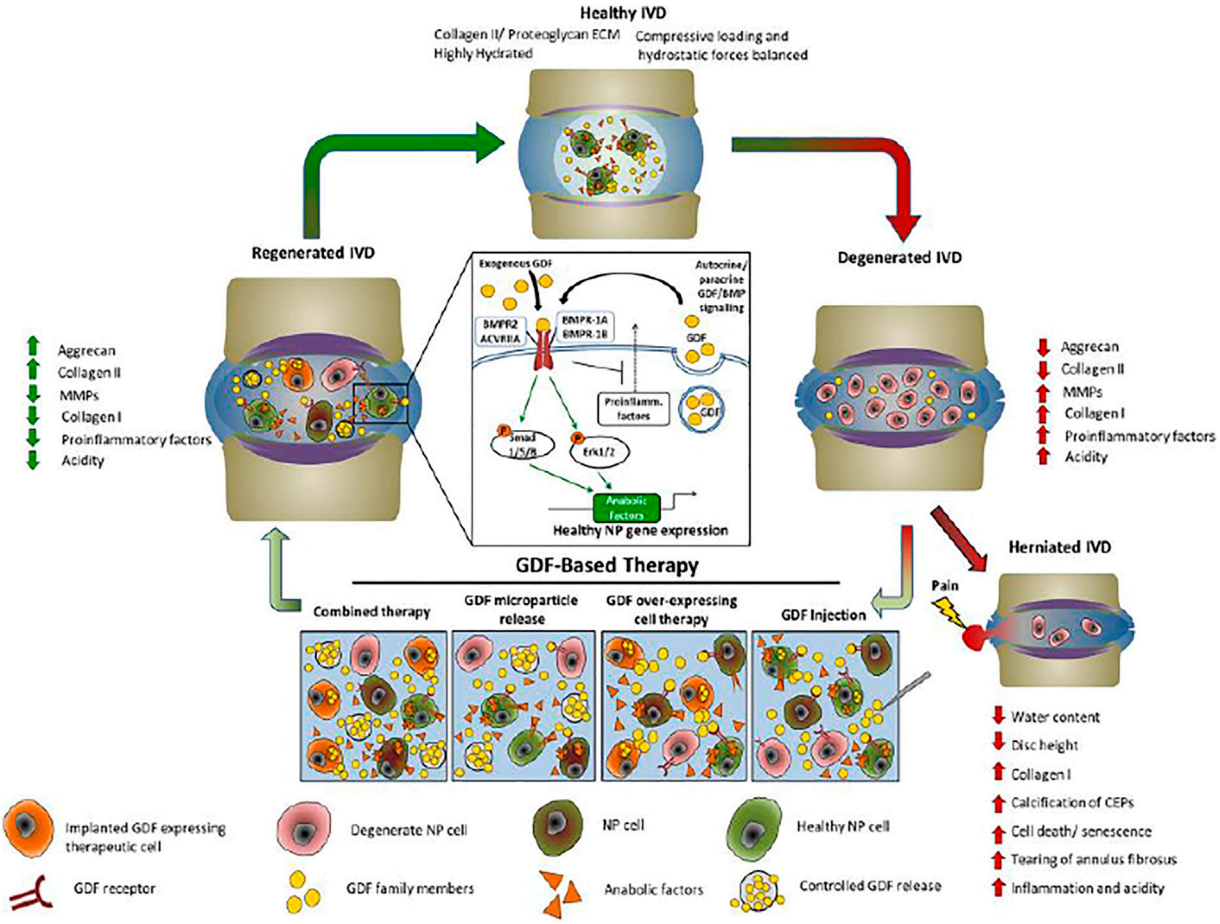

FIGURE 2 | The effect of GDF-based therapeutic cycle in IDD. The imbalance between synthesis and catabolism in normal IVDs and degenerate IVDs increase inflammation and alter ECM production. The processes accelerate increasing type I collagen and decreasing proteoglycan production, compromises tissue integrity, and cause NP herniation and CLBP. Moreover, injection of GDF has shown promise for readdressing the balance between catabolic and anabolic processes in the degenerate IVD, thereby restoring disc matrix integrity and function, and reducing pain. ECM, extracellular matrix; GDF, growth differentiation factor; IVD, intervertebral disc; MMP, matrix metalloproteinase; NP, nucleus pulposus. Reproduced with permission (Hodgkinson et al., 2019). Copyright 2019, Wiley.

the absence or presence of BMP6 and not GDF-5 under hypoxic conditions (Lui et al., 2021). Hypoxia renders cells more responsive to treatment with BMP6 as reflected by increased expression of ECM mRNA levels. These findings demonstrate that GDF-5 may be a useful growth factor to stimulate proteoglycan production in the human IDD and hence the repair of the ECM (Colombier et al., 2016). While not technically a member of the BMP family, GDF-5 is strictly associated with this family of proteins and has been shown to influence joint and skeletal development via ECM production and IVD cells growth and differentiation (Gruber et al., 2014; Luo et al., 2016).

GDF-5 has been regarded as the main regulator of ECM composition due to their capacity in enhancing production of beneficial components of the ECM while decreasing matrix metalloproteinase expression (Feng et al., 2015). Endogenously, GDF-5 expression is constant throughout different stages of degeneration (Li et al., 2015). GDF-5 is able to exert beneficial effects on IVDs and ECM without inducing heterotopic ossification because GDF-5 shows osteo-inductive activity only at high concentrations. Leslie Frapin et al. (2020) found that pullulan microbeads (PMBs) loaded with CCL5/TGF-β1/GDF-5 constitute an innovative and promising strategy for promoting cell recruitment and ECM. After injection of GDF-5 plasmid nano-microspheres were conducted in rabbits, the ECM proteins in chondrocytes was significantly increased (Chen et al., 2018). Liu et al. showed that miR-132 stimulated ECM degradation around human NP cells by direct targeting of GDF-5 and represented a therapeutic target for IDD treatments (Liu et al., 2017). Liu et al. demonstrated that miR-7 contributes to an impaired ECM in IVD through targeting GDF-5 and prevent IDD (Liu et al., 2016b) (**Figure 2**).

GDF-5 Promotes the Proliferation of IVD Cells

Many studies have assumed that a decreased cell count and ECM degradation are highly associated with the behavioural alterations

of IVD cells. Induced by various growth factors including TGFβ, IGF-1, FGF-2, and PDGF, MSCs have been modified towards NP-like differentiation in an effort to promote their therapeutic utility. However, current studies pay attention to general chondrogenic markers rather than specific NP differentiation markers. GDF-5 has been investigated as inducers of the expression of general chondrogenic genes (type II collagen; SOX9; ACAN) and, importantly, to also induce specific NP differentiation genes (SHH, KRT18, KRT19, CA12, CD24, HIF1α, and Glut-1) in MSCs. Although a significant increase in markers of hypertrophy and ossification including ALP, collagen types I and X, and OPN was observed, co-culture of high-density of MSCs together with a GDF-5 is therefore required for increased chondrogenic differentiation. However, sparse evidence showed a similar response to GDF-5 in NP cells, indicating an undesirable chondrogenic hypertrophy toward endochondral ossification. The injection of GDF-5 loaded microspheres leads to a restoration of disc height, improvement of sulfated glycosaminoglycan, DNA content, and increased mRNA levels of collagen type II (Yan et al., 2014). GDF-6 stimulates greater expression of NP-marker genes and PG production than GDF-5 in both MSCs and ASCs (Gantenbein-Ritter et al., 2011). Delivery of GDF-5 and GDF-6 through intradiscal injection into IDD models has shown promising results. For instance, in murine models, IDD after static compression showed signs of improvement with a single GDF-5 injection (Masuda et al., 2004). The number of cells expressing both aggrecan and collagen II increases significantly in the NP and AF. Similarly, delivery of GDF-5 improved disc height and histological appearance in stab models of IDD in rabbit (Chujo et al., 2006). The presence of GDF-5 was observed to colocalize with proliferating cells adjacent to the epiphyseal plate (Henriksson et al., 2012). GDF-5 suppress the expression of MMP-13 and ADAMTS-4 in human chondrocytes and expression of pro-inflammatory markers including TNF-α, IL-1β, and prostaglandinE2 (PGE2) in murine NP cells (Enochson et al., 2014). Increased miR-665 expression decreased expression of aggrecan and Col II and promoted NP cell proliferation. Furthermore, ectopic expression of miR-665 increased expression of MMP-3 and MMP-13 through suppressing GDF-5 expression in NP cells (Tan et al., 2018).

GDF-5 Inhibits Inflammation

Elevated inflammatory factors (TNF-α and IL-1β) levels have been showed to stimulate and deteriorate the development of IDD. Inflammatory molecules and signaling pathways are regarded as major contributors to the onset and development of IDD. Furthermore, the process of IDD is accompanied by an increasing of inflammatory mediators (TNF, IL-1α, IL-1β, IL-6, and IL-17) by IVD cells, which has been implicated in disc herniation, nerve irritation, and in-growth. Neurogenic factors produced by the IVD promote the expression of pain-related cation channels of the dorsal root ganglion, and the depolarization of these ion channels may induce discogenic and root-induced pain. These cytokines trigger a series of pathogenic responses by the IVD cells that can stimulate autophagy and apoptosis. They can not only up-regulate a variety of catabolic mediators that include ADAMTS-4/5, MMP-1, -2, -3, -13, -14, and can disrupt the balance of IVD tissue anabolism and catabolism, promote the degradation of extracellular matrix, which induce structural changes and spinal instability. Chemokines can promote the infiltration and activation of immune cells, thereby expanding the inflammatory cascade. The nuclear factor-κB (NF-κB) signaling pathway is implicated in various complex biological processes including inflammatory responses. The canonical pathway and non-canonical pathway contributing to the activation of the NF-κB signaling cascades. The inner region of the IVD is composed of collagen II and proteoglycans, inhibiting the NF-κB signaling pathway regulated the catabolism of IDD collagen II and aggrecan (Zhang et al., 2021b). Inflammatory mediators had degraded collagen and proteoglycan, although they had been substantially repaired. So inflammatory mediators exhibited a strictly association with IDD, with the mechanism complicated, which results in the promotion of process of IDD in multiple ways. Some of the key pro-inflammatory cytokines, such as TNF-α, IL-1α, IL-1β, IL-6, and IL-8, are found and released at sites of tissue injury which is mediated by NF-κB. Several studies have showed that GDF-5 inhibits the NF-κB signaling pathway, which reduces inflammatory factor gene transcription and diminishes inflammatory factor expression. IL-1 is naturally found within the IVD and is responsible for indirectly degrading ECM components through the production of degradative enzymes, upregulation of other cytokines, and preventing the production of ECM components. A delicate homeostasis is maintained by pro-inflammatory and anti-inflammatory subtypes of IL-1 *in vivo*, which is gradually disturbed by IDD and genetic polymorphisms.

Overexpression of GDF-5 in NP cells also dramatically decreased the protein expression levels of TNF-α, IL-1, PGE2, iNOS, COX-2, collagen-II, aggrecan, IκBα, and p-p65. Accordingly, GDF-5 suppressed the production and release of inflammatory components, relieving LPS-induced IDD. Meanwhile, IL-1β and TNF-α were both found to decrease GDF-5 expression significantly in AF cells in 3D culture (Gruber et al., 2014). The nanoparticles loaded with the dexamethasone and GDF-5 effectively inhibited proliferation of activated macrophages, indicating apoptotic induction and an anti-inflammatory effect (Wu et al., 2021) (**Figure 3**; **Table 1**).

GDFs Promotes the Differentiation of MSCs Toward an NP-cell-like Phenotype

Different types of both GDF and PDGF (in combination or not) have been shown to promote ADSC tenogenesis and cellular proliferation (Luo et al., 2009). *In vivo* and *in vitro* results illustrate that the growth factor injections has the potential to restore IDD at an early stage (Walsh et al., 2004). GDF-5 is involved in the development, maintenance and repair of cartilage and other musculoskeletal soft tissues. Similarly, the NP tissue demonstrates similar histological and biological characteristics. Moreover, a gene mutation in GDF-5 is related to IDD, as previously delineated (Williams et al., 2011). Combination of

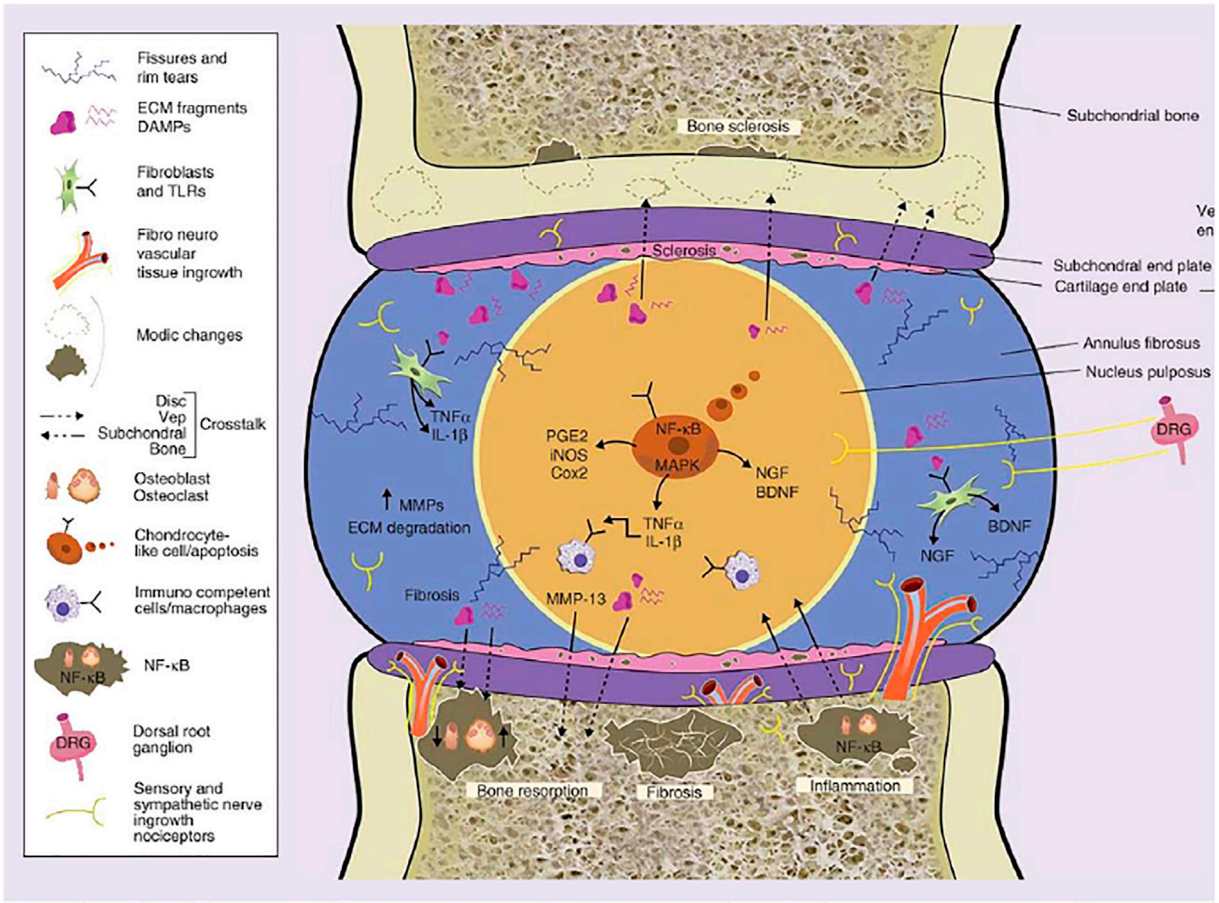

FIGURE 3 | The molecular mechanisms of low-grade inflammation in IVDJD and the crosstalk between intervertebral disc and subchondral bone. Reproduced from Eduardo et al. (Anitua and Padilla, 2018) with permission from Copyright 2018 Future Medicine.

MSCs and GDF-5-augmented fibrin hydrogel was used to glue collagen and hydrogel constructs onto bone disks to stimulate ALP activity *in vivo* model (Diederichs et al., 2018). Henry et al. (2017) propose injectable Si-HPMC/Pullulan microbeads hydrogel system for the GDF-5 and TGF-β1 delivery in IDD regenerative medicine. Du et al. showed that SOX-9 and GDF-5 co-transfected MSCs differentiated into KRT19-positive NP cells (Du et al., 2015). Notably, a consistent and potentially exploitable response during chondrogenesis of mesenchymal stem cells from osteoarthritis patients to the protein encoded by the susceptibility gene GDF-5 (Ratnayake et al., 2017). MSCs differentiated to an NP-like phenotype following direct co-culture with both nondegenerate and degenerate NP, as shown by upregulation of GDF-5, TGF-β1, IGF-1 and CTGF. Direct co-culture of MSCs with degenerated NP cells lead to upregulate matrix gene expression, accompanied by upregulation of TGF-β and GDF-5 gene expression (Strassburg et al., 2010). Yin et al. (2017) showed that miR-615-3p could inhibite the osteogenic differentiation of lumbar ligamentum flavum cells through suppression of osteogenic regulators GDF-5 and FOXO1. Henriksson et al. (2012) showed that a cellular MR from the IVD stem cell niche resulted in regeneration of the adult mammal IDD. They found that the presence of GDF-5, SLUG, SNAI1, SOX9, and β1-INTEGRIN was observed in the outer AF among rabbits in all age groups, indicating a gradual migration of cells. According to Christian et al. (Bucher et al., 2013), the GDF-5 gene transfer resulted in increased aggrecan and SOX9 expression, as well as more proteoglycans expressed in the GAG/DNA ratio. In addition, the GAG/DNA ratio was somewhat recovered in GDF-5 transfected MCS put into an IDD degeneration model. GDF-5 stimulates Smad 1/5/8 signaling, which improves chondrocyte phenotype. Furthermore, GDF-5 boosted aggrecan gene expression in chondrocyte pellet cultures while having little effect on collagen type X expression (Ayerst et al., 2017). Knocking down of GAS5 suppressed the osteogenic differentiation of hPDLSCs, whereas overexpressing GAS5 bolstered GDF-5 expression and boosted the phosphorylation of JNK and p38 in hPDLSCs (Zhang et al., 2021b). ADSCs could differentiate to the NP cell phenotype with a upregulation of multiple genes and proteins in pertinent growth factors (GDF-5, TGF-b1, IGF-1, and CTGF), and relative NP markers (HBB, FOXF1 PAX1 and CA12), ECM (ACAN, COL2A1, COL6A2 and SOX9). In addition, the expression of gene (COL2A1, ACAN, and COL6A2) in degenerate NP cells was also up-regulated (Wu et al.,

TABLE 1 | Effect of GDF5 on MSCs in culture.

GDF5 Concentration	Cell population	Culture duration	Culture conditions	Outcomes	References
100 μg/ml	hASCs	28 Days	Pullulan microbeads	Promote cell recruitment and ECM remodelling	Frapin et al. (2020)
100 ng/ml	hMSCs	18 Days	3D alginate bead	i) Up-regulate aggrecan and collagen II. ii) Promote expression of aggrecan in relation to collagen	Gantenbein-Ritter et al. (2011)
100 ng/ml	hACs and hMSCs	21 days	GE-silk fleece	GE-silk scaffold thrive hMSC towards a NP-cell-like phenotype or maintain the phenotype of native hAFC.	Frauchiger et al. (2018)
100 ng/ml	ADSCs	14 days	PNIPAAM-g-CS	i) Hydrogel support NP regeneration ii) PNIPAAM-g-CS supports the survival, proliferation, and differentiation of ADSCs toward an NP-cell-like phenotype	Christiani et al. (2021)
100 ng/ml	hACs and hMSCs	4 weeks	2D	i) Up-regulate chondrogenic gene expression in both hACs and hMSCs ii) Induce the upregulation of chondrogenic genes and synthesis of cartilage-specific matrix iii) Yield mechanically robust cartilage rich in collagen II and GAGs	Murphy et al. (2015)
50–500 ng/ml	hMSCs	21 Days	Pellet	i) Upregulate collagen II. ii) Potential synergistic relationship with TGFβ1 in driving chondrogenic differentiation	Coleman et al. (2013)
10 ng/ml; 100 ng/ml; 1,000 ng/ml	AD-MSCs	14 Days	type I collagen hydrogels	i) Differentiate to an NP-like phenotype and results in a more proteoglycan-rich matrix ii) GDF6-treated AD-MSCs have a less-stiff matrix composition iii) Induce a matrix that is more akin to the native NP-like tissue	Clarke et al. (2014)
100 ng/ml	hMSCs	Up to 7 Days	HA-pNIPAM	Support hMSC differente toward the disc phenotype	Peroglio et al. (2013)

2021). MSCs and chondrocytes from the central region of the IVD promote production of proteoglycans, collagens and other matrix proteins, making them promising candidates as cell-based IVD repair. MSCs transfected with the GDF-5 gene were added to an IVD organ culture and generated an insignificant amount of glycosaminoglycan (Bridgen et al., 2017).

MSCs are capable of self-renewal and multipotential characteristics, allowing them to differentiate into certain mesenchymal and non-mesenchymal lineages (Le Maitre et al., 2009). Beside, the differentiation of MSCs depends on various biological factors. The differentiation of MSCs into NP-like cells has been induced by the growth factors including TGF-β, IGF-1, FGF-2, and PDGF (Xia et al., 2019). These factors can activate proliferation and differentiation of endogenous stem or progenitor cells, stimulate the expression of ECM proteins, regulate the pro-inflammatory cytokines expression and suppress apoptosis and scarring of the remaining tissue (Novoseletskaya et al., 2020). MSCs are also considered to secrete a wide range of bioactive factors including ECM components to modulate the microenvironment at the primary site of action, referred to as "trophic activity" (Miranda et al., 2019). MSCs transplantation can increase the cells number and the ECM accumulation (Lu et al., 2008). NP cells can release soluble factors to direct differentiation of ASCs, which combinated with a nucleus-mimicking collagen II microenvironment enhances differentiation towards NP cell lineage. Influence of collagen type II and nucleus pulposus cells on aggregation and differentiation of adipose tissue-derived stem cells. For instance, GDF-5 can induce ADSCs differentiate into an NP-like phenotype (Zhu et al., 2019). However, the carrier might determine the fate of MSCs without the presence of GDF-5. For instance, MSCs cultured in a HA-pNIPAM under hypoxia can differentiate toward an NP-like phenotype, regardless of whether GDF-5 was added (Peroglio et al., 2013). Moreover, MSCs suspended in HA-pNIPAM without GDF-5 demonstrated stronger NP-like differentiation than MSCs pre-differentiated with GDF-5 in HA-pNIPAM in a bovine caudal disc organ culture model (Peroglio et al., 2013). This increased ratio in PG composition of ECM in comparison to collagenous matrix is a central property of NP tissue and is

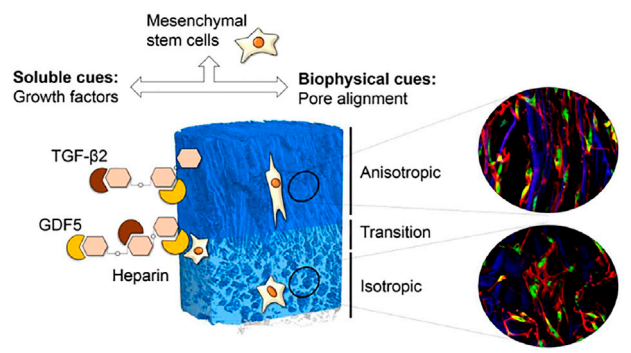

FIGURE 4 | Delivery of GDF-5 with functionalized scaffolds and their role in IVDs repair. The combined impact of GDF-5 and pore alignment can drive MSCs differentiate towards the desired NP cells phenotypes for IDD repair. Engineered scaffolds guide spatial positioning of GDF-5 at specific regions and the temporal control of quantal growth factors release. The delivery of GDF-5 enhanced the expression of markers and collagen II protein content on substrates with isotropic porosity. Reproduced from Font Tellado et al. (2018) with permission from Copyright 2018 Elsevier.

required for correct functionality. Importantly, reports to date indicate no increase in collagen X production in GDF-6 stimulated cultures as seen with other chondrogenic factors. This lack of hypertrophy and progression toward endochondral ossification when using GDF-6, coupled with the enhanced expression of NP markers, PG production and the higher aggrecan to type II collagen ratio observed in comparison to GDF-5 strongly suggests that GDF-6 is the most promising candidate to produce implantable NP cell phenotypes from MSCs or particularly ASCs. Xia et al. (2019) showed that the combination of GDF-5-loaded gelatin microspheres and NP-like cell could promote regeneration of the IVD after transplantation into rat coccygeal intervertebral discs. PMBs loaded with GDF-5/CCL5/TGF-β1 constitute an innovative sequential release system to promote hASCs recruitment and ECM remodeling (Frapin et al., 2020). This finding is confirmed using the self-assembling method to generate robust, scaffold-free neocartilage constructs using expanded hACs and MSCs. GDF-5, TGF-β1, and BMP-2 stimulation induces chondrogenesis in expanded human articular chondrocytes and marrow-derived stromal cells (Murphy et al., 2015). Human umbilical cord-mesenchymal stem cells (hUC-MSCs)-derived chondroprogenitors demonstrated expression of GDF-5, indicating better regeneration potential as compared to normal MSCs in an IDD model (Ekram et al., 2021). Benjamin et al. (Gantenbein-Ritter et al., 2011) found that GDF6 promotes greater expression of NP-marker genes and stimulates greater PG production than GDF-5 in MSCs. This increased ratio in PG composition of ECM in comparison to collagenous matrix is a central property of NP tissue (Clarke et al., 2014). Liang et al. (2010) injected an adenoviral vector carrying the GDF-5 gene into IVD and found that the gene was successfully expressed and active GDF-5 produced, which result in significant restoration of histology, and improved disc hydration as assessed through MRI. Consistently, adenoviral mediated GDF-5 delivery not only improves the expression of ECM proteins but also could promote the construction and function of NP cells at the level of transcription, translation and post-translation of ECM proteins (Feng et al., 2008) (**Figure 4**).

Limitations and Future Prospects

The aim of this review is to provide a review on the regulatory role of GDF-5 in IVD. Gene therapy for degenerative disc diseases is a promising area of research. Insertion of the GDF-5 gene demonstrates promise for applications in repairing the matrix of degenerated IDD. The aim is that the injection of growth factors could surmount the complex degenerative IVD phenotype. The inflammatory environment of the IDD is related with the convergence of GDF and cytokine signaling on kinase cascades. Moreover, the decreased presence of resident cells in IDD tissues renders GDF-5 a candidate for treating painful IDD where a pool of progenitor cells is still retained in the NP and AF. The possible limitations of GDF-5 could be speculated as follows. The mechanism of action of GDF-5 in IDD is very complex, and the study of many signaling pathways is still unclear. GDF-5 may not ultimately work in the avascular intervertebral disc tissue, and the effective dose of injection may be much higher than that of normal physiological agents due to the avascular intervertebral disc tissue. GDF-5 participates in multiple cellular processes in a time-dependent and stage-dependent manner, GDF-5 could be widely used as a therapeutic agent in the musculoskeletal system, indicating that it may help approaches for more functions in IDD. All these limitations suggest that single GDF-5 treatment might not reach its full effects. However, there are few literature reports on whether it can promote the proliferation of BMSCs. GDF-5 induce NP-like differentiation of MSCs, which is promising graft cells for IDD. The combination ofGDF-5 and MSCs and the manipulation of the tissue microenvironment allowing IDD to better respond to GDF-5 offer novel insights into the application. Moreover, to guarantee that the therapeutic effects of GDF-5 are sustained, any approach to improve the safety and feasibility of GDF-5 should be investigated.

AUTHOR CONTRIBUTIONS

BL, WKG, ZRC, and JTW wrote the manuscript. YHC revised the paper. KCZ and YKZ reviewed and edited the paper. All authors read and approved the paper.

FUNDING

This study was sponsored by the grants from the National Natural Science Foundation of China (81772391, 81974348, and 81902260).

REFERENCES

Ahlholm, V. H., Rönkkö, V., Ala-Mursula, L., Karppinen, J., and Oura, P. (2021). Modeling the Multidimensional Predictors of Multisite Musculoskeletal Pain across Adulthood-A Generalized Estimating Equations Approach. *Front. Public Health* 9, 709778. doi:10.3389/fpubh.2021.709778

Anitua, E., and Padilla, S. (2018). Biologic Therapies to Enhance Intervertebral Disc Repair. *Regen. Med.* 13 (1), 55–72. doi:10.2217/rme-2017-0111

Ayerst, B. I., Smith, R. A., Nurcombe, V., Day, A. J., Merry, C. L., and Cool, S. M. (2017). Growth Differentiation Factor 5-Mediated Enhancement of Chondrocyte Phenotype Is Inhibited by Heparin: Implications for the Use of Heparin in the Clinic and in Tissue Engineering Applications. *Tissue Eng. Part. A.* 23 (7-8), 275–292. doi:10.1089/ten.TEA.2016.0364

Bedore, J., Leask, A., and Séguin, C. A. (2014). Targeting the Extracellular Matrix: Matricellular Proteins Regulate Cell-Extracellular Matrix Communication within Distinct Niches of the Intervertebral Disc. *Matrix Biol.* 37, 124–130. doi:10.1016/j.matbio.2014.05.005

Belykh, E., Giers, M., Bardonova, L., Theodore, N., Preul, M., and Byvaltsev, V. (2015). The Role of Bone Morphogenetic Proteins 2, 7, and 14 in Approaches for Intervertebral Disk Restoration. *World Neurosurg.* 84 (4), 871–873. doi:10.1016/j.wneu.2015.08.011

Bridgen, D. T., Fearing, B. V., Jing, L., Sanchez-Adams, J., Cohan, M. C., Guilak, F., et al. (2017). Regulation of Human Nucleus Pulposus Cells by Peptide-Coupled Substrates. *Acta Biomater.* 55, 100–108. doi:10.1016/j.actbio.2017.04.019

Bucher, C., Gazdhar, A., Benneker, L. M., Geiser, T., and Gantenbein-Ritter, B. (2013). Nonviral Gene Delivery of Growth and Differentiation Factor 5 to Human Mesenchymal Stem Cells Injected into a 3D Bovine Intervertebral Disc Organ Culture System. *Stem Cell Int* 2013, 326828. doi:10.1155/2013/326828

Chen, Z., Deng, S., Yuan, D. C., Liu, K., Xiang, X. C., Cheng, L., et al. (2018). Novel Nano-Microspheres Containing Chitosan, Hyaluronic Acid, and Chondroitin Sulfate Deliver Growth and Differentiation Factor-5 Plasmid for Osteoarthritis Gene Therapy. *J. Zhejiang Univ. Sci. B* 19 (12), 910–923. doi:10.1631/jzus.B1800095

Christiani, T., Mys, K., Dyer, K., Kadlowec, J., Iftode, C., and Vernengo, A. J. (2021). Using Embedded Alginate Microparticles to Tune the Properties of *In Situ* Forming poly(N-Isopropylacrylamide)-Graft-Chondroitin Sulfate Bioadhesive Hydrogels for Replacement and Repair of the Nucleus Pulposus of the Intervertebral Disc. *JOR Spine* 4 (3), e1161. doi:10.1002/jsp2.1161

Chujo, T., An, H. S., Akeda, K., Miyamoto, K., Muehleman, C., Attawia, M., et al. (2006). Effects of Growth Differentiation Factor-5 on the Intervertebral Disc--In Vitro Bovine Study and *In Vivo* Rabbit Disc Degeneration Model Study. *Spine (Phila Pa 1976)* 31 (25), 2909–2917. doi:10.1097/01.brs.0000248428.22823.86

Clarke, L. E., McConnell, J. C., Sherratt, M. J., Derby, B., Richardson, S. M., and Hoyland, J. A. (2014). Growth Differentiation Factor 6 and Transforming Growth Factor-Beta Differentially Mediate Mesenchymal Stem Cell Differentiation, Composition, and Micromechanical Properties of Nucleus Pulposus Constructs. *Arthritis Res. Ther.* 16 (2), R67. doi:10.1186/ar4505

Coleman, C. M., Vaughan, E. E., Browe, D. C., Mooney, E., Howard, L., and Barry, F. (2013). Growth Differentiation Factor-5 Enhances *In Vitro* Mesenchymal Stromal Cell Chondrogenesis and Hypertrophy. *Stem Cell Dev* 22 (13), 1968–1976. doi:10.1089/scd.2012.0282

Colombier, P., Clouet, J., Boyer, C., Ruel, M., Bonin, G., Lesoeur, J., et al. (2016). TGF-β1 and GDF5 Act Synergistically to Drive the Differentiation of Human Adipose Stromal Cells toward Nucleus Pulposus-like Cells. *Stem Cells* 34 (3), 653–667. doi:10.1002/stem.2249

Daniels, J., Binch, A. A., and Le Maitre, C. L. (2017). Inhibiting IL-1 Signaling Pathways to Inhibit Catabolic Processes in Disc Degeneration. *J. Orthop. Res.* 35 (1), 74–85. doi:10.1002/jor.23363

Diederichs, S., Renz, Y., Hagmann, S., Lotz, B., Seebach, E., and Richter, W. (2018). Stimulation of a Calcified Cartilage Connecting Zone by GDF-5-Augmented Fibrin Hydrogel in a Novel Layered Ectopic *In Vivo* Model. *J. Biomed. Mater. Res. B Appl. Biomater.* 106 (6), 2214–2224. doi:10.1002/jbm.b.34027

Du, Z. Y. H., Li, S., Wu, H., Bai, M., Cao, Z., and Meng, G. (2015). Differentiation of SOX-9 and GDF-5 Co-transfected Bone Marrow Mesenchymal Stem Cells into Nucleus Pulposus Cells. *Zhongguo Zuzhigongcheng Yanjiu* 19 (19), 2953–2958. doi:10.3969/j.issn.2095-4344.2015.19.001

Ekram, S., Khalid, S., Bashir, I., Salim, A., and Khan, I. (2021). Human Umbilical Cord-Derived Mesenchymal Stem Cells and Their Chondroprogenitor Derivatives Reduced Pain and Inflammation Signaling and Promote Regeneration in a Rat Intervertebral Disc Degeneration Model. *Mol. Cel Biochem* 476 (8), 3191–3205. doi:10.1007/s11010-021-04155-9

Enochson, L., Stenberg, J., Brittberg, M., and Lindahl, A. (2014). GDF5 Reduces MMP13 Expression in Human Chondrocytes via DKK1 Mediated Canonical Wnt Signaling Inhibition. *Osteoarthritis Cartilage* 22 (4), 566–577. doi:10.1016/j.joca.2014.02.004

Feng, G., Wan, Y., Balian, G., Laurencin, C. T., and Li, X. (2008). Adenovirus-mediated Expression of Growth and Differentiation Factor-5 Promotes Chondrogenesis of Adipose Stem Cells. *Growth Factors* 26 (3), 132–142. doi:10.1080/08977190802105917

Feng, C., Liu, H., Yang, Y., Huang, B., and Zhou, Y. (2015). Growth and Differentiation Factor-5 Contributes to the Structural and Functional Maintenance of the Intervertebral Disc. *Cell Physiol Biochem* 35 (1), 1–16. doi:10.1159/000369670

Fitzgerald, M. J., Mustapich, T., Liang, H., Larsen, C. G., Nellans, K. W., and Grande, D. A. (2021). Tendon Transection Healing Can Be Improved with Adipose-Derived Stem Cells Cultured with Growth Differentiation Factor 5 and Platelet-Derived Growth Factor. *Hand (N Y)* 00 (0), 1–10. doi:10.1177/15589447211028929

Font Tellado, S., Chiera, S., Bonani, W., Poh, P. S. P., Migliaresi, C., Motta, A., et al. (2018). Heparin Functionalization Increases Retention of TGF-B2 and GDF5 on Biphasic Silk Fibroin Scaffolds for Tendon/ligament-To-Bone Tissue Engineering. *Acta Biomater.* 72, 150–166. doi:10.1016/j.actbio.2018.03.017

Frapin, L., Clouet, J., Chédeville, C., Moraru, C., Samarut, E., Henry, N., et al. (2020). Controlled Release of Biological Factors for Endogenous Progenitor Cell Migration and Intervertebral Disc Extracellular Matrix Remodelling. *Biomaterials* 253, 120107. doi:10.1016/j.biomaterials.2020.120107

Frauchiger, D. A., Heeb, S. R., May, R. D., Wöltje, M., Benneker, L. M., and Gantenbein, B. (2018). Differentiation of MSC and Annulus Fibrosus Cells on Genetically Engineered Silk Fleece-Membrane-Composites Enriched for GDF-6 or TGF-B3. *J. Orthop. Res.* 36 (5), 1324–1333. doi:10.1002/jor.23778

Gantenbein-Ritter, B., Benneker, L. M., Alini, M., and Grad, S. (2011). Differential Response of Human Bone Marrow Stromal Cells to Either TGF-B(1) or rhGDF-5. *Eur. Spine J.* 20 (6), 962–971. doi:10.1007/s00586-010-1619-z

Genovesi, M. L., Guadagnolo, D., Marchionni, E., Giovannetti, A., Traversa, A., Panzironi, N., et al. (2021). GDF5 Mutation Case Report and a Systematic Review of Molecular and Clinical Spectrum: Expanding Current Knowledge on Genotype-Phenotype Correlations. *Bone* 144, 115803. doi:10.1016/j.bone.2020.115803

Gruber, H. E., Hoelscher, G. L., Ingram, J. A., Bethea, S., and Hanley, E. N. (2014). Growth and Differentiation Factor-5 (GDF-5) in the Human Intervertebral Annulus Cells and its Modulation by IL-1ß and TNF-α *In Vitro*. *Exp. Mol. Pathol.* 96 (2), 225–229. doi:10.1016/j.yexmp.2014.02.005

Han, C., Ren, Y., Jia, Y., Kong, L., Eerdun, T., and Wu, L. (2016). The Effective Mode of Growth and Differentiation Factor-5 in Promoting the Chondrogenic Differentiation of Adipose-Derived Stromal Cells. *Cell Tissue Bank* 17 (1), 105–115. doi:10.1007/s10561-015-9517-6

Henriksson, H. B., Svala, E., Skioldebrand, E., Lindahl, A., and Brisby, H. (2012). Support of Concept that Migrating Progenitor Cells from Stem Cell Niches Contribute to normal Regeneration of the Adult Mammal Intervertebral Disc: a Descriptive Study in the New Zealand white Rabbit. *Spine (Phila Pa 1976)* 37 (9), 722–732. doi:10.1097/BRS.0b013e318231c2f7

Henriksson, H. B., Papadimitriou, N., Tschernitz, S., Svala, E., Skioldebrand, E., Windahl, S., et al. (2015). Indications of that Migration of Stem Cells Is Influenced by the Extra Cellular Matrix Architecture in the Mammalian Intervertebral Disk Region. *Tissue Cell* 47 (5), 439–455. doi:10.1016/j.tice.2015.08.001

Henry, N., Clouet, J., Fragale, A., Griveau, L., Chédeville, C., Véziers, J., et al. (2017). Pullulan microbeads/Si-HPMC Hydrogel Injectable System for the Sustained Delivery of GDF-5 and TGF-B1: New Insight into Intervertebral Disc Regenerative Medicine. *Drug Deliv.* 24 (1), 999–1010. doi:10.1080/10717544.2017.1340362

Hodgkinson, T., Shen, B., Diwan, A., Hoyland, J. A., and Richardson, S. M. (2019). Therapeutic Potential of Growth Differentiation Factors in the Treatment of Degenerative Disc Diseases. *JOR Spine* 2 (1), e1045. doi:10.1002/jsp2.1045

Jenner, J. M., van Eijk, F., Saris, D. B., Willems, W. J., Dhert, W. J., and Creemers, L. B. (2007). Effect of Transforming Growth Factor-Beta and Growth Differentiation Factor-5 on Proliferation and Matrix Production by Human Bone Marrow Stromal Cells Cultured on Braided Poly Lactic-Co-Glycolic Acid Scaffolds for Ligament Tissue Engineering. *Tissue Eng.* 13 (7), 1573–1582. doi:10.1089/ten.2006.0208

Jing, W., and Liu, W. (2021). HOXC13-AS Induced Extracellular Matrix Loss via Targeting miR-497-5p/ADAMTS5 in Intervertebral Disc. *Front. Mol. Biosci.* 8, 643997. doi:10.3389/fmolb.2021.643997

Kritschil, R., Scott, M., Sowa, G., and Vo, N. (2021). Role of Autophagy in Intervertebral Disc Degeneration. *J. Cel Physiol* 237, 1266–1284. doi:10.1002/jcp.30631

Le Maitre, C. L., Freemont, A. J., and Hoyland, J. A. (2009). Expression of Cartilage-Derived Morphogenetic Protein in Human Intervertebral Discs and its Effect on Matrix Synthesis in Degenerate Human Nucleus Pulposus Cells. *Arthritis Res. Ther.* 11 (5), R137. doi:10.1186/ar2808

Li, Y. F., Tang, X. Z., Liang, C. G., Hui, Y. M., Ji, Y. H., Xu, W., et al. (2015). Role of Growth Differentiation Factor-5 and Bone Morphogenetic Protein Type II Receptor in the Development of Lumbar Intervertebral Disc Degeneration. *Int. J. Clin. Exp. Pathol.* 8 (1), 719–726.

Liang, H., Ma, S. Y., Feng, G., Shen, F. H., and Joshua Li, X. (2010). Therapeutic Effects of Adenovirus-Mediated Growth and Differentiation Factor-5 in a Mice Disc Degeneration Model Induced by Annulus Needle Puncture. *Spine J.* 10 (1), 32–41. doi:10.1016/j.spinee.2009.10.006

Liu, W., Zhang, Y., Feng, X., Li, S., Gao, Y., Wang, K., et al. (2016). Inhibition of microRNA-34a Prevents IL-1β-induced Extracellular Matrix Degradation in Nucleus Pulposus by Increasing GDF5 Expression. *Exp. Biol. Med. (Maywood)* 241 (17), 1924–1932. doi:10.1177/1535370216657444

Liu, W., Zhang, Y., Xia, P., Li, S., Feng, X., Gao, Y., et al. (2016). MicroRNA-7 Regulates IL-1β-induced Extracellular Matrix Degeneration by Targeting GDF5 in Human Nucleus Pulposus Cells. *Biomed. Pharmacother.* 83, 1414–1421. doi:10.1016/j.biopha.2016.08.062

Liu, W., Xia, P., Feng, J., Kang, L., Huang, M., Wang, K., et al. (2017). MicroRNA-132 Upregulation Promotes Matrix Degradation in Intervertebral Disc Degeneration. *Exp. Cel Res* 359 (1), 39–49. doi:10.1016/j.yexcr.2017.08.011

Lu, Z. F., Doulabi, B. Z., Wuisman, P. I., Bank, R. A., and Helder, M. N. (2008). Influence of Collagen Type II and Nucleus Pulposus Cells on Aggregation and Differentiation of Adipose Tissue-Derived Stem Cells. *J. Cel Mol Med* 12 (6b), 2812–2822. doi:10.1111/j.1582-4934.2008.00278.x

Lui, H., Denbeigh, J., Vaquette, C., Tran, H. M., Dietz, A. B., Cool, S. M., et al. (2021). Fibroblastic Differentiation of Mesenchymal Stem/stromal Cells (MSCs) Is Enhanced by Hypoxia in 3D Cultures Treated with Bone Morphogenetic Protein 6 (BMP6) and Growth and Differentiation Factor 5 (GDF5). *Gene* 788, 145662. doi:10.1016/j.gene.2021.145662

Luo, Q., Song, G., Song, Y., Xu, B., Qin, J., and Shi, Y. (2009). Indirect Co-culture with Tenocytes Promotes Proliferation and mRNA Expression of Tendon/ligament Related Genes in Rat Bone Marrow Mesenchymal Stem Cells. *Cytotechnology* 61 (1-2), 1–10. doi:10.1007/s10616-009-9233-9

Luo, X. W., Liu, K., Chen, Z., Zhao, M., Han, X. W., Bai, Y. G., et al. (2016). Adenovirus-mediated GDF-5 Promotes the Extracellular Matrix Expression in Degenerative Nucleus Pulposus Cells. *J. Zhejiang Univ. Sci. B* 17 (1), 30–42. doi:10.1631/jzus.B1500182

Massagué, J. (2000). How Cells Read TGF-Beta Signals. *Nat. Rev. Mol. Cel Biol* 1 (3), 169–178. doi:10.1038/35043051

Masuda, K., Oegema, T. R., and An, H. S. (2004). Growth Factors and Treatment of Intervertebral Disc Degeneration. *Spine (Phila Pa 1976)* 29 (6 Suppl. l), 2757–2769. doi:10.1097/01.brs.0000146048.14946.af

Masuya, H., Nishida, K., Furuichi, T., Toki, H., Nishimura, G., Kawabata, H., et al. (2007). A Novel Dominant-Negative Mutation in Gdf5 Generated by ENU Mutagenesis Impairs Joint Formation and Causes Osteoarthritis in Mice. *Hum. Mol. Genet.* 16 (19), 2366–2375. doi:10.1093/hmg/ddm195

Mayer, J. E., Iatridis, J. C., Chan, D., Qureshi, S. A., Gottesman, O., and Hecht, A. C. (2013). Genetic Polymorphisms Associated with Intervertebral Disc Degeneration. *Spine J.* 13 (3), 299–317. doi:10.1016/j.spinee.2013.01.041

Miranda, J. P., Camões, S. P., Gaspar, M. M., Rodrigues, J. S., Carvalheiro, M., Bárcia, R. N., et al. (2019). The Secretome Derived from 3D-Cultured Umbilical Cord Tissue MSCs Counteracts Manifestations Typifying Rheumatoid Arthritis. *Front. Immunol.* 10, 18. doi:10.3389/fimmu.2019.00018

Murphy, M. K., Huey, D. J., Hu, J. C., and Athanasiou, K. A. (2015). TGF-β1, GDF-5, and BMP-2 Stimulation Induces Chondrogenesis in Expanded Human Articular Chondrocytes and Marrow-Derived Stromal Cells. *Stem Cells* 33 (3), 762–773. doi:10.1002/stem.1890

Novoseletskaya, E., Grigorieva, O., Nimiritsky, P., Basalova, N., Eremichev, R., Milovskaya, I., et al. (2020). Mesenchymal Stromal Cell-Produced Components of Extracellular Matrix Potentiate Multipotent Stem Cell Response to Differentiation Stimuli. *Front Cel Dev Biol* 8, 555378. doi:10.3389/fcell.2020.555378

Paesold, G., Nerlich, A. G., and Boos, N. (2007). Biological Treatment Strategies for Disc Degeneration: Potentials and Shortcomings. *Eur. Spine J.* 16 (4), 447–468. doi:10.1007/s00586-006-0220-y

Peroglio, M., Eglin, D., Benneker, L. M., Alini, M., and Grad, S. (2013). Thermoreversible Hyaluronan-Based Hydrogel Supports *In Vitro* and *Ex Vivo* Disc-like Differentiation of Human Mesenchymal Stem Cells. *Spine J.* 13 (11), 1627–1639. doi:10.1016/j.spinee.2013.05.029

Ratnayake, M., Tselepi, M., Bloxham, R., Plöger, F., Reynard, L. N., and Loughlin, J. (2017). A Consistent and Potentially Exploitable Response during Chondrogenesis of Mesenchymal Stem Cells from Osteoarthritis Patients to the Protein Encoded by the Susceptibility Gene GDF5. *PLoS One* 12 (5), e0176523. doi:10.1371/journal.pone.0176523

Strassburg, S., Richardson, S. M., Freemont, A. J., and Hoyland, J. A. (2010). Co-culture Induces Mesenchymal Stem Cell Differentiation and Modulation of the Degenerate Human Nucleus Pulposus Cell Phenotype. *Regen. Med.* 5 (5), 701–711. doi:10.2217/rme.10.59

Tan, H., Zhao, L., Song, R., Liu, Y., and Wang, L. (2018). microRNA-665 Promotes the Proliferation and Matrix Degradation of Nucleus Pulposus through Targeting GDF5 in Intervertebral Disc Degeneration. *J. Cel Biochem* 119 (9), 7218–7225. doi:10.1002/jcb.26888

Walsh, A. J., Bradford, D. S., and Lotz, J. C. (2004). *In Vivo* growth Factor Treatment of Degenerated Intervertebral Discs. *Spine (Phila Pa 1976)* 29 (2), 156–163. doi:10.1097/01.BRS.0000107231.67854.9F

Wang, Z., Wu, Y., Zhao, Z., Liu, C., and Zhang, L. (2021). Study on Transorgan Regulation of Intervertebral Disc and Extra-skeletal Organs through Exosomes Derived from Bone Marrow Mesenchymal Stem Cells. *Front. Cel Dev Biol* 9, 741183. doi:10.3389/fcell.2021.741183

Williams, F. M., Popham, M., Hart, D. J., de Schepper, E., Bierma-Zeinstra, S., Hofman, A., et al. (2011). GDF5 Single-Nucleotide Polymorphism Rs143383 Is Associated with Lumbar Disc Degeneration in Northern European Women. *Arthritis Rheum.* 63 (3), 708–712. doi:10.1002/art.30169

Wu, S. C., Chen, C. H., Wang, J. Y., Lin, Y. S., Chang, J. K., and Ho, M. L. (2018). Hyaluronan Size Alters Chondrogenesis of Adipose-Derived Stem Cells via the CD44/ERK/SOX-9 Pathway. *Acta Biomater.* 66, 224–237. doi:10.1016/j.actbio.2017.11.025

Wu, X., Li, P., Cheng, J., Xu, Q., Lu, B., Han, C., et al. (2021). ROS-sensitive Nanoparticles Co-delivering Dexamethasone and CDMP-1 for the Treatment of Osteoarthritis through Chondrogenic Differentiation Induction and Inflammation Inhibition. *Front. Bioeng. Biotechnol.* 9, 608150. doi:10.3389/fbioe.2021.608150

Xia, K., Zhu, J., Hua, J., Gong, Z., Yu, C., Zhou, X., et al. (2019). Intradiscal Injection of Induced Pluripotent Stem Cell-Derived Nucleus Pulposus-like Cell-Seeded Polymeric Microspheres Promotes Rat Disc Regeneration. *Stem Cell Int* 2019, 6806540. doi:10.1155/2019/6806540

Xu, Y., Wei, B., Zhou, J., Yao, Q., Wang, L., and Na, J. (2018). Dopamine Modified and Cartilage Derived Morphogenetic Protein 1 Laden Polycaprolactone-Hydroxyapatite Composite Scaffolds Fabricated by Three-Dimensional Printing Improve Chondrogenic Differentiation of Human Bone Marrow Mesenchymal Stem Cells. *Zhongguo Xiu Fu Chong Jian Wai Ke Za Zhi* 32 (2), 215–222. doi:10.7507/1002-1892.201708017

Xu, X., Hong, P., Wang, Z., Tang, Z., and Li, K. (2021). MicroRNAs in Transforming Growth Factor-Beta Signaling Pathway Associated with Fibrosis Involving Different Systems of the Human Body. *Front. Mol. Biosci.* 8, 707461. doi:10.3389/fmolb.2021.707461

Yan, J., Yang, S., Sun, H., Guo, D., Wu, B., Ji, F., et al. (2014). Effects of Releasing Recombinant Human Growth and Differentiation Factor-5 from Poly(lactic-Co-Glycolic Acid) Microspheres for Repair of the Rat Degenerated Intervertebral Disc. *J. Biomater. Appl.* 29 (1), 72–80. doi:10.1177/0885328213515034

Yang, Z., Gao, X. J., and Zhao, X. (2020). CDMP1 Promotes Type II Collagen and Aggrecan Synthesis of Nucleus Pulposus Cell via the Mediation of ALK6. *Eur. Rev. Med. Pharmacol. Sci.* 24 (21), 10975–10983. doi:10.26355/eurrev_202011_23581

Yin, J., Zhuang, G., Zhu, Y., Hu, X., Zhao, H., Zhang, R., et al. (2017). MiR-615-3p Inhibits the Osteogenic Differentiation of Human Lumbar Ligamentum Flavum Cells via Suppression of Osteogenic Regulators GDF5 and FOXO1. *Cell Biol Int* 41 (7), 779–786. doi:10.1002/cbin.10780

Zhang, W. L., Chen, Y. F., Meng, H. Z., Du, J. J., Luan, G. N., Wang, H. Q., et al. (2017). Role of miR-155 in the Regulation of MMP-16 Expression in Intervertebral Disc Degeneration. *J. Orthop. Res.* 35 (6), 1323–1334. doi:10.1002/jor.23313

Zhang, H. J., Liao, H. Y., Bai, D. Y., Wang, Z. Q., and Xie, X. W. (2021). MAPK/ERK Signaling Pathway: A Potential Target for the Treatment of Intervertebral Disc Degeneration. *Biomed. Pharmacother.* 143, 112170. doi:10.1016/j.biopha.2021.112170

Zhang, G. Z., Liu, M. Q., Chen, H. W., Wu, Z. L., Gao, Y. C., Ma, Z. J., et al. (2021). NF-κB Signalling Pathways in Nucleus Pulposus Cell Function and Intervertebral Disc Degeneration. *Cell Prolif* 54 (7), e13057. doi:10.1111/cpr.13057

Zhu, J., Xia, K., Yu, W., Wang, Y., Hua, J., Liu, B., et al. (2019). Sustained Release of GDF5 from a Designed Coacervate Attenuates Disc Degeneration in a Rat Model. *Acta Biomater.* 86, 300–311. doi:10.1016/j.actbio.2019.01.028

Conflict of Interest: The authors declare that the research was conducted in the absence of any commercial or financial relationships that could be construed as a potential conflict of interest.

Publisher's Note: All claims expressed in this article are solely those of the authors and do not necessarily represent those of their affiliated organizations, or those of the publisher, the editors and the reviewers. Any product that may be evaluated in this article, or claim that may be made by its manufacturer, is not guaranteed or endorsed by the publisher.

frontiers | Frontiers in Pharmacology

REVIEW
published: 23 June 2022
doi: 10.3389/fphar.2022.915355

Optimizing Antimicrobial Therapy by Integrating Multi-Omics With Pharmacokinetic/Pharmacodynamic Models and Precision Dosing

Hui-Yin Yow[1,2], *Kayatri Govindaraju*[3], *Audrey Huili Lim*[4] *and Nusaibah Abdul Rahim*[5]*

[1]Faculty of Health and Medical Sciences, School of Pharmacy, Taylor's University, Subang Jaya, Malaysia, [2]Centre for Drug Discovery and Molecular Pharmacology, Faculty of Health and Medical Sciences, Taylor's University, Subang Jaya, Malaysia, [3]Department of Pharmaceutical Life Sciences, Faculty of Pharmacy, Universiti Malaya, Kuala Lumpur, Malaysia, [4]Centre for Clinical Outcome Research (CCORE), Institute for Clinical Research, National Institutes of Health, Shah Alam, Malaysia, [5]Department of Clinical Pharmacy and Pharmacy Practice, Faculty of Pharmacy, Universiti Malaya, Kuala Lumpur, Malaysia

In the era of "*Bad Bugs, No Drugs*," optimizing antibiotic therapy against multi-drug resistant (MDR) pathogens is crucial. Mathematical modelling has been employed to further optimize dosing regimens. These models include mechanism-based PK/PD models, systems-based models, quantitative systems pharmacology (QSP) and population PK models. Quantitative systems pharmacology has significant potential in precision antimicrobial chemotherapy in the clinic. Population PK models have been employed in model-informed precision dosing (MIPD). Several antibiotics require close monitoring and dose adjustments in order to ensure optimal outcomes in patients with infectious diseases. Success or failure of antibiotic therapy is dependent on the patient, antibiotic and bacterium. For some drugs, treatment responses vary greatly between individuals due to genotype and disease characteristics. Thus, for these drugs, tailored dosing is required for successful therapy. With antibiotics, inappropriate dosing such as insufficient dosing may put patients at risk of therapeutic failure which could lead to mortality. Conversely, doses that are too high could lead to toxicities. Hence, precision dosing which customizes doses to individual patients is crucial for antibiotics especially those with a narrow therapeutic index. In this review, we discuss the various strategies in optimizing antimicrobial therapy to address the challenges in the management of infectious diseases and delivering personalized therapy.

Keywords: antimicrobial therapy, pharmacokinetic/pharmacodynamic (PK/PD), mechanism-based PK/PD models, multi-omics, systems pharmacology, precision dosing

OPEN ACCESS

Edited by:
Chuanpin Chen,
Central South University, China

Reviewed by:
Michael Super,
Harvard University, United States
Supatat Chumnumwat,
Mahidol University, Thailand

***Correspondence:**
Nusaibah Abdul Rahim
nusaibah.abdulrahim@um.edu.my

Specialty section:
This article was submitted to Translational Pharmacology, a section of the journal Frontiers in Pharmacology

Received: *07 April 2022*
Accepted: *01 June 2022*
Published: *23 June 2022*

Citation:
Yow H-Y, Govindaraju K, Lim AH and Abdul Rahim N (2022) Optimizing Antimicrobial Therapy by Integrating Multi-Omics With Pharmacokinetic/Pharmacodynamic Models and Precision Dosing. Front. Pharmacol. 13:915355. doi: 10.3389/fphar.2022.915355

INTRODUCTION

Antibiotics have been regarded as one of the most instrumental advances in modern healthcare from the beginning of their discovery until the present day in controlling infectious diseases that were the leading causes of human morbidity and mortality. However, despite their indispensable contribution to global healthcare, their equilibrium in the arms race against microorganisms is fragile. Inappropriate and overuse of antibiotics lead to the emergence and spread of antibiotic-resistant bacteria in the community, which significantly threaten human health and the global economy. In 2019 the World Health Organization (WHO), reported that antimicrobial resistance (AMR) is one of

the top 10 global public health threats facing humanity. The acceleration of antibiotic resistance is one of the most alarming consequences of antibiotic overuse. According to a recent study, 50% of all the antibiotics prescribed for people are not needed or are not optimally effective as prescribed in US hospitals (Magill et al., 2021).

AMR occurs naturally over time, usually through genetic changes, and antibiotics are becoming increasingly ineffective as drug resistance spreads globally, making it more difficult to treat infections and death. At the heart of this problem is the dearth of antimicrobial drugs development in the clinical pipeline. In 2019, WHO identified 32 antibiotics in clinical development that address the WHO list of priority pathogens, of which only six were classified as innovative. The findings clearly highlight the pressing need for greater innovation and investment in developing new antimicrobials for efficient control and management of infectious diseases.

Presently, the progress in the development of antimicrobials is driven by the modification of existing classes of antimicrobials rather than by the discovery of new antimicrobial classes (Aminov, 2017). Thus, hindering the discovery of new classes of antimicrobials for decades. However, acknowledging the battle against rapidly emerging bacterial resistance is a relentless clinical problem and cannot be solved once and for all; we can no longer rely entirely on discovering new antibiotics. Instead, implementing better strategies for the use of older and readily available antibiotics would be worthwhile pursuing to handle the problem as efficiently and safely as possible. These strategies should be formulated based on how antimicrobial resistance develops and on identifying critical checkpoints where preventive measures could be imposed to stop or at least hamper the process (Chernov et al., 2019).

One of the strategies to contain the rapid expansion of resistance could be to emphasize the reengineering and optimization of existing antimicrobials since the new antimicrobial drug development has been largely focused on extensive modifications of existing natural drugs. For example, due to toxicity concerns, antibiotics such as chloramphenicol which may cause neurotoxicity, and haematological disorders have had derivatives developed, including florfenicol and thiamphenicol, which exhibit less toxicity (Dinos et al., 2016). However, to date, florfenicol and thiamphenicol have only been used in animals (Shin et al., 2005; Wei et al., 2016). Promisingly, the application of pharmacokinetic and pharmacodynamics (PK/PD) strategies may allow more therapeutically effective use of some existing antibiotics. Antimicrobials that have previously been shelved due to toxicity concerns, such as daptomycin and colistin, are now being used to treat life-threatening infections, highlighting the importance of PK/PD data in the optimal use of old antimicrobials (Ortwine et al., 2015). Another strategy worthy of consideration is combining antibiotics with non-antimicrobial compounds that display synergistic effects to extend the useful life of some older antibiotics (Ejim et al., 2011). Mechanism-based PK/PD models have also been developed to further investigate and inform optimal dosing regimens. Moreover, the use of omics technologies could substantially contribute to the discovery/development of these compounds and identify novel targets. The advances in transcriptomics, proteomics, and metabolomics permit the profiling of bacteria during antimicrobial exposure and have revealed the involvement of many pathways in antimicrobial response and resistance (Pulido et al., 2016). This has led to the emergence of quantitative systems pharmacology (QSP) and model-informed precision dosing (MIPD).

Herein in this review, we discuss the various strategies for optimizing antimicrobial therapy to address the challenges in the management of infectious diseases and delivering personalized therapy.

PK/PD CONSIDERATIONS WHEN OPTIMIZING ANTIBIOTIC DOSING

In addition to the appropriateness of antimicrobial agent selection (both mono- and combination therapies), optimal antimicrobial dosing is another key factor for therapeutic success in managing infectious diseases, while minimizing the toxicity and preventing the emergence of antimicrobial resistance (**Figure 1**). Suboptimal antimicrobial dosing has been associated with poorer clinical outcomes, in terms of clinical cure rate and mortality (Roberts et al., 2014; Appaneal et al., 2021). This is attributed to inadequate drug exposure in achieving PK/PD targets in individual patients (Hoo et al., 2017). This issue is closely related to the physiological changes of patients, which are commonly observed in critically ill, comorbidities, elderly and obese patients (Pai and Bearden, 2007; Chai et al., 2020; Rawson et al., 2021). Pharmacokinetic variation is well-explained in critically ill patients, who often present with altered pharmacokinetic parameters. These include fluid shifts due to capillary leak syndrome leading to an increase in the volume of distribution of hydrophilic antimicrobial agents (e.g., beta-lactams and aminoglycosides) and a decrease in plasma concentration, hypoalbuminemia causing changes in protein binding for high protein-bound antimicrobials (e.g., ertapenem and flucloxacillin) and organ dysfunction that reduces or increases the drug clearance through renal and hepatic systems and therefore leading to pharmacokinetic variability (Cai et al., 2012; Chai et al., 2020; Rawson et al., 2021).

Besides inter-individual variability, antimicrobial dosing is also affected by two other factors: antimicrobial and microorganism factors. Antibiotics available vary in physicochemical and pharmacokinetic properties, including solubility, the volume of distribution, protein binding and drug clearance (Hoo et al., 2017). These properties must be taken into consideration to estimate the antimicrobial disposition in the body. To understand the application of antimicrobial dosing to efficacy, the pharmacology of antimicrobial agents in terms of pharmacokinetic and pharmacodynamic profiles need to be integrated (**Table 1**). Antimicrobial dosing is conventionally prescribed using a fixed-dose based on a one-size-fits-all approach, where pharmacokinetics and pharmacodynamic variabilities are not taken into account and the antimicrobial dosing regimen is chosen according to the drug exposure and pharmacokinetic

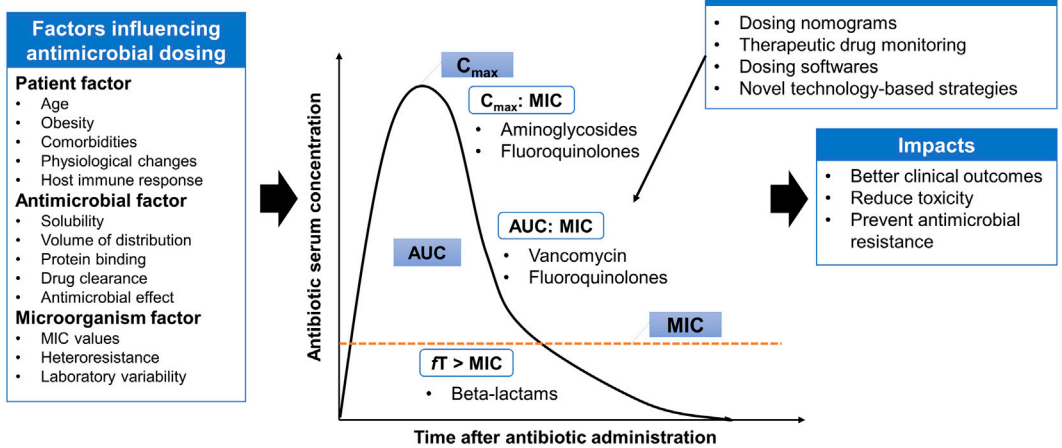

FIGURE 1 | Antimicrobial pharmacokinetic-pharmacodynamic is affected by three main factors: patient, antimicrobial and microorganism factors. Several approaches are implemented in the clinical practice settings or under the experimental phase to provide individualized dosing and address some degree of variabilities. AUC: area under the curve; MIC: minimum inhibitory concentration; C_{max}: maximum concentration; *f*T > MIC: Time that free serum concentration above minimum inhibitory concentration; C_{max}:MIC: ratio of maximum concentration to minimum inhibitory concentration; AUC:MIC: ratio of area under the concentration-curve to minimum inhibitory concentration.

TABLE 1 | Pharmacokinetic characteristics of commonly used antibiotics with their pattern of killing and pharmacokinetic/pharmacodynamic target.

Antibiotic	Pharmacokinetic properties (Hoo et al., 2017)				Pattern of antimicrobial activity	PK/PD index (Kowalska-Krochmal & Dudek-Wicher 2021; Rawson et al., 2021)
	Solubility	V_d[a]	Protein binding	CL		
Beta-lactams	Hydrophilic	Low	Low to moderate[b]	Renal	Time-dependent	*f*T > MIC
Vancomycin	Hydrophilic	Low	Moderate	Renal	Time- and concentration dependent	AUC:MIC
Fluoroquinolones	Lipophilic	Moderate	Low to moderate	Hepatic and renal	Concentration-dependent	C_{max}:MIC AUC:MIC
Aminoglycosides	Hydrophilic	Low	Low	Renal	Concentration-dependent	C_{max}:MIC

[a]*Low V_d: 0.1–0.4 L/kg, moderate V_d: 0.6–5 L/kg.*

[b]*Exceptions: Cefazolin (75%–85%), ceftriaxone (85%–95%), ertapenem (85%–95%), flucloxacillin (95%), dicloxacillin (97%), oxacillin (94%). V_d, volume of distribution; CL, clearance; fT > MIC, time that free serum concentration above minimum inhibitory concentration; C_{max}:MIC, ratio of maximum concentration to minimum inhibitory concentration; AUC:MIC, ratio of area under the concentration-curve to minimum inhibitory concentration.*

data from the general population (Tuntland et al., 2014). Together with the pharmacokinetic and pharmacodynamic variabilities driven by patients, determining optimal dosing of antimicrobial agents for individual patients is challenging.

Unfortunately, antimicrobial dosing is further complicated by the susceptibility of the pathogen to the antimicrobial agent, which is determined by measuring the minimum inhibitory concentration (MIC) of the antimicrobial agent in inhibiting microbial growth. MIC is the major indicator of antimicrobial effectiveness (Kowalska-Krochmal and Dudek-Wicher 2021). It is the denominator in the PK/PD index, which describes the quantitative relationship between the given dose and the bacterial killing effect in terms of rate and extent of killing (Hoo et al., 2017). European Committee on Antimicrobial Susceptibility Testing (EUCAST) and Clinical and Laboratory Standards Institute (CLSI) classified the susceptibility breakpoints that are useful for dose optimization depending on MIC values, which is vital when local laboratory antibiograms are not available (Clinical & Laboratory Standards Institute, 2022; European Committee on Antimicrobial Susceptibility Testing, 2022). The accuracy in MIC determination is subjected to a few factors, such as variation in a laboratory (intra-laboratory variability) and variation in determination method (intra-sample variability) (Mouton et al., 2018; Kowalska-Krochmal and Dudek-Wicher 2021). On the other hand, several studies reported that pathogens isolated from critically ill patients were less susceptible to antimicrobial agents with the presence of higher MIC values (Kiratisin et al., 2012; Leblebicioglu et al., 2012; Valenza et al., 2012; Pérez-Pitarch et al., 2018). This indicates that higher antimicrobial dosing is needed to achieve the PK/PD targets for better clinical outcomes.

In order to achieve optimal antimicrobial dosing, several approaches are implemented in the clinical practice settings or under the experimental phase to provide individualized dosing and address some degree of variabilities. These include dosing nomograms, therapeutic drug monitoring (TDM), dosing

software and other novel technology-based approaches, such as real-time drug monitoring using biosensors, closed-loop controlled systems, artificial intelligence and machine learning assisted systems (He et al., 2021; Rawson et al., 2021). These technology-based approaches have several barriers to applying in clinical practice including inadequate investigation on their applications, the issue of data integration with patient medical records (Rawson et al., 2021). Thus, advanced strategies that can offer rapid and precise antimicrobial dosing adjustments are needed to optimize the antimicrobial dosing. TDM and model-informed precision dosing (MIPD), which is an emerging approach, are further addressed in the sections below.

PHARMACOLOGY AND MECHANISM-BASED PK/PD MODELS

It is well known that bacteria behave differently *in vitro* and *in vivo*. As such, in antibiotic discovery and development, PK/PD studies are imperative to provide substantial insight into the therapeutic potential of lead compounds at the early discovery stage and assist in the establishment of optimal dosage regimens (de Araujo et al., 2011; Velkov et al., 2013). As Schmidt et al. (2008) described, ideal treatment optimization requires information on the mechanisms involved in the effect of the antibiotics (pharmacodynamics, PD) and the evolution of the antibiotic concentration in the patients (pharmacokinetics, PK).

PK is a central part of clinical pharmacology and pharmacometrics. It describes the relationship between drug dosing and the drug concentration-time profile in the body. Whilst PD describes the relationship between the concentration of an antibiotic and its ability to inhibit the growth of microorganisms. The major pharmacodynamic parameter is the drug's minimum inhibitory concentration (MIC) against the infecting pathogen. Despite MIC's well-established susceptibility parameter, which has been paramount to understanding antimicrobial dosing, it is a crude and mono-dimensional threshold value. The value can show high variability and does not provide information on the time course of antimicrobial activity or growth inhibition due to antibiotic exposure (Craig, 2003). In comparison, the evaluation of growth and kill profiles over time (time-kill curves) offer a more robust approach.

PK/PD models link the dose/concentration relationship (PK) and concentration/effect relationship (PD), thereby facilitating the description and prediction of the clinically relevant relationship between time and drug effects (Schmidt et al., 2008). The PK/PD approach implies the use of *in vitro*, *ex vivo*, and *in vivo* models, as well as mathematical models (Rodríguez-Gascón et al., 2021). Each one exhibits advantages and disadvantages and may be regarded as complementary. The mathematical modelling to analyze PK/PD data resulting from *in vitro*, *ex vivo* or *in vivo* experiments has an important impact on the development and optimization of antibiotic dosing.

Besides its main application, to optimize dosing strategies to improve the clinical outcome of antibiotic therapy, the PK/PD analysis also minimizes side effects and the emergence of resistances (Asín-Prieto et al., 2015). Furthermore, the PK/PD indices define the combination of pharmacokinetic and pharmacodynamic parameters. For instance, the ratio of the peak concentration of the antimicrobial (C_{max}) to the minimum inhibitory concentrations (MICs) (C_{max}/MIC) (McAleenan et al., 2020).

Three PK/PD indices have been set as the best descriptors of clinical efficacy and bacterial kill characteristics of the antibiotic based on the activity pattern of the antibiotic (**Table 1**). The first pattern of antimicrobial activity exhibits concentration-dependent activity and the PK/PD indices preferred are the ratios of the free-drug maximum concentration (fC_{max}) to the MIC (fC_{max}/MIC) or the area under the free-drug concentration-time curve, typically over a 24-h period, to the MIC ($fAUC_{24}$/MIC). The second is the time-dependent pattern, where the antibacterial effect is best described by the percentage of time the free drug concentration remains above the MIC throughout the dosing interval ($fT_{>MIC}$). Finally, the best PK/PD ratio for concentration-dependent with time-dependence antibiotics is $fAUC_{24}$/MIC (Jorda and Zeitlinger, 2020; McAleenan et al., 2020).

Over the last decades, the regulatory agencies recommended model-based drug development to strengthen scientific evidence as a basis for making key decisions. However, very few PK/PD models describe time courses of antibiotic drug effects in animals and patients. The model-based has its drawbacks as only a few PK/PD models describe time courses of antibiotic drug effects in animals and patients. To overcome the drawback, the mechanism-based model could help predict the time-course of bacteria growth and kill in patients, based on *in vitro* and/or *in vivo* information compared with more empirical models. Notably the mechanism-based PK/PD model (MBM) are more reliable for extrapolating different dosing regimens in the presence of resistant mutants in investigating how resistance selection can be reduced or overcome (Danhof et al., 2008; Khan et al., 2015).

The MBM includes equations that describe microorganism growth, the effect of antimicrobial drugs, and changing drug concentrations (Czock and Keller, 2007). The MBM takes into account several parameters, including MIC value, at minimum, a control growth rate constant (K_{growth}) and a killing rate (K_{death}), a maximum kill rate (E_{max}) and a potency value such as the half-maximum effect concentration (EC_{50}) (Nielsen and Friberg, 2013). Moreover, as only limited information on the drug effect may be needed when the underlying system is characterized, MBM can be useful for selecting between candidate drugs. As such, it allows more therapeutically effective use and has renewed interest in some old antibiotics. For example, colistin is administered as a last-line therapy for difficult-to-treat respiratory tract infections via intravenous administration or inhalation (Lin et al., 2018). However, both routes fail to achieve adequate exposure owing to poor penetration into the epithelial lining fluid and a lack of scientific evaluation with well-designed PK/PD studies, respectively (Landersdorfer et al., 2017; Yapa et al., 2014). When an MBM was used, optimal inhalational dosage regimens of colistin were developed to treat life-threatening respiratory tract infections caused by Gram-negative superbugs

TABLE 2 | Examples of microbial studies used omics technologies.

Omics strategies	Approach	Study objective	Drug/ compound	Pathogen	Reference
Genomics	Single-cell sequencing	Evaluate human microbiota	—	Microbiota of a healthy oral subject	Campbell et al. (2013)
Genomics	Single-cell sequencing	Identify bacteria that affect disease susceptibility and severity	—	Intestinal microbiome from 11 patients with inflammatory bowel disease	Palm et al. (2014)
Genomics and metagenomics	Single-cell sequencing + Shotgun sequencing	Evaluate the genomes of SAR86 marine bacterial lineage	—	SAR86 from seawater	Dupont et al. (2012)
Metagenomics	Shotgun sequencing	Assess health risk of antimicrobial resistance genes (ARGs)	—	1,921 gut microbiome genomes from 59 healthy stool donors	Zhang et al. (2021)
Metagenomics	Shotgun sequencing	Investigate the rates and targets of horizontal gene transfer (HGT) across thousands of bacterial strains	—	Samples were collected from 15 human populations spanning a range of industrialization	Groussin et al. (2021)
Transcriptomics	RNA-Seq	Analyze the regulation of adaptive resistance upon adaptation to disparate toxins	Ampicillin, tetracycline, n-butanol	*E. coli*	Erickson et al. (2017)
Transcriptomics	Microarray	Identify molecular mechanism of Licochalcone A	Licochalcone A from *Glycyrrhiza inflata*	*S. aureus*	Shen et al. (2015)
Transcriptomics, metabolomics, lipidomics and lipid A profiling data	Genome-scale metabolic modelling	Analyze bacterial metabolic changes at the systems levels	Polymyxins	*P. aeruginosa*	Zhu et al. (2018)
Proteomics	nanoLC-MS/MS	Analyze bacterial phosphoproteomic changes of prokaryotes for drug resistance	-	*A. baumannii, H. pylori, K. pneumoniae, V. vulnificus, A. platensis, M. taiwanensis, T. thermophilus, M. mazei, M. portucalensis*	Lai et al. (2017)
Proteomics	MS and 2D-DIGE	Identify changes in subproteome	Piperacillin/ tazobactam	*E. coli*	dos Santos et al. (2010)
Proteomics	2DE and iTRAQ	Investigate the mechanism of Plumbagin	Plumbagin	*B. subtilis*	Reddy et al. (2015)
Metabolomics and proteomics	Computational model	Identify the biomarkers to predict patient outcomes and guide therapeutic development	-	*S. aureus*	Wozniak et al. (2020)
Metabolomics	HPLC with MS	identify metabolic changes of bacteria	Methicillin, ampicillin, kanamycin, norfloxacin	Two isogenic *S. aureus* strains	Schelli et al. (2017)

Nano LC-MS/MS, nanoscale liquid chromatography coupled to tandem mass spectrometry; MS, mass spectrometry; 2D-DIGE, two-dimensional difference gel electrophoresis; 2DE, two-dimensional electrophoresis; iTRAQ, isobaric tag for relative and absolute quantification; HPLC, high performance liquid chromatography.

in patients (Lin et al., 2018). Nielsen et al. (2007) have previously developed a mechanism-based *in silico* model that successfully described the bacterial growth and killing kinetics for *Streptococcus pyogenes* exposed to antibiotics of different classes. The Nelson model structure provides valuable information for future studies' design and the development of improved dosing regimens. Therefore, the efforts taken to develop this model are rewarding in the battle against rapidly emerging bacterial resistance as we can no longer rely entirely on discovering new antibiotics.

Following established MBMs using parameter estimates including bacterial growth, bacterial killing and mutation frequency with the application of relevant software, dosing regimens of antibiotics can be further optimized *via* Monte Carlo simulation in conjunction with human population PK models. Monte Carlo simulation is a mathematical technique which can be performed to determine the probability of target attainment (PTA) under different dosing regimens by utilizing PK data and PK/PD targets (Llanos-Paez et al., 2017; Trang et al., 2017). The Monte Carlo simulation combines PK and microbiological data to predict the therapeutic outcome for different antimicrobial dosage regimens. Thus acting as an additional tool that can support antimicrobial dose optimization and guide empiric therapy. Overall, these *in silico* PK/PD models have been essential in optimizing therapy, including antibiotics dosage regimens (Yadav et al., 2017).

MULTI-OMICS AND METABOLIC MODELLING

Conventionally, growth inhibition assays in disk-diffusion, well diffusion, broth or agar dilution can be used for epidemiology, drug discovery and prediction of therapeutic outcomes (Balouiri et al., 2016). However, the procedures are laborious and time-consuming as only a few isolates can be studied at one time, while

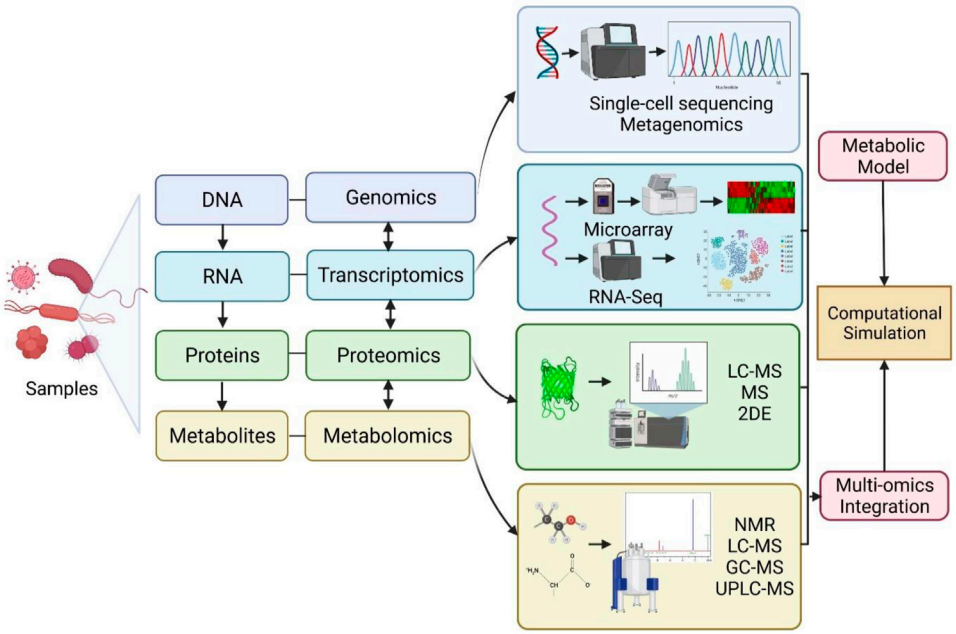

FIGURE 2 | Schematic representation of omics workflow for genomics, transcriptomics, proteomics and metabolomics approaches. Multi-omics data integration can be used for refining and reconciling modelling predictions to construct computational simulations. RNA-Seq: RNA-sequencing; LC-MS: liquid chromatography-mass spectrometry; MS: Mass spectrometry; 2DE: two-dimensional electrophoresis; NMR: nuclear magnetic resonance; GC-MS: gas chromatography coupled to mass spectrometry; UPLC-MS: ultra-high-performance liquid chromatography coupled to mass spectrometry. Created with BioRender.com.

some methods are highly subjected to the risk of errors in the preparation of dilutions or determining MIC values (Balouiri et al., 2016). Recent advances in "omics," which is an umbrella term for genomics, transcriptomics, proteomics, lipidomics and metabolomics, are emerging and provide valuable tools in getting deeper insights into bacterial physiology and virulence mechanism of antimicrobial resistance and mechanisms of potential antimicrobial compounds (**Table 2**). The schematic representation of omics workflow is depicted in **Figure 2**. The integration of high-throughput multi-omics data can unravel the relationship between genes and proteins, as well as the interaction of biological networks in a system-based model (Garcia et al., 2021). This explains the reason for the growing interest in using multi-omics analysis in microbiology research.

The advent of genetic sequencing technologies over the past decade, together with the bioinformatics tools, enable the decoding of microbial genomes with better taxonomic and functional annotation of genomic and metagenomic data, which leads to the identification of novel genes related to bacterial virulence, resistance and mutations (Roemer & Boone 2013; Scheffler et al., 2013). The incorporation of genomic technologies into microbiology research provides a large genomic dataset which is valuable in predicting the metabolic pathway of microorganisms (Garza and Dutilh, 2015), identification of promising candidate targets for novel antimicrobials in drug discovery and development (Santos et al., 2016), elucidating the antimicrobial resistance mechanisms via comparative genomic analysis (Chernov et al., 2019). Single-cell sequencing and metagenomic sequencing are widely used approaches for investigating microbiome, which refers to the microorganisms inhabiting a particular environment (Cheng et al., 2019). Single-cell sequencing provides high-quality genomic information for microbe strains with low abundance (which might be missing from metagenomic sequencing), by isolating individual cells for DNA extraction, whole-genomic amplification, high-throughput sequencing and lastly followed by genome assembly and genome analysis (Cheng et al., 2019). The application of single-cell sequencing in microbiology research has led to significant findings, including the discovery of bacteria with novel metabolic features and alternative genetic code (Campbell et al., 2013), and the identification of microbial taxa that induce specific disease (Palm et al., 2014).

However, single-cells genomics represents genomes of individual cells and may not provide the full genomic collection within a microbial community or biome. This shortcoming can be solved with the integration of metagenomics and single-cell genomics (Cheng et al., 2019). Metagenomics allows the assembly of basic genomes with microbial communities by investigating the whole genomes of all microbes in microbial communities contained within a certain environment. Antibiotic resistance can be transferred from one bacterium to another *via* horizontal gene transfer. A recent report demonstrated that it occurs at an elevated rate in the gut microbiome among individuals from industrialized and urban populations (Groussin et al., 2021). This approach has been employed to investigate microbial diversity and antibiotic resistance genes (Dupont et al., 2012; Zhang et al., 2021).

Integration of single-cell genomics and metagenomics produced better microbe genome assemblies from microbial communities (Dupont et al., 2012; Nobu et al., 2015).

Transcriptomics involves large-scale analysis of transcriptional changes in gene expression levels, which are produced by the microbes in response to a defined environmental condition, such as antimicrobial treatment. The mechanism controlling the activity of antimicrobial agents on microbial cells involves a complex interaction of multiple pathways at different levels, such as transcriptional, translational and post-translational levels (Dwyer et al., 2015; Erickson et al., 2017). Gene expression analysis, together with bioinformatics resources, may help in unveiling the mechanism of antimicrobial action (Shen et al., 2015), metabolic changes of bacteria (Zhu et al., 2018) and mechanism of bacterial adaptive resistance (Erickson et al., 2017). The microarray approach using microchip technology allows simultaneous analysis on gene expression levels in microbes at the transcription level, where the gene expression patterns (up-regulation or down-regulation) of microbes in response to a stimulus can be identified. Therefore, it can provide insights into the molecular mechanisms or pathways involved in the investigated phenomena at a systems level. It has been applied in microbiology research to elucidate the mechanism of action of several potential antimicrobial agents (Shen et al., 2015; Santos et al., 2016).

The application of microarray or gene probe-based methods are limited to the availability of the array for the specific microbe strain, completeness of genome sequence of an investigated organism, issue of result reproducibility and availability of instrument to read microchip (Chernov et al., 2019). As an alternative, the RNA sequencing (also termed as RNA-Seq) method is employed to provide quantitative analysis of gene expression, and at the same time, it allows the gene profiling of non-coding RNAs involved in regulating gene expression at transcriptional and post-transcriptional levels. Unlike probe-based approaches, RNA-Seq can be used to detect the transcripts in an organism without a complete sequenced genome and provides high accuracy and reproducibility in quantifying gene expression levels (Wang et al., 2009).

The assessment of protein expression level (qualitatively or quantitatively) at the whole-cell level can be achieved *via* proteomics analysis. It allows protein identification and evaluation of differential protein expression for the investigated phenomena, as well as provides information on post-translational modifications of proteins (Chernov et al., 2019). This information highlights the key proteins involved, pathways affected and the underlying mechanisms in response to stimuli, including identification of bacteria proteome and mechanism of drug resistance (Lai et al., 2017; dos Santos et al., 2010). Proteomic approaches are also adopted in drug discovery research to investigate the mechanism of actions of potential antimicrobial agents and reveal their cellular targets (Reddy et al., 2015). Various methods can be used for proteomics analysis, such as mass spectrometry and two-dimensional electrophoresis, liquid chromatography-mass spectrometry (LC-MS) (Lai et al., 2017; dos Santos et al., 2010).

Metabolomics offers the metabolic profiling of an organism by determining the metabolites present over a given time under certain conditions. In other words, it provides a snapshot of cell physiology in view of metabolites as end-products of cellular processes. Similar to proteomics, various approaches can be used for metabolomics, such as nuclear magnetic resonance (NMR), LC-MS, gas chromatography coupled to mass spectrometry (GC-MS) and ultra-high performance liquid chromatography coupled to mass spectrometry (UPLC-MS) (Chernov et al., 2019). This technology may help in determining metabolic changes related to antimicrobial resistance (Schelli et al., 2017), disease, toxins or drugs (Santos et al., 2016).

To unveil the complexity of the microbial system, data from multi-omics are integrated into metabolic modelling to improve model predictions and provide comprehensive insights into cellular networks at the system level (Fondi and Liò 2015). This is due to the limitation of inaccuracy prediction in a single layer network. Genomic-scale cellular network has become an important tool to bridge the gap between genomic-derived data (such as gene products, mRNA, proteins and metabolites) and their interactions, offering a comprehensive understanding of the dynamic physiological function of microbes under a specific condition (Hao et al., 2018). The cellular networks have been classified into: 1) genomic-scale metabolic network—allows systematic level predictions of metabolism in the organism, 2) transcriptional regulatory network—allows predictions of interactions between different transcriptional factors and target genes, and 3) signal transduction network—allows predictions of molecular cell response (protein-protein ad protein-gene interactions) to stimuli (Hao et al., 2018). Zhu et al. (2018) integrated multi-omics data with a genome-scale metabolic model (GSMM) to analyze the responses of *P. aeruginosa* to polymyxins. Abdul Rahim et al. (2021) employed a systems-based model to analyze the synergistic activity of polymyxin B and chloramphenicol. Wozniak et al. (2020) adopted a combination of metabolomics and proteomics analysis of *S. aureus* bacteraemia together with the computational tool as biomarkers to predict mortality risk and recommend personalized therapy.

In addition to exploring the genome information of the microbes and the response of the antimicrobial agents, multi-omics also provide a meaningful approach to address the inter-individual variability through exploration of genomic information from the host, which is important in optimizing antimicrobial therapy. Genetic polymorphisms of drug-metabolizing enzymes were reported to be associated with anti-tuberculosis drug-induced hepatitis, including *NAT2**4 and *CYP2E1**4 (Kim et al., 2009; Cai et al., 2012). These pharmacogenomic data are important in predicting the clinical response to antimicrobial agents and tailor an individualized antimicrobial therapy. Interestingly, mitochondrial pharmacogenomics is also useful to provide a personalized barcode for antimicrobial therapy in view of the mutational rate of mitochondrial DNA is much higher than nuclear DNA (Pacheu-Grau et al., 2010; Singh et al., 2014). Mitochondrial DNA genetic variants were found to be associated with different aminoglycosides-related ototoxicity susceptibility (Rydzanicz

et al., 2010; Muyderman et al., 2012). Integrating the data from pharmacogenomics into the drug's PK/PD could provide an approach in optimizing antibiotic doses while minimizing the toxicity of antimicrobial agents.

On the other hand, multi-omics technology is also supported by European Union as a framework for developing an omics-based personalized treatment scheme as an approach in addressing the emergence of antibiotic resistance (Cohen et al., 2015). This tailored-treatment approach integrates personalized patient data such as identification of genetic predisposition to specific infections (host genomics), host immune response to infections (proteomics, transcriptomics), microbiome analysis (transcriptomics) and characterization of pathogen resistance profile (microbial genomics) to generate a database and this database will be mined using bioinformatics tools to identify the significant associations between different datasets. This eventually will contribute to the building of treatment algorithms to implement the personalized treatment with an optimal treatment regimen for individual patients (Cohen et al., 2015).

QUANTITATIVE SYSTEMS PHARMACOLOGY

As highlighted above, PK/PD consideration is essential for antimicrobial dose optimization. Moreover, with multi-omics, there has been a paradigm shift from MBM to systems-based models. In recent years, there has been an increase in interest in quantitative systems pharmacology (QSP) (Ribba et al., 2017). QSP is an innovative, emerging interdisciplinary approach that integrates systems biology and PK/PD (Pichardo-Almarza and Diaz-Zuccarini, 2016). QSP modelling technique applies biology with findings of *in vitro* studies to determine the way drugs affect biological processes (Woodhead et al., 2017). It differs from other pharmacometrics approaches as QSP modelling enables the elucidation of the mechanisms of action and possibly resistance of drugs upon exposure on a systems level. This is done by quantitatively analyzing the dynamic interactions between drug(s) and a biological system (van der Graaf & Benson 2011). Unlike the traditional mechanism-based PK/PD models, which apply minimal mechanistic biology, QSP incorporates omics data, including transcriptomics and metabolomics, along with computational techniques to incorporate key interactions between the drug and its targets which result in changes in cellular processes (Zhao & Iyengar 2012).

This promising approach has led to the release of a US National Institutes of Health (NIH) white paper in 2011 (Sorger et al., 2011). There are many different applications of QSP, including evaluating the impact on the efficacy of novel mono- and combination therapies (Musante et al., 2017). The application of QSP modelling is evident in neoplasms, nervous system, cardiovascular system and nutritional and metabolic disease (Knight-Schrijver et al., 2016). Nonetheless, there are still barriers to QSP. Among them is the complexity of the models, and hence simplification via model reduction is recommended (Derbalah et al., 2022). Others include the cost and time of model development due to the large amount of datasets (Garcia et al., 2021).

To date, no QSP models have been published for antibiotics against "superbugs." Due to the rapidly emerging resistance of MDR Gram-negative bacteria, these *in silico* models are urgently needed to optimize antibiotic combinations and hence to meet the needs of the current global health problem.

MODEL-INFORMED PRECISION DOSING

Another emerging approach is model-informed precision dosing (MIPD). Treatment response in individuals for some drugs may vary due to genotype and phenotype differences (Peck, 2021). In order to ensure optimal outcomes in patients, drugs with certain characteristics would benefit from close monitoring and precision dosing (i.e., dosing tailored to individual patients). These characteristics include drugs with a narrow therapeutic index which may lead to serious adverse effects from overtreatment or severe consequences due to suboptimal treatment (Peck, 2021). Pharmacokinetics is the study of drug concentration changes in the body that results from various physiological processes over time. To identify significant covariates of response variability, population pharmacokinetic (popPK) modelling can be utilized for dose adjustments. The approach of using Bayesian popPK modelling to optimize dosing is called model-informed precision dosing (MIPD) (Abdulla et al., 2021). As PK/PD is employed, MIPD can be carried out if drug plasma concentrations are useful in predicting pharmacological effects.

Antibiotics with a narrow therapeutic window require close monitoring and are done with a therapeutic drug monitoring service (TDM). TDM service is offered in hospitals globally and is usually led by pharmacists (Ab Rahman et al., 2013). TDM involves the interpretation of drug plasma concentration levels which are compared to a therapeutic range. Based on this, recommendations are made, which often involve dose adjustments in order to optimize outcomes. Examples of antibiotics where TDM is conducted are vancomycin and aminoglycosides (amikacin and gentamicin). Suboptimal doses may lead to treatment failure and the emergence of AMR. Increased exposure, often demonstrated by levels above the recommended therapeutic range for vancomycin, amikacin and gentamicin, would lead to nephrotoxicity (Morales-Alvarez, 2020). Nonetheless, serious adverse effects and toxicities may also develop in patients with plasma concentration levels well within the therapeutic range.

Although TDM can assist individualized therapy, the TDM based dose optimization approach alone is not powerful enough to enable precision dosing for individual patients. The traditional TDM approach is associated with several limitations including the need for steady-state for sample collection, leading to delayed and suboptimal attainment of the PK/PD targets (Wicha et al., 2021). To address this, statistical and mathematical techniques are being applied using TDM results in dose optimization with the use of

TABLE 3 | Characteristics of model-informed precision dosing (MIPD) tools.

MIPD tool	Country	Mathematical software	Performance[#] (%) > 75%
Autokinetics	Netherlands	NONMEM®, R®	X
Bestdose	United States	—	X
DoseMeRx	United States	GNU scientific library	✓
ID-ODS	United States	Matlab®	X
InsightRX nova	United States	NONMEM®	✓
MwPharm++	Netherlands/Czech Republic	—	✓
NextDose	New Zealand	—	X
PrecisePK	United States	—	✓
TDMx	Germany	NONMEM®	X
Tucuxi	Switzerland	NONMEM®	X

Adapted from Abdulla et al., 2021; Kantasiripitak et al., 2020. NONMEM: non-linear mixed effects model.
[#]Criteria include user-friendliness and utilization, user support, computational aspects, population models, quality and validation, output generation, privacy, data security, and costs (Kantasiripitak et al., 2020).

dosing software (Chai et al., 2020). Model-informed precision dosing (MIPD) is a mathematical framework that integrates different sources of information to streamline the TDM process and maximize the success of antibacterial therapy. To provide precise dosing, many other factors and parameters must be taken into consideration. This is where PK/PD models play a crucial role where the models provide information on drug exposure and effect either efficacy or toxicity (Wakefield et al., 1999). Furthermore, the incorporation of population PK and PK/PD models using the Bayesian approach and dosing simulations (Monte Carlo simulation) are utilized in MIPD. For some antibiotics, MIPD has been successfully developed (Roggeveen et al., 2020) and even implemented, for example, vancomycin (Frymoyer et al., 2020). As there is a demand for MIPD, it is not surprising that software tools have been developed to meet this need. Recent reviews (Kantasiripitak et al., 2020; Abdulla et al., 2021) reported there are around 10 MIPD software tools available, as shown in **Table 3** below.

Although there are tools already available, there are still gaps in addressing unmet needs. As shown in **Table 3**, the performance of MIPD tools is based on 8 criteria: user-friendliness and utilization, user support, population models, quality and validation, output generation, privacy, data security and costs. Only four tools had a performance of more than 75%, with the highest scoring 83%. Thus, there is still room for improvement, including in aspects of validation and prospective evidence. Another crucial aspect of MIPD is continuous learning (Hughes et al., 2021). This involves the continuous update of the models and hence software tools based on data availability.

Notably, two MIPD tools have demonstrated cost-effectiveness, while for other products, trials are ongoing (Kantasiripitak et al., 2020). A study in 2018 by Tong et al. reported that the costs associated with pneumonia in the United States from 2008 to 2014 remain substantial and is a burden on the US healthcare system (Tong et al., 2018). Collectively, MIPD tools could potentially also save hospitalization costs in addition to saving lives.

FUTURE DIRECTIONS

Applying and utilizing antimicrobial PK/PD models are crucial in optimizing antimicrobial therapy. Nonetheless, in the fight against antimicrobial resistance, novel strategies integrating mechanistic data from systems biology with antimicrobial PK/PD are warranted. As high-throughput data become more widely available and the demand for model-informed precision dosing (MIPD) increases, especially for narrow therapeutic window antibiotics, the need for QSP will also be more evident. MIPD will continue to evolve, thus requiring more information on biomarkers and mechanistic data. These can be obtained and provided from systems-based models, including QSP models. More studies investigating host-pathogen interactions and identifying biomarkers are crucial to further inform the models to enable optimization of antimicrobial therapy and precision dosing. As MIPD involves pharmacometrics, software and training costs must also be considered before they can be applied. Integration of MIPD tools with electronic health records must also be seamless for wider implementation. Lastly, cost-effectiveness studies of MIPD tools are scarce and therefore warranted. With the advent and availability of cost-effective, user-friendly and validated MIPD tools, clinicians will be able to further optimize antimicrobial therapy for their patients and thus health outcomes.

AUTHOR CONTRIBUTIONS

NAR contributed to conception and design. All authors contributed to first and subsequent drafts and approved the submitted version.

ACKNOWLEDGMENTS

The authors acknowledge the financial support by the Faculty Research Grant (Geran Penyelidikan Fakulti), Faculty of Pharmacy, Universiti Malaya (GPF001B-2020).

REFERENCES

Ab Rahman, A. F., Ahmed Abdelrahim, H. E., and Mohamed Ibrahim, M. I. (2013). A Survey of Therapeutic Drug Monitoring Services in Malaysia. *Saudi Pharm. J.* 21 (1), 19–24. doi:10.1016/j.jsps.2012.01.002

Abdul Rahim, N., Zhu, Y., Cheah, S.-E., Johnson, M. D., Yu, H. H., Sidjabat, H. E., et al. (2021). Synergy of the Polymyxin-Chloramphenicol Combination against New Delhi Metallo-β-Lactamase-Producing *Klebsiella pneumoniae* Is Predominately Driven by Chloramphenicol. *ACS Infect. Dis.* 7, 1584–1595. doi:10.1021/acsinfecdis.0c00661

Abdulla, A., Edwina, A. E., Flint, R. B., Allegaert, K., Wildschut, E. D., Koch, B. C. P., et al. (2021). Model-Informed Precision Dosing of Antibiotics in Pediatric Patients: A Narrative Review. *Front. Pediatr.* 9, 624639. doi:10.3389/fped.2021.624639

Aminov, R. (2017). History of Antimicrobial Drug Discovery: Major Classes and Health Impact. *Biochem. Pharmacol.* 133, 4–19. doi:10.1016/j.bcp.2016.10.001

Appaneal, H. J., Shireman, T. I., Lopes, V. V., Mor, V., Dosa, D. M., LaPlante, K. L., et al. (2021). Poor Clinical Outcomes Associated with Suboptimal Antibiotic Treatment Among Older Long-Term Care Facility Residents with Urinary Tract Infection: a Retrospective Cohort Study. *BMC Geriatr.* 21 (1), 1–3. doi:10.1186/s12877-021-02378-5

Asín-Prieto, E., Rodríguez-Gascón, A., and Isla, A. (2015). Applications of the Pharmacokinetic/pharmacodynamic (PK/PD) Analysis of Antimicrobial Agents. *J. Infect. Chemother.* 21 (5), 319–329. doi:10.1016/j.jiac.2015.02.001

Balouiri, M., Sadiki, M., and Ibnsouda, S. K. (2016). Methods for *In Vitro* Evaluating Antimicrobial Activity: A Review. *J. Pharm. Anal.* 6 (2), 71–79. doi:10.1016/j.jpha.2015.11.005

Cai, Y., Yi, J., Zhou, C., and Shen, X. (2012). Pharmacogenetic Study of Drug-Metabolising Enzyme Polymorphisms on the Risk of Anti-tuberculosis Drug-Induced Liver Injury: a Meta-Analysis. *PLoS One* 7 (10), e47769. doi:10.1371/journal.pone.0047769

Campbell, J. H., O'Donoghue, P., Campbell, A. G., Schwientek, P., Sczyrba, A., Woyke, T., et al. (2013). UGA Is an Additional glycine Codon in Uncultured SR1 Bacteria from the Human Microbiota. *Proc. Natl. Acad. Sci. U. S. A.* 110, 5540–5545. doi:10.1073/pnas.1303090110

Chai, M. G., Cotta, M. O., Abdul-Aziz, M. H., and Roberts, J. A. (2020). What Are the Current Approaches to Optimising Antimicrobial Dosing in the Intensive Care Unit? *Pharmaceutics* 12 (7), 638. doi:10.3390/pharmaceutics12070638

Cheng, M., Cao, L., and Ning, K. (2019). Microbiome Big-Data Mining and Applications Using Single-Cell Technologies and Metagenomics Approaches Toward Precision Medicine. *Front. Genet.*, 972. doi:10.3389/fgene.2019.00972

Chernov, V. M., Chernova, O. A., Mouzykantov, A. A., Lopukhov, L. L., and Aminov, R. I. (2019). Omics of Antimicrobials and Antimicrobial Resistance. *Expert Opin. Drug Discov.* 14 (5), 455–468. doi:10.1080/17460441.2019.1588880

Clinical & Laboratory Standards Institute (CLSI) (2022). CLSI Breakpoints. Available at: https://clsi.org/standards/products/free-resources/access-our-free-resources/ (Accessed 03 04, 2022).

Cohen, A., Bont, L., Engelhard, D., Moore, E., Fernández, D., Kreisberg-Greenblatt, R., et al. (2015). A Multifaceted 'omics' Approach for Addressing the Challenge of Antimicrobial Resistance. *Future Microbiol.* 10 (3), 365–376. doi:10.2217/fmb.14.127

Craig, W. A. (2003). Basic Pharmacodynamics of Antibacterials with Clinical Applications to the Use of Beta-Lactams, Glycopeptides, and Linezolid. *Infect. Dis. Clin. North Am.* 17 (3), 479–501. doi:10.1016/S0891-5520(03)00065-5

Czock, D., and Keller, F. (2007). Mechanism-based Pharmacokinetic-Pharmacodynamic Modeling of Antimicrobial Drug Effects. *J. Pharmacokinet. Pharmacodyn.* 34 (6), 727–751. doi:10.1007/s10928-007-9069-x

Danhof, M., de Lange, E. C., Della Pasqua, O. E., Ploeger, B. A., and Voskuyl, R. A. (2008). Mechanism-based Pharmacokinetic-Pharmacodynamic (PK-PD) Modeling in Translational Drug Research. *Trends Pharmacol. Sci.* 29 (4), 186–191. doi:10.1016/j.tips.2008.01.007

de Araujo, B. V., Diniz, A., Palma, E. C., Buffé, C., and Dalla Costa, T. (2011). PK-PD Modeling of β-lactam Antibiotics: *In Vitro* or *In Vivo* Models? *J. Antibiot. (Tokyo)* 64 (6), 439–446. doi:10.1038/ja.2011.29

Derbalah, A., Al-Sallami, H., Hasegawa, C., Gulati, A., and Duffull, S. B. (2022). A Framework for Simplification of Quantitative Systems Pharmacology Models in Clinical Pharmacology. *Br. J. Clin. Pharmacol.* 88 (4), 1430–1440. doi:10.1111/bcp.14451

Dinos, G. P., Athanassopoulos, C. M., Missiri, D. A., Giannopoulou, P. C., Vlachogiannis, I. A., Papadopoulos, G. E., et al. (2016). Chloramphenicol Derivatives as Antibacterial and Anticancer Agents: Historic Problems and Current Solutions. *Antibiot. (Basel)* 5. doi:10.3390/antibiotics5020020

Dos Santos, B. S., Da Silva, L. C., da Silva, T. D., Rodrigues, J. F., Grisotto, M. A., Correia, M. T., et al. (2016). Application of Omics Technologies for Evaluation of Antibacterial Mechanisms of Action of Plant-Derived Products. *Front. Microbiol.* 7, 1466. doi:10.3389/fmicb.2016.01466

dos Santos, K. V., Diniz, C. G., de Castro Veloso, L., de Andrade, H. M., da Silva Giusta, M., da Fonseca Pires, S., et al. (2010). Proteomic Analysis of *Escherichia coli* with Experimentally Induced Resistance to Piperacillin/tazobactam. *Res. Microbiol.* 161 (4), 268–275. doi:10.1016/j.resmic.2010.03.006

Dupont, C. L., Rusch, D. B., Yooseph, S., Lombardo, M. J., Richter, R. A., Valas, R., et al. (2012). Genomic Insights to SAR86, an Abundant and Uncultivated Marine Bacterial Lineage. *ISME J.* 6 (6), 1186–1199. doi:10.1038/ismej.2011.189

Dwyer, D. J., Collins, J. J., and Walker, G. C. (2015). Unraveling the Physiological Complexities of Antibiotic Lethality. *Annu. Rev. Pharmacol. Toxicol.* 55, 313–332. doi:10.1146/annurev-pharmtox-010814-124712

Ejim, L., Farha, M. A., Falconer, S. B., Wildenhain, J., Coombes, B. K., Tyers, M., et al. (2011). Combinations of Antibiotics and Nonantibiotic Drugs Enhance Antimicrobial Efficacy. *Nat. Chem. Biol.* 7 (6), 348–350. doi:10.1038/nchembio.559

Erickson, K. E., Otoupal, P. B., and Chatterjee, A. (2017). Transcriptome-level Signatures in Gene Expression and Gene Expression Variability during Bacterial Adaptive Evolution. *Msphere* 2 (1), e00009–17. doi:10.1128/mSphere.00009-17

European Committee on Antimicrobial Susceptibility Testing (EUCAST) (2022). Clinical Breakpoints - Breakpoints and Guidance. Available at: https://eucast.org/clinical_breakpoints/ (Accessed 03 04, 2022).

Fondi, M., and Liò, P. (2015). Multi -omics and Metabolic Modelling Pipelines: Challenges and Tools for Systems Microbiology. *Microbiol. Res.* 171, 52–64. doi:10.1016/j.micres.2015.01.003

Frymoyer, A., Schwenk, H. T., Zorn, Y., Bio, L., Moss, J. D., Chasmawala, B., et al. (2020). Model-Informed Precision Dosing of Vancomycin in Hospitalized Children: Implementation and Adoption at an Academic Children's Hospital. *Front. Pharmacol.* 11, 551. doi:10.3389/fphar.2020.00551

Garcia, E., Ly, N., Diep, J. K., and Rao, G. G. (2021). Moving from Point-Based Analysis to Systems-Based Modeling: Integration of Knowledge to Address Antimicrobial Resistance against MDR Bacteria. *Clin Pharma Ther.* 110 (5), 1196–1206. doi:10.1002/cpt.2219

Garza, D. R., and Dutilh, B. E. (2015). From Cultured to Uncultured Genome Sequences: Metagenomics and Modeling Microbial Ecosystems. *Cell Mol. Life Sci.* 72 (22), 4287–4308. doi:10.1007/s00018-015-2004-1

Groussin, M., Poyet, M., Sistiaga, A., Kearney, S. M., Moniz, K., Noel, M., et al. (2021). Elevated Rates of Horizontal Gene Transfer in the Industrialized Human Microbiome. *Cell* 184 (8), 2053–e18. doi:10.1016/j.cell.2021.02.052

Hao, T., Wu, D., Zhao, L., Wang, Q., Wang, E., and Sun, J. (2018). The Genome-Scale Integrated Networks in Microorganisms. *Front. Microbiol.* 9, 296. doi:10.3389/fmicb.2018.00296

He, S., Leanse, L. G., and Feng, Y. (2021). Artificial Intelligence and Machine Learning Assisted Drug Delivery for Effective Treatment of Infectious Diseases. *Adv. Drug Deliv. Rev.* 178, 113922. doi:10.1016/j.addr.2021.113922

Hoo, G. S. R., Liew, Y. X., and Kwa, A. L. (2017). Optimisation of Antimicrobial Dosing Based on Pharmacokinetic and Pharmacodynamic Principles. *Indian J. Med. Microbiol.* 35 (3), 340–346. doi:10.4103/ijmm.IJMM_17_278

Hughes, J. H., Tong, D. M. H., Lucas, S. S., Faldasz, J. D., Goswami, S., and Keizer, R. J. (2021). Continuous Learning in Model-Informed Precision Dosing: A Case Study in Pediatric Dosing of Vancomycin. *Clin. Pharmacol. Ther.* 109 (1), 233–242. doi:10.1002/cpt.2088

Jorda, A., and Zeitlinger, M. (2020). Preclinical Pharmacokinetic/Pharmacodynamic Studies and Clinical Trials in the Drug Development Process of EMA-Approved Antibacterial Agents: A Review. *Clin. Pharmacokinet.* 59 (9), 1071–1084. doi:10.1007/s40262-020-00892-0

Kantasiripitak, W., Van Daele, R., Gijsen, M., Ferrante, M., Spriet, I., Dreesen, E., et al. (2020). Software Tools for Model-Informed Precision Dosing: How Well Do They Satisfy the Needs?. *Front. Pharmacol.* 11, 620. doi:10.3389/fphar.2020.00620

Khan, D. D., Lagerbäck, P., Cao, S., Lustig, U., Nielsen, E. I., Cars, O., et al. (2015). A Mechanism-Based Pharmacokinetic/pharmacodynamic Model Allows Prediction of Antibiotic Killing from MIC Values for WT and Mutants. *J. Antimicrob. Chemother.* 70 (11), 3051–3060. doi:10.1093/jac/dkv233

Kim, S. H., Kim, S. H., Bahn, J. W., Kim, Y. K., Chang, Y. S., Shin, E. S., et al. (2009). Genetic Polymorphisms of Drug-Metabolizing Enzymes and Anti-TB Drug-Induced Hepatitis. *Pharmacogenomics* 10 (11), 1767–1779. doi:10.2217/pgs.09.100

Kiratisin, P., Chongthaleong, A., Tan, T. Y., Lagamayo, E., Roberts, S., Garcia, J., et al. (2012). Comparative *In Vitro* Activity of Carbapenems against Major Gram-Negative Pathogens: Results of Asia-Pacific Surveillance from the COMPACT II Study. *Int. J. Antimicrob. Agents* 39 (4), 311–316. doi:10.1016/j.ijantimicag.2012.01.002

Knight-Schrijver, V. R., Chelliah, V., Cucurull-Sanchez, L., and Le Novère, N. (2016). The Promises of Quantitative Systems Pharmacology Modelling for Drug Development. *Comput. Struct. Biotechnol. J.* 14, 363–370. doi:10.1016/j.csbj.2016.09.002

Kowalska-Krochmal, B., and Dudek-Wicher, R. (2021). The Minimum Inhibitory Concentration of Antibiotics: Methods, Interpretation, Clinical Relevance. *Pathogens* 10 (2), 165. doi:10.3390/pathogens10020165

Lai, S.-J., Tu, I.-F., Wu, W.-L., Yang, J.-T., Luk, L. Y. P., Lai, M.-C., et al. (2017). Site-specific His/Asp Phosphoproteomic Analysis of Prokaryotes Reveals Putative Targets for Drug Resistance. *BMC Microbiol.* 17 (1), 1–10. doi:10.1186/s12866-017-1034-2

Landersdorfer, C. B., Nguyen, T.-H., Lieu, L. T., Nguyen, G., Bischof, R. J., Meeusen, E. N., et al. (2017). Substantial Targeting Advantage Achieved by Pulmonary Administration of Colistin Methanesulfonate in a Large-Animal Model. *Antimicrob. Agents Chemother.* 61 (1). doi:10.1128/aac.01934-16

Leblebicioglu, H., Cakir, N., Cakir, N., Celen, M., Kurt, H., Baris, H., et al. (2012). Comparative Activity of Carbapenem Testing (The COMPACT Study) in Turkey. *BMC Infect. Dis.* 12 (1), 1–8. doi:10.1186/1471-2334-12-42

Lin, Y.-W., Zhou, Q. T., Han, M.-L., Onufrak, N. J., Chen, K., Wang, J., et al. (2018). Mechanism-Based Pharmacokinetic/Pharmacodynamic Modeling of Aerosolized Colistin in a Mouse Lung Infection Model. *Antimicrob. Agen. Chemother.* 62 (3), e01965–e01917. doi:10.1128/AAC.01965-17

Llanos-Paez, C. C., Hennig, S., and Staatz, C. E. (2017). Population Pharmacokinetic Modelling, Monte Carlo Simulation and Semi-mechanistic Pharmacodynamic Modelling as Tools to Personalize Gentamicin Therapy. *J. Antimicrob. Chemother.* 72 (3), 639–667. doi:10.1093/jac/dkw461

Magill, S. S., O'Leary, E., Ray, S. M., Kainer, M. A., Evans, C., Bamberg, W. M., et al. (2021). Assessment of the Appropriateness of Antimicrobial Use in US Hospitals. *JAMA Netw. Open* 4 (3), e212007. doi:10.1001/jamanetworkopen.2021.2007

McAleenan, A., Ambrose, P. G., Bhavnani, S. M., Drusano, G. L., Hope, W. W., Mouton, J. W., et al. (2020). Methodological Features of Clinical Pharmacokinetic-Pharmacodynamic Studies of Antibacterials and Antifungals: a Systematic Review. *J. Antimicrob. Chemother.* 75 (6), 1374–1389. doi:10.1093/jac/dkaa005

Morales-Alvarez, M. C. (2020). Nephrotoxicity of Antimicrobials and Antibiotics. *Adv. Chronic Kidney Dis.* 27 (1), 31–37. doi:10.1053/j.ackd.2019.08.001

Mouton, J. W., Muller, A. E., Canton, R., Giske, C. G., Kahlmeter, G., and Turnidge, J. (2018). MIC-based Dose Adjustment: Facts and Fables. *J. Antimicrob. Chemother.* 73 (3), 564–568. doi:10.1093/jac/dkx427

Musante, C., Ramanujan, S., Schmidt, B., Ghobrial, O., Lu, J., and Heatherington, A. (2017). Quantitative Systems Pharmacology: A Case for Disease Models. *Clin. Pharmacol. Ther.* 101, 24–27. doi:10.1002/cpt.528

Muyderman, H., Sims, N. R., Tanaka, M., Fuku, N., Raghupathi, R., and Thyagarajan, D. (2012). The Mitochondrial T1095C Mutation Increases Gentamicin-Mediated Apoptosis. *Mitochondrion* 12 (4), 465–471. doi:10.1016/j.mito.2012.06.006

Nielsen, E. I., and Friberg, L. E. (2013). Pharmacokinetic-pharmacodynamic Modeling of Antibacterial Drugs. *Pharmacol. Rev.* 65 (3), 1053–1090. doi:10.1124/pr.111.005769

Nielsen, E. I., Viberg, A., Löwdin, E., Cars, O., Karlsson, M. O., and Sandström, M. (2007). Semimechanistic Pharmacokinetic/pharmacodynamic Model for Assessment of Activity of Antibacterial Agents from Time-Kill Curve Experiments. *Antimicrob. Agents Chemother.* 51 (1), 128–136. doi:10.1128/aac.00604-06

Nobu, M. K., Narihiro, T., Rinke, C., Kamagata, Y., Tringe, S. G., Woyke, T., et al. (2015). Microbial Dark Matter Ecogenomics Reveals Complex Synergistic Networks in a Methanogenic Bioreactor. *ISME J.* 9 (8), 1710–1722. doi:10.1038/ismej.2014.256

Ortwine, J. K., Kaye, K. S., Li, J., and Pogue, J. M. (2015). Colistin: Understanding and Applying Recent Pharmacokinetic Advances Pharmacotherapy. *J. Hum. Pharmacol. Drug Ther.* 35 (1), 11–16. doi:10.1002/phar.1484

Pacheu-Grau, D., Gómez-Durán, A., López-Pérez, M. J., Montoya, J., and Ruiz-Pesini, E. (2010). Mitochondrial Pharmacogenomics: Barcode for Antibiotic Therapy. *Drug Discov. Today* 15 (1-2), 33–39. doi:10.1016/j.drudis.2009.10.008

Pai, M. P., and Bearden, D. T. (2007). Antimicrobial Dosing Considerations in Obese Adult Patients. *Pharmacotherapy* 27 (8), 1081–1091. doi:10.1592/phco.27.8.1081

Palm, N. W., de Zoete, M. R., Cullen, T. W., Barry, N. A., Stefanowski, J., Hao, L., et al. (2014). Immunoglobulin A Coating Identifies Colitogenic Bacteria in Inflammatory Bowel Disease. *Cell* 158, 1000–1010. doi:10.1016/j.cell.2014.08.006

Peck, R. W. (2021). Precision Dosing: An Industry Perspective. *Clin. Pharmacol. Ther.* 109, 47–50. doi:10.1002/cpt.2064

Pérez-Pitarch, A., Ferriols-Lisart, R., Aguilar, G., Ezquer-Garín, C., Belda, F. J., and Guglieri-López, B. (2018). Dosing of Caspofungin Based on a Pharmacokinetic/pharmacodynamic Index for the Treatment of Invasive Fungal Infections in Critically Ill Patients on Continuous Venovenous Haemodiafiltration. *Int. J. Antimicrob. Agents* 51 (1), 115–121. doi:10.1016/j.ijantimicag.2017.05.013

Pichardo-Almarza, C., and Diaz-Zuccarini, V. (2016). From PK/PD to QSP: Understanding the Dynamic Effect of Cholesterol-Lowering Drugs on Atherosclerosis Progression and Stratified Medicine. *Curr. Pharm. Des.* 22, 6903–6910. doi:10.2174/1381612822666160905095402

Pulido, M. R., García-Quintanilla, M., Gil-Marqués, M. L., and McConnell, M. J. (2016). Identifying Targets for Antibiotic Development Using Omics Technologies. *Drug Discov. Today* 21 (3), 465–472. doi:10.1016/j.drudis.2015.11.014

Rawson, T. M., Wilson, R. C., O'Hare, D., Herrero, P., Kambugu, A., Lamorde, M., et al. (2021). Optimizing Antimicrobial Use: Challenges, Advances and Opportunities. *Nat. Rev. Microbiol.* 19 (12), 747–758. doi:10.1038/s41579-021-00578-9

Reddy, P. J., Ray, S., Sathe, G. J., Prasad, T. S. K., Rapole, S., Panda, D., et al. (2015). Proteomics Analyses ofBacillus Subtilisafter Treatment with Plumbagin, a Plant-Derived Naphthoquinone. *Omics a J. Integr. Biol.* 19 (1), 12–23. doi:10.1089/omi.2014.0099

Ribba, B., Grimm, H. P., Agoram, B., Davies, M. R., Gadkar, K., Niederer, S., et al. (2017). Methodologies for Quantitative Systems Pharmacology (QSP) Models: Design and Estimation. *CPT Pharmacometrics Syst. Pharmacol.* 6, 496–498. doi:10.1002/psp4.12206

Roberts, J. A., Paul, S. K., Akova, M., Bassetti, M., De Waele, J. J., Dimopoulos, G., et al. (2014). DALI: Defining Antibiotic Levels in Intensive Care Unit Patients: Are Current β-lactam Antibiotic Doses Sufficient for Critically Ill Patients? *Clin. Infect. Dis.* 58, 1072–1083. doi:10.1093/cid/ciu027

Rodríguez-Gascón, A., Solinís, M. Á., and Isla, A. (2021). The Role of PK/PD Analysis in the Development and Evaluation of Antimicrobials. *Pharmaceutics* 13 (6), 833. doi:10.3390/pharmaceutics13060833

Roemer, T., and Boone, C. (2013). Systems-Level Antimicrobial Drug and Drug Synergy Discovery. *Nat. Chem. Biol.* 9 (4), 222–231. doi:10.1038/nchembio.1205

Roggeveen, L. F., Guo, T., Driessen, R. H., Fleuren, L. M., Thoral, P., van der Voort, P. H. J., et al. (2020). Right Dose, Right Now: Development of AutoKinetics for Real Time Model Informed Precision Antibiotic Dosing Decision Support at the Bedside of Critically Ill Patients. *Front. Pharmacol.* 11, 646. doi:10.3389/fphar.2020.00646

Rydzanicz, M., Wróbel, M., Pollak, A., Gawecki, W., Brauze, D., Kostrzewska-Poczekaj, M., et al. (2010). Mutation Analysis of Mitochondrial 12S rRNA Gene in Polish Patients with Non-syndromic and Aminoglycoside-Induced Hearing

Loss. *Biochem. Biophys. Res. Commun.* 395 (1), 116–121. doi:10.1016/j.bbrc.2010.03.149

Schelli, K., Zhong, F., and Zhu, J. (2017). Comparative Metabolomics Revealing *Staphylococcus aureus* Metabolic Response to Different Antibiotics. *Microb. Biotechnol.* 10 (6), 1764–1774. doi:10.1111/1751-7915.12839

Scheffler, R. J., Colmer, S., Tynan, H., Demain, A. L., and Gullo, V. P. (2013). Antimicrobials, Drug Discovery, and Genome Mining. *Appl. Microbiol. Biotechnol.* 97 (3), 969–978. doi:10.1007/s00253-012-4609-8

Schmidt, S., Barbour, A., Sahre, M., Rand, K. H., and Derendorf, H. (2008). PK/PD: New Insights for Antibacterial and Antiviral Applications. *Curr. Opin. Pharmacol.* 8 (5), 549–556. doi:10.1016/j.coph.2008.06.010

Shen, F., Tang, X., Wang, Y., Yang, Z., Shi, X., Wang, C., et al. (2015). Phenotype and Expression Profile Analysis of *Staphylococcus aureus* Biofilms and Planktonic Cells in Response to Licochalcone A. *Appl. Microbiol. Biotechnol.* 99 (1), 359–373. doi:10.1007/s00253-014-6076-x

Shin, S. J., Kang, S. G., Nabin, R., Kang, M. L., and Yoo, H. S. (2005). Evaluation of the Antimicrobial Activity of Florfenicol against Bacteria Isolated from Bovine and Porcine Respiratory Disease. *Vet. Microbiol.* 106, 73–77. doi:10.1016/j.vetmic.2004.11.015

Singh, R., Sripada, L., and Singh, R. (2014). Side Effects of Antibiotics during Bacterial Infection: Mitochondria, the Main Target in Host Cell. *Mitochondrion* 16, 50–54. doi:10.1016/j.mito.2013.10.005

Sorger, P. K., Allerheiligen, S. R. B., Abernethy, D. R., Altmann, R. B., Brouwer, K. L. R., Califano, A., et al. (2011). "Quantitative and Systems Pharmacology in the Post-Genomic Era: New Approaches to Discovering Drugs and Understanding Therapeutic Mechanisms (White Paper)," in *An NIH White Paper by the QSP Workshop Group* (Rockville, MD, USA: Bethesda), 48.

Tong, S., Amand, C., Kieffer, A., and Kyaw, M. H. (2018). Trends in Healthcare Utilization and Costs Associated with Pneumonia in the United States during 2008-2014. *BMC Health Serv. Res.* 18, 715. doi:10.1186/s12913-018-3529-4

Trang, M., Dudley, M. N., and Bhavnani, S. M. (2017). Use of Monte Carlo Simulation and Considerations for PK-PD Targets to Support Antibacterial Dose Selection. *Curr. Opin. Pharmacol.* 36, 107–113. doi:10.1016/j.coph.2017.09.009

Tuntland, T., Ethell, B., Kosaka, T., Blasco, F., Zang, R. X., Jain, M., et al. (2014). Implementation of Pharmacokinetic and Pharmacodynamic Strategies in Early Research Phases of Drug Discovery and Development at Novartis Institute of Biomedical Research. *Front. Pharmacol.* 5, 174. doi:10.3389/fphar.2014.00174

Valenza, G., Seifert, H., Decker-Burgard, S., Laeuffer, J., Morrissey, I., Mutters, R., et al. (2012). Comparative Activity of Carbapenem Testing (COMPACT) Study in Germany. *Int. J. Antimicrob. Agents* 39 (3), 255–258. doi:10.1016/j.ijantimicag.2011.10.015

van der Graaf, P. H., and Benson, N. (2011). Systems Pharmacology: Bridging Systems Biology and Pharmacokinetics-Pharmacodynamics (PKPD) in Drug Discovery and Development. *Pharm. Res.* 28, 1460–1464. doi:10.1007/s11095-011-0467-9

Velkov, T., Bergen, P. J., Lora-Tamayo, J., Landersdorfer, C. B., and Li, J. (2013). PK/PD Models in Antibacterial Development. *Curr. Opin. Microbiol.* 16 (5), 573–579. doi:10.1016/j.mib.2013.06.010

Wakefield, J., Aarons, L., and Racine-Poon, A. (1999). "The Bayesian Approach to Population Pharmacokinetic/pharmacodynamic Modeling," in *Case Studies in Bayesian Statistics. Lecture Notes in Statistics*. Editor C. Gatsonis (New York, NY: Springer), 140. doi:10.1007/978-1-4612-1502-8_4

Wang, Z., Gerstein, M., and Snyder, M. (2009). RNA-seq: a Revolutionary Tool for Transcriptomics. *Nat. Rev. Genet.* 10 (1), 57–63. doi:10.1038/nrg2484

Wei, C. F., Shien, J. H., Chang, S. K., and Chou, C. C. (2016). Florfenicol as a Modulator Enhancing Antimicrobial Activity: Example Using Combination with Thiamphenicol against *Pasteurella Multocida*. *Front. Microbiol.* 7, 389. doi:10.3389/fmicb.2016.00389

Wicha, S. G., Märtson, A. G., Nielsen, E. I., Koch, B. C. P., Friberg, L. E., Alffenaar, J. W., et al. (2021). From Therapeutic Drug Monitoring to Model-Informed Precision Dosing for Antibiotics. *Clin. Pharmacol. Ther.* 109 (4), 928–941. doi:10.1002/cpt.2202

Woodhead, J. L., Brock, W. J., Roth, S. E., Shoaf, S. E., Brouwer, K. L., Church, R., et al. (2017). Application of a Mechanistic Model to Evaluate Putative Mechanisms of Tolvaptan Drug-Induced Liver Injury and Identify Patient Susceptibility Factors. *Toxicol. Sci.* 155, 61–74. doi:10.1093/toxsci/kfw193

Wozniak, J. M., Mills, R. H., Olson, J., Caldera, J. R., Sepich-Poore, G. D., Carrillo-Terrazas, M., et al. (2020). Mortality Risk Profiling of *Staphylococcus aureus* Bacteremia by Multi-Omic Serum Analysis Reveals Early Predictive and Pathogenic Signatures. *Cell* 182 (5), 1311–e14. doi:10.1016/j.cell.2020.07.040

Yadav, R., Bulitta, J. B., Wang, J., Nation, R. L., and Landersdorfer, C. B. (2017). Evaluation of Pharmacokinetic/Pharmacodynamic Model-Based Optimized Combination Regimens against Multidrug-Resistant *Pseudomonas aeruginosa* in a Murine Thigh Infection Model by Using Humanized Dosing Schemes. *Antimicrob. Agents Chemother.* 61, e01268–17. doi:10.1128/AAC.01268-17

Yapa, S. W. S., Li, J., Patel, K., Wilson, J. W., Dooley, M. J., George, J., et al. (2014). Pulmonary and Systemic Pharmacokinetics of Inhaled and Intravenous Colistin Methanesulfonate in Cystic Fibrosis Patients: Targeting Advantage of Inhalational Administration. *Antimicrob. Agents Chemother.* 58 (5), 2570–2579. doi:10.1128/AAC.01705-13

Zhang, A. N., Gaston, J. M., Dai, C. L., Zhao, S., Poyet, M., Groussin, M., et al. (2021). An Omics-Based Framework for Assessing the Health Risk of Antimicrobial Resistance Genes. *Nat. Commun.* 4765, 1–11. doi:10.1038/s41467-021-25096-3

Zhao, S., and Iyengar, R. (2012). Systems Pharmacology: Network Analysis to Identify Multiscale Mechanisms of Drug Action. *Annu. Rev. Pharmacol. Toxicol.* 52, 505–521. doi:10.1146/annurev-pharmtox-010611-134520

Zhu, Y., Czauderna, T., Zhao, J., Klapperstueck, M., Maifiah, M. H. M., Han, M. L., et al. (2018). Genome-scale Metabolic Modeling of Responses to Polymyxins in *Pseudomonas aeruginosa*. *Gigascience* 7, giy021. doi:10.1093/gigascience/giy021

Conflict of Interest: The authors declare that the research was conducted in the absence of any commercial or financial relationships that could be construed as a potential conflict of interest.

Publisher's Note: All claims expressed in this article are solely those of the authors and do not necessarily represent those of their affiliated organizations, or those of the publisher, the editors and the reviewers. Any product that may be evaluated in this article, or claim that may be made by its manufacturer, is not guaranteed or endorsed by the publisher.

frontiers | Frontiers in Pharmacology

ORIGINAL RESEARCH
published: 19 July 2022
doi: 10.3389/fphar.2022.910789

A Quantitative Systems Pharmacology Model of Liver Lipid Metabolism for Investigation of Non-Alcoholic Fatty Liver Disease

Theodore R. Rieger, Richard J. Allen and Cynthia J. Musante*

Quantitative Systems Pharmacology, Early Clinical Development, Pfizer Inc, Cambridge, MA, United States

Non-alcoholic fatty liver disease is a metabolic and inflammatory disease that afflicts many people worldwide and presently has few treatment options. To enhance the preclinical to clinical translation and the design of early clinical trials for novel therapeutics, we developed a Quantitative Systems Pharmacology model of human hepatocyte lipid metabolism. The intended application of the model is for simulating anti-steatotic therapies for reversing fatty liver. We parameterized the model using literature data from humans with both normal and elevated liver fat. We assessed that the model construct was sufficient to generate a virtual population of NAFLD patients that matched relevant statistics of a published clinical cohort, and then validated the model response to treatment by simulating pioglitazone and diet intervention in the virtual population. Finally, a sensitivity analysis was performed to determine the best points of intervention for reducing hepatic steatosis. Analysis of the model suggests the most potent method for reducing hepatic steatosis is by limiting non-esterified fatty acid flux from the adipose to the liver.

Keywords: QSP, NAFLD, liver, mathematical modeling, steatosis, triglyceride, metabolism

OPEN ACCESS

Edited by:
Amal Kaddoumi,
Auburn University, United States

Reviewed by:
Rajesh H. Amin,
Auburn University, United States
Joana Paiva Miranda,
University of Lisbon, Portugal

****Correspondence:***
Theodore R. Rieger
ted.rieger@pfizer.com

Specialty section:
This article was submitted to Translational Pharmacology, a section of the journal Frontiers in Pharmacology

Received: *01 April 2022*
Accepted: *21 June 2022*
Published: *19 July 2022*

Citation:
Rieger TR, Allen RJ and Musante CJ (2022) A Quantitative Systems Pharmacology Model of Liver Lipid Metabolism for Investigation of Non-Alcoholic Fatty Liver Disease. Front. Pharmacol. 13:910789. doi: 10.3389/fphar.2022.910789

1 INTRODUCTION

Non-alcoholic fatty liver disease (NAFLD) is a progressive disorder of the liver that may affect more than 25% of the worldwide population (Younossi et al., 2016; Mitra et al., 2020). While the more advanced stages of the disease (non-alcoholic steatohepatitis, NASH) are notable for inflammation and fibrosis of the liver, the early stages usually begin with steatosis, the accumulation of triglyceride in the hepatocytes (Parthasarathy et al., 2020). The exact molecular mechanism(s) that cause progression of the disease from simple steatosis to the more advanced forms are unknown; however, lipotoxicity from excess lipids inducing an inflammatory response is often postulated as an important driver (Marra and Svegliati-Baroni, 2018). For this reason, pharmacological intervention in the early stages of the disease, i.e., preventing and reversing the accumulation of lipids in the liver, is an attractive therapeutic hypothesis (Calle et al., 2021). Many questions arise in the pre-clinical stages of NAFLD drug development related to the translation of efficacy and safety assessments from animal models to humans. Common concerns include: is the preclinical model representative of the pathological state in humans? Do differences in eating patterns between rodents and humans affect our conclusions? Are there points of pathway intervention in humans that will have more "horsepower" than others for reducing steatosis? Mathematical models, based on human physiology and including mechanisms of disease, can supplement the knowledge we gain from pre-clinical *in vitro* and *in vivo* models to address some of these questions early in drug development.

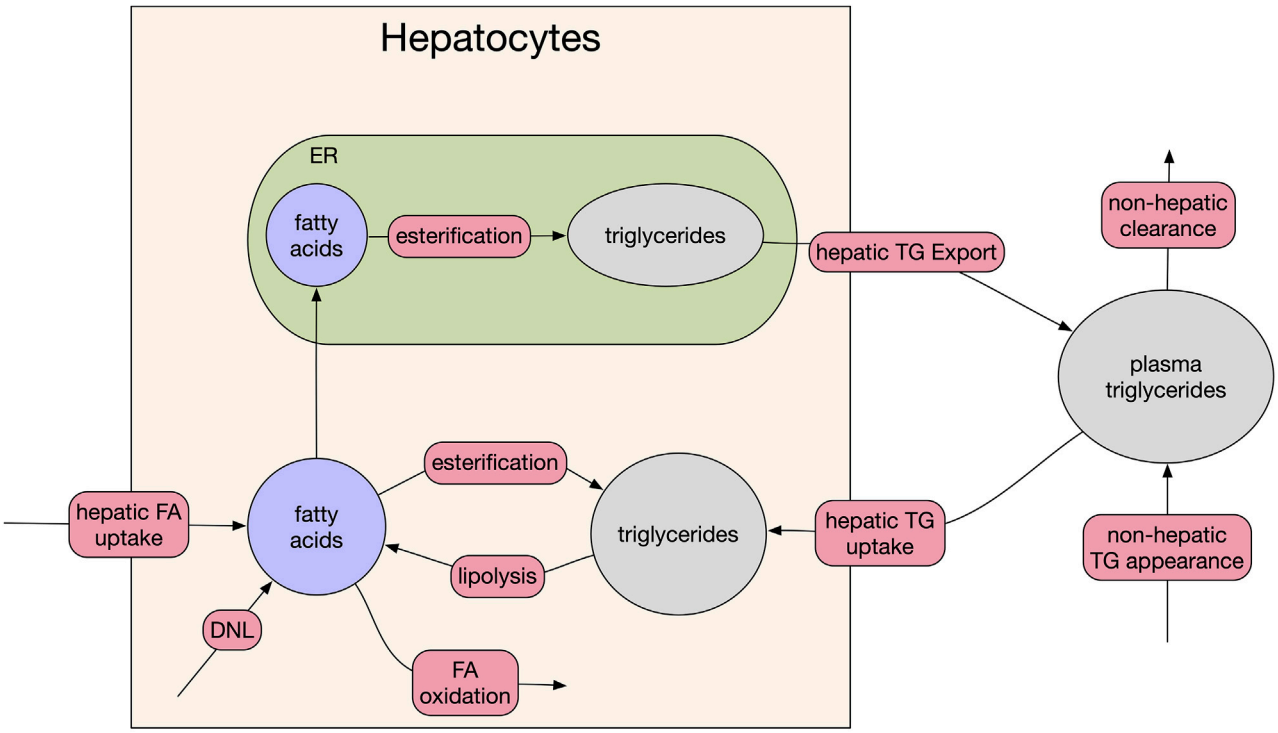

FIGURE 1 | Model schematic. The three compartments of the model are: plasma, hepatocyte cytosol, and hepatocyte endoplasmic reticulum (ER). Red bubbles on arrows represent fluxes of the model, filled ellipses are the five species of the model. For clarity, feedback between DNL and fatty acid (beta) oxidation and cytosolic fatty acid levels and FA uptake are omitted (see source code for full equations).

Quantitative Systems Pharmacology (QSP) models are mechanistic models that utilize our prior knowledge of the biological system, disease mechanisms, and response to treatment informed by data from various sources. QSP models have previously been applied to many physiological systems including COVID-19 (Dai et al., 2021). Notably for understanding NAFLD, there are several prior QSP models that successfully simulate aspects of liver metabolism (Allen and Musante 2018; Noorman et al., 2019; Holzhutter and Berndt 2021; Siler 2022).

Here we developed and analyzed a new model of liver lipid metabolism. In compliment to prior QSP models, we focused the model on simulating therapies for reducing hepatic steatosis in patients with early NAFLD. We focused on developing a "fit-for-purpose" QSP model to aid our goal of developing a model that is mechanistic but highly computationally efficient for simulating early phase clinical trials in NAFLD patients and developing large virtual populations. We demonstrate that the model successfully produces a virtual population with the statistics of a clinical population at steady state and appropriately responds to pioglitazone treatment or dietary intervention. Finally, we use the model and virtual population to perform a sensitivity analysis to identify the pathways that are the most promising intervention points for reducing steatosis as potential monotherapies.

2 METHODS

2.1 Biological Scope of the Model

The model consists of three biological compartments and five dynamic species focused on fatty acids and lipid metabolism (**Figure 1**). The species are hepatocyte cytosolic fatty acids, hepatocyte cytosolic triglyceride, hepatocyte endoplasmic reticulum (ER) fatty acids, hepatocyte ER triglycerides, and plasma triglycerides. In the model, plasma triglycerides are a lumped representation of all forms of circulating triglycerides including very-low-density lipoprotein (VLDL) synthesized in the liver and chylomicrons from intestinal enterocytes, as well as smaller diameter species such as high-density lipoproteins and low-density lipoproteins.

Since the primary dynamics of interest are the liver triglyceride pools, which do not change appreciably on an hourly basis, several simplifying assumptions were made:

1) The fluxes of the model represent the 24-h average flux (vs. an hourly dynamic). This choice is due to the sparsity of dynamic liver fat data in the literature, usually only being reported pre-/post-treatment after a time span of weeks to month.
2) All inputs to the model are constant (e.g., fatty acid flux from adipose tissue to liver), unless explicitly modified by therapy. Like (1) this choice reflects the sparsity of dynamic data vs.

time in clinical studies. Fat mass is usually reported at pre-/post-treatment.

3) No explicit modeling of dynamics such as receptor cycling. As above for (1) and (2), this reflects a time-resolution of available pre-clinical and clinical data. Adding faster dynamics would come at considerable computational cost for no additional certainty in prediction.
4) The mitochondria of hepatocytes will oxidize available fatty acids at a rate determined by the basal metabolic rate of the liver and there is no feedback from carbohydrate content of the hepatocytes.

The focus of the modeling on describing 24-h average fluxes reflects both the lack of data on the minute to hour timescale and the modeling goal of describing clinical trial data points collected weeks apart.

2.2 Implementation

We converted the conceptual model (**Figure 1**) into a system of five non-linear ordinary differential equations. By default, we assumed the kinetics of the model were non-saturating mass-action kinetics. We used saturating kinetics (i.e., Michaelis-Menten type) when we had explicit information for enzymatic constants (e.g., VLDL release from the liver). To reflect some known homeostatic feedback mechanisms, we added two feedback loops, which were free parameters in plausible patient fitting (**Sections 2.3**, **2.4**). First, we added feedback between the rate of *de novo* lipogenesis (DNL) and fatty acid oxidation (McGarry et al., 1977; McGarry et al., 1978). Second, we added feedback between the concentration of cytosolic fatty acids and the uptake rate to reflect homeostatic mechanisms potentially exerted by sterol response element binding protein 1 (SREBP1c), (Ferre and Foufelle 2010).

We implemented the model using the Julia Language, v1.7 (Bezanson et al., 2017). All source code is available online (Rieger et al., 2022).

2.3 Base Parameterization

The model contains 22 parameters including basal concentrations and excluding parameters related to therapies. Using published data and steady state constraints on all the pools of the model, we determined a basal value for 20 parameters. The remaining two parameters relate to how the system adapts to dynamic changes from baseline and were allowed to vary across the Virtual Population (**Section 2.5**).

For creating plausible patients, we established a plausible range for each parameter (log) centered around the pre-determined basal value described above. Absent specific published data, we set the standard deviation of each parameter such that 90% of values are between 0.25 × and 4 × the baseline. The full set of model parameters, their plausible ranges and the derivation of each value is included with the source code (Rieger et al., 2022). The baseline parameters are in **Supplementary Table S1**, as well as the included supplementary Microsoft Excel sheet: *parameters.xlsx* with the source code. The algebraic derivations of many of the model parameters, using literature or steady state constraints are included in the supplementary Pluto notebook: *derived_parameters.jl.*

2.4 NAFLD Virtual Population.

We based our selection of a virtual population on our previously published methodology using Metropolis-Hastings and acceptance-rejection sampling (Rieger and Musante 2016; Rieger et al., 2018). We used the baseline parameterization of **Supplementary Table S1** and our estimated variability for the parameters as a joint log-normal distribution. For our naïve search, we assumed the covariance matrix to be diagonal.

The two observables of interest for creating a virtual population were liver fat and plasma triglycerides. We wished to create a general-purpose population that could be sub-selected to make many different patient populations (e.g., healthy normal volunteers, steatotic, hypertriglycerdemic). We digitized the individual subject data shown in Kotronen et al. (2007). (Kotronen and Yki-Jarvinen, 2008), which contained simultaneous measurements of liver fat % and fasting serum triglycerides. Based on the digitized data, we fitted a joint log-normal distribution for the desired statistics of our virtual population. To avoid issues with having to truncate the observable distributions or our parameter distributions, we fitted the full distributions of Kotronen et al. (2007) including both healthy individuals, hyperlipidemics (elevated triglycerides), simple NAFLD, and NAFLD with hyperlipidemia. We allowed the Metropolis-Hastings algorithm to proceed until the algorithm accepted a pre-determined (500,000) number of plausible patients. We then selected our final virtual population using acceptance-rejection sampling (leaving 1,900 virtual patients). Since the data set was for the general population, our final virtual population included both subjects with normal (<5% liver fat) and high liver fat (>5%). We sub-selected all virtual patients with liver fat > 5% as our NAFLD cohort (900) (Chalasani et al., 2018). Due to the stochastic nature of the acceptance-rejection sampling, the final population size varied ± 5% between runs, but the variance of the virtual population selection was found to have no significant effect on the results or conclusions, thus we present the results as a single virtual population run of the model.

2.5 Simulation of Pioglitazone Therapy

Pioglitazone is a PPARγ agonist approved for the treatment of type 2 diabetes. While expression of PPARγ has been shown in several tissues of humans, it is highly enriched in adipocytes (Fajas et al., 1997), we assumed the primary pharmacodynamic effect of pioglitazone therapy in humans is insulin-sensitization of adipose tissue (Derosa et al., 2009; Gastaldelli et al., 2009). Thus, the pharmacodynamic effect of pioglitazone therapy was implemented as a reduction in non-esterified fatty acids (NEFAs) released from adipose to liver. For simulation and validation of our model, we selected a study by Belfort et al. (Belfort et al., 2006), which included 24 weeks of pioglitazone or placebo treatment in a randomized cohort of patients (26/group, 45 mg QD) with NAFLD (see Belfort et al. for additional details on the study population and protocol). We estimated the 24-h mean change in NEFAs as the averaged the percent changes observed on the meal challenge and at fasting,

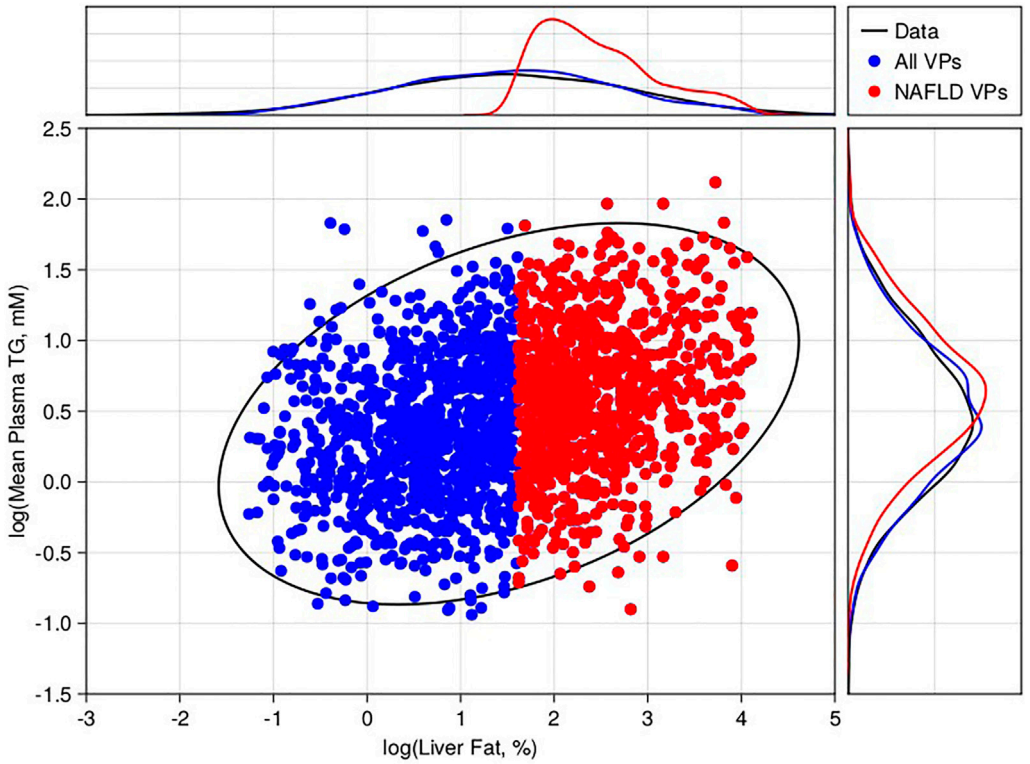

FIGURE 2 | Virtual population selection with comparison to literature-derived constraints. 2D scatter compares the steady state 24-h average plasma triglycerides versus liver fat % for 2,000 selected virtual patients (blue—non-NAFLD, red—NAFLD). For comparison, we calculated the 95% confidence interval of the 2D-lognormal distribution derived from literature (black ellipse). The marginal distributions for the virtual patients (blue and red lines) for liver fat % (top) and plasma triglycerides (top) are also shown versus the data (black lines).

representing roughly half the day is spent in the prandial/postprandial period (−28%, **Supplementary Material S1**). We implemented the effect of pioglitazone in the model as a step change to the uptake flux of NEFAs.

2.6 Simulation of Dietary Intervention

We represented the effects of sustained dietary intervention (i.e., reduced food intake) through three simultaneous changes in the model fluxes:

1) Reduced chylomicron influx to the model, representing the reduction in fat consumption.
2) Reduced DNL flux, representing reduced carbohydrate consumption.
3) Reduced NEFA flux to the liver, representing reduced adipose mass.

Importantly, for the purpose of model validation, we wanted to fix these three effects and compare the model predictions to an observed percent change in liver fat. We chose a 26-weeks weight loss study by Haufe et al. (2013). in NAFLD patients (50 patients) for testing our model, see original source for additional details on study protocol and demographics. We converted weight loss into a percentage change in food intake using a published body weight macronutrient model (Hall, 2010). Using the Hall model, we determined that a mean reduction caloric intake of 20% was necessary to achieve the same mean weight loss as Haufe et al. (2013) over 6 months. We fixed the effect on chylomicrons at -20% based on the food intake calculation. Similarly, for DNL flux we used the relationship measured in Schwarz et al. (1995). to calculate a 20% reduction in food intake will reduce DNL by 55% on average. Finally, the NEFA flux was based on the measured change in adipose mass in Haufe et al. (2013) scaled by the 2/3rd factor used by the Hall model for calculating lipolysis rates. Taking these factors together, we reduced NEFA flux by 11% (**Supplementary Material** for additional details).

2.7 Sensitivity Analysis.

Four potential therapeutic strategies were tested:

1) Inhibition of DNL.
2) Inhibition of NEFA uptake to liver.
3) Inhibition of Esterification of Triglycerides in Hepatocytes
4) Activation of VLDL synthesis, increasing triglycerides export from the liver

For each of these, we assumed constant, 24-h inhibition or activation (for VLDL synthesis). We swept each corresponding parameter from 0% → 95% inhibition and simulated our cohort of NAFLD patients for 26 weeks. For activation we swept the

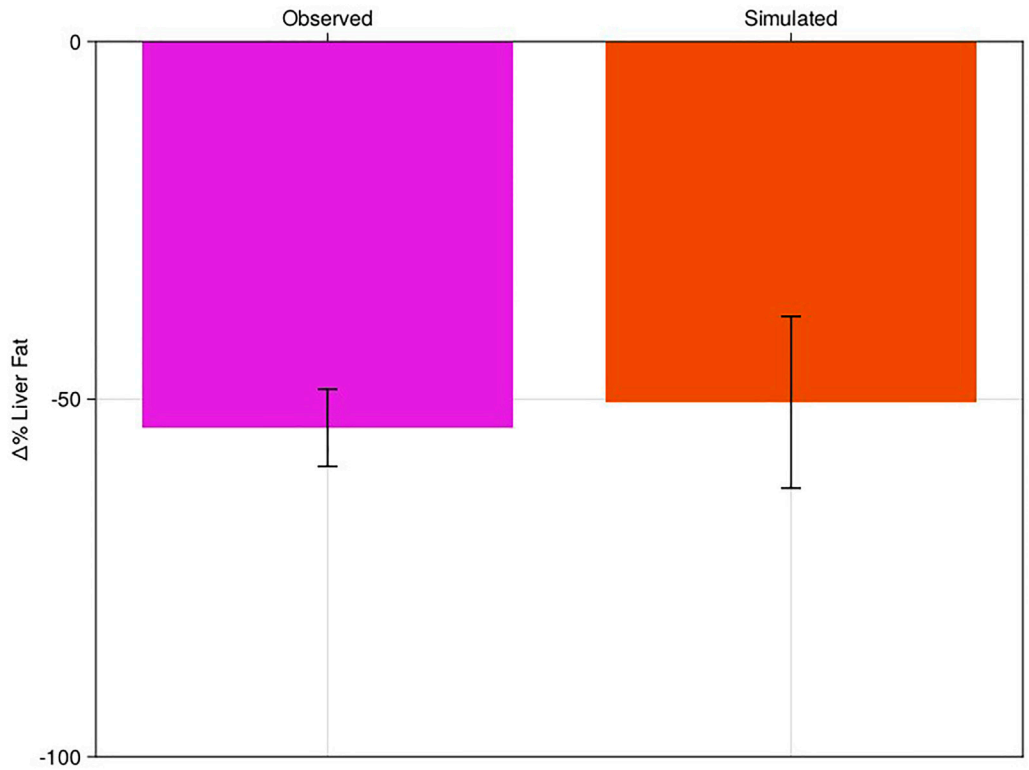

FIGURE 3 | Percent change in liver fat of virtual population to pioglitazone-like therapy with comparison to literature. Clinical results of Belfort et al. (pink bar) compared to the NAFLD virtual patient response to pioglitazone (red). Bars are mean response of the cohort or virtual patients; error bars are estimated standard deviations.

inverse of the inhibition (1 × → 20 × the baseline parameter value). The output comparator was the percentage change in liver fat from baseline value.

3 RESULTS

3.1 Virtual Patient Creation

Following the methodology of **Section 2.4**, we generated 500,000 plausible patients by drawing alternative parameters using a Metropolis-Hastings algorithm, simulating to steady state, and checking the final steady state was within the pre-defined state limits. From the initial plausible population, a final virtual population of 1,900 virtual patients was selected (**Figure 2**), including 900 virtual patients with baseline liver fat > 5% (NAFLD virtual patients). This cohort of NAFLD virtual patients was used to test the model's response to interventions.

3.2 Model Validation With Pioglitazone and Diet Intervention.

Pioglitazone is a peroxisome proliferators-activated receptor gamma (PPAR) agonist and putative insulin sensitizer approved for the treatment of type 2 diabetes due to its efficacy on reducing plasma glucose (Phatak and Yin 2006). Due to its mechanism of action, pioglitazone has also been investigated for the treatment of NAFLD (Belfort et al., 2006; Gastaldelli et al., 2021). Following the methods of **Section 2.5** we simulated pioglitazone as a validation of the model's response to intervention. We fixed the Virtual Population created in **Section 3.1** with no new fitting to the trial data. We induced a step change of −28% in the NEFA uptake to the model to simulate the estimated observed mean reduction in NEFAs in the Haufe et al. (2013) study. We then simulated the model for 24 weeks, allowing it to equilibrate at a new liver fat level for each patient and compared the results to the published cohort-level data from Belfort et al. (**Figure 3**; **Supplementary Figure S1A**).

Simulation of dietary intervention was like pioglitazone therapy, but the "pharmacodynamics" of the intervention are more complicated, allowing us to test additional sensitivities of the model (**Section 2.6**). Like the pioglitazone intervention, we started with the NAFLD cohort established in **Section 3.1** and did no additional fitting based on the dietary literature results. We simulated the model for 26 weeks and compared the % change in liver fat to the published values from Haufe et al. (2013) (**Figure 4**; **Supplementary Figure S1B**).

Based on our assessment of a reasonable mean response of the model, relative to clinical variability, we felt confident that the base model parameterization was reasonable to assess against novel interventions.

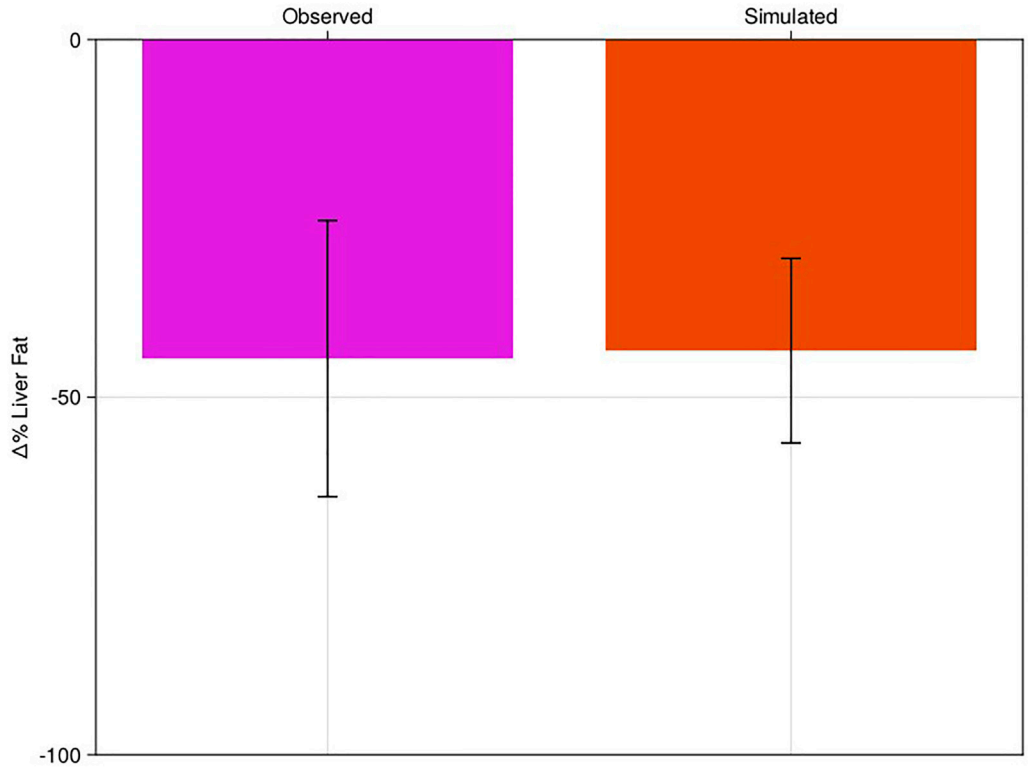

FIGURE 4 | Percent change of liver fat of virtual population to diet-like therapy with comparison to literature. Clinical results of Haufe et al. (pink bar) compared to the NAFLD virtual patient response to dietary intervention (red). Bars are mean response of the cohort or virtual patients; error bars are estimated standard deviations.

3.3 Sensitivity Analysis

Having established the model, at least at steady state, we wished to use the model as a tool to help us understand how future treatments for NAFLD may translate from preclinical to clinical efficacy. Dietary intervention and pioglitazone treatment demonstrated there are many ways to reduce liver fat, which may not all be equal for efficacy. We performed a sensitivity analysis on four points of intervention assuming a constant 24-h level of inhibition or activation for 26 weeks (**Section 2.7**). We observed that the model is most sensitive to NEFA uptake to the hepatocytes, followed by DNL and esterification, and least sensitive to VLDL activation (**Figure 5**; **Supplementary Figure S2**).

4 DISCUSSION

NAFLD is a complex disease whose etiology is poorly understood. We do not yet know the best point(s) of intervention and it is seeming unlikely that any one therapy will be the "silver bullet" for all forms of the disease. Therefore, the medical community will likely be attacking treatment of NAFLD/NASH from several angles: inflammation, fibrosis, and metabolic. The model presented here provides a starting point for understanding metabolic treatments.

The sensitivity analysis we performed provides a high-level indicator of the likelihood of success of a general therapeutic strategy. With a goal of reducing liver steatosis, the results of our simulation studies suggest that the most effective therapeutic strategy is to reduce the carbon flux *via* NEFAs from the adipose tissue to the liver. This observation agrees well with positive clinical trials for pioglitazone. Treatment of NAFLD patients with GLP-1 agonists, putatively acting through both anorexic effects and insulinotropic effects to suppress lipolysis, seems to support this prediction as well (Newsome et al., 2021). Direct inhibition of lipogenic flux in the liver, *via* DNL or esterification suppression, also was found to be a potent mechanism for reducing steatosis. With multiple viable avenues, the best therapeutic strategy may come down to the practical druggability of targets or a combination of different approaches.

Any model is a necessary simplification of the true biology; however, the goal is to create a model that is still fit-for-purpose. Here we presented a base model that can be expanded as required for specific research questions. As part of our model-building, we made the explicit assumptions to use coarser (24-h average) dynamics for the metabolic pools of the model. While potentially limiting for certain research questions (e.g., dose timing relative to a meal), this decision keeps the model dynamics on a timescale with the vast majority of published clinical data to date. In addition to allowing the model to be

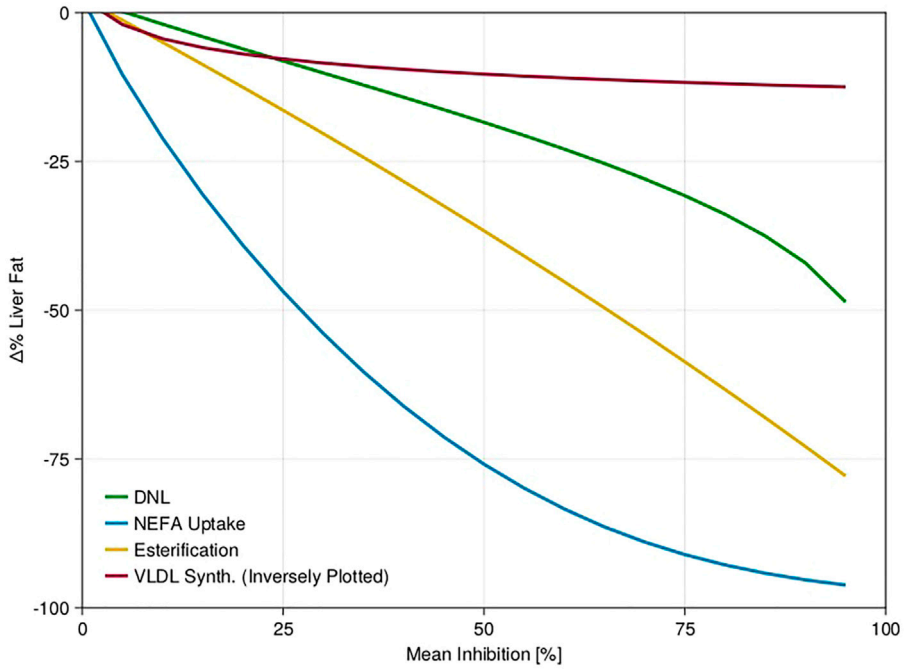

FIGURE 5 | Sensitivity analysis of mean NAFLD virtual population response to step changes in five model fluxes. Fluxes were varied as described in the text for four different fluxes. Three fluxes were inhibited, one flux (VLDL synthesis) was activated. For the activated flux we plotted it on the same scale as the other three by plotting the x-axis inversely. For clarity, only the mean response of the NAFLD virtual patients is shown.

reasonably constrained by the available data, an added benefit is coarser dynamics will have a significant numerical performance benefit for practical simulation of the model. Our assumption that a 24-h averaged model can still be of practical benefit is justified by the model's ability to reproduce liver fat changes for complex interventions, like diet or pioglitazone, without refitting a virtual population generated based on the general literature.

While the model showed a close quantitative match to the mean percent change in liver fat of the two intervention studies, it is worth noting that quantitatively capturing the clinical variability of any given study can be very difficult. Simulating the variability likely requires a specialized virtual population (subselected or specially generated) for the cohorts of that study and a careful assessment of variability of treatment (i.e., pharmacokinetics, adherence) and possibly interoccasion variability. One other limitation of the current validation studies are the pleiotropic effects of both pioglitazone and diet. For both we chose to focus on some of the best documented or hypothesized metabolic effects, but others are possible. Primarily this meant the effect would be driven through reductions of NEFAs and DNL. In the case of pioglitazone, PPARγ is expressed in both the liver and macrophages of rodents, but to a lower level than observed in adipose (Czaja 2009). However, we cannot necessarily discount the presence of PPARγ in these extra-adipose tissues contributes to NAFLD outcomes beyond steatosis (e.g., inflammation). While the approach taken here captured the steatosis endpoint reasonably, a more thorough understanding of pioglitazone's clinical efficacy should be systematically undertaken to understand treatment of the disease more holistically.

A few areas of potential interest for future expansion of the model include regulation of lipogenic genes by SREBP1c, hourly dynamics of DNL and lipolysis from adipose in response to food intake, and more detailed handling of lipoprotein dynamics in the plasma. Beyond these metabolism-centric additions, we could also consider the lifecycle of the hepatocyte and how it is affected by lipotoxicity. Incorporating the lifecycle of the hepatocyte and turnover will also allow the direct use of commonly collected biomarkers of liver function, like alanine aminotransferase (ALT) and aspartate aminotransferase (AST). Ultimately, considering hepatocyte apoptosis and necrosis in response to stress could lead to an evaluation of how to couple the metabolic disorder of NAFLD with the inflammatory response of NASH and consider the progression/reversal of the disease. However, each of these steps should be taken as required for a particular drug-discovery research question of translation or extrapolation from short-term to longer-term trials.

The model we presented is the basis of a flexible QSP platform for understanding metabolic therapies, easily expanded to include new targets, and amenable to exploring potential combination therapy approaches. Based on currently available clinical and biological data, any mechanistic model of NAFLD pathophysiology will necessarily require a detailed and thorough exploration of uncertainty. The advantage of the model we presented here is its size and speed, which allows for development and simulations of large virtual populations. This flexibility is a crucial facilitator for providing timely and robust simulations for clinical applications. By applying this model to existing and emerging clinical and biological data it

will provide further quantitative understanding of the human pathophysiology of NAFLD and how to best design treatments for the early phases of the disease.

DATA AVAILABILITY STATEMENT

The original contributions presented in the study are included in the article/**Supplementary Material**, further inquiries can be directed to the corresponding author.

AUTHOR CONTRIBUTIONS

TR and RA conceived the model and built the initial versions. TR, RA, and CM refined the model and its application to therapies for NAFLD. TR drafted the initial manuscript and source code for publication. TR, RA, and CM revised the final manuscript.

FUNDING

This research is supported by Pfizer, Inc.

ACKNOWLEDGMENTS

The authors wish to thank many colleagues from Pfizer's Internal Medicine Research Unit, Early Clinical Development, and Medicinal Chemistry groups who provided valuable insights that helped to develop and refine the model.

SUPPLEMENTARY MATERIAL

The Supplementary Material for this article can be found online at: https://www.frontiersin.org/articles/10.3389/fphar.2022.910789/full#supplementary-material

REFERENCES

Allen, R. J., and Musante, C. J. (2018). A Mathematical Analysis of Adaptations to the Metabolic Fate of Fructose in Essential Fructosuria Subjects. *Am. J. Physiol. Endocrinol. Metab.* 315 (3), E394–E403. doi:10.1152/ajpendo.00317.2017

Belfort, R., Harrison, S. A., Brown, K., Darland, C., Finch, J., Hardies, J., et al. (2006). A Placebo-Controlled Trial of Pioglitazone in Subjects with Nonalcoholic Steatohepatitis. *N. Engl. J. Med.* 355 (22), 2297–2307. doi:10.1056/NEJMoa060326

Bezanson, J., Edelman, A., Karpinski, S., and Shah, V. B. (2017). Julia: A Fresh Approach to Numerical Computing. *SIAM Rev.* 59 (1), 65–98. doi:10.1137/141000671

Calle, R. A., Amin, N. B., Carvajal-Gonzalez, S., Ross, T. T., Bergman, A., Aggarwal, S., et al. (2021). ACC Inhibitor Alone or Co-administered with a DGAT2 Inhibitor in Patients with Non-alcoholic Fatty Liver Disease: Two Parallel, Placebo-Controlled, Randomized Phase 2a Trials. *Nat. Med.* 27 (10), 1836–1848. doi:10.1038/s41591-021-01489-1

Chalasani, N., Younossi, Z., Lavine, J. E., Charlton, M., Cusi, K., Rinella, M., et al. (2018). The Diagnosis and Management of Nonalcoholic Fatty Liver Disease: Practice Guidance from the American Association for the Study of Liver Diseases. *Hepatology* 67 (1), 328–357. doi:10.1002/hep.29367

Czaja, M. J. (2009). Pioglitazone: More Than Just an Insulin Sensitizer. *Hepatology* 49 (5), 1427–1430. doi:10.1002/hep.22983

Dai, W., Rao, R., Sher, A., Tania, N., Musante, C. J., and Allen, R. (2021). A Prototype QSP Model of the Immune Response to SARS-CoV-2 for Community Development. *CPT Pharmacometrics Syst. Pharmacol.* 10 (1), 18–29. doi:10.1002/psp4.12574

Derosa, G., Maffioli, P., Salvadeo, S. A., Ferrari, I., Gravina, A., Mereu, R., et al. (2009). Direct Comparison Among Oral Hypoglycemic Agents and Their Association with Insulin Resistance Evaluated by Euglycemic Hyperinsulinemic Clamp: the 60's Study. *Metabolism* 58 (8), 1059–1066. doi:10.1016/j.metabol.2009.03.007

Fajas, L., Auboeuf, D., Raspé, E., Schoonjans, K., Lefebvre, A. M., Saladin, R., et al. (1997). The Organization, Promoter Analysis, and Expression of the Human PPARgamma Gene. *J. Biol. Chem.* 272 (30), 18779–18789. doi:10.1074/jbc.272.30.18779

Ferré, P., and Foufelle, F. (2010). Hepatic Steatosis: a Role for De Novo Lipogenesis and the Transcription Factor SREBP-1c. *Diabetes Obes. Metab.* 12 (Suppl. 2), 83–92. doi:10.1111/j.1463-1326.2010.01275.x

Gastaldelli, A., Harrison, S. A., Belfort-Aguilar, R., Hardies, L. J., Balas, B., Schenker, S., et al. (2009). Importance of Changes in Adipose Tissue Insulin Resistance to Histological Response during Thiazolidinedione Treatment of Patients with Nonalcoholic Steatohepatitis. *Hepatology* 50 (4), 1087–1093. doi:10.1002/hep.23116

Gastaldelli, A., Sabatini, S., Carli, F., Gaggini, M., Bril, F., Belfort-DeAguiar, R., et al. (2021). PPAR-γ-induced Changes in Visceral Fat and Adiponectin Levels Are Associated with Improvement of Steatohepatitis in Patients with NASH. *Liver Int.* 41 (11), 2659–2670. doi:10.1111/liv.15005

Hall, K. D. (2010). Predicting Metabolic Adaptation, Body Weight Change, and Energy Intake in Humans. *Am. J. Physiol. Endocrinol. Metab.* 298 (3), E449–E466. doi:10.1152/ajpendo.00559.2009

Haufe, S., Haas, V., Utz, W., Birkenfeld, A. L., Jeran, S., Böhnke, J., et al. (2013). Long-lasting Improvements in Liver Fat and Metabolism Despite Body Weight Regain after Dietary Weight Loss. *Diabetes Care* 36 (11), 3786–3792. doi:10.2337/dc13-0102

Holzhütter, H. G., and Berndt, N. (2021). Computational Hypothesis: How Intrahepatic Functional Heterogeneity May Influence the Cascading Progression of Free Fatty Acid-Induced Non-alcoholic Fatty Liver Disease (NAFLD). *Cells* 10 (3). doi:10.3390/cells10030578

Kotronen, A., Westerbacka, J., Bergholm, R., Yki-Järvinen, K. H. H., and Yki-Jarvinen, H. (2007). Liver Fat in the Metabolic Syndrome. *J. Clin. Endocrinol. Metab.* 92 (9), 3490–3497. doi:10.1210/jc.2007-0482

Kotronen, A., and Yki-Järvinen, H. (2008). Fatty Liver: a Novel Component of the Metabolic Syndrome. *Arterioscler. Thromb. Vasc. Biol.* 28 (1), 27–38. doi:10.1161/ATVBAHA.107.147538

Marra, F., and Svegliati-Baroni, G. (2018). Lipotoxicity and the Gut-Liver axis in NASH Pathogenesis. *J. Hepatol.* 68 (2), 280–295. doi:10.1016/j.jhep.2017.11.014

McGarry, J. D., Leatherman, G. F., and Foster, D. W. (1978). Carnitine Palmitoyltransferase I the Site of Inhibition of Hepatic Fatty Acid Oxidation by Malonyl-CoA. *J. Biol. Chem.* 253 (12), 4128–4136. doi:10.1016/s0021-9258(17)34693-8

McGarry, J. D., Mannaerts, G. P., and Foster, D. W. (1977). A Possible Role for Malonyl-CoA in the Regulation of Hepatic Fatty Acid Oxidation and Ketogenesis. *J. Clin. Invest.* 60 (1), 265–270. doi:10.1172/JCI108764

Mitra, S., De, A., and Chowdhury, A. (2020). Epidemiology of Non-alcoholic and Alcoholic Fatty Liver Diseases. *Transl. Gastroenterol. Hepatol.* 5, 16. doi:10.21037/tgh.2019.09.08

Newsome, P. N., Buchholtz, K., Cusi, K., Linder, M., Okanoue, T., Ratziu, V., et al. (2021). A Placebo-Controlled Trial of Subcutaneous Semaglutide in Nonalcoholic Steatohepatitis. *N. Engl. J. Med.* 384 (12), 1113–1124. doi:10.1056/NEJMoa2028395

Noorman, M., Allen, R., Musante, C. J., and Banks, H. T. (2019). Analysis of Compartments-In-Series Models of Liver Metabolism as Partial Differential Equations: the Effect of Dispersion and Number of Compartments. *Math. Biosci. Eng.* 16 (3), 1082–1114. doi:10.3934/mbe.2019052

Parthasarathy, G., Revelo, X., and Malhi, H. (2020). Pathogenesis of Nonalcoholic Steatohepatitis: An Overview. *Hepatol. Commun.* 4 (4), 478–492. doi:10.1002/hep4.1479

Phatak, H. M., and Yin, D. D. (2006). Factors Associated with the Effect-Size of Thiazolidinedione (TZD) Therapy on HbA(1c): a Meta-Analysis of Published Randomized Clinical Trials. *Curr. Med. Res. Opin.* 22 (11), 2267–2278. doi:10.1185/030079906X148328

Rieger, T. R., Allen, R. J., Bystricky, L., Chen, Y., Colopy, G. W., Cui, Y., et al. (2018). Improving the Generation and Selection of Virtual Populations in Quantitative Systems Pharmacology Models. *Prog. Biophys. Mol. Biol.* 139, 15–22. doi:10.1016/j.pbiomolbio.2018.06.002

Rieger, T. R., and Musante, C. J. (2016). Benefits and Challenges of a QSP Approach through Case Study: Evaluation of a Hypothetical GLP-1/GIP Dual Agonist Therapy. *Eur. J. Pharm. Sci.* 94, 15–19. doi:10.1016/j.ejps.2016.05.006

Rieger, T. R., Allen, R. J., and Musante, C. J. (2022). *Source Code for a Quantitative Pharmacology Model of Liver Lipid Metabolism for Investigation of Non-alcoholic Fatty Liver Disease*. v1.1. doi:10.5281/zenodo.6621096

Schwarz, J. M., Neese, R. A., Turner, S., Dare, D., and Hellerstein, M. K. (1995). Short-term Alterations in Carbohydrate Energy Intake in Humans. Striking Effects on Hepatic Glucose Production, De Novo Lipogenesis, Lipolysis, and Whole-Body Fuel Selection. *J. Clin. Invest.* 96 (6), 2735–2743. doi:10.1172/JCI118342

Siler, S. Q. (2022). Applications of Quantitative Systems Pharmacology (QSP) in Drug Development for NAFLD and NASH and its Regulatory Application. *Pharm. Res.* doi:10.1007/s11095-022-03295-x

Younossi, Z. M., Koenig, A. B., Abdelatif, D., Fazel, Y., Henry, L., and Wymer, M. (2016). Global Epidemiology of Nonalcoholic Fatty Liver Disease-Meta-Analytic Assessment of Prevalence, Incidence, and Outcomes. *Hepatology* 64 (1), 73–84. doi:10.1002/hep.28431

Conflict of Interest: TRR, RJA, and CJM were employees of Pfizer during the completion of this study.

Publisher's Note: All claims expressed in this article are solely those of the authors and do not necessarily represent those of their affiliated organizations, or those of the publisher, the editors and the reviewers. Any product that may be evaluated in this article, or claim that may be made by its manufacturer, is not guaranteed or endorsed by the publisher.

frontiers | Frontiers in Pharmacology

ORIGINAL RESEARCH
published: 10 August 2022
doi: 10.3389/fphar.2022.901559

Effects of GLP-1 Receptor Agonists on Biological Behavior of Colorectal Cancer Cells by Regulating PI3K/AKT/mTOR Signaling Pathway

*Guoxiang Tong[1,2,3], Tianhao Peng[3], Ya Chen[3], Lijuan Sha[3], Huikang Dai[3], Yidong Xiang[3], Zhiqi Zou[3], Heli He[4] and Sha Wang[1,2]**

[1]Academician Workstation, Changsha Medical University, Changsha, China, [2]Department of Endocrinology, The First Affiliated Hospital of Changsha Medical University, Changsha, China, [3]Hunan Evidence-based Biotechnology Co., Ltd., Changsha, China, [4]Department of Oncology, The First Affiliated Hospital of Changsha Medical University, Changsha, China

Colorectal cancer (CRC) has become one of the top ten malignant tumors with a high incidence rate and mortality. Due to the lack of a good CRC screening program, most of the CRC patients are being transferred at the time of treatment. The conventional treatment cannot effectively improve the prognosis of CRC patients, and the target drugs can significantly prolong the overall survival of patients in the advanced stage. However, the use of single drug may lead to acquired drug resistance and various serious complications. Therefore, combined targeted drug therapy is the main alternative treatment with poor effect of single targeted drug therapy, which has important research significance for the treatment of CRC. Therefore, this study intends to culture CRC cell lines *in vitro* at the cell level and intervene with the GLP-1 receptor agonist liraglutide. The effects of liraglutide on the PI3K/Akt/mTOR signal pathway and CRC cell proliferation, cycle, migration, invasion, and apoptosis are explored by detecting cell proliferation, cycle, migration, invasion, and apoptosis and the expression of related mRNA and protein. The results showed that liraglutide, a GLP-1 receptor agonist, could block the CRC cell cycle, reduce cell proliferation, migration, and invasion and promote apoptosis by inhibiting the PI3K/Akt/mTOR signal pathway.

Keywords: colorectal cancer, GLP-1 receptor agonist, liraglutide, PI3K/AKT/mTOR, migration, apoptosis

OPEN ACCESS

Edited by:
Weiguo Li,
Harbin Institute of Technology, China

Reviewed by:
Jianhua Xiao,
University of South China, China
Wenjie Song,
Fourth Military Medical University, China

****Correspondence:***
Sha Wang
846493283@126.com

Specialty section:
This article was submitted to Translational Pharmacology, a section of the journal Frontiers in Pharmacology

Received: *22 March 2022*
Accepted: *19 April 2022*
Published: *10 August 2022*

Citation:
Tong G, Peng T, Chen Y, Sha L, Dai H, Xiang Y, Zou Z, He H and Wang S (2022) Effects of GLP-1 Receptor Agonists on Biological Behavior of Colorectal Cancer Cells by Regulating PI3K/AKT/mTOR Signaling Pathway. Front. Pharmacol. 13:901559. doi: 10.3389/fphar.2022.901559

1 INTRODUCTION

Colorectal cancer (CRC) refers to cancers that occur in the epithelium of the large intestine, including colon cancer and rectal cancer. Adenocarcinoma is the most common pathological type, and a few are squamous cell carcinoma. In China, rectal cancer is the most common type, followed by colon cancer, and the colon includes the sigmoid colon, cecum, ascending colon, descending colon, and transverse colon, which are widely affected. The incidence rate of CRC is high, and CRC has become one of the top ten malignant tumors (Brittain et al., 2018; Geijsen et al., 2019). In recent years, the incidence rate and mortality rate of CRC in China has been increasing obviously. Due to the lack of perfect CRC examination programs in China, most CRC patients are treated for metastasis, 15%–20% of CRC patients have liver metastasis in the initial operation, and liver metastasis recurrence 2 years after surgery is up to 50 (Peng et al., 2021). Based on the fact that conventional treatment methods cannot effectively improve the prognosis of CRC patients,

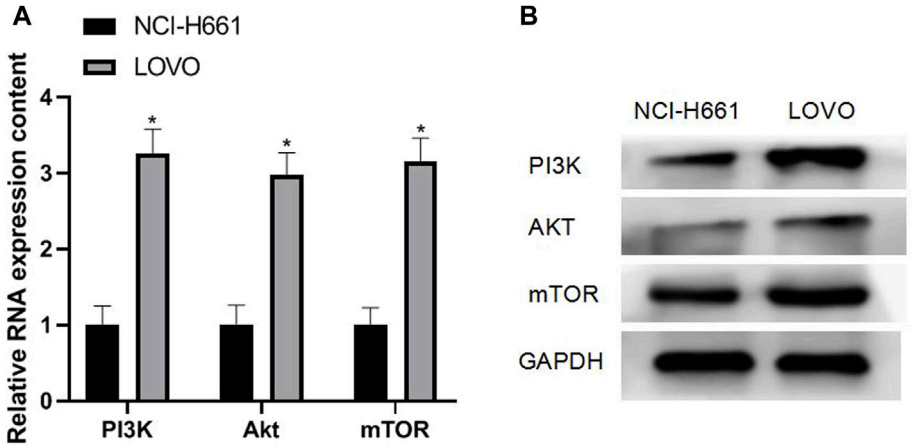

FIGURE 1 | Expression of PI3K/Akt/mTOR in CRC cells. Note: **(A)** qRT-PCR experiment; **(B)** Western blotting experiment, compared with NCI-H661, $*p < 0.05$.

molecular targeted drugs came into being. In addition to significantly prolonging the overall survival of patients with advanced stage, the high specificity of targeted drugs meets the requirements of current precision treatment. However, whether they are monoclonal antibodies or signal pathway inhibitors, except for patients with natural drug resistance, the use of single drug may lead to acquired drug resistance and various serious complications (Sadat et al., 2021; Teo et al., 2021; Huaiyu Zhang et al., 2021), making the treatment fail. Therefore, combined targeted drug therapy is the main alternative treatment with poor effect of single targeted drug therapy, which has important research significance for the treatment of CRC.

Glucagon-like peptide-1 (GLP-1) is widely distributed in the heart, brain, lung, gastrointestinal tract, pancreas, and other tissues. Activation of the GLP-1 receptor can promote a variety of cell proliferation and improve cell viability (Knudsen et al., 2018). Previous studies have shown that GLP-1 receptor agonists play an important role in the occurrence and development of a variety of tumor cells (Liu et al., 2019; Kojima et al., 2020; Mao et al., 2021). It has also been found that long-term injection of GLP-1 receptor agonists exenatide and liraglutide can promote the occurrence of thyroid cancer in rodents by activating the GLP-1 receptor in a dose-dependent manner (Sherman et al., 2018). GLP-1 receptor agonists have long-term effects on the occurrence and development of tumors originating from thyroid follicular cells (van den Brink et al., 2017). Therefore, GLP-1 receptor agonists may have a certain effect on tumor cells.

At present, academic circles believe that the accelerated progress of CRC is caused by PIK3CA gene mutation of the PI3K/Akt/mTOR signal pathway and the loss of expression of phosphatase and tensin homolog deleted on chromosome 10 (PTEN). PIK3CA mutation is closely related to the location, degree of tissue differentiation, and immunohistochemical type of CRC lesions (Zhihang Chen et al., 2020; Li et al., 2021; Wang et al., 2021; Jing Zhang et al., 2021). Cells carry out biological activities through proliferation, migration, invasion, and apoptosis, as well as cancer cells (Xie et al., 2021). So far, although there are many studies on CRC, the pathogenesis and pathophysiological mechanism of CRC are still not fully understood. Understanding and mastering the changes of CRC cell proliferation, migration, cycle, and apoptosis can provide an important theoretical basis for the research and treatment of CRC.

Based on the aforementioned points, the effects of GLP-1 receptor agonists on tumor cells, and the effects of the PI3K/Akt/mTOR signaling pathway on cell biology, we boldly put forward the scientific hypothesis that GLP-1 receptor agonists can affect the proliferation, cycle, migration, invasion, and apoptosis of CRC cells by mediating PI3K/Akt/mTOR. Therefore, this study intends to culture CRC cell lines *in vitro* at the cell level and intervene with the GLP-1 receptor agonist liraglutide. By detecting the changes in cell proliferation, cycle, migration, invasion, and apoptosis and the expression of related mRNAs and proteins, this study will explore the effects of liraglutide on the PI3K/Akt/mTOR signal pathway and CRC cell proliferation, cycle, migration, invasion, and apoptosis, and preliminarily explore its possible mechanisms of action so as to provide an experimental and theoretical basis for CRC, combined with targeted drug therapy.

2 MATERIALS AND METHODS

2.1 Cell Culture and Passage

Human normal colonic epithelial cell line NCI-H661 was cultured in high-glucose DMEM containing 10% fetal bovine serum, and human colon cancer cell line LOVO was cultured in RPMI1640 medium in a sterile incubator at 37°C with 5% CO_2 saturation humidity. When the cells reached 70%–80% confluence when observed under a microscope, they were digested and subcultured with 0.25% trypsin. Tumor cells in the logarithmic growth stage were taken for the experiment. Materials such as cells and culture medium were purchased from Beijing Dingguo Changsheng Biotechnology Co., Ltd.

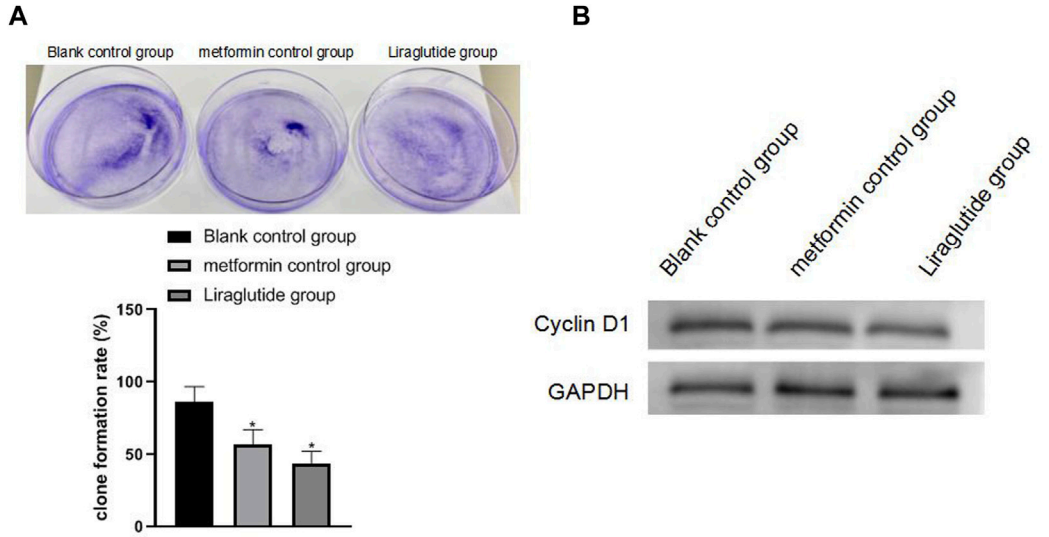

FIGURE 2 | Effects of GLP-1 receptor agonists on the proliferation and cycle of CRC cells. Note: **(A)** plate cloning experiment; **(B)** Western blotting experiment, compared with blank control group, $^{*}p < 0.05$.

2.2 Liraglutide Intervention and Grouping

LOVO cells in the logarithmic growth stage were inoculated into a 96-well culture plate with 5,000 cells/well, and the culture medium was 100 μ L/well, cultured in a sterile incubator at 37°C, 5% CO_2 saturation humidity for 24 h, and then the supernatant was gently sucked and discarded. In order to study the optimal intervention concentration, liraglutide (Macklin) at different concentrations (10^{-5} mol/L, 10^{-8} mol/L, 10^{-11} mol/L) was used to intervene. After 24, 48, and 72 h of intervention, 5 mg/ml MTT 20 μL was added to each well. It was incubated at 37°C for 4 h, the liquid in the hole was discarded, and DMSO 150 μL was added to each hole. After shaking for 10 min without light, the absorbance value (A value) of each hole was measured at 450 nm wavelength using the enzyme-linked immunosorbent assay instrument (Thermo Fisher Scientific). The intervention concentration with the highest inhibition rate of 10^{-8} mol/L was selected, and LOVO cells were randomly divided into three groups: 1) blank control group; 2) metformin (MedBio) control group: 20 mmol/L metformin; and 3) liraglutide group: 10^{-8} mol/L liraglutide.

2.3 Real-Time Fluorescence Quantitative PCR (qRT-PCR)

A certain amount of TRIzol solution (absin) was added to CRC cells to extract total RNA from the cells. After zeroing the micro-nucleic acid protein detector with 0.1% DEPC water, 1 μ L was used to detect the concentration and purity of the extracted RNA diluent. When 1.8 < A260/A280 < 2.0, it was indicated that the purity of the RNA was qualified and there was no pollution of protein and phenol. RNA concentration = 40 × A260ng/μ L. Then the reading was taken. RNA concentration at 500–1,000 ng/μ L room is the most suitable. An appropriate amount of 0.1% DEPC water was added for adjustment. The cDNA was synthesized using reverse transcription. The primers were purchased from Shanghai Jima. The primer sequence required for the reaction: GAPDH: F: 5′- tcaagatcagcaatgcc-3′, R: 5′- cgatacaca agttgtcatgga-3'; PI3K: F:5′- CAGACAGCGAGAGAGATGA-3′, R:5′-GGTGGATGGTGGTGCTGTATT-3'; Akt: F:5′- ATTGTGAAG GAGGGTTGGCTG-3′, R:5′-CCGCTCCTTGTAGCCAATGAA -3'; mTOR: F:5′- CCCTCCATCCACCTCATCAGT-3′, R:5′-CGCCAAGACACAGTAGCGAAT-3'. Pre-denaturation: 95°C 2min, amplification: 95 °C 5s, 60 °C 30s, melt curve program: 95 °C 15s, 60 °C 60s, 95 °C 10sec. The reverse transcription kit was purchased from Thermo Fisher. It was operated according to the user guide of the fluorescence quantitative kit, U6 and GAPDH were taken as internal parameters, and the relative content of PI3K/Akt/mTOR in CRC was calculated by using the $2^{-\triangle\triangle Ct}$ method (Wang et al., 2021).

2.4 Plate Cloning

Each group of cells in logarithmic growth stage was blown with 0.25% trypsin as a single cell, and the cells were suspended in the RPMI1640 medium containing 10% fetal bovine serum. The cell suspension was inoculated in a petri dish containing 10 ml of 37°C preheated medium, gently rotated to disperse the cells evenly, and placed in a sterile incubator with 37°C and 5% CO_2 saturation humidity for 2–3 weeks. The culture medium was changed according to the cell growth. When the cells had clones visible to the naked eye, the culture was terminated, the supernatant was discarded, and the cells were cleaned and fixed. Then an appropriate amount of Giemsa was added and dyed with the staining solution for 30 min The staining solution was then cleaned and dried, and the cells were made into a transparent film. The number of clones greater than 10 cells under the microscope and the clone formation rate were calculated = (number of clones/number of inoculated cells) × 100%。

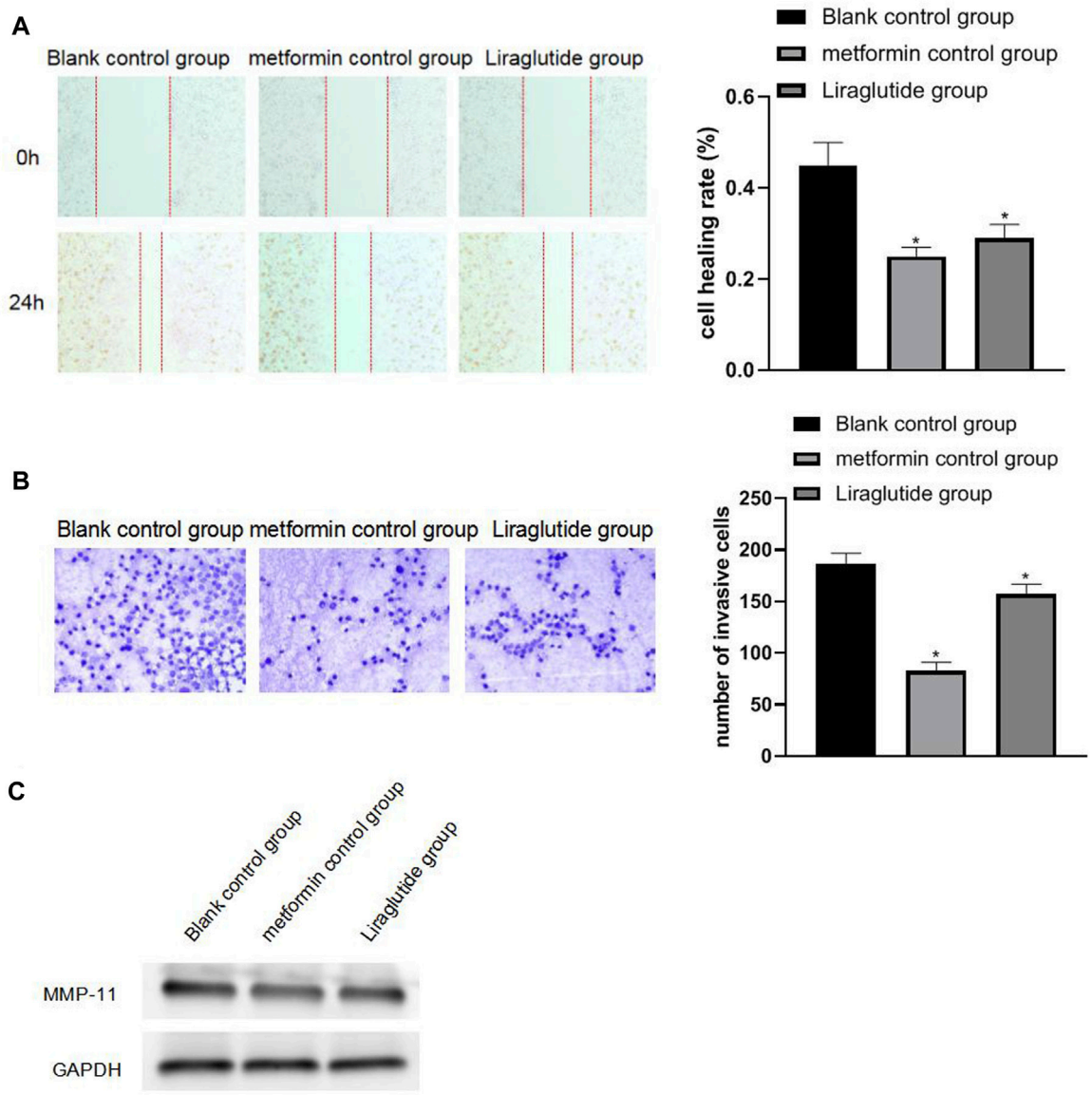

FIGURE 3 | Effects of GLP-1 receptor agonists on the migration and invasiveness of CRC cells. Note: **(A)** wound healing experiment; **(B)** Transwell experiment (20 ×); **(C)** Western blotting experiment, compared with blank control group, $^{*}p < 0.05$.

2.5 Wound Healing Experiment

LOVO cells in the logarithmic growth stage were taken and were divided into two cells per well × the density of 104 cells was inoculated on 96-well plates and incubated for 24 h, and scratches were made on the confluent adherent cell layer using wound healing inserts. The medium was sucked out, and the cells were gently washed with the medium twice. Then the plate was placed inside the imaging system, and scanning was repeated for 24 h. Calculation of mobility: mobility = (1–24 h scratch distance/ initial distance) × 100%.

2.6 Transwell

Matrigel (Corning) was dissolved at 4°C overnight 2 days in advance and was diluted in serum-free medium in the ratio of 1:7. All operations involving Matrigel needed to be carried out on ice. The Matrigel invasion chamber was placed in a sterile 24-well plate, and 20 μl of Matrigel was added to the chamber so that it was evenly spread on the bottom of the chamber. CRC cells in each group were prepared into single cell suspension in serum-free RPMI1640 medium and counted under the microscope (the concentration is about 60–80 × 10^4/ml). Medium 600 μl containing 10% fetal bovine serum was added to the small holes of the lower chamber, and 105 cells were added to each hole of the upper chamber to supplement 200 μl with serum-free medium. The cells were cultured at 37°C in an incubator with 5% carbon dioxide volume fraction for 24 h. When the cells had been worn for enough time, the upper chamber culture medium was discarded, the upper chamber was taken out carefully, and the

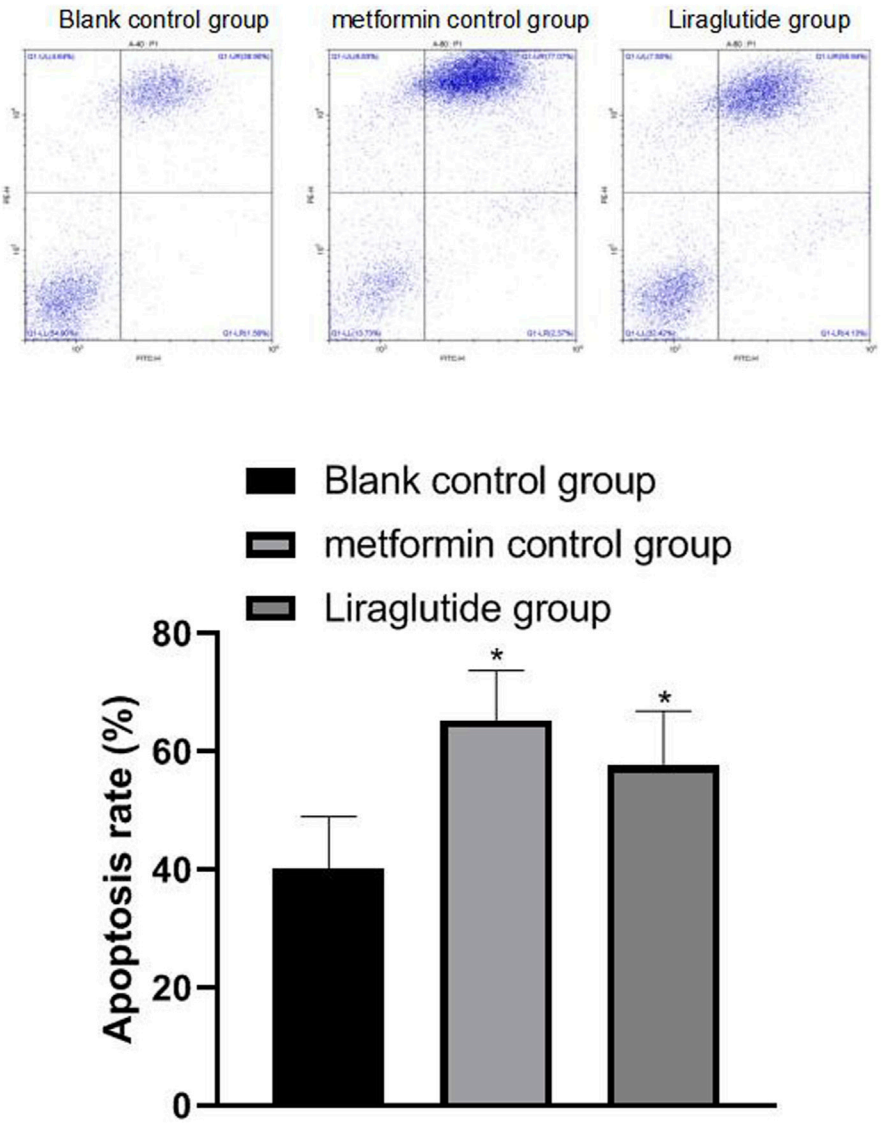

FIGURE 4 | Effects of GLP-1 receptor agonists on apoptosis of CRC cells. Note: flow cytometry experiment, compared with blank control group, $*p < 0.05$.

cells not passing through the membrane were gently wiped with a wet cotton swab. The chamber was washed with PBS 3 times, and the lower part of the chamber was fixed with 4% paraformaldehyde (Beijing Dingguo Changsheng Biotechnology Co., Ltd.) for 30 min, dyed with crystal violet for 20 min. Photos were taken under an inverted microscope. Randomly five visual fields were chosen, and the number of cells penetrating the stromal membrane was counted.

2.7 Flow Cytometry

Cells were washed twice with pre-chilled PBS, then washed, and resuspended with 1× binding buffer to adjust the cell concentration to 1×10^6 cells/mL; 100 μL of the adjusted cell suspension was taken into 5 mL of flow cytometry tube. Annexin V-labeled protein and corresponding nucleic acid dyes were added, then mixed evenly, and kept at room temperature for 15 min; 400 μL of 1× binding buffer was added to the flow cytometry tube, resuspended, and analyzed by using a flow cytometer in time. After the flow cytometer is installed, the data will be directly analyzed, and the time of reading the data will not be recorded.

2.8 Western Blotting

Total protein in CRC cells was extracted, and the BCA protein quantification kit was used for protein quantification and analysis. Protein sample weighing 50 μg was taken, added to the sample well of 5% stacking gel, and 3 μl protein marker was added to the sample well, and the total amount added to each well was equal. After identifying the positive and negative electrodes of the electrophoresis tank, electrophoresis was started. The initial constant voltage was 90 V. When the bottom of the bromophenol blue reached the surface of the

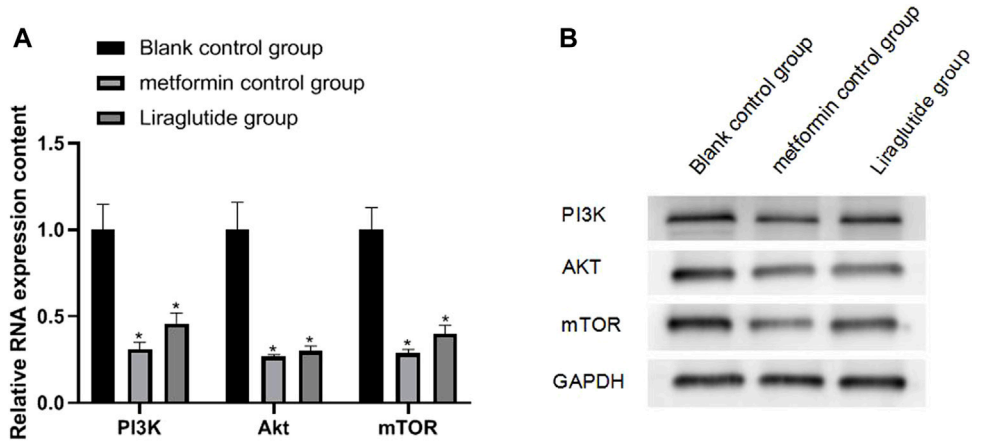

FIGURE 5 | Effects of GLP-1 receptor agonists on the expression of PI3K/Akt/mTOR in CRC cells. Note: **(A)** qRT-PCR experiment; **(B)** Western blotting experiment, compared with blank control group, $^*p < 0.05$.

separation gel, the voltage was adjusted to 120 V, and the electrophoresis was run until the bromophenol blue dye ran out of the separation gel. The electrophoresis instrument was turned off. The glass plate was gently removed, the stacking gel and excess separating gel were cut off according to the Marker strip, and the gel containing the target protein was soaked in transfer buffer. The membrane was transferred, blocked, and incubated with primary antibody: the PVDF membrane from the blocking solution was taken out, and the membrane was washed three times with TBST solution, 10 min/time. The primary antibodies (rabbit anti-human PI3K, 1:1,000; Akt, 1:1,000; mTOR, 1:1,000; cyclin D1, 1:1,000; MMP-11, 1:1,000) diluted with TBST were added and incubated at 4°C overnight. Reaction with secondary antibody: the PVDF membrane from the primary antibody was taken out and washed 3 times in TBST, 5 min/time. The IR fluorescently labeled secondary antibody (diluted with TBST) was added and incubated for 2 h in the dark on a shaker (pay attention to moderate speed). This procedure was repeated for the TBST cells 3 times, 5 min/time, and in the dark. The Odyssey dual-color infrared fluorescence scanning system was used to observe the colored bands, image, and analyze the data.

2.9 Statistical Analysis

The data of this study were processed by SPSS 19.0 software for statistical analysis. Measurement data were expressed as mean ± standard deviation. The comparison of means between groups was performed using one-way ANOVA, the comparison of data between two groups was performed using the *t*-test of two independent samples, and the comparison within two groups was performed using the SNK-q test. $p < 0.05$ was considered to be statistically significant.

3 RESULTS

3.1 Expression of PI3K/Akt/mTOR in Colorectal Cancer Cells

The results of qRT-PCR and Western blotting experiments showed that the mRNA and protein expressions of PI3K (3.26 ± 0.32), Akt (2.98 ± 0.29), and mTOR (3.16 ± 0.30) were all upregulated in CRC cells, and the difference was statistically significant ($p < 0.05$). As shown in **Figures 1A,B**

3.2 Effects of GLP-1 Receptor Agonists on the Proliferation and Cycle of Colorectal Cancer Cells

The results of plate cloning and Western blotting experiments showed that after the intervention of the GLP-1 receptor agonist liraglutide, the proliferation ability of CRC cells weakened (13.19 ± 8.85), the expression of cyclin D1 protein decreased, and the difference was statistically significant ($p < 0.05$), as shown in **Figures 2A,B**

3.3 Effects of GLP-1 Receptor Agonists on the Migration and Invasion of Colorectal Cancer Cells

The results of wound healing, Transwell, and Western blotting experiments showed that after the intervention of the GLP-1 receptor agonist liraglutide, the migration (0.29 ± 0.03) and invasion ability (157.11 ± 9.66) of CRC cells weakened, the expression of MMP-11 protein was decreased, and the differences were statistically significant ($p < 0.05$), as shown in **Figures 3A,B,C**.

3.4 Effects of GLP-1 Receptor Agonists on Apoptosis of Colorectal Cancer Cells

The results of flow cytometry showed that after the intervention of the GLP-1 receptor agonist liraglutide, the apoptosis (57.69 ± 9.21) of CRC cells increased and the difference was statistically significant ($p < 0.05$), as shown in **Figure 4**.

3.5 Effects of GLP-1 Receptor Agonists on the Expression of PI3K/Akt/mTOR in Colorectal Cancer Cells

The results of qRT-PCR and Western blotting experiments showed that after the intervention of the GLP-1 receptor agonist liraglutide, the expressions of PI3K (0.46 ± 0.06), Akt (0.30 ± 0.03), and mTOR (0.40 ± 0.05) proteins in CRC cells were decreased, and the difference was statistically significant ($p < 0.05$), as shown in **Figure 5A,B**.

4 DISCUSSION

According to the GLOBOCAN project of the WHO Cancer Research Center, the number of new cases of CRC in 2018 was about 1.8 million, and the number of deaths was about 880,000. The incidence of CRC is related to factors such as age, region, and gender (Takiyama et al., 2017; Zhou et al., 2022). The pathological types of CRC are divided into ulcerative, raised, and infiltrating. (Reid et al., 2021). In the early stage of CRC, there are no obvious symptoms, and some non-specific symptoms such as changes in bowel habits and changes in stool characteristics may appear, which are easy to be ignored. However, as the disease progressed, various gastrointestinal symptoms and systemic symptoms, such as blood in the stool and abdominal pain were seen (Zhang and Jiang, 2020). Conventional treatment methods cannot effectively improved the prognosis of CRC patients, and targeted drugs can significantly prolong the overall survival of advanced patients. However, the use of a single drug may lead to acquired drug resistance and various serious complications. Therefore, it is of great significance to explore new treatment methods for CRC.

Studies have shown that the activation of the PI3K/Akt/mTOR pathway begins with the activation of PIK3CA by the transmembrane tyrosine kinase growth factor receptor, which then activates Akt through phosphorylation and dephosphorylation reactions, which stimulate tuberous sclerosis 1 (TSC1). The TSC1/TSC2 complex generates Ras protein brain tissue homologous analogs, and the Ras protein brain tissue homologous analogs activate mTOR and then, respectively, controls the translation of specific subsets of messenger RNAs, thereby regulating protein synthesis and playing an important role in cell proliferation, invasion, metastasis, and metabolism (Huiqin Chen et al., 2020; Liu et al., 2021). This study found that in CRC cells, the expressions of PI3K, Akt, and mTOR were upregulated, indicating that the PI3K/Akt/mTOR pathway was activated, which is consistent with the aforementioned theory. Studies have shown that PIK3CA mutation can reduce the risk of CRC peritoneal metastasis (Lund-Andersen et al., 2021). Mutated BRAF, PIK3CA, and PTEN have also been confirmed to exist in the EGFR signal transduction pathway. Multi-site gene mutations lead to the complexity of tumor signal transduction, which explains the use of EGFR monoclonal antibodies in the treatment of CRC patients. The reason is that the prolongation of time and the time of disease progression of the patients did not form a significant promotion relationship, and because of this, the process of single-molecule targeted drugs as first-line drugs was gradually prolonged (Klupp et al., 2021). In addition, hypoxia-inducible factor-1α acts as a downstream regulatory unit of mTORC1, and its regulation of protein level is affected not only by the environmental oxygen concentration but also by interfering with the expression of hypoxia-inducible factor-1α in the PI3K/Akt signaling pathway, affecting the proliferation activity of CRC cells, thereby reducing the drug resistance of CRC cells (Deng et al., 2021), which further proves the necessity of in-depth research on PI3K/Akt/mTOR signaling pathway inhibitors.

GLP-1 receptor agonists act on islet beta cells in a glucose-dependent manner, promote insulin gene transcription, and inhibit islet beta cell apoptosis, thereby increasing the number of islet beta cells. The contents are emptied (Falkentoft et al., 2022). Zhao et al. (2014) studies confirm that GLP-1 receptor activation can inhibit the growth of human pancreatic cancer cells and promote cell apoptosis in a cAMP-dependent manner. Koehler et al. (2011) showed that GLP-1 receptor agonists can inhibit the growth and apoptosis of mouse CT26 colon cancer cells. Ligumsky et al.'s (2012) studies confirm that GLP-1 receptor agonists can inhibit the growth of breast cancer cells by activating cAMP (Hicks et al., 2016). Studies have shown that GLP-1 receptor agonists can mediate the signal pathway of phosphatidylinositol-3-kinase (PI3K)/protein kinase B (PKB/Akt)/mammalian target of rapamycin (mTOR), which has a protective effect on cerebral ischemia, but there are few studies on the role of PI3K/Akt/mTOR in CRC (Wang et al., 2019).

In the following elaboration, we explain that the cell cycle affects cell proliferation and thus correlates with the likelihood of cancer cell proliferation and spread. Therefore, it is necessary to block the growth and metastasis of cancer cells to curb the spread of cancer. After the intervention of the GLP-1 receptor agonist liraglutide, it was found that the proliferation, migration, and invasion of CRC cells weakened, cyclin D1 and MMP-11 decreased, and apoptosis increased. Cyclin D1 is an important protein in the cell cycle. As the regulator of cyclin-dependent kinase CDKs, cyclin D1 affects cell proliferation by regulating the transition from G1 the phase to S phase in the cell proliferation cycle (Cao et al., 2018; El-Gendi and Abu-Sheasha, 2018). MMP-11 is one of the matrix metalloproteinases (MMPs), which is the main enzyme causing the degradation of the basement membrane and extracellular matrix. Different family members of MMP may play a role in the occurrence and development of different tumors and are closely related to the low degree of tumor differentiation and strong ability of invasion and metastasis. Apoptotic pathways include the extracellular pathway and intracellular pathway. The expression of cyclin D1 and MMP-11 decreased, the cycle of cancer cells was blocked, and the metastatic ability of cancer cells was inhibited.

In conclusion, the PI3K/Akt/mTOR signaling pathway is activated in CRC. After intervention with a GLP-1 receptor agonist, CRC cells can block the cell cycle, inhibit cell proliferation, migration and

invasion, promote apoptosis, and reduce the expression of PI3K/Akt/mTOR pathway protein. Therefore, GLP-1 receptor agonists can reduce the development of biological behavior of CRC cells by inhibiting the PI3K/Akt/mTOR signaling pathway.

DATA AVAILABILITY STATEMENT

The data presented in the study are deposited in the repository of Hunan Evidence-Based Biotechnology Co., Ltd. (enterprise email, login number: hnxzsw888@vip.163.com).

AUTHOR CONTRIBUTIONS

GT is mainly responsible for the writing of the article. TP and YC are mainly responsible for research design. LS and HD are mainly responsible for data analysis. YX, ZZ, and HH are mainly responsible for data statistics. SW is responsible for the guidance of the entire research.

FUNDING

This study was funded by the Outstanding Youth Project of Scientific Research of Hunan Provincial Department of Education (No. 20B069).

SUPPLEMENTARY MATERIAL

The Supplementary Material for this article can be found online at: https://www.frontiersin.org/articles/10.3389/fphar.2022.901559/full#supplementary-material

REFERENCES

Brittain, K., Pennings Kamp, K. J., and Salaysay, Z. (2018). Colorectal Cancer Awareness for Women via Facebook: A Pilot Study. *Gastroenterol. Nurs.* 41 (1), 14–18. doi:10.1097/SGA.0000000000000294

Cao, L., Liu, Y., Wang, D., Huang, L., Li, F., Liu, J., et al. (2018). MiR-760 Suppresses Human Colorectal Cancer Growth by Targeting BATF3/AP-1/cyclinD1 Signaling. *J. Exp. Clin. Cancer Res.* 37 (1), 83. doi:10.1186/s13046-018-0757-8

Chen, H., Chen, N., Li, F., Sun, L., Du, J., Chen, Y., et al. (2020). Repeated Radon Exposure Induced Lung Injury and Epithelial-Mesenchymal Transition through the PI3K/AKT/mTOR Pathway in Human Bronchial Epithelial Cells and Mice. *Toxicol. Lett.* 334, 4–13. doi:10.1016/j.toxlet.2020.09.008

Chen, Z., Wang, C., Dong, H., Wang, X., Gao, F., Zhang, S., et al. (2020). Aspirin Has a Better Effect on PIK3CA Mutant Colorectal Cancer Cells by PI3K/Akt/Raptor Pathway. *Mol. Med.* 26 (1), 14. doi:10.1186/s10020-020-0139-5

Deng, X., Kong, F., Li, S., Jiang, H., Dong, L., Xu, X., et al. (2021). A KLF4/PiHL/EZH2/HMGA2 Regulatory axis and its Function in Promoting Oxaliplatin-Resistance of Colorectal Cancer. *Cell Death Dis.* 12 (5), 485. doi:10.1038/s41419-021-03753-1

El-Gendi, S., and Abu-Sheasha, G. (2018). Ki-67 and Cell Cycle Regulators P53, P63 and cyclinD1 as Prognostic Markers for Recurrence/Progression of Bladder Urothelial Carcinoma. *Pathol. Oncol. Res.* 24 (2), 309–322. doi:10.1007/s12253-017-0250-2

Falkentoft, A. C., Andersen, J., Malik, M. E., Selmer, C., Gæde, P. H., Staehr, P. B., et al. (2022). Impact of Socioeconomic Position on Initiation of SGLT-2 Inhibitors or GLP-1 Receptor Agonists in Patients with Type 2 Diabetes - a Danish Nationwide Observational Study. *Lancet Reg. Health Eur.* 14, 100308. doi:10.1016/j.lanepe.2022.100308

Geijsen, A. J. M. R., Brezina, S., Keski-Rahkonen, P., Baierl, A., Bachleitner-Hofmann, T., Bergmann, M. M., et al. (2019). Plasma Metabolites Associated with Colorectal Cancer: A Discovery-Replication Strategy. *Int. J. Cancer* 145 (5), 1221–1231. doi:10.1002/ijc.32146

Hicks, B. M., Yin, H., Yu, O. H., Pollak, M. N., Platt, R. W., and Azoulay, L. (2016). Glucagon-like Peptide-1 Analogues and Risk of Breast Cancer in Women with Type 2 Diabetes: Population Based Cohort Study Using the UK Clinical Practice Research Datalink. *BMJ* 355, i5340. doi:10.1136/bmj.i5340

Klupp, F., Sass, M., Bergmann, F., Khajeh, E., Ghamarnejad, O., Hassenpflug, M., et al. (2021). Impact of EGFR and EGFR Ligand Expression on Treatment Response in Patients with Metastatic Colorectal Cancer. *Oncol. Lett.* 21 (6), 448. doi:10.3892/ol.2021.12709

Knudsen, J. S., Thomsen, R. W., Pottegård, A., Knop, F. K., and Sørensen, H. T. (2018). Differences between Randomized Clinical Trial Patients and Real-World Initiators of the Glucagon-like Peptide 1 Receptor Agonist Liraglutide. *Diabetes Care* 41 (9), e133–e135. doi:10.2337/dc18-0999

Koehler, J. A., Kain, T., and Drucker, D. J. (2011). Glucagon-like Peptide-1 Receptor Activation Inhibits Growth and Augments Apoptosis in Murine CT26 colon Cancer Cells. *Endocrinology* 152 (9), 3362–3372. doi:10.1210/en.2011-1201

Kojima, M., Takahashi, H., Kuwashiro, T., Tanaka, K., Mori, H., Ozaki, I., et al. (2020). Glucagon-Like Peptide-1 Receptor Agonist Prevented the Progression of Hepatocellular Carcinoma in a Mouse Model of Nonalcoholic Steatohepatitis. *Int. J. Mol. Sci.* 21 (16), 5722. doi:10.3390/ijms21165722

Li, H., Huang, H., Li, S., Mei, H., Cao, T., and Lu, Q. (2021). Long Non-Coding RNA ADAMTS9-AS2 Inhibits Liver Cancer Cell Proliferation, Migration and Invasion. *Exp. Ther. Med.* 21 (6), 559. doi:10.3892/etm.2021.9991

Ligumsky, H., Wolf, I., Israeli, S., Haimsohn, M., Ferber, S., Karasik, A., et al. (2012). The Peptide-Hormone Glucagon-like Peptide-1 Activates cAMP and Inhibits Growth of Breast Cancer Cells. *Breast Cancer Res. Treat.* 132 (2), 449–461. doi:10.1007/s10549-011-1585-0

Liu, Y., Zhang, X., Chai, S., Zhao, X., and Ji, L. (2019). Risk of Malignant Neoplasia with Glucagon-like Peptide-1 Receptor Agonist Treatment in Patients with Type 2 Diabetes: A Meta-Analysis. *J. Diabetes Res.* 2019, 1534365. doi:10.1155/2019/1534365

Liu, Z., Sun, T., Piao, C., Zhang, Z., and Kong, C. (2021). METTL13 Inhibits Progression of clear Cell Renal Cell Carcinoma with Repression on PI3K/AKT/mTOR/HIF-1α Pathway and C-Myc Expression. *J. Transl Med.* 19 (1), 209. doi:10.1186/s12967-021-02879-2

Lund-Andersen, C., Torgunrud, A., Fleten, K. G., and Flatmark, K. (2021). Omics Analyses in Peritoneal Metastasis-Utility in the Management of Peritoneal Metastases from Colorectal Cancer and Pseudomyxoma Peritonei: a Narrative Review. *J. Gastrointest. Oncol.* 12 (Suppl. 1), S191–S203. doi:10.21037/jgo-20-136

Mao, D., Cao, H., Shi, M., Wang, C. C., Kwong, J., Li, J. J. X., et al. (2021). Increased Co-expression of PSMA2 and GLP-1 Receptor in Cervical Cancer Models in Type 2 Diabetes Attenuated by Exendin-4: A Translational Case-Control Study. *EBioMedicine* 65, 103242. doi:10.1016/j.ebiom.2021.103242

Peng, Y., Feng, H., Wang, C., Song, Z., Zhang, Y., Liu, K., et al. (2021). The Role of E26 Transformation-specific Variant Transcription Factor 5 in Colorectal Cancer Cell Proliferation and Cell Cycle Progression. *Cel Death Dis.* 12 (5), 427. doi:10.1038/s41419-021-03717-5

Reid, F. S. W., Egoroff, N., Pockney, P. G., and Smith, S. R. (2021). A Systematic Scoping Review on Natural Killer Cell Function in Colorectal Cancer. *Cancer Immunol. Immunother.* 70 (3), 597–606. doi:10.1007/s00262-020-02721-6

Sadat, S. M. A., Paiva, I. M., Shire, Z., Sanaee, F., Morgan, T. D. R., Paladino, M., et al. (2021). A Synthetically Lethal Nanomedicine Delivering Novel Inhibitors of Polynucleotide Kinase 3'-phosphatase (PNKP) for Targeted Therapy of PTEN-Deficient Colorectal Cancer. *J. Control. Release* 334, 335–352. doi:10.1016/j.jconrel.2021.04.034

Sherman, S. I., Kloos, R. T., Tuttle, R. M., Pontecorvi, A., Völzke, H., Harper, K., et al. (2018). No Calcitonin Change in a Person Taking Dulaglutide Diagnosed

with Pre-existing Medullary Thyroid Cancer. *Diabet Med.* 35 (3), 381–385. doi:10.1111/dme.13437

Takiyama, A., Tanaka, T., Yamamoto, Y., Hata, K., Ishihara, S., Nozawa, H., et al. (2017). Microsatellite Status of Primary Colorectal Cancer Predicts the Incidence of Postoperative Colorectal Neoplasms. *Anticancer Res.* 37 (10), 5785–5790. doi:10.21873/anticanres.12020

Teo, M. Y. M., Ng, J. J. C., Fong, J. Y., Hwang, J. S., Song, A. A., Lim, R. L. H., et al. (2021). Development of a Single-Chain Fragment Variable Fused-Mutant HALT-1 Recombinant Immunotoxin against G12V Mutated KRAS Colorectal Cancer Cells. *PeerJ* 9, e11063. doi:10.7717/peerj.11063

van den Brink, W., Emerenciana, A., Bellanti, F., Della Pasqua, O., and van der Laan, J. W. (2017). Prediction of Thyroid C-Cell Carcinogenicity after Chronic Administration of GLP1-R Agonists in Rodents. *Toxicol. Appl. Pharmacol.* 320, 51–59. doi:10.1016/j.taap.2017.02.010

Wang, J., Wang, A., He, H., She, X., He, Y., Li, S., et al. (2019). Trametenolic Acid B Protects against Cerebral Ischemia and Reperfusion Injury through Modulation of microRNA-10a and PI3K/Akt/mTOR Signaling Pathways. *Biomed. Pharmacother.* 112, 108692. doi:10.1016/j.biopha.2019.108692

Wang, J., Zhou, F., Li, F., Wang, B., Hu, Y., and Li, X. (2021). Autocrined Leptin Promotes Proliferation of Non-small Cell Lung Cancer (NSCLC) via PI3K/AKT and P53 Pathways. *Ann. Transl Med.* 9 (7), 568. doi:10.21037/atm-20-7482

Xie, J., Sun, Y., and Xu, Q. (2021). Inhibition of SRSF3 Alleviates Proliferation and Migration of Gastric Cancer Cells by Regulating the PI3K/AKT/mTOR Signalling Pathway. *Folia Biol. (Praha)* 67 (3), 102–107.

Zhang, H., Zhang, J., Liu, Y., Jiang, Y., and Li, Z. (2021). Molecular Targeted Agent and Immune Checkpoint Inhibitor Co-Loaded Thermosensitive Hydrogel for Synergistic Therapy of Rectal Cancer. *Front. Pharmacol.* 12, 671611. doi:10.3389/fphar.2021.671611

Zhang, J., Hu, J., Li, W., Zhang, C., Su, P., Wang, Y., et al. (2021). Rapamycin Antagonizes BCRP-Mediated Drug Resistance through the PI3K/Akt/mTOR Signaling Pathway in mPRα-Positive Breast Cancer. *Front. Oncol.* 11, 608570. doi:10.3389/fonc.2021.608570

Zhang, W., and Jiang, K. W. (2020). Role of Gut Microbiota in Carcinogenesis and Treatment for Colorectal Cancer. *Zhonghua Wei Chang Wai Ke Za Zhi* 23 (5), 516–520. doi:10.3389/fphar.2021.671611

Zhao, H., Wei, R., Wang, L., Tian, Q., Tao, M., Ke, J., et al. (2014). Activation of Glucagon-like Peptide-1 Receptor Inhibits Growth and Promotes Apoptosis of Human Pancreatic Cancer Cells in a cAMP-dependent Manner. *Am. J. Physiol. Endocrinol. Metab.* 306 (12), E1431–E1441. doi:10.1152/ajpendo.00017.2014

Zhou, X., Wang, L., Xiao, J., Sun, J., Yu, L., Zhang, H., et al. (2022). Alcohol Consumption, DNA Methylation and Colorectal Cancer Risk: Results from Pooled Cohort Studies and Mendelian Randomization Analysis. *Int. J. Cancer* 1, 25. doi:10.1002/ijc.33945

Conflict of Interest: The authors declare that the research was conducted in the absence of any commercial or financial relationships that could be construed as a potential conflict of interest. Authors GT, TP, YC, LS, HD, YX, and ZZ were employed by Hunan Evidence-based Biotechnology Co., Ltd.

Publisher's Note: All claims expressed in this article are solely those of the authors and do not necessarily represent those of their affiliated organizations, or those of the publisher, the editors, and the reviewers. Any product that may be evaluated in this article, or claim that may be made by its manufacturer, is not guaranteed or endorsed by the publisher.

Frontiers in Pharmacology

Explores the interactions between chemicals and living beings

The most cited journal in its field, which advances access to pharmacological discoveries to prevent and treat human disease.

Discover the latest Research Topics

See more →

Frontiers

Avenue du Tribunal-Fédéral 34
1005 Lausanne, Switzerland
frontiersin.org

Contact us

+41 (0)21 510 17 00
frontiersin.org/about/contact